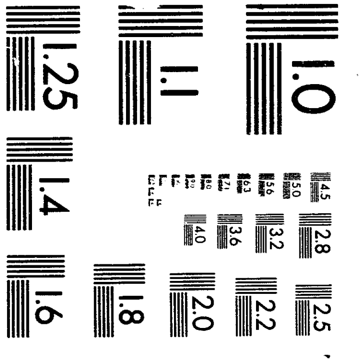
1.0
1.1
1.25
1.4
1.6
1.8
2.0
2.2
2.5
2.8
3.2
3.6
4.0
4.5
5.0
5.6

1 of 3

LA-12663-T
Thesis

UC-410
Issued: November 1993

Reaction $\pi N \rightarrow \pi\pi N$ Near Threshold

Emil Frlež*

*Graduate Research Assistant at Los Alamos Group MP-9.
University of Virginia, Department of Physics,
Charlottesville, VA 22901-2458.

Los Alamos
NATIONAL LABORATORY
Los Alamos, New Mexico 87545

Acknowledgements

A list of all the people, my colleagues and collaborators, faculty and staff at UVA and researchers, engineers and technicians at LAMPF who made this experiment possible and contributed in minor or major way to this thesis is a very long list indeed.

My gratitude, personal and professional, goes first and foremost to my research advisor and thesis supervisor Dinko Počanić. From the first weeks he conceived the idea for this measurement, through the design, development and building of the apparatus, feasibility run, test run and data acquisition runs, and replay, data analysis and physical interpretation, Dinko was the major driving force making sure that the final results lived up to the goals outlined in the original experiment proposal.

Our principal LAMPF collaborator Jim Knudson met with the members of the "advance" E1179 team at the LAMPF site for three consecutive years and worked with us months ahead of the allotted beam time to insure that with first droplet of the useful beam the cave would be ready and the equipment would be up and running. As the π^0 spectrometer custodian he was my last resort to ask for help with tough software bugs and occasional "unexplainable" behavior of the spectrometer hardware and electronics (and a few times the spectrometer misbehaved in the wee morning hours).

The important solutions concerning design of the charged particle range counters that had to be tightly packed were worked out by Rick Marshall. During the (always to short) change-over period in the experiment cave Rick was able to troubleshot all the connections, reconfigure the patch-panels, redesign the bases, defeat the reflections, to arrive at the best signals coming from plastic scintillators. He was less successful in trying to teach me to expertly use the soldering iron, though.

There is a place in a first logbook that says: "Ketevi gives blood for the experiment." My comrade Ketevi Assamagan would always work with such a dedication on assigned tasks that he would seldom notice that he cut himself! That's the spirit, Ketevi! His name is on every other page in all seven E1179 logbooks.

A few crucial insights into better understanding of the background sources were made by Cole Smith. In particular, Cole was the first one to clearly identify target-full backgrounds coming from two-step elastic scattering—charge exchange processes and purely elastic triggers that would subsequently charge exchange in the plastic detector material itself. His help with electronics setup and long and painstaking timing adjustments of the ADC gates and TDC signals is also appreciated.

Ralph Minehart developed the details of mechanical and optical coupling of scintillators to the light guides and phototubes and lead the group the assembled and light-proofed all the hodoscopes and thick plastic counters.

Kara Keeter joined our group when this experiment was in its early stages and became the reliable member who struggled successfully through day-shifts and night-shifts till the end. She worked out with me the design of the detector stand for the feasibility run. Kara's interest in the activation methods certainly improved our pion flux determination.

Bruce King initiated me to the LAMPF facility in the summer of 1990. Learning the basic experimental techniques during his thesis experiment I first appreciated what an impressive instrument the π^0 spectrometer is.

The portions of the data acquisition code were written and debugged by Gail Dodge. Her help in the LEP cave with π^0 spectrometer is particularly appreciated.

I was fortunate that Jian-Ping Chen was able to find the time between running the other experiments he was on and helped us in the set-up stages of both 1991 test run as well as 1992 data collection run.

In several weeks preceding the 1991 test run Cvjetan Jakovljević gave me a hand in replacing the π^0 spectrometer dead and "hot" hybrids. Together we increased the π^0 detection efficiency by 10%. He was also a valuable member of our data acquisition night-shift crew.

Stanly Hanna and Bill Cummings made contributions when and where they counted most: in the cave and the counting house when beam was on.

The LAMPF electronics pool people kept up with us, and tolerated my everyday requests for additional ADCs, TDCs, amplifiers, discriminators, delay boxes, cameras, and all that, even when I emptied all of their shelves.

Martin Cooper of the MEGA collaboration, lent us thousands of feet of high voltage and high quality signal cables. I wonder what we would do without his cables. Two dozen HV cables came from the SCRUNCHER setup, courtesy of John O'Donnell.

Ron Harrison of MP-8 participated in the design and supervised the construction of the charged particle detector stand, working always under tight time constraints. His group surveyed the detector positions relative to target using the "AIMS" computerized theodolite system.

I would like to thank the staff of LAMPF groups MP-7, MP-8 and HS-5 for very strong technical support. Without their skills, sharp eyes, and often their strong muscles this experiment would not have been possible. The resourcefulness of Clyde Kain I will especially remember.

I am particularly indebted to Bob Garcia who was responsible for the liquid hydrogen

target design and construction. Some of his and Chris Romero's technical drawings of the E1179 cave layout, liquid hydrogen target and the target stand are displayed in this thesis.

I gratefully acknowledge the help provided by Larry Suddarth, Mark Lesko and Andy Wall, of UVa in assembling the charged particle detector arm. Our colleague Todd Averett, of UVa helped us through the last weeks of routine shift-taking, when finally, everything was running fine, but all the rest of us were running exhausted.

Gilbert Backers collaborated as an undergraduate in the calibration of the charge particle prototype detectors. The results of the measurements have been incorporated in the Appendix C.

I thank Anatoly Bolokhov of Sankt Petersburg Nuclear Physics Institute for the helpful discussion of chiral Lagrangians and the model-independent extraction of $\pi\pi$ scattering amplitudes.

Jim Lowe kindly provided me with the data summary tapes of his Brookhaven E857 experiment. I was excited to start the analysis of his high-quality high-statistics data set to supplement our I=2 isospin channel. The potential results are touched upon in the conclusion of this thesis.

Thanks to Joe Mitchell for first demonstrating to me the `GEANT3` detector simulation package and showing me the flexibility of CERN's Physics Analysis Workstation software. The `PAW` data analysis tools greatly facilitated the implementation of the complicated set of particle identification and kinematical cuts that needed to be refined iteratively. My thanks also go to the authors of the product for increasing my productivity many times.

Pat Welch proved to be real-life computer wizard—not one question I was constantly bombarding him was left unanswered. Not bad, TPW.

When Pat left for MIT, Bryan Wright was the one I started (and never stopped since) bugging with my programming difficulties. Bryan introduced me to the applications of his `OPTICS` code for light propagation in a variety of counter shapes and provided the source code (with occasional custom-made enhancements!). The experimentally measured energy resolutions proved that a few months investment in simulating the light collection properties of possible detector geometries paid off.

A day-to-day use of the departmental Vax-cluster and peripheral devices was greatly facilitated by Pat Walsh. I just hope I did not ask Pat one question too many.

Thanks to Jim Shea for helping me when I got lost in the physics library and the interlibrary loans transactions.

The members of my thesis committee deserve special thanks for many helpful suggestions and excellent advice about how to improve the presentation in this thesis and straighten out my (I hope only occasionally) broken English.

The experiment was supported by the U. S. National Science foundation and the Department of Energy.

Table of Contents

List of Figures

List of Tables

Reaction $\pi N \to \pi\pi N$ Near Threshold

by

Emil Frlež

ABSTRACT

The LAMPF E1179 experiment used the π^0 spectrometer and an array of charged particle range counters to detect and record $\pi^+\pi^0$, $\pi^0 p$, and $\pi^+\pi^0 p$ coincidences following the reaction $\pi^+ p \to \pi^0\pi^+ p$ near threshold. The total cross sections for single pion production were measured at the incident pion kinetic energies 190, 200, 220, 240, and 260 MeV. Absolute normalizations were fixed by measuring $\pi^+ p$ elastic scattering at 260 MeV. A detailed analysis of the π^0 detection efficiency was performed using cosmic ray calibrations and pion single charge exchange measurements with a 30 MeV π^- beam. All published data on $\pi N \to \pi\pi N$, including our results, are simultaneously fitted to yield a common chiral symmetry breaking parameter $\xi = -0.25 \pm 0.10$. The threshold matrix element $|a_0(\pi^0\pi^+ p)|$ determined by linear extrapolation yields the value of the s-wave isospin-2 $\pi\pi$ scattering length $\alpha_0^2(\pi\pi) = -0.041 \pm 0.003\ m_\pi^{-1}$, within the framework of soft-pion theory.

Chapter I: Introduction

A. Physical Motivation

Understanding the nature of the strong interaction has long been at the heart of research in nuclear and elementary particle physics. As a particularly simple and common strong interaction process, pion-pion scattering has been vigorously investigated for the past three decades. Quantities characterising the $\pi\pi$ interaction are as important as the pion-nucleon interaction constants.

The motivation for study of the $\pi\pi$ interaction was provided by Chew and Low [Che-59]. Pion targets or intersecting pion beams do not exist: the pion is a short-lived unstable particle ($\tau_{\pi^\pm} = 2.60 \times 10^{-8}$ s). Chew and Low proposed to use the differential cross sections for the reaction $\pi N \longrightarrow \pi\pi N$ to extract $\pi\pi$ cross sections indirectly. Their method involves extrapolation of measured data relying on the assumption that only the one-pion exchange diagram plays an important role near the pion pole. The pedestrian derivation is given in Källen's monograph [Käl-64].

A number of other processes with pions in the final state such as the annihilation and decay processes $\bar{p}p \longrightarrow 2\pi$, $e^+e^- \longrightarrow 2\pi$, $K \longrightarrow 3\pi$, $K \longrightarrow \pi\pi e\nu_e$, $K \longrightarrow \pi\pi\mu\nu_\mu$ were used to extract information on the $\pi\pi$ interaction.

The early theoretical approaches to the subject were formulated within the framework of partially conserved axial-vector current (PCAC) and current algebra (CA). Nambu and Lurié [Nam-62] were the first to derive the matrix element of a light pseudoscalar meson in the kinematic limit of zero four-momentum by direct application of commutation and conservation relations of γ_5-invariant systems.

Weinberg [Wei-66a] proceeded to show how to calculate the matrix elements for the emission of any number of "soft" pions in an arbitrary process. In a subsequent paper [Wei-66b] he derived the scattering length for a pion scattering on any target particle, and extended that result to the more difficult case of $\pi\pi$ scattering. The emphasis was moved away from PCAC and CA to chiral symmetry when Weinberg [Wei-66c] constructed a chiral Lagrangian which in lowest order of perturbation theory reproduced the results of current algebra for soft-pion interactions. Weinberg's derivation started from the σ-model of Gell-Man and Lévy [Gel-60] in which a pion is in a chiral quartet with a 0^+ isoscalar σ. A space-time dependent chiral rotation transformed the $(\boldsymbol{\pi}, \sigma)$ quartet into $(0, \sigma)$ everywhere and the pion field was reintroduced as the chiral rotation "angle". Although the resulting Lagrangian had unfamiliar and complicated non-linear structure, the pion couplings were all derivative interactions suppressing the incalculable graphs in which soft pions are emitted from internal lines of a hard-particle process.

Weinberg's work provided the basis for study of alternative realizations of chiral symmetry breaking. Schwinger's Lagrangian [Sch-67] contained a chiral symmetry breaking term which implied that the divergence of the axial vector current is proportional to the physical pion field. Chang and Gürsey [Cha-67] proposed a systematic and unified treatment of the effective Lagrangians based on the partially chiral-invariant nonlinear theory of π-N interactions advanced in a series of papers by Gürsey [Gür-60a] [Gür-60b] [Gür-61]. As an example of the general model they explicitly discussed three special cases that all agree with Weinberg's variant up to second order in the π-N pseudovector coupling constant. Although equivalent overall, the three schemes gave different predictions for the ratio of isospin 0 and 2 s-wave $\pi\pi$ scattering length.

Building on the ideas of Schwinger, Weinberg [Wei-68] worked out a general theory of non-linear realizations of chiral $\mathrm{SU_L(2)}\times\mathrm{SU(2)_R}$. His framework was soon extended to arbitrary groups in elegant papers of Callan, Coleman, Wess, and Zumino [Col-68] [Cal-68]. The methods of current algebra and the departures from chiral symmetry are extensively reviewed in [Lee-72], [Pag-75], [Sca-81], and [Gas-81].

In terms of $\pi\pi$ scattering models these developments were put in perspective by Olsson and Turner [Ols-68] [Ols-69] who showed that the different approaches discussed above can be distinguished in terms of a single chiral symmetry breaking parameter ξ in the effective Lagrangian. The pion production cross sections in $\pi N \rightarrow \pi\pi N$ reactions near threshold and $\pi\pi$ scattering lengths were parameterized as a function of ξ, f_π, the pion decay constant, the π-N coupling constant $G_{NN\pi}$, and f_A/f_V, the ratio of vector to axial vector form factor of the nucleon. Consequently, all existing near-threshold $\pi N \rightarrow \pi\pi N$ data have been used to extract parameter ξ from the measured total cross sections. For such an approach to make sense, of course, precise values of f_π, $G_{NN\pi}$, are f_A/f_V are imperative.

In a recent review [Wei-79] Weinberg summarized the above work and concluded that phenomenological Lagrangians can be used not only to reproduce the soft-pion results of current algebra but also to justify them, in essence doing the much easier work of "current algebra without current algebra". Showing how easily a theoretician can calculate the leading order corrections to the tree amplitudes he demonstrated that there was not a great for refinements in the theory of $\pi\pi$ scattering. Subsequent theoretical works considered corrections to the soft-pion and kaon theorems in processes like $\pi N \rightarrow \pi\pi N$, $K \rightarrow 2\pi$, $K \rightarrow 3\pi$, $K \rightarrow \pi\mu\nu$, $\eta \rightarrow 3\pi$.

The recent microscopic (initially non-relativistic) models of Jäkel and collaborators [Jäk-90] apply to the $(\pi, 2\pi)$ reactions on both the nucleon and nuclei. The extensions to the model [Jäk-91] introduce leading relativistic corrections to the static treatment of baryons and feature $\pi\pi$ interactions in the initial and final states via σ- and ρ- meson exchange. These results were tested experimentally in a very limited way by examining the sensitivity of exclusive $\pi\pi$ angular distributions to calculated corrections. Other theoretical work dedicated to pion-induced single pion production on nuclei include [Roc-75], [Roc-83] [Bha-84], [Eis-70], [Eis-80], and [Coh-83a], [Coh-83b]. Two comparisons with kinematically complete experiments are available [Gri-89] [Cam-93].

From the more fundamental point of view, these Lagrangians are only phenomenological. When calculating graphs to higher and higher order in the energies of interacting particles, more and more unknown parameters are encountered. The free parameters in the phenomenological expressions should be fixed in a fundamental quantum field theory of strong interactions. Today it is accepted that quantum chromodynamics (QCD), a renormalizable gauge theory, is that underlying theory. It exhibits the property called "asymptotic freedom": strong effective couplings go to zero as the momentum transfers increase and the characteristic distances of the phenomena decrease. The QCD predictions in the high-energy regime carried out by familiar perturbative methods are so far in agreement with experiment.

In the low and medium energy regime, the program proposed by Weinberg was carried out with considerable success. The chiral symmetry as a fundamental symmetry of QCD in the limit of zero quark masses was applied to the "hybrid" systems of quarks and pions [Mei-88]. The symmetry-breaking terms in the Lagrangian account for the small quark masses and the small ratio between the mass of the pion to masses of heavier mesons.

The experimental data hinted that the Born approximation to the chiral Lagrangian that corresponds to the p^2 order in the expansion of the amplitudes in powers of the momenta of interacting particles is already inadequate [Bel-87].

Gasser and Leutwyler [Gas-84] used the QCD Lagrangian to calculate the Green's functions associated with quark currents. The Ward identities of chiral symmetry determined the expansions up to and including terms of order p^4. The low-energy representation constrained the threshold parameters and low-energy phase shifts. The differences between soft-pion approximation and one-loop perturbation expansion is expressed in terms of the scalar radius of pion.

An alternative approach [Ser-79] [Vol-78] corrects the Born approximation by using the results of dispersion methods which take into account the unitarity and analyticity of strong interaction amplitudes to extrapolate the theory into the region of higher energies.

A third method expands the minimal Lagrangian by introducing additional derivative terms constrained by the requirements of chiral transformations and reliably measured static properties of a baryon [Bel-87].

Another calculation of the $\pi\pi$ scattering lengths is made by Ivanov and Troitskaya [Iva-86] in the framework of the model of dominance by quark loop anomalies. Jacob and Scadron [Jac-82] argued that the Weinberg soft-pion results could be significantly improved by simply including the background contribution of the $f_0(975)$ isobar resonance. Both calculations increase Weinberg's scattering lengths by 30%.

All of the above mentioned phenomenological and QCD-inspired schemes claim proofs from the existing experimental data. But a review of the available $\pi N \rightarrow \pi\pi N$ measurements in the next section shows that even the total cross sections in the near threshold region are scarce and often inconsistent.

From the point of view of a modern experimentalist a framework for extraction of $\pi\pi$ amplitudes from the $\pi N \rightarrow \pi\pi N$ reaction in a model-independent way is most appealing. In the series papers Bolokhov, Vereshchagin and Sherman (BVS) provided just such an approximation that describes all the low-energy characteristics of the $\pi\pi$ interaction up to D-waves. The BVS parametrization is given in a Appendix C.

The last section of this introduction describes the E1179 proposal, the feasibility and test run that proved the soundness of the experimental method and the accomplished activities and timetable of data acquisition runs. The more formal theoretical discussions of the topics outlined on these pages in the historical order are relegated to the appendices.

Derivation of phenomenological chiral Lagrangian preceded by short exposition of the σ model is given in Appendix D.

B. Previous Near-Threshold $\pi N \rightarrow \pi\pi N$ Measurements

Five charge channels of the $\pi N \rightarrow \pi\pi N$ reaction are accessible to measurement:

$$\pi^- p \rightarrow \pi^- \pi^+ n \tag{1.1}$$

$$\pi^- p \rightarrow \pi^- \pi^0 p \tag{1.2}$$

$$\pi^- p \rightarrow \pi^0 \pi^0 n \tag{1.3}$$

$$\pi^+ p \rightarrow \pi^+ \pi^+ n \tag{1.4}$$

$$\pi^+ p \rightarrow \pi^+ \pi^0 p \tag{1.5}$$

While data on all channels listed above exist, in most cases they do not possess the statistics and accuracy necessary for a model-independent analysis or even a simple threshold extrapolation. In the region of interest near the threshold (T_{π} ~170 MeV) measurements become exceedingly difficult due to small cross section ($\sim 1\mu b$) and background processes five orders of magnitude higher. Three measurement techniques have been used in these studies: (a) photographic emulsion or bubble chamber tracks, (b) single-arm detection of the produced pion, and (c) coincident detection of final state particles.

An exhaustive search of literature shows that the available data base today would consist of 121 data points below the center-of-momentum kinetic energy 250 MeV. The $\pi + \pi^-$ channel is most extensivwely studied—measurements exist at 43 different energies below $T_{\rm inc}$ =454 MeV, but a few data points are not consistent with the majority.

The reaction (1.2) is measured at 18 different energies below 430 MeV.

26 measurements exist in the $\pi^0\pi^0$ channel below 454 MeV. The largest data set—measurements of Lowe should be corrected for a few percent error in phase space weights calculation that alters apparatus acceptance and, therefore total cross sections [Frl-91]. In addition, Makarov *et al.* [Mak-73] and Bolokhov [Bol-93] point out that the early data [Che-70], [Bar-64], [Chi-67] are incorrect.

The $\pi^+\pi^+$ channel is sensitive exclusively to the $I_{\pi\pi}$ = 1 isospin amplitude. Measurements exist at 20 energies below 550 MeV. Two recent experiments discussed below, comprising 16 data points, contradict each other. If older measurements are included, the extracted reduced amplitudes do not appear to be linear in the 100 MeV region above the threshold.

The $\pi^+\pi^0$ is covered by only 6 measurements bellow 550 MeV. Four data points are deduced from emulsion and bubble chamber photographs made in the mid-1960's, comprising only 9 events total with considerable (~20-50 MeV) incident energy uncertainties. A fifth point comes from parasitic trigger in a pion-proton bremsstrahlung experiment [Sob-75], and the last one is preliminary number published in conference proceedings [Ker-91b].

Within the last five years several groups have proposed and completed the experiments that tried to fill gaps and resolve ambiguities in old data sets. The OMICRON collaboration working at the CERN synchrocyclotron supplemented the existing data on four channels with at least one charged particle in the final state with full kinematics measurements resulting in about fifty coincidenct events at 8-10 energies near threshold. Their measurements relied on a multi-arm magnetic spectrometer in which the incident pion and two secondary charged particles were detected. Their apparatus and its performance are described in detail in references [Ker-83], [Ker-86]. The cross sections and soft pion analysis are reported in [Ker-89a], [Ker-89b], [Ker-90], and [Ker91a]. The chiral symmetry breaking parameter describing the excitation function of $\pi^+p \rightarrow \pi^+\pi^+n$ was claimed to be incompatible with the other channels. The deviations from the phase space shapes in the measured angular and invariant mass distributions affecting the apparatus acceptance were not addressed. A more detailed study of the $\pi^+\pi^-$ system at small invariant masses was published in a separate paper [Ker-91]. Ortner *et al.* [Ort-93] recently criticized OMICRON's total cross sections which are based on a poorly understood extrapolation of in-plane data to the unobserved regions of the phase space.

The Brookhaven experiment E857 is the first measurement of $\pi^-p \to \pi^0\pi^0n$ reaction all the way down to threshold [Low-91a], [Low-91b]. The LAMPF "crystal box" calorimeter [Wil-88] was used to detect ~10000 coincidences at 12 different energies. The disappearance of signal below the threshold was confirmed in an independent measurement. The extracted values of scattering lengths were consistent with chiral symmetry broken by the Weinberg $\pi\pi$ interaction and the effects of the $f_0(975)$ scalar meson. The coincident analysis was limited to a presentation of angular and invariant mass distributions and their (dis)agreement with the phase space distributions.

The measurement of $\pi^+p \to \pi^+\pi^+n$ by Sevior and collaborators at TRIUMF [Sev-91a], [Sev-91b], employed a novel technique. The stopped $\pi^+\pi^+$ pairs were detected in an active plastic target while a large-volume scintillator bar array was positioned downstream to capture the neutrons. The pion beam was swept away from the bars by a clearing magnet placed between the target and the array. Data were accumulated for four energies close to threshold and the below-threshold run was used to constrain the backgrounds. A similar setup was used to carry out the runs with a π^- beam; the analysis is in progress [Gal-92].

Ortner, Hofmann *et al.* [Ort-90a] [Jäk-90] collected kinematically complete $\pi^+\pi^-n$ data in the accesable part of the phase space at PSI. The two-part detector arrangement consisted of a magnetic spectrometer followed by a scintillator stack for π^+ detection and three wire chambers enabling track reconstruction of the coincident π^- ejectile. About 3.5×10^4 events were recorded yielding triple differential cross sections and angular distributions, but problems with acceptance and efficiency calculations prevented the extraction of total cross sections. Attempts were made to describe the data qualitatively using the microscopic theory of Jäckel that describes only the pion as a relativistic particle and uses the nonrelativistic, static limit for the nucleon [Jäc-90].

Experiment TRIUMF-624 scheduled to run in the summer of 1993 [Gal-92] will attempt to measure all $\pi\pi N$ channels with charged particle ejectiles using the CHAOS detector.

Two papers analyze large portions of the available data base. The work of Manley [84] collects all data available up to 1984 and extracts the scattering lengths discarding some mutually inconsistent points. The more recent study of Burkhart and Lowe [Bur-91] encompasses the majority of new experiments (33 data points total) and indicates that the pion-pion system at low energies can be described by the Weinberg interaction modified by the contribution of $f_0(975)$ scalar meson.

The only existing exclusive measurements of near-threshold $(\pi, 2\pi)$ reaction on nuclei are one of Grion *et al.* (^{16}O 280 at MeV, [Gri-89]) and one by Camerini *et al.* (^{2}H, ^{4}He, ^{16}O, ^{208}Pb at 280 MeV, [Cam-93]). The four-fold-differential cross sections and invariant dipion mass spectra were reproduced qualitatively when a pion dispersion relation in the nuclear medium was considered.

For completeness, it should be mentioned that the K_{e4} decay measurements can in principle yield the value of a_0^0 scattering length with comparable accuracy. The most recent and precise experimental study involves 30000 decays $K \rightarrow \pi^+\pi^-e^+\nu_e$; it was performed by Rosselet *et al.* at the CERN proton synchrotron [Ros-77].

Two sets of tables in the Appendix A itemize all the published measurements. The first set of tables (A1-A5) summarizes the results of the experiments in terms of reported total cross sections. The Tables A6-A10 contain the reduced threshold amplitudes calculated from these cross sections using common values for the parameters f_π and f_A/f_V. The energy dependence of total cross sections and isospin amplitudes are shown on Figures A1-A10.

C. LAMPF Experiment E1179: A Synopsis

The experiment E1179 at LAMPF was proposed in August 1989 with an objective of measuring the total and differential cross sections of the reaction $\pi^+p \rightarrow \pi^+\pi^0p$ near threshold [Poč-89]. Initially, the intention was to cover the relatively narrow energy range 220-260 MeV (threshold is at 164.8 MeV). with the 10-30% statistical accuracy in the exclusive cross section bins, and systematic uncertainties of ~10%. The University of Virginia group provided the nucleus of the collaboration and was joined by collaborators from Stanford University and LAMPF.

A feasibility run was carried out in the LEP channel in October of 1990 using an existing liquid hydrogen target [Poč-91]. The LAMPF π^0 spectrometer [Bae-81] was used to detect neutral pions produced in π^+p collisions, while charged ejectiles were detected in an array of 8 existing ΔE-E telescope counters made of plastic scintillator, previously used at LAMPF for π^0p coincident measurements [Gil-86].

The 30 MeV π^- beam was used for calibrations of the π^0 spectrometer efficiency. The weakly focusing tune was successfully achieved for the LEP beam-line with low divergence (12 mrad horizontal and vertical), minimal beam spot (9 mm FWHM), small momentum spread (3% $\Delta p/p$) and pion flux of $\geq 10^6$ π^- s^{-1}. That facilitated shielding design (two encompassing

30 cm thick lead walls) and resulted in very quiet operation of the π^0 spectrometer with the target empty to target full π^0's yield ratio $\leq 3\%$. The narrow 2 mm proton beam-tune with the energy of 70 MeV was developed for the liquid hydrogen target scan to ascertain the correct location of the target and double-check its thickness profiles for elastically scattered charged particles.

Table 1.1 E1179: 1990 approved and completed beam time activities. A shift is an eight hour long interval. The average run was three hours long and corresponded to $\sim 10^{10}$ incident "live" π^-'s at 30 MeV, and $\sim 10^{11}$ π^+'s at 160-260 MeV, respectively.

Date (1990)	Activity—Energy (MeV)	Number of shifts/runs
8/1-8/15	CP and π^0 detector calibrations	30/na
8/15-9/15	detector stand construction	62/na
9/15-9/27	detector assembly and cabling	24/na
9/27-10/4	beam tuning and activations	21/na
10/4-10/8	efficiency calibration, 30 MeV π^-	$2\frac{1}{3}$/15
10/12	target scan, 30 MeV p	1/2
10/15-10/17	data acquisition, 260 MeV π^+	$2\frac{1}{2}$/12

The important study of the π^0 spectrometer acceptance for the background SCX sources was done by measuring the yields from ^{12}C target at six different positions along the beam axis. The results of that measurement dictated the placement of the future upstream and downstream windows and the over-all design of the new scattering chamber.

Data for single charge exchange on CH_2, ^{12}C, LH_2 and air (no target) have been collected and all raw π^0 hardware triggers were written to tape.

The data acquisition beam tune at 260 MeV was characterised by small spot size (11 mm FWHM), moderate divergences (30 mrad horizontal 2 mrad vertical) and high π^+ flux ($\geq 10^7$ π^+ s^{-1}). That arrangement was in place for both the runs with the liquid hydrogen and carbon target. The inclusive and raw coincident hardware triggers as well as the special prescaled charged particle singles were taped.

The preliminary exclusive cross section were extracted from 120 detected coincident event in the replay analysis. The value $\sigma_t = 31 \pm 4 \pm 5$ μb was reported in [Poč-91].

The relying on the results of the test run the new set of the 14 charged particle detectors was designed specially for the 1991 experiment. The dimensions, shapes, materials and treatments of optical surfaces have been designed using Monte Carlo codes developed at

Table 1.2 E1179: 1991 approved and completed beam time activities.

Date (1991)	Activity—Energy (MeV)	Number of shifts/runs
7/2-7/30	detector assembly and cabling	44/na
7/15-7/30	CP and π^0 detectors calibration	18/na
7/31-8/4	beam tuning and activations	21/na
8/5-8/12	efficiency calibration, 30 MeV π^-	$4\frac{3}{4}/26$
8/20,21	data acquisition, 160 MeV π^+	$1\frac{1}{2}/11$
8/19	data acquisition, 180 MeV π^+	1/6
8/18	data acquisition, 190 MeV π^+	$\frac{3}{4}/7$
8/17	data acquisition, 200 MeV π^+	$\frac{3}{4}/7$
8/16	data acquisition, 220 MeV π^+	$\frac{1}{3}/4$
8/15-8/18,23	data acquisition, 240 MeV π^+	1/8
8/13-8/15,21,23	data acquisition, 260 MeV π^+	$1\frac{3}{4}/15$

the University of Virginia. The components were manufactured at the UVa machine shop and the College of William and Mary and assembled at LAMPF site. The newly built array doubled the solid angle coverage for the charged ejectiles in $\pi^+p \rightarrow \pi^+\pi^0p$ reaction as compared with the old setup, introducing 66 different hodoscope angular directions. The individual counter shapes were optimized for dense packing arrangement and proved to have better energy resolution ($\Delta E/E \leq 5\%$ at 50 MeV). A customized detector stand was designed and build at LAMPF easily allowing the detector positioning precision better than 0.1°.

The cylindrical liquid hydrogen target with 3 mil thick mylar walls and the eccentrically mounted aluminum scattering chamber with 10 mil thick mylar windows were constructed at the LAMPF cryogenic shop.

The MWPC spectrometer readout electronics was tested with cosmic ray triggers in May 1991 and all PCOS hybrids reporting hot and missing wires were replaced. The decision was then made to supplement in-beam π^0 spectrometer measurements with the cosmics ray calibrations. Using various triggers for one spectrometer arm at a time the intrinsic MWPC's efficiencies, scintillator plane efficiencies, and potential backsplashes were monitored. The study of replayed calibration runs yielded the decomposition of π^0 detection efficiency that entered as the largest systematic uncertainty. Complete set of π^0 cosmics calibration runs making use of four different triggers were taped preceding both 1991 and 1992 data acquisition runs.

The 1991 LAMPF accelerator operations ended a month earlier than planned to allow the preparations for the Department of Energy audit of the laboratory. That change cut 10 days from the experiment running schedule and lead to the approval of the additional beam time request for 1992. The good quality coincidence data were obtained at 260 MeV as well as below the threshold at 160 MeV.

Table 1.3 E1179: 1992 approved and completed beam time activities.

Date (1992)	Activity—Energy (MeV)	Number of shifts/runs
5/6-6/28	detector assembly and cabling	44/na
5/28-6/5	CP and π^0 detectors calibration	18/na
6/6-6/13	beam tuning and activations	21/na
6/12-6/14, 6/20	efficiency calibration, 30 MeV π^-	3/25
6/6/16	target calibration, 30 MeV p	$\frac{1}{2}$/2
6/16-6/19, 7/8,9	data acquisition, 160 MeV π^+	$3\frac{1}{4}$/14
7/3,47/9-7/11	data acquisition, 190 MeV π^+	$1\frac{3}{4}$/18
6/22,23	data acquisition, 200 MeV π^+	2/17
6/21,22, 6/23-6/25	data acquisition, 220 MeV π^+	$2\frac{1}{2}$/20
6/21, 6/25,26	data acquisition, 240 MeV π^+	$2\frac{1}{2}$/16
6/26-6/28, 7/4-7/8	data acquisition, 260 MeV π^+	18/45

The experiment was run in a routine manner in the summer of 1992 providing besides the repeated calibrations of the inclusive and exclusive arm the coincident measurements at five different energies near threshold as well as below the threshold. The completely redesigned target with 2 mil thick copper walls operated flawlessly increasing the inclusive π^0's yields by ~30% with respect to 1991 design. All the checks for the beam contamination, target position and thickness, detector efficiencies and the background sources developed in the previous runs have been extended to all studied energies.

The completed activities in 1990, 1991, and 1992 runs, closely corresponding to the requested allocation of the beam time, are summarized in the Tables 1.1-1.3.

The partial results presented here have been reported in preliminary form in [Poč-91a,b]. The more complete letter discussing the extracted total cross sections has been submitted to *Physical Review Letters*.

Chapter II: Experimental Method

A. LAMPF Linac

The Los Alamos Meson Physics Facility—LAMPF was and still currently is the highest intensity proton accelerator of 0.5 to 1.0 GeV serving the world nuclear and particle physics community. As a prime example of a "meson factory" its primary proton beam is used to deliver a great variety of intense secondary nucleon, pion, muon, gamma and neutrino beams. The most complete collection of commented reprints documenting the history, accelerator characteristics with major instrumentation and present and future physics applications of LAMPF as well as other meson facilities is a recent monograph by Ericson, Hughes and Nagle [Eri-91]. The following paragraphs are limited to the brief description of the LAMPF laboratory relevant to this thesis experiment. In addition to the articles in [Eri-90] the exposition is understandably drawing from the LAMPF *Users Handbook* [How-74].

The high energy portion of the LAMPF machine is a proton linear accelerator that delivers high average proton current of 100 μA to 1 mA at an energy of 800 MeV. It has all the advantages of a linac with high current capability, variable energy (212-800 MeV) and small energy spread ($\leq$0.3% FWHM), good beam quality, superior extraction efficiency ($\geq$99%), low loss of internal beam ($\leq$1%), and moderate duty factor ($\leq$10%) [Ros-69].

Three injectors consisting of a 50-mA ion source, a high-voltage dc supply and Cockcroft-Walton column accept 750 keV H^+ and H^- ions simultaneously. The $H^\pm$ beams from the injectors are passed into a 100 MeV drift-tube linac through a bunching system. The output ions are injected into a linac comprised of side-coupled *rf* cavities operating at 201.25 MHz that increase the continuously variable particle energy from 100 MeV up to a maximum of 800 MeV. The cavities are grouped together in four series known as a tanks and operated in a non-conventional highly stabilizing $\pi/2$ mode in which the field alternates not only in adjacent cells but additional resonant posts contain no field [Nag-67]. The overall layout of the main accelerator is illustrated in Figure 2.1. The proton beam consisting of $H^\pm$ ions enters the experimental areas after first traversing a beam switchyard with a variety of redirecting and focusing magnets. The main H^+ beam at full intensity is transported to the experimental area A where it traverses two production targets known as A-1 and A-2 providing five secondary pion beams (Figure 2. 4). These beams are guided to the shielded areas for experiments through the customized meson channels with the permanently assembled arrays of bending and focusing magnets and slit systems. The target cell A-1 made of 3 cm thick graphite (density 1.73 g/cm^3) delivers a good momentum resolution pion beam to the low energy pion channel (LEP) at 5-10 mm FWHM proton spot size transmitting 92% of primary protons.

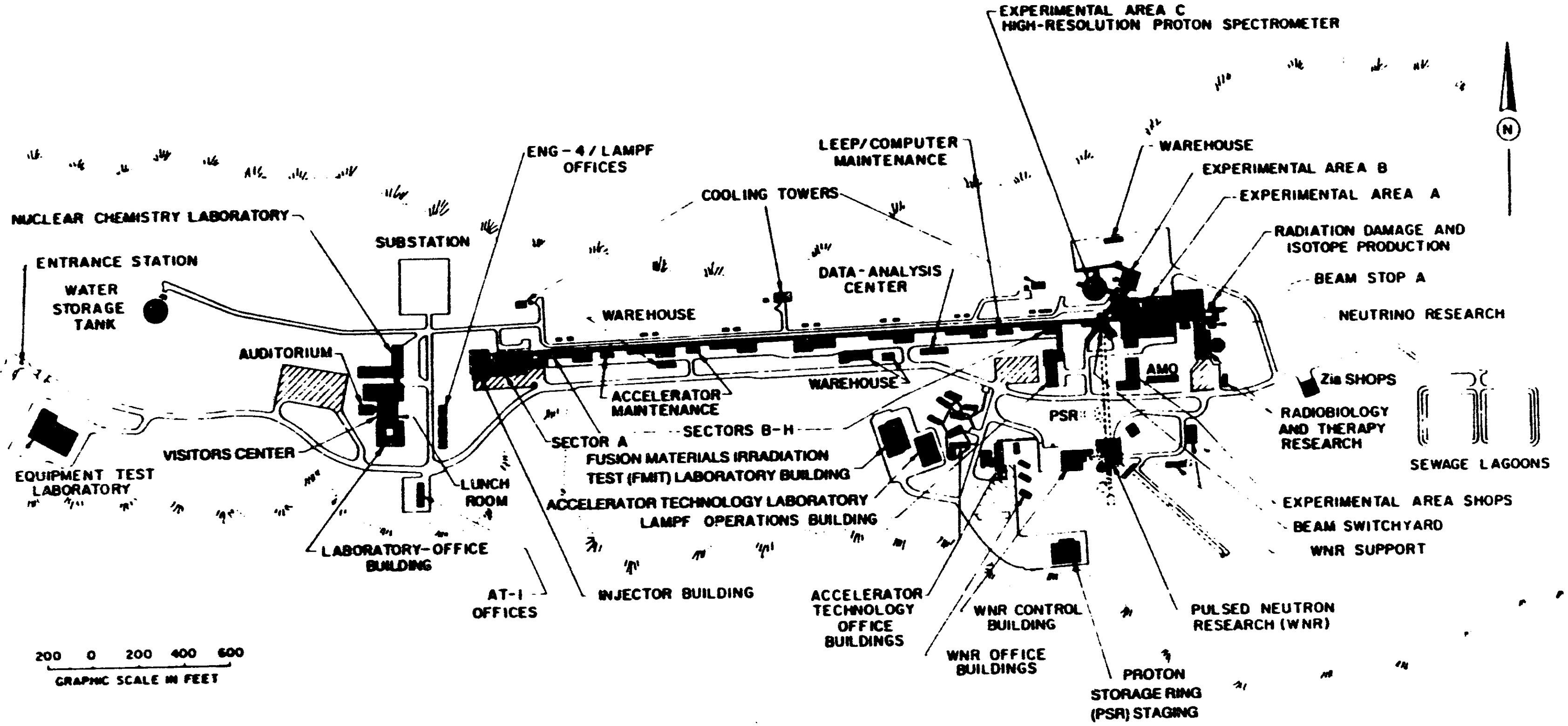

Figure 2.1 The Clinton P. Anderson Meson Physics Facility. Shown are the administrative buildings, data analysis center and electronics equipment pool, the 800 MeV proton linac itself and the experimental areas [How-87]. The experimental area A houses the low-energy pion line (LEP).

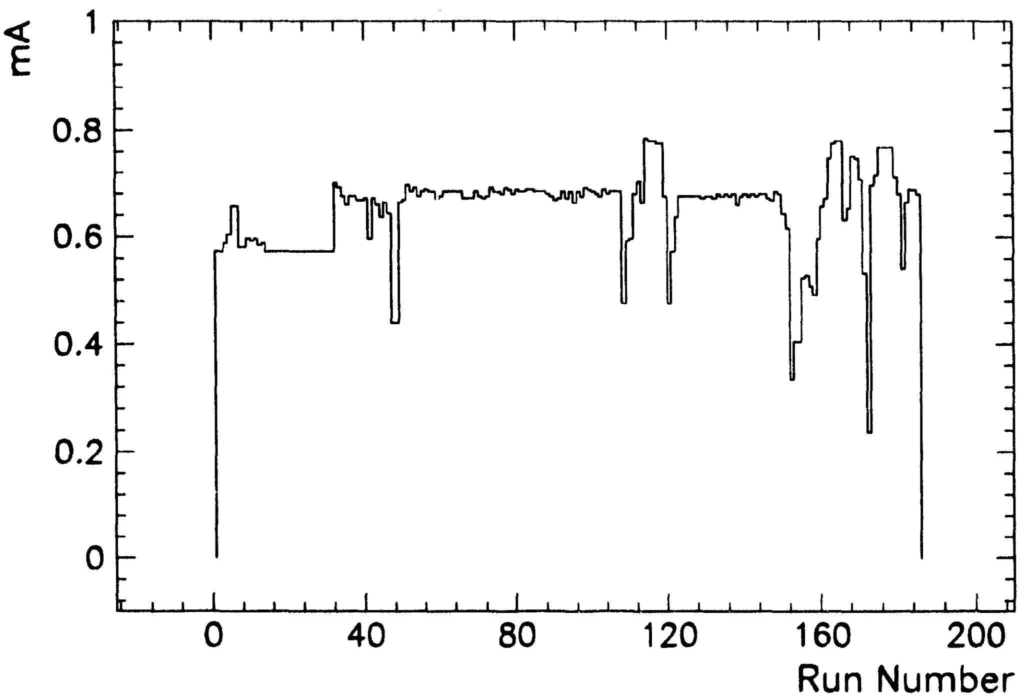

Figure 2.2 Primary proton current during the LAMPF production cycle number 61 (summer 1992).

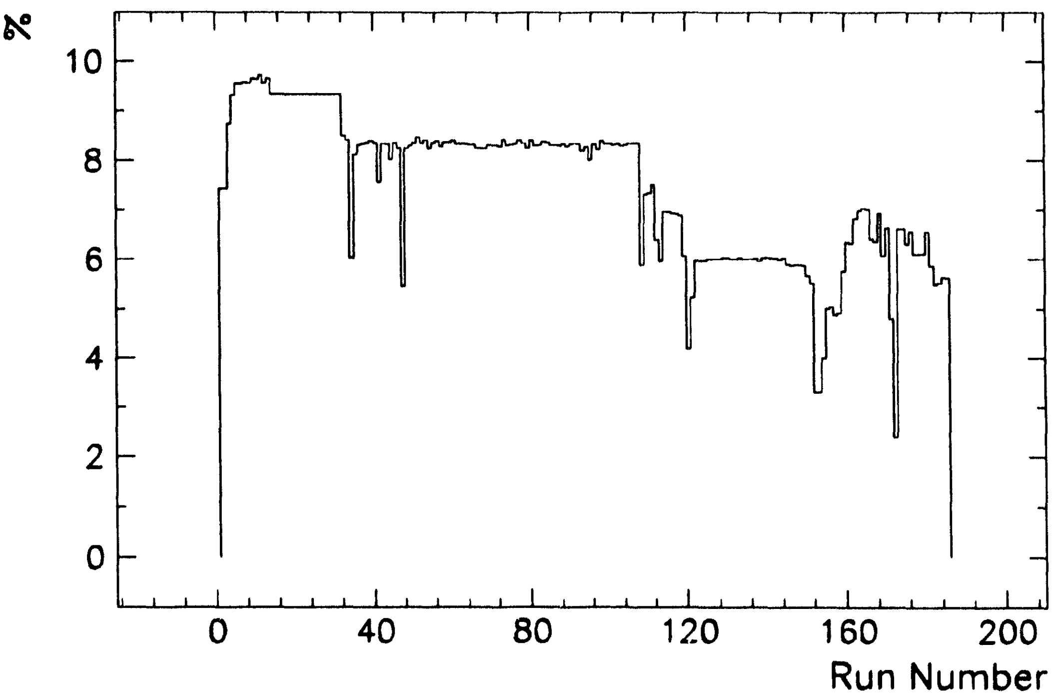

Figure 2.3 The accelerator duty factor for all 1992 data acquisition runs.

The accelerating time profile is characterized by a macrostructure of 120 pulses per second with a maximum macropulse length 900 μs. The microstructure of the macropulse consists of a 0.25-ns burst every 5 ns.

The primary proton currents and corresponding duty factors during E1179 1992 data acquisition runs are displayed in two panels of Figures 2.2 and 2.3. The maximum delivered primary beam currents reached 1 mA and the duty factor varied between 4% and 10% during the routine production cycles number 58, 60, and 61.

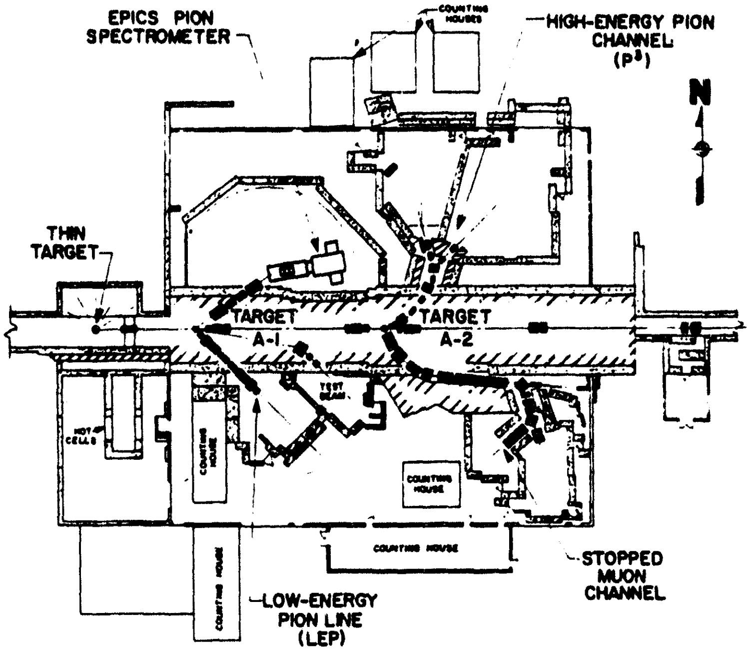

Figure 2.4 The experimental area A. The experiment E1179 was done in the Low Energy Pion Channel (LEP) that uses the secondary pion beam produced on 3 cm thick graphite target A-1 [How-87].

B. LEP Channel and Beam Tunes

The experiment E1179 was run three consecutive years in the low energy pion cave. The choice of LEP channel was preferred due to the 20-300 MeV energy range of useful pion beams the transport system of the channel was designed for. The location of the experimental cave and the adjacent counting house within the experimental area A hall are indicated in Figure 2.5.

The mechanical design of the LEP channel is described in a paper by Fulton [Ful-73].

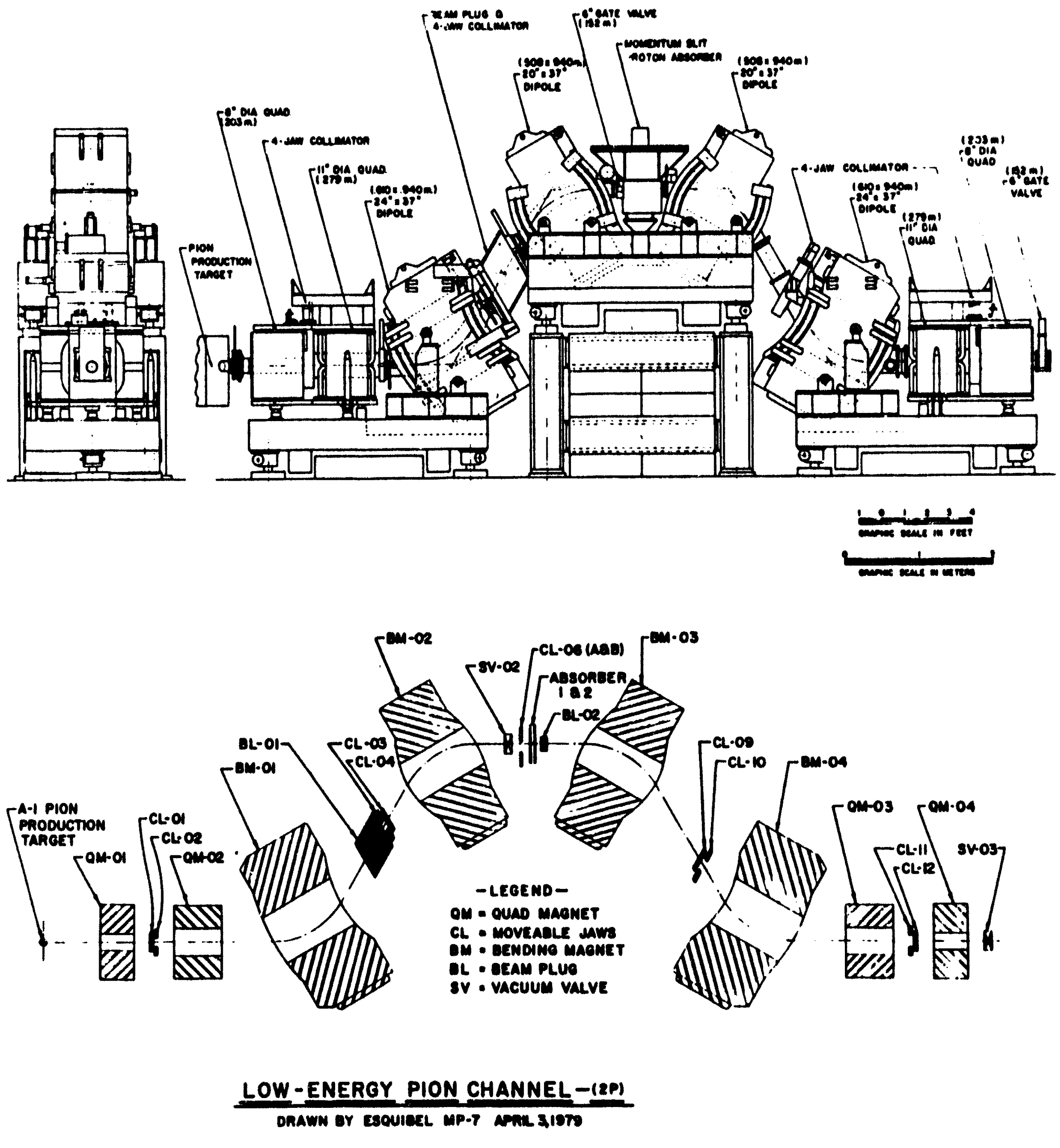

Figure 2.5 (a) A Low-Energy Pion Channel in a front and side elevation view [Bur-75a]. (b) Schematic layout of the channel bending dipole magnets and focusing quadrupoles [How-87]. With the vertical bend plane the height of the beam centerline at channel entrance and exit is 158 cm.

The optical characteristics of the beam line are presented in references [Fur-73], [Bur-75]. The described symmetric design is achromatic, essentially isochronous and nondispersive to high order. It is built around four rectangular bending dipole magnets and entrance and exit quadrupoles pairs as illustrated in Fig. 1. The magnets define the vertical bending plane in order to better optically match to the forwardly-directed 45° production angle on primary target. The entrance and exit edges of the bending magnets are engineered to provide sextupole focusing correcting second order terms in the beam transport. The gaps are 15 cm wide limiting the maximum acceptance solid angle to 20 msr. The transmitted momentum spread can be varied in the wide interval from ±0.05 to ±4% $\Delta p/p$ by independently driving two centrally located 2 cm thick jaws. The beam spot size at the channel exit can be controlled by varying the fields of the exit quadrupoles. Additional control is provided by four 4-jaw collimator slits that are kept in pairs at an equal distance from the beam centerline. These collimation jaws mounted on opposite end ball screws are moved in vacuum by a stepping motor through a bellows-sealed rotary feedthrough. The 14 m long beam centerline making 60° bends with 1 m curvature radius is designed as short as possible to minimize in-flight pion decay losses.

The protons present in the positive pion beams were removed before the last bending magnet by differential absorption. Two mid-channel wheels each carry three different absorbers providing 16 different combinations of thicknesses. For the 1992 runs the wheels were rebuilt to provide the combinations customized for the E1179 beam tunes developed in test runs. The pion-proton separation of 6-10% insured the proton contamination $\lesssim$3%. The muon fraction in the final image originating from the production target (~3%) dominates the muon surface flux formed in the last quadrupoles (typically ~10% distributed over 10 cm^2 for 100 MeV beam). The neutron contamination values at the channel exit are approximately constant at $\sim 10^{-4}$ for both positive and negative beams in the range 50-200 MeV and are due primarily to pion and proton-induced production in the beam line. The electron (positron) contamination is serious only at low energies: for 25 MeV π^- the e^-/π^- fraction is ~10 while for 200 MeV π^+ beam the positron contamination is less then a percent [Dyc-79]. The detailed exposition of two alternative methods employed for estimation of the non-pionic beam contaminations is contained in the section III.B.

The beam-design program TRACE originally written by Burman and Chavez [Bur-75b] was used to arrive at initial magnet settings. The code is a miniature version of the computer program TRANSPORT [Bro-80] which handles magnetostatic charged particle optics systems including both first and second-order fitting capabilities.

The program was used in the simple input variant that requires the specification of the incident pion energy in MeV as well as the desired degrader combination. The TRACE outputs the final transport matrix for the LEP line, first and second-order beam profiles, the beam divergence and all the channel magnet settings. The strengths of quadrupoles were subsequently fine-tuned to the most narrow attainable beam spot at the target position.

The optimal collimator openings were determined for one slit at a time by calibrating the collimator setting vs beam flux. The goal was to cut down the beam envelope until the beam intensity was reduced to 90% of the noncollimated value.

The analysis was done during the 1990 feasibility run of weak and strong focusing tunes at the limiting energies 165 and 260 MeV. The conclusion was that the strong focusing tune provides ~50% higher intensities but the beam spot horizontally broadens (14 → 20 mm) and it is not possible to collimate it. The further advantage of weaker quadrupole fields was good beam transmittance and lower scattering backgrounds resulting from small-to-moderate beam divergence.

Table 2.1 1991 LEP beam parameters. The nominal kinetic energies and momenta of the pion beam together with the energy spread and $\Delta p/p$ bite are shown in the first two columns followed by the contamination proton energies. The full width at half maximum of the beam spot, the range of the fluxes and intensity normalized to the primary beam toroid count fill in the rest of the table. The values marked with an asterix correspond to the 1990 run.

T_π (MeV)	p_π (MeV)	T_p (MeV)	$\Delta x \times \Delta y$ (FWHM, mm)	$I_{min} \rightarrow I_{max}$ 10^6 π/sec	$\langle \pi / A_1 \rangle$ 10^2 π/sec/tor_1
$30 \pm 1.64^*$	96.30 (±3%)	4.93 ± 0.74	$6 \times 8^*$	0.76→1.43	0.41^*
30 ± 1.64	96.30 (±3%)	4.93 ± 0.74	15×16	0.43→0.51	0.28
160 ± 0.47	265.07 (±0.2%)	36.72 ± 0.31	14×14	7.4→7.8	3.80
180 ± 0.52	287.48 (±0.2%)	43.05 ± 0.36	11×13	8.1→8.8	4.25
190 ± 0.54	298.56 (±0.2%)	46.35 ± 0.36	11×13	11.4→12.9	6.10
200 ± 0.56	309.56 (±0.2%)	49.75 ± 0.40	11×11	12.6→13.3	6.83
220 ± 0.61	331.38 (±0.2%)	56.80 ± 0.45	10×11	13.5→13.9	7.08
240 ± 0.66	352.98 (±0.2%)	64.20 ± 0.49	12×11	8.6→9.4	5.36
$260 \pm 0.70^*$	374.40 (±0.2%)	71.94 ± 0.54	$12 \times 11^*$	7.1→11.3	3.78^*
260 ± 0.70	374.40 (±0.2%)	71.94 ± 0.54	14×13	5.9→35.0	5.77

The location and profile of the beam spot were established with the LAMPF profile monitor, a single multiwire proportional chamber with two perpendicular wire grids covering area of 6×6 cm^2. The final beam vertical and horizontal profiles were documented in the oscilloscope polaroids of the monitor response. The two-dimensional beam contours were reconstructed from excitations of 0.9 mm separated wires in two chamber planes. The contour plots of all used pion and proton beams are displayed in Figures 2.6 and 2.7.

The horizontal bending magnet known as Werbecka was positioned against the exit wall at the beam height. The calibrations of the Werbecka and final vertical bending magnet are done at the limiting energies of 30 and 260 MeV to ascertain the orthogonal beam

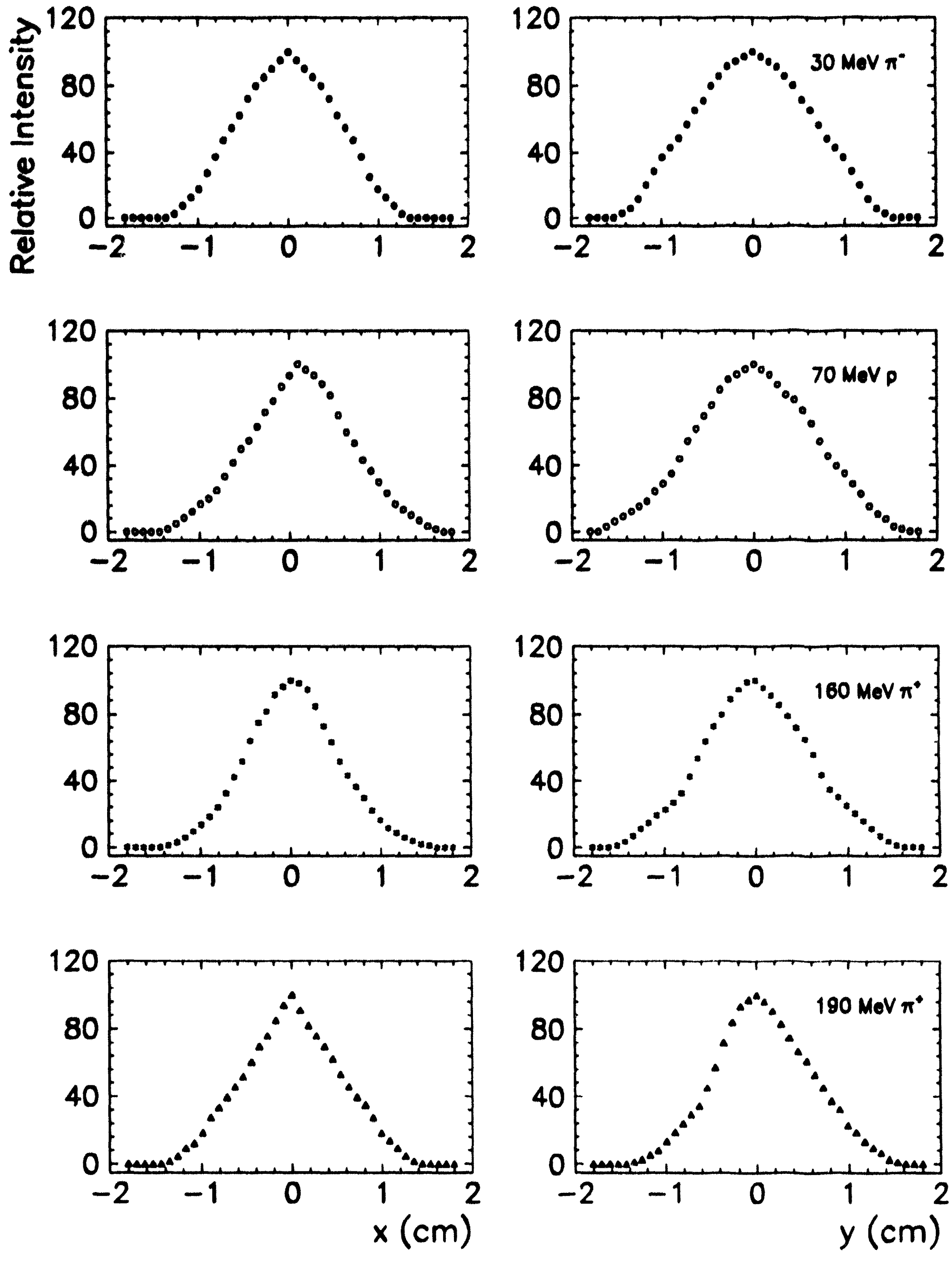

Figure 2.6 The horizontal (x) and vertical (y) beam profiles for the 30 MeV π^- (•) and 70 MeV p (∘) tune and 160 (∗), 190 MeV π^+ (▵) tune. For 30 MeV π^- tune the beam spot size as measured on the wire chamber reflects primarily the electron component of the beam.

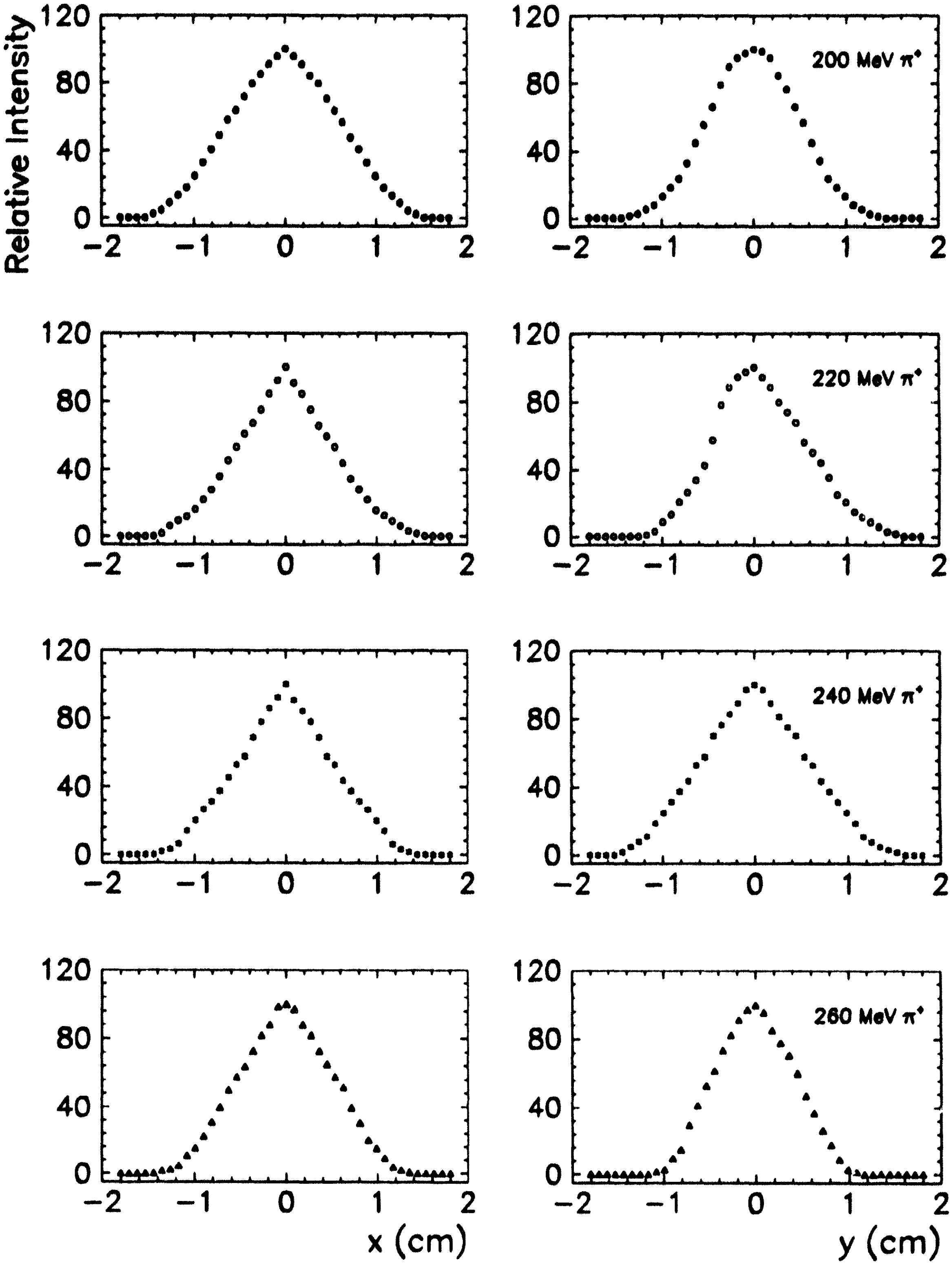

Figure 2.7 The horizontal (x) and vertical (y) beam profiles for the 200 (•), 220 (∘), 240 (∗), and 260 MeV π^+ (▵) tune.

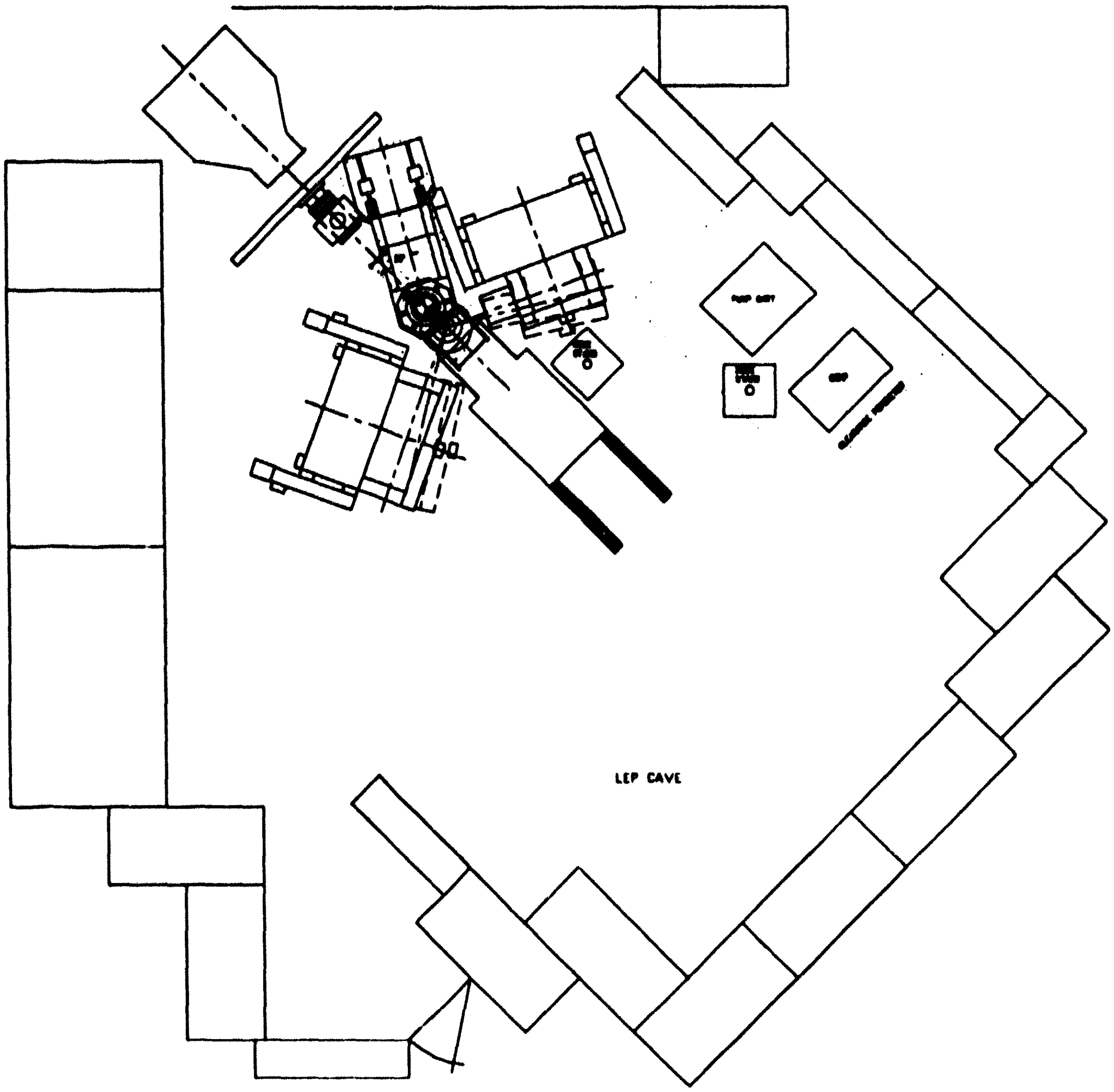

Figure 2.8 The LEP cave layout of the experiment E1179. The horizontal stearing magnet is backed to the "blue wall" matching the last channel quadrupole on the exit flange. The arrangement of the π^0 spectrometer, the charged particle stand, target stand and the scattering chamber as well as the cryogenic equipment is shown.

displacements for specific changes in magnetic fields. The field strengths were carefully monitored during the data acquisition runs, periodically adjusted for drifts exceeding 0.2 G and logged at least two times per shift. That procedure assured the beam centered on targets with beam spot drifts less then 2 mm. The final drift distance, the separation between the LEP channel "blue wall" and the pivot position, was 250.2 cm. The parameters describing the accepted and used beam tunes are summarized in Tables 2.1 and 1.1.

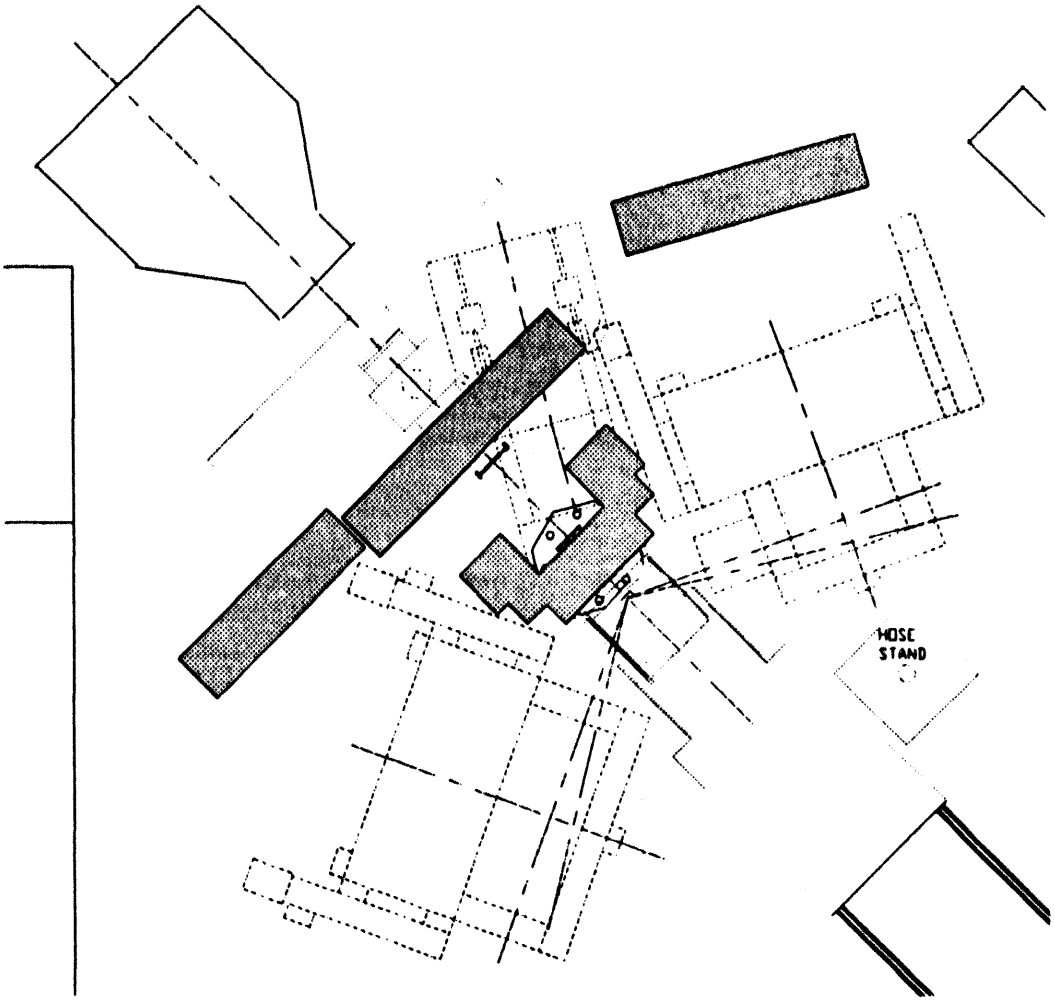

Figure 2.9 The shielding design for the charged particle detectors and the π^0 spectrometer. The outlines of the CP stand, target stand and spectrometer crates are shown. The lead brick walls built on 6 layers of .15×30 cm^3 concrete blocks were 2 m high and 30 cm wide. Total of 2500 5×10×20 cm^3 lead bricks were used.

The previous experience with LEP tunes confirms that the central momentum of the channel is correct to within experimental uncertainty of 0.5%. That check was done by measuring the energies of spallation particles with momentum 128 MeV from the pion production target in the experiment [Hoe-82].

The shielding was arranged to fit into the constrained available space between the Werbecka's exit flange and the detector arrangement. The two 30 cm thick lead brick walls were built on concrete block stands 2.5 meters high to shield both the charged particle detectors as well as the π^0 spectrometer glass from the background particles coming from the direction of the primary target. The thickness of the walls was appropriate to stop the highest energy muons originating from in-flight pion decays. The muon background was expected to be particularly intense in the charged particle detectors at small angles. The distribution of the decay muon polar angles is determined by a relativistic boost γ_π and peaks near the maximum allowed laboratory angle $\theta_{\max}$:

$$\tan\theta_{\max} = \frac{1}{\gamma_\pi\sqrt{13.6\beta_\pi^2 - 1}}. \tag{2.1}$$

The opening of the muon cone was 6.0° at the highest energy of 260 MeV, 8.5° for 160 MeV pion beam, and 24.1° for 30 MeV pions. For the runs with solid targets the evacuated 20 cm-diameter steel spool with 5 mil mylar windows on both ends was encased in the lead shielding extruding to 30 cm upstream of pivot position. Eight specially cut lead bricks were used to make a tight cylindrical collimator around the spool circumference.

The liquid hydrogen target shielding was built around the aluminum scattering chamber that accepted the beam through a 1 m long steel tube attached to it upstream.

The relative arrangement of shielding elements with respect to the active detectors, the target, target stand and scattering chamber is shown schematically on Figure 2.9

The described shielding design reduced the rates in the π^0 spectrometer glass elements to $\sim 10^3$ s^{-1} for 260 MeV beam-off gate and $\sim 10^5$ s^{-1} during beam on gate. The average background rates in the charged particle hodoscope counters were $\sim 5 \times 10^3$ s^{-1}. For the low energy 30 MeV π^- beam the π^0 spectrometer operated very quietly with the scaled background rates an order of magnitude smaller.

C. Target and the Scattering Chamber

The calibration of out hydrogen target thickness and the π^0 spectrometer efficiency required measurements with 30 MeV π^- beam in air. The CH_2 target with dimensions 78×78×7.772 mm was mounted on 3.2 mm thick aluminum frame with the 10×12 cm window opening. The areal density was established by weighing the target to be 0.721 ± 0.004 gr cm^{-2}. The target nonuniformity was estimated to be $\leq 1\%$.

Determination of the single charge exchange cross section on hydrogen discussed in Chapter III required the subtraction of ^{12}C yield. Runs with ^{12}C were made using four different rectangular carbon sheets with areal densities comparable to the CH_2 target. The dimensions and thicknesses of all the targets used in the experiment are listed in Table 2.2.

Table 2.2 List of targets used in 1990, 1991, and 1992 experiments. For the liquid hydrogen targets the diameters of the cylindrical (1990, 1991) or spherical (1992) cells were quoted.

Target (Symbol)	Description	Thickness (mm)	Areal Density (g cm^{-2})	Density (g cm^{-3})	Areal Density (mb^{-1})
^{12}C "90"	Graphite Sheet	3.18 ± 0.02	0.5289 ± 0.0040	1.66	26.54 ± 0.17
^{12}C "A"	Graphite Sheet	6.82 ± 0.02	1.0787 ± 0.0045	1.582	54.13 ± 0.35
^{12}C "B"	Graphite Sheet	3.40 ± 0.02	0.5374 ± 0.0023	1.581	26.97 ± 0.17
^{12}C "C"	Graphite Sheet	4.95 ± 0.02	0.7826 ± 0.0050	1.581	39.27 ± 0.25
CH_2	Polyethylene	7.772 ± 0.002	0.7112 ± 0.0020	0.920	91.77 ± 0.26
LH_2 "90"	Liquid Hydrogen	38.1 ± 1.0	0.267 ± 0.007	0.070	161.0 ± 5.0
LH_2 "91"	Liquid Hydrogen	38.1 ± 1.0	0.267 ± 0.007	0.070	161.0 ± 5.0
LH_2 "92"	Liquid Hydrogen	38.1 ± 1.0	0.267 ± 0.007	0.070	161.0 ± 5.0

Solid targets were oriented perpendicular to the beam direction with their upstream face positioned above the π^0 spectrometer pivot point. That arrangement improves the π^0 energy resolution because of partial compensation for the energy loss of beam pions in the target [Bae-81].

The data collected with no target installed were useful for fixing the small background resulting from pion single charge exchange in air.

For 1990 runs a existing liquid hydrogen target was used. The target cell was vertical-axis 7.6 μm thick mylar ($C_5H_4O_2$, $\rho = 1.39$ g cm^{-3}) cylinder epoxied to the brass frame. The cell was insulated with 10 layers of 6.4μm thick aluminized mylar superinsulation. The effective cross-sectional area of the mylar cell perpendicular to the beam was 3.81W×7.62H cm. The target vacuum chamber was an upright cylinder with 25 cm diameter and height made of

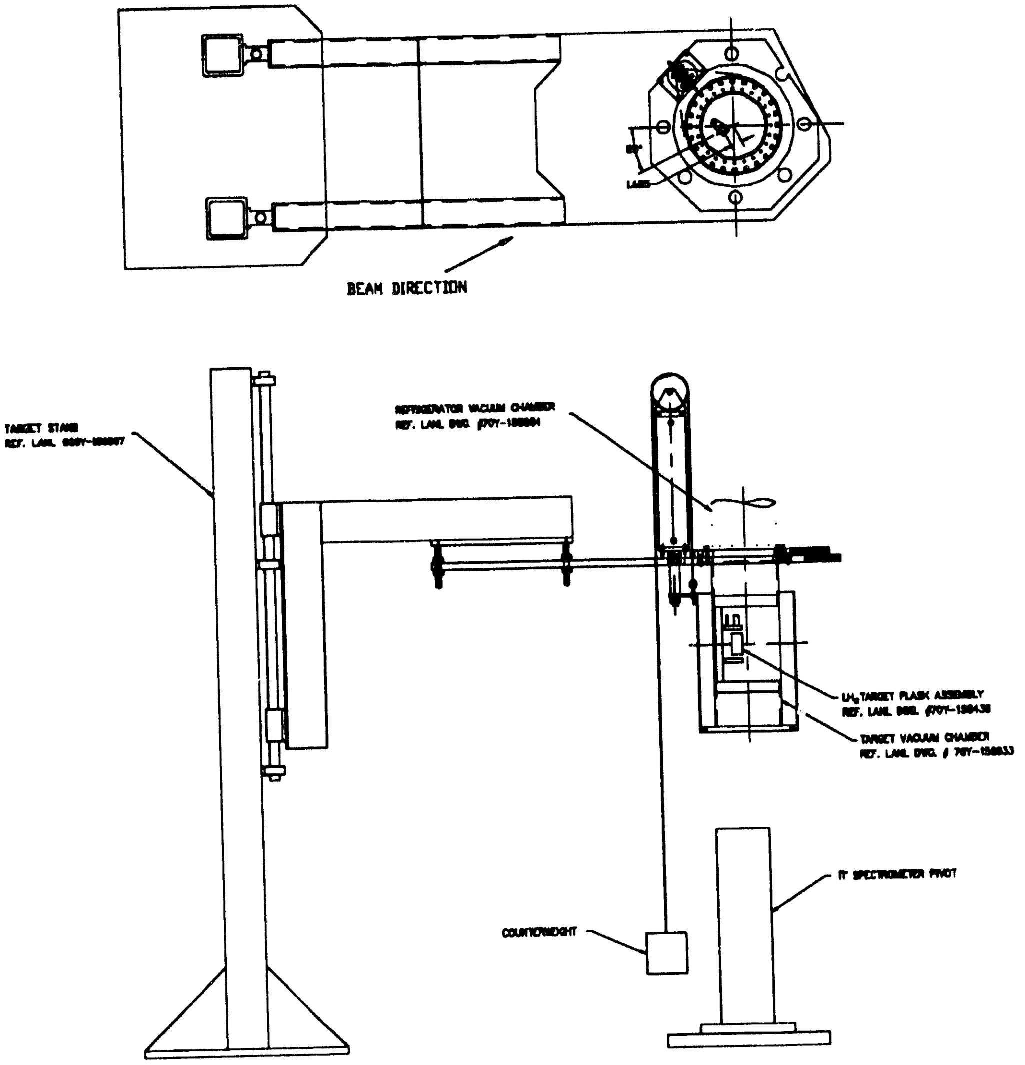

Figure 2.10 The LH_2 target cell, mylar-kevlar scattering chamber and target stand used in the 1990 run. The target could be raised up for the no-target runs.

Table 2.10 The effective thicknesses of LH_2 targets. The results were obtained in Monte Carlo simulation using measured beam profiles and target shape.

Target (Symbol)	Description	Beam Particle	T_π (MeV)	Effective Thickness (mm)	π^0 Absorption Loss Probability
LH_2 "91"	Liquid Hydrogen	π^+	259.5	35.3 ± 2.0	0.1207 ± 0.0015
LH_2 "92"	Liquid Hydrogen	π^-	28.2	30.6 ± 2.0	0.3559 ± 0.0055
LH_2 "92"	Liquid Hydrogen	π^+	259.5	33.7 ± 2.0	0.1496 ± 0.0016

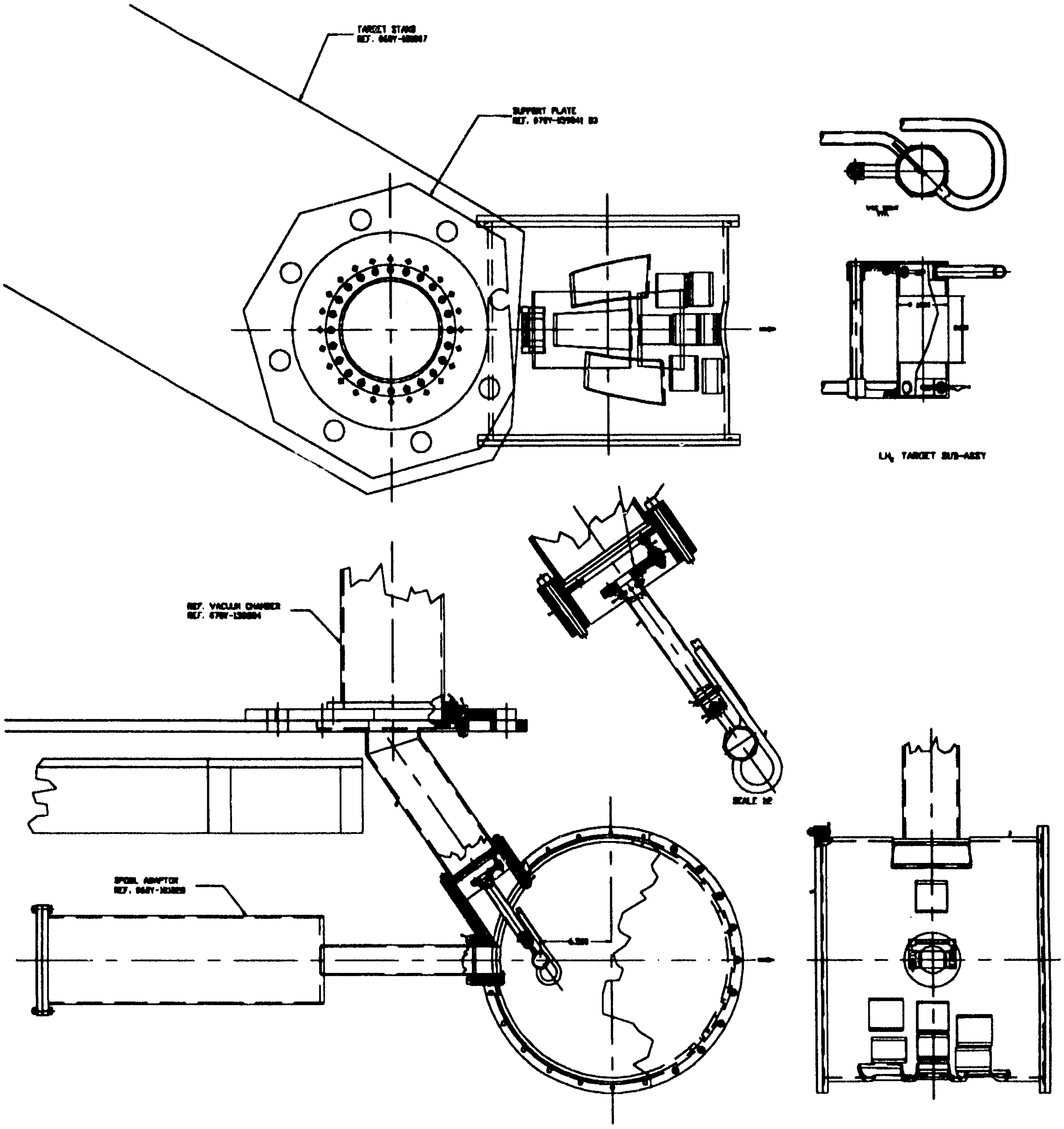

Figure 2.11 The LH_2 target flask and aluminum scattering chamber with custom-made mylar windows and G10 endplates used in the 1991 run.

12.7 μm mylar film and reinforced with three 1.3 μm thick layers of kevlar [$(HNOC)_n$, $\rho = 1.44$ g cm^{-3}]. The total thickness of target assembly to the beam as well as outgoing charged particles was 71 mg cm^{-2}. The geometry of the assembly is shown on Figure 2.10. The complete description of the target system is given in the experiment's *Standard Operating Procedure* [Nov-90].

The second part of the E1179 cryogenic target consisted of standard the LAMPF 10 watt

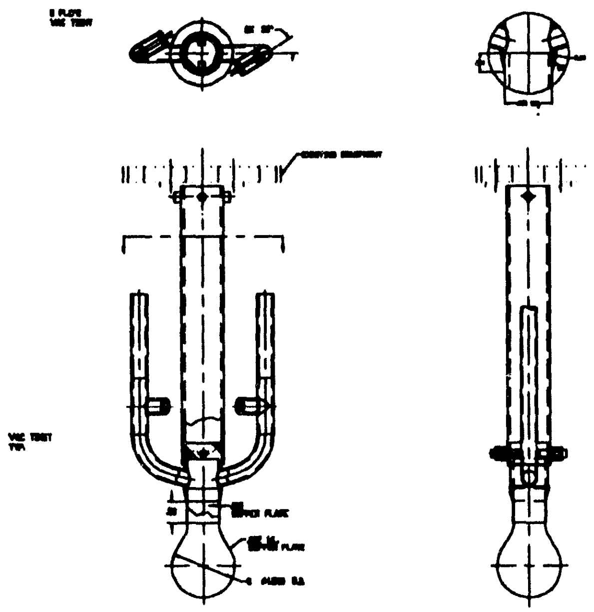

Figure 2.12 The LH_2 target cell used in 1992 run. The 5.1 μm thick copper walls of the target bulb are shown in the cross-section.

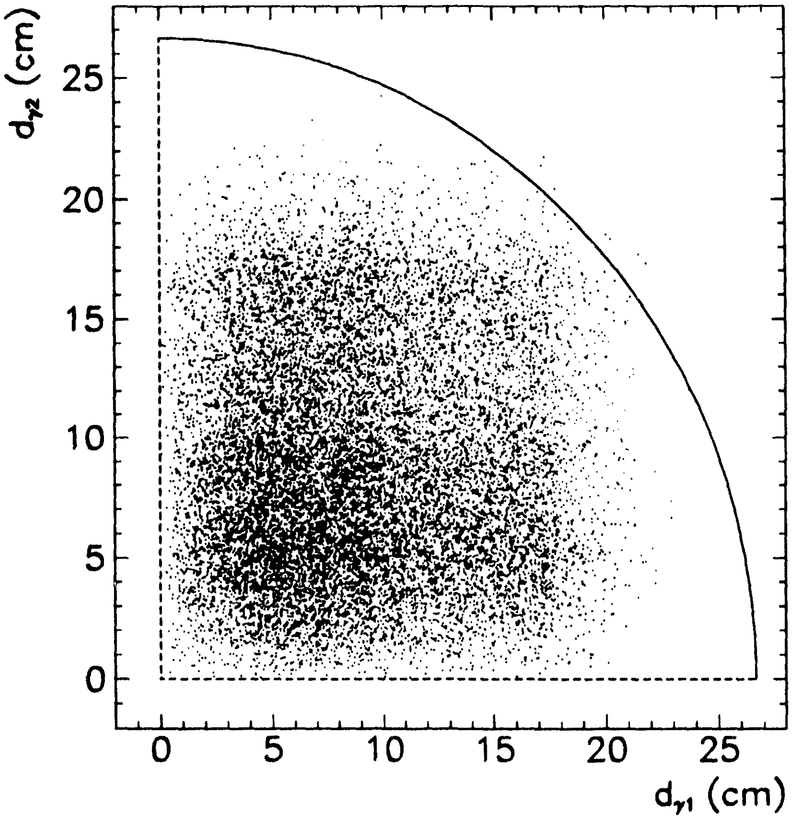

Figure 2.13 Simulated π^0 gammas intersecting scattering chamber endplates. All the converted γ's are missing scattering chamber aluminum drum and pass through endplates made from G10 (1991 run, 0.065 radiation lengths) or mylar-kevlar sheets (1992 run, 0.013 radiation lengths). The boundary of the endplate disk is indicated. The absorption in the chamber was taken into account in detection efficiency calculation.

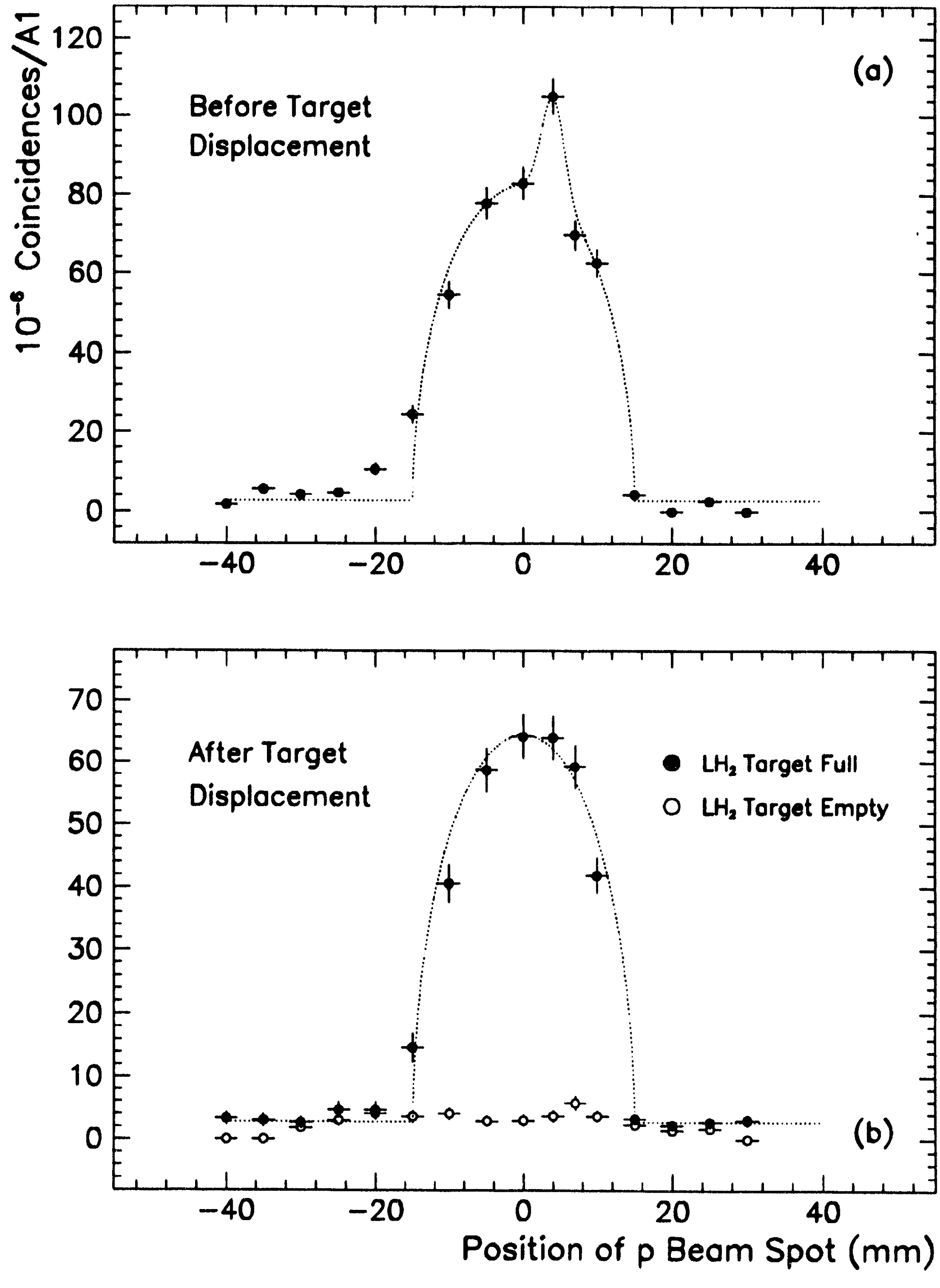

Figure 2.14 The 1990 LH_2 horizontal target scan using $pp \rightarrow pp$ scattering. The scan proved that the target was horizontally mispositioned relative to beam line. The 9 mm displacement corrected the problem as evidenced in the lower panel. The proton beam was tightly collimated with lead bricks to 1 mm FWHM spot; the scan profile therefore reflects the true LH_2 target width of 30 mm. The dotted line is expected geometrical target profile. The spike in the top panel is caused by the brass-covered fill post that was in the way of the beam in the first measurement.

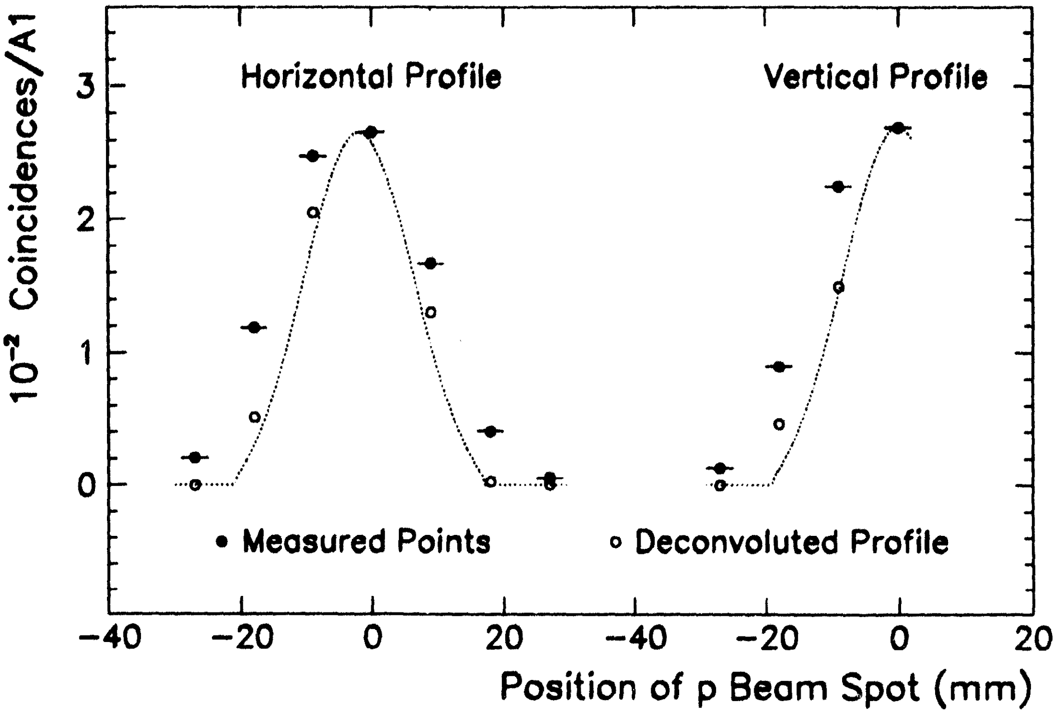

Figure 2.15 The 1992 horizontal and vertical scan of LH_2 target with $^1H(p,p)p$ coincidence rates. The horizontal and the vertical profile of the liquid hydrogen target was performed using narrowly collimated proton beam and detecting proton-proton coincidences. The proton beam was swept across the target by scaling the dipole magnet strengths in the channel beam line. The expected geometrical target cell profiles are shown by the dotted curves. The measured points (•) are plotted alongside the Fast Fourier Transform (FFT) deconvolution (○) that used the proton beam spot profile of Figure 2.6 and indicates the real target dimensions. A 2 mm beam-left horizontal target offset is revealed.

refrigeration system. The compressor module furnished high pressure, high purity helium gas to the refrigerator. Gas was expanded in the refrigerator in two stages, operating at 50 to 80 K in the first step, and at 10-20 K in the second step, thus producing 10 watts of cooling at 20 K. The compressor and expander were coupled forming a closed system in which the cooled gas was returned to the initial stage for recompression. The hydrogen was liquefied in a condensing chamber that received gas through a purifying system, and was stored in a reservoir and then passed on to the target cell. The schematic diagram of the cryogenic system is displayed in Figure 2.16 and described in detail in the reference [Nov-90].

The flask and the connecting pipes filled with 0.15 liters of liquid in ~3 hours starting from a warm state. Carbon resistor level sensors in the flask were wired to the light indicators in the counting house showing full and empty conditions.

The 1991 run used a redesigned scattering chamber and a new target cell. The LH_2 flask was made of 7.6 μm thick mylar film, in the shape of horizontal cylinder epoxied to stainless steel endcaps. It presented a 2.0W× 1.5H cm cross section to the beam and contained 0.12 liters. The scattering chamber was a 1.3 cm thick aluminum drum with an outer diameter 55.9 cm and a horizontal axis 50.8 cm long. Windows matching the charged particle detector directions and openings for beam entry and exit were cut in the envelope and covered in order to preserve vacuum tightness with a 25.4 μm thick mylar band wrapped completely around the chamber drum. The end plates of the chamber were constructed from a 1.3 cm thick G10 plate having 19.4 cm radiation length. The upstream vacuum window was moved away from the pivot point by putting it on the spool bolted on the chamber as illustrated on Figure 2.11.

All gamma rays originating from the decays of low energy ($\leq$100 MeV) neutral pions in a target were intersecting the chamber end plates and not passing through the aluminum envelope. That important feature was established in the realistic Monte Carlo simulation of π^0 gamma paths that fall within the spectrometer fiducial areas. Figure 2.13 shows the distances of the intersection points for γ pairs d_{γ_1} and d_{γ_2} with respect to the centers of the endplates.

Insights gained in the analysis of 1991 data led to an improved target cell design. The charged particle energy losses in the target assembly were equalised for different outscattering directions. The background processes and photon conversions were considerably reduced by avoiding the metal endcaps and the effective target thickness was increased 30%. The manufacturing process involved electroplating an condom-shaped aluminum mandrel with 5.1 μm copper skin. The aluminum core was then etched out with an acid solution leaving a 5 μm thick, uniform ($\pm$1.3 μm) copper flask, Figure 2.12.

For the 1992 runs G10 chamber endplates were replaced with 12.7μm mylar shell sandwiched between 2 kevlar layers of the same thickness.

The condition of the target was documented in a separate logbook usually twice per shift. The position of the target cell relative to the beam was checked with a precision theodolite both before installing the vacuum chamber as well as after the experiment. An independent check of the target positioning was provided by scans of the in-beam material with target full/empty using elastic proton-proton scattering. In the 1990 feasibility run the scan established error in target position that was promptly corrected before the data acquisition stage, Figure 2.14.

The effective thickness of the target cells to the beam particles was found in a simple Monte Carlo calculation. The simulated particle paths taken from measured beam profiles (Figures 2.6 and 2.7) were passed through the appropriate flask shapes. The average path length was fixed with 0.1% statistical uncertainty, Table 2.3.

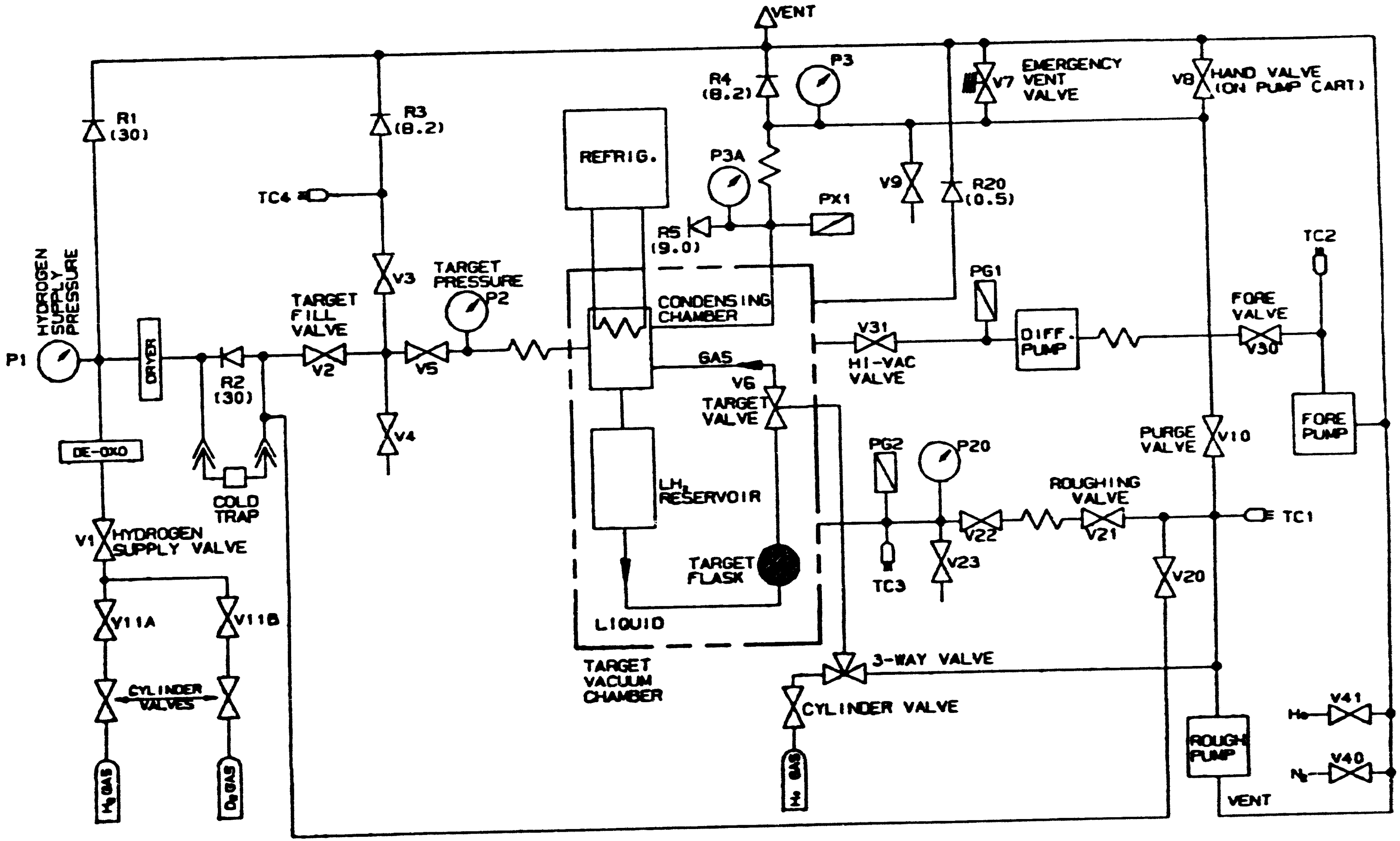

Figure 2.16 The 10-watt refrigerated liquid hydrogen target system [Nov-92]. The basic components of the assembly are as follows: (a) the refrigeration system with compressor and expander module, (b) liquefied gas system consisting of condensing chamber reservoir, target cell, vacuum containment and target material supply system, (c) vacuum support, (d) electrical power supply, and (e) liquid nitrogen supply.

D. LAMPF π^0 Spectrometer

The neutral pions created in $\pi^+p \rightarrow \pi^+\pi^0p$ collisions were detected in the LAMPF π^0 spectrometer. The instrument was designed, constructed and tested by a collaboration of LAMPF, Tel Aviv University and Case Western Reserve University in 1979 [Gil-79].

The π^0 spectrometer has an energy resolution of 2-5 MeV and an effective solid angle of 1 mrad for the π^0's with kinetic energies less then 300 MeV.

The instrument detects only the dominant π^0 decay mode

$$\pi^0 \rightarrow \gamma\gamma, \tag{2.2}$$

which proceeds with the branching ratio of $(98.798 \pm 0.032)\%$ [Her-90]. Therefore the undetected Dalitz decays

$$\pi^0 \rightarrow e^+e^-\gamma, \tag{2.3}$$

with branching ratio of $(1.198 \pm 0.032)\%$ are taken into account as a correction.

The π^0 spectrometer detects and measures the kinematic parameters of the π^0's by measuring the energies and directions of two gamma rays from decay (2.2). The basic equations expressing the π^0 total energy T_{π^0} and polar angle θ_{π^0} in the laboratory in terms of the measured quantities are

$$T^2_{\pi^0} = \gamma^2 m^2_{\pi^0} = \frac{2m^2_{\pi^0}}{(1-\cos\eta)(1-X^2)}, \tag{2.4}$$

$$\cos\theta_{\pi^0} = \frac{E_1\cos\theta_1 + E_2\cos\theta_2}{\sqrt{E_1^2 + E_2^2 + 2E_1E_2\cos\eta}}, \tag{2.5}$$

where E_1, E_2, θ_1, θ_2 are the energies and direction of the two photons, η is their opening angle and $\gamma = \sqrt{1-\beta^2}$ is a relativistic factor. The energy asymmetry parameter is defined by:

$$X = \frac{E_1 - E_2}{E_1 + E_2}, \tag{2.6}$$

and is physically restricted to the values $\pm\beta = \pm v/c$. The step-by-step kinematic derivations of these relationships are provided in Gilad's thesis [Gil-79].

A schematic illustration of the two π^0 spectrometer crates (J—beam left and K—beam right) in the two-post configuration with vertical scattering plane is given in Figure 2.17a. Each crate is an independent position sensitive γ ray detector optimized for energies from 50 to 300 MeV. The front face of each detector is covered with a 3.6 g cm^{-2} polyethylene "hardener" (not shown) to absorb low-energy particles and photons followed by a 3 mm thick plastic scintillator that vetoes the incoming charged particles.

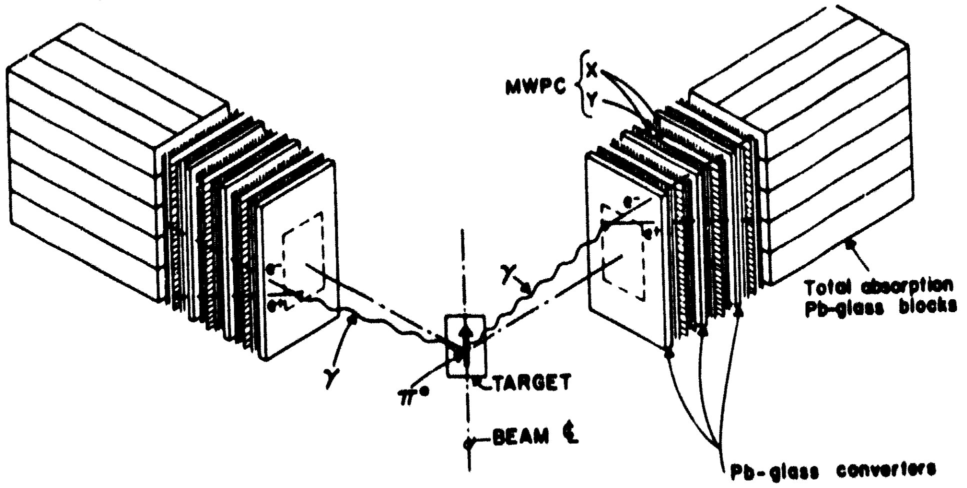

Figure 2.17 A schematic drawing of the π^0 spectrometer [Bae-81]. (a) The orientation of J and K arm in two post configuration with respect to each other and to the target is shown. (b) The details of one spectrometer arm. Three sets of converter-scintilator-MWPCs, as well as the array of lead glass total absorption blocks can be seen. The convention for 2-post setting coordinate system orientation is indicated.

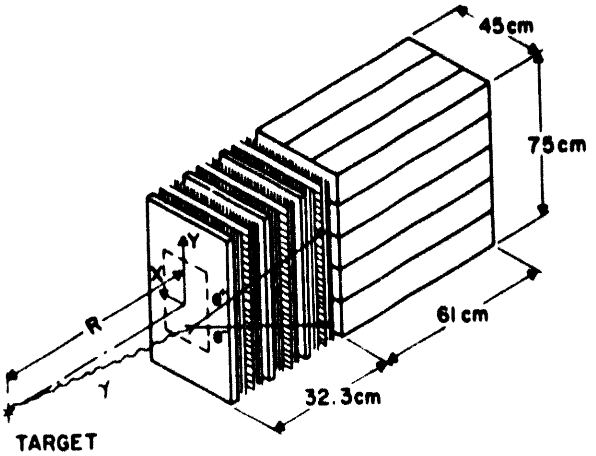

Three identical conversion systems provide the basis for γ detection. Each consists of a 2.46 cm (0.58 radiation length) thick lead glass converters that initiate the showers and three multiwire proportional chamber (MWPC) planes used for determination of the conversion point coordinates. The active converters were segmented into five strips each coupled to its own photomultiplier tube in order to reduce the signal pile-up due to high singles rates and 250 ns long signal decay tails. The two MWPC planes labeled X and X′ have 2 mm wire spacing in more critical (x) direction of the line between a chamber center and the detector's bisector. The third chamber (Y) is sandwiched between X and X′ planes and has 4 mm resolution in the orthogonal y coordinates. At the back of each system is a 3 mm thick scintillator sheet that tags the conversion event. The shower is contained in a 3×5 array of $15\times15\times61$ cm^3 total-absorption lead glass blocks. The Čerenkov light output in the converters and calorimeter blocks plus scintillator light is a measure of the incident γ ray energy. The properties of lead glass necessary for reliable Monte Carlo simulation of the spectrometer response and the tracking of particles through the detector elements are summarized in Table 2.5. The energy resolution of individual block detectors was determined

Table 2.4 The π^0 spectrometer multiwire proportional chamber parameters [Gil-79].

Parameter	Value
Chamber active area	64 × 38 cm
Frame composition	G-10 fiberglass-epoxy laminate
Gap size	5.7 mm
Anode wire spacing	2 mm
Anode wire tension	50 g weight
Planar cathode	2.54 μm aluminized mylar
Total number of wires	3264
Number of wires in each X plane	192
Position resolution in X plane	2 mm
Number of wires in Y plane	160
Position resolution in Y plane	4 mm
Operating voltage	−3.15 kV
Gas mixture	
Argon	75%
Isobutan	20%
Methylal	5%
Freon	0.5%

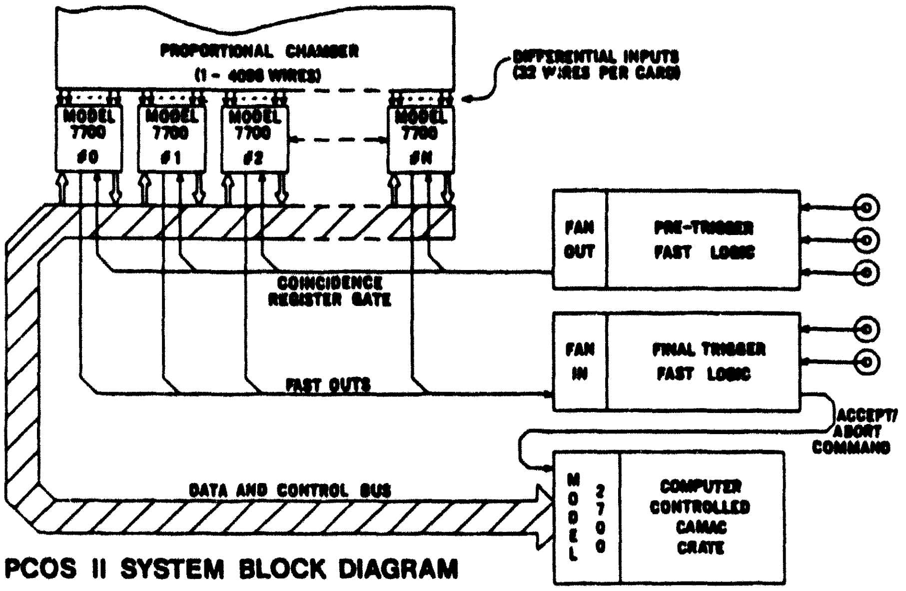

Figure 2.18 Schematic layout of PCOS II—proportional chamber operating system by Le Croy [Lec-87]. The model 7700 boards mounted on the chambers amplify, discriminate, delay and latch the multi-hit data signals subsequently encoded by four CAMAC LCR 2700 units. The outside low voltage is provided to set the discriminator threshold (−5 mA) and laser-trimmed delay (400 ± 60) ns.

by Baer *et al.* [Bae-81] to be

$$\Delta E_B(\mathrm{MeV}) = 2.4\sqrt{E}. \tag{2.7}$$

All Čerenkov and scintillator detectors are viewed by 5 inch phototubes (EMI9618KR, EMI9530KR, and RCA4525) which have linearity and amplitude stability of ±1% over 48 hours and were successfully tested for rate instabilities at 0.65 MHz [Gil-79].

The approximate dimensions of a spectrometer crate are indicated on Figure 2.17b while the precise dimensions of every active detector element in both arms and their absolute separations can be found in the unpublished notes of H. Baer [Bae-84].

The gains of the 60 lead glass Čerenkov detectors are monitored using ^{207}Bi sources embedded in plastic scintillator capsules attached to each detector [Bol-80]. After adjusting the amplifier gains to match the reference ^{207}Bi spectra, this method provided ±2% stability throughout our experimental runs requiring little maintenance.

Table 2.5 Summary of LF5 lead glass properties [Gil-79] [Bae-84]. The chemical composition of the glass is by weight 33.8 ± 1.0% PbO, 52.7 ± 1.0% SiO_2, 7.00 ± 0.05% K_2O, 6.50 ± 0.05% Na_2O and is coded into GEANT detector description.

Radiation Length (cm)	Density (gm cm^{-2})	Refraction Index	dE/dx (MeV cm^{2}g^{-1})	Internal Transmission
4.20 ± 0.10	3.23 ± 0.02	1.581	1.55	0.985-0.999

Apart from effects of beam momentum dispersion and nonzero target thickness the instrumental π^0 energy resolution, ΔT_{π^0}, is determined by the uncertainties in gamma energies ΔE_{γ_1}, and ΔE_{γ_2} and the uncertainty in the opening angle $\Delta\eta$:

$$\begin{aligned}\Delta T_{\pi^0} &= \left[\left(\frac{\partial T_{\pi^0}}{\partial E_\gamma}\Delta E_\gamma\right)^2 + \left(\frac{\partial T_{\pi^0}}{\partial \eta}\Delta\eta\right)^2\right]^{\frac{1}{2}} = \\ &= \left[\frac{3T^2_{\pi^0}}{(1-X^2)^2}\frac{\sigma^4_{E_\gamma}}{(E_{\gamma_1}+E_{\gamma_2})^4} + \frac{m^2_{\pi^0}}{4}\gamma^4\beta^2\Delta\eta^2\right]^{\frac{1}{2}}.\end{aligned} \tag{2.8}$$

The contribution from the gamma energy resolution depends only weakly on π^0 energy because measurements of Baer *et al.* [Bae-81] show that

$$\sigma_{E_\gamma} = 1.1\sqrt{E_\gamma}.\ (\mathrm{MeV}), \tag{2.9}$$

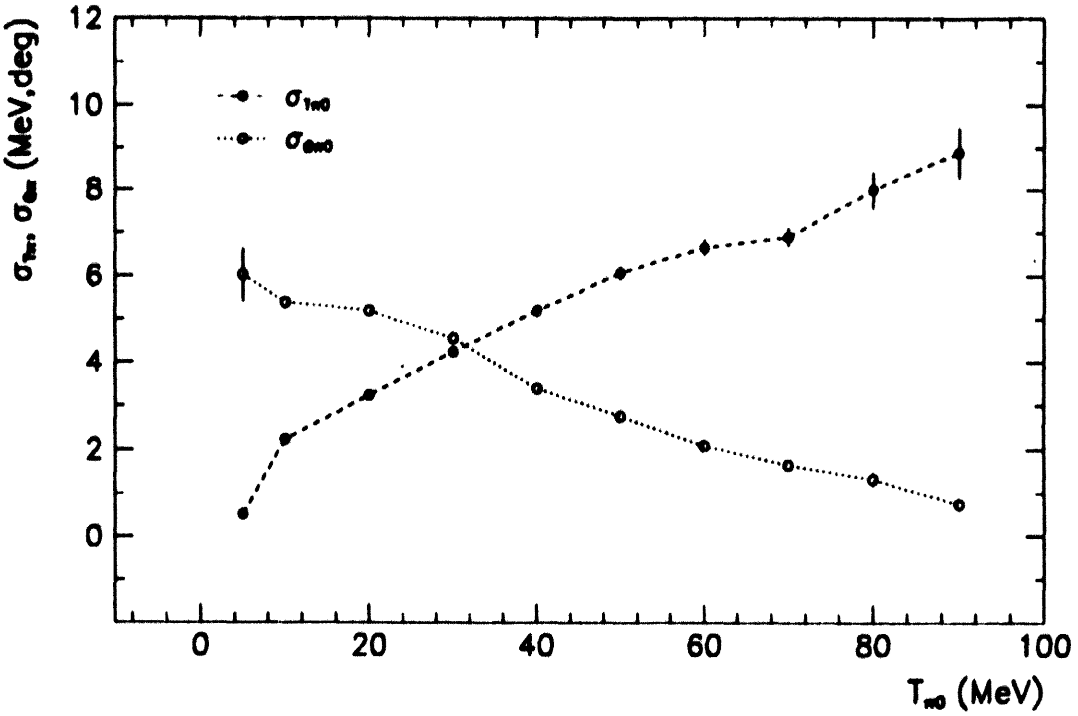

Figure 2.19 Energy and angular resolution of the π^0 spectrometer in the E1179 configuration as a function of π^0 energy for unrestricted X parameter obtained in **PIANG** Monte Carlo.

The energy-dependent contribution is caused by $\Delta\eta$ uncertainty that for a nominal target-to-detector distance R and the conversion point resolution Δx (~4 mm) has the form

$$\Delta\eta = \frac{\sqrt{2}\Delta x}{R}. \tag{2.10}$$

The dominant instrumental contributions to the π^0 angular resolution are the uncertainties associated with the magnitudes of photon momenta registered by the spectrometer. For symmetric π^0 decays ($E_{\gamma_1}=E_{\gamma_2}$) the directional resolution $\Delta\theta_{\pi^0}$ is directly proportional to the fractional energy resolution of the lead-glass calorimeter $\Delta E_\gamma / E_\gamma$:

$$\Delta\theta_{\pi^0} = \frac{\tan(\eta(T_{\pi^0},\quad)}{\sqrt{2}}\frac{\Delta E_\gamma}{E_\gamma}, \tag{2.11}$$

because the contribution from $\Delta\eta$ is negligible ($\leq 0.5°$) even at small distances or high energies.

The energy and angular resolution corresponding to the spectrometer geometry used in experiment E1179 are shown as a function of π^0 energy in Figure 2.19.

An improved instrument called the Neutral Meson Spectrometer (NMS) has been built recently at LAMPF [Bou-89]. It will become available for routine use in 1993.

E. π^0 Spectrometer Electronics and Software

The raw hardware trigger for a neutral pion is designed to select coincident gamma events in two spectrometer crates. A gamma event in one spectrometer arm is defined by the logic condition

$$\Gamma_9 = (S_1 + S_2 + S_3) \times \bar{V} \times \sum_{i,j}(C_i + B_j), \tag{2.12}$$

corresponding to a signal in at least one scintillator plane S_i, the absence of the veto signal V, and the summed signals in converters C_i and blocks B_j exceeding threshold level.

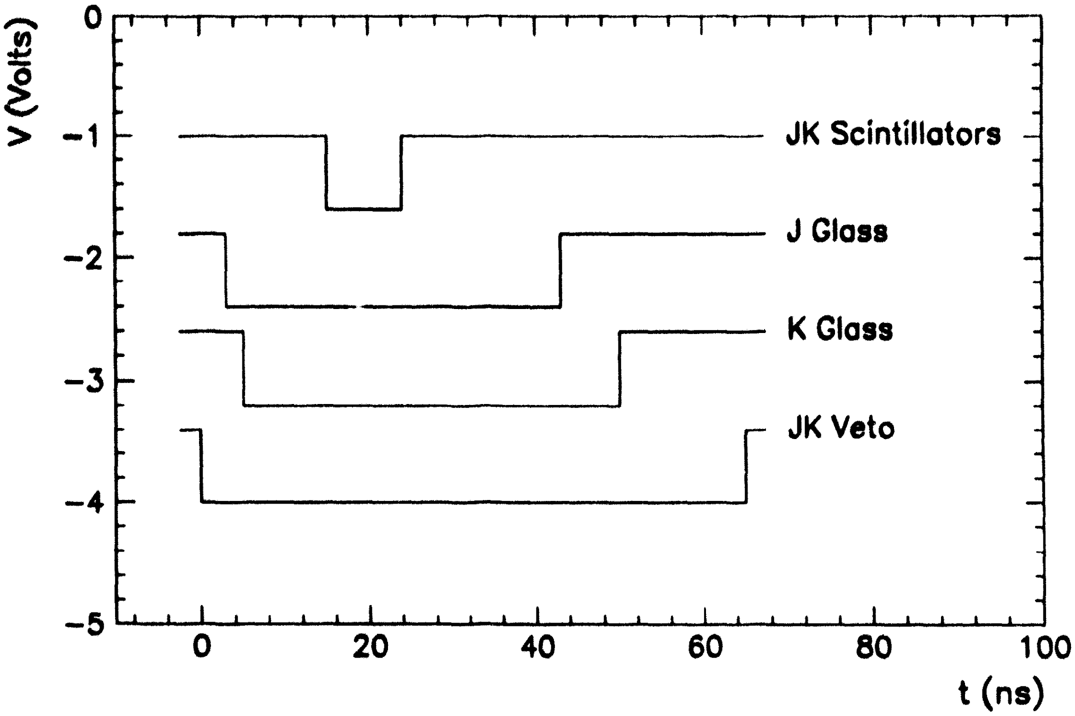

Figure 2.46 The π^0 event timing is determined by the coincidence between two spectrometer crate scintillator tags. The MWPC's are not in the trigger. The charged particle hardware veto thresholds were set at approximately one third of minimum ionizing peak.

Analog signals of the photomultiplier tubes (PMT) coupled to the plastic and Čerenkov detectors are amplified tenfold before being split and discriminated. The Čerenkov signals are first summed in linear fan-in modules and subsequently discriminated in constant fraction discriminators with thresholds set to ~20 MeV. That discrimination level suppresed the low-energy background events that would otherwise dominate the rate.

A good π^0 is defined as a fast logical AND of two coincident Γ events provided that the secondary beam is present, the computer is not busy and the manual run switch is turned on:

$$\mathrm{EVENT\ 9} = \mathrm{BEAM} \times \mathrm{SWITCH} \times \overline{\mathrm{COMPUTER\ BUSY}} \times \Gamma_J \times \Gamma_K, \qquad (2.13)$$

Schematic diagrams detailing the spectrometer NIM and CAMAC electronics logic and interfacing are provided on the pages 38-44, in Figures 2.20-2.45.

The link between the external trigger (2.13) and the data acquisition system is provided by a LAMPF event trigger module which resides in the CAMAC crate. The module supports 32 different trigger inputs, eight of which can be set by the external NIM or CAMAC signal [Koz-89].

We used the standard LAMPF Q data acquisition program loaded into a microprogrammable branch driver (MBD) connected to a Micro-VAX computer [Oot-85]. The Q system is general-purpose software that provides a set of facilities to control a typical data acquisition and replay system supplemented by the histogramming (`HPL`) and test (`TSU`) packages. [Oot-89] [Amm-88]. All Q tasks share a common region created dynamically at run time in memory and can use a general parameter array system (`PRM`) that maintains a set of integer and real parameters defined and modifiable by user programs. [And-85] [And-89].

The Q Acquisition Language and compiler (`QAL`) were used to define the layout of electronics modules in CAMAC system and specify the CAMAC operations to be executed for each event following the trigger module signal. The raw data buffers were passed to user processing subroutines (`PROCs`) where there were padded with calculated user data words and taped subsequently on 1600-bpi (1990 and 1991) and 8-mm magnetic tapes (1992 runs). The events that were defined in Q analyzer and enabled in Trigger Module were:

- EVENT 4—scaler event, triggered every 4 seconds reads 84 π^0 and 84 charged particle scalers, writes every event to tape, and keeps the running sums in the region.
- EVENT 5—stabilization event active during the beam-off and no-beam intervals. The `PROC5` subroutine establishes that just one timing group (see Figure 2.23) in one arm fired above the software threshold and then enters the ADC data for each converter and block element in the group into the `STABLE` histogram. If the number of the counts in the histogram is above the preset limit (10^5) the `ANLLST` program analyzes the data by comparing it with the reference spectra, calculates the gains, writes the results to the tape and updates the gain parameters in the dynamic memory region.

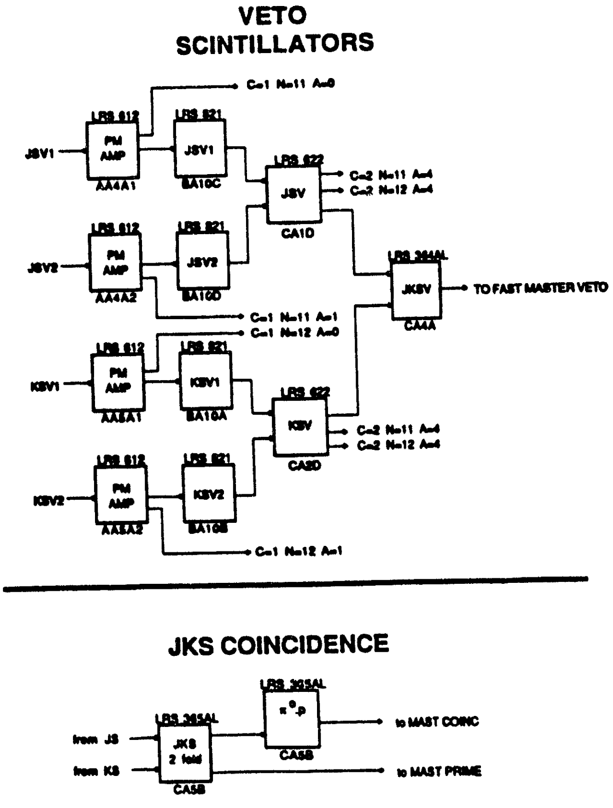

Figure 2.20

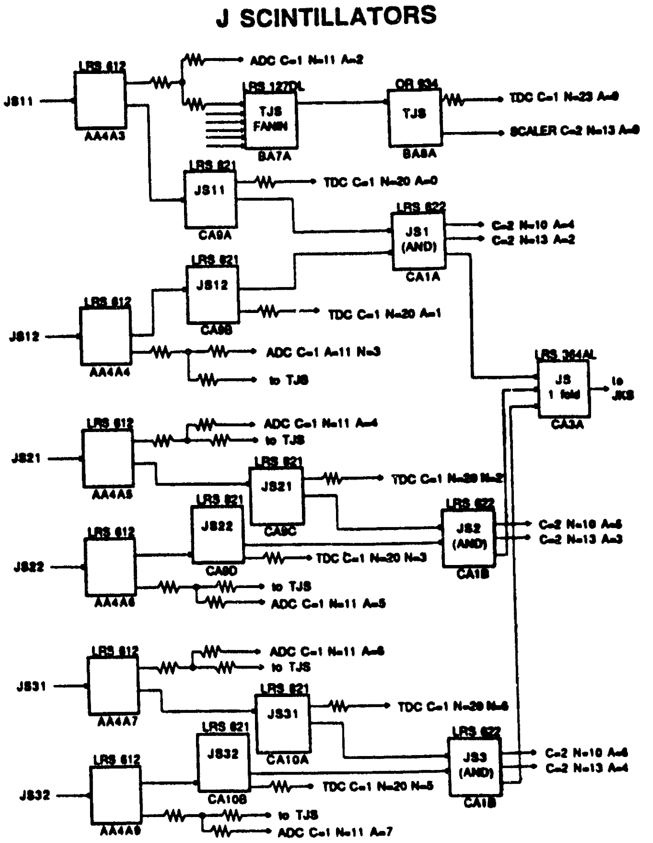

Figure 2.21

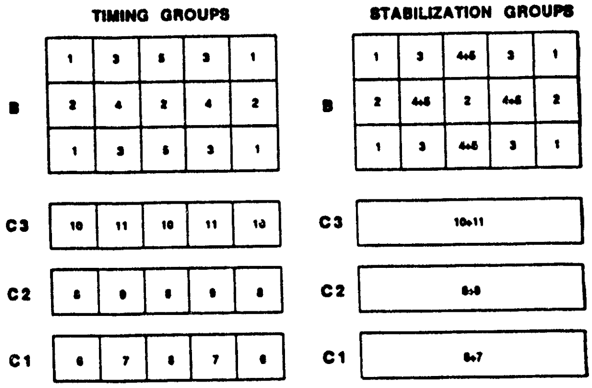

TIMING GROUPS

	1	3	5	3	1
B	2	4	2	4	2
	1	3	5	3	1
C3	10	11	10	11	10
C2	8	9	8	9	8
C1	6	7	6	7	6

STABILIZATION GROUPS

	1	3	4+5	3	1
B	2	4+5	2	4+5	2
	1	3	4+5	3	1
C3	10+11				
C2	8+9				
C1	6+7				

Figure 2.22

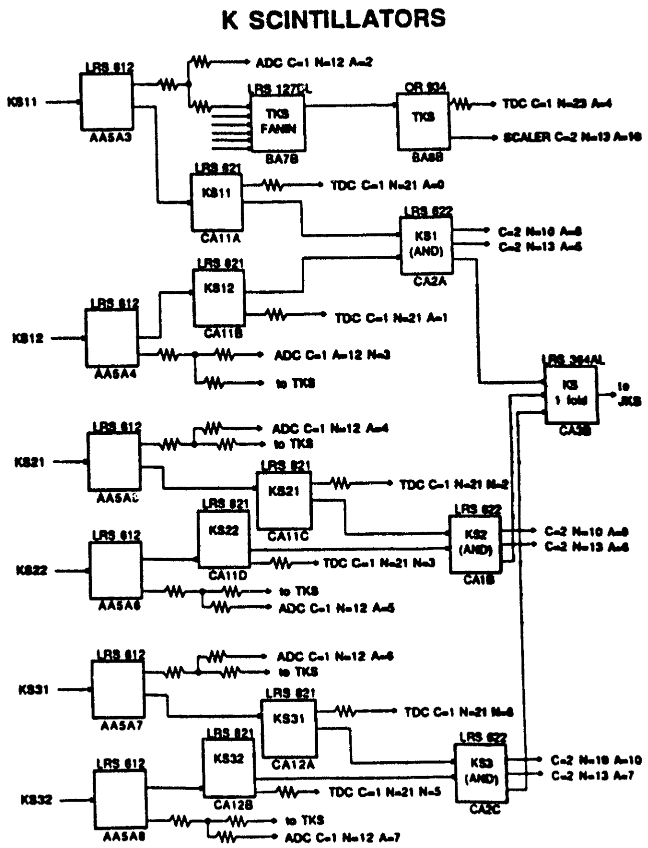

Figure 2.23

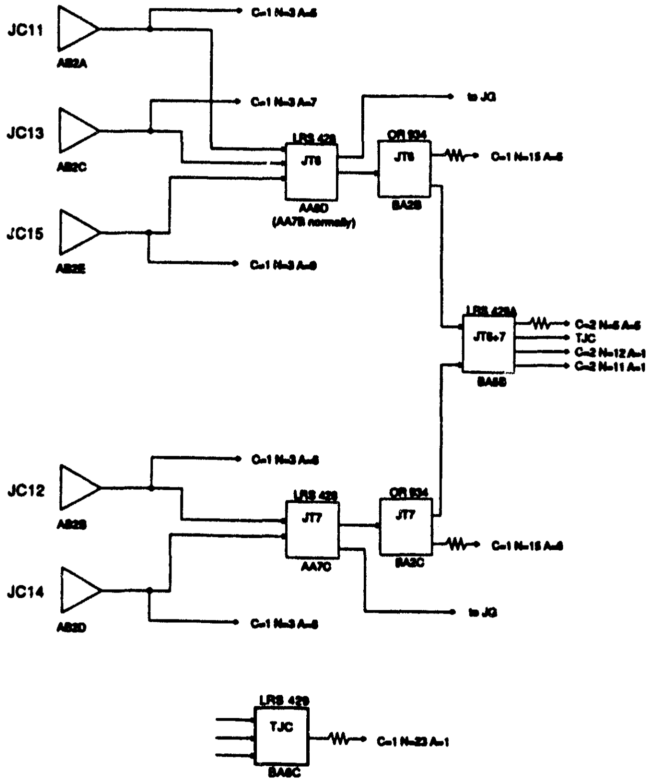

Figure 2.24

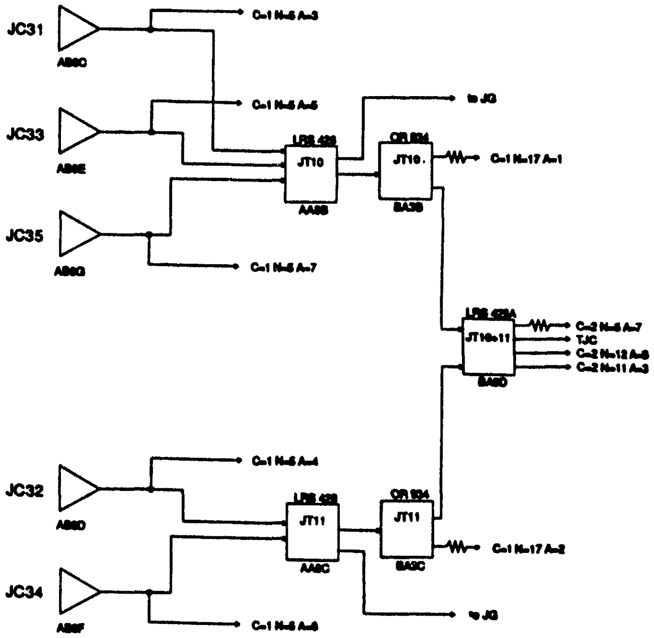

Figure 2.25

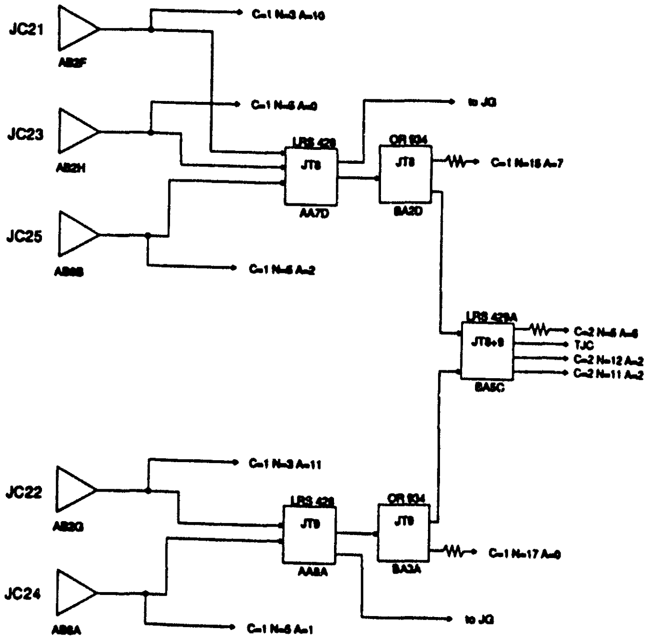

Figure 2.26

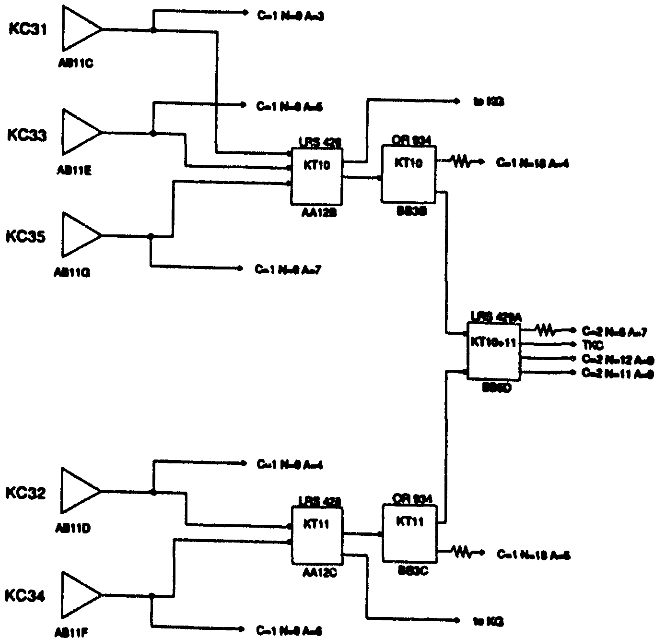

Figure 2.27

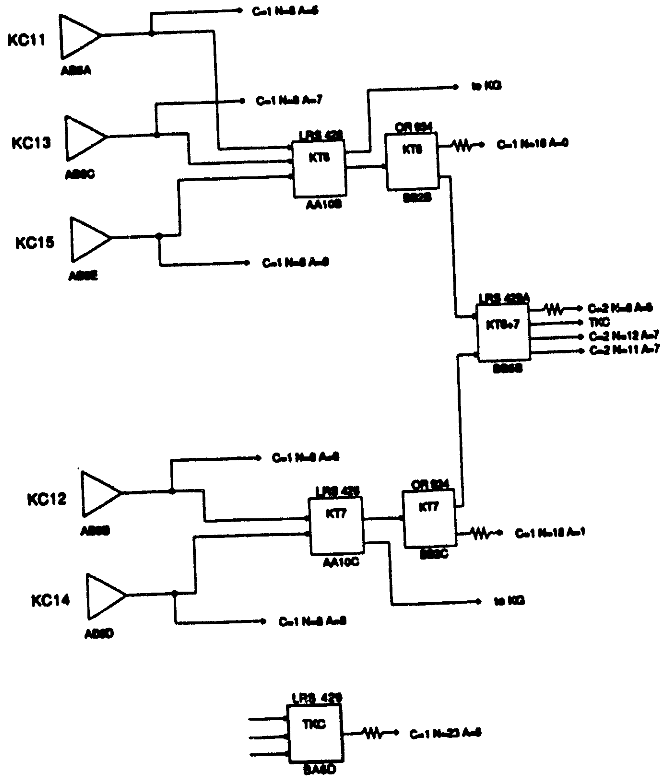

Figure 2.28

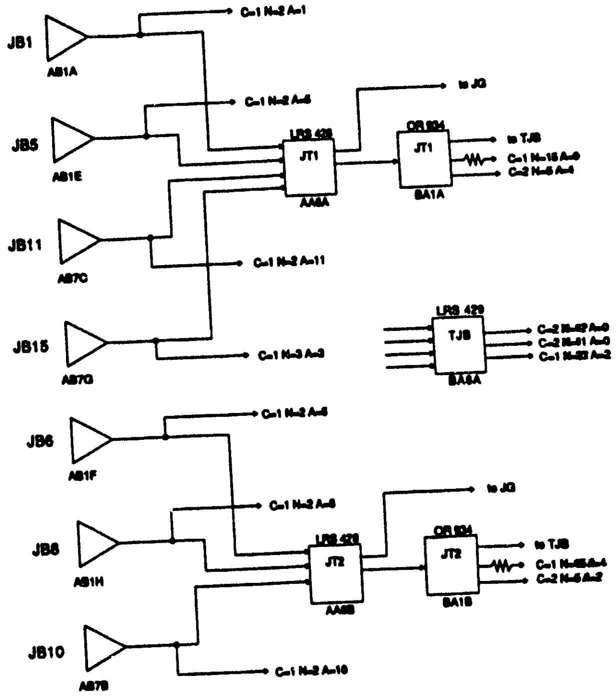

Figure 2.29

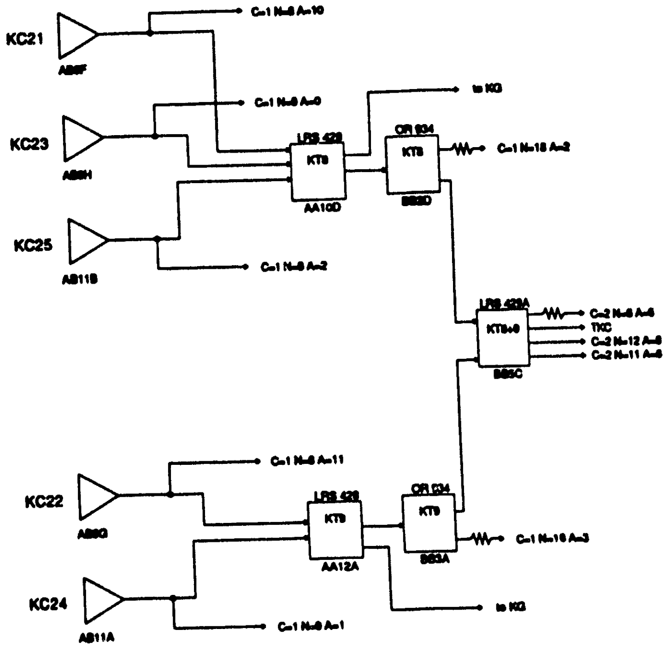

Figure 2.30

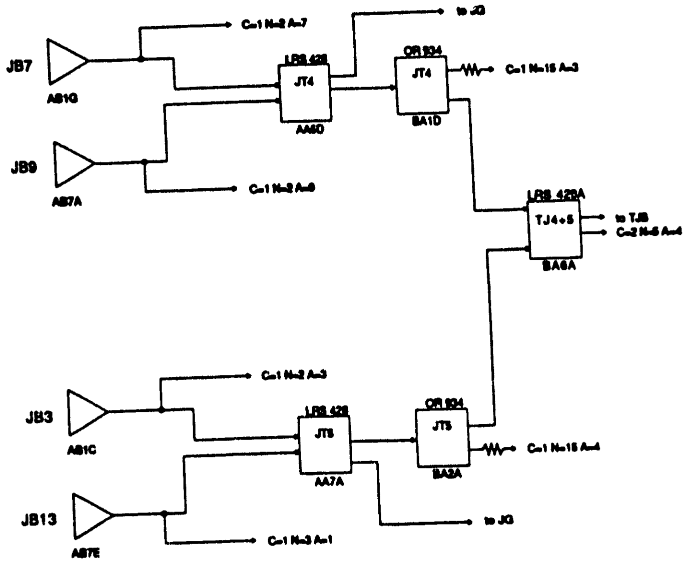

Figure 2.31

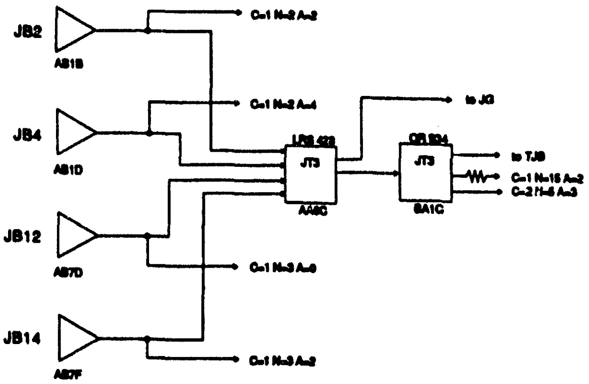

Figure 2.32

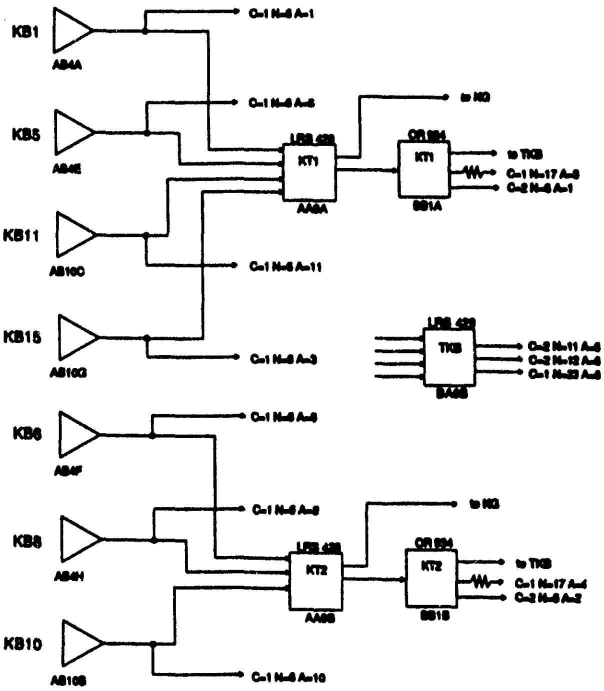

Figure 2.33

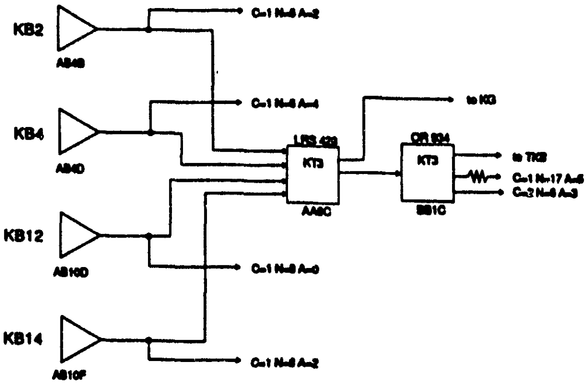

Figure 2.34

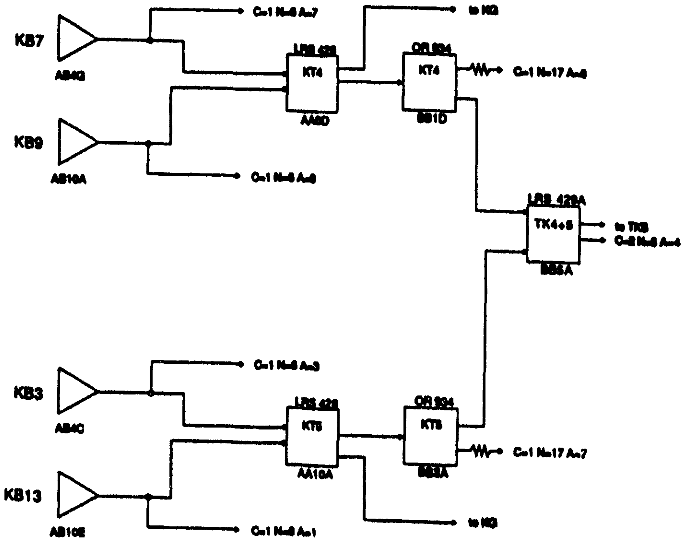

Figure 2.35

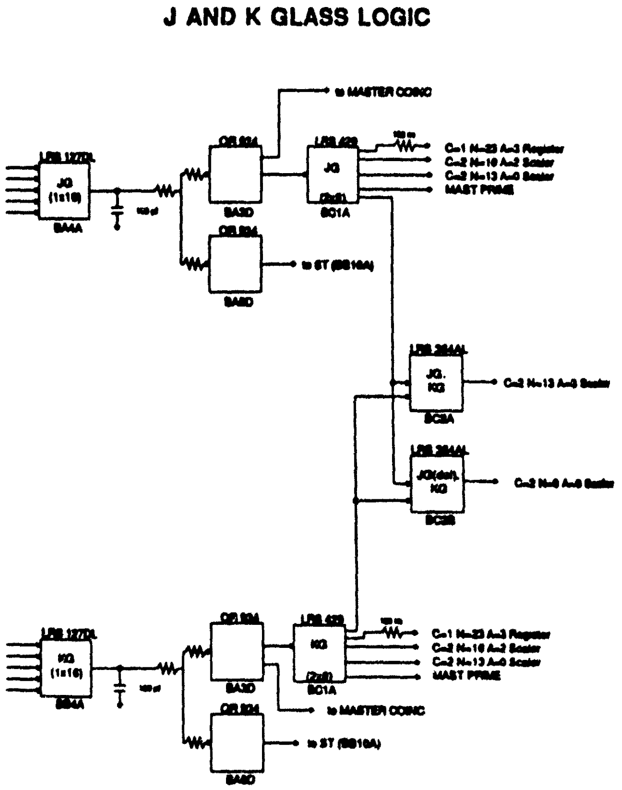

Figure 2.36

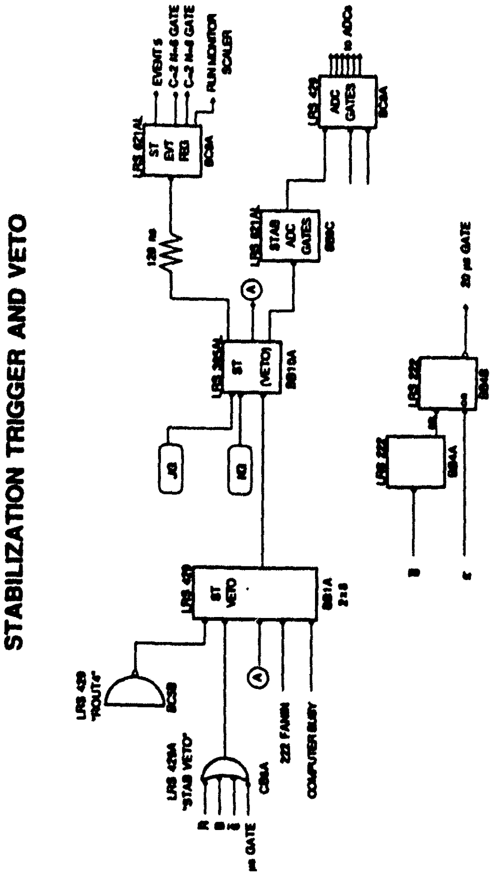

Figure 2.37

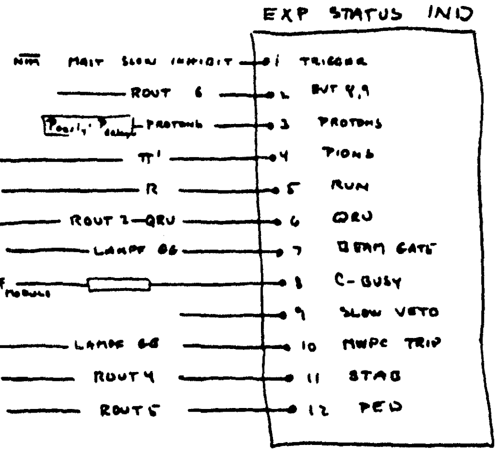

Figure 2.38

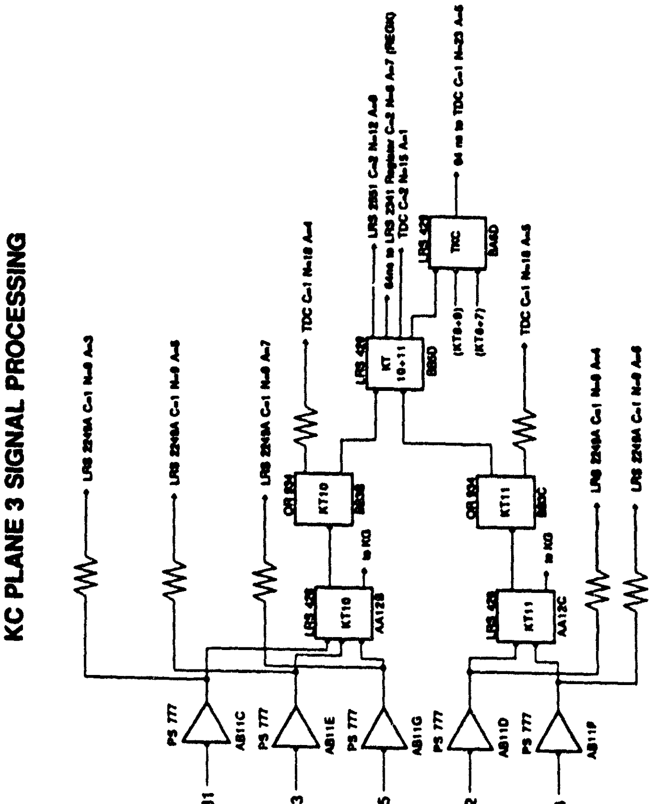

Figure 2.39

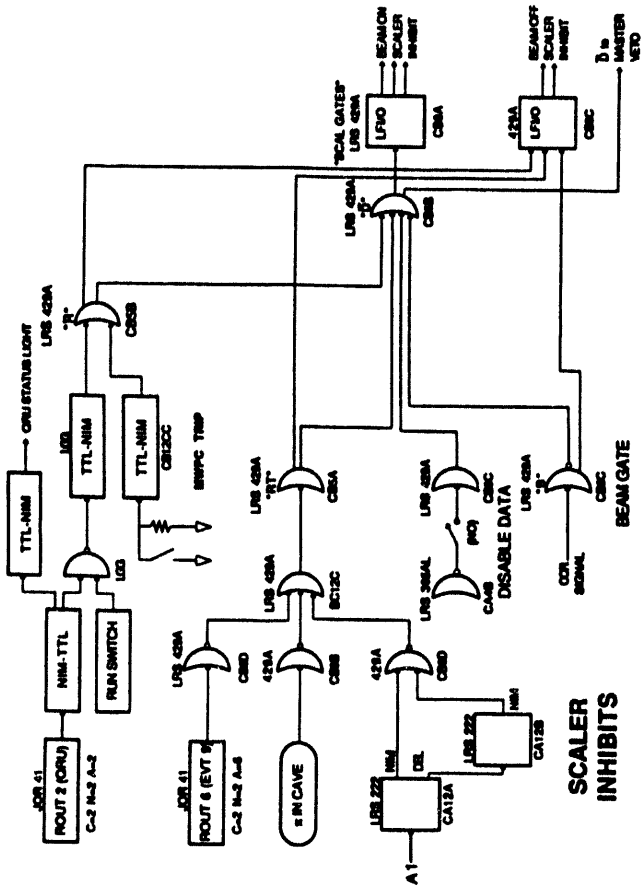

Figure 2.40

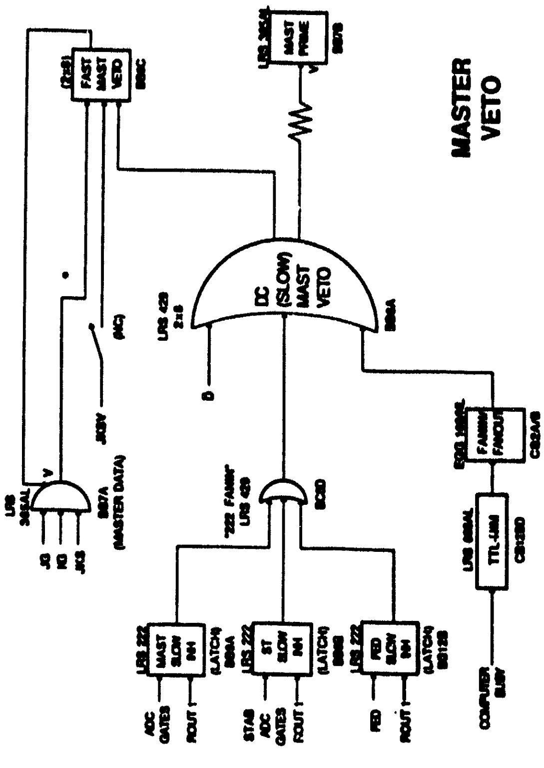

Figure 2.41

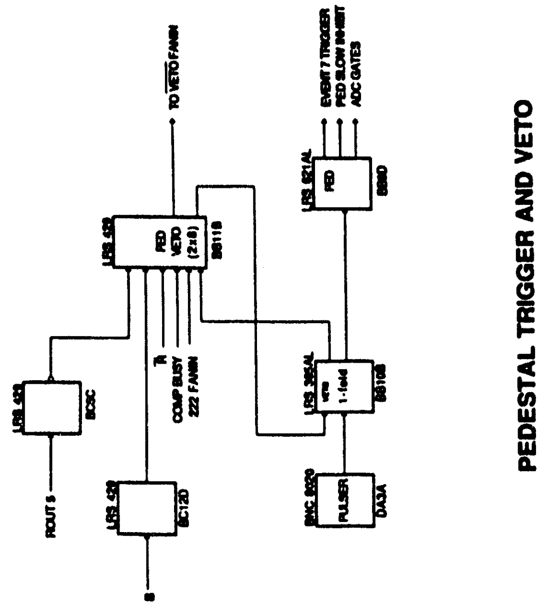

Figure 2.42

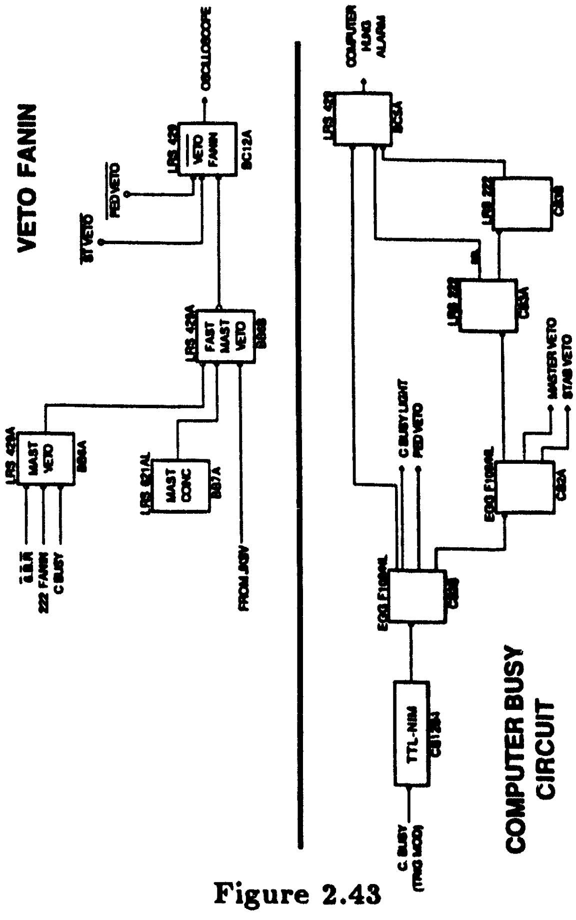

Figure 2.43

Figure 2.45

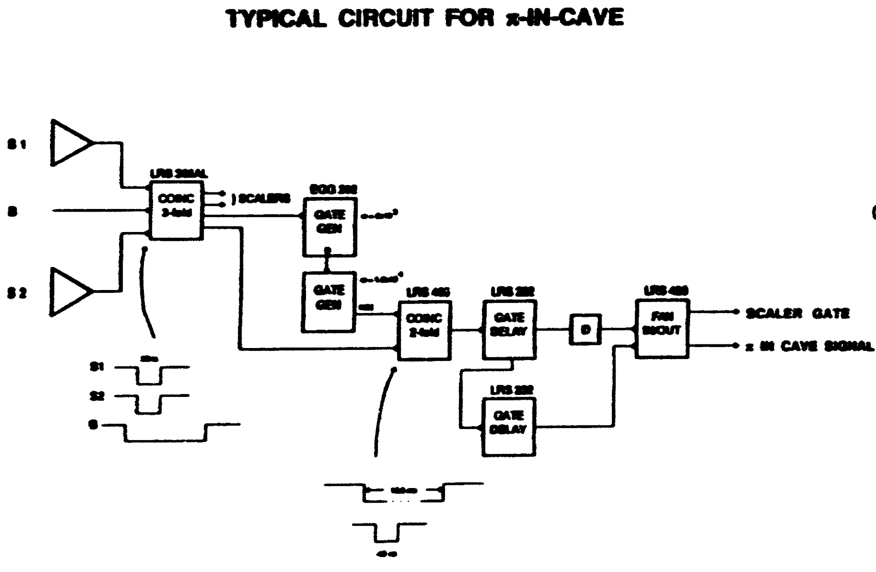

Figure 2.44

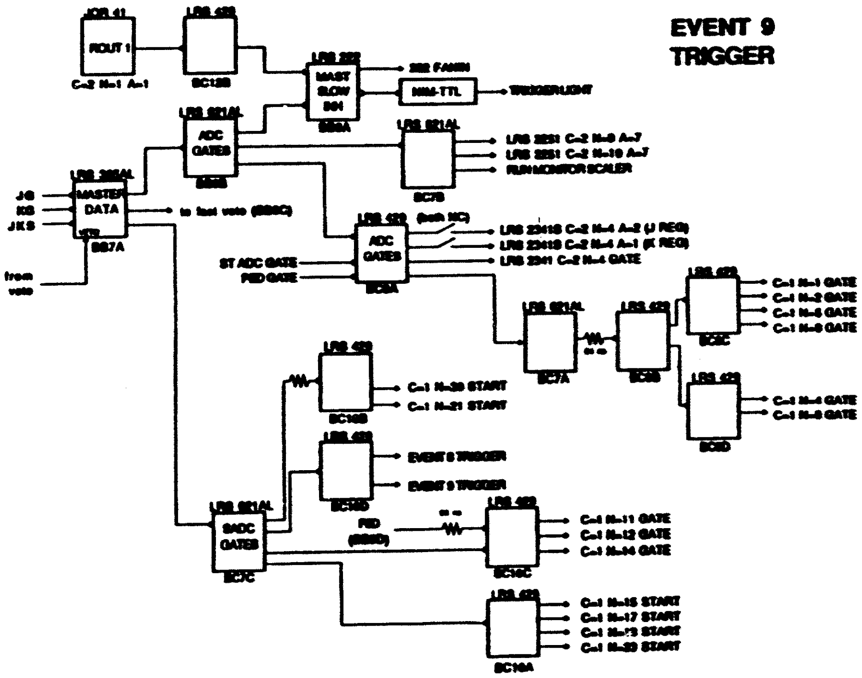

Figures 2.20-2.45 A Shematic diagrams of π^0 spectrometer electronics logic [Knu-89]. The whole spectrometer data aquisition is organized into four standard 19-inch cabinets. The positions of the NIM input and output signals are labeled with the rack name (A,B,C,D), NIM bin code (A,B,C,D), module station number (1-25), and module channel location (A,B,C,...). The CAMAC electronics is set up in three CAMAC crates designated with C=1 (2,3). The input CAMAC analog and digital signals are associated with the crate slots (N=1-25) and module addresses (A=1,2,3, ...). For example, the fan-in/fan-out unit labelled as BA6A can by find in second rack, sixth station of the top NIM crate and uses the first section of quad LeCroy 429A model. The diagrams are logically organized starting from the spectrometer charged particle veto signals and moving to the J and K scintillators, convertor planes and lead glass blocks, pedestal, stablization and master veto logic and concluding with formation of hardware EVENT 9.

- EVENT 6—single charge particle (CP) event or logically orthogonal π^0·CP coincidence.
- EVENT 7—pedestal event, that is triggered at the beginning of every run and then runs periodically in predefined (1 hour) intervals. The `PROC7` routine accumulates the data from 60 π^0 and 66 CP ADCs until `PEDLST` program is activated, which averages the data and calculates the new pedestal values.
- EVENT 9—hardware π^0 event, consisting of up to 256 words of information summarizing the ADC and TDC addresses of all 60 active spectrometer detectors in addition to the MWPC information and scaler data.

F. π^0 Spectrometer Timing

The relative timing of the scintillator, converter and lead glass block elements were adjusted using cosmic rays by turning on one PMT at a time. The adjustments were made by changing the lengths of the signal cables. The scintillator TDC spectra were adjusted relative to one another with a spread of less than ±1 ns, and the glass detectors within ±2 ns.

The two spectrometer arms were timed relative to each other usind a pion beam and real γ-γ coincidence. The uncorrected software timing of the π^0 events, $t^r_{\pi^0}$, was defined as the difference of TDC readings for two scintillator planes behind the showering converters. Coordinates of gamma ray conversions $x_{J(K)}$, $y_{J(K)}$, $z_{J(K)}$ in J (K) arm are available on line so that the geometrical time-of-flight correction for both photons could be applied in software. Corrections for propagation time of the light in the tagging scintillators improve the instrumental timing resolution. Cosmic ray calibration runs were used in replay to determine the coefficients of the relationship between $t^c_{\pi^0}$ and $t^r_{\pi^0}$ by minimizing $\chi^2 = \sum(t^r_{\pi^0} - t^c_{\pi^0})^2$ using `MINUIT` [Jam-89a]. The result

$$t^c_{\pi^0} = t^r_{\pi^0} - 0.04 \times \sqrt{x_J^2 + (y_J + 90)^2} + 0.04 \times \sqrt{x_K^2 + (y_K - 90)^2} + 0.148, \qquad (2.14)$$

is easy to interpret: constants multiplying the square roots are close to the speed of scintillation light propagation in the plastic scintillator detectors (c/n_r), while the y offset is related to the PMT positions in the local coordinate frame of the crate.

G. Calibration of the π^0 Spectrometer Efficiency

The π^0 spectrometer efficiency is one of the most sensitive ingredients in the overall normalization because of the complexity of the instrument. In the past, the spectrometer

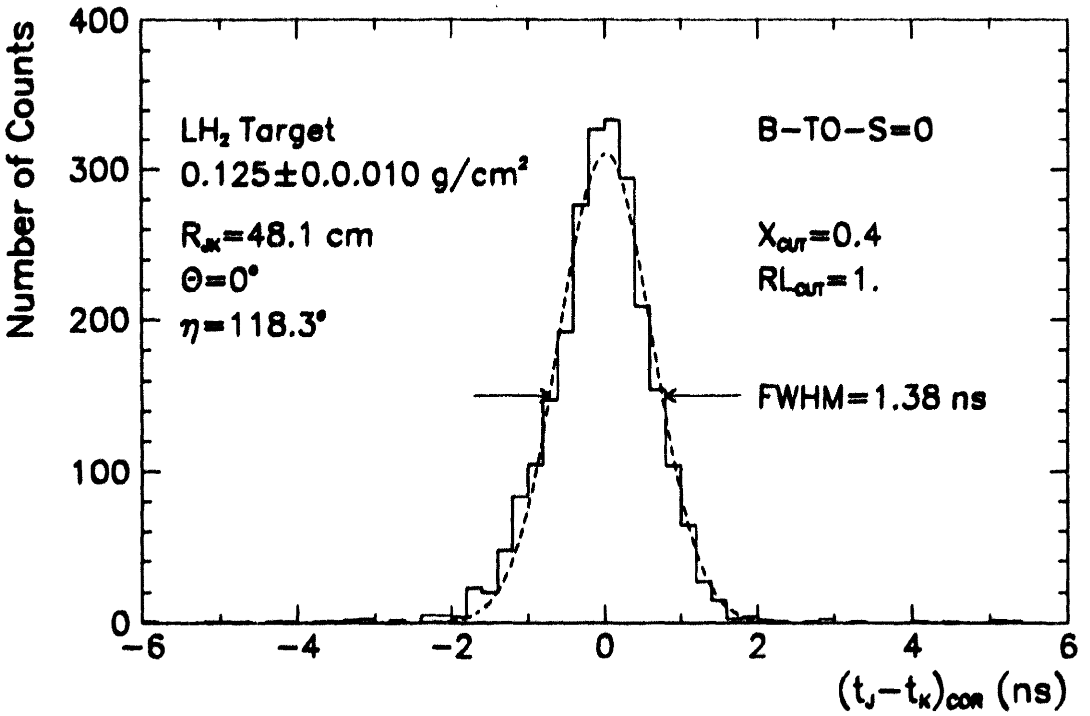

Figure 2.47 Inclusive π^0 timing for SCX with LH_2 target at 30 MeV. The TDC hits of J and K gammas in scintillator planes were corrected for trivial time-of-flight interval between target and the conversion points as well as for light propagation delay in scintillators. The best FWHM resolution achieved was 1.40 ns.

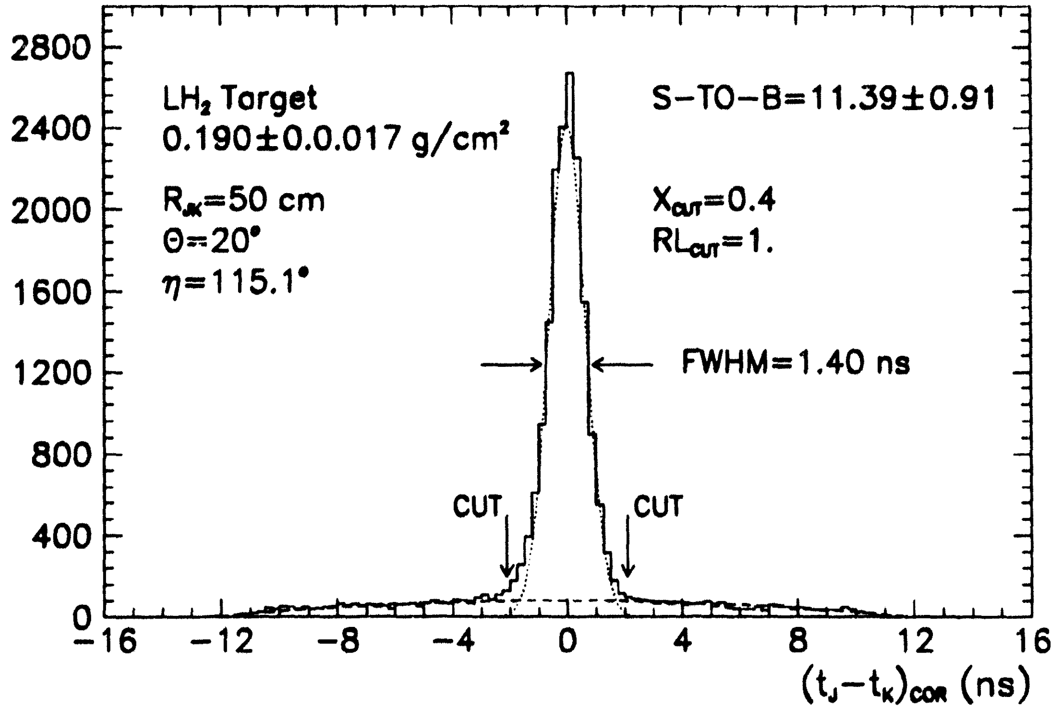

Figure 2.48 Inclusive π^0 timing with LH_2 target and 260 MeV π^+ beam. The signal-to-background ratio in the inclusive arm can be deduced from accidental out-of-time events.

instrumental efficiency was calibrated to 1% accuracy at 522 MeV by Gaille *et al.* [Gai-84] [McF-85].

One of the goals of the experiment E1179 was an calibration of the π^0 spectrometer efficiency. Cosmic ray calibration runs were used to measure directly the intrinsic instrumental efficiencies of the lead glass and plastic scintillator elements and MWPC's. The trigger logic was appropriately reconfigured, software limits removed and all events were taped. J and K arm calibrations were performed separately. Each run collected $\geq 10^5$ cosmic ray events ensuring a ~0.3% statistical uncertainty in the deduced efficiencies. The most constraining trigger logic condition was set to measure the intrinsic MWPC chamber efficiency:

$$V \times S1 \times S2 \times S3 \times B, \tag{2.15}$$

with the coincident hits in veto, all three scintillator planes and the glass blocks required.

Table 2.6 1991 π^0 spectrometer MWP efficiencies: the independent J and K cosmic ray calibration runs were done with the trigger logic requirement V × S1 × S2 × S3 × GB. Average values of instrumental chamber efficiencies for each crate and and their spread is also tabulated.

MWPC Name	no hits	One Wire	Two Wires	Three Wires	Four Wires	> 4 Wires	Percentage of Hot Wires	Intrinsic Efficiency
MJ1X	6.31	81.76	8.36	2.08	0.71	0.78	1.04	94.73
MJ1Y	6.65	82.64	8.13	1.62	0.49	0.47	0.00	93.35
MJ1XP	4.61	86.25	7.08	1.67	0.60	0.35	0.00	95.39
MJ2X	3.79	80.46	11.37	2.55	0.86	0.97	0.52	96.73
MJ2Y	3.33	86.06	7.89	1.74	0.51	0.46	0.00	96.67
MJ2XP	3.45	85.81	7.50	1.81	0.66	0.77	0.00	96.55
MJ3X	4.63	82.42	8.86	2.31	0.78	1.00	1.04	96.41
MJ3Y	5.49	83.44	8.43	1.71	0.53	0.40	0.00	94.51
MJ3XP	8.75	80.86	7.58	1.60	0.57	0.63	0.52	91.77
J Crate	5.22	83.30	8.36	1.90	0.63	0.65	0.35	95.1 ± 1.7
MK1X	4.12	83.76	8.72	2.29	0.81	0.90	1.04	96.92
MK1Y	5.39	82.57	8.93	2.00	0.81	0.30	0.00	94.61
MK1XP	4.38	83.30	8.45	2.20	0.73	1.12	0.52	95.87
MK2X	2.06	84.88	8.89	2.28	0.83	1.06	0.52	98.46
MK2Y	6.06	82.31	8.49	1.94	0.62	0.58	0.00	93.94
MK2XP	2.35	82.51	11.42	2.17	0.78	0.77	0.52	98.17
MK3X	2.63	84.05	9.01	2.36	0.88	1.07	0.00	97.37
MK3Y	3.12	85.75	8.40	1.71	0.51	0.51	0.00	96.88
MK3XP	8.36	81.31	7.43	1.71	0.56	0.63	1.04	92.68
K Crate	4.27	83.38	8.86	2.05	0.73	0.71	0.40	96.1 ± 2.0
J& K	4.75	83.34	8.61	1.98	0.68	0.68	0.38	95.6 ± 2.6

The veto and scintillator efficiencies were determined with triggers of the types:

$$\mathrm{S1} \times \mathrm{S3}, \text{ and } \mathrm{V1} \times \mathrm{B}, \tag{2.16}$$

where in the first case the fiducial area was restricted using MWPC information to constrain the geometrical path of the cosmic rays through the veto plane. The 1991 calibration data are summarized in Tables 2.6 and 2.8. The results of 1992 cosmic ray measurements reported in Tables 2.7 and 2.8 remain consistent. The average MWPC chamber efficiency was 95.6% in 1991 and 94.4% in 1992. The numbers are changed sligthly when weighted with the theoretical conversion probabilities for particular conversion plane pair to 95.6% and 94.6%. The weighted veto and scintillator efficiencies were measured to be 96.9% and 96.1%, respectively.

The "analyzed" fraction η_a, defined as a ratio of the number of π^0 triggers to **MTSJKC**, the number of "analyzable" events with good wire chamber information can be understand entirely in terms of instrumental MWPC efficiencies. Over the period of experiment, for each individual run, η_a was equal within the statistical uncertainty to the appropriately weighted product of six intrinsic chamber efficiencies (compare Tables 2.6, 2.7 and 3.1).

The overall spectrometer π^0 detection efficiency ϵ_{π^0} can be decomposed into a product of individual efficiencies

$$\epsilon_{\pi^0} = \epsilon_{\pi^0}^{jk} \epsilon_m \epsilon_{ct} \epsilon_s \epsilon_t \epsilon_b, \tag{2.17}$$

where $\epsilon_{\pi^0}^{jk}$ is the coincident $\gamma\gamma$ conversion probability in the J and K arms, ϵ_m is the properly weighted MWP chamber efficiency, ϵ_{ct} is the converter transparency for charged showers, ϵ_b is a correction due to the shower backsplash, ϵ_s is the weighted scintillator efficiency and ϵ_t represents the tracking algorithm efficiency for a good neutral pion.

The π^0 conversion probability $\epsilon_{\pi^0}^{jk}$ is a function of the single converter plane conversion probability ϵ_c^γ:

$$\epsilon_{\pi^0}^{jk} = [1 - (1 - \epsilon_c^\gamma)^3]^2. \tag{2.18}$$

The quantity ϵ_c^γ is extracted in the off-line analysis of pion single charge exchange events which pass all the hardware trigger logic requirements. The accepted events at 8 different incident $\pi^\pm$ energies all involve detection of coincident γ-γ pairs with $E_\gamma \sim 90$ MeV. The conversion planes were tabulated in 3×3 matrices for each event. The entries in the matrix correspond to the number of good conversions in a given pair of J and K-arm converter planes. The effective solid angles s_i of the three scintillator planes in an arm were in the ratio 1 : 0.9876 : 0.9792. The solid angle coverage of a scintillator pair is $s_{ij} = s_i s_j$. The efficiency ϵ_c is then calculated in a simultaneous fit to all nine matrix elements. The results

Table 2.7 1992 π^0 spectrometer MWPC efficiencies: the independent J and K cosmic ray calibration runs were done with the trigger logic requirement V × S1 × S2 × S3 × GB.

MWPC Name	no hits	One Wire	Two Wires	Three Wires	Four Wires	> 4 Wires	Percentage of Hot Wires	Intrinsic Efficiency
MJ1X	5.74	82.76	8.14	2.10	0.69	0.57	1.04	92.65
MJ1Y	5.34	84.79	7.40	1.56	0.47	0.44	0.00	94.22
MJ1XP	3.92	86.68	7.02	1.61	0.60	0.17	0.00	95.91
MJ2X	3.40	83.09	9.36	2.42	0.79	0.94	0.00	95.66
MJ2Y	3.04	86.29	7.83	1.78	0.56	0.50	0.00	96.46
MJ2XP	5.49	82.79	7.93	1.96	0.82	1.01	0.00	93.50
MJ3X	4.46	82.68	8.67	2.25	0.85	1.09	1.04	93.41
MJ3Y	5.21	84.77	7.47	1.64	0.51	0.40	0.00	94.39
MJ3XP	5.12	81.52	7.02	1.58	0.54	0.69	0.52	90.14
J Crate	4.64	83.93	7.87	1.88	0.65	0.65	0.29	94.0 ± 1.9
MK1X	3.21	83.64	8.94	2.33	0.86	1.02	0.00	95.77
MK1Y	4.33	84.20	8.43	1.90	0.60	0.54	0.00	95.13
MK1XP	3.07	85.46	7.73	1.84	0.79	1.11	0.52	95.30
MK2X	2.15	85.05	8.67	2.23	0.86	1.04	0.52	96.29
MK2Y	4.55	84.07	8.20	1.97	0.63	0.58	0.00	94.87
MK2XP	2.40	85.55	8.55	1.90	0.71	0.89	0.52	96.19
MK3X	3.43	83.59	8.73	2.21	0.89	1.15	2.08	93.34
MK3Y	3.07	86.14	8.03	1.72	0.53	0.51	0.00	96.42
MK3XP	8.25	78.58	9.77	2.06	0.68	0.66	1.56	89.53
K Crate	3.83	84.03	8.56	2.02	0.73	0.33	0.58	94.8 ± 2.2
J & K	4.24	83.98	82.15	1.95	0.69	0.49	0.44	94.4 ± 2.1

Table 2.8 1991 and 1992 π^0 spectrometer scintilator efficiencies. The trigger logic requirement for the cosmic ray calibration runs was V × S1 × S3 in 1991 and V × GB in 1992.

Scintilator Name	1991 Efficiency (%)	1992 Efficiency (%)
JSA1	-	96.99
JSA2	-	97.04
JSA3	95.47	96.15
JSA4	95.51	96.01
JSA5	-	95.85
JSA6	-	95.66
KSA1	-	95.23
KSA2	-	96.57
KSA3	97.19	96.34
KSA4	97.09	96.34
KSA5	-	96.62
KSA6	-	96.56

Table 2.9 π^0 conversion efficiencies for 1991 run: the extracted single-plane conversion probability is $\bar{\epsilon}_c^\gamma = 0.272 \pm 0.011$ while the theoretical prediction gives $\epsilon_{th}^\gamma = 0.279 \pm 0.003$.

T_π (MeV)	−30	160	180	190
ϵ_c^γ	0.305 ± 0.057	0.286 ± 0.036	0.259 ± 0.020	0.259 ± 0.033
T_π (MeV)	200	220	240	260
ϵ_c^γ	0.259 ± 0.026	0.276 ± 0.052	0.260 ± 0.064	0.302 ± 0.027

Table 2.10 π^0 conversion efficiencies for 1992 run. The example of the conversion matrix for the 260 MeV LH_2 runs is shown. The effective solid angle extended by the ij scintillator pair is s_{ij}. The average conversion probability of ~ 90 MeV photon is $\bar{\epsilon}_c^\gamma = 0.292 \pm 0.020$. The theoretical value calculated from the photon interaction probability tables [Hub-70] is $\epsilon_{th}^\gamma = 0.279 \pm 0.003$.

$$\begin{pmatrix} 4290 & 2988 & 2028 \\ 3395 & 2450 & 1536 \\ 2108 & 1420 & 980 \end{pmatrix} \propto \begin{pmatrix} \epsilon_c^2/s_{11} & (1-\epsilon_c)\epsilon_c^2/s_{12} & (1-\epsilon_c)^2\epsilon_c^2/s_{13} \\ (1-\epsilon_c)\epsilon_c^2/s_{21} & (1-\epsilon_c)^2\epsilon_c^2/s_{22} & (1-\epsilon_c)^3\epsilon_c^2/s_{23} \\ (1-\epsilon_c)^2\epsilon_c^2/s_{13} & (1-\epsilon_c)^3\epsilon_c^2/s_{23} & (1-\epsilon_c)^4\epsilon_c^2/s_{33} \end{pmatrix} \Rightarrow \epsilon_c = 0.31 \pm 0.05$$

T_π (MeV)	−30	160	190	200	220	240
ϵ_c	0.30 ± 0.07	0.28 ± 0.07	0.28 ± 0.05	0.29 ± 0.05	0.30 ± 0.05	0.28 ± 0.05

of the calculations for the 1991 and 1992 replay data are given in Tables 2.9 and 2.10 and displayed as in Fig. 1 together with all published measurements.

ϵ_c^γ have been previously determined semi-empirically by Baer *et al.* [Bae-80]:

$$\epsilon_c = 0.86[0.327 + 0.1\log(0.1E_\gamma(\text{MeV})], \tag{2.19}$$

based on Hubbel's [Hub-80] photon interaction probabilities and the known converter specifications. The factor 0.86 which does not appear in [Bae-80] reflects the reduced converter thickness of 2.4 cm from the original design value of 2.8 cm.

Properties of the Schott LF5 lead glass from which the converters are made have been taken from the original manufacturer's specification. Table 2.5 lists the material parameters that were required for the GEANT3 simulation.

Efficiency of the π^0 spectrometer shower tracking algorithm was extracted from the SCX runs at 30 MeV, after subtraction of the empty target and ^{12}C target backgrounds from

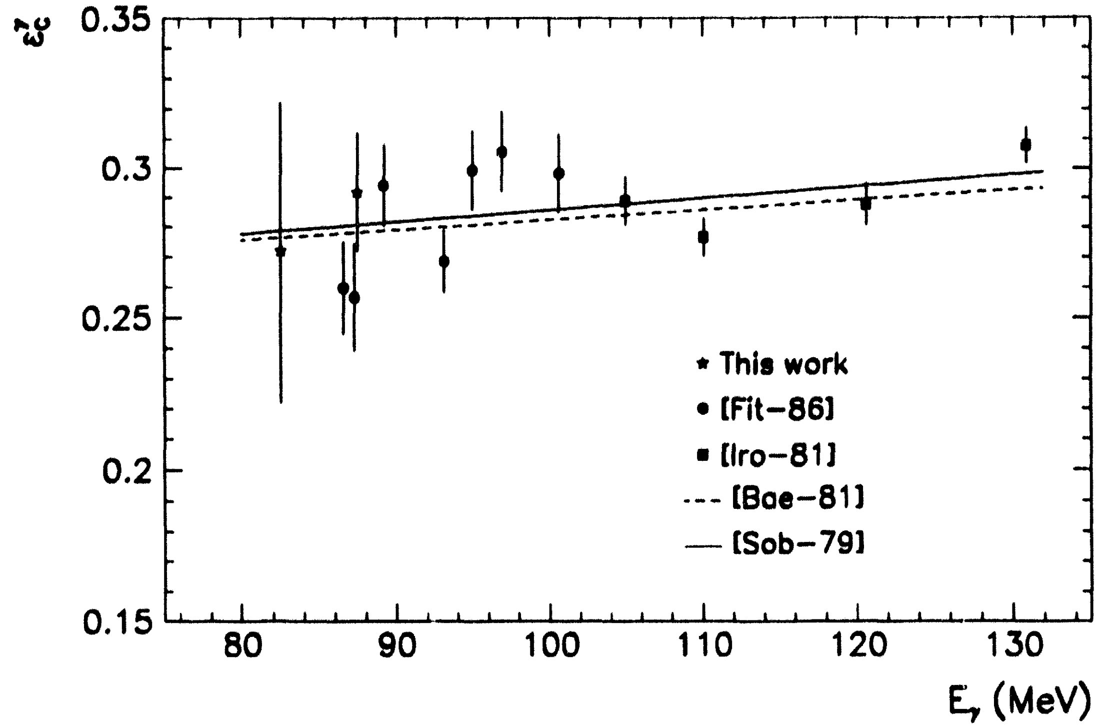

Figure 2.49 Single-plane gamma conversion efficiency for the π^0 spectrometer. The solid curve is a fit to a Monte Carlo calculation of [Bae-81] and the dashed curve is the result of a semiempirical calculation by Sober [Sob-79]. The E1179 experiment measured conversion efficiencies at 30 MeV and 160-260 MeV (full stars). Full circles represent the measurements in reference [Fit-86] while solid squares are data obtained by comparison of single charge exchange yields with cross sections from partial wave analysis [Iro-81].

the measurements with LH_2 and CH_2 targets respectively. Ratio of `TPICUT`, the number of events which survive all software cuts, to `MTSJKC`, the events that satisfy cuts for good MWPC hits inside predefined fiducial areas, is defined as tracking efficiency ϵ_t:

$$\epsilon_t = \frac{\mathtt{TPICUT} \times F_a}{\mathtt{MTSJKC}} = 0.76 \pm 0.02, \tag{2.20}$$

where F_a, the fiducial are fraction, was determined in the Monte Carlo simulation. The measured efficiency was constant for 1990, 1991 and 1992 data sets and averaged to 0.76 ± 0.02, Figure 2.50.

The instrumental and software aspects of π^0 detection in the spectrometer were studied in greater detail in a full-fledged `GEANT3` simulation (Figure 4.6). The Monte Carlo calculation reproduced 29% single-plane conversion efficiency. The event was counted as a "conversion" if a photon interacted in converter material by photoelectric effect, Compton scattering or pair production and generated secondary particles which deposited more than 1 MeV in the lead glass. The agreement between the measured and simulated probability assured us that the converter composition listed in Table 2.5 is appropriate.

Simulated showers converting into neutrals inside the converter or the ones that fail to provide the necessary tracking pulses in scintillators and wire-chamber planes have to be taken into account separately. Probability that π^0's γ's generated showers containing at least one detectable charged particle in the volume occupied by the follow-up MWPC's sandwich defined the converter transparency ϵ_{ct}. In high-statistics simulation ϵ_{ct} had a value of $5.6 \pm 0.2\%$ that should be compared with the early calculation and measurement of Gilad and collaborators [Gil-78] in Table 2.11. Their measurement of $7.6 \pm 0.5\%$ was done using the original 2.8 cm converters.

Of particular importance for the tracking efficiency are tests imposed **TRACER** routine in the analyzer which reconstruct the trajectory of the charged particles in the shower through a spectrometer arm. The routine returns a failure code in three different cases:

- the number of wires hit in X, Y, or X′ MWPC chamber following the predetermined converter plane is greater than a preset value (4),
- x and y coordinates of the wire hits fall outside a preset window (10×20 cm) whose center is calculated by weighting central coordinates of all calorimeter blocks with deposited energy exceeding 1 MeV,
- the slope parameter, defined as the smallest angle in the horizontal plane between the line connecting the conversion point to the target center and one of the lines through the hits in the X and X′ chambers exceeding the preset value of 17.1°.

These cuts were simulated in the **GUSTEP** subroutine of **GEANT** where shower particles were tracked through the experimental apparatus. The histograms that show the (dis)agreement between the measured and simulated spectra for total energy deposition in one arm, weighted calorimeter block centroids, the **TRACER** window cuts and **TRACER** slope cuts are shown in Figure 2.53. The tracking efficiency deduced from the number of simulated π^0 conversions that pass all cuts was 0.73 ± 0.05, where most of the uncertainty is due to the approximations involved in the Monte Carlo description. This uncertainty can be reduced further by performing a more refined Monte Carlo calculation which is planned for the future. In the present analysis the Monte Carlo result gives the independent confirmation of the measured result.

In summary, the over-all detection efficiency of the π^0 spectrometer was calibrated in the energy range below 100 MeV with 5% uncertainty, Table 2.12. The value of ϵ_{π^0} for our choice of adjustable analyzer cuts is 0.175. The general approach outlined in this section, however, can be followed to calculate the spectrometer detection efficiency for different set of applied tests and/or different π^0 energies. A goal of the work in progress is to tabulate

ϵ_{π^0} for commonly used analyzer versions and potentially rescale the results of previously published experiments.

Table 2.11 Multiplicity of charged particle prongs in MWPCs: experiment and simulation [Gil-79]. A tagged 100 MeV bremsstrahlung photon beam initiated electromagnetic showers in 0.6 radiation lengths Pb-glass converter. Uncorrected Monte Carlo results, as well as those corrected for finite geometry and MWPC efficiency are shown. The estimated systematic uncertainty of calculation is $\leq 5\%$.

No. of Charged Prongs	Calculated Percentage (%)	Calculated with Correction (%)	Measured Precentage (%)
0	1.3 ± 0.36	13.2 ± 1.2	7.4 ± 0.5
1	30.2 ± 1.7	52.5 ± 2.3	58.7 ± 1.5
2	60.7 ± 2.5	32.1 ± 1.8	30.8 ± 1.1
3	6.7 ± 0.8	2.2 ± 0.4	2.7 ± 0.3
4	1.1 ± 0.33	NA	0.2 ± 0.08

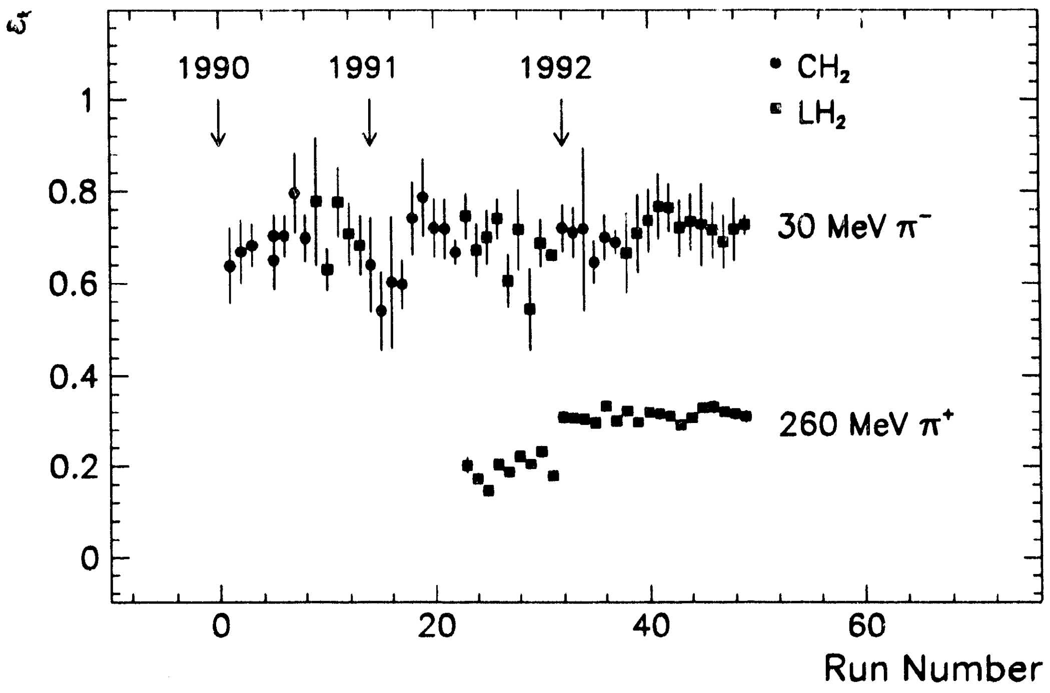

Figure 2.50 The variation of tracking efficiency ϵ_t for selected 1990, 1991, and 1992 runs. At 30 MeV where the π^0 background is negligible (signal-to-background in TOF spectra) ϵ_t is essentially constant. For the 160-260 MeV runs random background, single charge exchange reactions originating away from the target and misidentified pion-proton bremsstrahlung events decrease the tracking efficiency depending upon the shielding design.

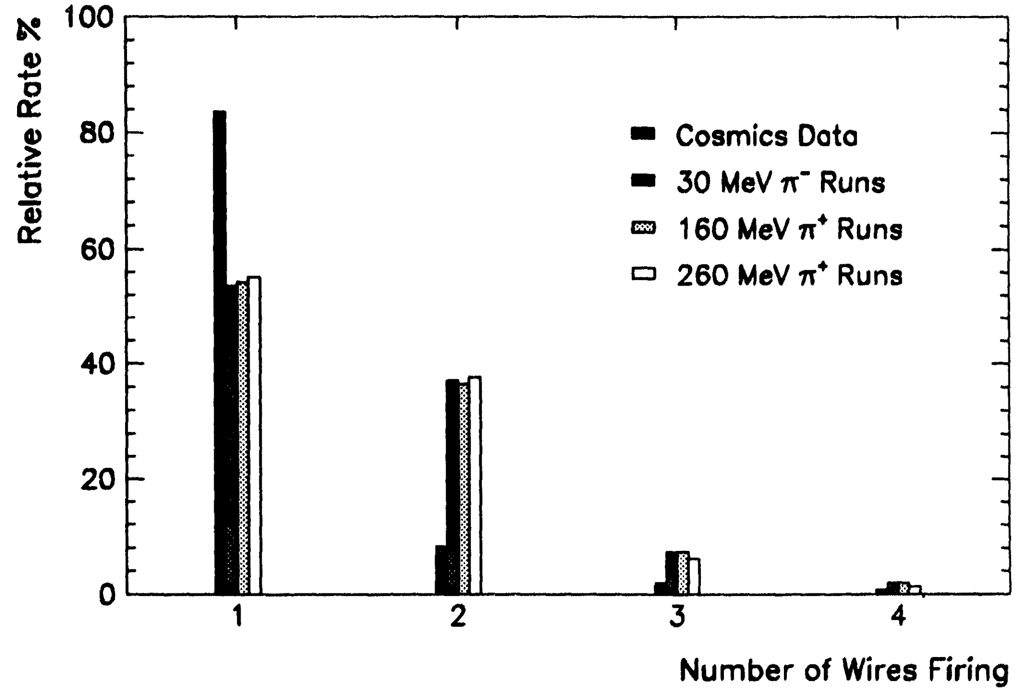

Figure 2.51 Distribution of the number of chamber wires firing for the cosmic minimum ionizing (MI) single muons and the raw EVENT 9 gammas showers at three different energies (30 MeV, 160 MeV, and 260 MeV) done with LH_2 target. Average rates of incident charged particles per crate were 10^2 s^{-1} in the cosmics run, 10^3 s^{-1} in 30 MeV and 10^4 s^{-1} for 160-260 MeV runs. It is evident that the distribution does not depend on the rate of π^0 triggers. From the comparison of the pion beam data with the cosmic ray data, using Poisson statistics, the average number of 1.37 ± 0.17 charged particles per one ~100 MeV gamma shower follows.

Table 2.12 Factors contributing to the π^0 detection efficiency: $\epsilon_{\pi^0} = 0.175 \pm 0.008$. The measurement of Gilad *et al.* [Gil-77] is scaled down for new thiner converters (2.86 → 2.46 cm) but corresponds to 100 MeV photons as compared to lower energy gammas in our simulation (87.5 MeV from 30 MeV neutral pions).

Symbol	Description	Method	Efficiency (%)	Stat/Syst Error (%)
ϵ_c^γ	single-plane detection efficiency	SCX π^0 detection	29.2	2.0
		[Hub-70] theory	27.9	1.0
ϵ_s	average scintillator efficiency	cosmics trigger	96.2	0.5
ϵ_v	average veto efficiency	cosmics trigger	97.0	0.5
ϵ_m	instrumental MWPC efficiency	cosmics trigger	95.6	0.2
$(1-f_v)^2$	CP vetoing efficiency	cosmics trigger	96.0	0.5
$(1-f_b)^2$	back-splash self-vetoing	GEANT3 code	99.4	0.2
$(1-f_p)^6$	max number of prongs cuts	cosmic ray trigger+SCX	92.39	1.0
		[Gil-79] thesis	91.4	2.0
$(1-f_d)^2$	TRACER shower window cuts	GEANT3 simulation	73.0	5.0
		SCX π^0 detection	76.0	2.0
$(1-f_{ct})^2$	MI $e^\pm$ converter transparency	GEANT3 simulation	88.9	0.4
		[Gil-77] experiment	87.6	1.0

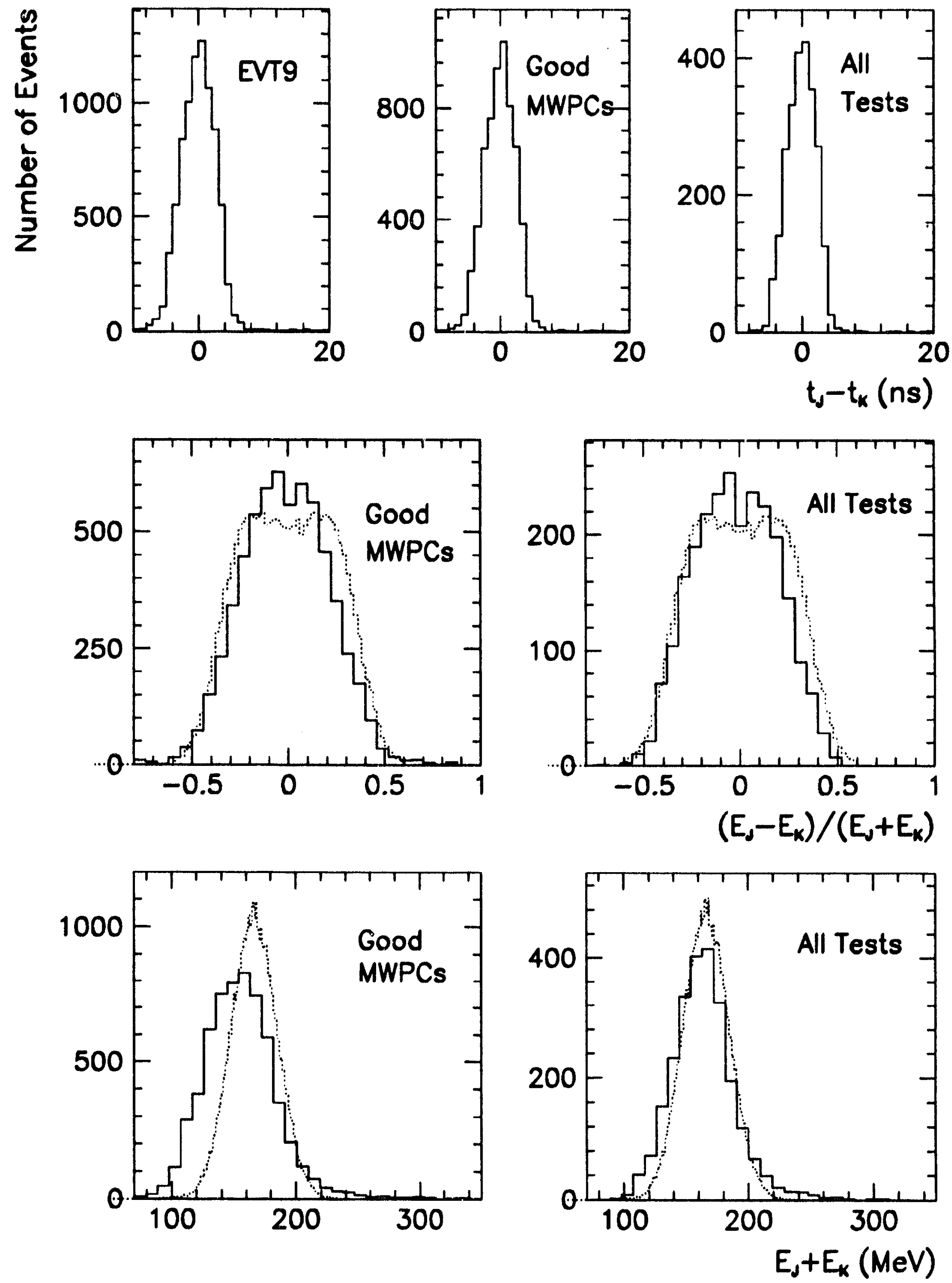

Figure 2.52 The "clean" π^0 signatures from SCX at 30 MeV. Histograms of unfiltered π^0's, events with good MWPC hits, and events that pass all software cuts illustrate that $\geq 99\%$ of detected events are good π^0 particles. PIANG Monte Carlo simulation spectra are shown in dotted lines. The cuts select π^0's that could be reconstructed with better energy and directional resolution.

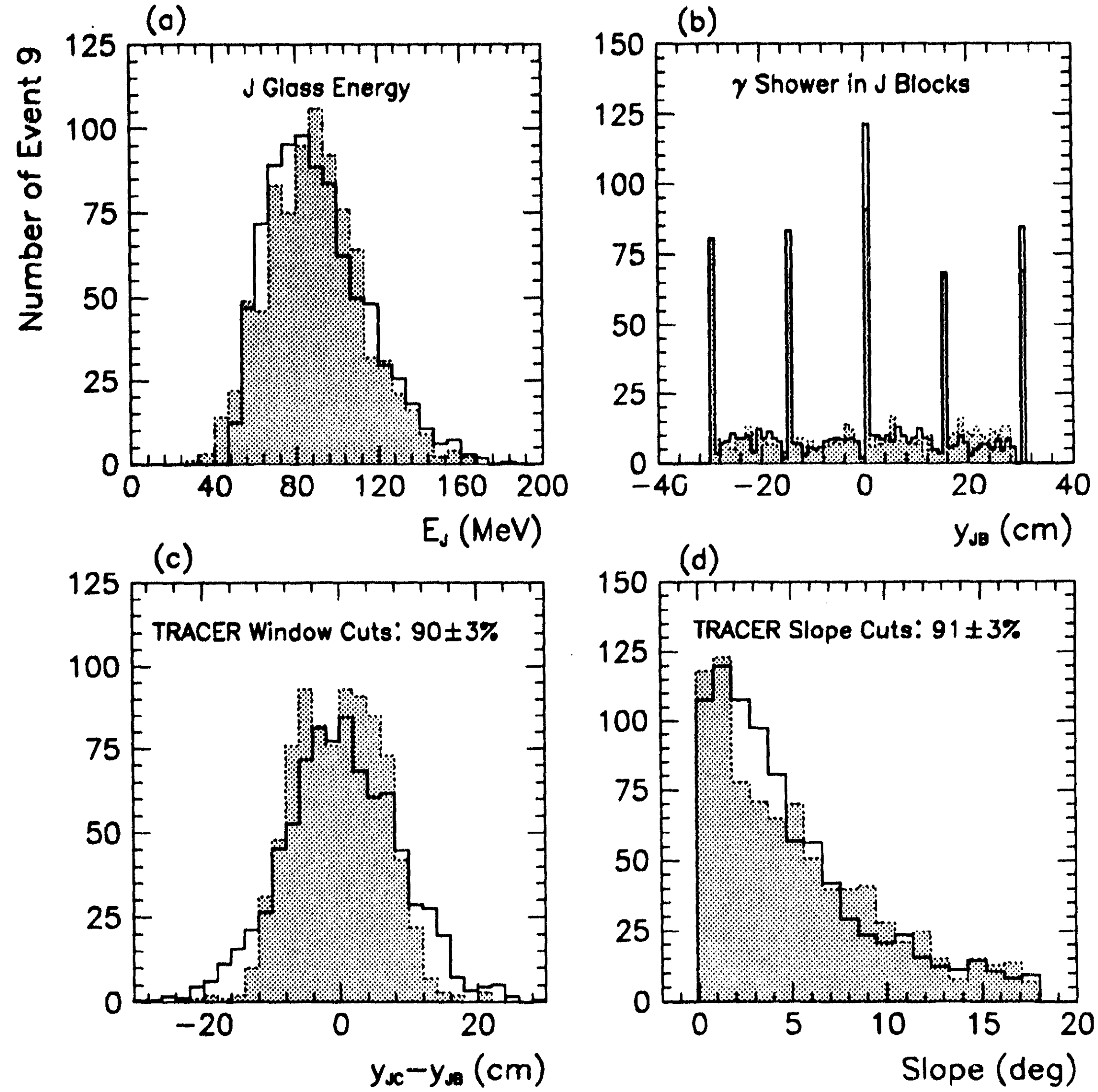

Figure 2.53 GEANT3 simulation of the software tracking efficiency. The Monte Carlo SCX π^0 generated from 30 MeV π^- beam interactions in the LH_2 target were identified by the gamma showers tracked through in the modeled spectrometer crate. On average, the showers produced 1.37 ± 0.03 charged MI particles exiting the converter. The percentage of γ-γ two-arm conversions surviving the TRACER window and slope cuts and maximal number of hit wires limit in this simulation was $73 \pm 3\%$. The result should be compared with the measured tracking fraction of $76 \pm 2\%$. The panels show (a) measured (full histogram) and simulated (hatched histogram) energy spectra in J glass, (b) distribution of the weighted coordinates of lead glass blocks with the deposited energy above the threshold, (c) differences between the coordinates of reconstructed γ conversion point and mean block energy deposition location, and (d) measured and simulated "best" angle between the back-projected line from the conversion point to target center and shower charged particle direction deduced from hits in X and X′ wire chambers.

H. The Charged Particle Detector Array

In our experiment charged particles were detected in 14 ΔE_1-ΔE_2-E range counters made of plastic scintillator BC408. Each of the eight "proton" detectors positioned 50 cm from the target center covered a solid angle of 10 msr. They were packed closely spanning 15-45° in the polar angle. The six "pion" detectors covered polar angles between 40° and 80°. They were positioned 38-42 cm away from the target subtending solid angles of 76 to 88 msr. The charged particle detector orientations, summarized in Tables 2.13 and 2.14 were chosen so as to maximize the acceptance for the $\pi^+p \rightarrow \pi^+\pi^0p$ reaction below 260 MeV, covering at the same time the most important part of the reaction phase space.

Table 2.13 Parameters of the "proton" detectors. The symbols θ and ϕ denote the polar and azimuthal angle, respectively, of the detector axis, ι is the inclination, Φ is the floor angle and the R is the target-to-ΔE_1 (detector face) distance. The last two columns show the solid angle for directly scattered pions, $d\Omega$, and the solid angle for detecting the elastically knocked-out protons at 260 MeV, $d\bar{\Omega}$.

Detector	θ	ϕ	ι	Φ	R (cm)	$d\Omega$ (msr)	$d\bar{\Omega}$ (msr)
PR1	18.0°	180.0°	−18.00°	0.00°	50	10.0	62.5
PR2	26.0°	208.0°	−22.77°	−12.90°	50	10.0	50.9
PR3	22.0°	146.0°	−18.09°	12.73°	50	10.0	58.0
PR4	30.0°	180.0°	−30.00°	0.00°	50	10.0	44.3
PR5	38.0°	200.0°	−35.35°	−14.96°	50	10.0	32.7
PR6	34.0°	156.5°	−30.85°	15.05°	50	10.0	38.1
PR7	42.0°	180.0°	−42.00°	0.00°	50	10.0	27.9
PR8	20.0°	0.0°	20.00°	0.00°	50	10.0	61.6

Table 2.14 Parameters of the "pion" detectors. For explanation of symbols see Table 2.13.

Detector	θ	ϕ	ι	Φ	R (cm)	$d\Omega$ (msr)	$d\bar{\Omega}$ (msr)
PI1	60.0°	202.0°	−53.41°	−32.98°	42	72.6	92.9
PI2	55.0°	158.0°	−49.42°	28.15°	42	72.6	116.6
PI3	65.0°	180.0°	−65.00°	0.00°	38	88.6	88.6
PI4	40.0°	0.0°	40.00°	0.00°	41	76.2	230.1
PI5	60.0°	0.0°	60.00°	0.00°	38	88.6	113.4
PI6	80.0°	0.0°	80.00°	0.00°	38	88.6	31.1

Table 2.15 Charge particle hodoscope directions.

Hodoscope No	θ (deg)	ϕ (deg)	R (cm)	$d\Omega$ (msr)
1	18.0	180.0	50.0	10.00
2	26.0	208.0	50.0	10.00
3	22.0	146.0	50.0	10.00
4	30.0	180.0	50.0	10.00
5	38.0	200.0	50.0	10.00
6	34.0	156.5	50.0	10.00
7	42.0	180.0	50.0	10.00
8	20.0	0.0	50.0	10.00
9	68.5	203.1	42.5	8.87
10	67.5	197.4	42.5	8.87
11	63.2	204.4	42.1	9.03
12	62.2	198.4	42.1	9.03
13	57.9	205.8	42.1	9.03
14	56.8	199.4	42.1	9.03
15	52.7	207.4	42.5	8.87
16	51.5	200.7	42.5	8.87
17	62.4	163.0	42.5	8.87
18	63.5	157.1	42.5	8.87
19	57.1	161.9	42.1	9.03
21	51.8	160.6	42.1	9.03
20	58.3	155.6	42.1	9.03
22	53.0	153.9	42.1	9.03
23	46.5	159.1	42.5	8.87
24	47.8	152.0	42.5	8.87
25	74.0	183.1	38.5	10.78
26	74.0	176.9	38.5	10.78
27	68.0	183.2	38.1	11.02
28	68.0	176.8	38.1	11.02
29	62.0	183.4	38.1	11.02
30	62.0	176.6	38.1	11.02
31	56.1	183.6	38.5	10.78
32	56.1	176.4	38.5	10.78
33	38.0	346.4	41.5	9.30
34	43.4	347.9	41.5	9.30
35	37.3	355.4	41.1	9.47
36	42.9	355.9	41.1	9.47
37	37.3	4.6	41.1	9.47
38	42.9	4.1	41.1	9.47
39	38.0	13.6	41.5	9.30
40	43.4	12.1	41.5	9.30
41	57.4	349.4	38.5	10.78
42	63.4	350.0	38.5	10.78
43	57.0	356.4	38.1	11.02
44	63.0	356.6	38.1	11.02
45	57.0	3.6	38.1	11.02
46	63.0	3.4	38.1	11.02
47	57.4	10.6	38.5	10.78
48	63.4	10.0	38.5	10.78
49	77.2	350.8	38.5	10.78
50	83.1	351.0	38.5	10.78
51	77.0	356.9	38.1	11.02
52	83.0	357.0	38.1	11.02
53	77.0	3.1	38.1	11.02
54	83.0	3.0	38.1	11.02
55	77.2	9.2	38.5	10.78
56	83.1	9.0	38.5	10.78
57	68.0	200.3	42.4	17.77
58	62.7	201.4	42.0	18.10
59	57.3	202.6	42.0	18.10
60	52.0	204.0	42.4	17.77
61	62.9	160.1	42.4	17.77
62	57.7	158.7	42.0	18.10
63	52.3	157.2	42.0	18.10
64	47.1	155.5	42.4	17.77
65	74.0	180.0	38.5	21.62
66	68.0	180.0	38.0	22.10
67	62.0	180.0	38.0	22.10
68	56.0	180.0	38.5	21.62
69	40.7	347.2	41.4	18.63
70	40.1	355.7	41.0	18.99
71	40.1	4.3	41.0	18.99
72	40.7	12.8	41.4	18.63
73	60.4	349.7	38.5	21.62
74	60.0	356.5	38.0	22.10
75	60.0	3.5	38.0	22.10
76	60.4	10.3	38.5	21.62
77	80.1	350.9	38.5	21.62
78	80.0	356.9	38.0	22.10
79	80.0	3.1	38.0	22.10
80	80.1	9.1	38.5	21.62

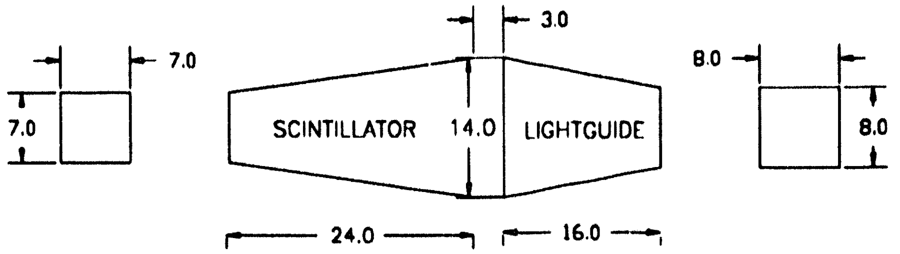

Figure 2.54 Dimensions of a "proton" E counter made of plastic scintillator BC 408. A ultraviolet-transparent (UVT) light guide made of aclylic plastic is also shown. The side scintillator surfaces were painted with diffuse reflector. The scintillator and light guide portions of the detector were glued together permanently. All linear dimensions are expressed in centimeters.

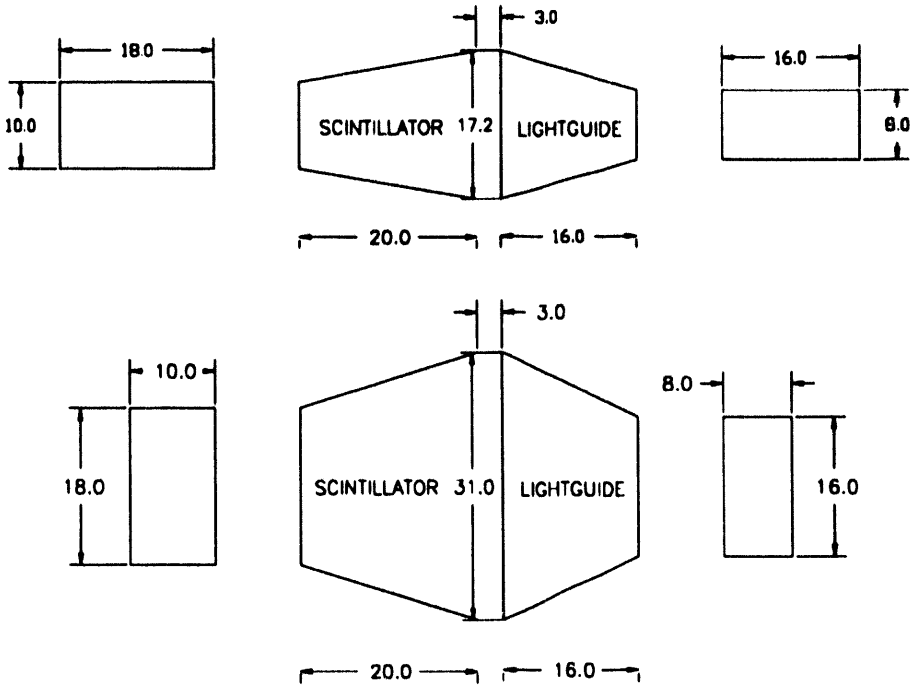

Figure 2.55 Dimensions of a "pion" E counter made of plastic scintillator BC 408. A ultraviolet-transparent (UVT) light guide made of aclylic plastic is also shown. The details of the design were described in Appendix B.

The thicknesses of the thin (ΔE_1) and thick (ΔE_2) counters were 3.2, 25.2 mm. The length of the "proton" total absorption (E) counter was 27 cm while the "pion" E detector was 23 cm long.

The different charged particles were identified by using the signals in the thin and thick detectors detectors. Dimensions of the thin proton counters were $0.32\times5\times5$ cm^3. Proton ΔE_2 counters were rectangular $2.52\times5.5\times5.5$ cm^3. Together with the total absorption E detectors they formed a very efficient range counters. The pion telescope coverage was defined by four adjacent thin hodoscope counters measuring $0.32\times4\times4$ cm^3, followed by

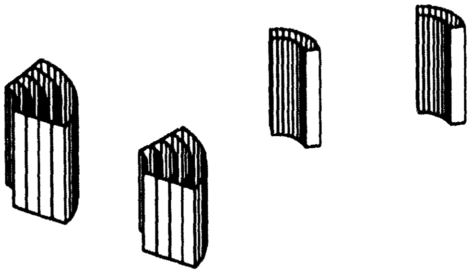

Figure 2.56 The thin ΔE_1 and thick ΔE_2 hodoscope counters were coupled to the straight light guides via plastic cylindrical sections. Monte Carlo studies of light collection and laboratory measurements using radioactive sources indicated that the best way to turn the sharp corner is to use the curved guides with thicknesses up 6 mm. The design solution for 2.5 cm thick ΔE_2 counter-guide transition involves 4 cylindrical shells with matching inner and outer radii. The individual cylinder sections were polished and optically separated with aluminized mylar strips. The resulting light collection efficiency was measured to be $\sim 80\%$.

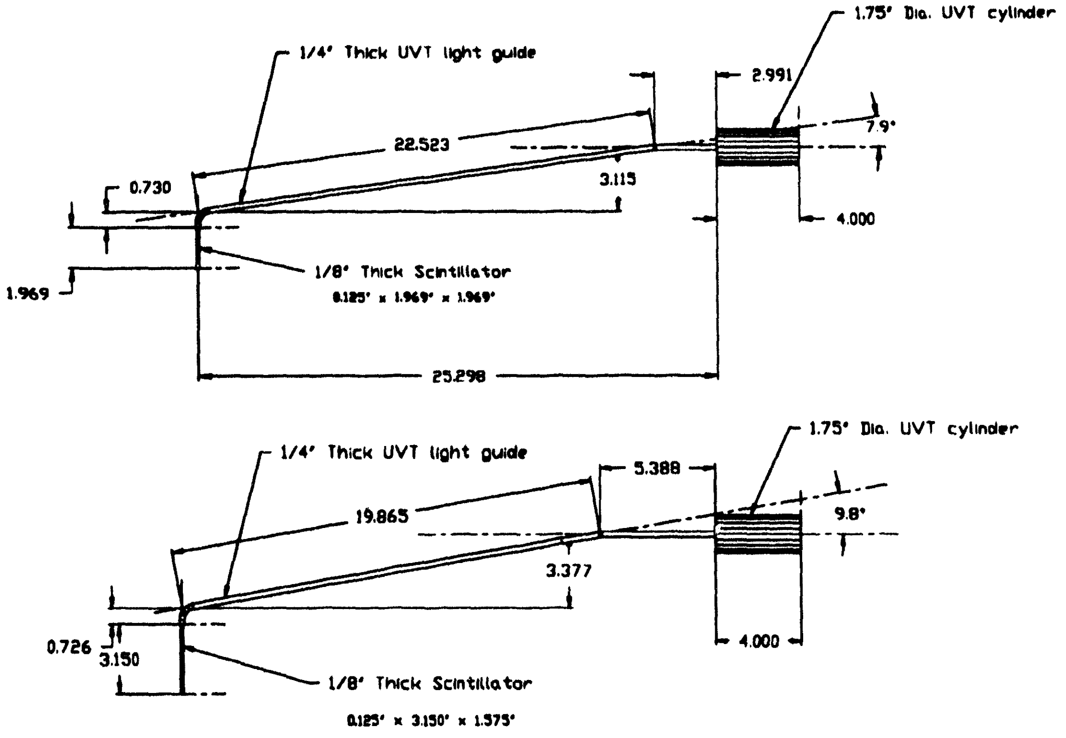

Figure 2.57 The thin hodoscope counters for pion and proton detectors. Width of the light guide is that of the scintilator (4 cm). Light guides are cut from ultraviolent-transparent plastic. The 7.9° and 9.8° bends were made on a wooden mold after the plastic was softened over a commercial toaster.

two 2.52×5×8 cm^3 counters. The hodoscope sections of the CP array defined a total of 80 different angular directions listed in Table 2.15.

The arrangements of the described range telescopes are depicted on Figures 2.58, 2.59 and 2.60.

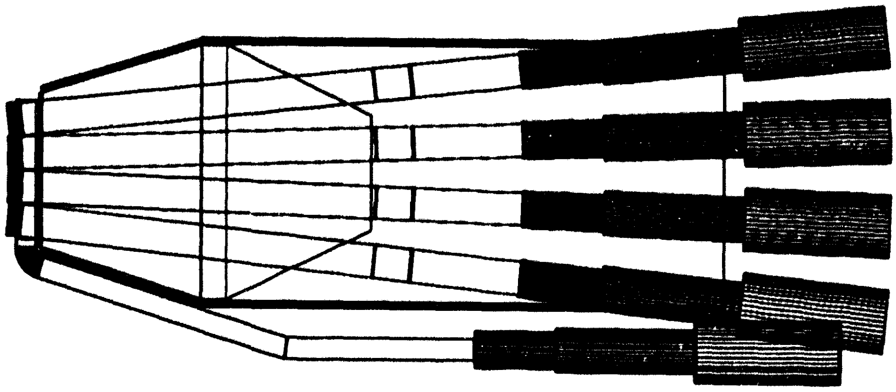

Figure 2.58 View of an assembled pion detector. The thin and thick hodoscope counters with light guides coupled to the 2 inch phototubes as well as full absorption counter are shown.

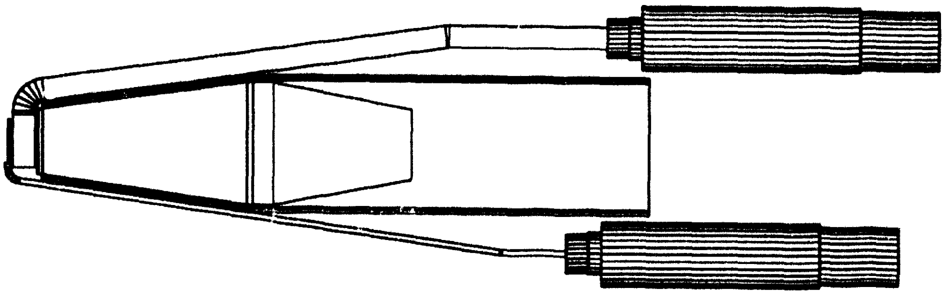

Figure 2.59 Cross section through an assembled proton detector. Thin and thick counter telescopes are coupled to the 2 inch phototubes via plastic guides with a gentle bends assuring good light collection. The total absorption counter is housed in light-proof aluminum box together with a light guide and 3 inch phototube (not shown).

The front face of the total absorption scintillator was sanded and then covered with black paper. The scintillator pyramids were permanently glued to the lightguide blocks with BICRON BC-600 optical cement, making sure that the gluing proccess does not introduce air bubbles in the interface layer that could degrade the light collection. The optical cement is a clear epoxy resin which sets at room temperature and has a refractive index 1.58 matched to that of the plastic scintillators. In order to strengthen the coupling between the scintilator and the light guide their end faces were polished and sanded before being glued. The whole pair was then wrapped in a 25 μm thick aluminum foil reaching up to 1 cm away from the light guide back face in order to avoid electric interference with the photocathode.

Both thin and thick hodoscope counters were first wrapped in 25 μm thick optically opaque aluminum foil that was secured in place with 1-2 layers of 0.18 cm thick Scotch 33^+ tape. After the assembly every detector was carefully checked for potential light leaks by two

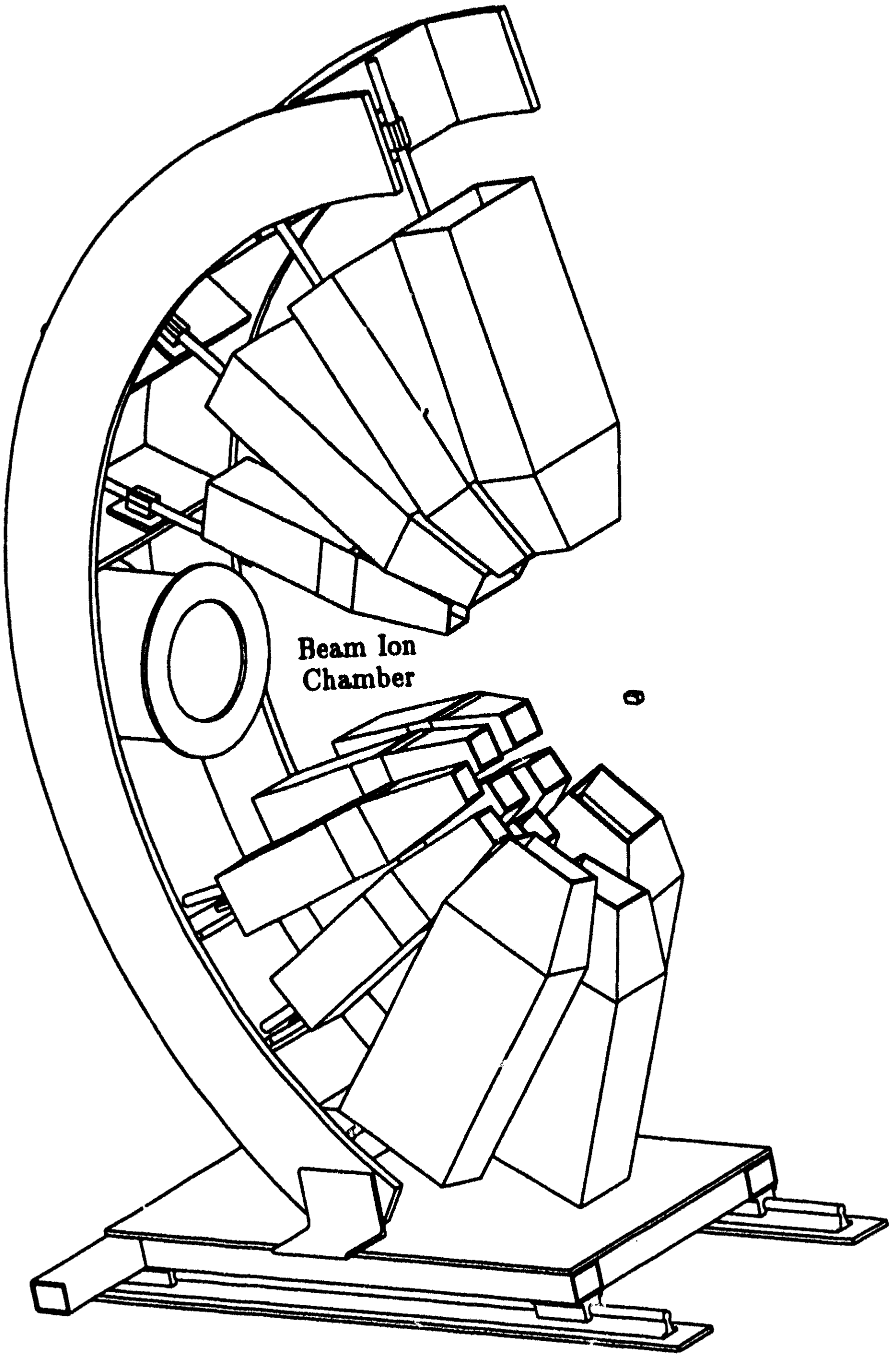

Figure 2.60 Charged particle detector stand. Fourteen aluminum boxes housing E counters attach to the rods that can be adjusted in length and direction. The ion chamber which counts beam charge is mounted at beam height, 65 cm away from the target. The whole stand move on rails in order to allow access to the target area and facilitate tasks like beam activations and beam profile measurements.

independently working teams. The established leaks were removed by reassembling the light-proofing material thus keeping the total thickness in front of the counter face unchanged. These detectors were designed to be able to detect low-energy 3 MeV pions and 10 MeV protons.

I. Charged Particle Arm Electronics

Analog signals from the 66 charged particle detectors were delayed between the experimental cave and the counting house by 150 ns long RG 58C/U 50 Ω cables in order to enable the interface with π^0 spectrometer logic electronics. The reflections, ground loops, noisy PMTs and faulty base voltage dividers were eliminated, repaired and replaced to achieve at stable pulses with the baseline levels varying less then 2 mV relative to ground. All signals coming from the counting house patch panel were divided by matched-impedance passive signal splitters into an analog branch that connected to adjustable delay boxes, and logic branch that was first amplified (Phillips 777) before discrimination. One output of a constant fraction discriminator (Phillips 715) for each detector was channeled directly to a CAMAC scaler input (LeCroy 2551 and Joerger S12). The other one was connected to a time-to-digital converter (TDC) module [LeCroy 2228(A)] after being appropriately delayed. The logic pulses of 32 thin charged particle detectors were used to define the charged particle trigger (CP OR). The discriminator thresholds for thin counters were set at the ~1/3 of the minimum ionizing (MI) peak, corresponding to ~0.7 MeV energy deposition. Loss of MI pions due to Landau straggling below the threshold was in that way kept below 1%. In the first stage, four thin counters defining the hodoscope of one pion detector were summed in a logical OR (Le Croy 429) unit and 14 individual detector signals were then fed into a common 16-channel fan-in/out module (LeCroy 429A).

The output of the CP OR provided two types of the charged particle events: charged particle singles (CP) and neutral pion-charged particle coincidences (π^0·CP). The TDC starts of coincident events were set by the π^0 pulses and stops were effected by coincident logic that included the single charged particles as an orthogonal class, Figure 2.61. The timing of the coincidence was determined by the narrow charged particle pulse while the π^0 gate was wide enough to include protons in the range 1-100 MeV spanning 30 ns time-of-flight (TOF) and thus provided the broad sampling of the accidental background, Figure 2.62.

Analog signals coming from thin, thick and total absorption counters of one "proton/pion" detector were grouped together and input into one analog-to-digital converter (ADC) CAMAC module (LCR 2249A and 2250). The signals were split by a four-channel linear fan-in/fan-out units with each output delayed differently in relation to the ADC gate before being input into individual ADC channels. The signal timing relative to ADC gate

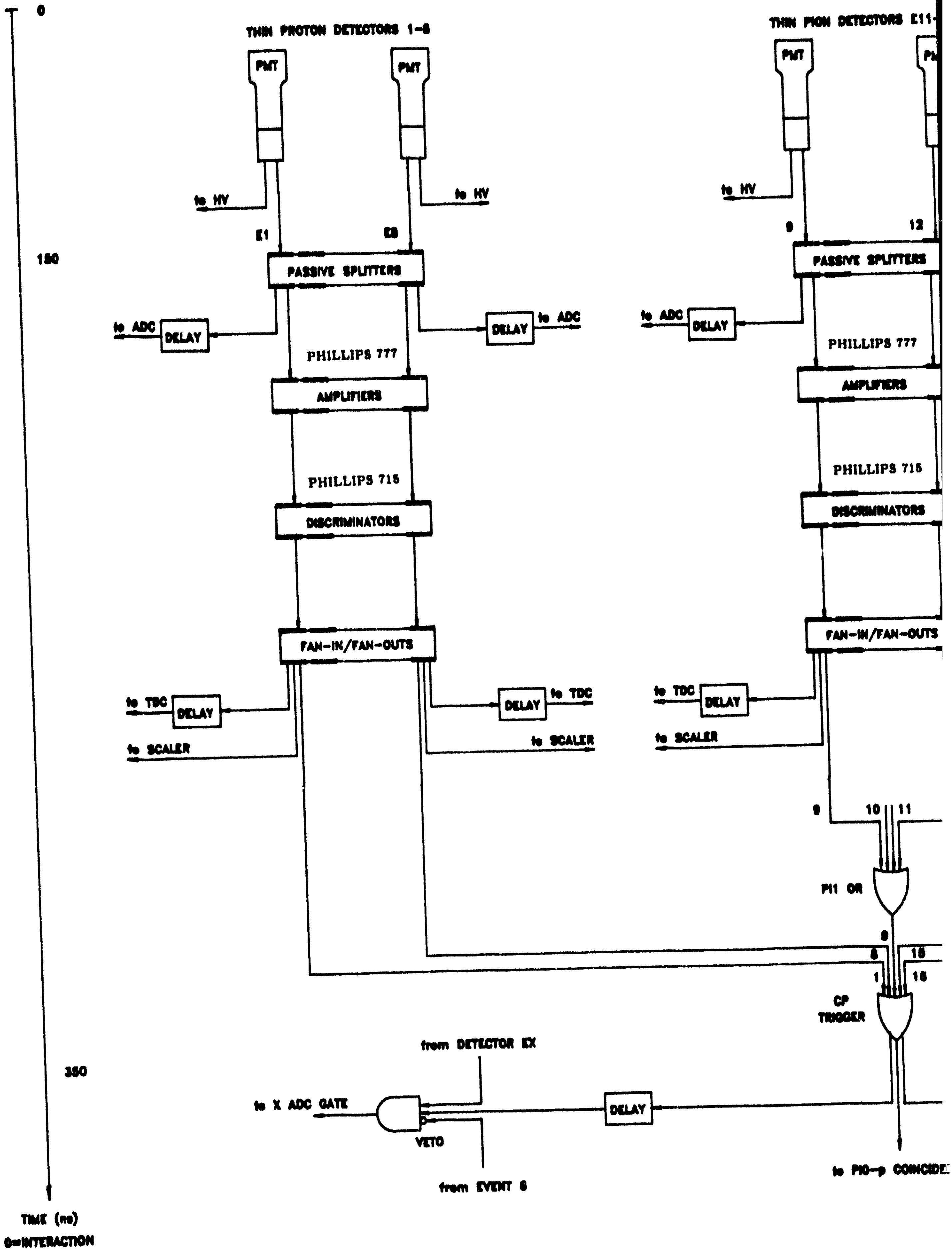
0
150
350
TIME (ns)
0=INTERACTION
THIN PROTON DETECTORS 1-8
PMT
PMT
to HV
to HV
E1
E8
PASSIVE SPLITTERS
to ADC
DELAY
DELAY
to ADC
PHILLIPS 777
AMPLIFIERS
PHILLIPS 715
DISCRIMINATORS
FAN-IN/FAN-OUTS
to TDC
DELAY
DELAY
to TDC
to SCALER
to SCALER
THIN PION DETECTORS E11-
PMT
to HV
9
12
PASSIVE SPLITTERS
to ADC
DELAY
PHILLIPS 777
AMPLIFIERS
PHILLIPS 715
DISCRIMINATORS
FAN-IN/FAN-OUTS
to TDC
DELAY
to SCALER
9
10
11
PI1 OR
9
8
15
1
16
CP
TRIGGER
from DETECTOR EX
to X ADC GATE
DELAY
VETO
from EVENT 6
to PI0-p COINCIDE

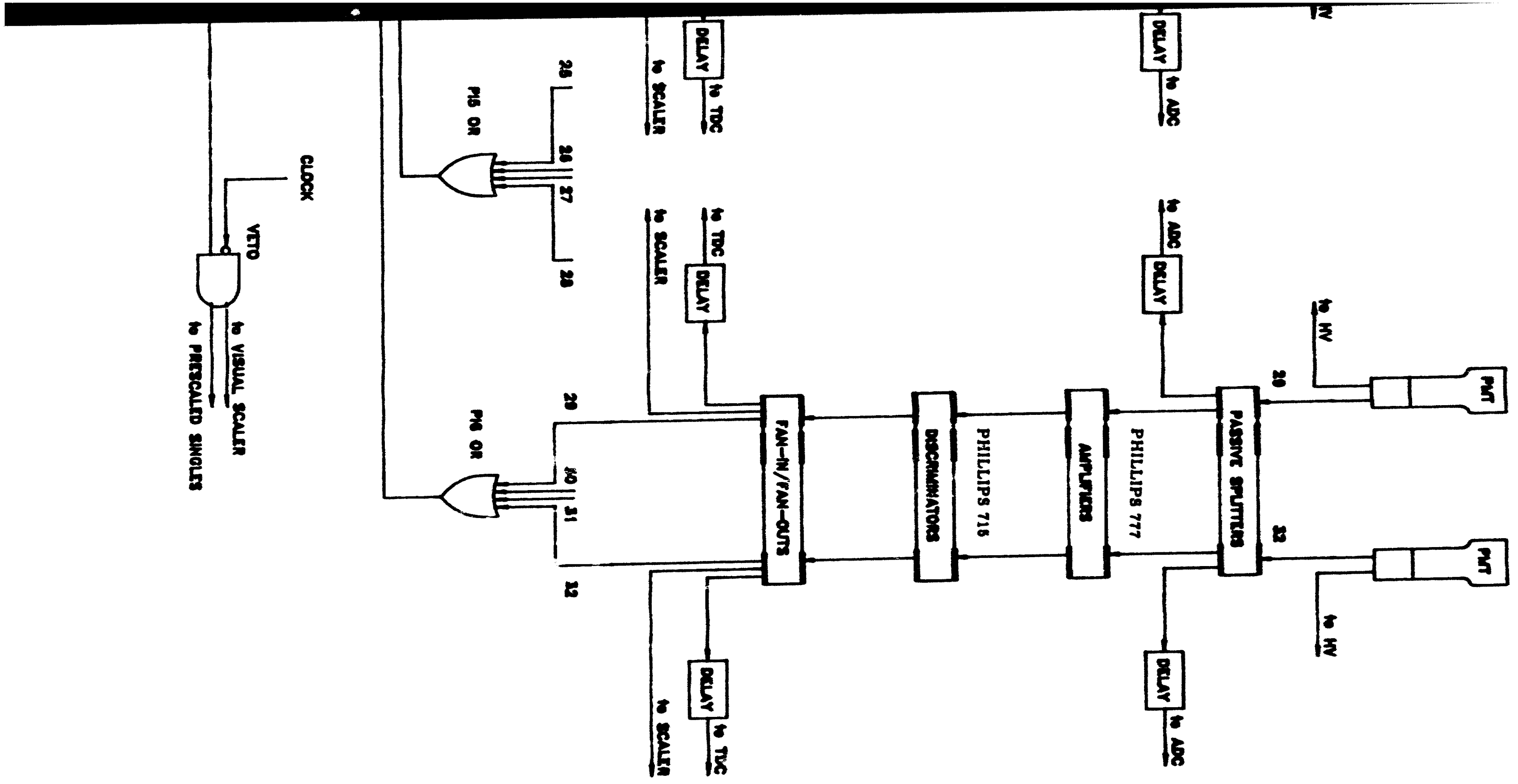

Figure 2.64 Shematic diagram of the charged particle logic electronics and its interface with the π^0 spectrometer logic (EVENT 9) resulting in the coincidence triggers (EVENT 6). The charged particle event is a logic OR of 32 precisely timed thin ΔE detector logic signals. One output of the CP trigger is scaled with the clock providing prescaled singles event, while the other is ANDed with the π^0 logic signal in the π^0 spectrometer electronics. The formation of charged particle ADC gates is also shown. Eight thin proton detectors are labeled as ΔE_1-ΔE_8 while 24 pion hodoscope thin segments are $\Delta E_{11},\ldots\Delta E_{14},\Delta E_{21},\ldots\Delta E_{64}$. The time from interaction (π^0 creation= 0) representing the accumulated delay due to signal cables, delay boxes and electronic module processing times, is marked along the vertical axis at left.

was adjusted so as to digitize the baseline, prompt, late and very late portions of analog pulse, as shown in Figure 2.63. The gate for a ADC module serving one detector was derived from the common CP trigger but was subsequently vetoed if a thin hodoscope counters associated with the detector did not fire.

The shematic layout of the charged particle trigger logic is shown on Figure 2.64, pages 64-65.

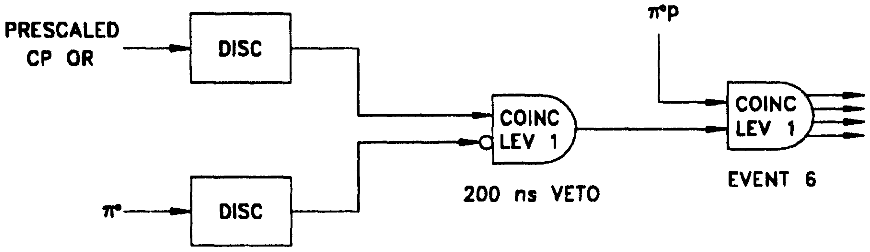

Figure 2.61 Shematic diagram of the prescaled charged particle singles event implemented with π^0 veto. The EVENT 6 includes both prescaled CP singles and true $\pi^0 p$, $\pi^0\pi^+$ coincidences. These two event types are made mutually exclusive by wide π^0 veto. Event identification is made relying on presence or absence of a π^0 (EVENT 9) stop signal.

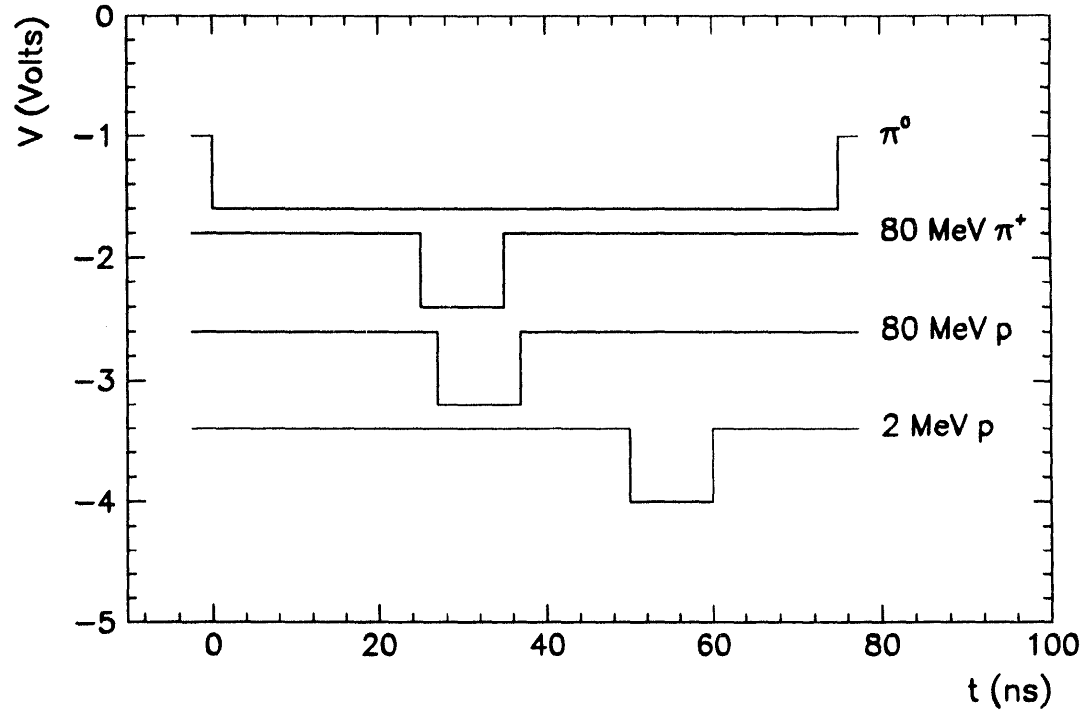

Figure 2.62 Timing of $\pi^0 \cdot$ CP coincident event (EVENT 6). Timing of the event is determined by the charged particle. The neutral pion gate is set wide enough to bracket protons in energy range 1-100 MeV. The length of the π^0 gate (76 ns in 1990 and 1991 shown here, and 126 ns for 1992 runs) sampled the accidental coincidences necessary for the background subtraction.

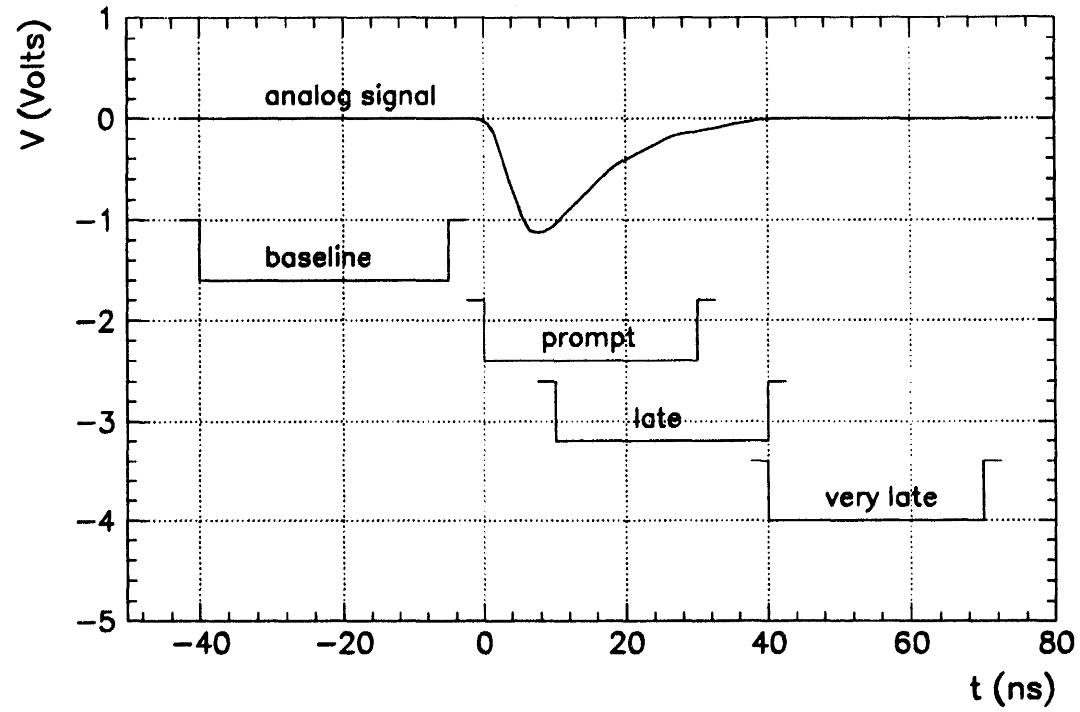

Figure 2.63 Charged particle ADC timing, as adjusted by oscilloscope. The baseline gate was sampling accidental pile-up. The ADC signals in prompt, late and very late gates were combined in software. The very late gate signal facilitates the detection of low-energy pion decays $\pi^{\pm} \to \mu\nu_{\mu}$ reinforcing the ΔE-E particle identification.

Chapter III: Inclusive Cross Sections

A. First and Second Pass Replay Analysis

All stages of the off-line analysis are shown in the order they were executed in the flow-chart in Figure 3.1. Q-files corresponding to individual runs were copied from the magnetic tapes onto disk and replayed on a VAXstation computer using an essentially unmodified run-time Q analyzer. A `FORTRAN` `write` statement was added to the `PROC6` subroutine to write the ADC and TDC data words collected in the charged particle arm to an ASCII file.

The `PRM` hot wire table and the `RR` scaler arrays were first cleared, the π^0 spectrometer geometry parameters confirmed and dynamical gain parameters restored to their initial values.

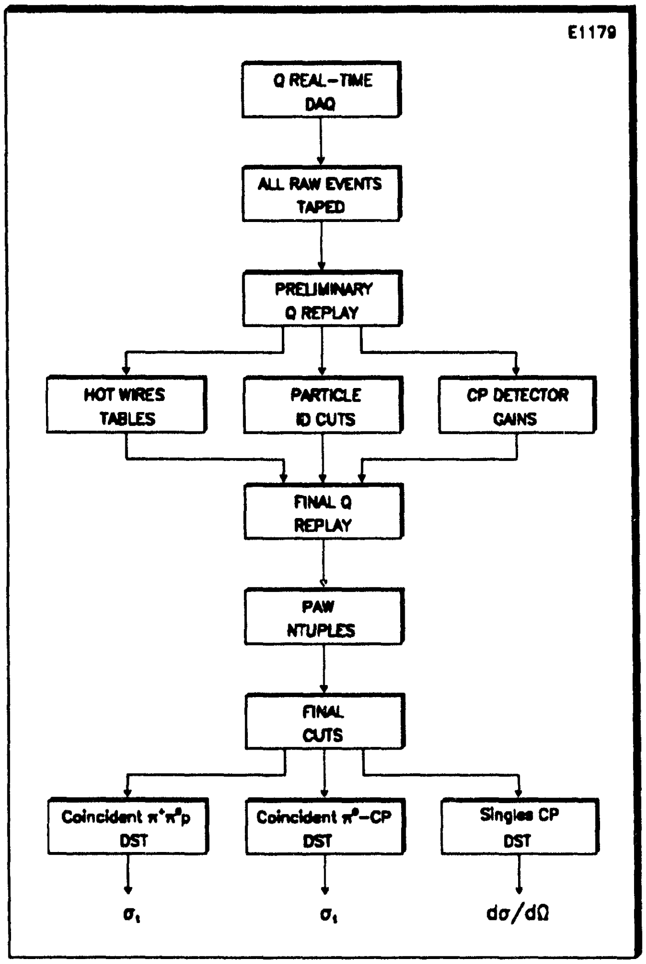

Figure 3.1 The flow-chart of the E1179 off-line analysis. The first pass replay involved the establishing tables of the MWPC hot, warm and missing wires for every run and the charged particle gains for every tenth run. In the second pass these values were entered manually into the dynamical `PRM` array before the individual run was replayed. The second pass Q replay produced ASCII data summary tapes that were consequently translated into `PAW` Ntuples for interactive cut analysis. The timing and higher order kinematic cuts result in yields for the reaction under study. Final data summary tapes (DST) are separate files for target-full and target-empty runs. They are labeled by the nominal momentum of incident beam and contain x, y, and z momentum components of three particles in the final state. Individual files are kept for $\pi^0\pi^+$, π^0p, and $\pi^0\pi^+p$ coincidences, as well as inclusive π^0's and CP singles.

Following each run the `WIRES` histograms featuring MWPCs hits in every chamber were inspected. Every hot wire (firing every time the chamber was strobed), warm wire (registering at least five times more often than the average rate), cold wire (registering at least five times less frequently than average rate), and missing wire (not present at all in the histograms) was documented in a separate logbook. Summary scaler printout was produced at the end of replay of each run, and raw ion chamber counts, computer live-time, spectrometer veto live-time and accelerator duty factor were extracted and logged. The scaler data array was then zeroed and the procedure was repeated for each of the 27 1990 runs, 84 1991 runs and 159 1992 runs resulting in the E1179 replay `RATs` logbook and hot wires logbook.

The analysis then proceeded to treat the charged particle energy and timing information. ADC and TDC data were transformed into a `HBOOK` structures from ASCII form. The `HBOOK` package is a `CERNLIB` collection [Cer-89] of several hundred `FORTRAN` subroutines which are used to define, book, edit and output one-, two-dimensional histograms and Ntuples. An Ntuple is a two-dimensional data summary tape where each event is characterized by its entry number and user array with a fixed number of elements. ADC data were first corrected by subtraction the constant charge offset, "pedestal", for each channel separately. The pedestal-corrected ADC data as well as TDC values for 66 charged particle detectors were packed into separate Ntuples for each individual run. Absolute energy calibration of the charged particle detectors was done by fitting the energy spectra of elastically scattered pions and protons from two reactions:

$$\pi^+ p \rightarrow \pi^+ p \tag{3.1}$$

$$pp \rightarrow pp \tag{3.2}$$

Events (3.1) were monitored throughout the experiment by a prescaled charged particle trigger, yielding $\sim 10^5$ events per run. The runs (3.2) were done using a 70 MeV proton beam with no degrader in the beam line (Figure B1). Particle identification was done using the interactive facilities of `PAW`—Physics analysis workstation [Bru-90]. `PAW` is an interactive data analysis and presentation package operational on a large variety of computer platforms including the fast DECstation 5000/200 used in this analysis. The graphical polygonal cuts were imposed on ΔE_1-E and ΔE_{12}-E histograms. The ΔE_1, ΔE_2 and E charged particle spectra were projected from the master Ntuple subject to the particle ID cut and the clearly identifiable peak positions due to nearly minimum ionizing pions and highly ionizing protons were measured for ten runs (Figure 3.8). The extracted gains (ADC channel MeV^{-1}) were found to be stable within the estimated accuracy of the method (10% for thin and thick counters, 5% for total absorption counters).

All TDC spectra were aligned relying on a strong high energy $\leq$100 MeV) signal coming from the pion quasi-free SCX on nuclei followed by the proton knockout. After applying the time-of-flight correction, the coincident proton ADC-TDC band was still curved because of

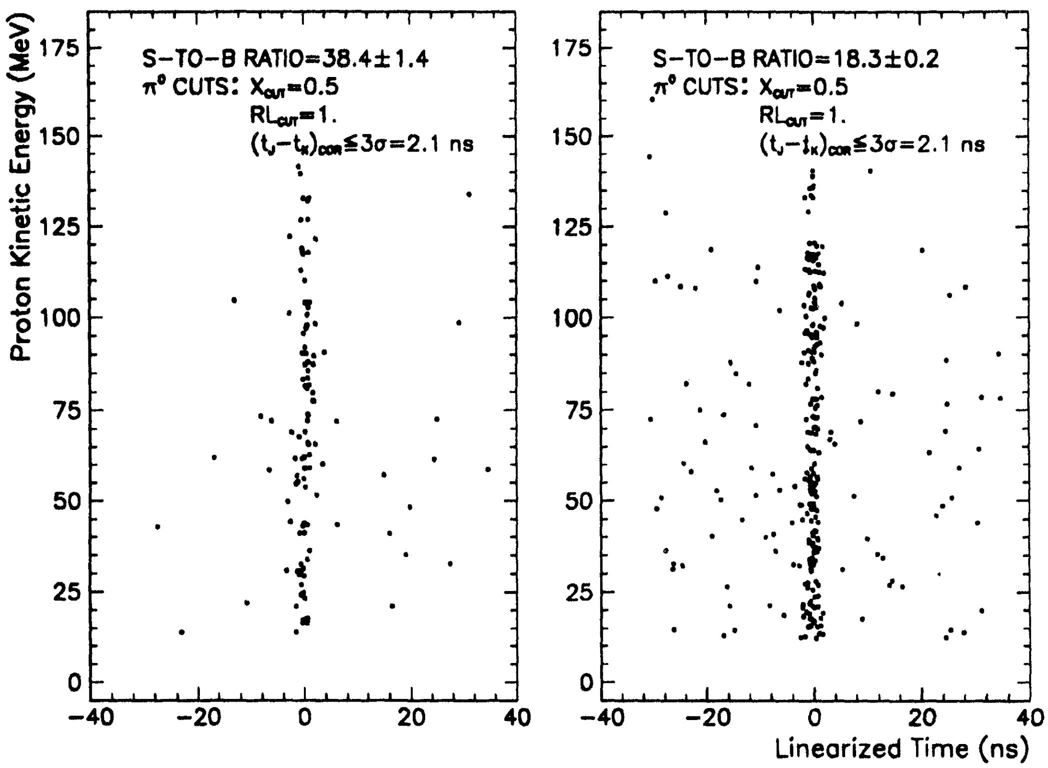

Figure 3.2 Scatter plot of coincident proton kinetic energy against its linearized timing with respect to detected π^0 for 1990 data set. The signal—to—background ratios in the coincident arm and the cuts imposed on π^0 events are indicated. The FWHM of the coincident charged particle timing peak is 2.10 ns for target-full and 2.20 ns for target-empty runs.

leading edge discrimination. A fully linearizing time-of-flight look-up table was coded into the second-pass analysis software, with the timing offsets discussed above (Figure 3.2).

In the second-pass replay FORTRAN `write` statements were included in π^0 event and π^0-CP subroutines listing 44 parameters associated with the inclusive π^0 event and 53 variables describing the charged particle—π^0 coincidence events. The hot and warm wires were entered into the PRM hot wire table manually, and were updated after every run. The FCD task which lists the results of the replay cut fail-codes and the individual and composite MWPC efficiencies was executed following every run and the hard copies of the lists were filed. Detailed listings of 223 test file cuts provided by the testing package task TPR were printed for use in the analysis of the π^0 spectrometer efficiency. The fraction of π^0 events with good wire chamber information (η_a, "analyzed fraction") was also documented, Table 3.1.

The final stage of the data organization was the creation of the data summary tapes from ASCII replay data output. The following files booking the energies, polar and azimuthal angles and timings in addition to the other ancillary parameters were obtained :

TABLE 3.1 Average values of assorted efficiencies, live-time and pile-up fractions. The fist column is the FCD MWPC replay efficiency ϵ_m, the second column contains η_a, the "analyzed fractions" (see text), and the last two list the computer live time η_{cl} and the π^0 spectrometer veto live time η_{vp}, respectively.

$T_\pi^\pm$ (MeV)	ϵ_m (%)	η_a (%)	η_{cl} (%)	η_{vp} (%)
−30	89.8 ± 1.1	72.7 ± 1.5	96.5 ± 1.5	99.2 ± 0.2
160	86.6 ± 0.7	61.5 ± 1.1	81.1 ± 4.6	92.5 ± 1.2
190	85.8 ± 0.5	58.9 ± 0.8	79.4 ± 3.8	90.1 ± 0.5
200	85.9 ± 0.5	59.5 ± 0.5	79.9 ± 4.0	91.4 ± 0.5
220	86.0 ± 0.6	60.3 ± 0.9	83.9 ± 2.1	93.2 ± 0.7
240	85.3 ± 0.7	61.4 ± 0.8	87.8 ± 1.9	95.1 ± 0.8
260	86.7 ± 1.0	61.6 ± 1.4	87.5 ± 1.9	95.1 ± 0.6

- inclusive 30 MeV SCX π^0 Ntuples for (i) CH_2 target, (ii) ^{12}C target, (iii) LH_2 target full, (iv) LH_2 target empty, (v) runs in air (no solid target),
- coincident π^0-CP Ntuples for runs at 260, 240, 220, 200, 190, and 160 MeV booked separately for LH_2 target full and empty,
- triple coincidence $\pi^+\pi^0p$ Ntuples for runs at 260, 240, 220, 200, 190, and 160 MeV booked separately for LH_2 target full and empty,
- coincident 260 MeV π^0-CP Ntuples for runs with (i) ^{12}C target, and (ii) no solid target (in air),
- prescaled charged particle Ntuples for runs at 260, 240, 220, 200, 190, and 160 MeV booked separately for LH_2 target full and empty,
- prescaled proton Ntuples for runs with 70 MeV proton beam with LH_2 target full and empty.

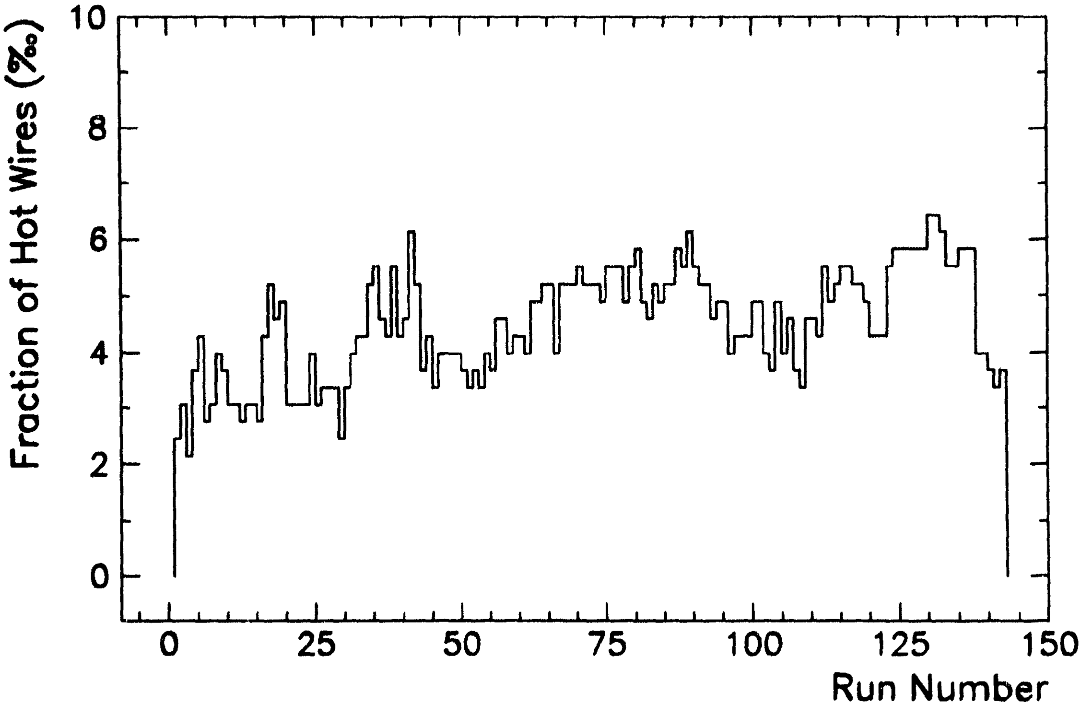

Figure 3.3 The percentage of the hot wires for individual runs in 1991 replay analysis. The wire is considered hot if it fired more the five times more often then the average wire rate.

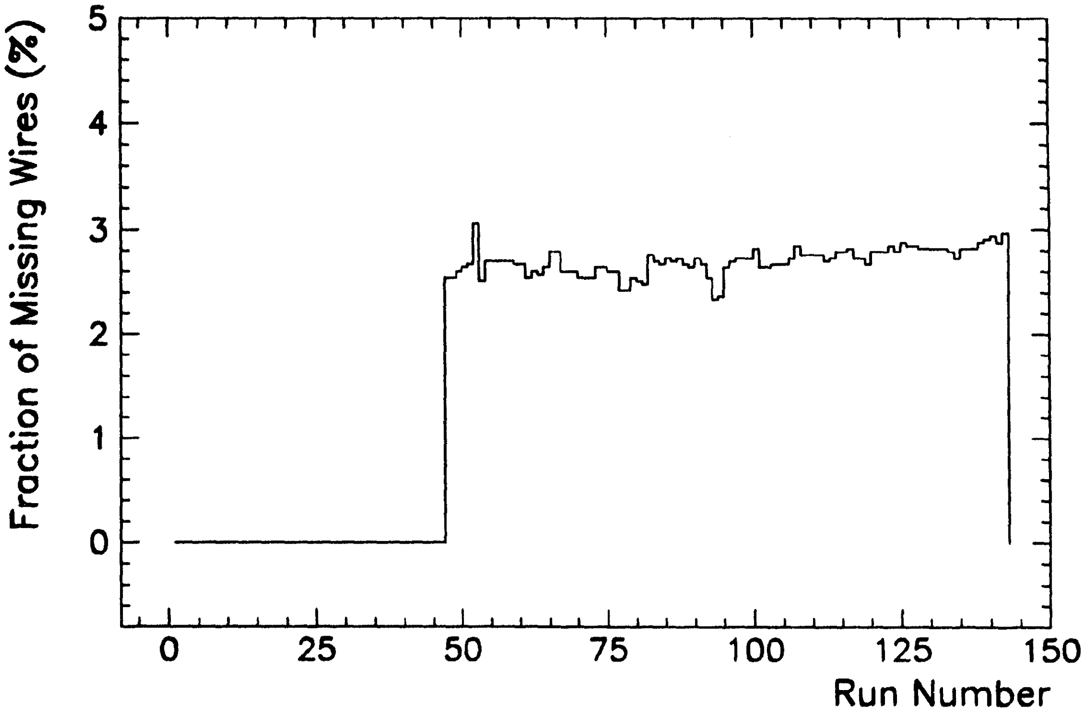

Figure 3.4 The fraction of missing wires for individual runs in 1991 replay analysis. The wire is considered missing if it does not fire at all or has a rate that is at least five times lower than the average.

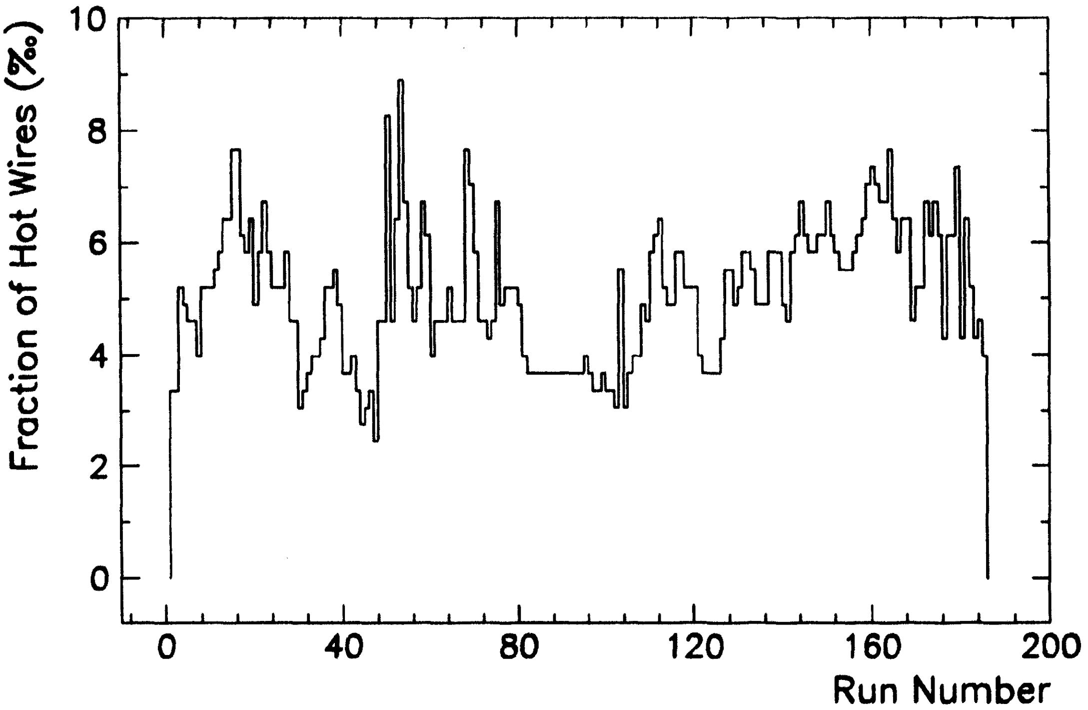

Figure 3.5 The percentage of the hot wires for individual runs in 1992 replay analysis. The fraction was basically unchanged in 1990, 1991, and 1992 runs.

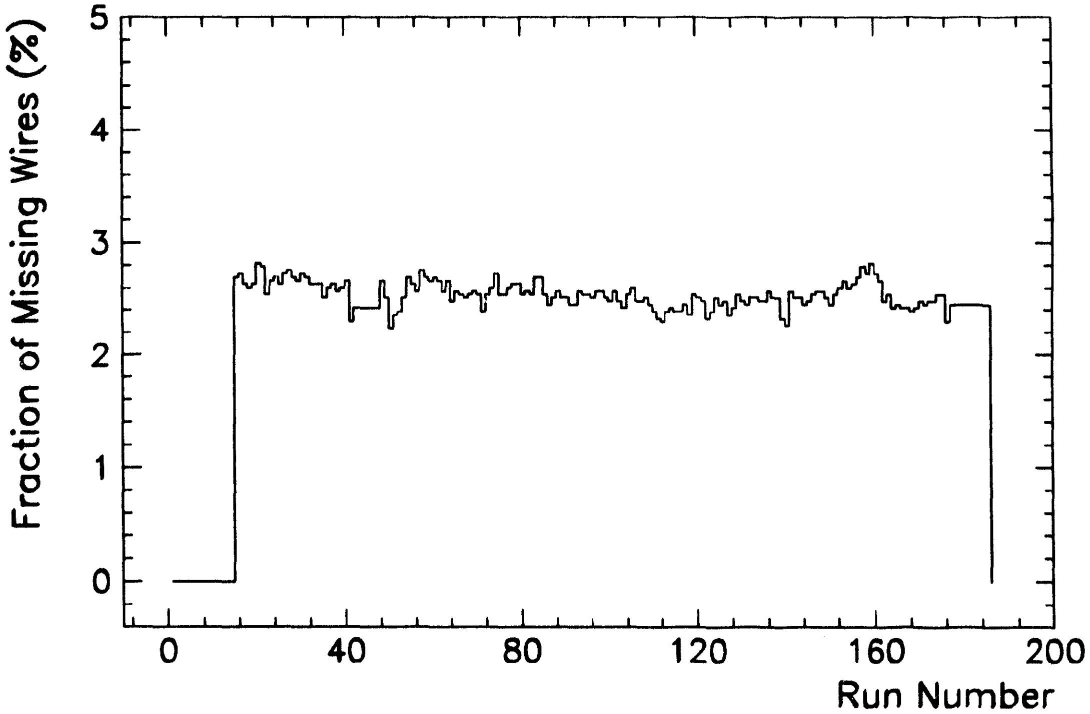

Figure 3.6 The fraction of missing wires on for individual runs in 1992 replay analysis. Knowing the percentange of hot and missing wires is important in understanding in detail the spectrometer detection efficiency.

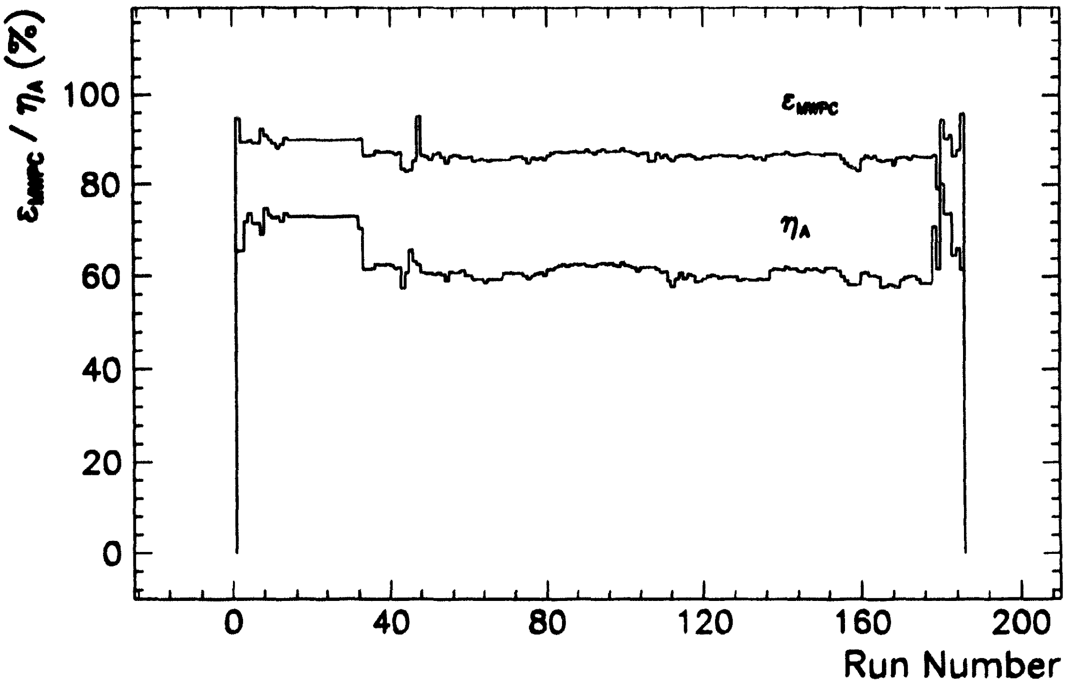

Figure 3.7 ϵ_{mwpc}, the replay MWPC instrumental efficiency and η_a, the "analyzed fraction" for 185 runs.

Table 3.2 Number of incident π^+'s: 1990 run. *IC* is an ion chamber scaler, η_L is live time of the π^0 spectrometer vetoes, η_a is the replay "analyzed fraction" indentical to the composite MWPC instrumental efficiency ϵ_m, and τ_L is computer live time.

T_{π^+} (MeV)	$10^5 IC\eta_L\eta_A\tau_L$ TGT FULL	$10^5 IC\eta_L\eta_A\tau_L$ TGT EMP	$10^{10}\pi^+_{inc}$ TGT FULL	$10^{10}\pi^+_{inc}$ TGT EMP
30	4.1607	1.5556	2.6628	0.9956
260	3.0009	2.0394	15.4247	10.4823

Table 3.3 Number of incident π^+'s: 1991 run

T_{π^+} (MeV)	$10^5 IC\eta_L\eta_A\tau_L$ TGT FULL	$10^5 IC\eta_L\eta_A\tau_L$ TGT EMP	$10^{10}\pi^+_{inc}$ TGT FULL	$10^{10}\pi^+_{inc}$ TGT EMP
30	4.7630	1.2385	1.5003	0.3901
160	2.8009	2.1741	14.7890	11.4793
180	1.6994	0.4991	9.6016	2.8199
190	2.7166	1.7485	15.4851	9.9665
200	2.7900	1.5326	16.0430	8.8125
220	1.4197	0.3511	8.1775	2.0223
240	1.9417	1.8882	11.8638	11.5370
260	5.3853	2.0659	33.8200	12.9739

Thin ΔE_1 Detector Number	Run Number									
	25	38	62	71	83	110	125	143	155	165
32	111	98	106	98	104	98	91	94	96	100
31	117	98	99	94	94	94	97	103	99	101
30	103	97	94	103	92	100	100	100	107	99
29	101	100	101	101	89	91	96	106	106	105
28	98	101	93	93	101	101	98	101	107	101
27	116	109	92	100	92	106	94	97	103	87
26	123	102	91	96	94	94	94	103	110	88
25	104	122	89	87	115	92	87	107	104	89
24	100	97	81	101	120	107	126	86	94	85
23	102	94	95	92	102	103	100	102	91	113
22	109	96	97	110	103	94	97	109	103	78
21	114	98	99	102	95	87	99	101	90	111
20	105	100	91	101	112	95	96	93	106	96
19	95	91	98	102	101	109	111	101	95	92
18	107	98	99	116	76	109	94	107	91	99
17	88	108	91	80	83	102	104	109	118	112
16	81	113	87	93	93	93	130	109	109	88
15	94	104	94	108	89	106	100	100	106	95
14	107	105	89	101	89	101	95	101	115	91
13	92	99	95	101	85	101	101	107	107	109
12	112	96	92	98	84	91	107	123	104	88
11	105	113	115	96	79	101	93	100	95	99
10	104	89	107	106	88	106	101	93	98	102
9	122	89	85	105	90	105	93	109	109	86
8	114	101	96	90	107	101	87	101	95	103
7	100	106	84	90	86	95	101	112	119	103
6	117	101	94	81	87	117	94	107	122	74
5	94	110	100	85	89	99	106	104	111	96
4	97	104	113	98	59	98	106	110	110	100
3	118	115	102	90	99	93	88	103	103	82
2	93	99	109	107	101	94	88	101	111	92
1	97	101	89	88	117	96	97	100	103	105

Table 3.4 Gain variation in thin ΔE counters. The gain conversion factors for charged particle counters were determined from elastically scattered near-minimum ionizing pions and knocked-out protons and were monitored for each run. The table lists the relative gains (100 is an average detector gain) for 32 thin detectors measured for 10 runs. The estimated accuracy of the method is 10 % and the maximal real gain variation around 10 %. This dispersion is used in Monte Carlo simulation.

Table 3.5 Number of incident π^+'s: 1992 run

T_{π^+} (MeV)	$10^5 IC\eta_L\eta_A\tau_L$ TGT FULL	$10^5 IC\eta_L\eta_A\tau_L$ TGT EMP	$10^{10}\pi^+_{inc}$ TGT FULL	$10^{10}\pi^+_{inc}$ TGT EMP
30	4.5018	2.5071	1.8824	1.0483
160	7.0546	3.5503	37.8127	19.0296
190	8.6683	2.8610	51.2123	16.9028
200	9.0423	3.8905	52.9517	22.7828
220	12.8136	3.7199	73.8191	21.4303
240	10.6761	2.8586	63.9925	17.1314
260	33.2319	3.4234	199.8570	20.5883

B. Non-pionic Contamination of $\pi^\pm$ Beams

1. Proton Contamination

Precise knowledge of the leptonic and/or proton fractions in the beam is essential for absolute determination of $\pi^\pm$ flux.

π^+ beams with energy 190 MeV and higher are accompanied by more than 50 protons/π^+ at the entrance of the LEP beam line. These momentum-analyzed protons have much lower energy than the beam pions, and, correspondingly, much higher stopping power. The proton beam fraction was directly extracted by monitoring elastic $pp \to pp$ scattering. A pair of conjugate-angle charged particle detectors at the largest available polar angle was chosen at each energy to monitor elastically scattered and recoil protons in coincidence. The position of such events in a two-dimensional ΔE_1 vs $(\Delta E_1 + \Delta E_2)$ scatter plot depends strongly on the energy loss of protons in the target. An example of coincident p-p detection is shown in Figure 3.8: a 70 MeV proton beam was transported through the beam line without an absorber.

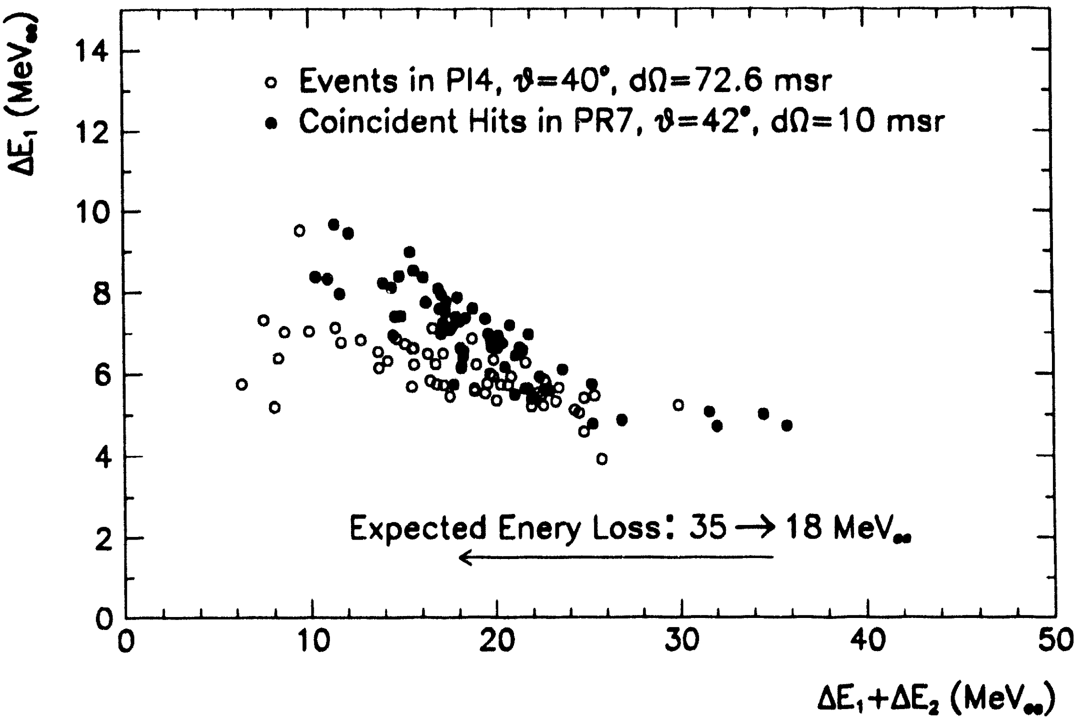

Figure 3.8 Coincident pp events in conjugate-angle detectors PI4 and PR7 with 70 MeV proton beam and LH_2 target. Of the two detectors, PI4 has the larger solid angle, and therefore detects the recoil proton coincident with any proton scattered into PR7 by the LH_2 target. Relying on this calibration pp events are used as an additional monitor of proton contamination in π^+ beams at 160-260 MeV. In case of 260 MeV pion beam proton fraction is found to be $(0.5 \pm 0.3)\%$.

For pion beams between 160 and 260 MeV the corresponding beam proton energies varied between 33 and 70 MeV at the target center. The number of protons Y_{pp} normalized to the i_m, the number of ion chamber counts, is given by the expression:

$$\frac{Y_{pp}}{i_m} = \frac{d\sigma}{d\Omega}(pp \rightarrow pp) t_{LH_2} d\Omega_p s_l, \tag{3.3}$$

where $\frac{d\sigma}{d\Omega}(pp \rightarrow pp)$ is the proton-proton elastic scattering cross section calculated by the SAID phase shift computer program [Arn-87], t_{LH_2} is the target thickness, $d\Omega_p$ is the solid angle element for a coicident proton pair and s_l is the singles prescaled fraction. The instrumental charge particle detector efficiency for monoenergetic protons was taken to be ~100% from target thickness calibration runs. The proton identification efficiency was also ~100% due to very unconstrained poligonal cut defined on ΔE-E histograms.

The non-pionic fractions determined in that way for the 160-260 beam tunes were consistently $0.5 \pm 0.3)\%$. The constancy is not suprising because the mid-channel degrader wheel was equipped with thickness options which provided consistent ~8% pion-proton separation throughout the studied energy range for our 1992 runs.

The proton contamination was independently determined from the pion-proton momentum separation scans. Magnetic fields in two bending magnets and exit quadrupoles downstream of the beam degrader were scaled linearly around the nominal momentum in small steps. Three independent measurements of i_m/i_{Al}, the number of ion chamber counts per primary beam toroid count were recorded for each exit momentum setting p/p_0. The beam ion chamber is a 30 cm long aluminum cylinder sealed with 5 mil steel windows and filled with argon gas ($\rho = 1.78$ mg/cm^3 at sea level) having the thickness 0.0427 g cm^{-2} at Los Alamos altitude. The pion and proton peaks were scanned together with long-range plural and single scattering wings. Resulting curves were represented by a sum of two Gaussians superimposed on the backgrounds falling with $[(p-p_0)^3+\delta^2]^{-1}$, see Figures 3.9-3.14. In the final step toroid-normalised ion chamber count had to be converted to particle fluxes.

The energy transfer from the charged particle to the detector medium is described satisfactorily with the Bethe-Bloch formula:

$$-\frac{dE}{dx} = 2\pi N_a r_e^2 m_e c^2 \rho \frac{Z}{A} \frac{z^2}{\beta^2} \left[\ln \left(\frac{2 m_e \gamma^2 v^2 W_{\max}}{I^2} \right) - 2\beta^2 \right], \tag{3.4}$$

where the constants N_a, r_e, m_e, and c are Avogardo's number (6.022×10^{23} mol^{-1}), classical electron radius (2.817×10^{-13} cm), electron mass (9.100×10^{-31} g), and speed of light (2.998×10^8 cm s^{-1}). Z and A are atomic number and weight of absorbing material, z is charge of incident particle in units of e, $\beta = v/c$ is speed of incident particle in terms of c,

$\gamma = 1/\sqrt{1-\beta^2}$ is a relativistic factor. Mean excitation potential I_{ex} can be calculated from the semi-empirical formula [Leo-90]

$$\frac{I_{ex}}{Z} = 12 + 7/Z \text{ eV}, \ Z \leq 13, \tag{3.5}$$

or better taken from empirical tables [Gre-867]. I_{ex} for argon, gas in our beam ion chamber, is 194.4 eV. Maximum energy deposition $W_{\max}$, is produced by a head-on collision. Kinematics for an incident particle with mass M gives

$$W_{\max} = \frac{2m_e c^2 \eta^2}{1 + 2\sqrt{1+\eta^2+s^2}}, \tag{3.6}$$

where $s = m_e/M$ and $\eta = \beta\gamma$.

The ratio of specific energy losses for pions in the ion chamber and protons was calculated using the Bethe-Bloch formula (3.4) and the relative particle intensity curves are displayed in the lower panels of Figures 3.9-3.16.

2. Lepton Contamination

Average energy loss for nearly-minimum ionizing 260 MeV π^+ beam traversing the beam ion chamber was 61.9 keV while the contaminating proton losses were in the range approximated by the linear equation:

$$\Delta E_p(\text{keV}) = 595.8 - 4.49 \ T_p(\text{MeV}), \tag{3.7}$$

with $40 \leq T_p \leq 80$ MeV. For the 30 MeV π^- beam the IC energy losses were 64.5 keV for MI electrons and

$$\Delta E_{\pi^-}(\text{keV}) = 215.5 - 4.18 \ T_{\pi^-}(\text{MeV}), \tag{3.8}$$

for pions in the range $20 \leq T_{\pi^-} \leq 40$ MeV [Gre-87].

Pion and electron activation cross sections were measured at 30, 40 an 50 MeV but not published by Leitch *et al.* [Lei-90]. That measurement was carried out at LAMPF in the LEP beam channel using an electrostatic separator. Results of Leitch *et al.* are summarized in Table 3.6. Quadratic interpolation formulas through two measured points as well as the 19 MeV reaction threshold point were used to calculate activation cross sections in the 20-50 MeV range:

$$\sigma_{\pi^-}(mb) = -1.93 + 4.75 \times 10^{-2} \ T_{\pi^-} + 2.45 \times 10^{-3} \ T_{\pi^-}^2, \tag{3.9}$$

$$\sigma_{e^-}(\mu b) = -245.0 + 16.0 \ T_{\pi^-} -- 0.187 \ T_{\pi^-}^2, \tag{3.10}$$

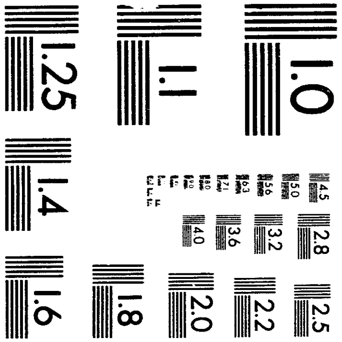
1.25
1.1
1.0
1.4
4.5
5.0
5.6
6.3
4.0
3.6
3.2
2.8
1.6
1.8
2.0
2.2
2.5

2 of 3

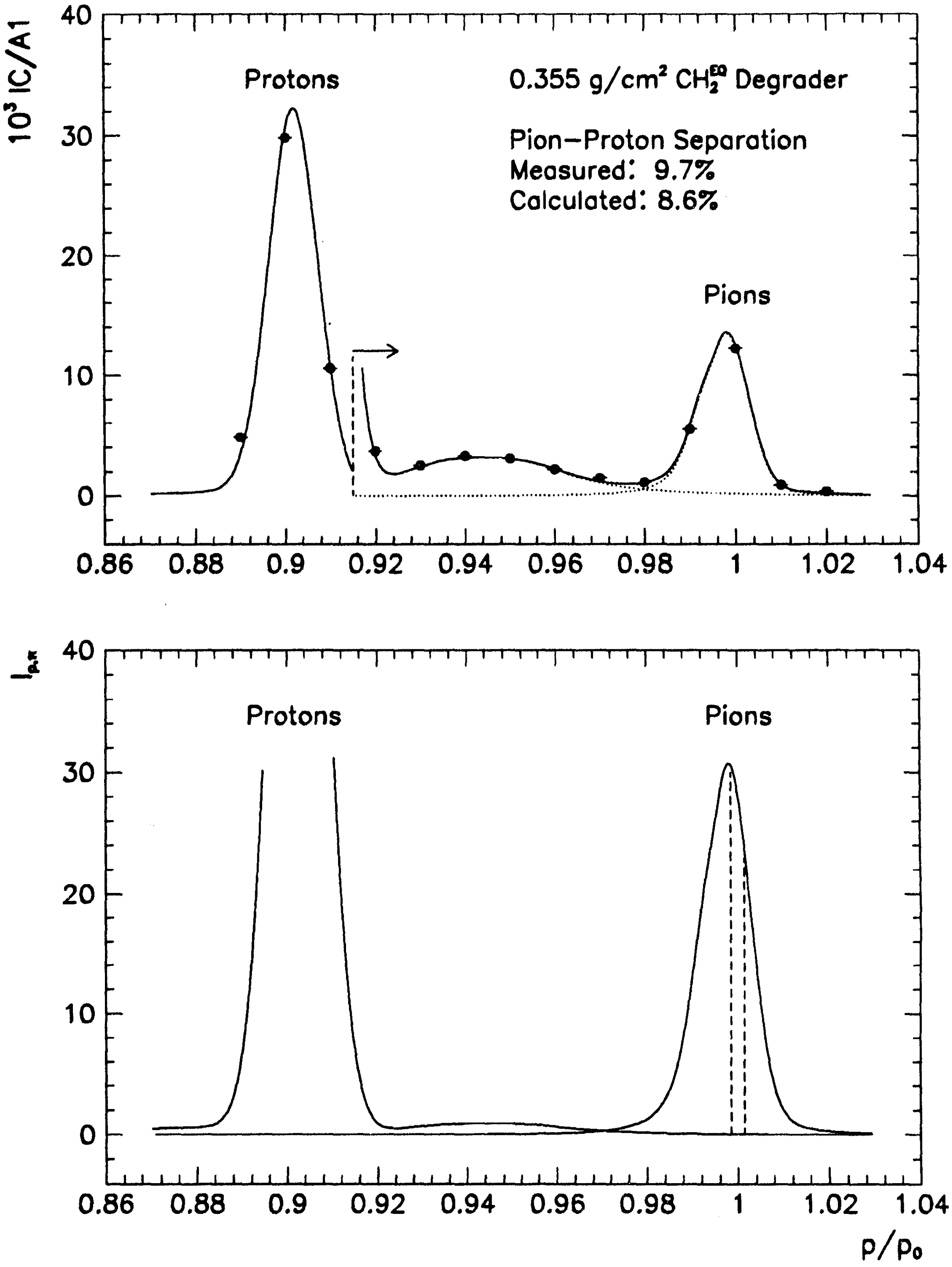

Figure 3.9 Pion-proton separation in the 160 MeV π^+ beam. The ionization chamber counts (IC) are plotted vs the momentum of charged particles. Pion and proton peaks are fitted simultaneously with Gaussian small-angle multiple scattering and wide-angle single scattering shapes. In the lower panel IC rates are appropriately scaled with Bethe-Block weights to obtain particle fluxes. Fixing the momentum spread of the beam (0.15%, shown as vertical dashed lines) the deconvoluted curves exhibit the proton contamination of the beam. The extracted proton fraction is 0.2%.

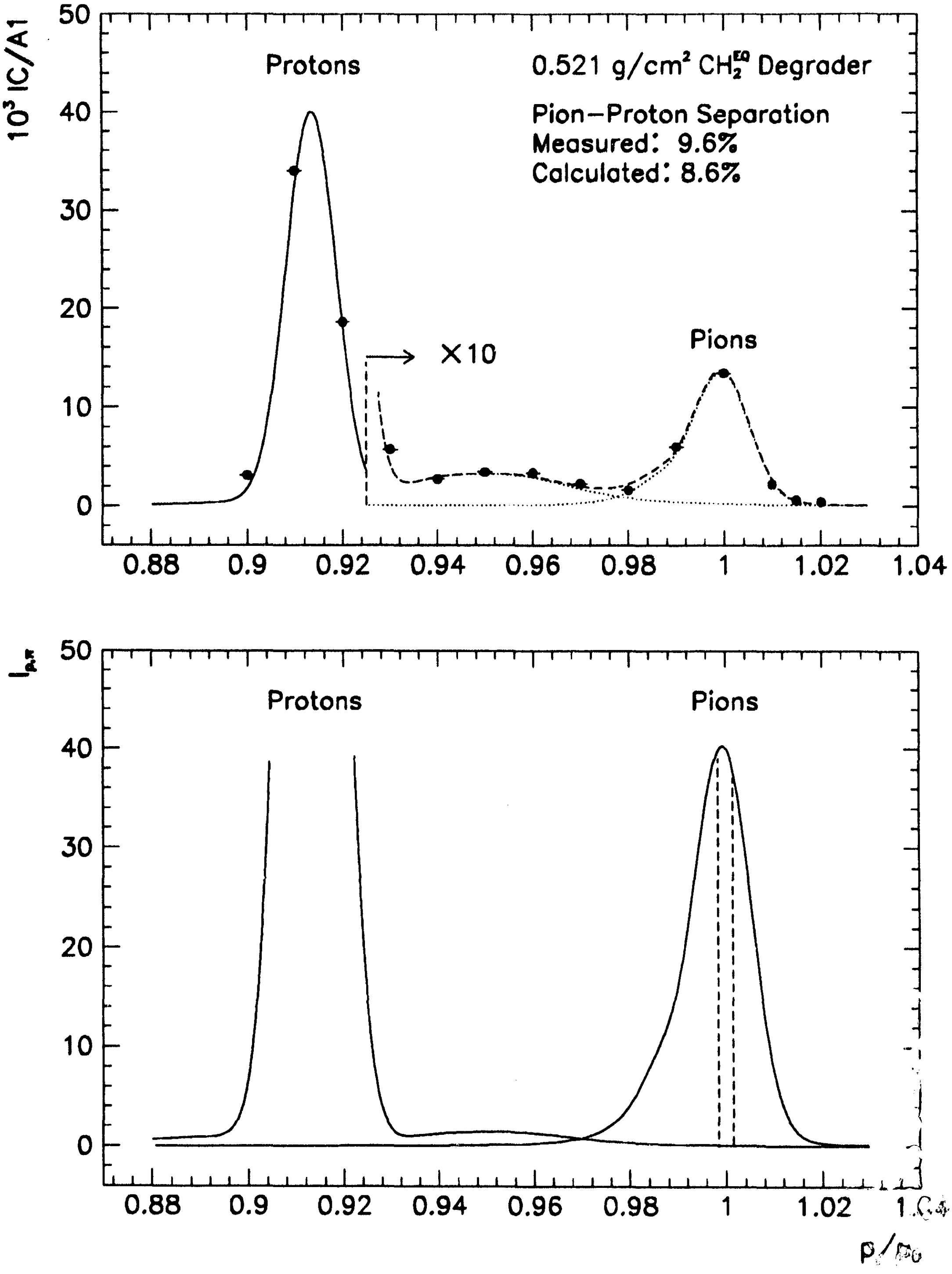

Figure 3.10 Pion-proton separation in 190 MeV π^+ beam. The extracted proton fraction is 0.3%.

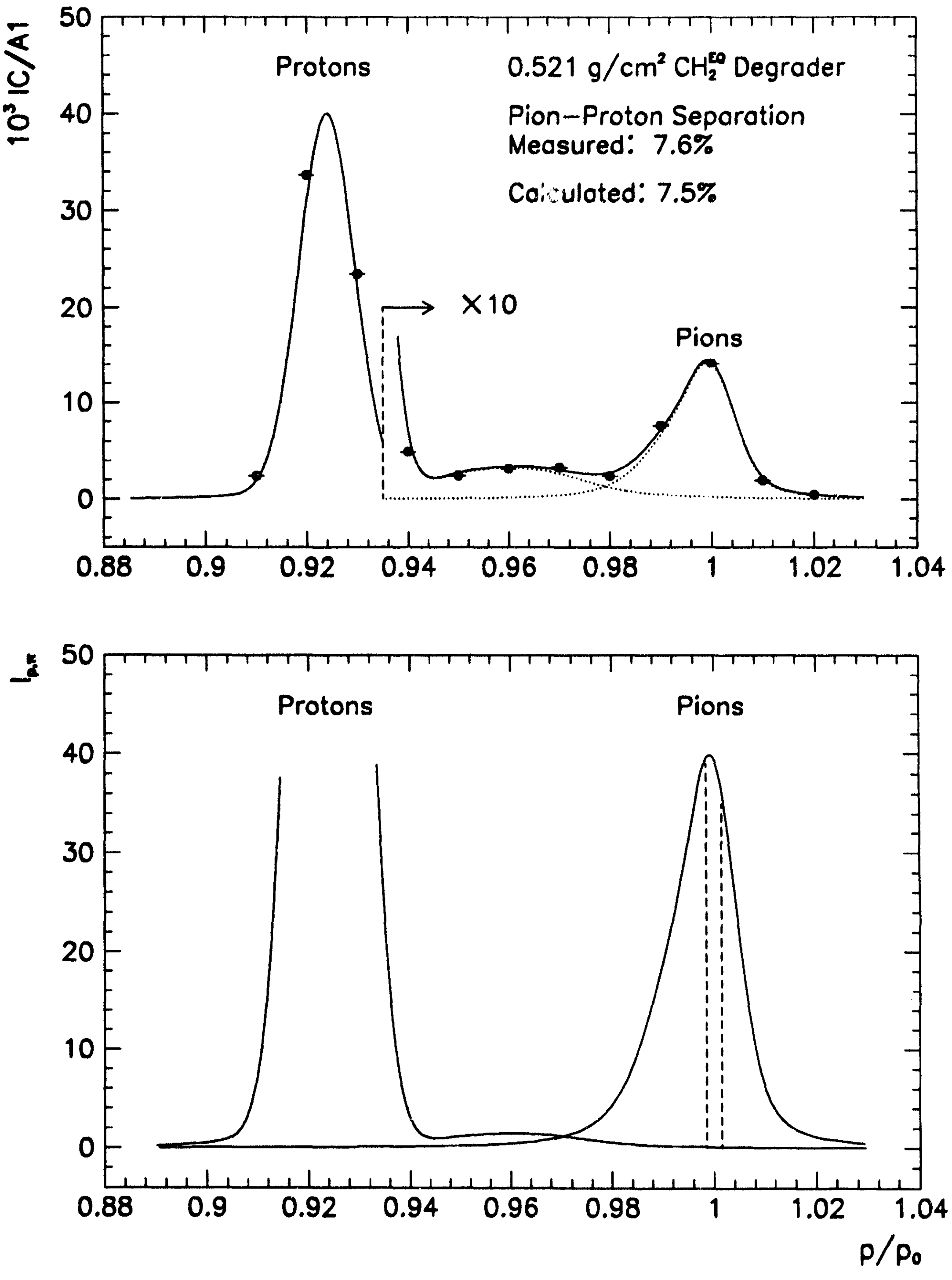

Figure 3.11 Pion-proton separation in 200 MeV π^+ beam. The extracted proton fraction is 0.3%.

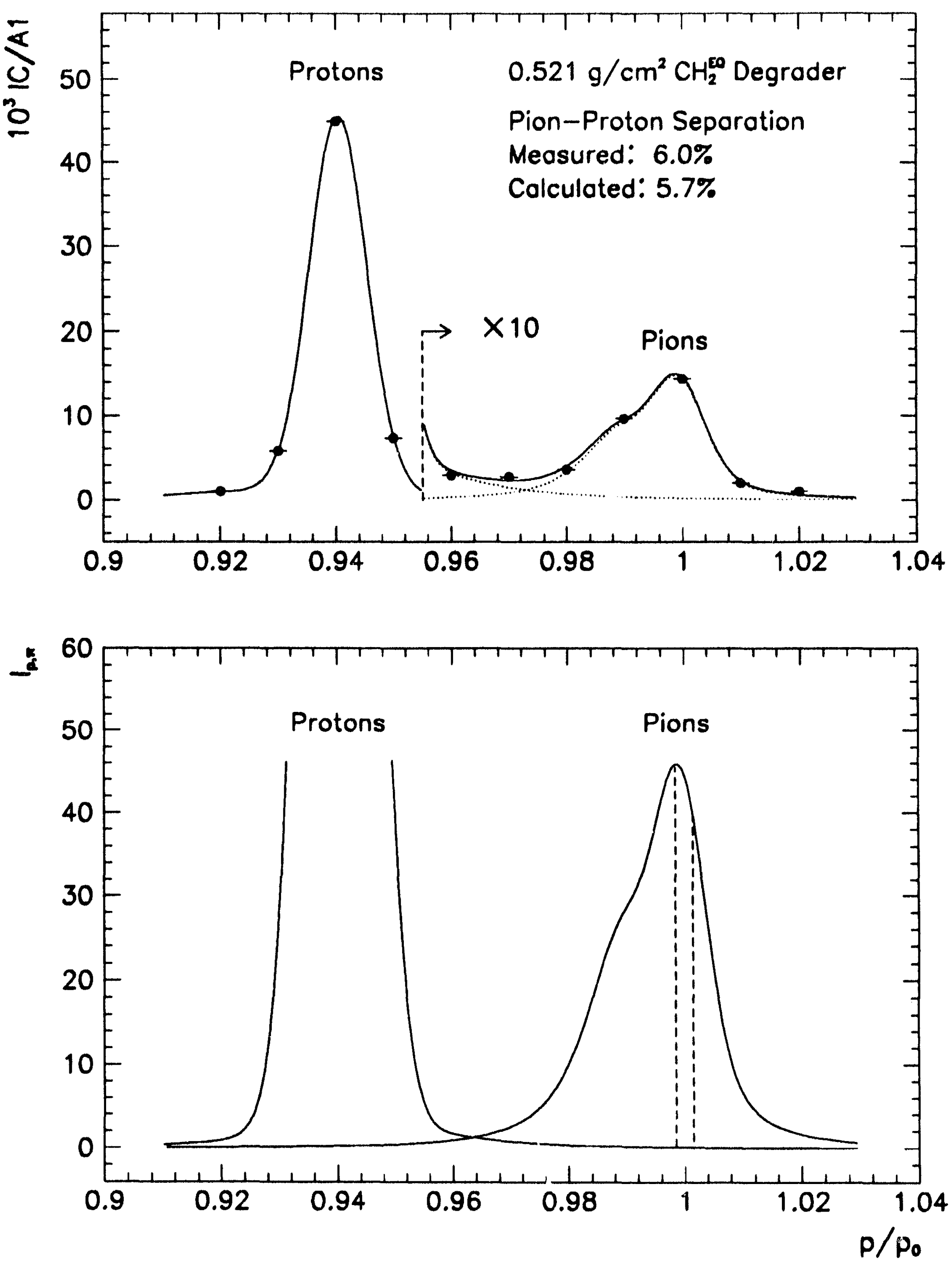

Figure 3.12 Pion-proton separation in 220 MeV π^+ beam. The extracted proton fraction is 0.3%.

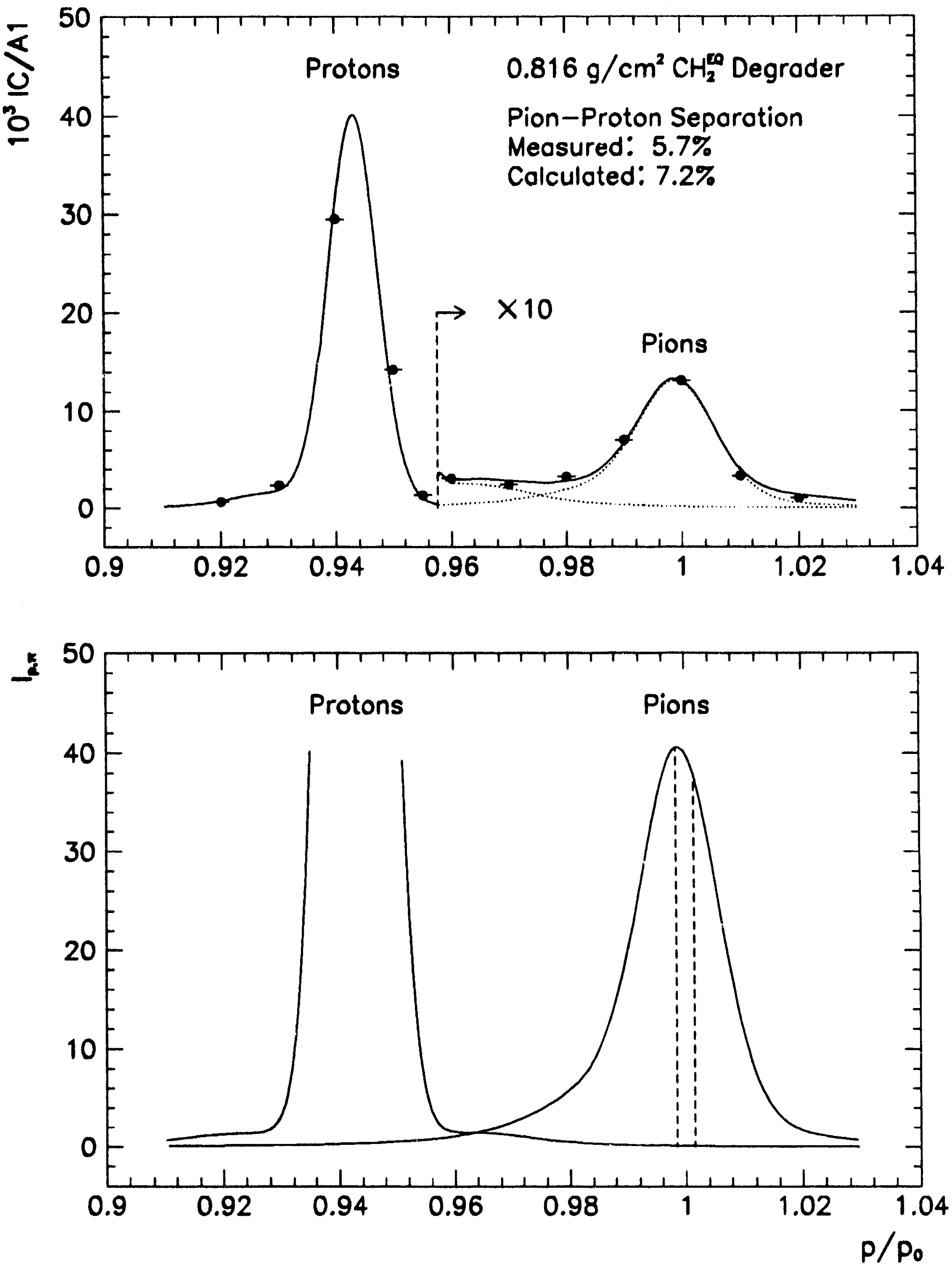

Figure 3.13 Pion-proton separation in 240 MeV π^+ beam. The extracted proton fraction is 0.2%.

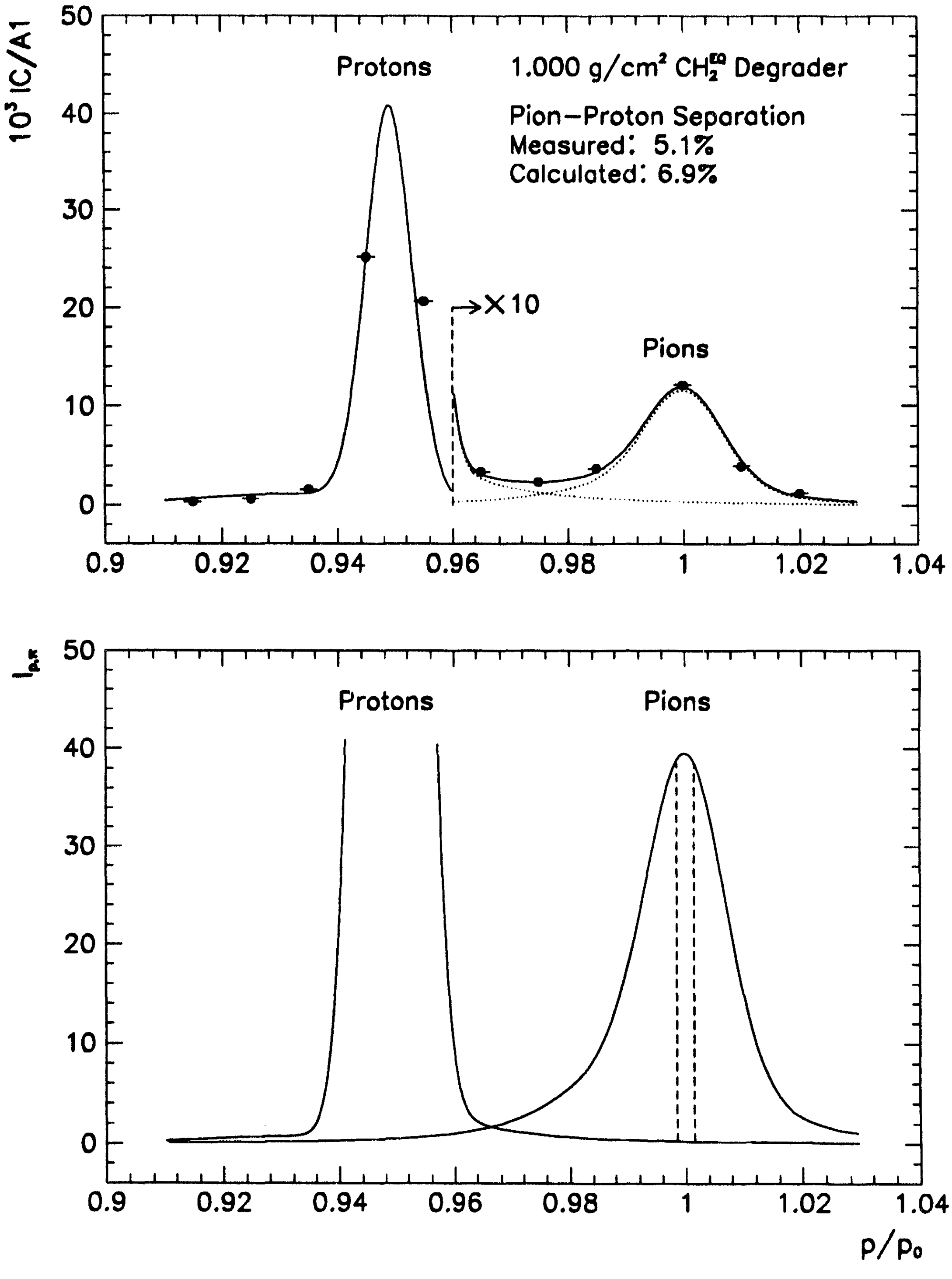

Figure 3.14 Pion-proton separation in 260 MeV π^+ beam. The extracted proton fraction is 0.7%.

with kinetic energy in MeV always corresponding to π^- particles.

Pion flux at the location of our activation disks (65 cm downstream from the target) is reduced due to in-flight decay compared to the flux on target. This correction is 11.5%, at 29 MeV. The rate of IC counts per MeV of deposited energy is a constant parameter of our ion chamber. This rate was measured with positive pion beams with known proton fraction f_p (0.6%) at 260 MeV:

$$I_c/E_{\text{dep}} = (2.57 \pm 0.11) \times 10^{-5}\ \text{MeV}^{-1}. \tag{3.11}$$

This parameter was used to extract the electron contamination of the 30 MeV negative pion beam. Both beam pions and beam electrons contribute to the induced activity in an activation disk. The total activity is proportional to N_p, the total number of beam particles

$$N_p = n_{\pi^-} + n_{e^-} = n_{\pi^-}\left(1 + f_{e^-}\frac{\sigma_{e^-}}{\sigma_{\pi^-}}\right), \tag{3.12}$$

where f_e is the electron fraction in the beam, and σ_{e^-} and σ_{π^-} are the electron and pion activation cross sections, respectively (see Table B.1).

Thus, the apparent number of pions deduced from an activation measurement must be reduced by the factor $(1 + f_e\sigma_{e^-}/\sigma_{\pi^-})$. On the other hand, the actual number of pions must satisfy:

$$N_p = n_{\pi^-}\frac{IC}{i_m}\Delta E_{\pi^-}\left(1 + f_e\frac{\Delta E_e}{\Delta E_\pi}\right), \tag{3.13}$$

where ΔE_{π^-} and ΔE_{e^-} are the energy loss of pions and electrons in the ion chamber, respectively. Eliminating N_p from (3.12) and (3.13) we obtain

$$\left(1 + f_e\frac{\sigma_e}{\sigma_\pi}\right)\frac{i_m}{N_p\Delta E_\pi I_c} = 1 + f_e\frac{\Delta E_e}{\Delta E_\pi}, \tag{3.14}$$

which is used to determine f_{e^-}. As expected, electron contamination were found to depend on the shielding and collimationg configuration, as follows:

$$\left.\begin{array}{l}
\bullet\ \text{1991 runs with CH}_2\text{ target shielding: } e^-/\pi^- = 12 \pm 2 \\
\bullet\ \text{1992 runs with CH}_2\text{ target shielding: } e^-/\pi^- = 12 \pm 2 \\
\bullet\ \text{1991 runs with LH}_2\text{ target shielding: } e^-/\pi^- = 22 \pm 3 \\
\bullet\ \text{1992 runs with LH}_2\text{ target shielding: } e^-/\pi^- = 19 \pm 3
\end{array}\right\} \tag{3.15}$$

These electron fraction values are in reasonable agreement with the *LAMPF User's Handbook* fraction [How-87] when the latter is interpolated to 29 MeV and extrapolated to the target location (expected $e^-/\pi^- \sim 19$).

Table 3.5 The LEP channel degraders and proton fraction. The subsequent columns tabulate the kinetic energy of the incident pion beam, the used degrader CH_2-equivalent areal thickness, the expected π^+-p separation of momentum-analysed particles and extracted proton fraction, pions-per-monitor constant obtained in the comprehensive activation measurements analysis and the product $\pi/IC \times \frac{\partial x}{\partial E}$ that is expected to be constant.

T_π (MeV)	Degrader g/cm^2 CH_2^{EQ}	πp Separation (%)	Proton Fraction (%)	π/IC 10^5	$\pi/\mathrm{IC}\times\frac{\partial x}{\partial E}$ 10^6 g/cm^2/MeV
30 ± 1.64[a]	-	-	-	0.640 ± 0.009	0.20 ± 0.01
30 ± 1.64[b]	-	-	-	0.513 ± 0.011	0.20 ± 0.01
30 ± 1.64[c]	-	-	-	0.512 ± 0.011	0.20 ± 0.01
160 ± 0.47	0.377	9.8	0.4	5.28 ± 0.15	1.02 ± 0.03
180 ± 0.52	0.521	10.1	0.4	5.65 ± 0.17	1.07 ± 0.03
190 ± 0.54	0.521	8.6	0.4	5.70 ± 0.15	1.08 ± 0.03
200 ± 0.56	0.521	7.5	0.6	5.75 ± 0.14	1.08 ± 0.03
220 ± 0.61	0.521	5.7	0.7	5.76 ± 0.13	1.07 ± 0.03
240 ± 0.66	1.284	12.2	0.6	6.11 ± 0.11	1.13 ± 0.02
260 ± 0.70[a]	1.385	10.4	0.6	5.14 ± 0.09	-
260 ± 0.70	1.385	10.4	3.6	6.28 ± 0.09	1.15 ± 0.02

Table 3.6 $\pi^\pm$ and contaminating p kinetic energies in LEP channel/cave

Degrader (g/cm^2 CH_2)	T_π^{in} (MeV)	T_π^{out} (MeV)	T_π^{tgt} (MeV)	T_p^{in} (MeV)	T_p^{out} (MeV)	T_p^{tgt} (MeV)
-	30.00	30.00	28.86	-	-	-
0.355	160.81	160.00	159.48	36.97	36.72	32.89
0.521	181.17	180.00	179.49	43.43	43.05	39.74
0.521	191.16	190.00	189.50	46.74	46.36	43.26
0.521	201.14	200.00	199.50	50.14	49.75	46.84
0.521	221.13	220.00	219.51	57.21	56.80	54.20
0.816	241.76	240.00	239.52	64.86	64.20	61.86
1.000	262.13	260.00	259.53	72.78	71.94	69.81

M. D. Cooper [Coo-74] has measured π:e^-:μ^- relative fractions at the exit of LEP beam line by time-of-flight method. From TOF spectra clear separation of pions, electrons and muons was obtained in proportions 0.32 : 0.62 : 0.06. Most of the detected muons came from the production target.

C. Single Charge Exchange on CH_2, ^{12}C, and LH_2 at 30 MeV

Goals of the single charge exchange measurements performed with 30 MeV π^- beam were:

- to ascertain proper functioning of the π^0 spectrometer detectors, electronics, and computer data acquisition,
- to confirm by direct measurement selected efficiency factors which enter into the over-all π^0 spectrometer detection efficiency and were determined independently in cosmic ray calibration runs and Monte Carlo studies,
- to calibrate the LH_2 target thickness by comparison with a well-described CH_2 target,
- to identify background sources with both full and empty target.

All stated goals have been achieved, enabling the extraction of the independent SCX differential cross sections with CH_2, LH_2 and ^{12}C targets.

The π^0 spectrometer was set to operate in the two-post configuration, with J and K arms positioned symmetrically left and right with respect to the beam. Three different choices of setup parameters—scattering plane polar angle, γ-γ opening angle and nominal crate distances—were used and are listed in Table 3.7. They were optimized for maximal geometrical acceptance of 25 MeV neutral pions.

Table 3.7 The π^0 spectrometer setup parameters. First column lists year and the configuration label, second, third and fourth give the vertical scattering angle, the opening angle of the two arms, and the corresponding π^0 kinetic energy, respectively. The dimensions of an ideal conversion plane located at a depth equivalent to 5/6th of the converter thickness from the front face of second converter are labeled $\Delta x_2 \times \Delta y_2$ while the plane itself is at $R + 12.63$ cm from a target center, R being the nominal arm radius.

Setup (Year)	θ (deg)	η (deg)	T_{π^0} (MeV)	$\Delta x_2 \times \Delta y_2$ (cm)	R (cm)
1990A	0°	118.25°	22.28	32.04 × 53.42	48.12
1990B	20°	115.07°	25.00	32.32 × 53.88	50.00
1991/92A	20°	115.07°	25.00	33.10 × 52.64	55.00
1991B	50°	106.94°	33.00	28.54 × 54.16	73.00

The mechanical alignment was accomplished using standard techniques [Bae-84]. A self-leveling theodolite, inclinometer, and calibrated levels were required for this task. The spectrometer alignment parameters for a given scattering angle and π^0 kinetic energy were calculated using the existing program `GEO`, and were passed on to the Q data acquisition and analysis program on-line by means of a `PRM` array.

The nominal distance from the pivot was measured with a standard tape engraved on the cart frame with an estimated accuracy of ±1 mm. The azimuth circle was laid out on the cave floor and two floor angles from Table 3.7 were marked at 4 m radius. The angles were changed by rotating the carts on the air pads and aligning the plumb bob with the marks to within 0.1°. The detector assembly inclinations were set using an inclinometer with crates pointing to the target within 1 minute of arc. The J and K carts were leveled by 3 jacks mounted on the base frames: the maximal estimated vertical column deviation from plumb was ±5 arc seconds. The vertical and horizontal offsets of the crates with respect to the post columns were measured using a theodolite set at beam height before and after the experiment. The offset corrections of the order of 1 mm were entered in the analyzer software.

The x and y wire chamber fiducial limits were adjustable as 1-dimensional gates in the Q test file. These cuts imposed on every wire chamber require that the reconstructed vertex of photon conversion in the lead-glass conversion plane lies within the pyramidal volume whose apex is located at the target and whose base is a plane located n_{rl} radiation lengths deep in the calorimeter blocks. The measured π^0 yields were determined as a function of fiducial area widths during the 1990 test run, Figure 3.15. The results scaled with the Monte Carlo effective solid angle without any evidence of shower leakage, even with the maximum geometrically allowed fiducial openings corresponding to 2 radiation lengths at 55 cm nominal crate radius. Leaving the fiducial area wide open with $n_{rl} = 2$ the resolution and the line shape of monoenergetic 30 MeV π^0's were affected by less than 10%.

The spectrometer acceptance for monoenergetic π^0's and π^0's with uniform energy distribution was calculated with Monte Carlo program `PIANG` [Gil-79]. That program was used extensively in the π^0 spectrometer design, as well as in all subsequent published experiments. `PIANG` simulates the detection of neutral pions by the π^0 spectrometer as a function of three classes of input parameters:

- geometrical settings of the detector crates including the scattering plane orientation, nominal target-to-converter distances, converter fiducial areas, the opening angle between detector arms, and the polar angle of the detector's bisector,
- performance parameters of the instrument given by the photon energy resolution in the calorimeter (33% for gammas at 100 MeV) and conversion position resolution in MWPC's ($\Delta x_m \times \Delta y_m$, full widths at half maximum: 0.6×1.2 mm), and

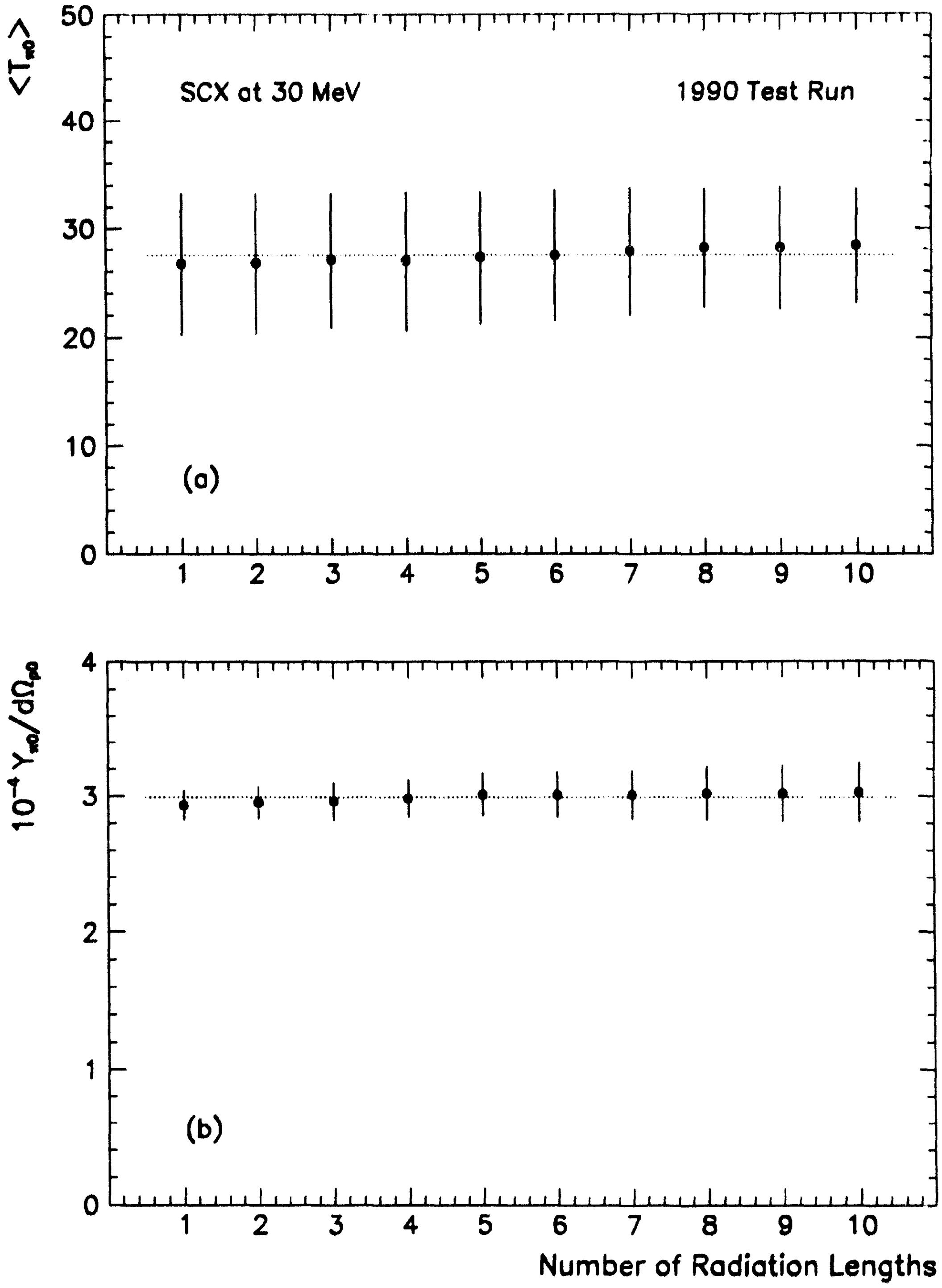

Figure 3.15 (a) Top panel shows the median kinetic energy and root-mean-square values for SCX π^0's at 30 MeV incident beam and CH_2 target. There is no evidence of significant electromagnetic shower leakage. (b) Bottom panel confirms that the ratio of π^0 yield to Monte Carlo spectrometer acceptance does not depend on the number-of-radiation-lengths constraint n_{rl} imposed on fiducial areas for this low energy spectrometer configuration.

Table 3.8 The π^0 spectrometer acceptance for $\pi^- p \to \pi^0 n$ at 28.2 MeV vs $X_{\rm CUT}$

$X_{\rm CUT}$ $n_{rl} = 3$	$d\Omega$ (msr)	$\int A(\Omega)(\frac{d\sigma}{d\Omega})d\Omega$ (μb)
0.03	3.470 ± 0.005	0.3767 ± 0.0006
0.05	5.804 ± 0.008	0.6309 ± 0.0009
0.07	8.116 ± 0.011	0.8839 ± 0.0014
0.10	11.640 ± 0.016	1.2747 ± 0.0018
0.15	17.944 ± 0.025	1.9210 ± 0.0027
0.20	23.287 ± 0.033	2.6252 ± 0.0037
0.25	28.761 ± 0.041	3.3081 ± 0.0047
0.30	33.589 ± 0.048	3.9493 ± 0.0056
0.35	37.552 ± 0.053	4.5138 ± 0.0064
0.40	40.163 ± 0.057	4.9197 ± 0.0070
0.45	41.788 ± 0.042	5.1865 ± 0.0052
0.50	42.554 ± 0.043	5.3226 ± 0.0054
0.55	42.837 ± 0.043	5.3787 ± 0.0054
0.60	42.950 ± 0.030	5.4053 ± 0.0038

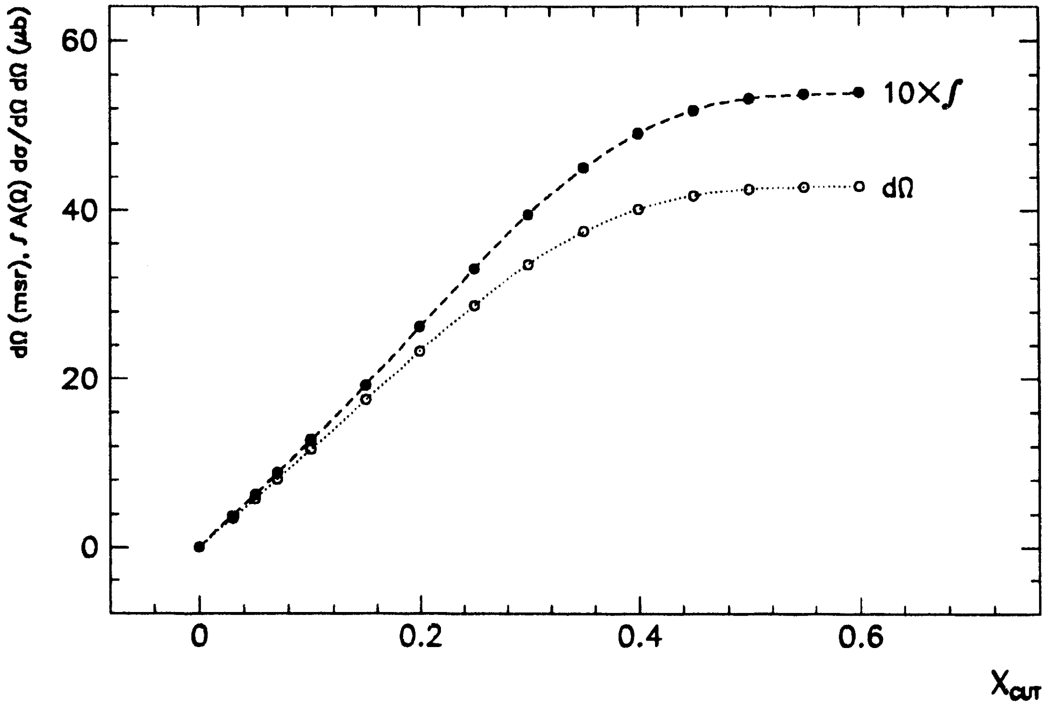

Figure 3.16 The π^0 spectrometer acceptance for 30 MeV incident π^- beam calculated in **PIANG** Monte Carlo simulation. The opening angle of the crates is optimized for 25 MeV π^0's while the polar angle is 20°. The MWPC's fiducial areas are wide open and correspond to 2 radiation length shower containment within the lead glass calorimeter. The dotted curve follows the effective detection solid angle in msr (•) as a function of the γ-γ energy asymmetry parameter $X_{\rm CUT}$. The dashed line connects the simulated solid angles (o) weighted with theoretical differential cross sections calculated by the phase-shift program **SAID** ("scattering analysis interactive dail-in") [Arn-87].

- beam and target related effects including the kinetic energy and momentum spread of the incident beam, horizontal and vertical beam profiles, target location and orientation, and energy loss and straggling in the target.

`PIANG` output routines were rewritten for this analysis calling the `CERNLIB HBOOK` subroutines which create one- and two-dimensional histograms and Ntuples. Histogrammed quantities included the kinetic energy, polar and azimuthal angle of "thrown" and "detected" π^0's, distribution of X, energy-sharing parameter, and simulated wire chamber hits as well as all the resolution functions.

Charge-exchange differential cross sections have been determined for three polar angle bins. Angular bin sized were determined by requiring an equal number of π^0 events in each bin. That condition obviously assured equal statistical uncertainties for the three polar angle bins. The differential cross sections were calculated from the yields:

$$\frac{d\sigma(\theta)}{d\Omega} = \frac{Y_{\pi^- p \to \pi^0 n} J}{N_{\pi^-} t_x d\Omega_{\pi^0} \epsilon_{\pi^0} f_{\text{abs}} \Gamma_{\pi^0 \to \gamma\gamma} \eta_{cl} \eta_{vp}}, \tag{3.16}$$

where Y is the number of detected π^0's after background subtraction, J is the Jacobian of transformation from the LAB to the CM frame, N_{π^-} is number of beam π^- incident on target x, t_x is the effective target thickness, $d\Omega_{\pi^0}$ is the laboratory solid angle of the spectrometer for π^0 detection, ϵ_{π^0} is the overall π^0 spectrometer detection efficiency, f_{abs} is the fraction of photons not absorbed before conversion, $\Gamma_{\pi^0 \to \gamma\gamma}$ is $\pi^0 \to \gamma\gamma$ decay branching ratio, η_{cl} is the computer live time, and η_{cp} is the spectrometer veto live time.

Partial wave expansion of the CM cross sections in terms of Legendre polynomials is

$$\frac{d\sigma(\theta)}{d\Omega} = \sum_{l=0}^{m} A_l P_l(\cos\theta), \tag{3.17}$$

where θ is the π^0 emission angle relative to the incident π^-.

For π^- energies up to 200 MeV a satisfactory description is provided by the truncated expansion

$$\frac{d\sigma(\theta)}{d\Omega} = A_0 + A_1 P_1 \cos(\theta) + A_2 P_2 \cos(\theta), \tag{3.18}$$

equivalent to keeping only six S and P phase shifts in the description.

The total SCX cross section follows from integration over θ:

$$\sigma_t^{\text{scx}} = 4\pi A_0, \tag{3.19}$$

A least square fit through 9 measured differential cross sections gives:

$$\frac{d\sigma(\theta)}{d\Omega} = [0.448 - 0.506 P_1 \cos(\theta) + 0.155 P_2 \cos(\theta)] \text{ mb/sr}, \quad \sigma_t = 5.6 \pm 2.1 \text{ mb}, \quad \chi^2 = 1.3. \tag{3.20}$$

Table 3.9 Differential cross sections for pion SCX at 27.7 MeV, measured with the CH_2 target with hydrogen thickness 61.18 mb^{-1}. Shower tracking efficiencies calculated for every angular bin in GEANT3 Monte Carlo varied between between 73.7% and 74.9% and agreed within ~2% with the measured average shower tracking efficiency of 76%. J is the Jacobian of the transformation of the π^0 spectrometer solid angle from the laboratory to the center-of-momentum frame. The comparison with the partial-wave analysis of Arndt *et al.* [Arn-87] is shown.

Year	$\cos\theta_{cm}$	$d\Omega^{lab}_{\pi^0}$ (msr)	J	$(d\sigma/d\Omega)^{cm}_{exp}$ (μb/sr)	$(d\sigma/d\Omega)^{cm}_{said}$ (μb/sr)	$\frac{\text{E1179}}{\text{SAID}}$ ratio
1990	$0.9603^{+0.0397}_{-0.0535}$	22.66 ± 0.02	0.7484	92.7 ± 6.3	71.0	1.31 ± 0.09
	$0.8138^{+0.0930}_{-0.0242}$	22.14 ± 0.02	0.7839	110.4 ± 7.2	103.0	1.07 ± 0.07
	$0.6833^{+0.1063}_{-0.3710}$	18.90 ± 0.02	0.8171	135.0 ± 8.4	138.5	0.97 ± 0.06
1991	$0.9385^{+0.0615}_{-0.0677}$	15.92 ± 0.02	0.7536	102.7 ± 6.6	75.8	1.35 ± 0.09
	$0.8151^{+0.0557}_{-0.0660}$	14.13 ± 0.02	0.7836	114.8 ± 7.2	104.8	1.10 ± 0.07
	$0.6481^{+0.1009}_{-0.3201}$	12.87 ± 0.02	0.8263	140.5 ± 7.8	148.1	0.95 ± 0.05
1992	$0.9385^{+0.0615}_{-0.0677}$	15.92 ± 0.02	0.7536	106.2 ± 6.2	75.8	1.40 ± 0.08
	$0.8151^{+0.0557}_{-0.0660}$	14.13 ± 0.02	0.7836	109.3 ± 6.6	104.8	1.04 ± 0.06
	$0.6481^{+0.1009}_{-0.3201}$	12.87 ± 0.02	0.8263	139.0 ± 7.1	148.1	0.94 ± 0.05

The diagonal elements of the symmetric covariance matrix in the units $(mb/sr)^2$ are standard deviations of fitted parameters:

$$\begin{array}{l} \\ A_0 - \frac{1}{2}A_2 \\ A_1 \\ \frac{3}{2}A_2 \end{array} \begin{array}{c} \begin{array}{ccc} A_0 - \frac{1}{2}A_2 & A_1 & \frac{3}{2}A_2 \end{array} \\ \left(\begin{array}{ccc} 0.0297 & -0.0751 & 0.0465 \\ \cdots & 0.1906 & -0.1185 \\ \cdots & \cdots & 0.0739 \end{array} \right) \end{array}, \qquad (3.21)$$

The LH_2 target thickness was extracted by direct comparison with the yield measured using the CH_2 target with the known thickness after applying the following corrections: (i) the fraction of π^0 photons absorbed (−2%), (ii) pion decay corrections (−11%), (iii) electron contamination fraction (+23%), (iv) pion beam profile on the target (+3%), (v) SCX energy dependence from phase-shift analysis (+10%), (vi) π/i_m factor (+20%). The resulting LH_2 target thickness for 30 MeV π^- is 0.116 b^{-1}. This thickness is consistent with value obtained from π^+p elastic scattering data when the difference in beam profile and fraction of π^0's converting in the target assembly are taken into account. The compatible thickness is calculated by integrating actual target shape weighted by 2-dimensional beam contour.

Table 3.10 Effective LH_2 target thickness for π^0's: 1990, 1991 and 1992 runs. f_{abs} is a loss due to the absorption of π^0 photons preceding conversion in the target assembly, the π^0 spectrometer polyethylene "hardener" sheet and veto scintillator.

X_{cut}	$f_{abs} \cdot t_{LH_2}$ 1990 (g cm^{-2})	$f_{abs} \cdot t_{LH_2}$ 1991 (g cm^{-2})	$f_{abs} \cdot t_{LH_2}$ 1992 (g cm^{-2})
0.10	0.136 ± 0.012	0.107 ± 0.016	0.137 ± 0.015
0.20	0.139 ± 0.010	0.106 ± 0.013	0.146 ± 0.012
0.30	0.133 ± 0.008	0.102 ± 0.010	0.130 ± 0.010
0.40	0.131 ± 0.006	0.105 ± 0.008	0.132 ± 0.008

The $\pi^- p \rightarrow \pi^0 n$ differential cross sections measured with CH_2 target for 9 polar-angle bins are summarized in Table 3.9. Listed uncertainties are the statistical ones and correspond to ~400-600 events per bin with 2–10% of subtracted ^{12}C background contribution. The polar angle centroids are the average values for each variable-size bin, while ±2.7° angular error bars represent the π^0 spectrometer resolution in that configuration. The comparison with the SAID phase shift analysis [Arn-87] is provided. The SAID ("scattering analysis interactive dial-in") package of programs and data files encodes π-nucleon partial-wave solutions for a pion incident energies below 1100 MeV. The data base contains 717 $\pi^- p$ charge exchange measurements, but only two published experiments cover the energies below 100 MeV. Fitzgerald *et al.* [Fit-86] used the LAMPF π^0 spectrometer to determine pion single charge exchange for center-of-momentum angles less then 20° at 7 beam energies between 32.5 and 63.2 MeV. The discussion of π^0 spectrometer calibration in the section II.F suggests that [Fit-87] considerably overestimated the product of the charged-particle detection efficiency and the track-reconstruction efficiency. Apparently omitting some relevant factors, such as a converter charged-particle transparency, the efficiency product in their differential cross section calculation ranged from 0.78 to 0.85. Our experimental experience supplemented with extensive Monte Carlo simulations of the π^0 spectrometer response as well as the study of standard analyzer programs led us to the conclusion that the equivalent efficiency product have to be $\leq$60%, even with unrestrictive TRACER cuts. That accounts in part for the difference between their results and our differential cross sections.

The experiments of Salomon, Bagheri and collaborators [Sal-83], [Bag-88], studied the reaction $\pi^0 p \rightarrow \pi^0 n$ using a large NaI crystal at 8 pion energies between 27.4 to 121.9 MeV. Covered polar angles spanned the range from 45° to 142°. Their differential cross sections extrapolated to the angular range 0°–45° are factor of two smaller then the results reported in this Thesis.

Figure 3.20 shows E1179 SCX differential cross sections increasing more slowly with the polar angle in the range from 0° to $\theta_{\pi^0}^{\rm cm}$ = 50°, when compared with SAID values. In conclusion, the published measurements underestimate $\pi^- p \rightarrow \pi^0 n$ differential cross sections for forward scattering angles ($\theta \lesssim 30°$) at beam energies ~30 MeV. Global SAID fit which includes the broader energy range is in better the agreement with E1179 data but still short by ≈30% at forward scattering angles.

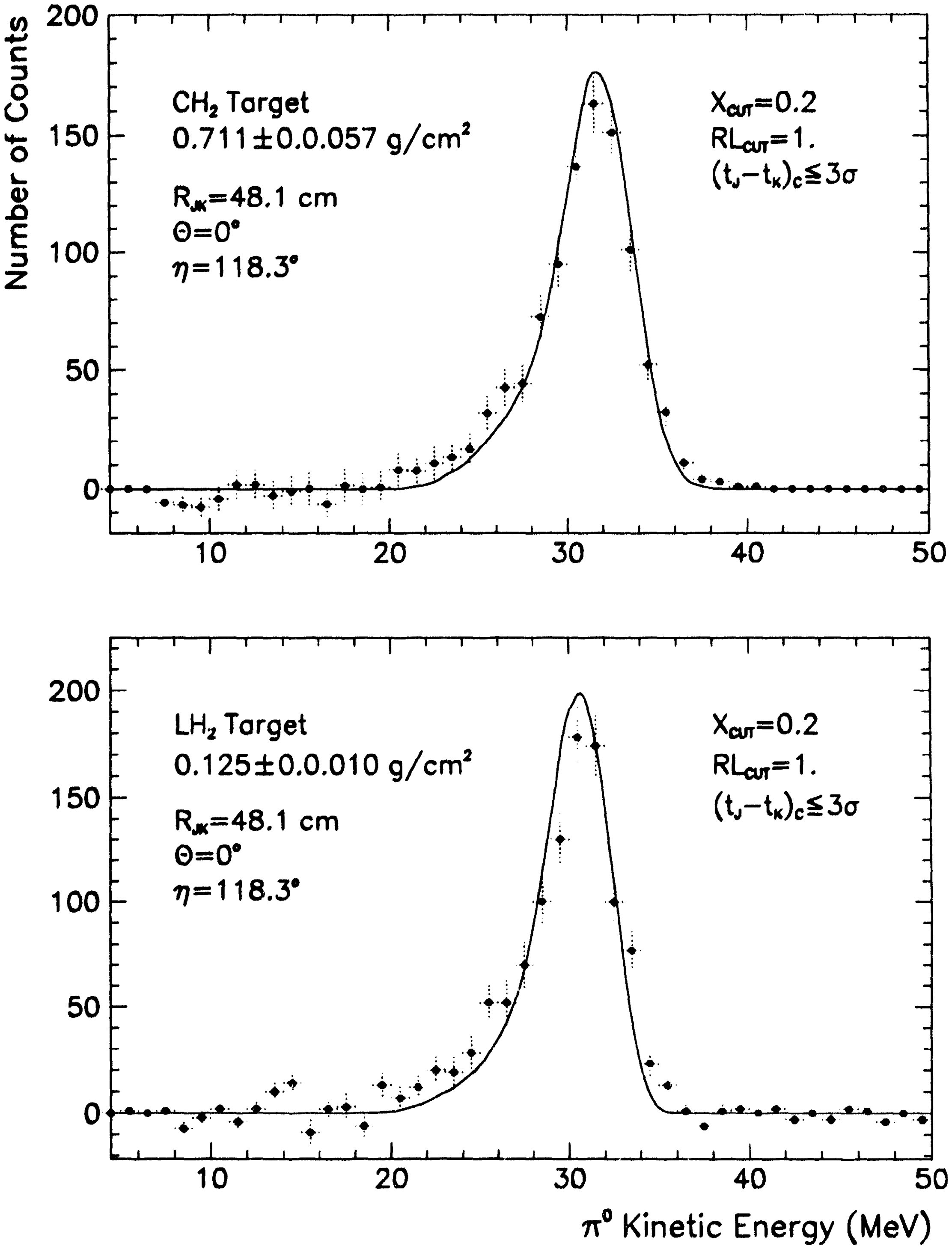

Figure 3.17 Background-subtracted inclusive π^0 energy spectra for the single charge exchange reaction on hydrogen at 30 MeV measured in 1990 run. The upper panel shows data obtained with a 0.71 g/cm^2 thick CH$_2$ target, while the lower panel shows data measured with the liquid hydrogen target (•). The latter set of data was corrected in replay for the misalignment of the target. In both panels the solid histograms represent results of Monte Carlo calculations of the π^0 spectrometer acceptance with the modified code **PIANG** [Frl-92a].

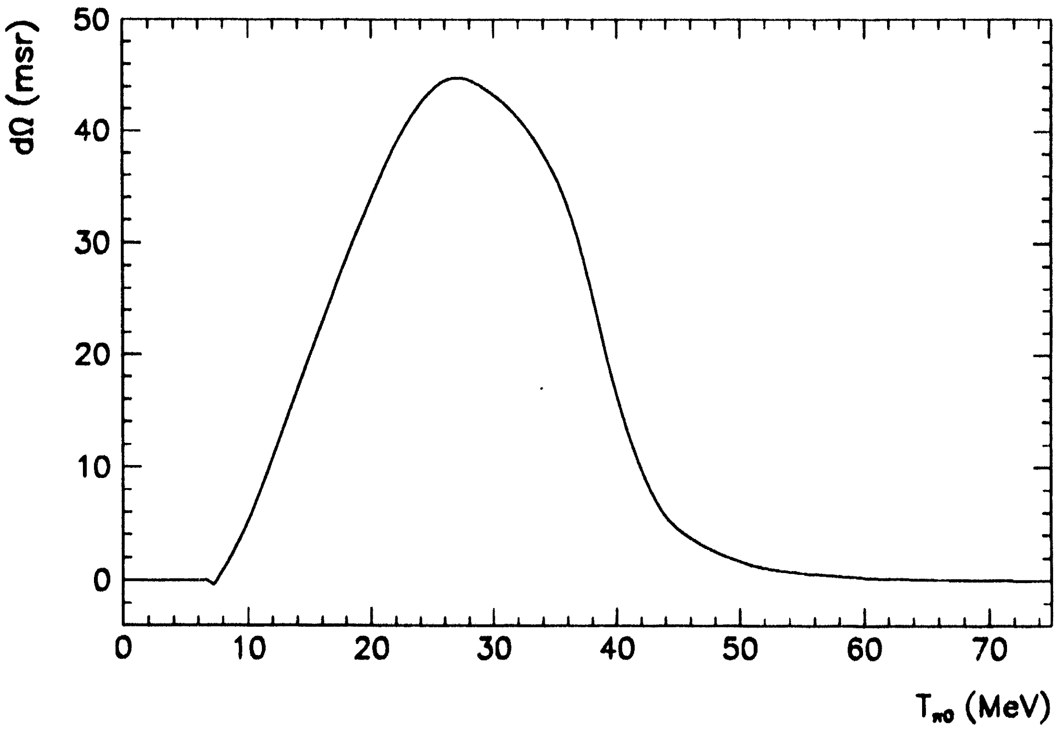

Figure 3.18 π^0 spectrometer acceptance as a function of kinetic energy of the detected pion. The calculation was done by Monte Carlo program **PIANG** for a two-radiation-lengths fiducial area and unconstrained energy sharing parameter X. The "thrown" π^0 had flat kinetic energy spectrum from 0 to $T_{\text{inc}} + Q \approx 34$ MeV.

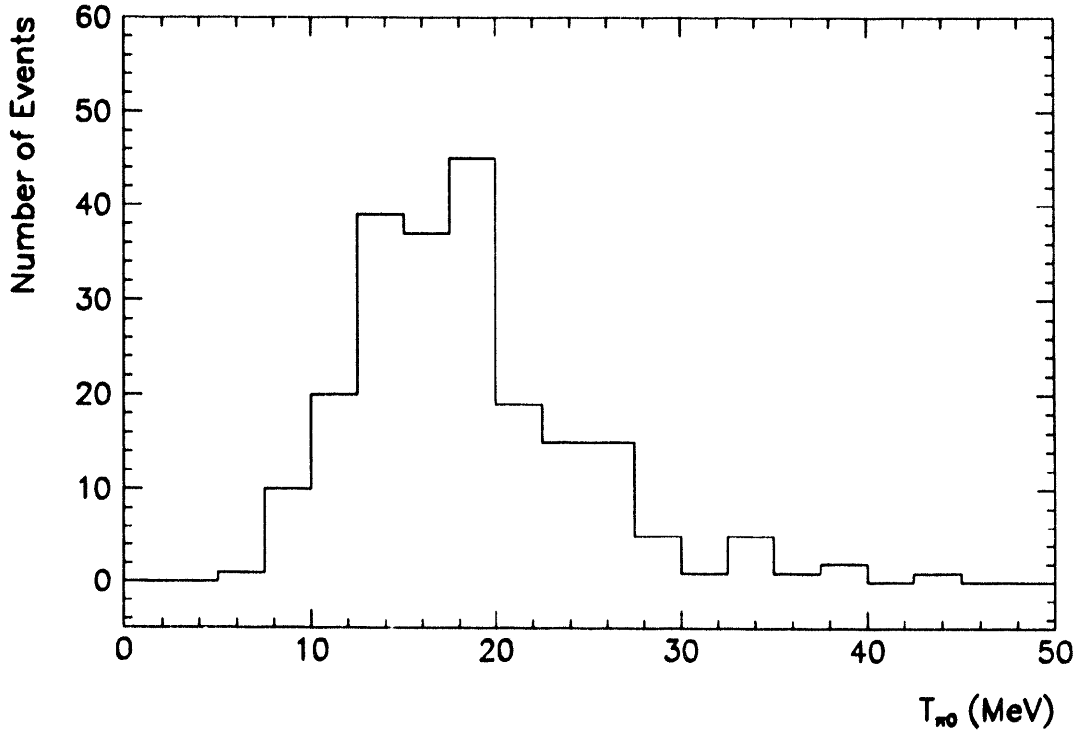

Figure 3.19 Pion single charge exchange on the ^{12}C target with 28 MeV combined to a single π^0 energy spectrum; the small background due to air around the target is subtracted using no-target runs.

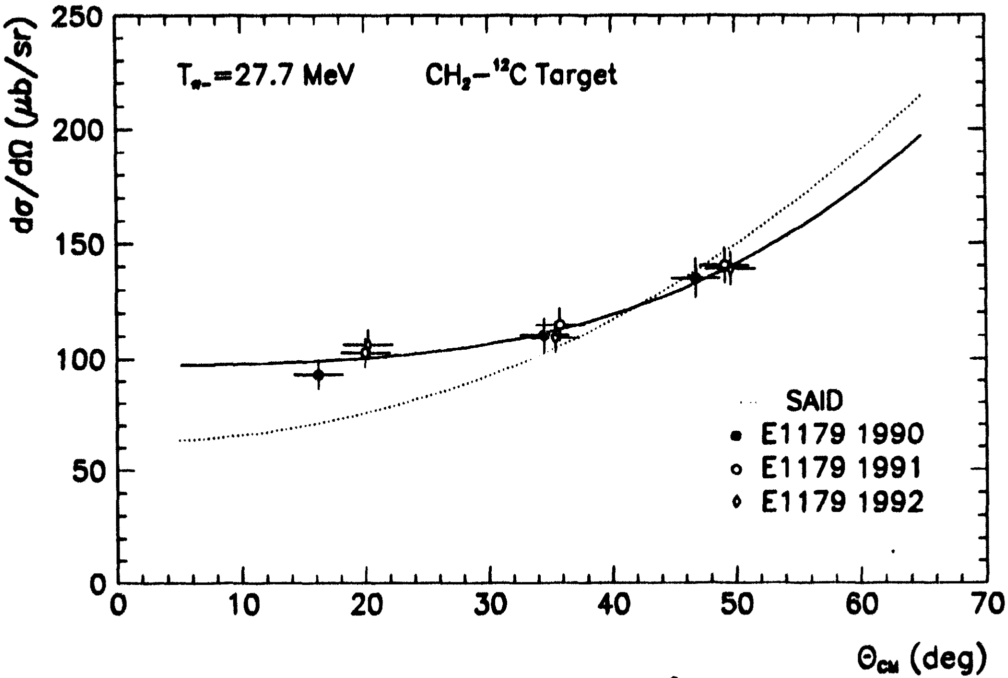

Figure 3.20 The differential cross sections for $\pi^- p \rightarrow \pi^0 n$ at 27.7 MeV. The raw yields were obtained by subtracting measured ^{12}C contribution from the runs with CH_2 target. The plotted error bars are statistical: there is an estimated 5% systematic uncertainty between 1990 and 1991/92 data. The π^0 spectrometer efficiency was determined to 5%. The full curve is a fit with first three Legendre polynomials, the dotted line represents SAID [Arn-87] solution.

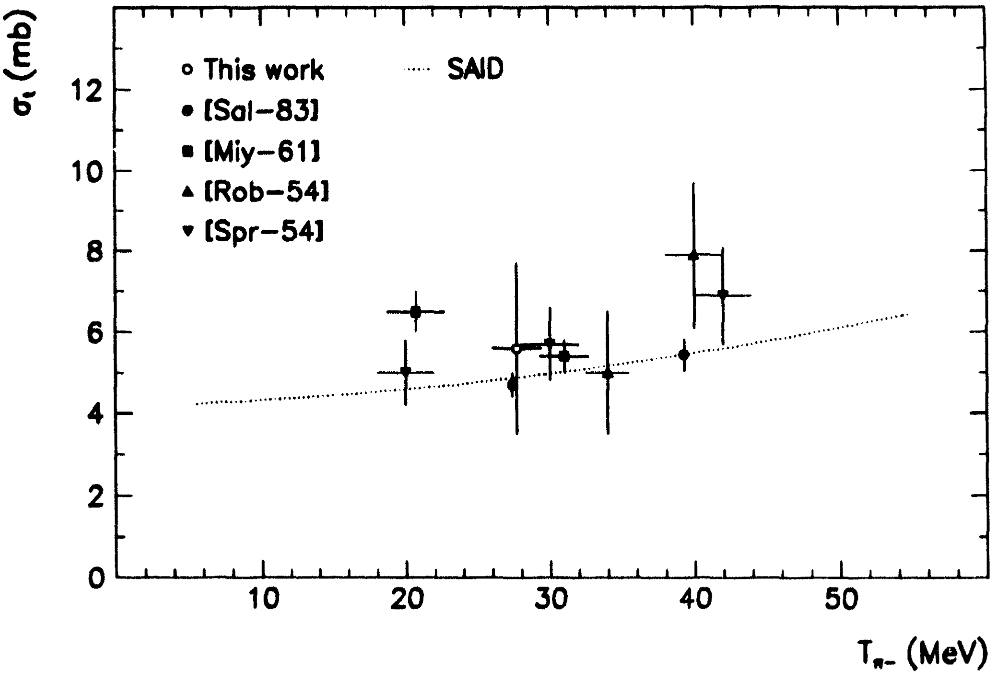

Figure 3.21 The total pion charge exchange cross section at 27.7 MeV (○) derived from a fit to 9 differential cross sections (Figure 3.14). All published measurements in the energy range 20-50 MeV are plotted alongside the SAID solution.

D. Charged Particle Identification

Light output of a scintillation detector is a nonlinear function of particle type and specific ionization. The semi-empirical model put forward by Birks [Bir-51] gave an early decsription of departures from linear behavior. Quenching interactions between the incident particle and excited molecules along its path drain the deposited energy that would otherwise appear as scintillation light. Light output L_p generated by a proton with kinetic energy T_p MeV for NE-228A scintillator (equivalent to BC 408 used in this work) was measured by [Mad-77] and parametrized in the form

$$L_p = -8.4(1.0 - e^{-0.10 T_p^{0.90}}) + 0.95 T_p. \tag{3.22}$$

Particle identification was effected by software windows on the integrated PMT charges in detectors ΔE_1 vs $(\Delta E_1 + \Delta E_2 + E)$ and $(\Delta E_1 + \Delta E_2)$ vs $(\Delta E_1 + \Delta E_2 + E)$.

The boundaries were conveniently approximated by curves of the form

$$\Delta E_i = A_i e^{-B_i(\Delta E_1 + \Delta E_2 + E)}. \tag{3.23}$$

Protons were selected by imposing the constraints

$$\Delta E_1^{\mathrm{max}} = 63.73 e^{-0.634(\Delta E_1 + \Delta E_2 + E)}, \tag{3.24}$$

$$\Delta E_1^{\mathrm{min}} = 21.51 e^{-0.604(\Delta E_1 + \Delta E_2 + E)}, \tag{3.25}$$

$$\Delta E_{12}^{\mathrm{max}} = 5725 e^{-1.184(\Delta E_1 + \Delta E_2 + E)}, \tag{3.26}$$

$$\Delta E_{12}^{\mathrm{min}} = 1661 e^{-1.064(\Delta E_1 + \Delta E_2 + E)}, \tag{3.27}$$

where $\Delta E_{12} = \Delta E_1 + \Delta E_2$, and all energies are in electron-equivalent MeV.

Pions events were found inside the following bounds:

$$\Delta E_1^{\mathrm{max}} = 8.24 e^{-0.378(\Delta E_1 + \Delta E_2 + E)}, \tag{3.28}$$

$$\Delta E_1^{\mathrm{min}} = 3.63 e^{-0.336(\Delta E_1 + \Delta E_2 + E)}, \tag{3.29}$$

$$\Delta E_{12}^{\mathrm{max}} = 117.77 e^{-0.557(\Delta E_1 + \Delta E_2 + E)}, \tag{3.30}$$

$$\Delta E_{12}^{\mathrm{min}} = 28.97 e^{-0.314(\Delta E_1 + \Delta E_2 + E)}. \tag{3.31}$$

In order to verify the bounds (3.24)-(3.31) photoelectron statistics were simulated by sampling random Poisson distribution defined by the average measured number of photoelectrons for the energy under consideration. Energy straggling effects in thin ΔE_1 counters, which are non-neglible for near-minimum ionizing pions were described with Landau random numbers generator available though the `CERNLIB` Landau package `RANLAN` [Cer-89]. The PMT gain factor uncertainty was estimated at ~7%, while the gain drifts were $\leq$ 7%. The geometrical variation of the path length in the thin and thick ΔE counters was $\leq$1%.

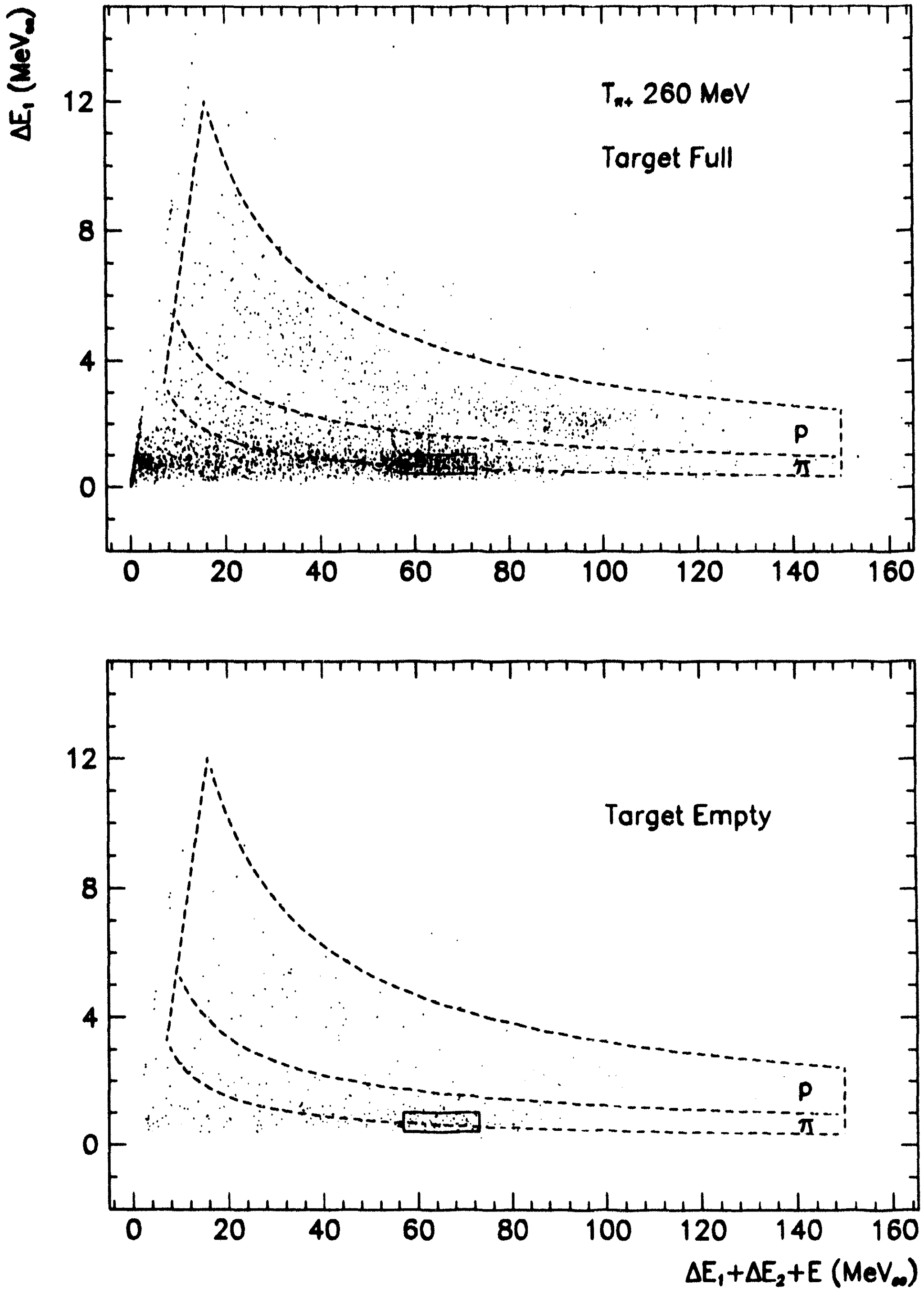

Figure 3.22 Coincident charged particle identification: ΔE_1 vs $\Delta E_1 + \Delta E_2 + E$. Protons (especially the more energetic ones) are not separated as well as when using the information from the thick ΔE_2 counter. Elastically scattered pions are nearly minimally ionizing particles which cluster around $\Delta E_1 = 0.7$ MeV$_{ee}$, $\Delta E_1 + \Delta E_2 + E = 60$ MeV$_{ee}$. The band of MI particles that extends below the pion lower band are nearly minimum ionizing pions scattered at large angles into CP detectors, triggering the charged particle electronics and subsequently charge exchanging in detector material. Resultant neutral pions, when detected, appear displaced 2-4 ns in the TOF spectrum.

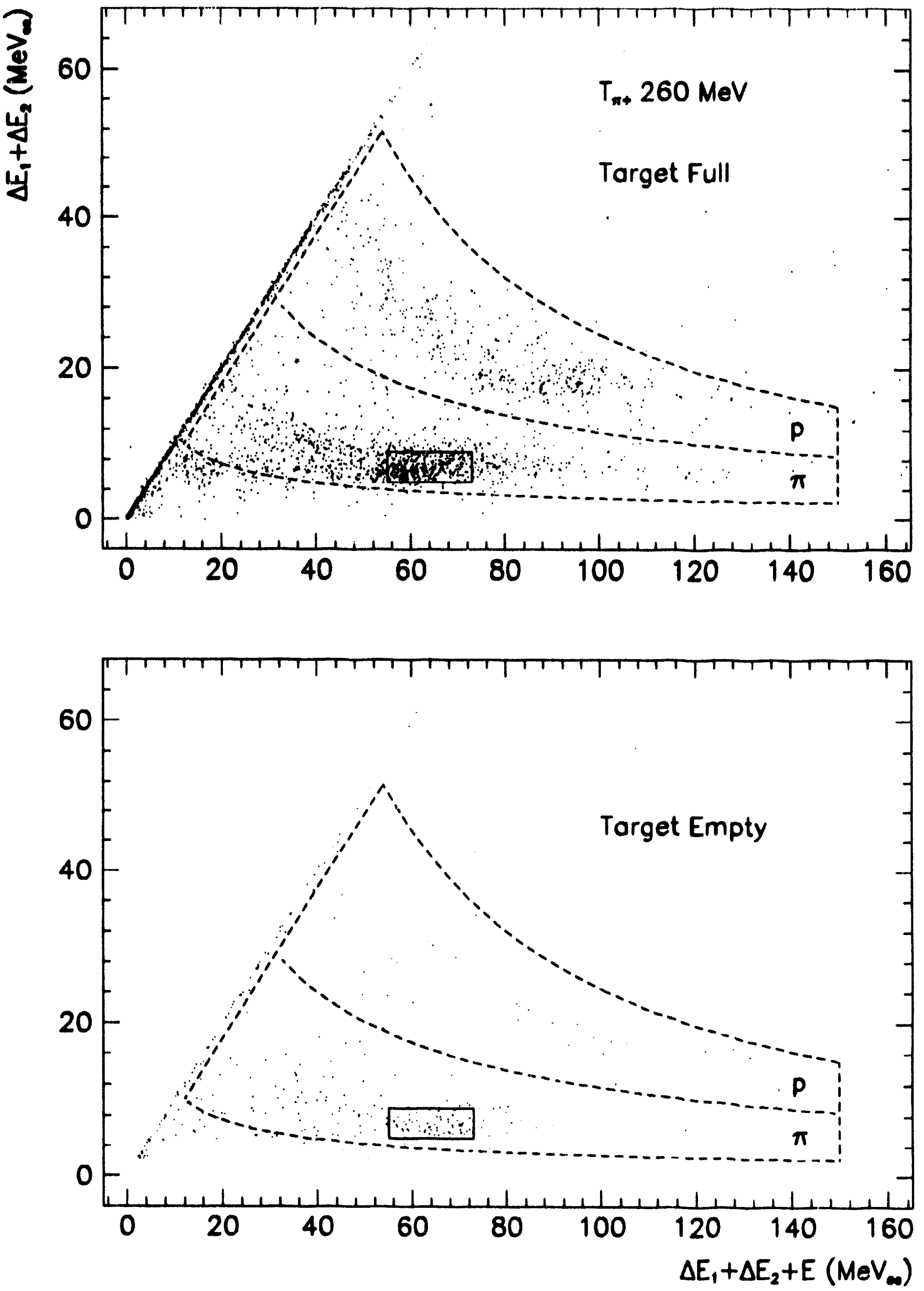

Figure 3.23 Coincident charged particle identification: $(\Delta E_1 + \Delta E_2)$ vs $(\Delta E_1 + \Delta E_2 + E)$. Particle identification windowss are consistent with curves calculated with program RANGER [Mar-85], corrected for the quenching effect in scintillator material. The deposited energies are therefore expressed in light-equivalent MeVs.

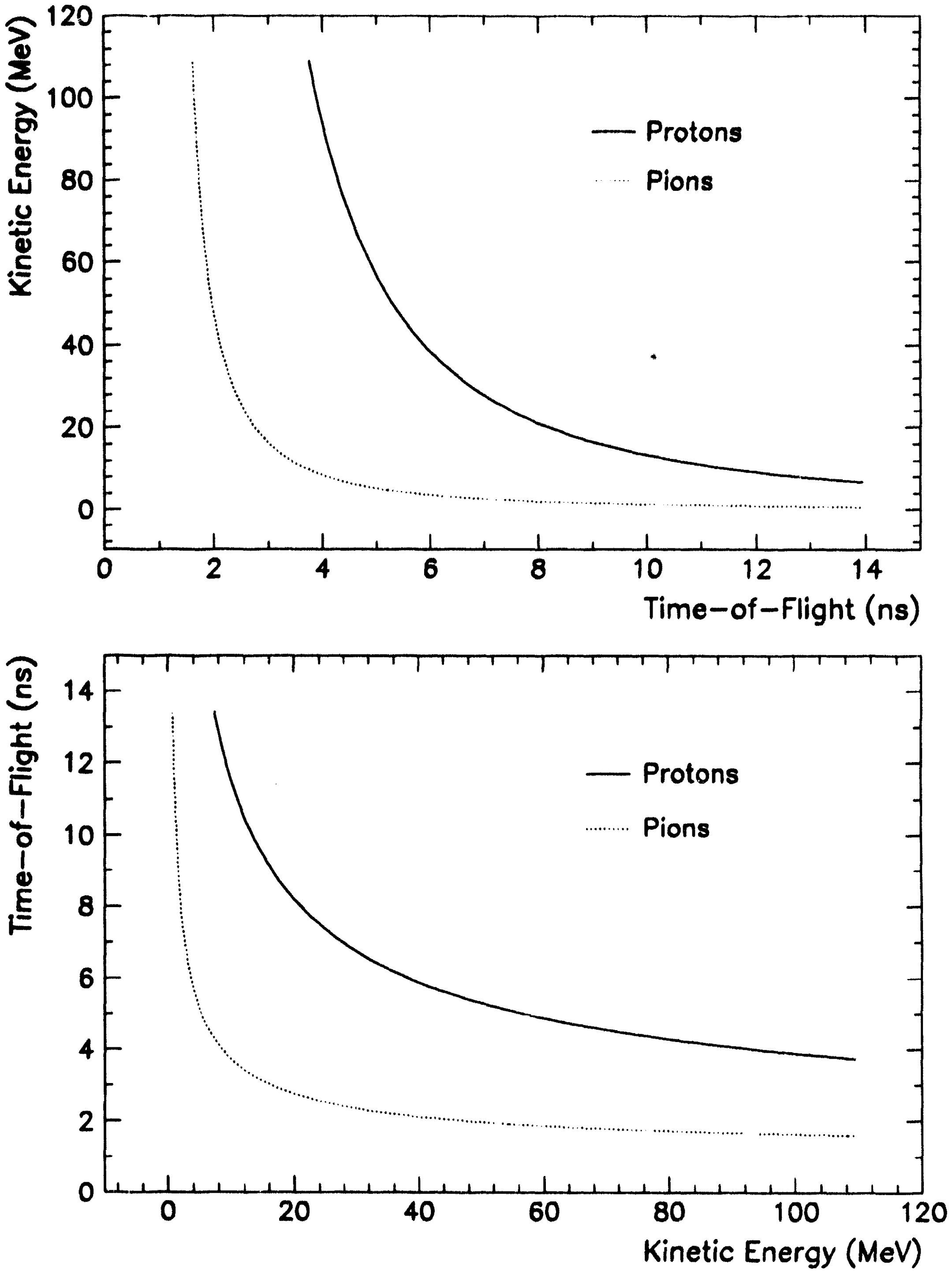

Figure 3.24 Calculated time-of-flight for the coincident charged particles with respect to the detected π^0. The expected 2-4 ns time difference between higher-energy (> 30 MeV) pions and protons shows up in TOF spectra.

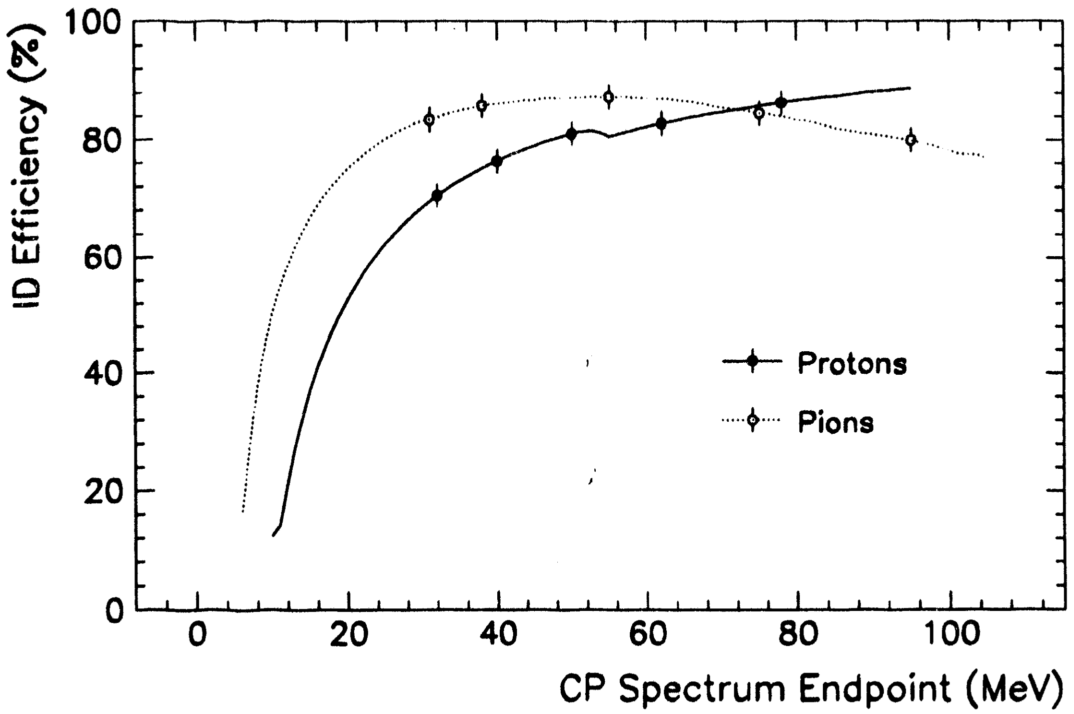

Figure 3.25 Calculated efficiency of the particle identification cuts for pions and protons. Energies of the Monte Carlo simulated coincident charged particles from $\pi^+ p \rightarrow \pi^+ \pi^0 p$ were smeared with the detector light collection probability distribution, photoelectron statistics, the Landau straggling in thin ΔE_1 and thick ΔE_2 counters and PMT gain uncertainties and drifts. The identical particle identification code is used as in the replay analysis for real coincident data. The efficiency shown as a function of the endpoint of energy spectrum of detected coincident protons (•) and pions (∘), with the five energies of interest 190-260 MeV indicated, varies between 80% and 90%.

When the timing offsets are adjusted in off-line analysis by lining up the time-of-flight histograms, a small but noticeable difference in time of arrival of pions and protons became evident. Because of the overlap of the pion-proton TOF spectra timing information could be used only to disqualify unphysicaly early protons from consideration.

Table 3.11 Factors contributing to the charged particle detection efficiency ϵ_{cp}.

Symbol	Description	Method	Value (%)	Stat/Syst Error (%)
ϵ_{pr}	intrinsic detector efficiency, p	$\pi^+ p \rightarrow \pi^+ p$	100	1
$\epsilon_{\pi^\pm}$	intrinsic detector efficiency, $\pi^\pm$	$\pi^+ p \rightarrow \pi^+ p$	100	1
f_{lp}	p interactions+out-scattering	$\pi^+ p \rightarrow \pi^+ p$	$1 \rightarrow 8$	1
$f_{l\pi^\pm}$	$\pi^\pm$ interactions+out-scattering+decay	$\pi^+ p \rightarrow \pi^+ p$	$20 \rightarrow 6$	1
$\epsilon_{id}^{\pi^\pm}$	$\pi^\pm$ software identification efficiency	Monte Carlo	$79.9 \rightarrow 87.3$	2
ϵ_{id}^{p}	p software identification efficiency	Monte Carlo	$79.9 \rightarrow 87.3$	2

E. π^+p Elastic Scattering at 160-260 MeV

A separate trigger for detection of a single charged particle was implemented in the CP logic electronics . Instantaneous particle rate in the counters varied between $(0.028-2.80)\times 10^4$. These signal rates were prescaled with a periodic clock signal at $(3.64-42.12)\times 10^{-5}$ making it comparable to the inclusive π^0 rate.

At the incident pion momentum of 378 MeV/c the differential cross sections for π^+p elastic scattering were measured with statistical uncertainties less than 1% and estimated systematic uncertainties of ~1% by Sadler *et al.* [Sad-87]. These measurements were used to monitor the LH2 target thickness during each run at an incident pion momentum 374.4 MeV/c. From the detected $\pi^+p\rightarrow\pi^+p$ yields with the target full $Y^{\mathrm{F}}_{\pi^+p}$ and target empty $Y^{\mathrm{E}}_{\pi^+p}$ the target thickness can be deduced

$$t_{\mathrm{LH_2}}=\frac{1}{N_{\pi^+}/IC\cdot(d\sigma/d\Omega)_{\mathrm{SAID}}\cdot d\Omega}\left\{\left[\frac{Y^{\mathrm{F}}_{\pi^+p}}{IC\cdot\eta_l\cdot d_l}\right]_{\mathrm{F}}-\left[\frac{Y^{\mathrm{E}}_{\pi^+p}}{IC\cdot\eta_l\cdot d_l}\right]_{\mathrm{E}}\right\}, \tag{3.32}$$

where IC is the beam ion chamber count, N_{π^+}/IC is number of incident pions per IC count, η_l is the computer live time, d_l is the prescaled factor, $d\Omega$ is the effective detector solid angle for elastically scattered pions or conjugate protons, and $d\sigma/d\Omega_{\mathrm{SAID}}$ is the differential cross section calculated from phase shifts [Arn-87]. The subscripts F and E denote the target full and target empty runs which are strongly constrained by [Sad-87] data.

Charged particle hodoscope sections have a finite angular acceptance of 10–22 msr so the scattering angles deviated slightly from the counter central angle. Differences of the order of ~1° were established in the Monte Carlo program with the realistic x and y beam profiles and geometrical target shape with the elastically scattered π^+'s distributed in polar angles according to the SAID [Arn-87] solution. Effective scattering angles of the individual detectors were entered in the Tables 3.12-3.19. Knock-out proton angles were calculated for every incident π^+ energy and the corresponding detector solid angles were derived evaluating the Jacobian factor $d\cos(\theta_p)/d\cos(\theta_{\pi^+})$.

With the LH2 target thickness confirmed using three independent methods, the equation (3.18) was inverted and the differential π^+p cross sections were calculated for the incident beam energies 160, 190, 200, 220, and 240 MeV. The results are summarized in Tables 3.15-3.19 and the data points are plotted in Figures 3.31-3.32. The angular distributions were fitted with three term Legendre polynomial expansions and the total elastic cross section obtained by integration are in agreement with the SAID solution. About 10% of the CP singles data was analyzed, resulting in statistical uncertainties of 3-10% and estimated systematic errors of ~5% in $d\sigma_{\pi^+p\rightarrow\pi^+p}/d\Omega$.

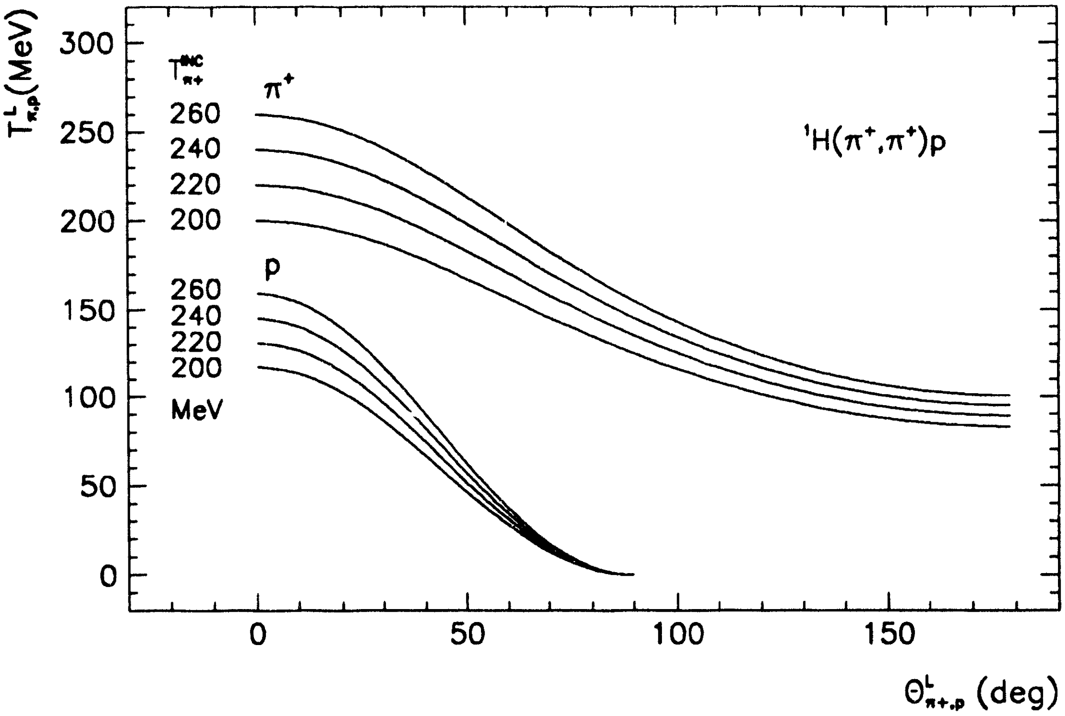

Figure 3.26 Kinematic relationship between the laboratory kinetic energy and polar angle for elastically scattered pions and knocked-out protons at four beam energies of interest.

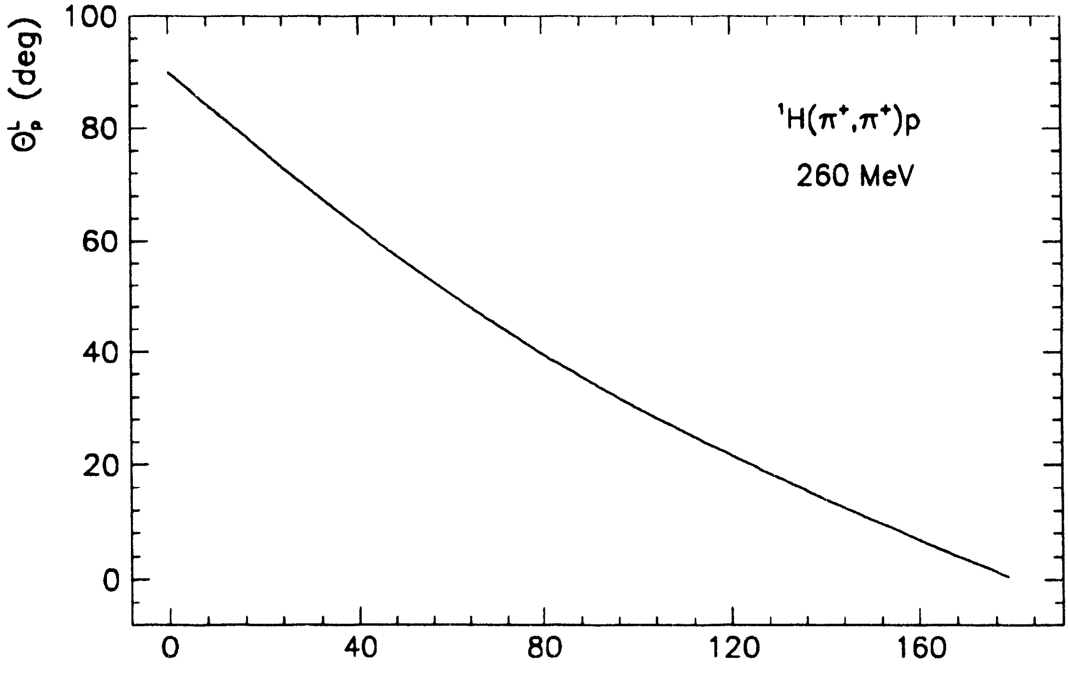

Figure 3.27 Kinematic relationship between the laboratory polar angles of the scattered pions and conjugate protons from ^{1}H$(\pi^+,\pi^+)p$ at 260 MeV. Curves corresponding to incident pion energies from 160 to 240 MeV are essentially indistinguishable.

Table 3.12 1991 $\pi^+p \rightarrow \pi^+p$ differential cross sections at 260 MeV, $t_{\rm LH_2} = 0.138$ b^{-2}.

Detector	θ_π (deg)	$d\Omega_\pi$ (msr)	$[\frac{d\sigma}{d\Omega_\pi}]^{\rm SAID}$ (mb/sr)	$[\frac{d\sigma}{d\Omega_\pi}]^{\rm exp}$ (mb/sr)	$\bar{\theta}_\pi$ (deg)	$d\bar{\Omega}_\pi$ (msr)	$[\frac{d\sigma}{d\bar{\Omega}_\pi}]^{\rm SAID}$ (mb/sr)	$[\frac{d\sigma}{d\bar{\Omega}_\pi}]^{\rm exp}$ (mb/sr)
PR1	18.0	10.0	34.9	-	129.5	65.2	4.47	5.00 ± 0.70
PR2	26.0	10.0	28.1	-	109.6	50.9	3.52	3.98 ± 0.56
PR3	22.0	10.0	31.4	-	119.3	58.0	4.01	3.57 ± 0.50
PR4	30.0	10.0	24.7	-	100.3	44.2	3.06	3.22 ± 0.55
PR5	38.0	10.0	18.4	15.21 ± 2.08	83.3	32.7	2.81	2.60 ± 0.54
PR6	34.0	10.0	21.5	-	91.7	38.2	2.78	2.79 ± 0.53
PR7	42.0	10.0	15.7	14.49 ± 1.88	75.4	27.9	3.31	3.69 ± 0.70
PR8	20.0	10.0	33.2	-	124.3	61.6	4.24	3.20 ± 0.45
PI1	60.0	72.6	6.51	7.00 ± 0.98	44.0	92.8	14.3	-
PI2	55.0	72.6	8.40	9.74 ± 1.56	52.1	116.7	9.72	-
PI3	65.0	88.6	5.08	5.73 ± 0.97	36.1	88.4	19.9	-
PI4	40.0	76.2	17.0	19.37 ± 2.30	79.3	230.0	2.99	-
PI5	60.0	88.6	6.51	6.42 ± 1.28	44.0	113.3	14.3	-
PI6	80.0	88.6	2.95	3.52 ± 1.28	14.1	31.2	38.7	-

Table 3.13 1991 $\pi^+p \rightarrow \pi^+p$ differential cross sections at 160 MeV, $t_{\rm LH_2} = 0.116$ b^{-2}.

Detector	θ_π (deg)	$d\Omega_\pi$ (msr)	$[\frac{d\sigma}{d\Omega_\pi}]^{\rm SAID}$ (mb/sr)	$[\frac{d\sigma}{d\Omega_\pi}]^{\rm exp}$ (mb/sr)	$\bar{\theta}_\pi$ (deg)	$d\bar{\Omega}_\pi$ (msr)	$[\frac{d\sigma}{d\bar{\Omega}_\pi}]^{\rm SAID}$ (mb/sr)	$[\frac{d\sigma}{d\bar{\Omega}_\pi}]^{\rm exp}$ (mb/sr)
PR1	18.0	10.0	39.6	-	132.8	58.9	15.5	14.80 ± 1.54
PR2	26.0	10.0	34.3	-	113.7	48.1	13.0	14.19 ± 1.62
PR3	22.0	10.0	37.2	-	123.1	53.6	14.4	12.35 ± 1.53
PR4	30.0	10.0	31.3	-	104.6	42.8	11.6	10.95 ± 1.69
PR5	38.0	10.0	24.9	-	87.7	33.1	9.39	6.90 ± 1.47
PR6	34.0	10.0	28.0	-	96.0	37.7	10.3	14.18 ± 1.21
PR7	42.0	10.0	21.9	-	79.7	28.8	8.99	9.43 ± 1.68
PR8	20.0	10.0	38.4	-	127.9	56.3	15.0	15.29 ± 1.57
PI1	60.0	72.6	12.1	13.83 ± 2.07	47.1	103.3	18.5	-
PI2	55.0	72.6	14.1	13.77 ± 2.07	55.7	127.7	13.8	-
PI3	65.0	88.6	10.6	12.00 ± 1.92	38.8	99.9	24.3	-
PI4	40.0	76.2	23.4	18.33 ± 2.38	83.6	235.1	9.10	-
PI5	60.0	88.6	12.1	12.23 ± 1.71	47.1	126.1	18.5	-
PI6	80.0	88.6	8.99	9.06 ± 1.60	15.2	36.2	40.8	-

Table 3.14 $\pi^+p \rightarrow \pi^+p$ at 260 MeV, t_{LH_2} = 0.138 b^{-2}

Detector	θ_π (deg)	$d\Omega_\pi$ (msr)	$[\frac{d\sigma}{d\Omega_\pi}]^{\mathrm{SAID}}$ (mb/sr)	$[\frac{d\sigma}{d\Omega_\pi}]^{\mathrm{exp}}$ (mb/sr)	$\bar{\theta}_\pi$ (deg)	$d\bar{\Omega}_\pi$ (msr)	$[\frac{d\sigma}{d\bar{\Omega}_\pi}]^{\mathrm{SAID}}$ (mb/sr)	$[\frac{d\sigma}{d\bar{\Omega}_\pi}]^{\mathrm{exp}}$ (mb/sr)
PR1	17.8	10.0	35.22	27.61 ± 5.31	130.1	65.59	4.53	2.94 ± 0.21
PR2	25.8	10.0	28.32	25.66 ± 2.68	110.1	51.29	3.57	3.64 ± 0.24
PR3	21.8	10.0	31.72	27.14 ± 3.60	119.9	58.43	4.07	3.49 ± 0.22
PR4	29.9	10.0	24.90	24.25 ± 2.45	100.9	44.63	3.12	2.96 ± 0.25
PR5	37.9	10.0	18.50	10.82 ± 1.30	83.3	32.68	2.83	2.13 ± 0.25
PR6	33.9	10.0	21.66	12.43 ± 1.75	91.9	38.34	2.81	2.93 ± 0.26
PR7	41.8	10.0	15.80	8.72 ± 1.12	75.1	27.69	3.37	3.26 ± 0.33
PR8	19.9	10.0	33.36	29.67 ± 3.79	125.0	62.06	4.31	4.92 ± 0.27
PI1	58.4	72.6	7.10	8.36 ± 0.42	41.7	86.67	15.87	-
PI2	53.3	72.6	9.20	9.28 ± 0.43	49.4	108.40	11.14	-
PI3	62.4	88.6	5.80	3.71 ± 0.26	33.1	79.55	22.29	-
PI4	39.7	76.2	17.26	14.34 ± 0.55	78.2	224.98	3.09	-
PI5	59.5	88.6	6.72	6.66 ± 0.27	42.4	108.06	15.39	-
PI6	79.7	88.6	2.99	3.87 ± 0.20	-	-	-	-

Table 3.15 $\pi^+p \rightarrow \pi^+p$ at 160 MeV, t_{LH_2} = 0.138 b^{-2}

Detector	θ_π (deg)	$d\Omega_\pi$ (msr)	$[\frac{d\sigma}{d\Omega_\pi}]^{\mathrm{SAID}}$ (mb/sr)	$[\frac{d\sigma}{d\Omega_\pi}]^{\mathrm{exp}}$ (mb/sr)	$\bar{\theta}_\pi$ (deg)	$d\bar{\Omega}_\pi$ (msr)	$[\frac{d\sigma}{d\bar{\Omega}_\pi}]^{\mathrm{SAID}}$ (mb/sr)	$[\frac{d\sigma}{d\bar{\Omega}_\pi}]^{\mathrm{exp}}$ (mb/sr)
PR1	17.9	10.0	39.27	282.07 ± 11.51	133.2	59.11	15.57	18.48 ± 0.63
PR2	25.9	10.0	34.11	237.75 ± 7.82	114.0	48.32	13.04	15.74 ± 0.65
PR3	21.9	10.0	36.91	53.12 ± 4.72	123.6	53.88	14.41	17.54 ± 0.65
PR4	29.9	10.0	31.05	32.53 ± 3.06	105.1	43.07	11.66	15.30 ± 0.68
PR5	37.9	10.0	24.79	18.95 ± 1.64	87.9	33.19	9.39	8.94 ± 0.59
PR6	33.9	10.0	27.89	23.09 ± 2.13	96.4	37.99	10.37	10.15 ± 0.59
PR7	41.9	10.0	21.83	19.19 ± 1.70	79.9	28.90	8.97	11.83 ± 0.75
PR8	19.9	10.0	38.16	48.06 ± 5.80	128.4	56.55	15.02	20.58 ± 0.69
PI1	59.0	72.6	12.36	25.88 ± 0.71	45.3	98.46	19.49	-
PI2	53.8	72.6	14.59	18.08 ± 0.62	54.0	122.73	14.49	-
PI3	63.6	88.6	10.89	15.79 ± 0.50	36.3	92.39	26.02	-
PI4	39.9	76.2	23.28	19.95 ± 0.69	83.7	235.49	9.09	-
PI5	59.8	88.6	12.07	19.32 ± 0.54	45.9	122.11	19.10	-
PI6	80.1	88.6	8.97	15.45 ± 0.48	-	-	-	-

Table 3.16 $\pi^+p \to \pi^+p$ at 190 MeV, $t_{\mathrm{LH_2}} = 0.138$ b^{-2}

Detector	θ_π (deg)	$d\Omega_\pi$ (msr)	$[\frac{d\sigma}{d\Omega_\pi}]^{\mathrm{SAID}}$ (mb/sr)	$[\frac{d\sigma}{d\Omega_\pi}]^{\mathrm{exp}}$ (mb/sr)	$\bar{\theta}_\pi$ (deg)	$d\bar{\Omega}_\pi$ (msr)	$[\frac{d\sigma}{d\bar{\Omega}_\pi}]^{\mathrm{SAID}}$ (mb/sr)	$[\frac{d\sigma}{d\bar{\Omega}_\pi}]^{\mathrm{exp}}$ (mb/sr)
PR1	17.9	10.0	50.42	10.76 ± 6.57	132.2	61.04	13.62	12.14 ± 0.43
PR2	25.9	10.0	42.31	53.45 ± 3.32	112.8	49.26	11.25	14.07 ± 0.51
PR3	21.9	10.0	46.46	76.69 ± 4.54	122.4	55.25	12.52	14.34 ± 0.49
PR4	29.9	10.0	38.05	39.73 ± 2.90	103.8	43.58	10.01	13.10 ± 0.53
PR5	37.8	10.0	29.74	19.81 ± 1.61	86.5	33.09	8.26	8.65 ± 0.50
PR6	33.8	10.0	33.88	31.78 ± 2.13	94.9	38.07	8.91	10.61 ± 0.51
PR7	41.9	10.0	25.74	25.81 ± 1.71	78.4	28.55	8.31	11.35 ± 0.62
PR8	19.9	10.0	48.46	37.54 ± 2.82	127.3	58.20	13.10	17.08 ± 0.32
PI1	58.9	72.6	13.37	24.06 ± 0.61	44.1	94.57	23.73	-
PI2	53.7	72.6	16.33	17.69 ± 0.54	52.4	117.83	17.19	-
PI3	63.2	88.6	11.48	15.14 ± 0.42	35.2	88.03	32.42	-
PI4	39.8	76.2	27.75	33.66 ± 0.73	82.0	232.65	8.18	-
PI5	59.7	88.6	12.99	20.20 ± 0.48	44.9	118.02	23.02	-
PI6	80.0	88.6	8.37	14.67 ± 0.39	-	-	-	-

Table 3.17 $\pi^+p \to \pi^+p$ at 200 MeV, $t_{\mathrm{LH_2}} = 0.138$ b^{-2}

Detector	θ_π (deg)	$d\Omega_\pi$ (msr)	$[\frac{d\sigma}{d\Omega_\pi}]^{\mathrm{SAID}}$ (mb/sr)	$[\frac{d\sigma}{d\Omega_\pi}]^{\mathrm{exp}}$ (mb/sr)	$\bar{\theta}_\pi$ (deg)	$d\bar{\Omega}_\pi$ (msr)	$[\frac{d\sigma}{d\bar{\Omega}_\pi}]^{\mathrm{SAID}}$ (mb/sr)	$[\frac{d\sigma}{d\bar{\Omega}_\pi}]^{\mathrm{exp}}$ (mb/sr)
PR1	17.9	10.0	49.95	92.19 ± 10.78	131.9	61.70	12.03	12.54 ± 0.68
PR2	25.8	10.0	41.67	42.95 ± 5.19	112.4	49.56	9.88	12.81 ± 0.76
PR3	21.9	10.0	45.82	76.48 ± 7.31	122.0	55.69	11.02	13.33 ± 0.73
PR4	29.8	10.0	37.36	40.66 ± 4.52	103.3	43.70	8.76	10.88 ± 0.75
PR5	37.9	10.0	28.82	26.88 ± 2.86	86.0	33.02	7.31	9.34 ± 0.80
PR6	33.8	10.0	33.07	32.36 ± 3.50	94.6	38.21	7.83	9.77 ± 0.79
PR7	41.9	10.0	24.93	20.06 ± 2.46	78.1	28.54	7.49	10.70 ± 0.96
PR8	19.8	10.0	47.99	49.20 ± 7.39	127.0	58.78	11.56	14.46 ± 0.76
PI1	58.8	72.6	12.66	22.85 ± 0.92	43.7	93.28	23.28	-
PI2	53.6	72.6	15.63	15.67 ± 0.82	51.8	115.99	16.82	-
PI3	63.1	88.6	10.80	13.61 ± 0.65	34.9	86.79	31.91	-
PI4	39.8	76.2	26.93	26.47 ± 1.10	81.5	231.89	7.31	-
PI5	59.6	88.6	12.27	17.17 ± 0.70	44.5	116.45	22.56	-
PI6	79.9	88.6	7.38	12.75 ± 0.59	-	-	-	-

Table 3.18 $\pi^+p \rightarrow \pi^+p$ at 220 MeV, $t_{\mathrm{LH}_2} = 0.138$ b^{-2}

Detector	θ_π (deg)	$d\Omega_\pi$ (msr)	$[\frac{d\sigma}{d\Omega_\pi}]^{\mathrm{SAID}}$ (mb/sr)	$[\frac{d\sigma}{d\Omega_\pi}]^{\mathrm{exp}}$ (mb/sr)	$\bar{\theta}_\pi$ (deg)	$d\bar{\Omega}_\pi$ (msr)	$[\frac{d\sigma}{d\bar{\Omega}_\pi}]^{\mathrm{SAID}}$ (mb/sr)	$[\frac{d\sigma}{d\bar{\Omega}_\pi}]^{\mathrm{exp}}$ (mb/sr)
PR1	17.8	10.0	45.85	63.67 ± 12.07	131.3	63.00	8.86	9.57 ± 0.44
PR2	25.9	10.0	37.54	21.46 ± 5.62	111.7	50.21	7.20	8.71 ± 0.46
PR3	21.9	10.0	41.64	50.00 ± 7.16	121.4	56.69	8.08	9.54 ± 0.42
PR4	29.8	10.0	33.54	31.02 ± 4.68	102.6	44.10	6.35	8.63 ± 0.49
PR5	37.8	10.0	25.63	17.31 ± 2.12	85.1	32.93	5.42	6.45 ± 0.50
PR6	33.9	10.0	29.40	21.35 ± 3.17	93.8	38.35	5.69	6.01 ± 0.52
PR7	41.8	10.0	22.00	18.91 ± 1.84	77.0	28.22	5.80	8.03 ± 0.64
PR8	19.8	10.0	43.78	46.27 ± 8.43	126.3	59.87	8.48	11.56 ± 0.49
PI1	58.6	72.6	10.69	13.55 ± 0.70	43.0	90.97	20.98	–
PI2	53.4	72.6	13.45	11.45 ± 0.65	50.9	113.17	15.02	–
PI3	62.9	88.6	8.91	9.00 ± 0.60	34.2	84.05	29.11	–
PI4	39.8	76.2	23.78	23.10 ± 0.95	80.4	229.78	5.55	–
PI5	59.6	88.6	10.24	12.84 ± 0.48	43.8	113.64	20.31	–
PI6	80.0	88.6	5.57	10.73 ± 0.39	–	–	–	–

Table 3.19 $\pi^+p \rightarrow \pi^+p$ at 240 MeV, $t_{\mathrm{LH}_2} = 0.138$ b^{-2}

Detector	θ_π (deg)	$d\Omega_\pi$ (msr)	$[\frac{d\sigma}{d\Omega_\pi}]^{\mathrm{SAID}}$ (mb/sr)	$[\frac{d\sigma}{d\Omega_\pi}]^{\mathrm{exp}}$ (mb/sr)	$\bar{\theta}_\pi$ (deg)	$d\bar{\Omega}_\pi$ (msr)	$[\frac{d\sigma}{d\bar{\Omega}_\pi}]^{\mathrm{SAID}}$ (mb/sr)	$[\frac{d\sigma}{d\bar{\Omega}_\pi}]^{\mathrm{exp}}$ (mb/sr)
PR1	17.8	10.0	40.33	54.78 ± 6.65	130.8	64.37	6.34	6.20 ± 0.29
PR2	25.9	10.0	32.64	27.80 ± 3.12	110.9	50.76	5.07	5.30 ± 0.30
PR3	21.9	10.0	36.40	40.89 ± 4.15	120.6	57.54	5.73	6.01 ± 0.30
PR4	29.9	10.0	28.92	24.97 ± 2.79	101.5	44.21	4.44	4.67 ± 0.31
PR5	37.8	10.0	21.91	15.30 ± 1.46	84.3	32.88	3.91	4.96 ± 0.36
PR6	33.8	10.0	25.38	17.90 ± 2.03	92.9	38.39	4.00	4.28 ± 0.32
PR7	41.8	10.0	18.68	12.82 ± 1.34	76.1	27.99	4.39	4.88 ± 0.39
PR8	19.8	10.0	38.39	39.62 ± 4.68	125.5	60.87	6.04	7.33 ± 0.32
PI1	58.6	72.6	8.68	9.58 ± 0.42	42.3	88.68	18.29	–
PI2	53.3	72.6	11.16	9.37 ± 0.44	50.1	110.65	12.97	–
PI3	62.7	88.6	7.17	6.37 ± 0.31	33.7	81.93	25.47	–
PI4	39.8	76.2	20.27	17.55 ± 0.61	79.4	227.92	4.11	–
PI5	59.5	88.6	8.32	7.34 ± 0.30	43.1	110.84	17.69	–
PI6	79.8	88.6	4.09	5.23 ± 0.23	–	–	–	–

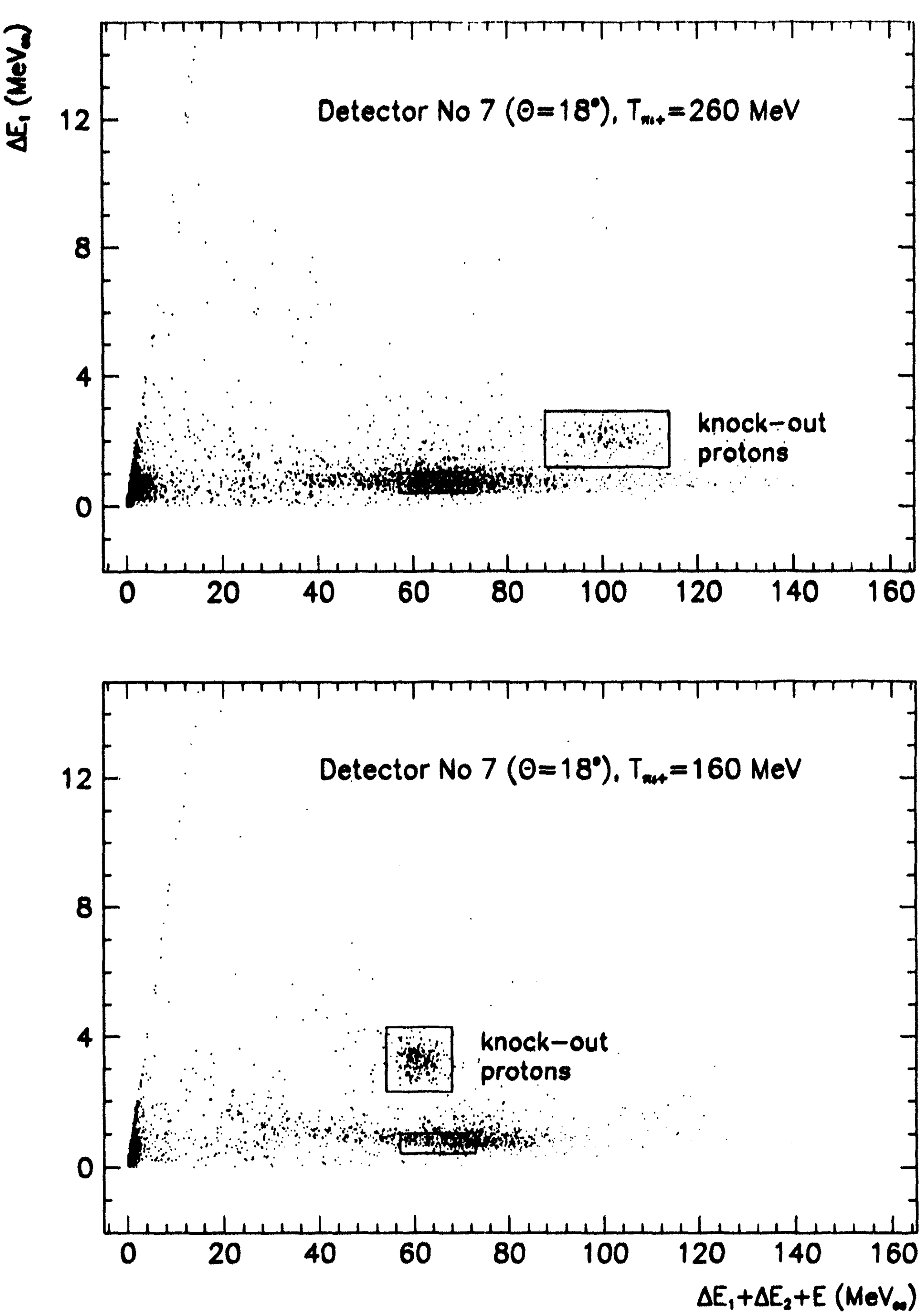

Figure 3.28 Recoil proton particle identification in $\pi^+p \rightarrow \pi^+p$ at 160 and 260 MeV. Hits in the proton detector at smallest polar angle are shown. The elastically scattered pions are nearly minimum-ionizing at both energies; the protons deposit around 55 electron-equivalent MeV at 160 MeV, and around 100 MeV with the 260 MeV pion beam. Detector energy resolution for these monoenergetic protons is about 5%, precisely the designed value.

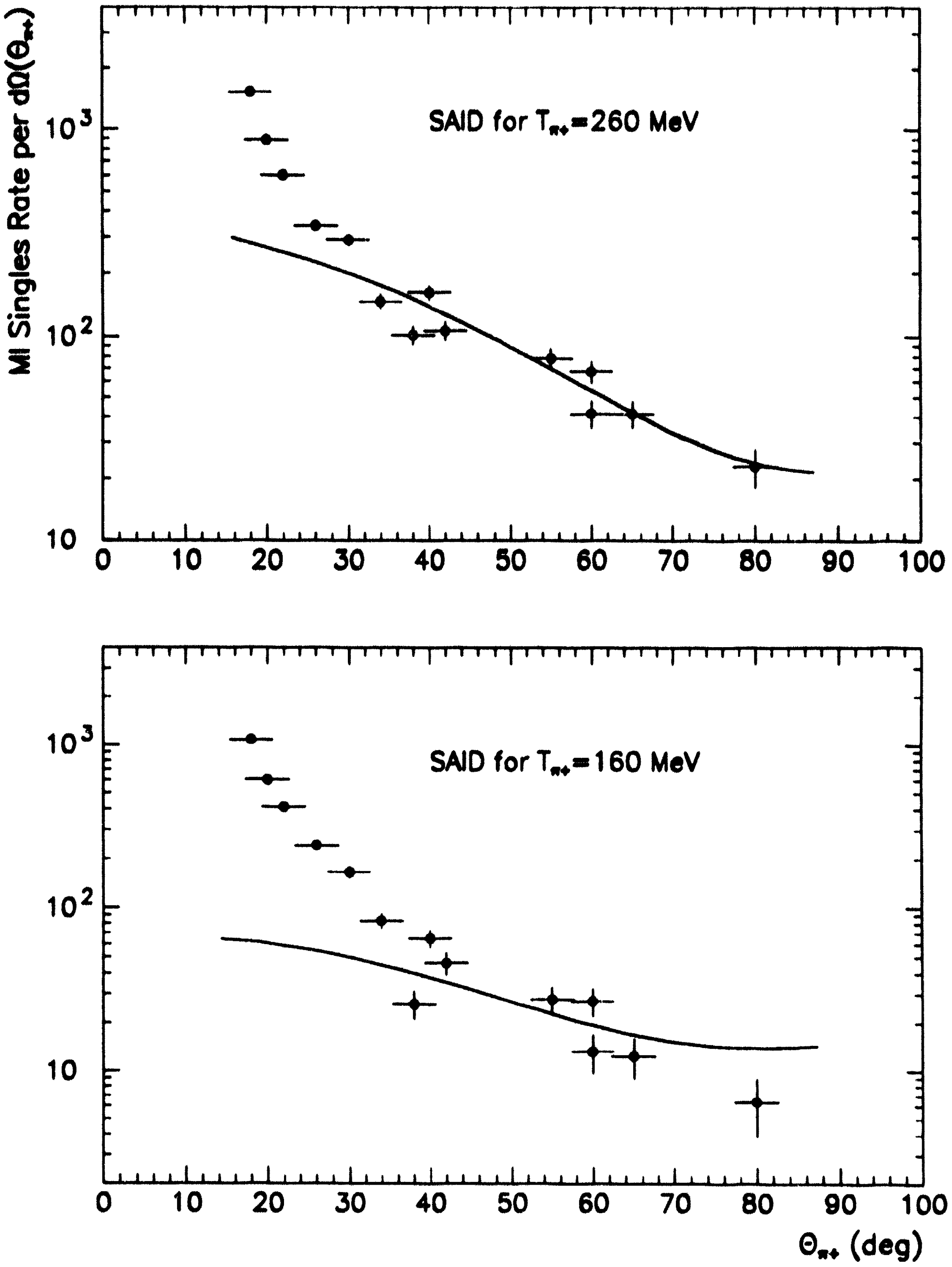

Figure 3.29 Nearly-minimum ionizing singles event rates in the charged particle counters at 160 and 260 MeV. The expected form of angular distribution for elastic $\pi^+p \rightarrow \pi^+p$ scattering is superimposed on measurements. At small polar angles the detectors are overwhelmed with MIP triggers caused apparently by the beam muon cone due to beam pion decays in flight.

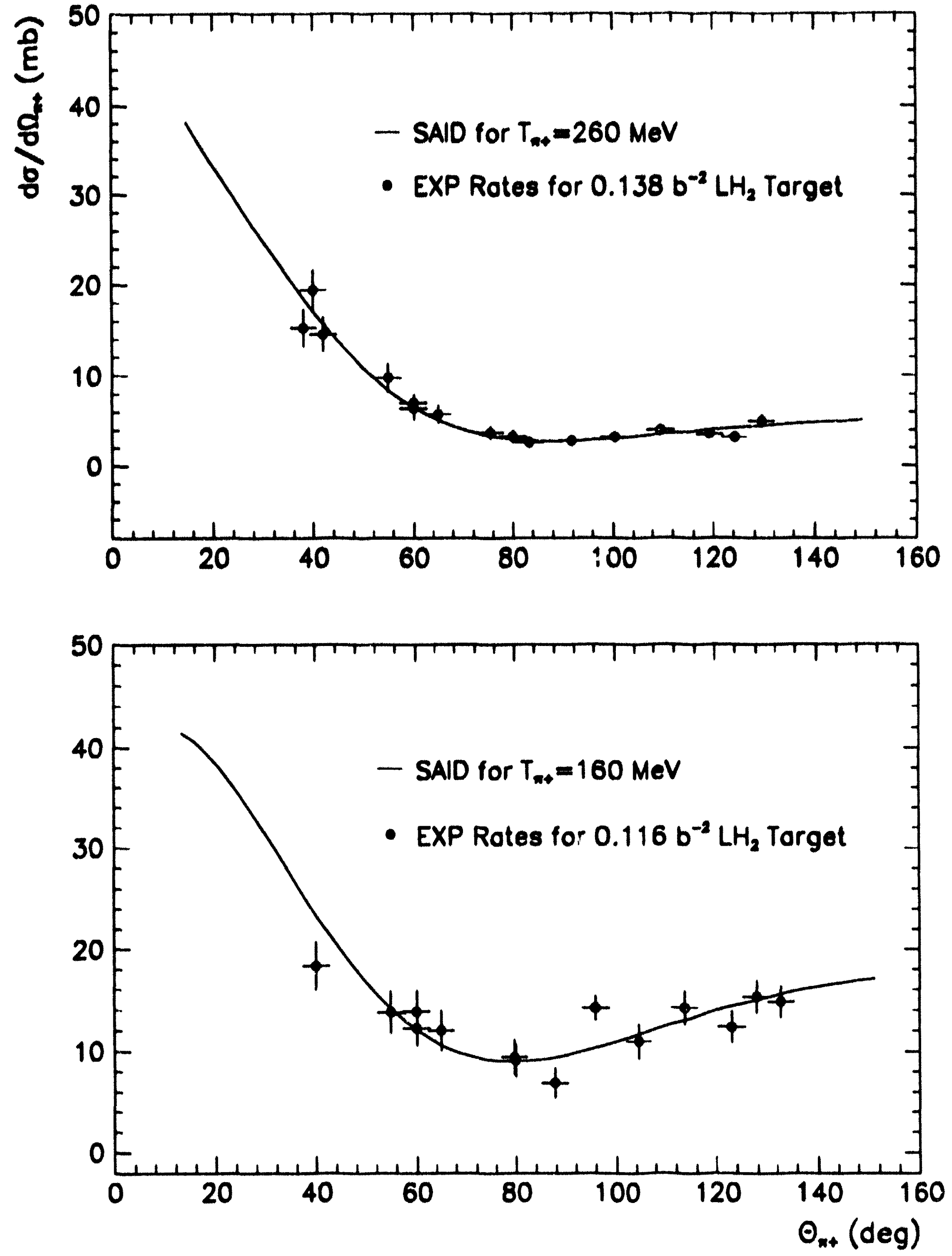

Figure 3.30 Agreement between SAID $\pi^+p \rightarrow \pi^+p$ differential scattering cross sections and the geometrical target thickness. For the "pion" detectors ($\theta > 40°$) elastically scattered pions are used, while in the "proton" detectors ($\theta < 40°$) conjugate proton events are substituted. The average polar scattering angle for each detector was calculated in Monte Carlo simulation taking into account the actual beam spot shape and target geometry.

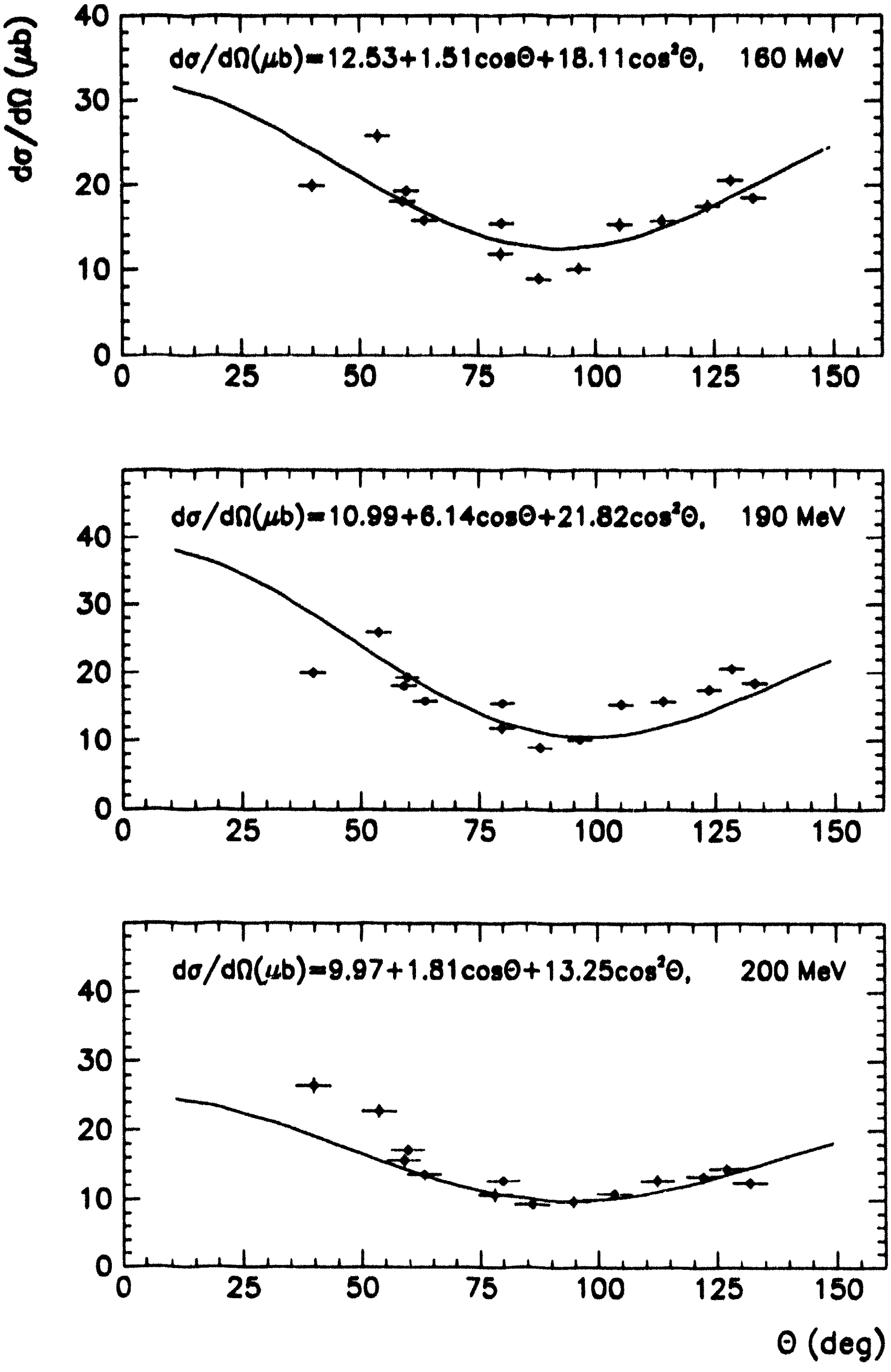

Figure 3.31 $\pi^+p \rightarrow \pi^+p$ differential elastic scattering cross section at 160, 190, and 200 MeV with LH_2 target. Just one run with target full and empty was analyzed here at each energy leading to the statistical uncertainties 5-30%.

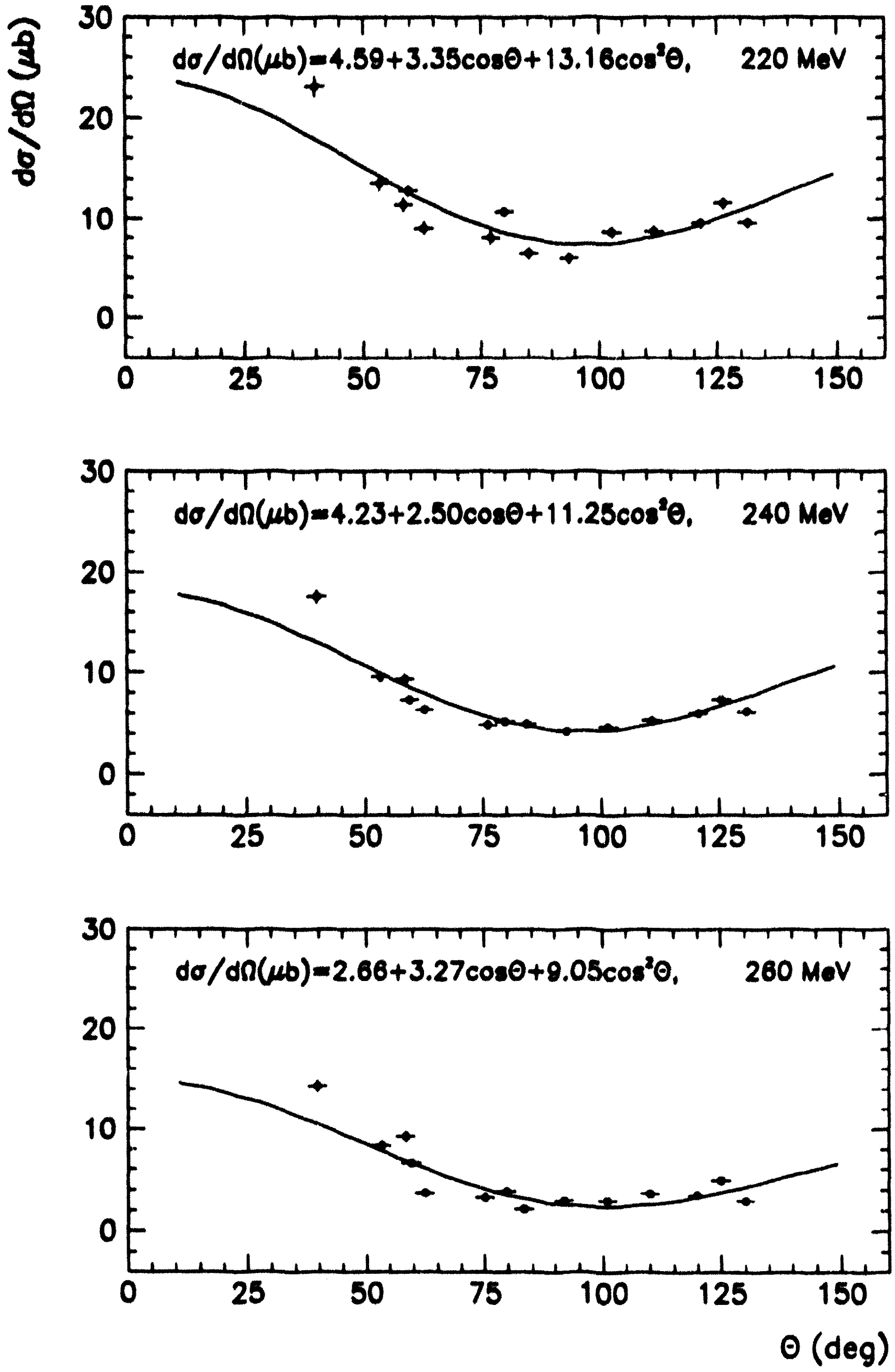

Figure 3.32 $\pi^+p \to \pi^+p$ differential elastic scattering cross section at 220, 240, and 260 MeV with LH_2 target. Just one run with target full and empty was analyzed here at each energy leading to the statistical uncertainties 5-30%.

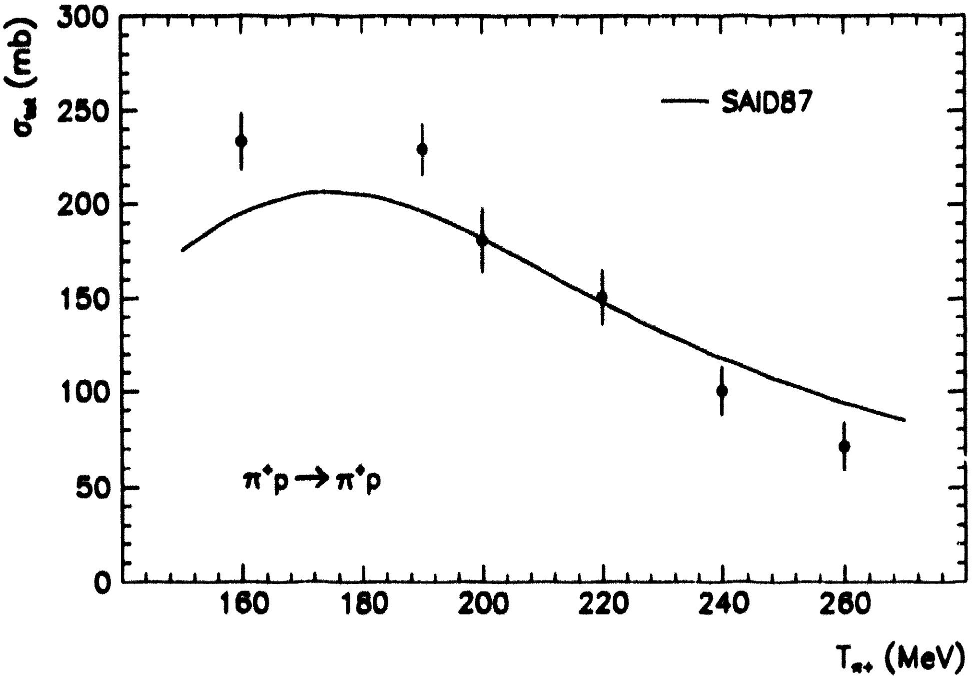

Figure 3.33 The total π^+p elastic scattering cross sections at 160, 190, 200, 220, 240, and 260 MeV measured with the LH_2 target. The points are integration results of differential cross section fits on Figures 3.25 and 3.26. The theoretical SAID excitation function is also shown.

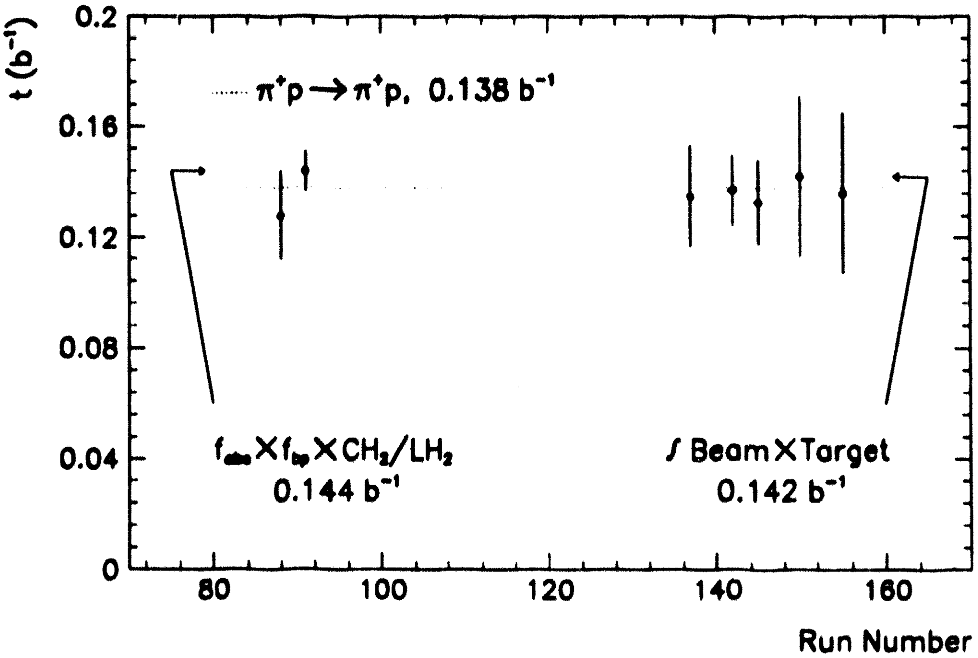

Figure 3.34 The liquid hydrogen target thickness. The π^+p elastic scattering monitored through the separate prescaled singles trigger fixes the target thickness for each run. The elastic differential scattering cross sections used in calculation come from [Sad-87] (1 % statistical and systematic uncertainty at 262 MeV). The Monte Carlo integration of two-dimensional beam profiles convoluted with target shape yields the consistent value. The comparison of charge exchange on the liquid hydrogen target with yield from the known CH_2 target is the third independent measurement, when corrected for beam size differences and π^0 conversion fraction.

Chapter IV: $\pi N \rightarrow \pi\pi N$ Total Cross Sections

A. Inclusive and Exclusive Acceptance of E1179 Apparatus

Determination of $\pi^+ p \rightarrow \pi^+ \pi^0 p$ total cross sections requires the knowledge of the absolute acceptance of the apparatus for various types of coincident events. The π^0 arm was described in the `PIANG_3B` and `PIANG_PAW` `FORTRAN` programs [Frl-92a,92b]. The programs were expanded to include 14 charged particle detectors defined by the front face detection surfaces at the predefined target distances, inclinations, and floor angles with respect to the pivot point.

$\pi^+ \pi^0 p$ final states for a fixed incident pion energy were generated using the `GENBOD` routine from `CERNLIB` library [Jam-89b]. The reaction vertex points within the LH_2 target were chosen by drawing random x and y coordinates from measured beam profile distributions (Figures 2.6 and 2.7) by the `CERNLIB HISRAN` routine [Jam-89c]. The z coordinates were distributed uniformly throughout the target geometry. Four-momenta of all three particles generated in the barycentric frame were Lorentz boosted to the LAB system. The individual events were weighted in proportion to the phase space probability, assuming a constant matrix element.

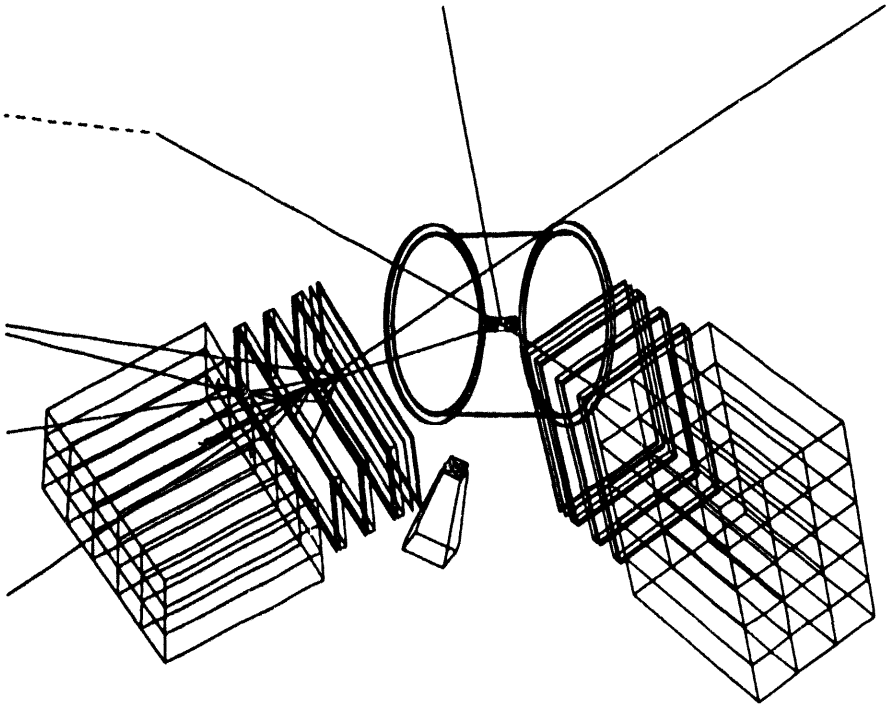

Figure 4.1 The `GEANT3` simulation of one $\pi^+ p \rightarrow \pi^0 \pi^+ p$ event in the realistic LAMPF E1179 geometry. One γ from π^0 decay starts showering in J crate. π^+ decays in flight into μ^+ and (invisible) ν_μ. The one charge particle detector (PR1) and the outgoing proton are also shown.

Energy losses of the charged particles were simulated in a separate **GEANT** program which propagates pions and protons from points inside the LH_2 target through the scattering chamber and surrounding material to the individual detectors. Proton nuclear interaction losses in the plastic scintillator detectors, pion in-flight decays and the charged particle multiple scattering were included in the simulation. Thus obtained smooth charged particle detection thresholds provided the lower bounds for passing detected coincident events in the main Monte Carlo simulation. The lower threshold was 4 MeV for pions and 12 MeV for reaction protons, Figures 4.2 and 4.3.

Kinematic parameters and phase space weights of all detected π^0 and all encountered π^0·CP coincidences as well as of the subset (1%) of all thrown events were written to the **PAW** Ntuple file. Ntuple entries included the generated kinetic energies and momenta of the particles, and the "measured" values of these parameters obtained by smearing the initial values to account for the detector resolution in energy and angular resolution functions, and beam-target geometry, and the higher order calculated parameters such as missing masses and relative angles. Selected resolution functions for 260 MeV run are shown in Figure 4.4.

The complete E1179 detector arrangement was defined independently within the **GEANT3** geometry package and the acceptance values obtained agreed with the **PIANG_PAW** results within ~1% statistical uncertainty of the calculation. The values of the inclusive and exclusive acceptances are summarized in Table 4.1.

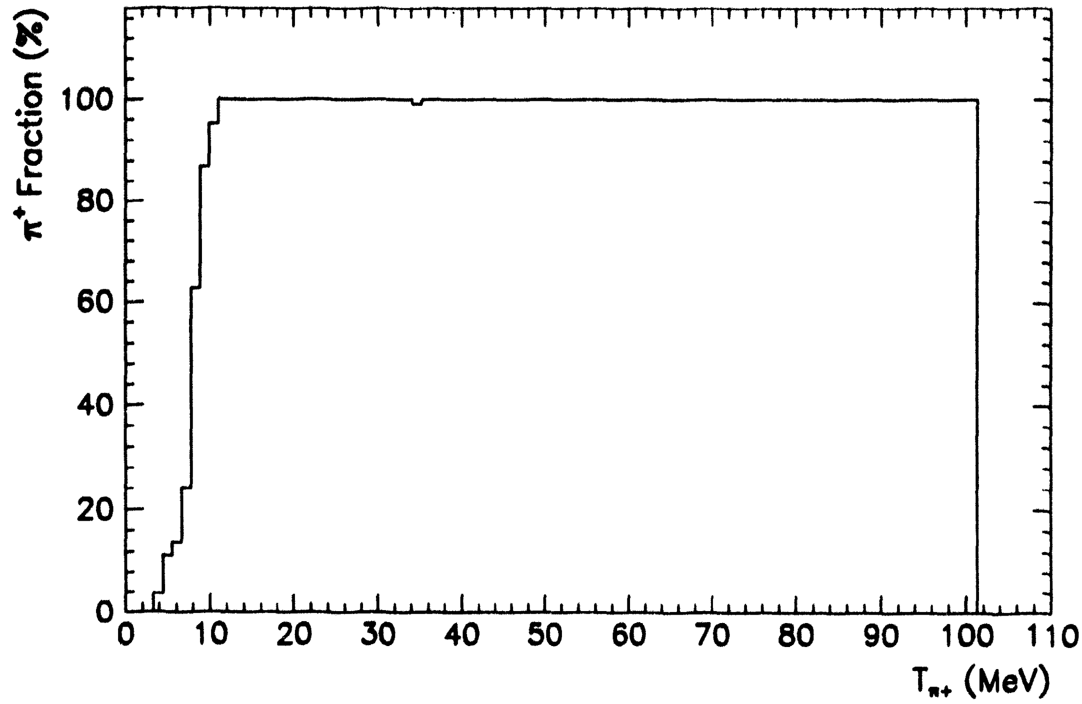

Figure 4.2 Coincident π loss fraction: modified GEANT3 simulation. The charged particle loss due to energy losses in liquid hydrogen target, scattering chamber material and air was carefully modeled to arrive at smooth, realistic detection thresholds used in acceptance calculations.

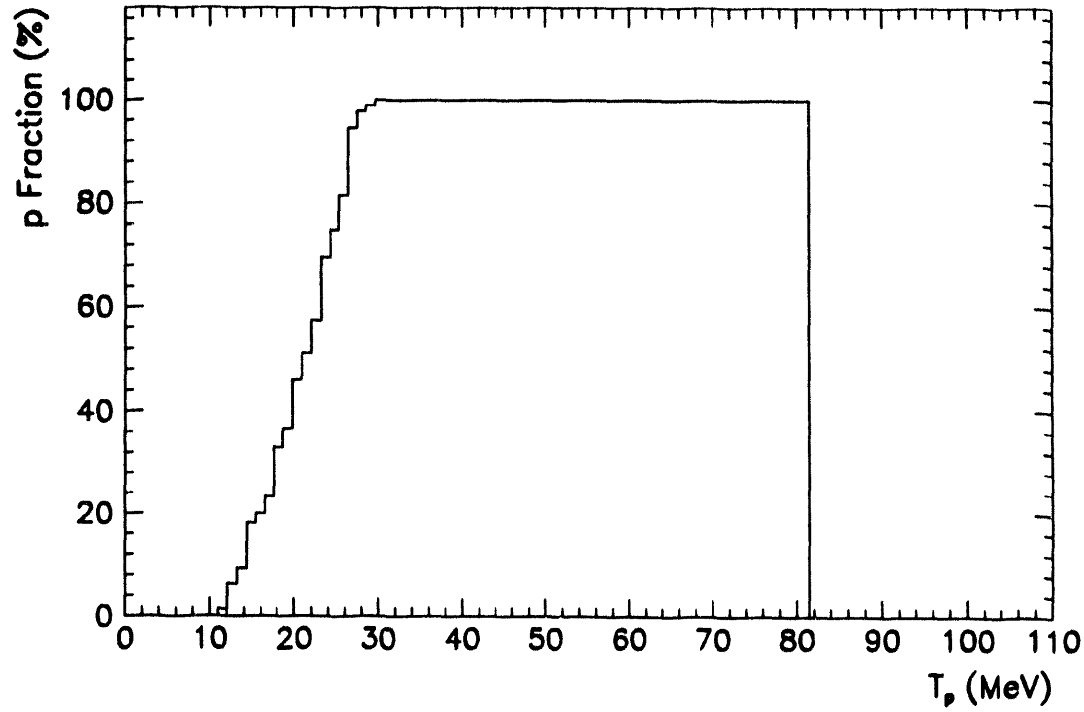

Figure 4.3 Coincident proton loss fraction: modified GEANT3 simulation. The extra thin-walled LH_2 targets were specially designed to equalise the energy losses and decrease the minimum proton detection threshold. The calculation shows that coincident protons with kinetic energies greater then 10 MeV were detectable.

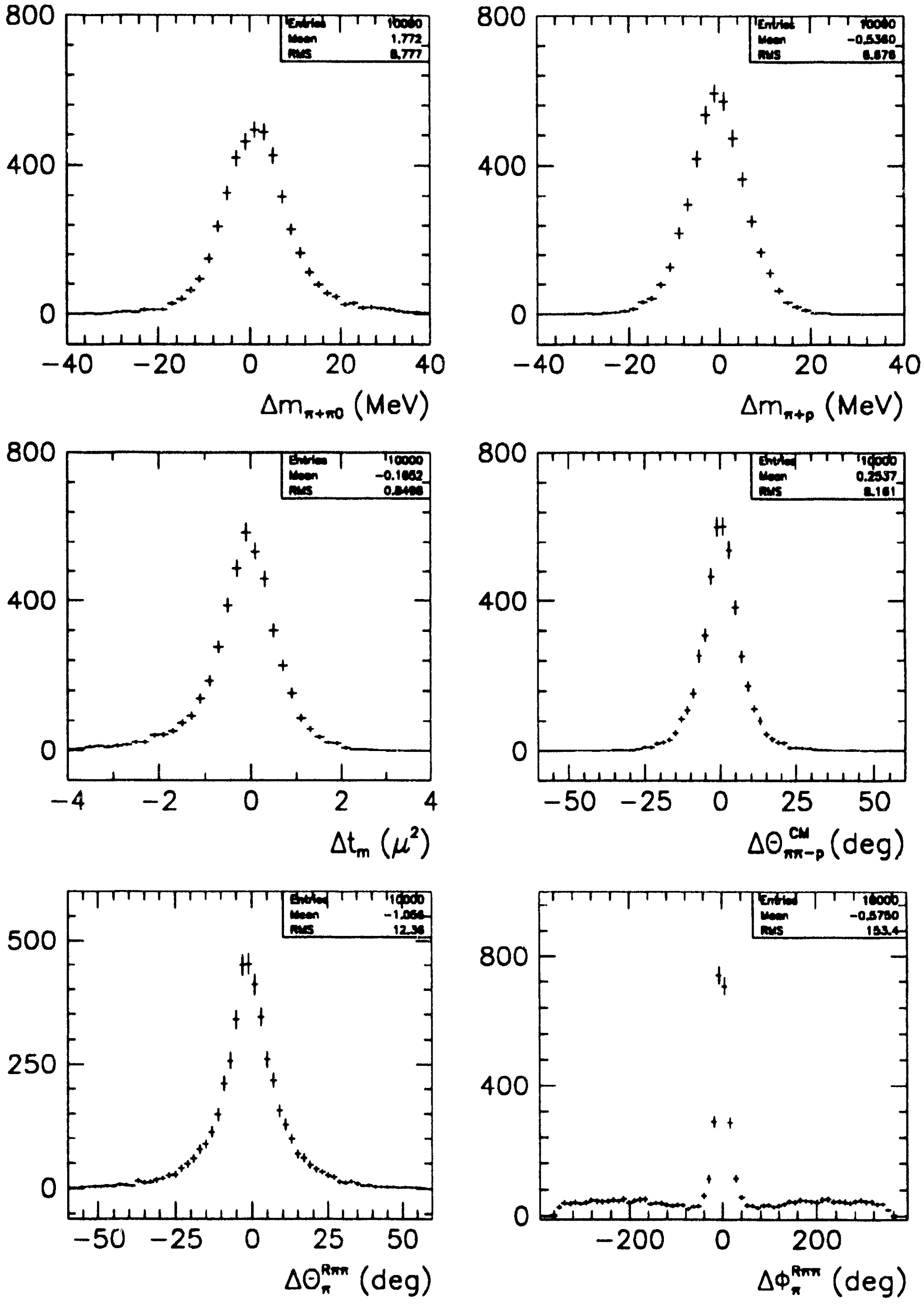

Figure 4.4 Monte Carlo resolution functions of selected kinematic variables at 260 MeV. The six panels show the differences between the generated and the measured values of $m_{\pi^+\pi^0}$, m_{π^+p}, the invariant masses, t_m, invariant four-momentum transfer, $\theta_{\pi^+\pi^0-p}$, dipion-proton angle in the CMS, $\theta_{\pi^+}^{R\pi^+\pi^0}$, the Jackson angle, and $\phi_{\pi^+}^{R\pi^+\pi^0}$, Treiman-Yang angle. Effects of the finite beam spot and target geometry, π^0 and charged-particle energy and direction resolution functions and detector gain variations have been taken into account.

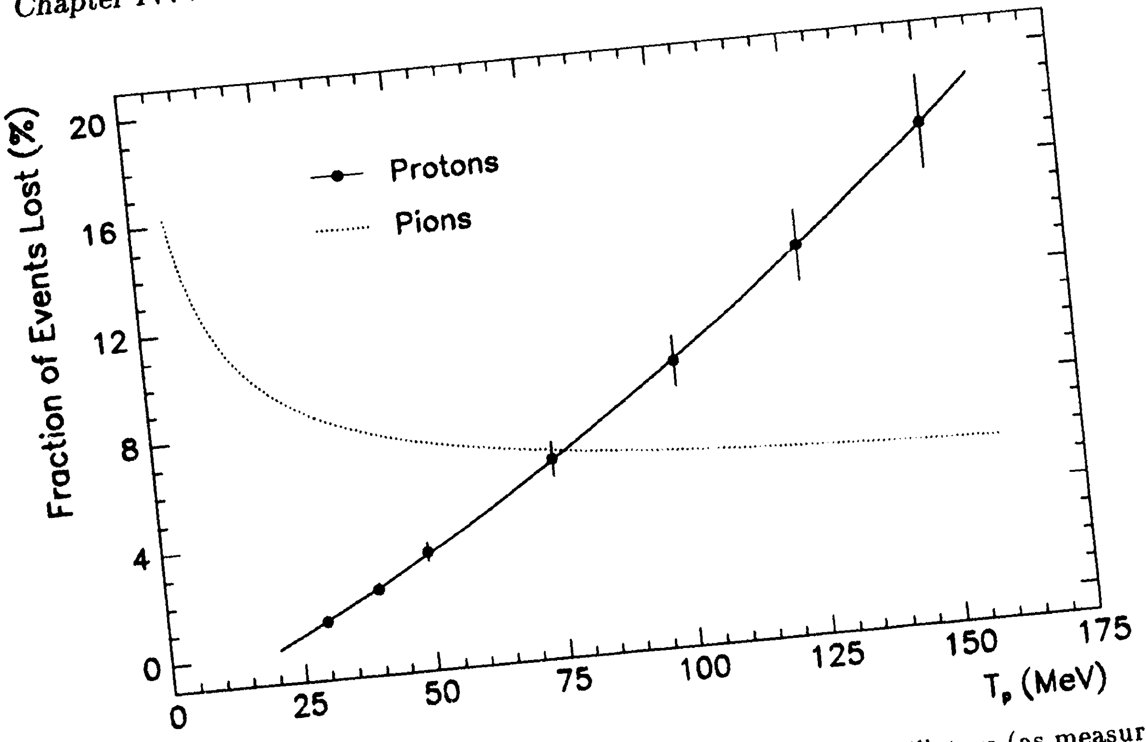

Figure 4.5 Proton nuclear inelastic interaction losses in plastic scintillators (as measured by [Mea-69a, 69b]). The calculated averaged pion decay losses for a set of E1179 detectors.

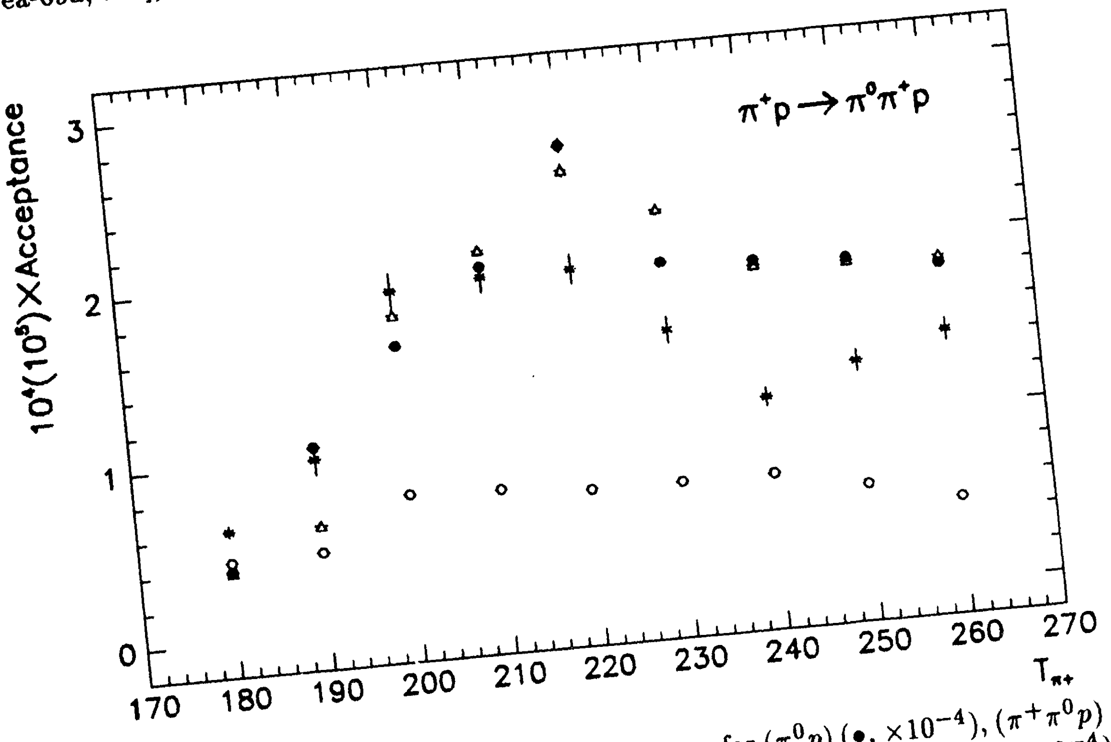

Figure 4.6 Effective acceptance of the E1179 apparatus for $(\pi^0 p)$ (•, $\times 10^{-4}$), $(\pi^+\pi^0 p)$ (∗, $\times 10^{-5}$), and $(\pi^+\pi^0)$ coincidences in proton (○, $\times 10^{-4}$) and pion detectors (▵, $\times 10^{-4}$) as a function of an incident pion energy. The points are calculated in a realistic Monte Carlo simulation using modified **PIANG_PAW** code [Gil-80], [Frl-92b], and confirmed independently in **GEANT3** simulation.

Table 4.1 The acceptance of the E1179 Apparatus for $\pi^+ p \to \pi^+\pi^0 p$ events as a function of beam energy. The first column lists the nominal energy of the incident beam. The inclusive π^0 and exclusive π^0-CP acceptances are listed next, followed by the acceptance values for various types of coincident events in all detectors as well as in the subsets of "proton" (PR1-PR8) and "pion" (PI1-PR6) detectors. The γ-γ energy asymmetry window cut was wide open: $X_{\rm cut} < 0.88$. The quoted uncertainties are due to the limited statistics of the Monte Carlo runs (10^4 π^0·CP events). The estimated systematic uncertainty of the detector setup description is ~3%, from the comparison of `PIANG_PAW` and `GEANT3` results. The exclusive acceptance $\mathcal{A}_{\pi^0 \mathrm{CP}_1(\mathrm{CP}_2)}$ takes into account the smooth charged particle thresholds, hardware and software charged particle detection efficiencies and corrections for π^+ decay-in-flight as well as proton nuclear interaction losses.

T_{π^+} (MeV)	$\mathcal{A}_{\pi^0}$ $\times 10^{-3}$	$\mathcal{A}_C$ $\times 10^{-4}$	$\mathcal{A}_{\pi^0 p}$ $\times 10^{-4}$	$\mathcal{A}_{\pi^0\pi^+}$ $\times 10^{-4}$	$\mathcal{A}_{\pi^0\pi^+ p}$ $\times 10^{-5}$
160	0.000 ± 0.000	0.000 ± 0.000	0.000 ± 0.000	0.000 ± 0.000	0.000 ± 0.000
180	14.13 ± 0.030	1.261 ± 0.013	0.407 ± 0.009	0.854 ± 0.009	0.633 ± 0.034
190	7.367 ± 0.020	2.167 ± 0.022	1.071 ± 0.018	1.096 ± 0.013	1.003 ± 0.089
200	7.484 ± 0.022	4.123 ± 0.041	1.601 ± 0.026	2.531 ± 0.012	1.914 ± 0.106
210	7.233 ± 0.022	4.853 ± 0.048	2.010 ± 0.031	2.843 ± 0.036	1.949 ± 0.089
220	6.665 ± 0.021	5.872 ± 0.059	2.661 ± 0.047	3.211 ± 0.037	1.950 ± 0.086
230	6.114 ± 0.020	4.882 ± 0.049	1.942 ± 0.029	2.940 ± 0.038	1.553 ± 0.077
240	5.580 ± 0.018	3.691 ± 0.037	1.904 ± 0.015	2.564 ± 0.033	1.127 ± 0.052
250	5.110 ± 0.016	4.313 ± 0.043	1.880 ± 0.028	2.433 ± 0.032	1.284 ± 0.062
260	5.124 ± 0.016	4.116 ± 0.041	1.810 ± 0.027	2.306 ± 0.030	1.417 ± 0.064

T_{π^+} (MeV)	$\mathcal{A}^{PR}_{\pi^0 p}$ $\times 10^{-4}$	$\mathcal{A}^{PI}_{\pi^0 p}$ $\times 10^{-6}$	$\mathcal{A}^{PR}_{\pi^0\pi^+}$ $\times 10^{-4}$	$\mathcal{A}^{PI}_{\pi^0\pi^+}$ $\times 10^{-4}$
160	0.000 ± 0.000	0.000 ± 0.000	0.000 ± 0.000	0.000 ± 0.000
180	0.407 ± 0.009	0.000 ± 0.000	0.455 ± 0.007	0.399 ± 0.006
190	1.071 ± 0.018	0.000 ± 0.000	0.472 ± 0.010	0.624 ± 0.009
200	1.601 ± 0.026	0.000 ± 0.000	0.755 ± 0.019	1.776 ± 0.025
210	2.010 ± 0.031	0.000 ± 0.000	0.737 ± 0.020	2.106 ± 0.030
220	2.661 ± 0.040	0.000 ± 0.000	0.691 ± 0.019	2.520 ± 0.036
230	1.942 ± 0.029	0.000 ± 0.000	0.690 ± 0.019	2.250 ± 0.033
240	1.904 ± 0.028	0.000 ± 0.000	0.689 ± 0.020	1.875 ± 0.027
250	1.873 ± 0.028	0.648 ± 0.180	0.582 ± 0.017	1.851 ± 0.027
260	1.795 ± 0.027	1.461 ± 0.276	0.468 ± 0.014	1.838 ± 0.027

B. $\pi^+ p \to \pi^+ \pi^0 p$ Total Cross Sections at 190-260 MeV

Total cross sections were deduced from the time-of-flight spectra projected from the master Ntuples after making the following kinematic cuts:

- a tight (± 2.0 ns) $\gamma\gamma$ timing requirement imposed on software-corrected π^0 time-of-flight $t^c_{\pi^0}$,
- charged particle identification cuts, identifying $\pi^0 p$ and $\pi^0 \pi^+$ events (described in Chapter III.C),
- charged particle time-of-flight cuts imposed separately for coincident pions ($|\mathrm{TOF}+1| \le 5$ ns) and protons ($|\mathrm{TOF}-1| \le 5$ ns) identified from E-ΔE information,
- a limit on the maximum kinetic energy of a charged particle detected at a given polar angle (discussed in Appendix C).

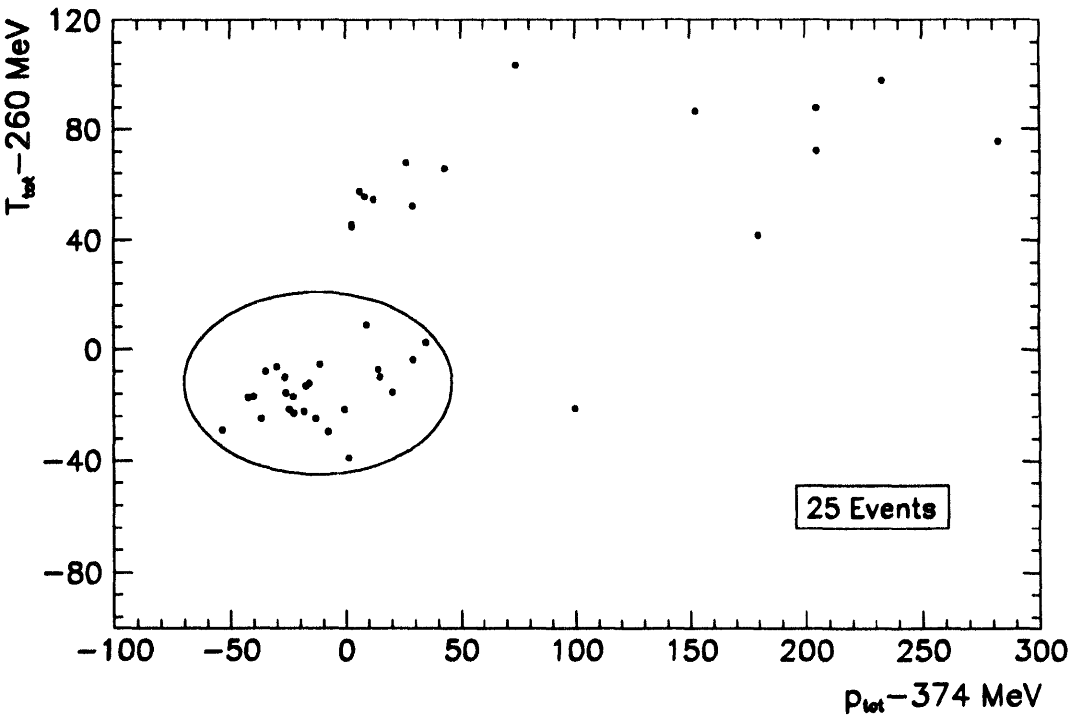

Figure 4.12 The 1992 detected triple $\pi^+\pi^0 p$ coincidences at 260 MeV. Total of 25 real events reveal themselves in this energy-momentum balance scatter plot. The boundary ellipse is determined from Monte Carlo resolution studies and should contain 96% of thrown simulated events. All the plotted coincidences fall within time-of flight window ± 5 ns and have the canceling x and y components of total momentum.

The detector light output-to-kinetic energy conversions and the average corrections for the energy losses in the target material and support structure were applied at this point.

The missing momentum $\mathbf{p}_3 = (x_3, y_3, z_3)$ and the missing mass of the third particle m_3 were calculated interactively in `PAW COMIS` routine for π^0·CP coincidences using the definitions:

$$x_3 = -x_{\pi^0} - x_{\rm cp} \qquad y_3 = -y_{\pi^0} - y_{\rm cp} \qquad z_3 = z_{\pi^+}^{\rm inc} - z_{\pi^0} - z_{\rm cp}$$
$$p_3^2 = x_3^2 + y_3^2 + z_3^2 \qquad E_3 = T_{\pi^+}^{\rm inc} - T_{\pi^0} - T_{\rm cp} + Q_{\rm cp} \qquad m_3^2 = E_3^2 - P_3^2$$

and used as a final kinematic cut. The $Q_{\rm cp}$ value for $\pi^0\pi^+$ coincidences is $m_p - m_{\pi^0}$=803.2 MeV and for $\pi^0 p$ events $m_{\pi^+} - m_{\pi^0}$=4.6 MeV. The resolution in the missing mass of the third particle for the subset of the events surviving all cuts is shown in Figure 4.17.

Four classes of coincident events were studied separately: $\pi^0 p$ coincidences (restricted kinematically to the proton telescope angles), $\pi^0\pi^+$ coincidences in the proton telescopes ($\theta_{\pi^+} \leq 42°$), $\pi^0\pi^+$ coincidences in the pion telescopes ($\theta_{\pi^+} \geq 42°$), and $\pi^+\pi^0 p$ triple coincidences. The $\pi^+\pi^0 p$ coincidences are well separated from background in the two-dimensional energy-momentum final state space. Monte Carlo spectra of detected products were used to identify the accepted triple coincidences in Figure 4.12. The total numbers of accepted events in all runs are tabulated in Tables 4.6-4.9. These are the yields from which total cross sections were calculated. Statistical uncertainties were propagated through the subtraction procedure and total cross sections at one energy were averaged by weighting with fractional inverse errors. The acceptance for each class was calculated separately, Table 4.5. The Monte Carlo simulation was carried out assuming a constant matrix element and purely s-wave interactions in the $\pi\pi$ and $\pi\pi$-p channel. The assumption is strengthened by the appearance of the dipion invariant mass spectra $m_{\pi\pi}$ and by the distribution of $\theta_{\pi\pi}$, the dipion polar angle. These distributions do not show statistically significant departures from phase space determined shapes in Figure 4.18. Accepting therefore, that the final-state $\pi^+\pi^0 p$ kinematic variables follow phase space distributions, total cross sections can be expressed as:

$$\sigma_t = \frac{Y_{\pi^+ p \rightarrow \pi^0 {\rm CP}_1({\rm CP}_2)}}{N_{\pi^+} t_x \mathcal{A}_x \epsilon_{\pi^0} f_{\rm abs} \Gamma_{\pi^0 \rightarrow \gamma\gamma} \eta_{cl} p_{cp} \eta_{vp}}, \tag{4.3}$$

where Y is the background-subtracted number of detected $\pi^0 \cdot$ CP (or $\pi^+\pi^0 p$), N_{π^+} is the number of beam π^+'s incident on the target, t_x is the effective target thickness, $\mathcal{A}_x$ is the corresponding acceptance of the E1179 coincident apparatus, ϵ_{π^0} is the over-all π^0 spectrometer detection efficiency, $f_{\rm abs}$ is the fraction of photons not absorbed before the conversion, $\Gamma_{\pi^0 \pi^0 \rightarrow \gamma\gamma}$ is $\pi^0 \rightarrow \gamma\gamma$ decay branching ratio, η_{cl} is the computer live time, p_{cp} is coincident charged-particle pile-up, and η_{vp} is the spectrometer veto live time. The exclusive acceptance $\mathcal{A}_{\pi^0 {\rm CP}_1({\rm CP}_2)}$ takes into account the smooth charged particle thresholds, hardware and software charged particle detection efficiencies and corrections for π^+ decay-in-flight as well

Table 4.2 ($\pi^0 p$) coincidences and total cross sections: physical $m_{\pi\pi}$, m_3, and kinematic cut on T_p^{max}. In-time window is ±5 ns and out-of-time window ±45 ns.

$T_{\pi^+}^{inc}$ (MeV)	Target Full In-Time	Target Full Out-of-Time	Target Empty In-Time	Target Empty Out-of-time	Yield #	Cross Section (μb)
260	654	81/9	37	7/9	293.4	24.8 ± 5.5
240	142	17/9	22	4/9	59.6	14.9 ± 4.5

Table 4.3 ($\pi^0\pi^+$) coincidences in the "pion" detectors: yields and total cross sections. Kinematic cut on $T_{\pi^+}^{max}$, physical m_3 and $m_{\pi\pi}$. In-time window is ±5 ns, out-of-time window sampling random coincidences is nine times wider. At subthreshold energy of 160 MeV we use the same $T_{\pi^+}^{max}$ as for 190 MeV. At subthreshold energy of 160 MeV we use the same $T_{\pi^+}^{max}$ as for 260 MeV.

$T_{\pi^+}^{inc}$ (MeV)	Target Full In-Time	Target Full Out-of-Time	Target Empty In-Time	Target Empty Out-of-time	Yield #	Cross Section (μb)
260	488	455/9	14	20/9	323.1	26.9 ± 5.0
240	117	132/9	11	7/9	64.2	16.3 ± 5.0
220	103	141/9	16	12/9	36.9	5.9 ± 2.5
200	30	54/9	8	5/9	6.4	2.0 ± 1.5
190	10	33/9	2	3/9	1.3	1.1 ± 2.9
160	3	20/9	1	1/9	1.0	0

as proton nuclear interaction losses. All relevant quantities were measured and evaluated in the laboratory reference frame.

The factors for the cumulative LH$_2$ target full runs were:

$$\text{260 MeV:} \quad \sigma(\mu\text{b}) = 1.53 \times 10^{-5}\frac{Y}{A} = (26.0 \pm 2.7)\ \mu\text{b}, \tag{4.4}$$

$$\text{240 MeV:} \quad \sigma(\mu\text{b}) = 4.76 \times 10^{-5}\frac{Y}{A} = (14.6 \pm 2.6)\ \mu\text{b}, \tag{4.5}$$

$$\text{220 MeV:} \quad \sigma(\mu\text{b}) = 4.03 \times 10^{-5}\frac{Y}{A} = (6.8 \pm 1.8)\ \mu\text{b}, \tag{4.6}$$

$$\text{200 MeV:} \quad \sigma(\mu\text{b}) = 5.55 \times 10^{-5}\frac{Y}{A} = (2.7 \pm 1.2)\ \mu\text{b}, \tag{4.7}$$

$$\text{190 MeV:} \quad \sigma(\mu\text{b}) = 5.28 \times 10^{-5}\frac{Y}{A} = (1.0 \pm 1.7)\ \mu\text{b}, \tag{4.8}$$

Table 4.4 ($\pi^0\pi^+$) coincidences in the "proton" detectors: yields and total cross sections

$T^{inc}_{\pi^+}$ (MeV)	Target Full In-Time	Target Full Out-of-Time	Target Empty In-Time	Target Empty Out-of-time	Yield #	Cross Section (μb)
260	126	250/9	4	15/9	75.6	25.1 ± 5.5
240	32	54/9	2	6/9	21.0	14.5 ± 5.5
220	32	77/9	2	7/9	19.2	11.2 ± 5.0
200	12	33/9	1	6/9	6.8	5.0 ± 3.0
190	2	12/9	0	3/9	1.7	1.9 ± 3.1
160	1	13/9	0	4/9	0.4	0

Table 4.5 $\pi^0\pi^+p$ triple coincidences: yields and total cross sections, $|TOF| \leq 5$ ns.

$T^{inc}_{\pi^+}$ (MeV)	Target Full	Target Empty	Cross Section (μb)
260	25	0	27.0 ± 5.4
240	3	0	11.1 ± 6.4
220	3	0	6.2 ± 3.4
200	1	0	2.9 ± 2.9
190	0	0	0.0 ± 3.0
160	0	0	0.0 ± 3.0

As seen in Tables 4.6-4.9 at 160 MeV and in Figures 4.13-14, the signal disappears below the reaction threshold.

Listed errors are statistical uncertainties calculated by propagating errors in the interactive `PAW COMIS` command file which executed target full/target empty and coincident/out-of-time event subtraction.

The factors contributing to the systematic uncertainty of total cross sections are summarized in Table 4.7. The most significant contributions to the total systematic error are: (i) liquid hydrogen target thickness (5%), (ii) π^0 spectrometer detection efficiency (5%), (iii) absolute beam intensity normalization (4.2%), and (iv) charged particle detection efficiencies (3%). Therefore, the over-all systematic uncertainty of E1179 total cross sections (4.4-4.8) is ~10%.

Table 4.6 Charged particle multipicities in π^0-CP coincidences at 260 MeV (1992).

LH$_2$ Target	Single (%)	Double (%)	Triple (%)	Quad (%)	$\pi\pi p$ (%)
FULL	92.49	7.14	0.34	0.03	0.0015
EMPTY	95.97	3.97	0.06	0.00	0.00

Table 4.7 Quantities used in total cross section calculation and their associated uncertainties. Systematic errors are shown in parentheses. Statistical yield uncertainties are calculated by propagating the errors in the subtraction procedure.

Symbol	Description	Method	Value	Stat(Syst) Error (%)
$Y_{\pi^0\pi^+(p)}$	Number of Double Coincidences	$\pi^+p \rightarrow \pi^+\pi^0p$	1-323	12-100
$Y_{\pi^0\pi^+p}$	Number of Triple Coincidences	$\pi^+p \rightarrow \pi^+\pi^0p$	0-25	20-100
t_{π^0}	LH$_2$ Target Thickness for π^0's	Y_{CH_2} vs Y_{LH_2}	0.144	6.0(5.0)
$t_{\pi^+(p)}$	LH$_2$ Target Thickness for $\pi^+(p)$	$\pi^+p \rightarrow \pi^+p$	0.138	2.5(5.0)
t_{geo}	LH$_2$ Geometrical Target Thickness	Monte Carlo	0.142	1.0(5.0)
N_{π^+}	Incident π^+ Flux	$^{12}C(\pi^\pm,\pi^\pm N)^{11}C$	10^6-10^7	1.6(4.2)
f_{abs}	π^0 absorption loss	Monte Carlo	0.85	1.0(3.0)
ϵ_{π^0}	π^0 Spectrometer Detection Efficiency	Cosmics+Monte Carlo	0.221	3.2(5.0)
ϵ_{cp}	Charged Particle Detection Efficiency	$\pi^+p \rightarrow \pi^+p$	75-85	2.2(3.0)
$A_{\pi^0\pi^+}$	E1179 Apparatus $\pi^0\pi^+$ Acceptance	Monte Carlo	$\simeq 10^{-4}$	1.8(3.0)
A_{π^0p}	E1179 Apparatus π^0p Acceptance	Monte Carlo	$\simeq 10^{-4}$	2.0(3.0)
$A_{\pi^0\pi^+p}$	E1179 Apparatus $\pi^0\pi^+p$ Acceptance	Monte Carlo	$\simeq 10^{-5}$	5.0(3.0)
$\Delta p/p$	Incident Beam Momentum Spread	LEP Channel Controls	0.15	0.4(0.2)

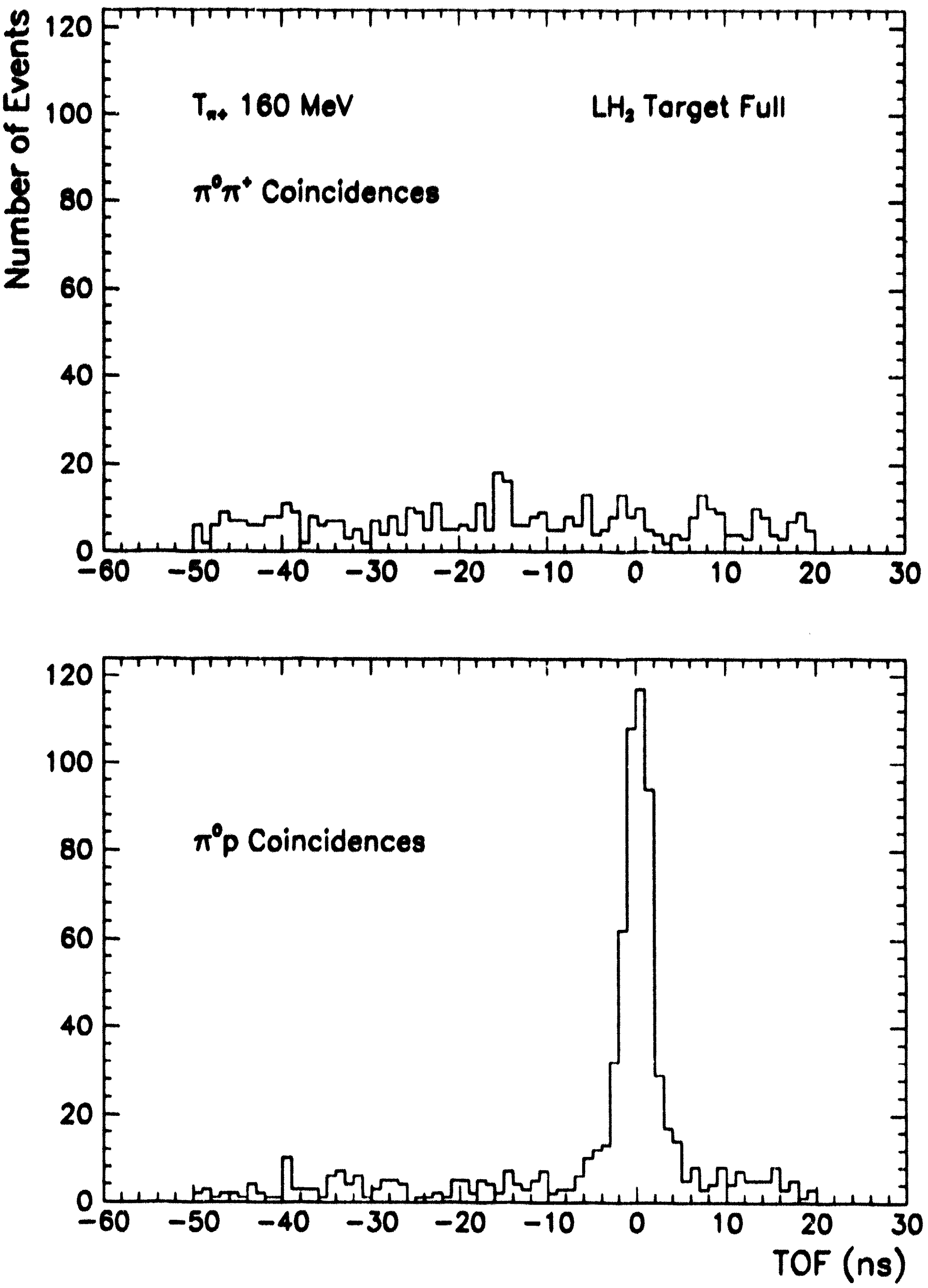

Figure 4.13 Representative unconstrained coincident charged particle time-of-flight relative to the π^0, measured with the full LH$_2$ target at 160 MeV ($\pi^+p \to \pi^+\pi^0p$ threshold: 164.8 MeV). $\pi^+\pi^0$ coincident signal disappears below the reaction threshold. The subthreshold π^+p events come from quasi-free charge exchange on nuclei followed by proton knockout ($\pi^+A \to \pi^0pB$), radiative pion-proton scattering with pion in spectrometer veto below the hardware threshold ($\pi^+p \to \pi^+\gamma p$), and two-step processes ($\pi^+p \to \pi^+p$, $\pi^+n \to \pi^0p$). These events were removed in the analysis by imposing appropriate kinematical cuts.

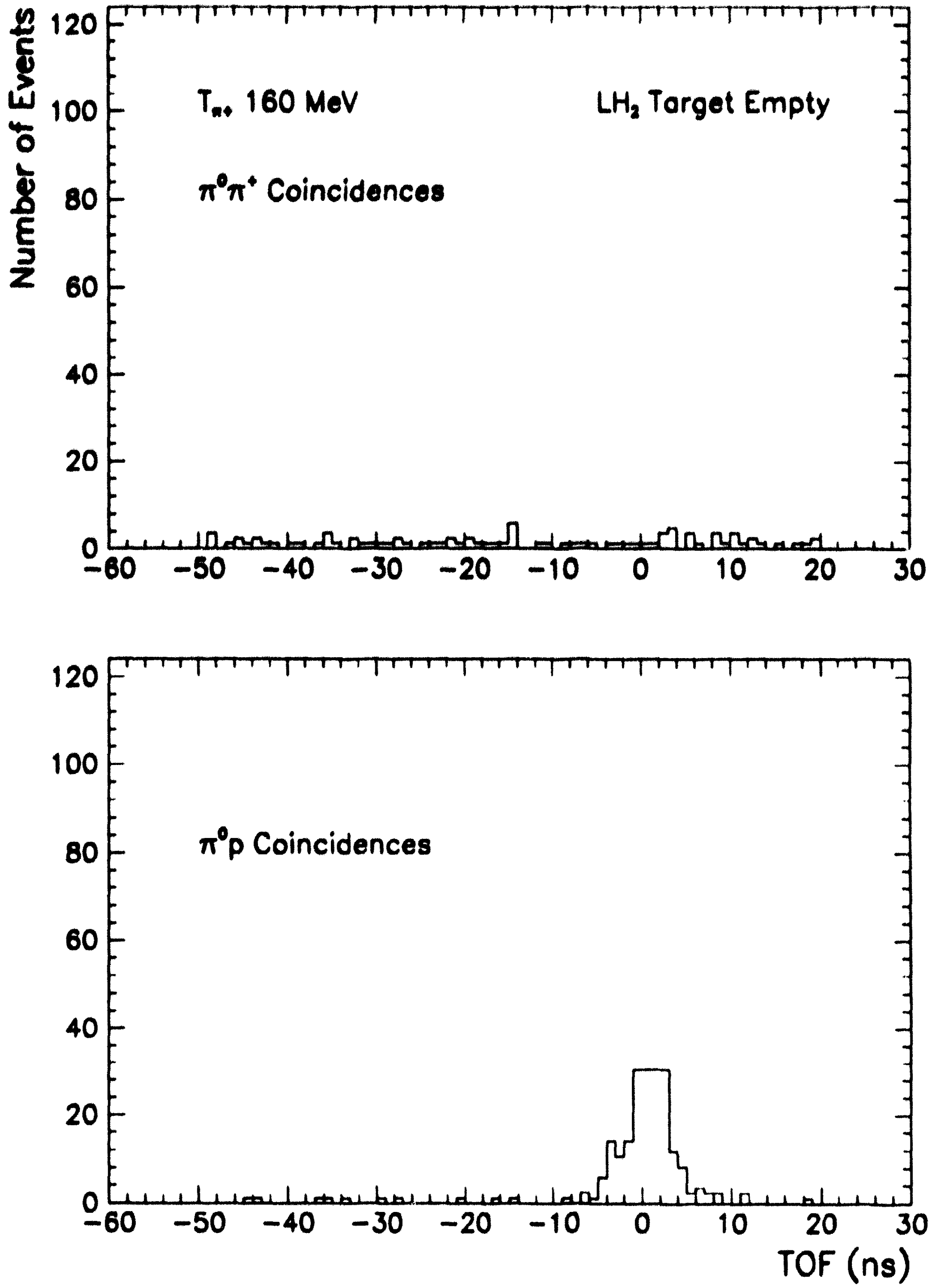

Figure 4.14 Representative coincident charged particle time-of-flight relative to the π^0, measured with the empty LH$_2$ target at 160 MeV ($\pi^+p \rightarrow \pi^+\pi^0p$ threshold: 164.8 MeV). $\pi^+\pi^0$ events are accidental coincidences, subthreshold π^0p events represent quasi-free charge exchange candidates with small admixture of two-step processes.

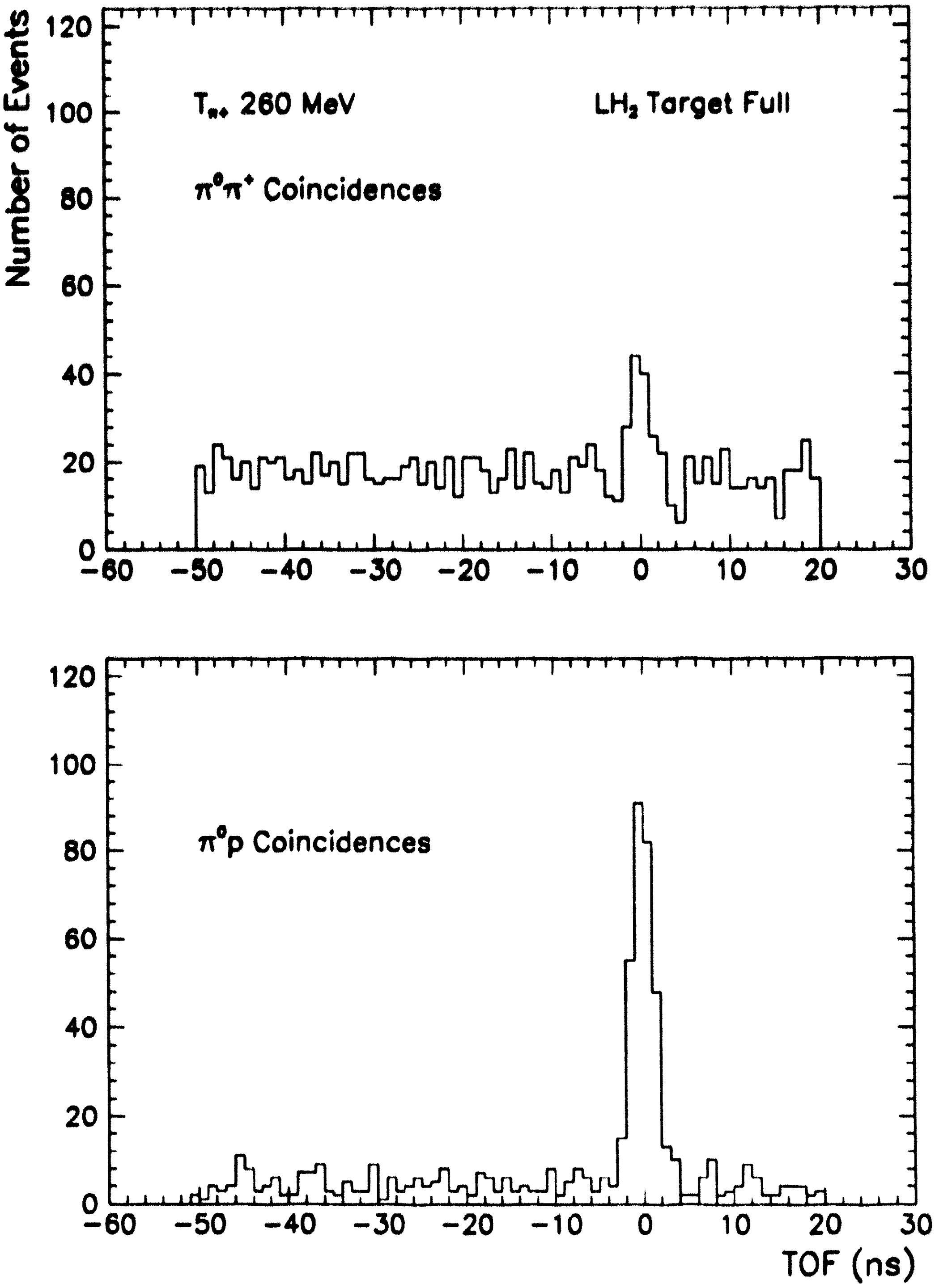

Figure 4.15 Representative coincident charged particle time-of-flight relative to the π^0, measured with the full LH$_2$ target at 260 MeV. $\pi^+\pi^0$ coincidences are the clear signature of the reaction $\pi^+p \rightarrow \pi^+\pi^0p$. More than half of π^0p events are background that does not satisfy kinematical constraints for the reaction $\pi^+p \rightarrow \pi^+\pi^0p$.

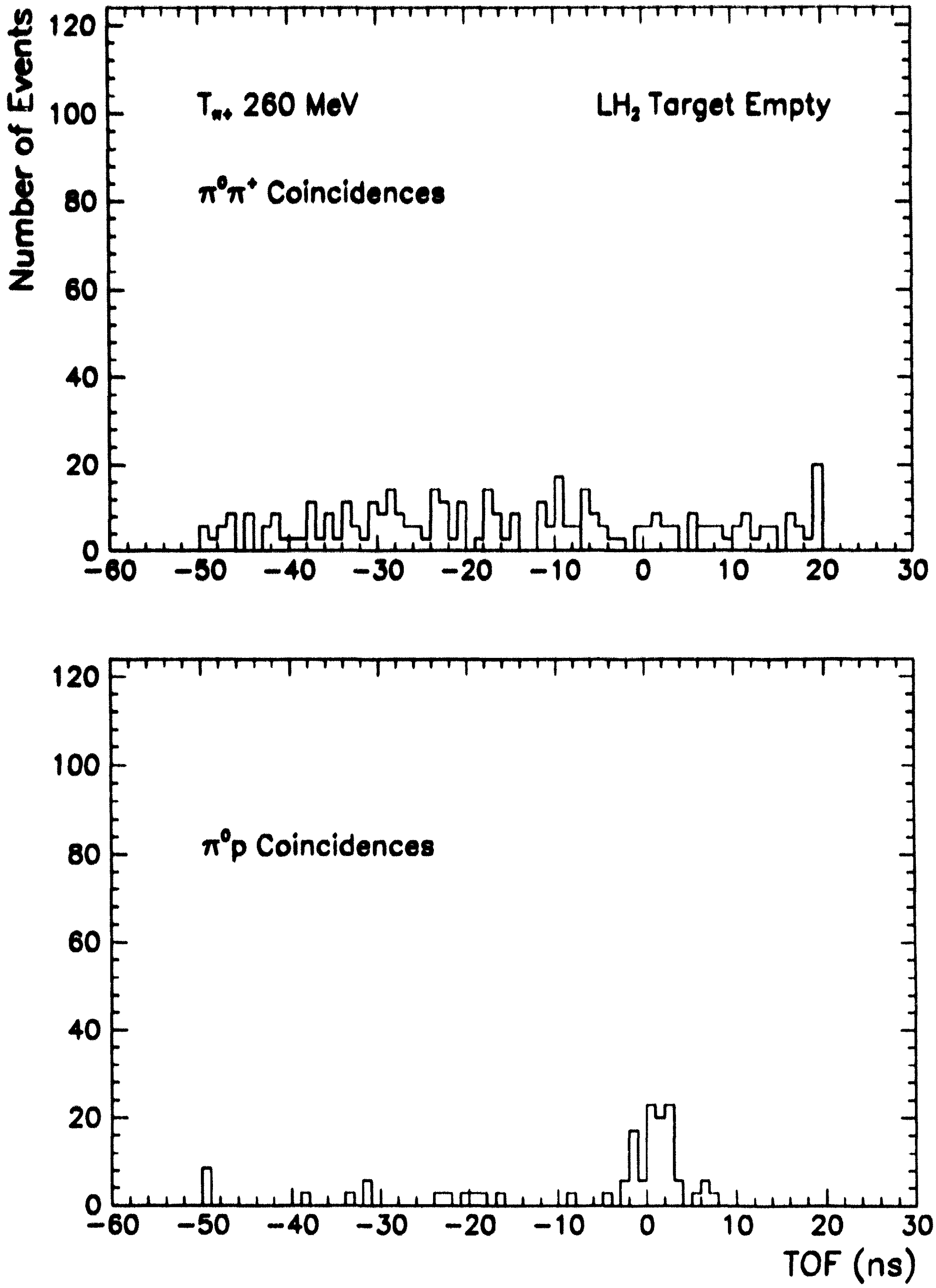

Figure 4.16 Representative coincident charged particle time-of-flight relative to the π^0, measured with the empty LH$_2$ target at 260 MeV. The disappearance of $\pi^+\pi^0$ signal proves that the data are free of background in dipion channel. Detected events are expected flat random accidentals.

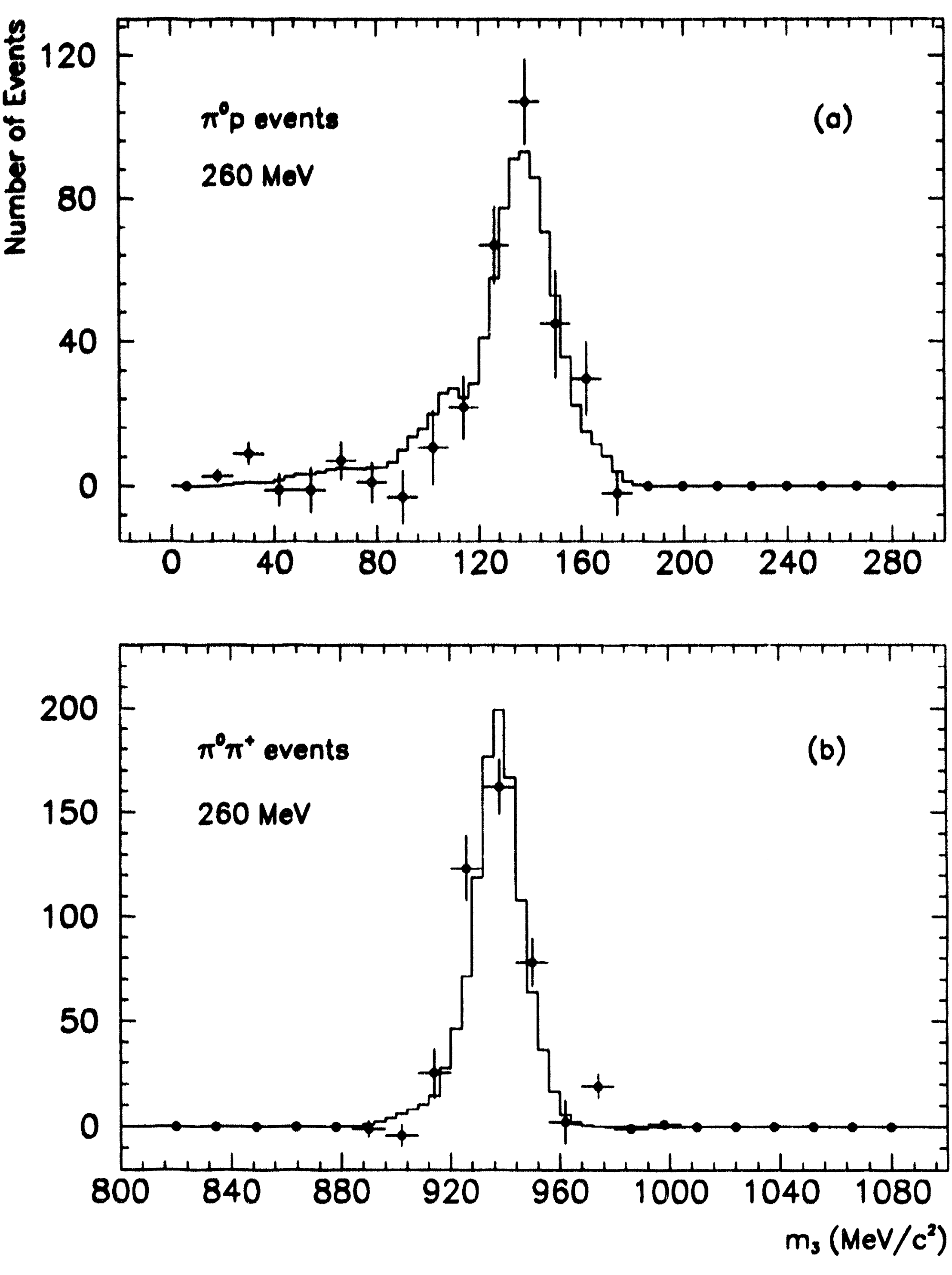

Figure 4.17 Measured spectra of m_3, the invariant mass of the missing (undetected) particle for π^+p (a), and $\pi^+\pi^0$ (b) coincidences, after subtraction of accidental and target-empty backgrounds (•), at 260 MeV. Histograms are the result of a Monte Carlo calculation which incorporates the effects of detector acceptance, instrumental resolution, charged particle detection thresholds, and target size. Results at lower energies are similar.

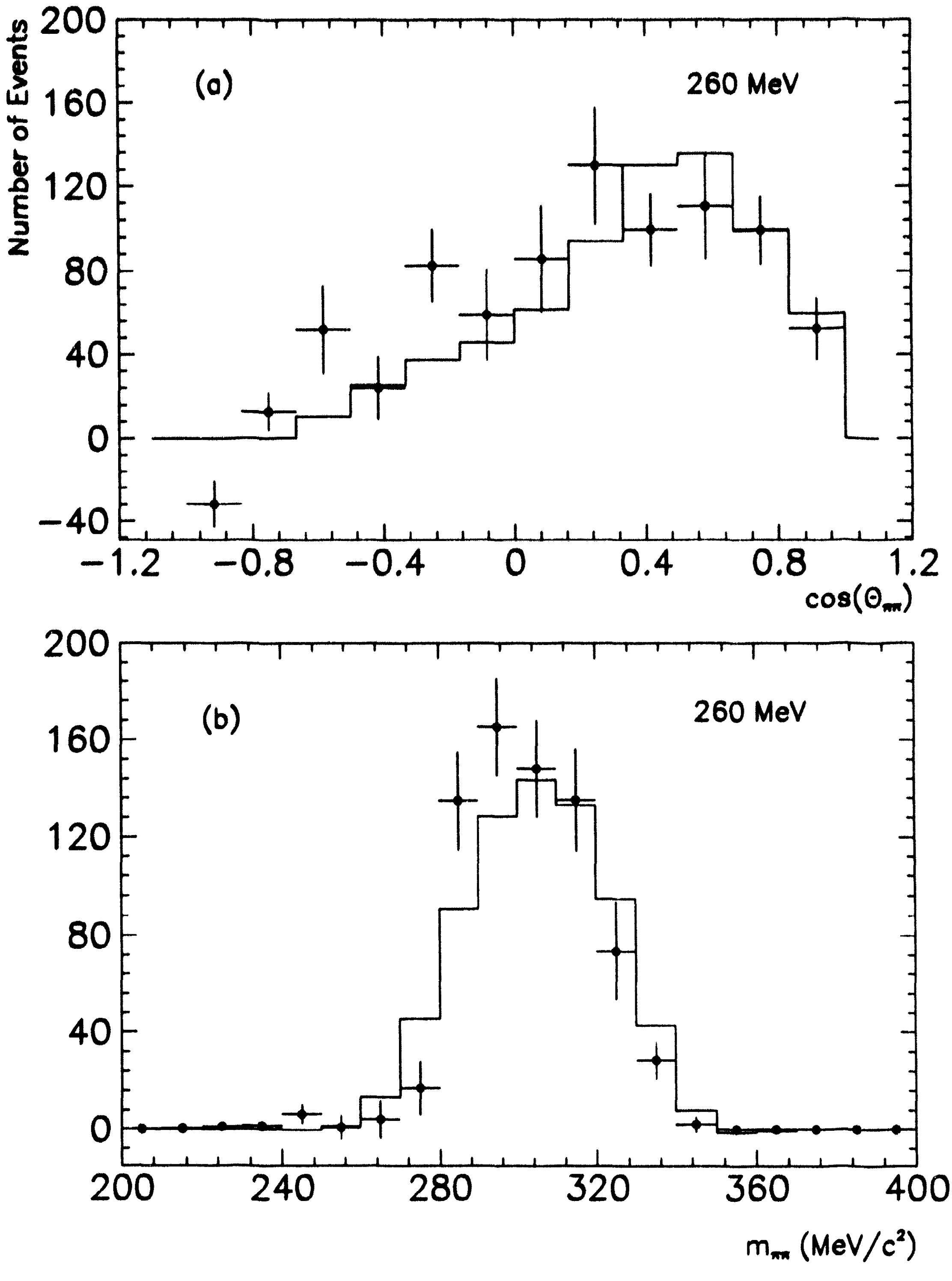

Figure 4.18 Distribution of $\theta_{\pi\pi}$, the dipion polar angle, measured at 260 MeV (•), and the results of a Monte Carlo simulation (histogram). (b) Dipion invariant mass distribution measured at 260 MeV (•), and simulated (histogram). The Monte Carlo simulation is based on pure s-wave dynamics (phase-space probability distributions), and incorporates the actual detector acceptances, resolution, and target size.

Table 4.8 Ingredients of absolute $\pi^\pm$ flux normalization. Systematic uncertainties are listed in parentheses. Over-all beam flux normalization uncertainty is 4.2% for 160–260 π^+ beams and 8.8% for 30 MeV π^- beam.

Symbol	Description	Method	Value	Stat(Syst) Error (%)
σ^-_{act}	30 MeV ACT Cross Sections	[Lei-90]	1.70 mb	6.0(4.7)
σ^+_{act}	160–260 MeV ACT Cross Sections	[Lei-90]	45.1–28.7 mb	1.6(3.7)
f_p	Proton Contamination	π^+-p Separation	0.2–0.7%	0.5(0.6)
f_{e^-}	Electron Contamination	Activation	$12\text{–}20 \times N_{\pi^-}$	5.0(7.0)
ϵ_{cp49}	Activation Apparatus Efficiency	$e^+\gamma$ Coincidence	96.6/23.9%	0.7(0.5)
t_d	ACT Disk Thickness	Scale Measurement	.150–.350 g cm^{-2}	0.1(0.1)

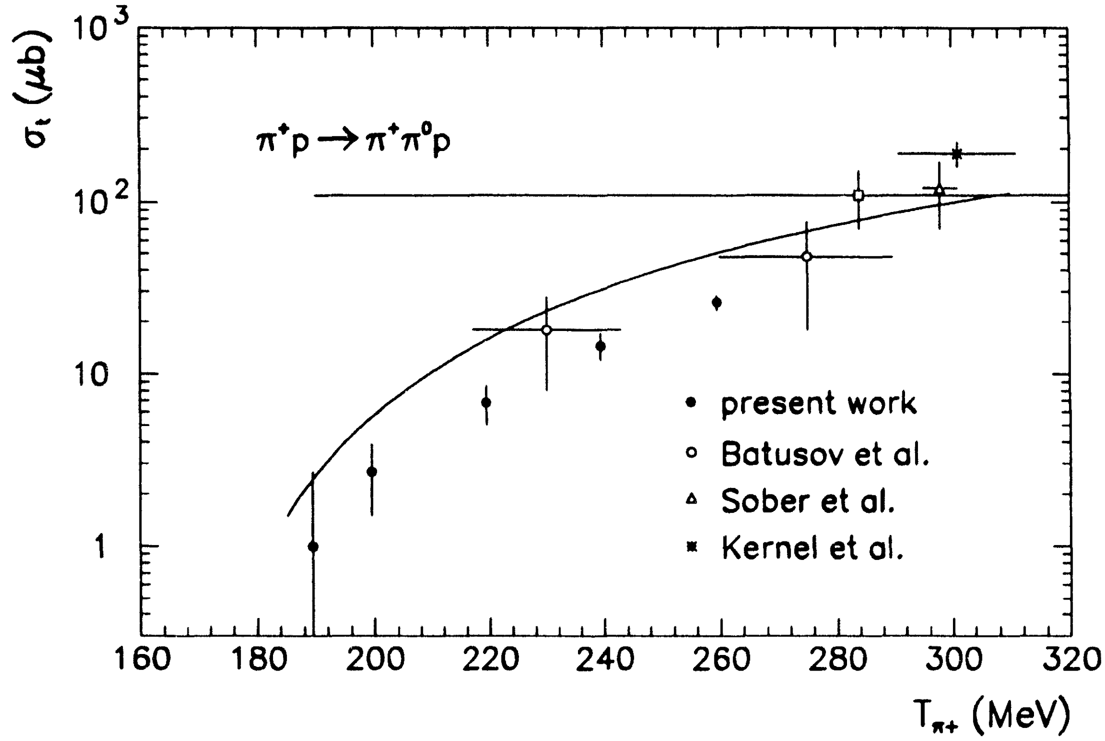

Figure 4.19 Total cross sections for the reaction $\pi^+p \to \pi^+\pi^0p$ measured in this work (•), and previously published (○ [Bat-75], △ [Sob75], and * [Ker-91b]). Full curve: global fit of $\pi\pi \to \pi\pi N$ isospin amplitudes of Burkhardt and Lowe [Bur-92].

C. Background Sources and Rates

One arm of the coincident trigger required the presence of π^0 and other registered one or more charged particles in the final state. Background reactions resulting in a neutral pion and a charged pion and/or proton in the final state include:

- accidental coincidences of pion SCX $\pi^+ n \rightarrow \pi^0 p$ and pion-proton elastic scattering $\pi^+ p \rightarrow \pi^+ p$,
- quasi-free pion SCX on nuclei followed by proton knockout, $\pi^+ A \rightarrow \pi^0 p B$,
- two-step processes involving pion elastic scattering followed by subsequent pion SCX in the material surrounding the target, $\pi^+ p \rightarrow \pi^+ (A \rightarrow \pi^0 B) p$,
- two-step processes involving the pion elastic scattering into the charged particle detector followed by subsequent pion SCX in the detector material, $\pi^+ p \rightarrow \pi^+ (A \rightarrow \pi^0 B) p$,
- $\pi^+ p \rightarrow \pi^+ \gamma p$, radiative pion-proton bremsstrahlung in which the charged pion is not detected in the π^0 spectrometer veto.

Table 4.8 Representative proton detector pile-up fraction. The pile-up was indicated by the signals in the baseline gate (E_b) exceeding the software threshold of 5 – 20% of the prompt signal gate (E_p). The coincident charged-particle pile-up correction was estimated on basis of these raw pile-up rates using Monte Carlo program as $\leq$1%.

Detector	PR1	PR2	PR3	PR4	PR5	PR6	PR7	PR8
Baseline Pedestal	22	22	20	19	22	13	27	32
$E_b/E_p \leq 5\%$	7.9	6.4	5.4	11.9	4.1	10.3	9.6	21.2
$E_b/E_p \leq 10\%$	7.3	3.2	4.7	7.5	2.1	7.0	6.4	16.1
$E_b/E_p \leq 20\%$	4.2	1.9	3.6	5.7	2.1	4.9	4.5	12.2
$E_b/E_p \leq 10\%$ & $E_{pr} \geq 5$ MeV	4.8	1.3	1.1	2.4	0.0	2.1	3.8	9.4

Table 4.9 $\pi^0 p$ background yields: 1992 run. Average yields for the liquid hydrogen target full and empty, with a π^0 and proton in coincidence ($|t^c_{\pi^0} - t^l_{pr}| \leq 5$ ns) and out of coincidence, are shown.

T_π (MeV)	$10^9\ (\pi^0 p)/\pi_{\rm inc}$ Full, In-Time	$10^9\ (\pi^0 p)/\pi_{\rm inc}$ Full, Out-of-Time	$10^{10}\ (\pi^0 p)/\pi_{\rm inc}$ Empty, In-Time	$10^{10}\ (\pi^0 p)/\pi_{\rm inc}$ Empty, Out-of-Time
160	1.75	1.39	.485	.075
190	1.86	1.25	.454	.086
200	1.84	1.23	.460	.089
220	1.63	0.78	.415	.084
240	1.22	0.37	.498	.069
260	1.11	0.30	.405	.042

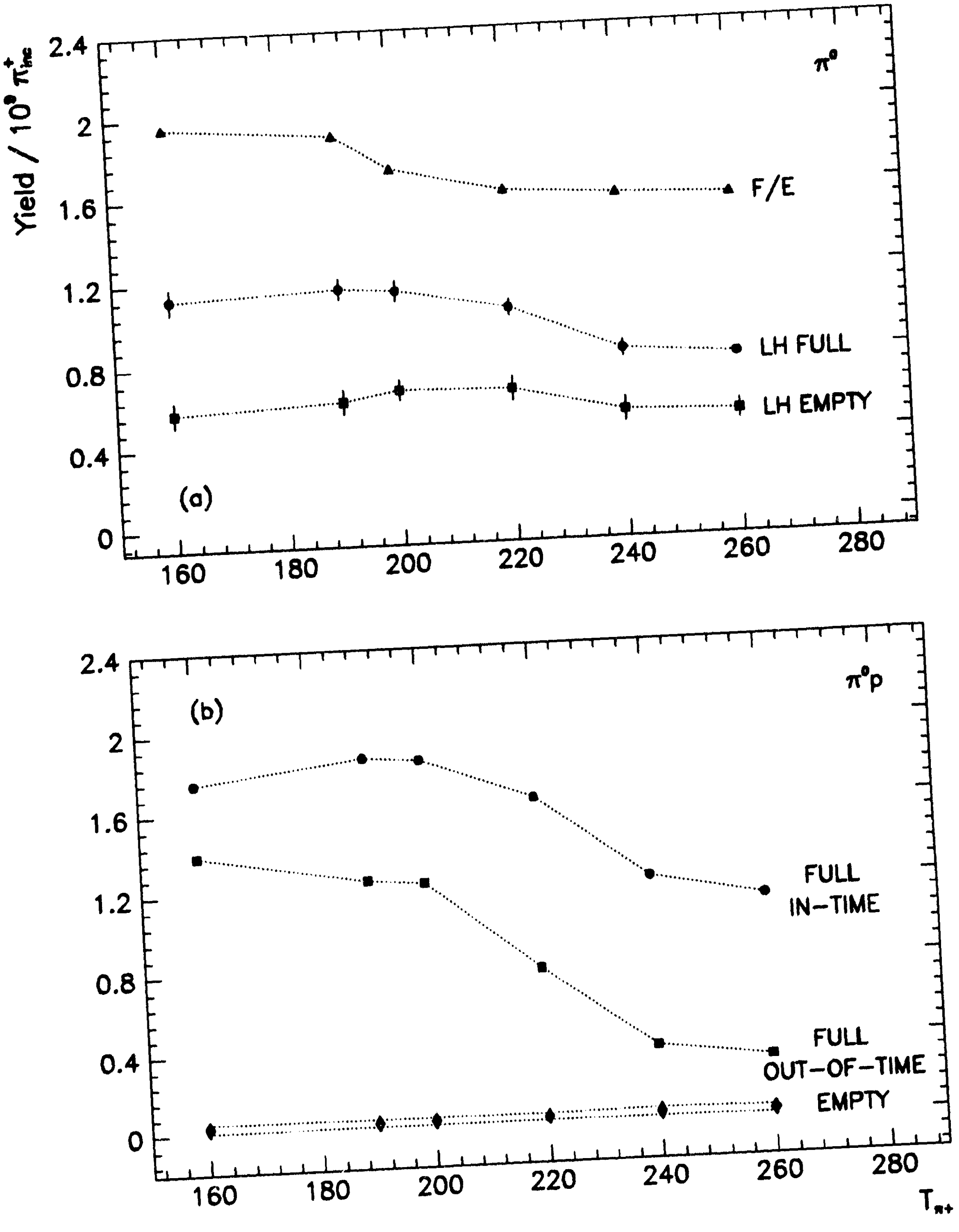

Figure 4.20 The inclusive π^0 and exclusive $\pi^0 p$ background yields as a function of incident pion energy. The exclusive background sources are accidental coincidences that should scale with SCX and elastic $\pi^+ p$ cross sections, as well as quasi-free SCX with proton knockout and radiative π^+ scattering (rising with incident pion energy).

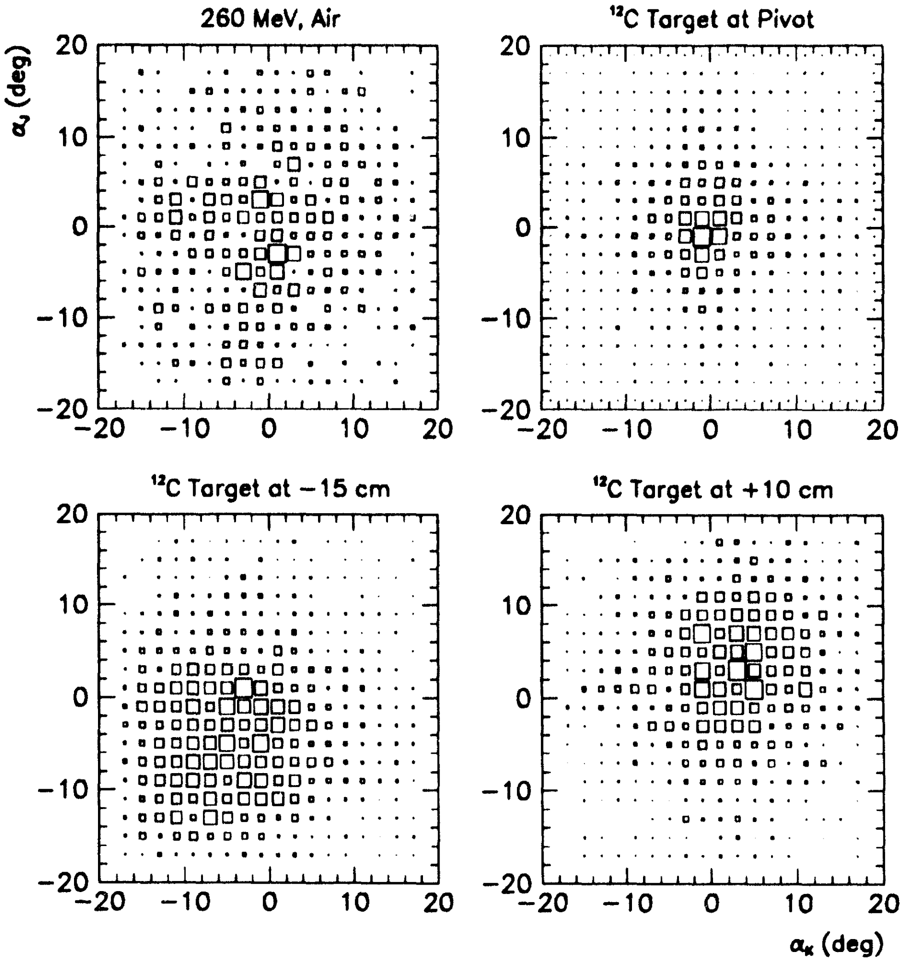
260 MeV, Air

^{12}C Target at Pivot

^{12}C Target at −15 cm

^{12}C Target at +10 cm

Figure 4.21 ^{12}C target position resolution from π^0 spectrometer MWPC hits. Two-dimensional histograms showing the floor angles between line back-projected from gamma conversion point to pivot center and gamma direction deduced from hits in X and X$'$ chambers for J and K arm. The carbon target was moved along the beamline on tracks in 5 cm steps.

Table 4.10 π^0 yields with LH_2 target: 1991 Run. * 1990 test run.

T_π (MeV)	$10^8\ \pi^0/\pi_{inc}$ Target Full	$10^8\ \pi^0/\pi_{inc}$ Target Empty	Full/Empty
$30 \pm 1.64^*$	8.61 ± 0.26	$1.54 \pm 0.13^*$	5.59 ± 0.51
30 ± 1.64	9.27 ± 0.28	0.90 ± 0.12	10.30 ± 1.37
160 ± 0.47	9.58 ± 0.29	5.34 ± 0.17	1.79 ± 0.08
180 ± 0.52	10.76 ± 0.34	4.86 ± 0.14	2.21 ± 0.11
190 ± 0.54	10.11 ± 0.28	4.78 ± 0.14	2.12 ± 0.09
200 ± 0.56	9.53 ± 0.25	4.51 ± 0.13	2.11 ± 0.08
220 ± 0.61	8.23 ± 0.21	3.61 ± 0.16	2.28 ± 0.11
240 ± 0.66	10.97 ± 0.24	7.25 ± 0.15	1.51 ± 0.05
$260 \pm 0.70^*$	13.74 ± 0.22	$11.31 \pm 0.21^*$	1.21 ± 0.03
260 ± 0.70	10.02 ± 0.21	6.99 ± 0.15	1.43 ± 0.04

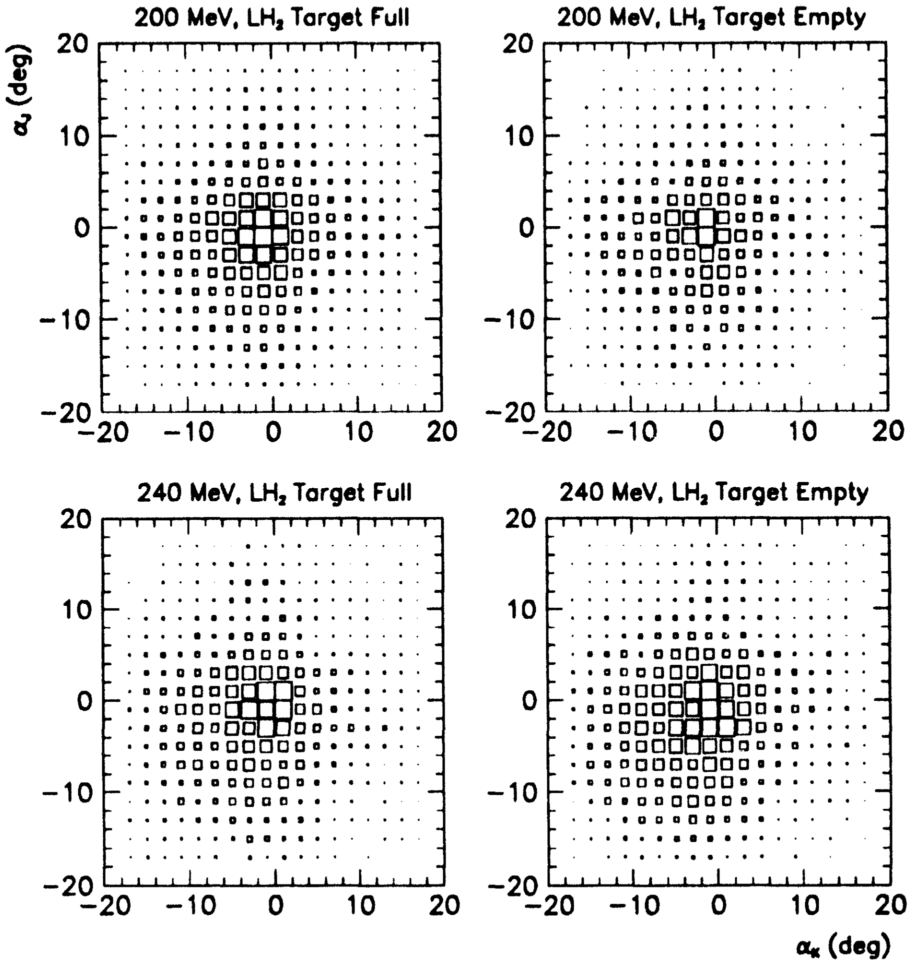

Figure 4.22 LH_2 target position resolution from π^0 spectrometer MWPC hits. The bulk of the background π^0's comes from SCX on upstream material where both angles are negative.

Table 4.11 π^0 Yields with LH_2 Targets: 1992 Run

T_π (MeV)	$10^8\ \pi^0/\pi_{\text{inc}}$ Target Full	$10^8\ \pi^0/\pi_{\text{inc}}$ Target Empty	Full/Empty
30 ± 1.64	10.67 ± 0.22	1.33 ± 0.10	8.02 ± 0.63
160 ± 0.47	11.20 ± 0.06	5.75 ± 0.06	1.95 ± 0.02
190 ± 0.54	11.54 ± 0.05	6.12 ± 0.06	1.89 ± 0.02
200 ± 0.56	11.36 ± 0.05	6.61 ± 0.05	1.72 ± 0.02
220 ± 0.61	10.37 ± 0.04	6.47 ± 0.06	1.60 ± 0.02
240 ± 0.66	8.21 ± 0.04	5.23 ± 0.06	1.57 ± 0.02
260 ± 0.70	7.83 ± 0.02	5.04 ± 0.05	1.55 ± 0.02

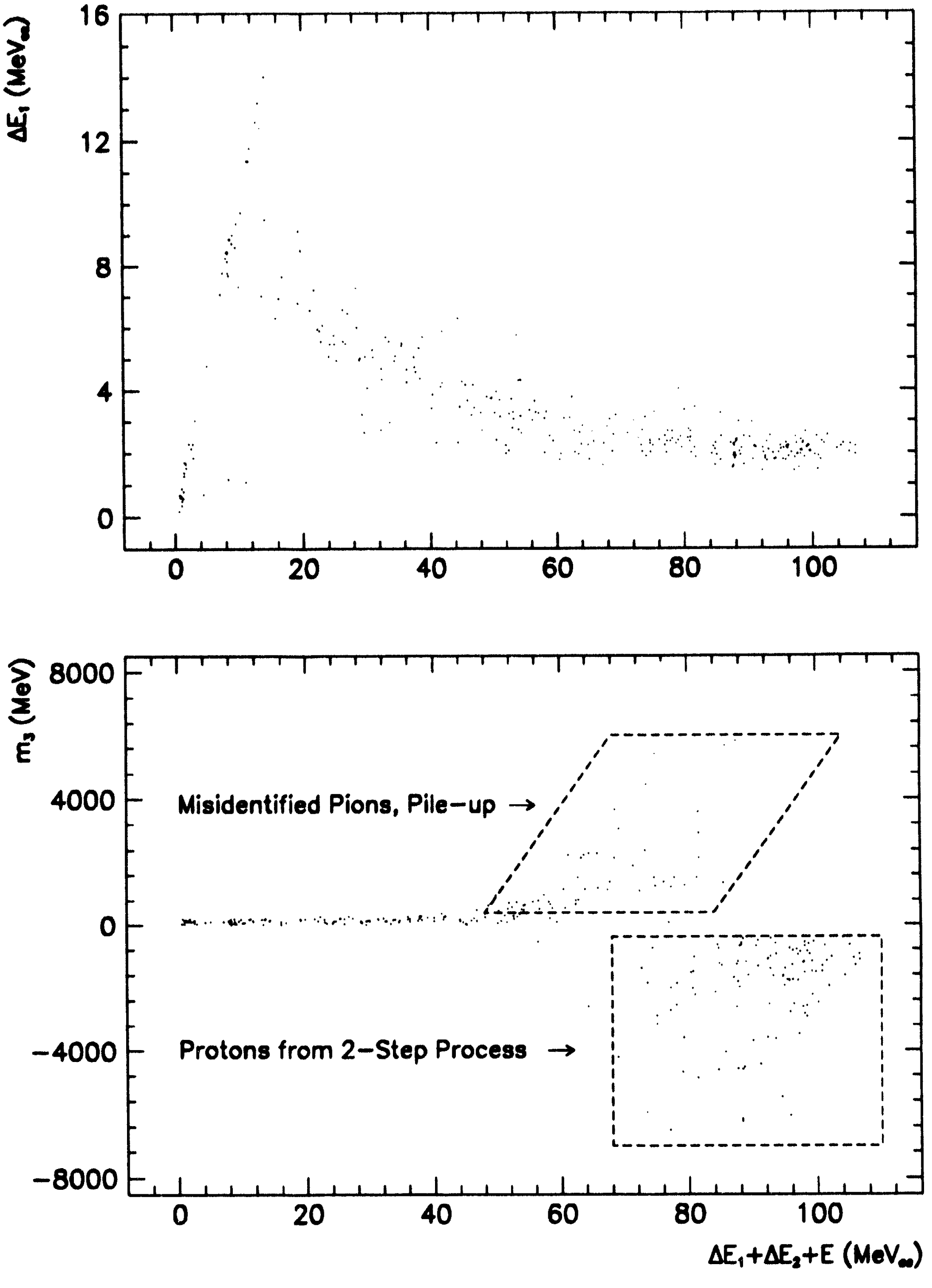

Figure 4.23 1991 $\pi^0 p$ coincidences at 260 MeV passing all cuts except the missing energy-momentum cut. Background events are clearly separated from real coincidences.

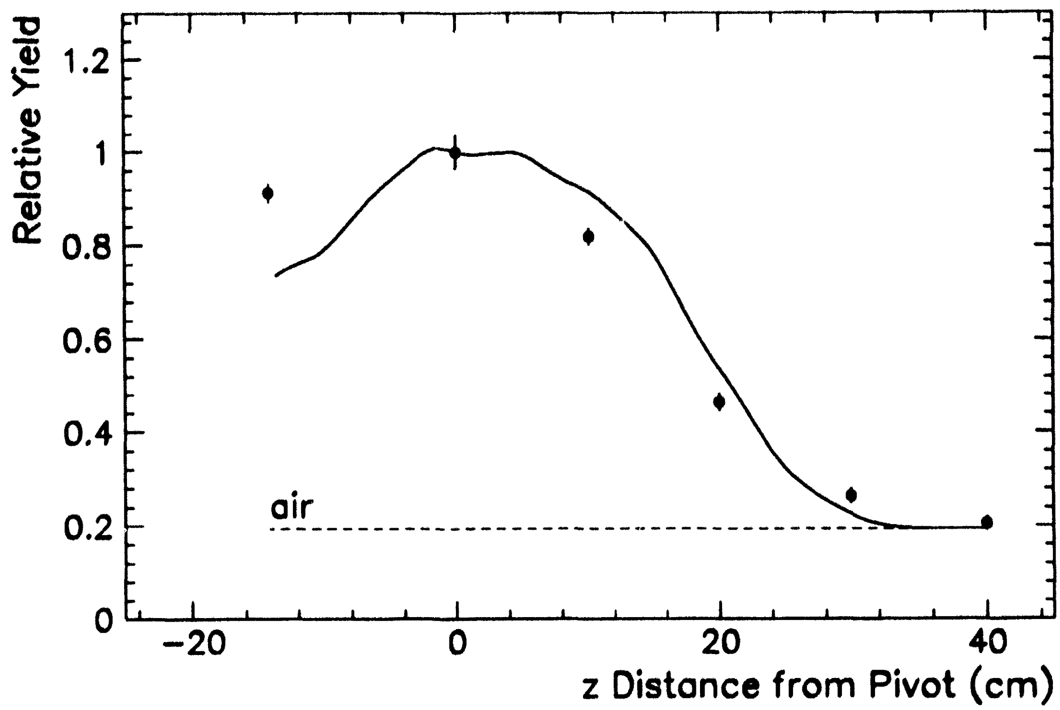

Figure 4.24 Inclusive π^0 rates measured with the π^0 spectrometer positioned at the polar angle of 20°, with a $\gamma\gamma$ opening angle of 115.1°, and nominal radius 50 cm. A 529 mg cm^{-2} ^{12}C target was moved along the beam axis upstream and downstream of the pivot position as indicated on the abscissa (positive distance is downstream). The measured π^0 yields are compared to a target-out run in air (dashed line). The solid curve is a result of Monte Carlo simulation using a π^0 source with a flat energy spectrum spread along beam axis.

The sensitivity of the π^0 spectrometer in the main E1179 configuration to the matter in the beam, as a function of z, displacement along beam axis, is measured in the 1990 runs. The results of that measurement are shown in Figure 4.24. They clearly indicated that: (a) there should be no upstream window on scattering chamber, and (b) the downstream window should be placed at least 40 cm away from the target center. Both constraints were incorporated in the 1992 scattering chamber design. For the same thickness of empty liquid hydrogen target that design reduced backgrounds by 40%, Tables 4.10 and 4.11. The off-axis π^0 background originates mainly from the downstream hemisphere of a scattering chamber and shielding material. These events are most effectively suppressed by the kinematical cuts on missing mass of the third (undetected) particle. One example from the first pass replay is shown in Figure 4.23. The Figures 4.21 and 4.22 indicate the spatial resolution of target and the smeared background source locations projected on horizontal plane.

D. Reduced Amplitudes and Threshold Extrapolation

Isospin invariance limits the form of the $\pi N \to \pi\pi N$ amplitudes, so that only four independent amplitudes, $A_{2I,I_{\pi\pi}}$, determine all five reaction channels. Two final-state pions can couple into a state with combined isospin $I_{\pi\pi} = 0, 1, 2$ while the dipion-nucleon system can have total isospin $I = \frac{1}{2}, \frac{3}{2}$. At threshold, when the pions are at rest in the CM frame Bose symmetry necessitates an even isospin state, $I_{\pi\pi} = 0$ or $I_{\pi\pi} = 2$.

Conservation of parity and total angular momentum requires that threshold single pion production proceed from the initial $P_{\frac{1}{2}}$ state to a final $S_{\frac{1}{2}}$ state. With these restrictions the decomposition of the measurable $\pi N \to \pi\pi N$ reaction amplitudes is

$$A(\pi^- p \to \pi^0\pi^0 n) = \frac{2}{3\sqrt{5}}A_{32} + \frac{\sqrt{2}}{3}A_{10}, \tag{4.10}$$

$$A(\pi^- p \to \pi^+\pi^- n) = \frac{1}{3\sqrt{5}}A_{32} - \frac{\sqrt{2}}{3}A_{10} + \frac{1}{3}A_{31} - \frac{1}{3}A_{11}, \tag{4.11}$$

$$A(\pi^- p \to \pi^-\pi^0 p) = -\frac{1}{\sqrt{10}}A_{32} + \frac{1}{3\sqrt{2}}A_{31} + \frac{\sqrt{2}}{3}A_{11}, \tag{4.12}$$

$$A(\pi^+ p \to \pi^+\pi^0 p) = -\frac{1}{\sqrt{10}}A_{32} - \frac{1}{\sqrt{2}}A_{31}, \tag{4.13}$$

$$A(\pi^+ p \to \pi^+\pi^+ n) = \frac{2}{\sqrt{5}}A_{32}. \tag{4.14}$$

Low-energy isospin amplitudes can be conveniently parametrized in the form

$$A_{32} = a_{32}\chi_f^\dagger \mathbf{Q}\boldsymbol{\sigma}\chi_i, \tag{4.15}$$

$$A_{10} = a_{10}\chi_f^\dagger \mathbf{Q}\boldsymbol{\sigma}\chi_i, \tag{4.16}$$

$$A_{31} = a_{31}\chi_f^\dagger (\mathbf{q}_1 - \mathbf{q}_2)\boldsymbol{\sigma}\chi_i, \tag{4.17}$$

$$A_{11} = a_{11}\chi_f^\dagger (\mathbf{q}_1 - \mathbf{q}_2)\boldsymbol{\sigma}\chi_i, \tag{4.18}$$

where $a_{2I,I_{\pi\pi}}$ are reduced isospin amplitudes, χ_i and χ_f are spinors for the initial and final nucleons, $\mathbf{Q}$ is the CM momentum of the incident pion, $\mathbf{q}_1$ and $\mathbf{q}_2$ are the CM momenta of the final state pions, and $\boldsymbol{\sigma}$ are the Pauli spin matrices.

Total cross section σ_t for pion production: $\pi(Q) + N(p_i) \to \pi(q_1) + \pi(q_2) + N(p_f)$ can be written as

$$\sigma_t = \int \delta^{(4)}(p_i + Q - p_f - q_1 - q_2)\frac{|A|^2}{(2\pi)^5 v}\frac{d^3p_f d^3q_1 d^3q_2}{[(E_i/m)(E_f/m)2\omega_Q 2\omega_1 2\omega_2]}, \tag{4.19}$$

where v is the relative velocity between the incident pion and the target nucleon, m is the nucleon mass, E_i and E_f are the energies of the initial and final nucleons and ω_Q, ω_1 and ω_2

are the energies of the pions. The parametrization (4.15-4.18) allows the total cross section to be calculated as a one-dimensional integral over three body final phase space R_3 [Tur-69]

$$\sigma_t = a_{if}^2 \times Q^2 \times R_3 \tag{4.20}$$

Phase space integrals for the various final charge states are shown in Figure 4.25 as a function of incident pion kinetic energy. Total cross sections can be obtained by multiplying the curves with the actual values of the reduced matrix elements.

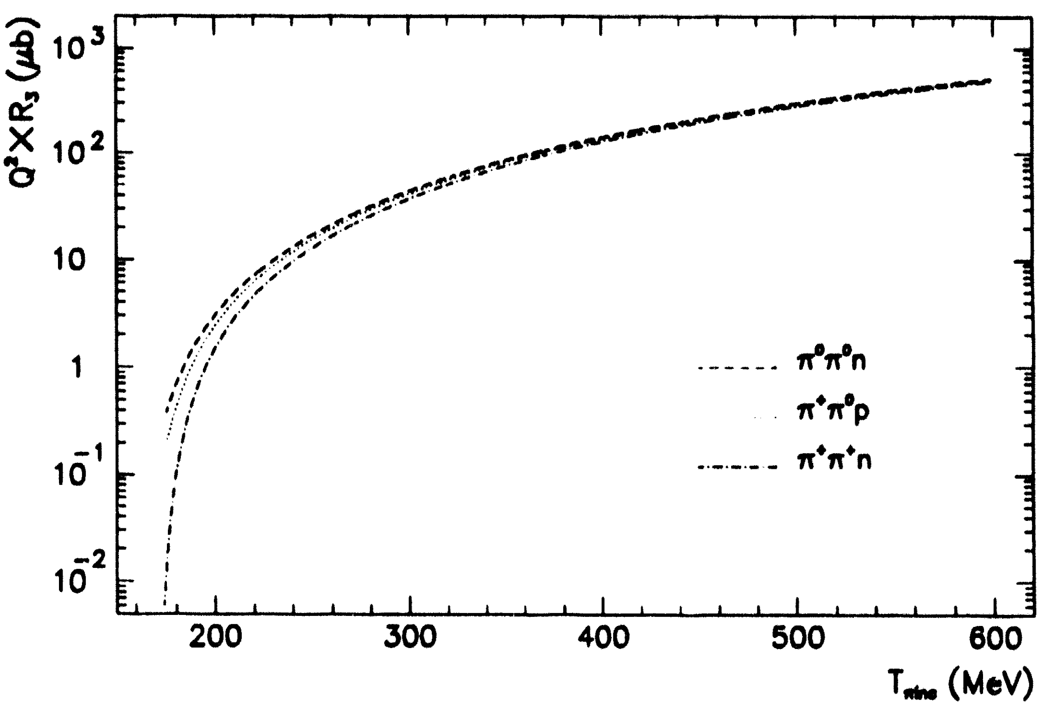

Figure 4.25 T_π dependence of $Q^2 \times R_3$ for $\pi N \rightarrow \pi\pi N$. Phase space dependence of the total cross section is obtained by single numerical integration.

The invariant amplitude $\mathcal{A}$ in the lowest order of perturbation theory is given by the Weinberg effective Lagrangian derived in Appendix D:

$$\mathcal{A} = \mathcal{A}^{(1)} + \mathcal{A}^{(2)} + \mathcal{A}^{(3)} + \mathcal{A}^{(K)} \tag{4.21}$$

The term $\mathcal{A}^{(K)}$ is caused by the anomalous magnetic moment in the Lagrangian [Bha-84]. One-point $\mathcal{A}^{(1)}$, two-point $\mathcal{A}^{(2)}$, and three-point $\mathcal{A}^{(3)}$ tree diagrams are shown in Figure 4.26. The explicit form of these matrix elements is given in the work of Arndt *et al.* [Arn-79]. Olsson and Turner [Ols-68] have calculated one- and two-point contributions in the threshold approximation for the $\pi^+\pi^-n$ and $\pi^+\pi^+n$ final charged states. The terms in the amplitude $\mathcal{A}(\pi^+\pi^-n)$ are

$$\mathcal{A}^{(1)} = i\frac{g_\pi}{2m}\frac{\sqrt{2}}{4f_\pi^2}(-2m)\left[-2-\frac{m_\pi}{m}+\frac{2\omega_q-m_\pi\xi}{\omega_Q-m_\pi}\right]\frac{\chi_f^\dagger(-\sigma\mathbf{Q})\chi_i}{\sqrt{2m(E_i+m)}}, \tag{4.22}$$

$$\mathcal{A}^{(2)} = -i\frac{g_\pi}{2m}\frac{\sqrt{2}}{4f_\pi^2}(-2m)\left[-\frac{3m_\pi}{m}-\frac{2m_\pi}{2m+m_\pi}+\frac{2m_\pi}{2E_i-m_\pi}\right]\frac{\chi_f^\dagger(-\sigma\mathbf{Q})\chi_i}{\sqrt{2m(E_i+m)}}, \tag{4.23}$$

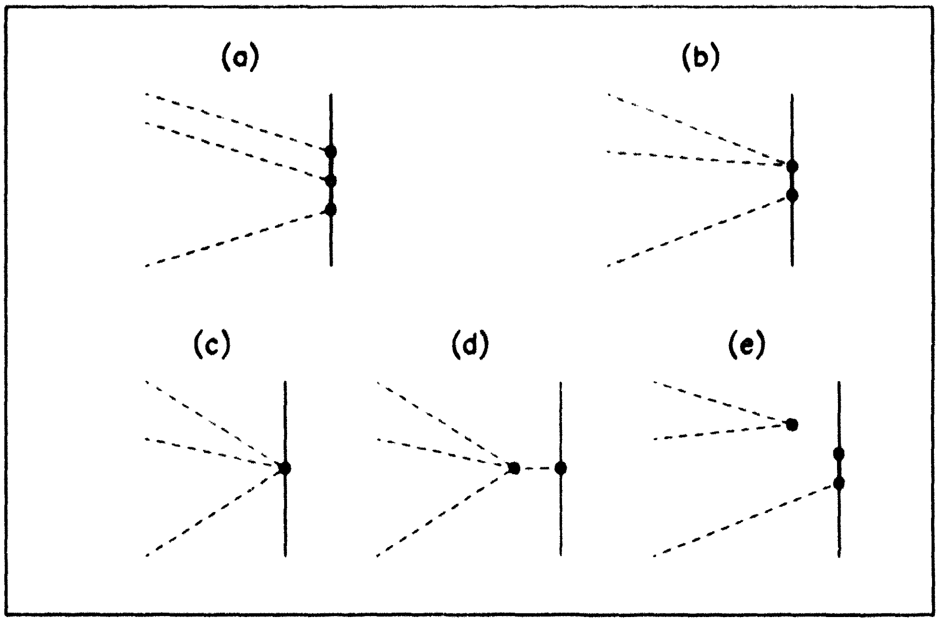

Figure 4.26 (c) and (d) one-point, (b) and (e) two-point and (a) three-point tree diagrams for the reaction $\pi N \to \pi\pi N$. Diagram (d) corresponds to the pion-pole term and diagram (c) to the contact term.

where g_π is the πNN strong coupling constant, f_π is the pion decay constant, and ξ, known as a chiral-symmetry-breaking parameter, characterizes the symmetry-breaking tensor term in Lagrangian. Therefore

$$\mathcal{A}^{\mathrm{OT}}_{\pi^+\pi^-n} = i\frac{g_\pi}{2m}\frac{\sqrt{2}}{4f_\pi^2}(-2m)\left[\frac{2\omega_q-m_\pi\xi}{\omega_Q-m_\pi}+\frac{2m_\pi}{m}-2-\frac{2m_\pi}{2m+m_\pi}+\frac{2m_\pi}{2E_i-m_\pi}\right]\frac{\chi_f^\dagger(-\sigma\mathbf{Q})\chi_i}{\sqrt{2m(E_i+m)}}, \tag{4.24}$$

The amplitude $\mathcal{A}(\pi^+\pi^+n)$ is

$$\mathcal{A}^{\rm OT}_{\pi^+\pi^+n} = i\frac{g_\pi}{2m}\frac{\sqrt{2}}{4f_\pi^2}(-2m)\left[\frac{-4m_\pi}{2E_i - m_\pi} - \frac{4m_\pi}{m} + \frac{4m_\pi}{2m + m_\pi} - \frac{(2+\xi)m_\pi}{\omega_Q - m_\pi}\right]\frac{\chi_f^\dagger(-\sigma\mathbf{Q})\chi_i}{\sqrt{2m(E_i + m)}}, \tag{4.25}$$

Threshold values of reduced amplitudes can, therefore, be expressed in terms of a single parameter ξ:

$$a_0(\pi^-p \rightarrow \pi^+\pi^-n) = -1.351 + 0.598\xi, \tag{4.26}$$

$$a_0(\pi^+p \rightarrow \pi^+\pi^+n) = 1.505 + 0.598\xi, \tag{4.27}$$

$$a_0(\pi^\pm p \rightarrow \pi^\pm\pi^0 p) = -0.532 - 0.212\xi, \tag{4.28}$$

$$a_0(\pi^-p \rightarrow \pi^0\pi^0 n) = 2.149 - 0.307\xi, \tag{4.29}$$

where the electromagnetic mass splitting significantly affects the phase space integral for charged states other than $\pi^-p \rightarrow \pi^+\pi^-n$ in the energy region of a few MeV above threshold.

The s-wave, $I = 0$ and $I = 2$ scattering lengths α_0^0 and α_0^2 in the Olsson-Turner chiral symmetry breaking model [Ols-68,69,72] depend on the parameter ξ

$$\alpha_0^0 = \frac{14 - 5\xi}{48}\frac{3m_\pi}{4\pi f_\pi^2}, \tag{4.30}$$

$$\alpha_0^2 = -\frac{2 + \xi}{24}\frac{3m_\pi}{4\pi f_\pi^2} \tag{4.31}$$

Chiral limit values recommended by Coon and Scadron [Coo-90] were used in this work for g_π, g_A/g_V and M.

Threshold extrapolation of the $\pi^+p \rightarrow \pi^+\pi^0 p$ amplitude was done for the five E1179 data points plus five other published results, using three different functional dependences of a_{if} on the total kinetic energy above the threshold: linear T^*, quadratic T^{*2} and $\sqrt{T^*}$, Figure 4.27. The statistical and systematic uncertainties in total cross sections as well as in the incident beam energies were taken into account in an iterative least squares procedure by replacing the standard deviation σ_i of each data point by [Lyb-84] [Ore-82]

$$\sigma_i \rightarrow \sigma_{\sigma_t}^2 + \left(\frac{da(T^*)}{dT^*}\right)^2 \sigma_{T^*}, \tag{4.32}$$

where σ_{σ_t} is the rms error in the total cross section and σ_{T^*} is the standard deviation of the CM total kinetic energy.

Table 4.12 The $\pi^+p \to \pi^+\pi^0p$ extrapolation of reduced amplitudes to threshold. The two values of xi follow from sign ambiguity in the amplitude.

Fit Type	$\lvert a(\pi^+\pi^0p)\rvert\ (T^*)$	χ^2/N	ξ
Linear	$\lvert 0.58 \pm 0.18\rvert + (9.95 \pm 2.84) \cdot 10^{-3}T^*$	1.36	$-5.30 \pm 0.87 \Leftrightarrow 0.25 \pm 0.87$
Square Root	$\lvert 0.15 \pm 0.34\rvert + (0.134 \pm 0.044) \cdot \sqrt{T^*}$	1.52	$-3.25 \pm 1.62 \Leftrightarrow -1.80 \pm 1.62$
Quadratic	$\lvert 0.85 \pm 0.11\rvert + (8.46 \pm 1.31) \cdot 10^{-5}T^{*2}$	0.82	$-6.54 \pm 0.50 \Leftrightarrow 1.50 \pm 0.50$

Results of the fits are only loosely constraining as evidenced by the coefficients of the different extrapolation procedures and error bars on the chiral symmetry breaking parameter ξ, Table 4.12.

All published measurements of the total cross sections for the five charge states of $\pi N \to \pi\pi N$ reaction have been used to calculate the reduced amplitudes by numerical integration of relativistic phase space from equation (4.20). Reduced χ^2 for the global fit is shown as a function of the chiral-symmetry-breaking parameter in Figure 4.27 for a full set of 109 data points as well as for a data set excluding the apparently incompatible [Ker-89] data.

The complete experimental data set extrapolated linearly to the threshold has $\chi^2/N = 1.19$ for $\xi = -0.15 \pm 0.10$. Using different extrapolation functions for each channel improves the goodness of fit by a mere 4%, with ξ remaining essentially stable. The threshold amplitudes $a_0(\pi\pi N)$, all determined by only two isospin threshold amplitudes a_{10} and a_{32}, are related by:

$$a_0(\pi^+\pi^+n) = -2\sqrt{2}a_0(\pi^-\pi^0p) = 2[a_0(\pi^-\pi^+n) + a_0(\pi^0\pi^0n)]. \tag{4.33}$$

Using these relations as a guide and visually inspecting reduced amplitude plots as a function of CM kinetic energy, the data set summarized in Tables A1-A10 can be restricted to 99 measured cross sections, 57 of which were obtained in the last five years. After removing the data of [Ker-89] from the analysis the global fit has a minimum χ^2/N=1.04 at $\xi = -0.24 \pm 0.10$. The s-wave $\pi\pi$ scattering lengths α_l^I then follow from relations (4.30-31):

$$\alpha_0^0 = 0.176 \pm 0.006, \quad \alpha_0^2 = -0.041 \pm 0.003. \tag{4.34}$$

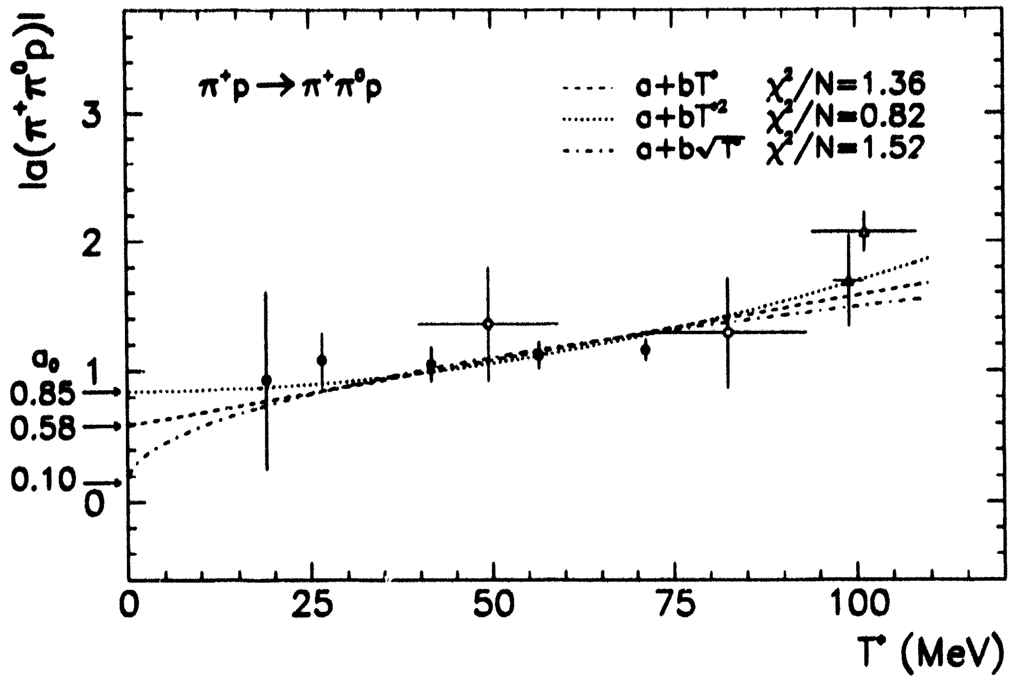

Figure 4.27 Absolute value of the $\pi^+\pi^0 p$ matrix element obtained from the total cross sections measured in this work (•), and by Batusov *et al.* (o [Bat75]) and Sober *et al.* (△ [Sob75]), as a function of the total kinetic energy in the barycentric frame. Linear, quadratic and square root fits and extrapolation to $T^* = 0$ are shown.

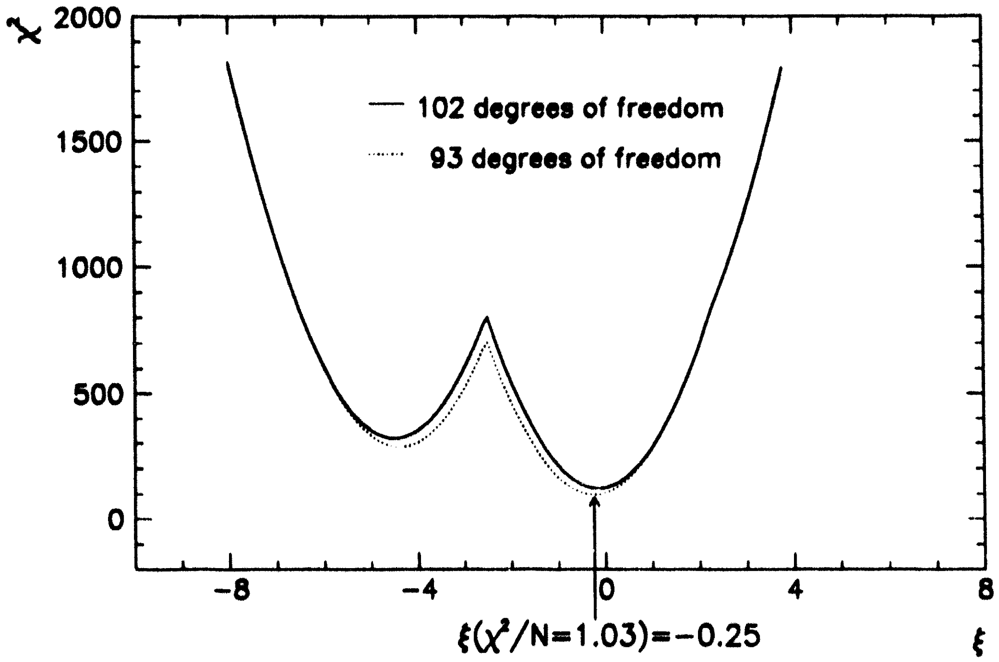

Figure 4.28 Global linear fit to all the available data below 160 MeV in the barycentric system, including E1179 cross sections, in the chiral-symmetry-breaking model of Olsson and Turner as a function of the parameter ξ. The "unpruned" data set gives $\xi = -0.15$ in a fit with $\chi^2_{\min} = 121$ for 102 degrees of freedom. The "pruned" database without cross sections from reference [Ker-89] has $\xi = -0.24 \pm 0.10$ with $\chi^2/N = 1.04$.

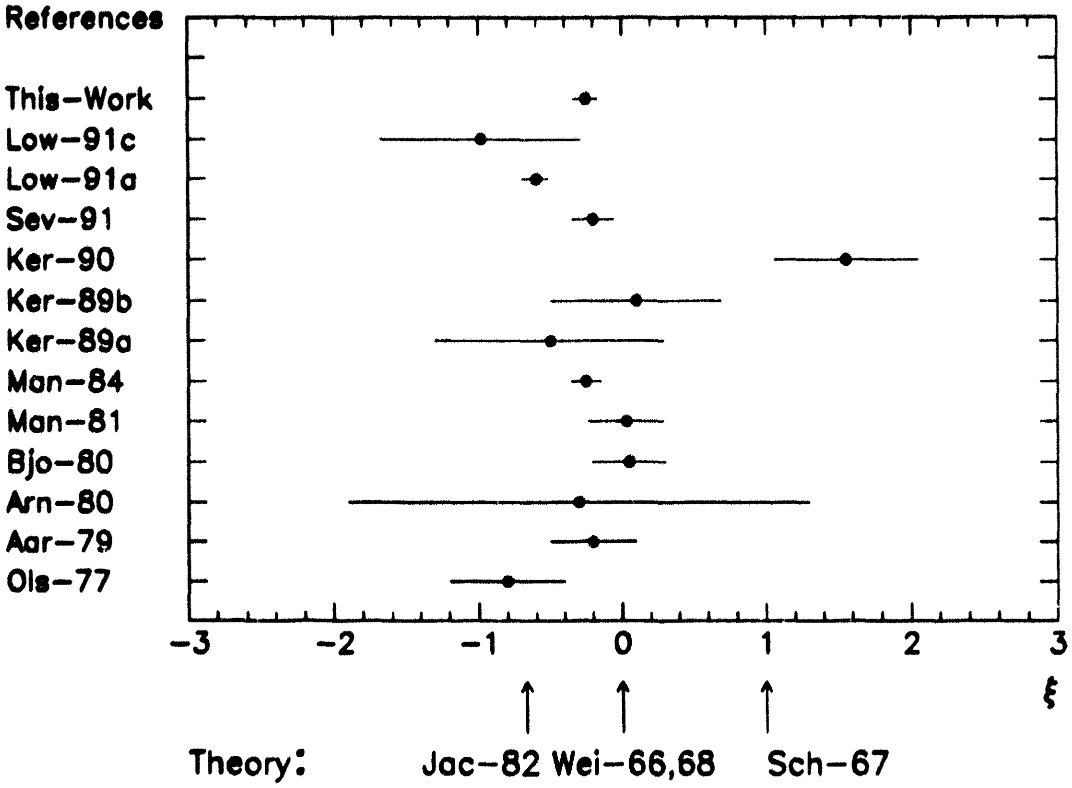

Figure 4.29 Published values of ξ, the chiral symmetry breaking parameter. All plotted values are extracted from published total cross sections using the procedure of Olsson and Turner. Three theoretical calculations are also indicated.

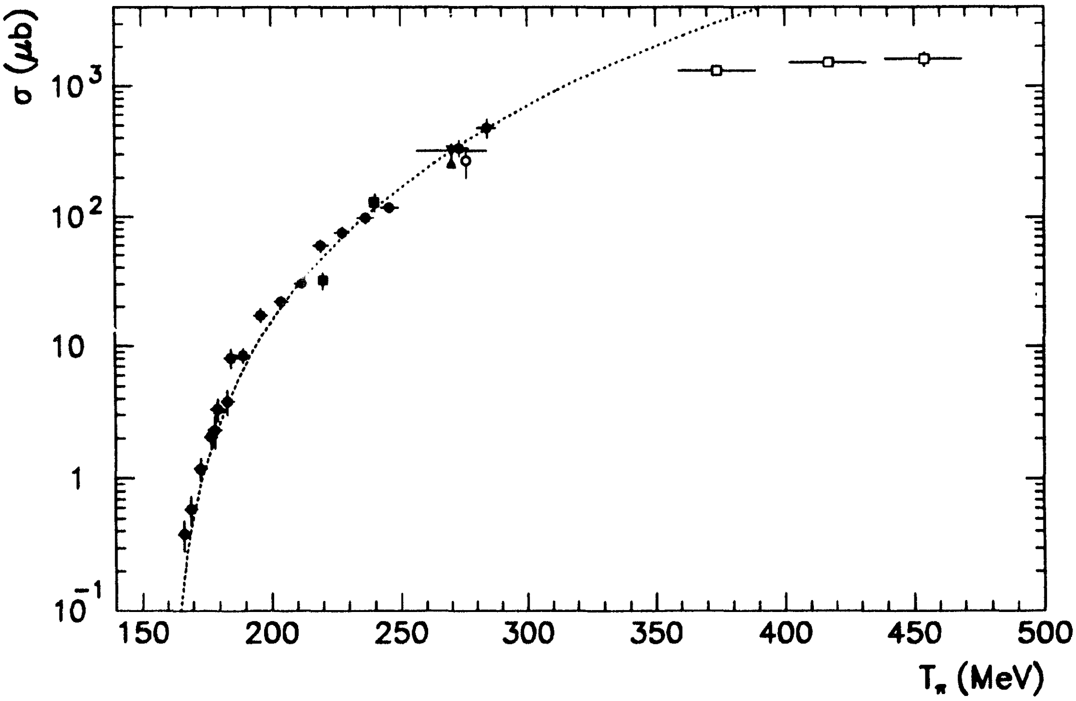

Figure 4.30 $\pi^- p \to \pi^0\pi^0 n$ total cross sections near threshold. The references are [Low-91c] (•), [Bel-80] (▪), [Bel-78] (▴), [Bun-77] (▾), [Kra-74] (○), and [Bar-64] (□). The dotted curve is a result of $\pi\pi N$ global fit.

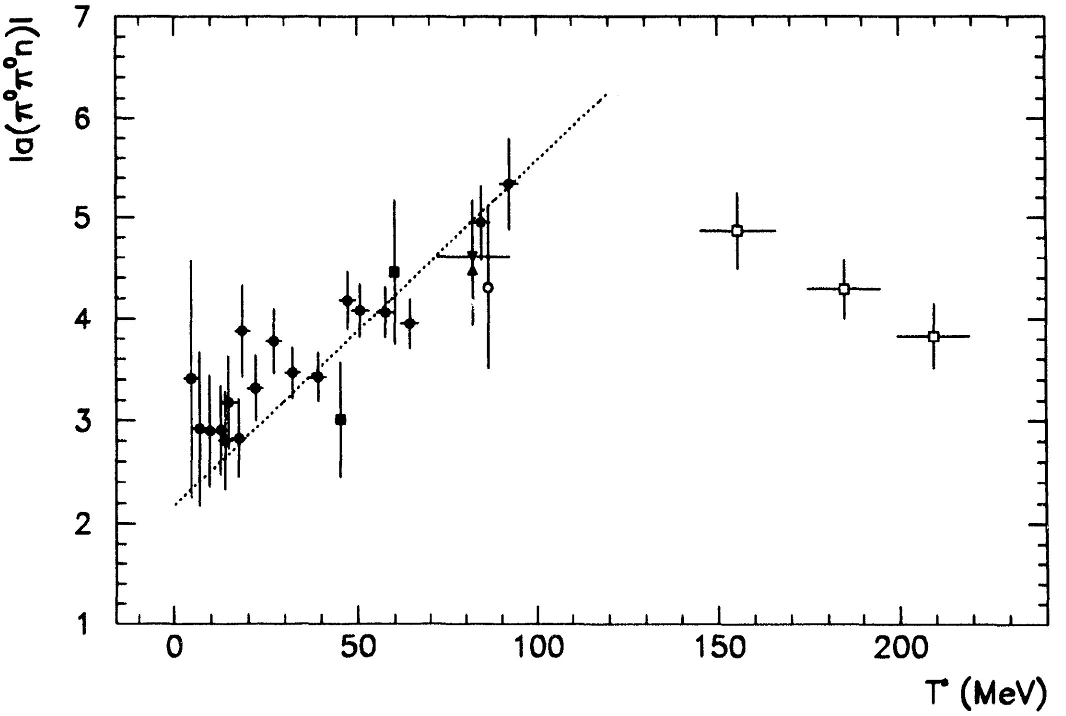

Figure 4.31 $\pi^- p \to \pi^0\pi^0 n$ reduced amplitudes near threshold. The references are [Low-91c] (•), [Bel-80] (▪), [Bel-78] (▴), [Bun-77] (▾), [Kra-74] (○), and [Bar-64] (□). The dotted line corresponds to $\pi\pi N$ global fit.

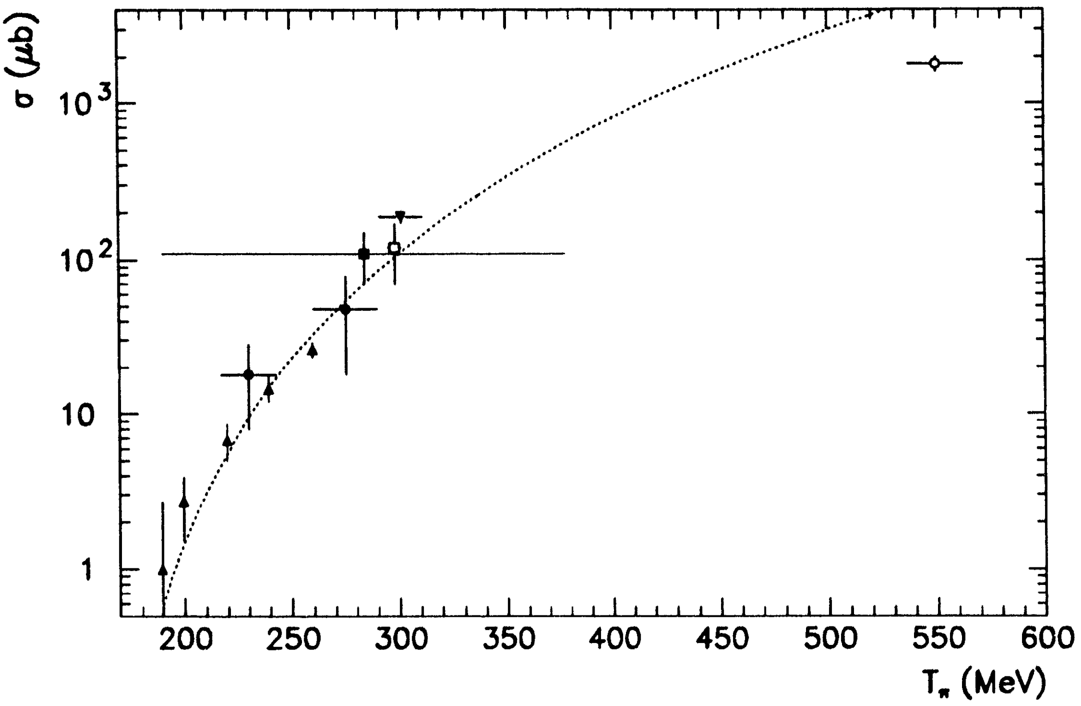

Figure 4.32 $\pi^+p \rightarrow \pi^+\pi^0p$ total cross sections near threshold. Besides this work (▲), the references are [Bat-75] (●), [Bar-63] (■), [Sob-75] (▼), [Ker-91b] (□), and [Deb-64] (○).

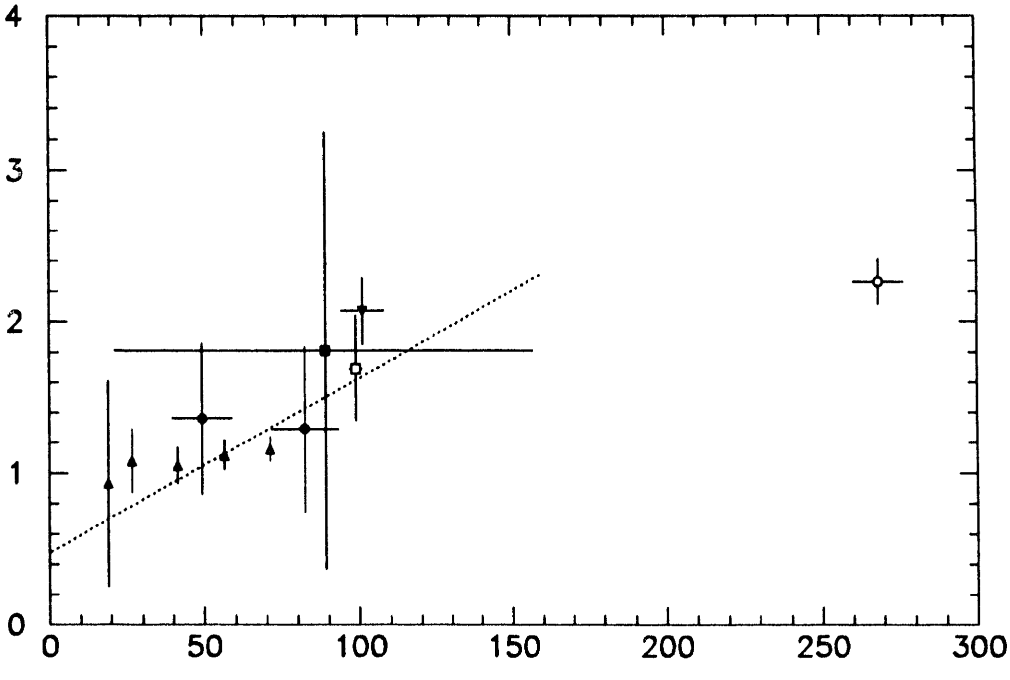

Figure 4.33 $\pi^+p \rightarrow \pi^+\pi^0p$ reduced amplitudes near threshold. Besides this work (▲), the references are [Bat-75] (●), [Bar-63] (■), [Sob-75] (▼), [Ker-91b] (□), and [Deb-64] (○).

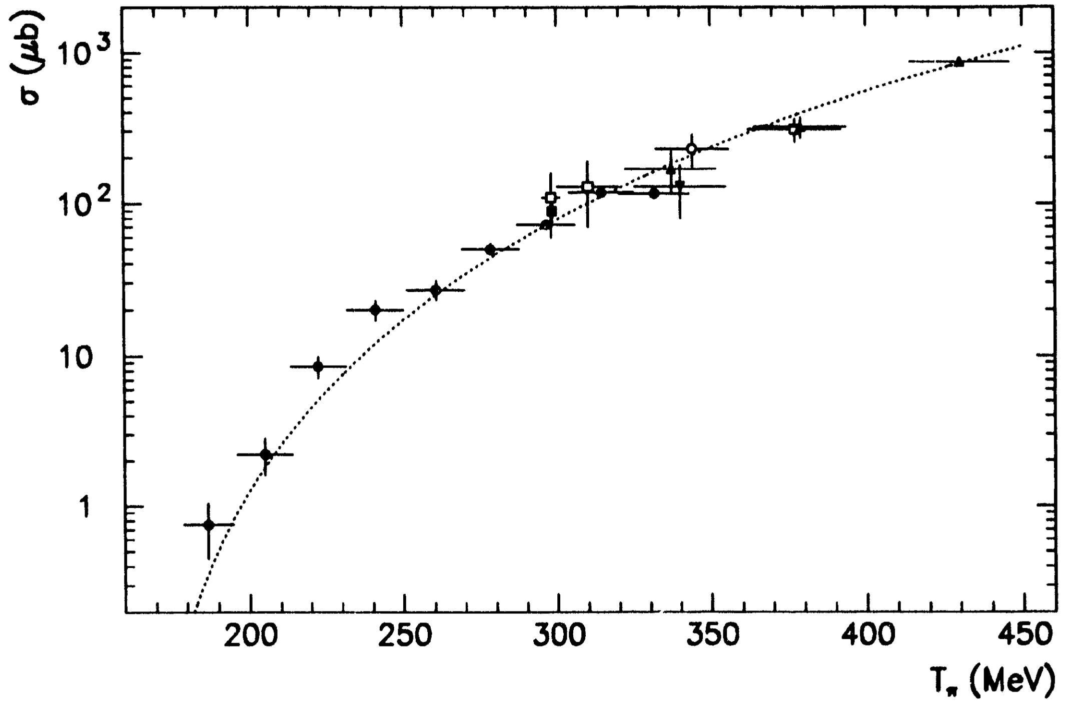

Figure 4.34 $\pi^- p \rightarrow \pi^-\pi^0 n$ total cross sections near threshold. The references are [Ker-89b] (●), [Sob-75] (■), [Jon-74] (▲), [Bar-64] (▼), [Sax-70] (○), [Blo-63] (□), and [Blo-65] (△).

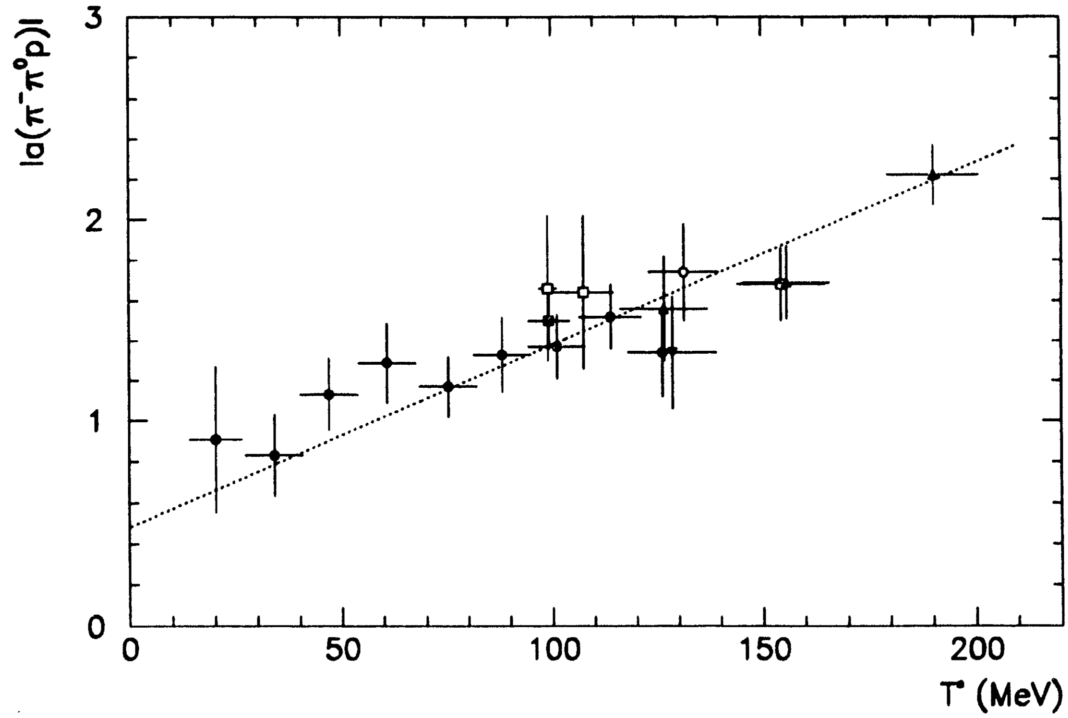

Figure 4.35 $\pi^- p \rightarrow \pi^-\pi^0 p$ reduced amplitudes near threshold. The references are [Ker-89b] (●), [Sob-75] (■), [Jon-74] (▲), [Bar-64] (▼), [Sax-70] (○), [Blo-63] (□), and [Blo-65] (△).

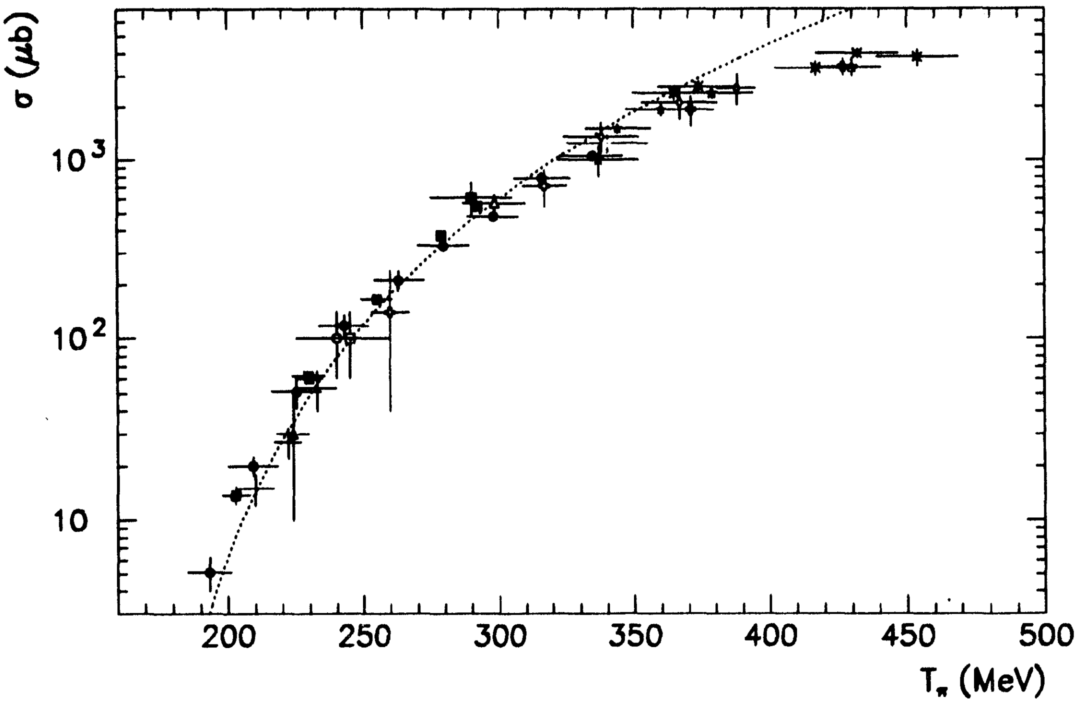

Figure 4.36 $\pi^-p \to \pi^-\pi^+n$ total cross sections near threshold. The references are [Ker-89a] (•), [Bjo-80] (■), [Bat-64] (▲), [Dea-61] (▼), [Aar-79] (○), [Bat-63] (□), [Bla-70] (△), [Per-60] (◇), [Blo-65] ( ), [Jon-74] (★), [Sax-70] ( ), [Arn-79] (∗), [Blo-63] (†), and [Bar-64] (†).

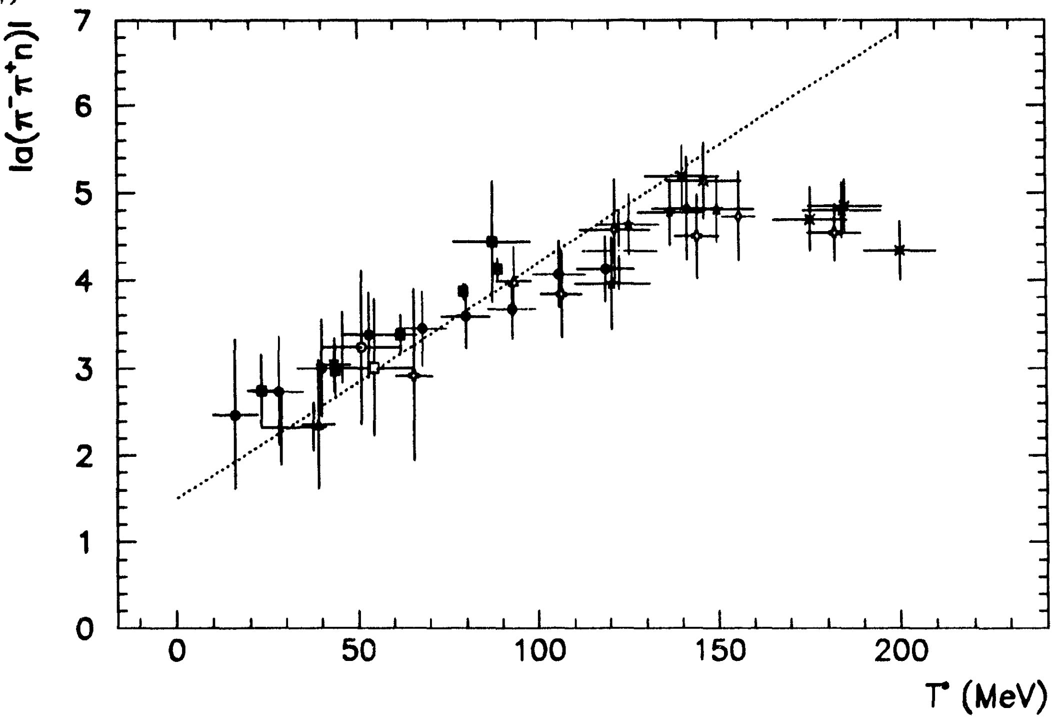

Figure 4.37 $\pi^-p \to \pi^-\pi^+n$ reduced amplitudes near threshold. The references are [Ker-89a] (•), [Bjo-80] (■), [Bat-64] (▲), [Dea-61] (▼), [Aar-79] (○), [Bat-63] (□), [Bla-70] (△), [Per-60] (◇), [Blo-65] ( ), [Jon-74] (★), [Sax-70] ( ), [Arn-79] (∗), [Blo-63] (†), and [Bar-64] (†).

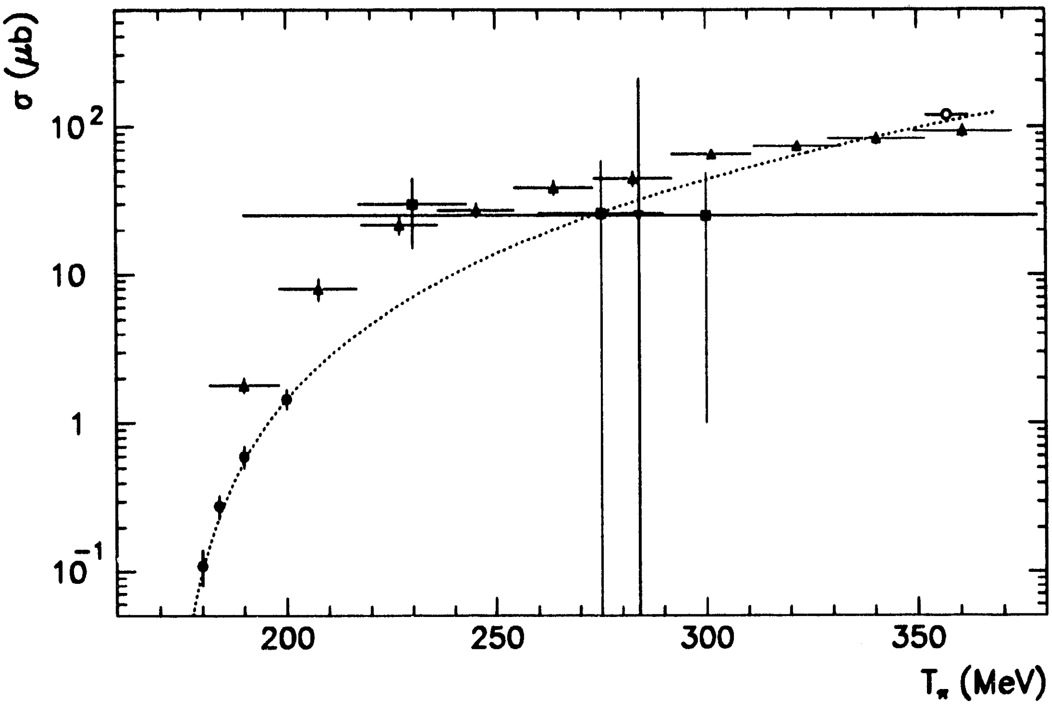

Figure 4.38 $\pi^+p \to \pi^+\pi^+n$ total cross sections near threshold. The references are [Sev-91] (•), [Ker-90] (▴), [Bat-75] (▪), [Bar-63] (▾), [Kir-62] (○), and [Deb-64] (□).

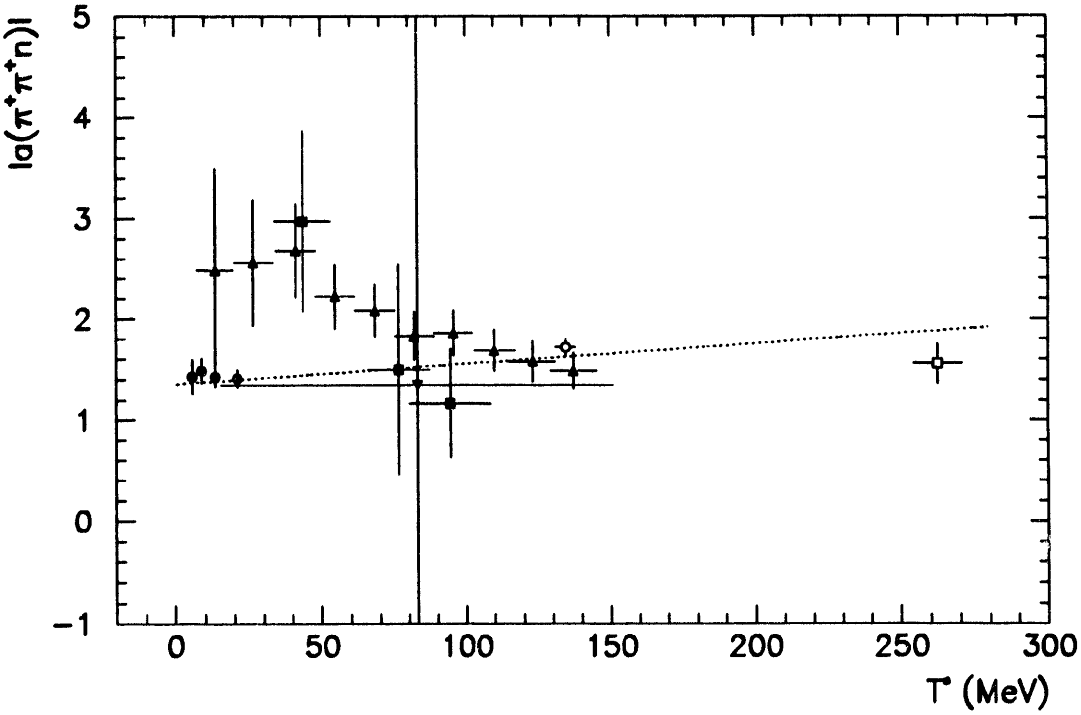

Figure 4.39 $\pi^+p \to \pi^+\pi^+n$ reduced amplitudes near threshold. The references are [Sev-91] (•), [Ker-90] (▴), [Bat-75] (▪), [Bar-63] (▾), [Kir-62] (○), and [Deb-64] (□).

Chapter V: Conclusions

Detailed analysis of data presented in Chapter IV can be summarized as follows. Total cross sections for $\pi^+p \rightarrow \pi^+\pi^0p$ reaction at 260 and 240 MeV were measured with 10% and 17% statistical and 9% systematic uncertainty, as originaly proposed. At the energies 220, 200, and 190 MeV, closer to the threshold, the available beam time limited the collected data sample and the increasing backgrounds influenced target-empty and out-of-time events subtraction resulting in larger statistical uncertainties in total cross sections.

Post-experiment review of the charged particle arm and replay data analysis assured us that the experimental method was a sound one leaving little room for improvements. In the π^0 spectrometer arm there is a possibility that the more detailed understanding of TRACER software cuts could justify wider window and slope gate limits increasing the statistics by ~20%; that would, however, decrease the energy and angular resolution of the π^0 data. The use of newly commissioned the LAMPF Neutral Meson Spectrometer was also studied in the Monte Carlo simulations. The effect would be an improvement in solid angle coverage (factor ~3) while over-all resolution of the $\pi^+\pi^0p$ final states would be dominated by the charged particle energy and direction resolutions and the target thickness.

The charged particle detectors designed and built for this experiment performed beautifully; charged particle detection efficiency was limited to ~80% because of difficulties associated with high backgrounds. The only reasonable option for reducing the elastically scattered π^+ background rate would be a redesign of the charged particle detectors. The total absorption counters could be doubled in length to ~50 cm to facilitate a clear separation of MI triggers. That design modification would considerably increase the cost of the CP arm for the same solid angle coverage and likely worsen the energy resolution.

Table 5.1 Threshold extrapolation of reduced amplitudes. The number of fitted data points for each channel is labeled by N. Second row gives dimensionless reduced matrix elements in linear fits to the individual channel data. Third row shows results of a global fit to all five channels for 93 degrees of freedom. The deduced parameter of chiral symmetry breaking ξ is -0.25 ± 0.10.

Fit Type	$a_0(\pi^0\pi^0n)$	$a_0(\pi^+\pi^0p)$	$a_0(\pi^-\pi^0p)$	$a_0(\pi^-\pi^+n)$	$a_0(\pi^+\pi^+n)$
N, $\Sigma = 99$	23	10	18	38	10
Channel	2.81 ± 0.18	-0.54 ± 0.18	-0.73 ± 0.12	-2.04 ± 0.16	1.44 ± 0.06
Global	2.18 ± 0.03	-0.48 ± 0.02	-0.48 ± 0.02	-1.50 ± 0.06	1.36 ± 0.06

The E1179 total cross sections are close to those of the charge conjugate channel $\pi^-\pi^0p$ [Ker-89b], which is to be expected from isospin symmetry.

Table 5.2 s-wave $\pi\pi$ scattering lengths a_l^I from a global fit to a $\pi N \to \pi\pi N$ reduced amplitudes and theoretical models. Pion decay constant f_π = 90.1 MeV equal to the experimental value extrapolated to chiral limit is used.

Source	a_0^0 (m_π^{-1})	a_0^2 (m_π^{-1})	χ^2/N
This work	0.176 ± 0.006	-0.041 ± 0.003	1.04
[Wei-66,68]	0.156	−0.045	...
[Jac-82]	0.201	−0.028	...
[Bur-91]	0.197 ± 0.010	-0.032 ± 0.004	0.97
[Ros-77]	0.26 ± 0.05	...	...
[Gas-81,84]	0.20	−0.042	...

The reaction matrix elements moduli were extracted using exact relativistic phase space factors with parameters m_π = 137.5 MeV, f_π = 90.1 MeV , and g_A/g_V = 1.29 [Coo-90]. On the physical grounds there is no reason to expect the approach to threshold to be linear. The various extrapolation functions were considered in previous sections, but on the basis of χ^2 tests, no need was found to introduce the terms higher than linear in the CM kinetic energy dependence.

Supplementing the previously existing experimental data with the E1179 total cross sections, the global analysis in the framework of the chiral symmetry breaking model of Olsson and Turner gives linear fits with χ^2 as good as 96 for the 99 data points. The resulting chiral-symmetry-breaking parameter ξ is then -0.25 ± 0.10, value between original Weinberg result and one corrected by Jacob and Scadron [Jac-82] for the contribution of $f_0(975)$ scalar meson.

The E1179 extracted total cross sections taken separately in linear extrapolation to threshold yield a value of the dimensionless reduced matrix element $|a_0(\pi^\pm\pi^0p)|$ that is consistent with the global fit.

The work has started on decomposing the E1179 kinematically complete data set for analysis in a model-independent way. The data will be supplemented by the 10^4 $\pi^0\pi^0n$ coincident events collected in the Brookhaven experiment E857 at 16 incident π^- kinetic energies between 166.6 and 284.0 MeV. Relying on the requirements of isospin and discrete CPT symmetries, Poincaré invariance, cross symmetry and Bose statistics for pions the $\pi\pi$ scattering amplitude from $\pi N \to \pi\pi N$ reaction can be expressed as a sum of a "basic" one-pion exchange graph and the background contribution. In the linear approximation for the background contribution [Bol-92] the amplitude has 15 free parameters, four of which describe the OPE mechanism and contain the complete description of $\pi\pi$ scattering up to D-waves. The phase space coverage of the E1179 and E857 data sets in terms of the BVS invariant variables is summarized in Table 5.3.

The theoretical cross section will be calculated analytically using the **REDUCE** symbolical computational tools from

$$\sigma_{\{i\}} = \frac{f_{\{i\}}}{2\pi^4\sqrt{3}J^2} \int_{\tau_1(0)}^{\tau_2(0)} d\tau \int_0^{\omega_\tau} d\omega \int_{\theta_I^-}^{\theta_I^+} d\theta_I \int_{\nu_I^-}^{\nu_I^+} d\nu_I \frac{\Sigma_{\{i\}}}{\sqrt{-\Delta_4}}, \tag{4.34}$$

where $J = \sqrt{(k_1 \cdot p) - m^2 m_\pi^2}$, $f_{\{i\}}$ is the statistical factor and the squared matrix element summed over polarizations $\Sigma_{\{i\}}$ contains the 15 adjustable parameters to be fitted to the data.

Table 5.3 E1179 and E857 phase space coverage in terms of invariant variables τ_I, θ_I, ω_τ, and τ defined in the Appendix C.

EXP	Energy (MeV)	$\Delta\tau_I$ (%)	$\Delta\theta_I$ (%)	$\Delta\omega_\tau$ (%)	$\Delta\tau$ (%)	$\Delta\tau_I\Delta\theta_I\Delta\omega_\tau\Delta\tau$. (%)
E1179	260.0	74.4	98.3	72.7	89.4	47.5
E857	247.0	91.4	97.5	88.3	84.9	66.7

Appendix A

1. Published $\pi N \rightarrow \pi\pi N$ Near-Threshold Measurements

An exhaustive survey of physics literature was conducted with the goal of compiling database of all published total cross sections for reactions $\pi N \rightarrow \pi\pi N$ near threshold ($T_\pi \leq 500$ MeV). Tables A1-5. give the central kinetic energy and momentum with the corresponding momentum spread, the number of collected coincident events (when available), the total cross section with the statistical (and systematic, when reported) uncertainty and the reference paper. The threshold momentum p_0 and incident beam energy T_0 for each channel are included in the caption lines. Tables A1-5 list results published before May 1993.

Table A1. $\pi^- p \rightarrow \pi^0 \pi^0 n$ total cross sections, (p_0 =265.6 MeV, T_0 =160.5 MeV).

Beam Momentum (MeV)	Beam Energy (MeV)	Number of Events	Total Cross Section (μb)	Reference
272.5 ± 2.7	166.6 ± 2.4	28	0.382 ± 0.096 ± 0.023	[Low-91c]
275.5 ± 2.8	169.3 ± 2.5	34	0.59 ± 0.14 ± 0.04	[Low-91c]
279.7 ± 2.8	173.0 ± 2.5	43	1.18 ± 0.22 ± 0.07	[Low-91c]
283.9 ± 2.8	176.8 ± 2.5	65	2.05 ± 0.35 ± 0.12	[Low-91c]
285.7 ± 2.9	178.4 ± 2.6	36	2.31 ± 0.65 ± 0.14	[Low-91c]
286.9 ± 2.9	179.5 ± 2.6	25	3.33 ± 0.64 ± 0.20	[Low-91c]
291.0 ± 2.9	183.2 ± 2.6	69	3.81 ± 0.81 ± 0.23	[Low-91c]
292.6 ± 2.9	184.6 ± 2.6	77	8.1 ± 1.3 ± 0.5	[Low-91c]
297.7 ± 3.0	189.2 ± 2.7	192	8.5 ± 1.0 ± 0.5	[Low-91c]
304.7 ± 3.0	196.0 ± 2.7	94	17.1 ± 1.9 ± 1.0	[Low-91c]
313.8 ± 3.1	203.9 ± 2.8	555	21.9 ± 2.0 ± 1.3	[Low-91c]
322.5 ± 3.2	211.8 ± 2.9	517	30.3 ± 3.0 ± 1.8	[Low-91c]
330.5 ± 3.3	219.2 ± 3.0	406	59.8 ± 6.4 ± 3.6	[Low-91c]
331.4 ± 14	220.0 ± 12.0	1170	32 ± 5	[Bel-80]
339.4 ± 3.4	227.4 ± 3.1	806	75.2 ± 7.3 ± 4.5	[Low-91c]
349.4 ± 3.5	236.7 ± 3.3	979	98.1 ± 9.3 ± 5.9	[Low-91c]
353.0 ± 14.0	240.0 ± 13.0	3964	130 ± 20	[Bel-80]
359.1 ± 3.6	245.7 ± 3.4	1147	118 ± 11 ± 7	[Low-91c]
385.1 ± 14.9	270.0 ± 14.0	3146	260 ± 20	[Bel-78]
385.1 ± 14.9	270.0 ± 14		320 ± 40	[Bun-77]
389.6 ± 3.9	273.3 ± 3.7	1195	338 ± 46 ± 20	[Low-91c]
391.4 ± 19.1	276.0 ± 18.0	2249	270 ± 70	[Kra-74]
399.9 ± 4.0	284.0 ± 3.8	3517	479 ± 79 ± 29	[Low-91c]
494 ± 16	374 ± 15		1300 ± 100	[Bar-64]
539 ± 16	417 ± 15		1500 ± 100	[Bar-64]
577 ± 15	454 ± 15		1600 ± 200	[Bar-64]

Table A2. $\pi^+ p \to \pi^+\pi^0 p$ total cross sections, (p_0 =270.4 MeV, T_0 =164.8 MeV).

Beam Momentum (MeV)	Beam Energy (MeV)	Number of Events	Total Cross Section (μb)	Reference
298.0 ± 0.6	189.5 ± 0.5	3	1.0 ± 1.7	[Poč-92]
309.0 ± 0.6	199.5 ± 0.6	13	2.7 ± 1.2	[Poč-92]
330.8 ± 0.7	219.5 ± 0.6	56	6.8 ± 1.8	[Poč-92]
342.2 ± 14.0	230 ± 13	5	18^{+12}_{-9}	[Bat-75]
352.4 ± 0.7	239.5 ± 0.7	145	14.6 ± 2.6	[Poč-92]
373.8 ± 0.7	259.5 ± 0.7	120	27 ± 5	[Poč-91]
373.8 ± 0.8	259.5 ± 0.7	692	26.0 ± 2.7	[Poč-92]
390.4 ± 15.9	275 ± 15	4	48^{+34}_{-25}	[Bat-75]
400 ± 100	284 ± 94	9	110 ± 40	[Bar-63]
414 ± 3	298 ± 3	430	120 ± 50	[Sob-75]
418 ± 10	301 ± 10		189 ± 8 ± 28	[Ker-91b]
675 ± 14	550 ± 13	159	1800 ± 200	[Deb-64]

Table A3. $\pi^- p \to \pi^-\pi^0 p$ total cross sections, (p_0 =270.4 MeV, T_0 =164.8 MeV).

Beam Momentum (MeV)	Beam Energy (MeV)	Number of Events	Total Cross Section (μb)	Reference
295 ± 9	186.8 ± 8.1	6	0.75 ± 0.3 ± 0.3	[Ker-89b]
315 ± 10	205.0 ± 9.1		2.2 ± 0.6 ± 0.4	[Ker-89b]
334 ± 10	222.4 ± 9.2		8.5 ± 1.4 ± 0.8	[Ker-89b]
354 ± 10	241.0 ± 9.3		20 ± 3 ± 4	[Ker-89b]
375 ± 10	260.6 ± 9.4		27 ± 4 ± 4	[Ker-89b]
394 ± 10	278.4 ± 9.4		50 ± 4 ± 12	[Ker-89b]
413 ± 10	296.4 ± 9.5		73 ± 4 ± 14	[Ker-89b]
414 ± 3	298 ± 3		110 ± 50	[Sob-75]
415 ± 12.1	298.3 ± 11.5	140	90 ± 10	[Jon-74]
427 ± 11	310 ± 10		130 ± 60	[Bar-64]
432 ± 11	314.4 ± 10.5		119 ± 8 ± 18	[Ker-89b]
450 ± 12	331.6 ± 11.5	430	117 ± 9 ± 36	[Ker-89b]
456 ± 16	337 ± 15		170 ± 50	[Sax-70]
459 ± 16	340 ± 15	11	130^{+60}_{-40}	[Blo-63]
463 ± 13	344 ± 12	51	230^{+40}_{-70}	[Blo-65]
497 ± 16	377 ± 15		310^{+70}_{-40}	[Bar-64]
499 ± 16	379 ± 15	47	320 ± 50	[Sax-70]
552 ± 16	430 ± 16	528	870 ± 50	[Sax-70]

Table A4. $\pi^- p \rightarrow \pi^-\pi^+ n$ total cross sections, (p_0 =279.0 MeV, T_0 =172.4 MeV).

Beam Momentum (MeV)	Beam Energy (MeV)	Number of Events	Total Cross Section (μb)	Reference
295 ± 9	186.8 ± 8.1		5.1 ± 1.1 ± 0.5	[Ker-89a]
312.9 ± 5.5	203 ± 5		13.8 ± 1.5	[Bjo-80]
315 ± 10	205.0 ± 9.1		20 ± 2.4 ± 1.8	[Ker-89a]
321 ± 8	210 ± 7		15 ± 3	[Bat-64]
334 ± 5	222 ± 5		27 ± 5	[Bat-64]
334 ± 10	222.4 ± 9.2		51 ± 10 ± 6	[Ker-89a]
336 ± 7	224 ± 6	3	30 ± 20	[Dea-61]
341.8 ± 6.8	229.6 ± 6.0		62 ± 4	[Aar-79]
342.0 ± 6.5	230 ± 6		60.3 ± 3.2	[Bjo-80]
345 ± 8	233 ± 7		53 ± 13	[Bat-64]
353.0 ± 16.1	240 ± 15		100 ± 40	[Bat-63]
354 ± 10	241.0 ± 9.3		118 ± 15 ± 13	[Ker-89a]
358.4 ± 16.1	245 ± 15	38	100 ± 40	[Bat-60]
360.5 ± 4.3	247 ± 4	357	60 ± 15	[Bla-70]
369.1 ± 6.3	255 ± 6		166 ± 6	[Bjo-80]
374 ± 7	260 ± 7		140 ± 100	[Per-60]
375 ± 10	260.6 ± 9.4		211 ± 27 ± 24	[Ker-89a]
394 ± 10	278.4 ± 9.4		327 ± 18 ± 37	[Ker-89a]
394.6 ± 1.7	279.0 ± 1.6		374 ± 15	[Bjo-80]
406 ± 16	290 ± 15	100	610 ± 130	[Bat-60]
406 ± 11	290 ± 10	300	610 ± 130	[Blo-65]
408.4 ± 1.8	292.0 ± 1.7		546 ± 31	[Bjo-80]
413 ± 10	296.4 ± 9.5		477 ± 17 ± 53	[Ker-89a]
415 ± 12.1	298.3 ± 11.5	881	570 ± 60	[Jon-74]
432 ± 11	314.4 ± 10.5		785 ± 55 ± 88	[Ker-89a]
435 ± 8	317 ± 8		710 ± 170	[Per-60]
450 ± 12	331.6 ± 11.5		1052 ± 42 ± 118	[Ker-89a]
456 ± 16	337 ± 15	2591	1000 ± 200	[Sax-70]
457 ± 15	338 ± 14	1227	1350 ± 270	[Arn-79]
459 ± 15	340 ± 15	108	1240 ± 140	[Blo-63]
463 ± 13	344 ± 12	324	1500 ± 100	[Blo-65]
480 ± 14	360 ± 13	573	1930 ± 160	[Blo-65]
485 ± 16	365 ± 15		2400 ± 200	[Bar-64]
487 ± 15	367 ± 14	1481	2120 ± 424	[Arn-79]
491 ± 10	371 ± 9		1930 ± 370	[Per-60]
494 ± 16	374 ± 15		2600 ± 200	[Bar-64]
499 ± 16	379 ± 15	298	2400 ± 160	[Sax-70]
509 ± 7	388 ± 7	1375	2550 ± 510	[Arn-79]
539 ± 16	417 ± 15		3300 ± 300	[Bar-64]
549 ± 11	427 ± 11		3360 ± 370	[Per-60]
552 ± 16	430 ± 16	2241	3840 ± 160	[Sax-70]
554 ± 15	432 ± 15		4000 ± 200	[Bar-64]
577 ± 15	454 ± 15		3800 ± 400	[Bar-64]

Table A5. $\pi^+ p \to \pi^+\pi^+ n$ total cross sections, (p_0 =279.0 MeV, T_0 =172.4 MeV).

Beam Momentum (MeV)	Beam Energy (MeV)	Number of Events	Total Cross Section (μb)	Reference
287.5 ± 0.3	180.0 ± 0.3	8	0.11 ± 0.03	[Sev-91]
291.9 ± 0.3	184.0 ± 0.3	65	0.28 ± 0.05	[Sev-91]
297 ± 9	188.6 ± 8.2		1.8 ± 0.2 ± 0.3	[Ker-90]
298.6 ± 0.3	190.0 ± 0.3	74	0.60 ± 0.10	[Sev-91]
309.6 ± 0.3	200.0 ± 0.3	124	1.46 ± 0.22	[Sev-91]
317 ± 10	206.8 ± 9.2	47	8.0 ± 1.3 ± 1.2	[Ker-90]
338 ± 10	226.1 ± 9.2		21.7 ± 3.0 ± 3.3	[Ker-90]
342.2 ± 14.0	230 ± 13	6	30^{+18}_{-12}	[Bat-75]
358 ± 10	244.7 ± 9.3		27.4 ± 3.2 ± 4.1	[Ker-90]
378 ± 10	263.4 ± 9.4		39.0 ± 4.4 ± 5.5	[Ker-90]
390.4 ± 15.9	275 ± 15	1	26^{+55}_{-20}	[Bat-75]
398 ± 10	282.2 ± 9.4		45.1 ± 5.2 ± 8.9	[Ker-90]
400 ± 100	284 ± 94	2	25 ± 184	[Bar-63]
416.8 ± 21.1	300 ± 20		25^{+31}_{-16}	[Bat-75]
418 ± 10	301.1 ± 9.5		65.0 ± 4.7 ± 12.7	[Ker-90]
439 ± 11	321.1 ± 10.5		74.0 ± 5.3 ± 14.4	[Ker-90]
459 ± 12	340.2 ± 11.5		83.0 ± 7.3 ± 16.2	[Ker-90]
477 ± 5	357 ± 5	213	120 ± 10	[Kir-62]
480 ± 12	360.3 ± 11.5		94.0 ± 8.0 ± 18.4	[Ker-90]
675 ± 13	550 ± 13	39	460 ± 100	[Deb-64]

The set of Tables A6-10. listing the reduced amplitudes $|a_0(\pi\pi N)|$ as a function of barycentric momentum, total energy and kinetic energy above the reaction threshold is derived from the total cross sections by numerical phase space integration. Values of physical constants used in this work are the chiral limits recommended by Coon and Scadron [Coo-90].

Table A6. $\pi^- p \rightarrow \pi^0\pi^0 n$ reduced amplitudes, (p_0 =265.6 MeV, T_0 =160.5 MeV).

CMS Momentum (MeV)	CMS Energy (MeV)	CMS Kinetic Energy (MeV)	$\lvert a(\pi^0\pi^0 p)\rvert$	Referent Cross Section
210.6 ± 2.1	1214.2 ± 1.9	4.7 ± 1.9	3.41 ± 1.16	[Low-91c]
212.5 ± 2.2	1216.3 ± 1.9	6.9 ± 1.9	2.92 ± 0.75	[Low-91c]
215.2 ± 2.2	1219.2 ± 1.9	9.7 ± 1.9	2.90 ± 0.54	[Low-91c]
218.0 ± 2.2	1222.1 ± 1.9	12.6 ± 1.9	2.91 ± 0.43	[Low-91c]
219.1 ± 2.2	1223.3 ± 2.0	13.8 ± 2.0	2.81 ± 0.48	[Low-91c]
219.9 ± 2.2	1224.2 ± 2.0	14.7 ± 2.0	3.18 ± 0.45	[Low-91c]
222.5 ± 2.2	1227.0 ± 2.0	17.5 ± 2.0	2.83 ± 0.38	[Low-91c]
223.5 ± 2.2	1228.1 ± 2.0	18.6 ± 2.0	3.88 ± 0.45	[Low-91c]
226.8 ± 2.3	1231.6 ± 2.1	22.1 ± 2.1	3.32 ± 0.32	[Low-91c]
231.5 ± 2.3	1236.7 ± 2.1	27.2 ± 2.1	3.78 ± 0.32	[Low-91c]
236.9 ± 2.3	1242.7 ± 2.1	32.2 ± 2.1	3.47 ± 0.25	[Low-91c]
242.3 ± 2.4	1248.7 ± 2.2	39.2 ± 2.2	3.43 ± 0.24	[Low-91c]
247.2 ± 2.5	1254.2 ± 2.2	47.4 ± 2.2	4.18 ± 0.29	[Low-91c]
247.8 ± 9.9	1254.8 ± 9.0	45.3 ± 9.0	3.01 ± 0.56	[Bel-80]
252.7 ± 2.5	1260.3 ± 2.3	50.8 ± 2.4	4.08 ± 0.26	[Low-91c]
258.7 ± 2.7	1267.2 ± 2.4	57.7 ± 2.4	4.06 ± 0.25	[Low-91c]
260.8 ± 10.5	1269.7 ± 9.6	60.2 ± 9.6	4.46 ± 0.71	[Bel-80]
264.5 ± 2.7	1273.9 ± 2.5	64.4 ± 2.5	3.95 ± 0.24	[Low-91c]
279.7 ± 11.0	1291.7 ± 10.2	82.2 ± 10.2	4.48 ± 0.54	[Bel-78]
279.7 ± 11.0	1291.7 ± 10.2	82.2 ± 10.2	4.61 ± 0.56	[Bun-77]
281.7 ± 2.9	1294.1 ± 2.7	84.5 ± 2.7	4.95 ± 0.37	[Low-91c]
283.4 ± 14.1	1296.0 ± 13.0	86.5 ± 13.0	4.31 ± 0.80	[Kra-74]
288.2 ± 3.0	1301.8 ± 2.7	92.3 ± 2.7	5.34 ± 0.46	[Low-91c]
339.7 ± 11.0	1365.1 ± 10.3	155.6 ± 10.3	4.87 ± 0.38	[Bar-64]
362.5 ± 10.8	1394.4 ± 10.1	184.9 ± 10.1	4.29 ± 0.29	[Bar-64]
381.5 ± 10.5	1419.0 ± 9.9	209.5 ± 9.9	3.83 ± 0.32	[Bar-64]

Table A7. $\pi^+p \to \pi^+\pi^0p$ reduced amplitudes, (p_0 =270.4 MeV, T_0 =164.8 MeV).

CMS Momentum (MeV)	CMS Energy (MeV)	CMS Kinetic Energy (MeV)	$\lvert a(\pi^+\pi^0p)\rvert$	Referent Cross Section
227.3 ± 0.5	1232.2 ± 0.4	19.0 ± 0.4	0.93 ± 0.68	[Poč-92]
234.3 ± 0.5	1239.8 ± 0.4	26.6 ± 0.4	1.08 ± 0.21	[Poč-92]
247.8 ± 0.5	1254.8 ± 0.5	41.6 ± 0.5	1.06 ± 0.13	[Poč-92]
254.4 ± 10.6	1262.3 ± 9.7	49.5 ± 9.7	$1.44^{+0.50}_{-0.41}$	[Bat-75]
260.8 ± 0.5	1269.7 ± 0.5	56.5 ± 0.5	1.12 ± 0.10	[Poč-92]
273.5 ± 0.6	1284.4 ± 0.5	71.2 ± 0.5	1.19 ± 0.14	[Poč-91]
273.5 ± 0.6	1284.4 ± 0.5	71.2 ± 0.5	1.16 ± 0.08	[Poč-92]
282.8 ± 11.8	1295.3 ± 10.9	82.5 ± 10.9	$1.34^{+0.47}_{-0.36}$	[Bat-75]
288.2 ± 73.3	1301.8 ± 67.8	89.0 ± 67.8	1.87 ± 1.39	[Bar-63]
296.6 ± 2.3	1311.8 ± 2.1	99.0 ± 2.1	1.73 ± 0.34	[Sob-75]
298.4 ± 7.7	1314.0 ± 7.1	101.2 ± 7.1	2.12 ± 0.21	[Ker-91b]
427.8 ± 8.7	1481.2 ± 8.2	268.3 ± 8.2	2.14 ± 0.15	[Deb-64]

Table A8. $\pi^-p \to \pi^-\pi^0p$ reduced amplitudes, (p_0 =270.4 MeV, T_0 =164.8 MeV).

CMS Momentum (MeV)	CMS Energy (MeV)	CMS Kinetic Energy (MeV)	$\lvert a(\pi^-\pi^0p)\rvert$	Referent Cross Section
225.1 ± 6.9	1229.7 ± 6.2	16.9 ± 6.2	0.91 ± 0.36	[Ker-89b]
237.7 ± 7.6	1243.6 ± 6.9	30.7 ± 6.9	0.83 ± 0.20	[Ker-89b]
249.4 ± 7.6	1256.6 ± 6.9	43.8 ± 6.9	1.13 ± 0.18	[Ker-89b]
261.5 ± 7.5	1270.4 ± 6.9	57.6 ± 6.9	1.29 ± 0.20	[Ker-89b]
273.9 ± 7.5	1284.8 ± 6.9	72.0 ± 6.9	1.17 ± 0.15	[Ker-89b]
284.8 ± 7.4	1297.8 ± 6.8	84.9 ± 6.8	1.33 ± 0.19	[Ker-89b]
295.7 ± 7.3	1310.7 ± 6.8	97.9 ± 6.8	1.37 ± 0.16	[Ker-89b]
296.6 ± 2.3	1311.8 ± 2.1	99.0 ± 2.1	1.66 ± 0.36	[Sob-75]
296.8 ± 8.9	1312.1 ± 8.2	99.3 ± 8.2	1.50 ± 0.14	[Jon-74]
303.7 ± 7.7	1320.4 ± 7.1	107.6 ± 7.1	1.64 ± 0.38	[Bar-64]
306.2 ± 8.0	1323.5 ± 7.4	110.7 ± 7.4	1.52 ± 0.16	[Ker-89b]
316.1 ± 8.7	1335.7 ± 8.1	122.9 ± 8.1	1.34 ± 0.22	[Ker-89b]
319.2 ± 11.3	1339.5 ± 10.5	126.6 ± 10.5	1.56 ± 0.26	[Sax-70]
320.9 ± 11.2	1341.6 ± 10.5	128.7 ± 10.5	$1.34^{+0.32}_{-0.23}$	[Blo-63]
323.1 ± 9.0	1344.3 ± 8.4	131.5 ± 8.4	$1.74^{+0.19}_{-0.28}$	[Blo-65]
341.3 ± 11.0	1367.2 ± 10.3	154.4 ± 10.3	$1.68^{+0.22}_{-0.16}$	[Bar-64]
342.4 ± 11.0	1368.6 ± 10.3	155.7 ± 10.3	1.69 ± 0.18	[Sax-70]
369.3 ± 11.4	1403.1 ± 10.7	190.3 ± 10.7	2.12 ± 0.15	[Sax-70]

Table A9. $\pi^- p \to \pi^-\pi^+ n$ reduced amplitudes, (p_0 =279.0 MeV, T_0 =172.4 MeV).

CMS Momentum (MeV)	CMS Energy (MeV)	CMS Kinetic Energy (MeV)	$\lvert a(\pi^-\pi^+n)\rvert$	Referent Cross Section
225.1 ± 6.9	1229.7 ± 6.2	11.0 ± 6.2	2.47 ± 0.86	[Ker-89a]
236.3 ± 4.2	1242.0 ± 3.8	23.3 ± 3.8	2.75 ± 0.41	[Bjo-80]
237.7 ± 7.6	1243.6 ± 6.9	24.9 ± 6.9	2.74 ± 0.62	[Ker-89a]
241.1 ± 5.8	1247.3 ± 5.3	28.6 ± 5.3	2.32 ± 0.43	[Bat-64]
249.1 ± 4.1	1256.3 ± 3.7	37.6 ± 3.7	2.33 ± 0.28	[Bat-64]
249.4 ± 7.6	1256.6 ± 6.9	37.9 ± 6.9	3.00 ± 0.55	[Ker-89a]
250.4 ± 4.9	1257.8 ± 4.5	39.1 ± 4.5	2.36 ± 0.74	[Dea-61]
254.1 ± 5.1	1262.0 ± 4.7	43.3 ± 4.7	3.04 ± 0.30	[Aar-79]
254.4 ± 4.9	1262.3 ± 4.5	43.6 ± 4.5	2.98 ± 0.28	[Bjo-80]
256.3 ± 5.7	1264.5 ± 5.2	45.8 ± 5.2	2.65 ± 0.40	[Bat-64]
260.8 ± 12.1	1269.7 ± 11.1	51.0 ± 11.1	3.24 ± 0.87	[Bat-63]
261.5 ± 7.5	1270.4 ± 6.9	51.7 ± 6.9	3.38 ± 0.48	[Ker-89a]
264.0 ± 12.1	1273.4 ± 11.1	54.7 ± 11.1	3.01 ± 0.78	[Bat-60]
265.3 ± 3.2	1274.9 ± 2.9	56.2 ± 2.9	2.26 ± 0.28	[Bla-70]
270.4 ± 4.8	1280.7 ± 4.4	62.0 ± 4.4	3.38 ± 0.23	[Bjo-80]
273.5 ± 5.6	1284.4 ± 5.1	65.7 ± 5.1	2.92 ± 0.98	[Per-60]
273.9 ± 7.5	1284.8 ± 6.9	66.1 ± 6.9	3.45 ± 0.42	[Ker-89a]
284.8 ± 7.4	1297.8 ± 6.8	79.1 ± 6.8	3.59 ± 0.36	[Ker-89a]
285.2 ± 1.3	1298.2 ± 1.2	79.5 ± 1.2	3.87 ± 0.09	[Bjo-80]
291.8 ± 11.6	1306.1 ± 10.8	87.4 ± 10.8	4.44 ± 0.69	[Bat-60]
291.8 ± 7.8	1306.1 ± 7.2	87.4 ± 7.2	4.44 ± 0.57	[Blo-65]
293.0 ± 1.3	1307.6 ± 1.2	88.9 ± 1.2	4.13 ± 0.12	[Bjo-80]
295.7 ± 7.3	1310.7 ± 6.8	92.0 ± 6.8	3.67 ± 0.33	[Ker-89a]
296.8 ± 8.9	1312.1 ± 8.2	93.4 ± 8.2	3.99 ± 0.39	[Jon-74]
306.2 ± 8.0	1323.5 ± 7.4	104.8 ± 7.4	4.07 ± 0.38	[Ker-89a]
307.7 ± 6.1	1325.4 ± 5.7	106.7 ± 5.7	3.84 ± 0.49	[Per-60]
316.1 ± 8.7	1335.7 ± 8.1	117.0 ± 8.1	4.13 ± 0.37	[Ker-89a]
319.2 ± 11.3	1339.5 ± 10.5	120.8 ± 10.5	3.96 ± 0.52	[Sax-70]
319.8 ± 10.5	1340.2 ± 9.8	121.5 ± 9.8	4.58 ± 0.58	[Arn-79]
320.9 ± 11.2	1341.6 ± 10.5	122.9 ± 10.5	4.33 ± 0.44	[Blo-63]
323.1 ± 9.0	1344.3 ± 8.4	125.6 ± 8.4	4.64 ± 0.35	[Blo-65]
332.0 ± 9.6	1355.5 ± 9.0	136.8 ± 9.0	4.78 ± 0.38	[Blo-65]
334.8 ± 11.1	1358.9 ± 10.4	140.2 ± 10.4	5.19 ± 0.45	[Bar-64]
335.9 ± 10.3	1360.3 ± 9.7	141.6 ± 9.7	4.82 ± 0.59	[Arn-79]
338.1 ± 6.6	1363.1 ± 6.2	144.4 ± 6.2	4.50 ± 0.48	[Per-60]
339.7 ± 11.0	1365.1 ± 10.3	146.4 ± 10.3	5.14 ± 0.43	[Bar-64]
342.4 ± 11.0	1368.6 ± 10.3	149.9 ± 10.3	4.81 ± 0.38	[Sax-70]
347.2 ± 5.1	1374.7 ± 4.8	156.0 ± 4.8	4.73 ± 0.51	[Arn-79]
362.5 ± 10.8	1394.4 ± 10.1	175.7 ± 10.1	4.70 ± 0.37	[Bar-64]
367.7 ± 7.8	1401.1 ± 7.4	182.4 ± 7.4	4.54 ± 0.33	[Per-60]
369.3 ± 11.4	1403.1 ± 10.7	184.4 ± 10.7	4.80 ± 0.32	[Sax-70]
370.3 ± 10.7	1404.4 ± 10.0	185.7 ± 10.0	4.85 ± 0.31	[Bar-64]
381.5 ± 10.5	1419.0 ± 9.9	200.3 ± 9.9	4.34 ± 0.34	[Bar-64]

Table A10. $\pi^+ p \rightarrow \pi^+\pi^+ n$ reduced amplitudes, (p_0 =279.0 MeV, T_0 =172.4 MeV).

CMS Momentum (MeV)	CMS Energy (MeV)	CMS Kinetic Energy (MeV)	$\lvert a(\pi^+\pi^+ n)\rvert$	Referent Cross Section
220.3 ± 0.3	1224.5 ± 0.2	5.8 ± 0.2	1.43 ± 0.17	[Sev-91]
223.1 ± 0.3	1227.6 ± 0.2	8.9 ± 0.2	1.49 ± 0.12	[Sev-91]
226.4 ± 7.0	1231.1 ± 6.2	12.4 ± 6.2	2.48 ± 1.01	[Ker-90]
227.3 ± 0.3	1232.2 ± 0.2	13.5 ± 0.2	1.43 ± 0.10	[Sev-91]
234.3 ± 0.3	1239.8 ± 0.2	21.1 ± 0.2	1.41 ± 0.09	[Sev-91]
238.9 ± 7.7	1244.9 ± 6.9	26.2 ± 6.9	2.56 ± 0.63	[Ker-90]
251.8 ± 7.5	1259.4 ± 6.9	40.7 ± 6.9	2.68 ± 0.47	[Ker-90]
254.4 ± 10.6	1262.3 ± 9.7	43.6 ± 9.7	$2.97^{+1.00}_{-0.80}$	[Bat-75]
263.9 ± 7.5	1273.2 ± 6.9	54.5 ± 6.9	2.22 ± 0.32	[Ker-90]
275.6 ± 7.5	1286.9 ± 6.9	68.2 ± 6.9	2.08 ± 0.26	[Ker-90]
282.8 ± 11.8	1295.3 ± 10.9	76.6 ± 10.9	$1.50^{+1.50}_{-0.58}$	[Bat-75]
287.1 ± 7.3	1300.5 ± 6.8	81.8 ± 6.8	1.83 ± 0.24	[Ker-90]
288.2 ± 73.3	1301.8 ± 67.8	83.1 ± 67.8	1.35 ± 4.77	[Bar-63]
297.8 ± 15.4	1313.3 ± 14.3	94.6 ± 14.3	$1.17^{+0.71}_{-0.39}$	[Bat-75]
298.4 ± 7.3	1314.1 ± 6.8	95.4 ± 6.8	1.86 ± 0.22	[Ker-90]
310.1 ± 8.0	1328.3 ± 7.4	109.8 ± 7.4	1.69 ± 0.20	[Ker-90]
321.0 ± 8.6	1341.7 ± 8.0	123.0 ± 8.0	1.58 ± 0.20	[Ker-90]
330.4 ± 3.7	1353.4 ± 3.5	134.7 ± 3.5	1.72 ± 0.08	[Kir-62]
332.2 ± 8.5	1355.7 ± 8.0	137.0 ± 8.0	1.49 ± 0.18	[Ker-90]
427.8 ± 8.7	1481.2 ± 8.2	262.5 ± 8.2	1.56 ± 0.20	[Deb-64]

Appendix B

1. $^{12}C(\pi^{\pm},\pi^{\pm}N)^{11}C$ Activation Measurements

Evaluation of absolute cross sections in experiment E1179 required the knowledge of absolute pion beam fluxes. The incident pion intensities of $\sim 10^7$ π^+ s^{-1} are too high for accurate direct counting of beam particles. Relative on-target beam intensity was therefore monitored with a beam ion chamber in combination with a precision charge integrator whose output was recorded on tape. Cross-calibration of ionization counts readings was obtained through activation measurements using plastic scintillator targets. The technique is described in general terms in the reference [Fri-64].

The activation targets were 3.2 mm thick by 38 mm diameter PILOT B plastic scintillators with precisely measured weight containing 91.6% carbon by weight. For every energy and for every shielding arrangement an activation disk intercepting the full beam spot was irradiated for 10-20 minutes at least once per 8-hour shift. The disks were placed at target position during the runs with solid CH_2 and ^{12}C targets and 65 cm down-stream of the target pivot position facing the scattering chamber exit window in the course of LH_2 data acquisition. The precise alignment was ensured by using a customized positioning frame and checked in each instance with a theodolite. A polaroid film was taped to the frame in order to document that the disk circle included the full beam profile.

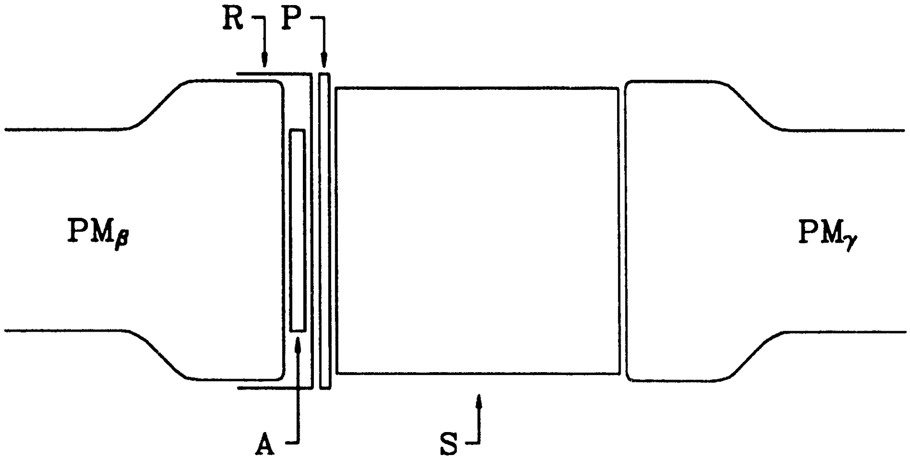

Figure B.1 Apparatus for measuring ^{11}C activity of the plastic scintillator target A by e^+-γ coincidence method. R is a thin aluminum reflector, P is a 1.6 mm thick copper plate ensuring positron annihilation close to scintillator disk, and S represents 75 mm thick × 75 mm diameter NaI(Tl) scintillator. PM$_\beta$ is a phototube used to count positron scintillation pulses while PM$_\gamma$ had the electronic window set to include only 511 keV photopeak pulses ([Høi-89], [Dro-79]).

Table B.1 Recommended ^{12}C($\pi^{\pm}$, πN)^{11}C activation cross sections and electron and proton-induced backgrounds. In this work we rely on the tables refined in a pair of papers by Dropesky, Butler and collaborators ([Dro-79], [But-82]). The measured activation cross sections σ_{e^-} for the contaminating electrons in the low energy negative pion beams are published by Kuhl and Kneissl [Kul-72]. Cross sections for ^{12}C(p,pn)^{11}C reaction come from the review of Cummings [Cum-63]. The $\mu^{\pm}$ induced ^{11}C production can safely be neglected due to the exceedingly small cross section [Ort-79]. At 30, 40 and 50 MeV we use new unpublished values of σ_{π^-} recommanded by Leitch [Lei-90].

$T_{\pi^{\pm}}$ (MeV)	σ_{π^+} (mb)	σ_{π^-} (mb)	σ_{e^-} (mb)	σ_p (mb)
−30	3.2 ± 0.4	1.70 ± 0.08	$.664 \pm .035$	–
−40	6.5 ± 0.4	3.89 ± 0.15	$.954 \pm .140$	–
−50	10.3 ± 0.6	6.10 ± 0.50	1.24 ± 0.20	–
160	45.1 ± 1.6	68.0 ± 2.0	–	90.6 ± 4.6
180	44.0 ± 1.5	70.0 ± 2.0	–	87.2 ± 4.4
190	42.6 ± 1.5	70.2 ± 2.1	–	85.5 ± 4.3
200	40.9 ± 1.4	69.8 ± 2.1	–	83.8 ± 4.2
220	36.9 ± 1.3	66.6 ± 2.0	–	80.4 ± 4.1
240	32.7 ± 1.2	61.1 ± 1.9	–	77.0 ± 3.9
260	28.7 ± 1.1	66.2 ± 1.7	–	73.5 ± 3.7

Pion beam irradiation induces the production of ^{11}C nuclei in plastic scintillator by the decay process ^{12}C($\pi^{\pm}$, $\pi^{\pm}N$)^{11}C. Absolute cross sections for that reaction are relatively large and are known with better than 5% relative uncertainty between 30 and 300 MeV [Dro-79] . The activation produces β-decays of ^{11}C with a conveniently short half-life of 20.4 minutes:

$$^{11}\mathrm{C} \rightarrow {}^{11}\mathrm{B} + e^{+} + \nu_e. \tag{B.1}$$

After each irradiation the scintillator disk was transported promptly to a LAMPF Nuclear Radiochemistry counting room where it was placed into a standard $e^{+}\gamma$ coincidence counter, Figures B.1 The recommended measuring procedure was described in an unpublished document by Vieira [Vie-87]. In the coincidence setup the activated disk was coupled with optical grease to the PMT window. An aluminum reflector foil was pressed against the disk with a special 1.6 mm thick copper cap which enhanced e^{+} annihilations close to the scintillator. Positrons were therefore self-detected in the plastic scintillator while the annihilation 511-keV photons revealed themselves by conversion in NaI(Tl) detector (see Figure B.1). The whole apparatus was enclosed in a light-tight lead box.

Electron, photon and coincidence counts were collected during at least three ^{11}C decay half-lives. The ^{11}C disintegration rate could in principle be determined from the measured net e^+, γ and e^+-γ coincidence rates: R_e, R_γ and $R_{e^+\gamma}$. R_0, the true number of ^{11}C β-decays is directly proportional to the measured quantities:

$$R_e = \epsilon_e R_0, \tag{B.2}$$

$$R_\gamma = \epsilon_\gamma R_0, \tag{B.3}$$

$$R_{e\gamma} = \epsilon_{e\gamma} R_0 \approx \epsilon_e \epsilon_\gamma R_0. \tag{B.4}$$

The coefficients ϵ_e, ϵ_γ and $\epsilon_{e\gamma}$ can be interpreted as defined by these equations, and are obviously products of intrinsic detection efficiencies, solid angle coverage and absorption and bremsstrahlung corrections. The effective efficiencies of the NaI(Tl) gamma counter and the positron scintillation detector were determined in high-statistics activations with higher energy beams (≥160 MeV) and showed about 1% stability over three years (Table B.2).

Table B.2 The activation apparatus efficiencies. The effective efficiencies of e^+ and γ counter were determined during three consecutive running years from high-statistics low-background runs at incident pion beam energies ≥160 MeV. The first measured point for the activated disk on average represented $\sim 10^6$ e^+ pulses while the independently measured background rate was $\sim 10^2$.

Year	e^+ Counter Efficiency (%)	γ Counter Efficency (%)
1990	96.30 ± 0.49	25.37 ± 0.91
1991	96.60 ± 0.80	23.91 ± 0.74
1992	97.26 ± 0.41	23.69 ± 1.24

Average background rates in the activation apparatus for dummy non-activated disks were determined in separate high-statistics calibrations once a week, and remained stable in the course of the experiment. Background counts are due to PMT dark currents, random cosmic ray coincidences and radioactive material naturally present in the disks and devices in the apparatus.

Activity induced by 30 MeV π^- beam was comparable with the background count rates. To obtain pion flux measurement within 1% accuracy this background rate had to be determined precisely for each activation. These rates were obtained with a `MINUIT` least-χ^2 fit keeping the instrumental counter efficiencies constrained as explained above.

Reliability of activation measurements with positive pion beams is affected by the non-pionic contamination of the beam. The upper bound on the beam proton fraction was set in pion-proton separation scans (Appendix A). That contamination component was further confirmed in monitoring $pp \rightarrow pp$ elastic scattering in conjugate charged particle detectors. Correction due to ^{12}C$(p,pn)^{11}$C reaction in the disintegration rate was made in the code.

Absolute $\pi^\pm$ intensities were calculated with the program ACTP [Lei-89] that was modified to take into account the proton contamination of the beam. Inputs to the code are rates R_{e^+}, R_γ and $R_{e^+\gamma}$ for 6-10 successive five minute intervals, the target irradiation time, the decay time between the end of irradiation and the beginning of activation measurement, the tabulated disk number, the beam energy and particle type, proton fraction and the ion chamber integrated charge. ACTP output inxcludes $\pi^\pm/IC$ calibration constant, statistical and systematic uncertainties and the χ^2 goodness of the fit.

The total number of activation measurements for every studied energy together with the accepted IC/π coefficients are summarized in Table B.3. Table B.4 contains the corrections applied to these coefficients due to differential energy losses in the activation disks and upstream target which are significant at lower energies.

Table B.3 Activation flux corrections due to differential energy loss in the targets. The effect of the differential energy loss in an in-beam target on the ion chamber counting was measured in 1990. The dummy activation disk in place of target increased the IC count rate by 1.3 ± 0.2%. Knowing that 30 MeV incident pion losses 1.5 MeV transversing the disk, the agreement with the ratio expected from Bethe-Bloch ionization formula is exact.

Target and 30 MeV π^-	Thickness (cm)	$E_{\rm act}$ (MeV)	$(dE_{\pi^-}/dx)_{\rm tgt}$ (MeV)
Act Disk	1.50	29.35	1.50
CH_2	3.64	25.71	3.64
^{12}C	3.20	26.15	3.20
LH90 FULL	1.34	27.52	1.34
LH91 FULL	2.16	26.70	2.16
LH92 FULL	2.07	26.79	2.07
LH EMPTY	0.80	28.86	0.80

Appendix C

1. Three-particle Final State Kinematics

The scattering of two particles into a three particle final state $p_a + p_b \to p_1 + p_2 + p_3$ can be kinematically described by the set of five standard invariant variables constructed from four-momenta p_i, Figure C.1(a):

$$s_1 \equiv s_{12} = (p_1 + p_2)^2 = (p_a + p_b - p_3)^2, \tag{C.1}$$

$$s_2 \equiv s_{23} = (p_2 + p_3)^2 = (p_a + p_b - p_1)^2, \tag{C.2}$$

$$t_1 \equiv t_{a1} = (p_a - p_1)^2 = (p_2 + p_3 - p_b)^2, \tag{C.3}$$

$$t_2 \equiv t_{b3} = (p_b - p_3)^2 = (p_1 + p_2 - p_a)^2, \tag{C.4}$$

$$s \equiv s_{ab} = (p_a + p_b)^2 = (p_1 + p_2 + p_3)^2, \tag{C.5}$$

using the symbols of reference [Byc-73].

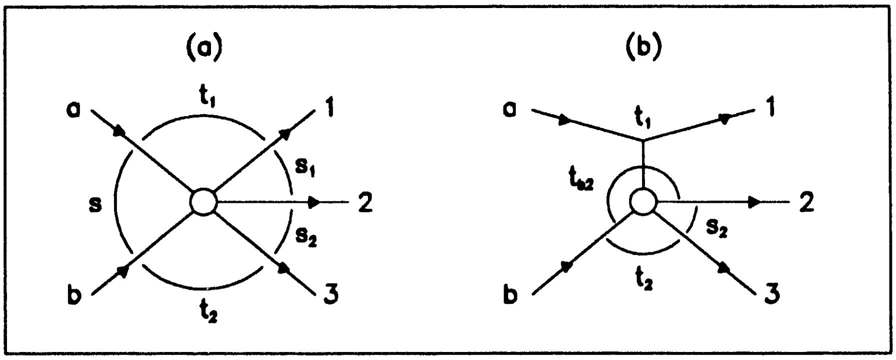

Figure C.1 (a) The invariant variables in 2 → 3 scattering. In the phase space of $\pi(p_b)N(p_a) \to \pi(p_2)\pi(p_3)N(p_1)$, s is fixed and only four invariants vary. (b) Connection between the variable $t_{b2} = (p_b - p_2)^2$ and the standard invariants follows from the reduction of lower vertex to 2→2 scattering.

By considering not-adjacent particle pair in Figure C.1(b) one obtains a linearly dependent invariant set. Rearranging the pairing as on Figure 1.1b the application of four-momentum conservation to the 2→2 scattering at the lower vertex gives

$$t_{a2} = (p_a - p_2)^2 = t_2 - t_1 - s_1 + m_a^2 + m_1^2 + m_2^2, \tag{C.6}$$

and similarly

$$t_{b2} = (p_b - p_2)^2 = t_1 - t_2 - s_2 + m_b^2 + m_2^2 + m_3^2, \tag{C.7}$$

$$t_{a3} = (p_a - p_3)^2 = s_1 - s - t_2 + m_a^2 + m_b^2 + m_3^2, \tag{C.8}$$

$$t_{b1} = (p_b - p_1)^2 = s_2 - s - t_1 + m_a^2 + m_b^2 + m_1^2, \tag{C.9}$$

$$s_{13} = (p_1 + p_3)^2 = s - s_1 - s_2 + m_1^2 + m_2^2 + m_3^2, \tag{C.10}$$

s is fixed for $2 \rightarrow 3$ scattering and the total number of independent variables is four. All permutations of the scalar products $p_i p_j$ can be expressed in terms of invariant quantities:

$$2p_a p_b = s - m_a^2 - m_b^2, \tag{C.11}$$

$$2p_a p_1 = m_a^2 + m_1^2 - t_1, \tag{C.12}$$

$$2p_a p_2 = s_1 + t_1 - t_2 - m_1^2, \tag{C.13}$$

$$2p_a p_3 = s - s_1 + t_2 - m_b^2, \tag{C.14}$$

$$2p_b p_1 = s - s_2 + t_1 - m_a^2, \tag{C.15}$$

$$2p_b p_a = s_2 + t_2 - t_1 - m_3^2, \tag{C.16}$$

$$2p_b p_3 = m_b^2 + m_3^2 - t_2, \tag{C.17}$$

$$2p_1 p_2 = s_1 - m_1^2 - m_2^2, \tag{C.18}$$

$$2p_1 p_3 = s - s_1 - s_2 + m_2^2, \tag{C.19}$$

$$2p_2 p_3 = s_2 - m_2^2 - m_3^2, \tag{C.20}$$

The reaction $\pi(p_b)N(p_a) \rightarrow \pi(p_2)\pi(p_3)N'(p_1)$ can be discussed in terms of the energies E_i, three-momenta $\mathbf{p}_i$ and momentum magnitudes P_i in the CM reference frame ($\mathbf{p}_a = -\mathbf{p}_b = \mathbf{p}$). Then s is the square of the total energy in the CM frame, t_1 and t_2 are 4-momentum transfers to the nucleon and incident pion, respectively, while s_1 and s_2 are the squares of invariant masses labeled as $m_{\pi p}^2$ and $m_{\pi\pi}$, respectively. The CM variables for particles in the ijk final state and for the jk pair are connected by the defining equations

$$P_{jk}^2 = P_i^2 = E_i^2 - m_i^2 = (\sqrt{s} - E_i)^2 - m_{jk}^2, \tag{C.21}$$

$$E_i = \sqrt{s} - E_{jk} = \frac{s - m_{jk}^2 + m_i^2}{2\sqrt{s}} \tag{C.22}$$

Conservation of energy requires

$$m_{12}^2 + m_{13}^3 + m_2 3^3 = s + m_1^2 + m_2^2 + m_3^2. \tag{C.23}$$

Limits on the invariant mass of the ij pair are

$$m_{ij}^{\text{min}} = m_i + m_j, \tag{C.24}$$

$$m_{ij}^{\text{max}} = \sqrt{s} - m_k, \tag{C.25}$$

where the velocities of particles i and j are equal in the first configuration and their momenta are collinear, while in the second case particle is k at rest in the over-all CM system.

The experimental detector arrangement is constrained by the kinematical limits on the kinetic energy T^L of the $\pi N \rightarrow \pi\pi N$ ejectiles at a given polar angle θ^L. In the laboratory system near the reaction threshold the recoil nucleon has polar angles restricted to a narrow forward cone. Limits the final state nucleon kinetic energy as a function of θ_2^L have the form

$$T_{1\text{min}}^L = \frac{m_a E_a^* E_{1\text{max}}^* - m_1 P \cos\theta_1^L \sqrt{(\frac{m_a}{m_1}) E_{1\text{max}}^{*2} - E_a^{*2} + P^2 \cos^2\theta_1^L}}{E_a^{*2} - P^2 \cos^2\theta_1^L} - m_1, \tag{C.26}$$

$$T_{1\text{max}}^L = \frac{m_a E_a^* E_{1\text{max}}^* + m_1 P \cos\theta_1^L \sqrt{(\frac{m_a}{m_1}) E_{1\text{max}}^{*2} - E_a^{*2} + P^2 \cos^2\theta_1^L}}{E_a^{*2} - P^2 \cos^2\theta_1^L} - m_1, \tag{C.27}$$

where m_a and m_1 are the masses of the initial and final state nucleon and for physical θ^L kinetic energies are positive and real:

$$0 \le T^*_{1\min} \le T^*_N \le T^*_{1\max}. \qquad \text{(C.28)}$$

Pion scattering angle θ_2^L can assume all values from 0° to 180° in the laboratory system and the T_2^L-$\cos\theta_2^L$ relation has the form of (C.26-27) with appropriate masses and energies substituted. The energy limits $E^*_{1\max}$ and $E^*_{2\max}$ follow from the equations (C.22), (C.24) and (C.25). The limiting final state pion and proton T^L-θ^L curves for the E1179 choices of incident pion energies are shown on Figures C.2 and C.3.

The kinematic function λ is defined as

$$\lambda(x,y,z) = (x-y-z)^2 - 4yz = x^2 + y^2 + z^2 - 2xy - 2yz - 2xz, \qquad \text{(C.29)}$$

The Dalitz plot [Dal-53] is defined as the physically allowed region of $p_a + p_b \rightarrow p_1 + p_2 + p_3$ in the s_1-s_2 space.

Assuming a constant reaction matrix element, probability of a specific three body final state is proportional to the invariant phase space integral

$$R_3(s) = \int \frac{d^3p_1 d^3p_2 d^3p_3}{2E_1 2E_2 2E_3} \delta^4(p_a + p_b - p_1 - p_2 - p_3), \qquad \text{(C.30)}$$

By performing the integration over the δ function in the CM frame, and using the Jacobian for transforming (E_1, E_3) variables to a (s_1, s_2) pair, the phase space density can be expressed in terms of the squares of invariant masses s_1 and s_2:

$$R_3(s) = \frac{1}{32s} \int ds_1 ds_2 d\Omega_1 d\phi_3 \Theta[-G(s_1, s_2, s, m_2^2, m_1^2, m_3^2)], \qquad \text{(C.31)}$$

where the Θ function restricts the variables to physical values. Phase space density in the $s_1 s_2$ space is independent of s_1 and s_2. The matrix element for 2 → 3 scattering is in general a function of four independent invariants. Dalitz plot density gives the integral of a matrix element over the undisplayed variables.

The physical limits on the Dalitz plot are

$$s_1^{\pm} = m_1^2 + m_2^2 - \frac{1}{2s_2}[(s_2 - s + m_1^2)(s_2 + m_2^2 - m_3^2) \pm \lambda^{\frac{1}{2}}(s_2, s, m_1^2)\lambda^{\frac{1}{2}}(s_2, m_2^2, m_3^2). \qquad \text{(C.32)}$$

Written in terms of t_1 and s_2 invariants the phase space density has the form

$$R_3(s) = \frac{1}{8\sqrt{s}P_a^*} \int_0^{2\pi} d\phi \int dt_1 ds_2 \frac{\lambda^{\frac{1}{2}}(s_2, m_2^2, m_3^2)}{8s_2} \int d\Omega_3^{\mathrm{R23}}. \qquad \text{(C.33)}$$

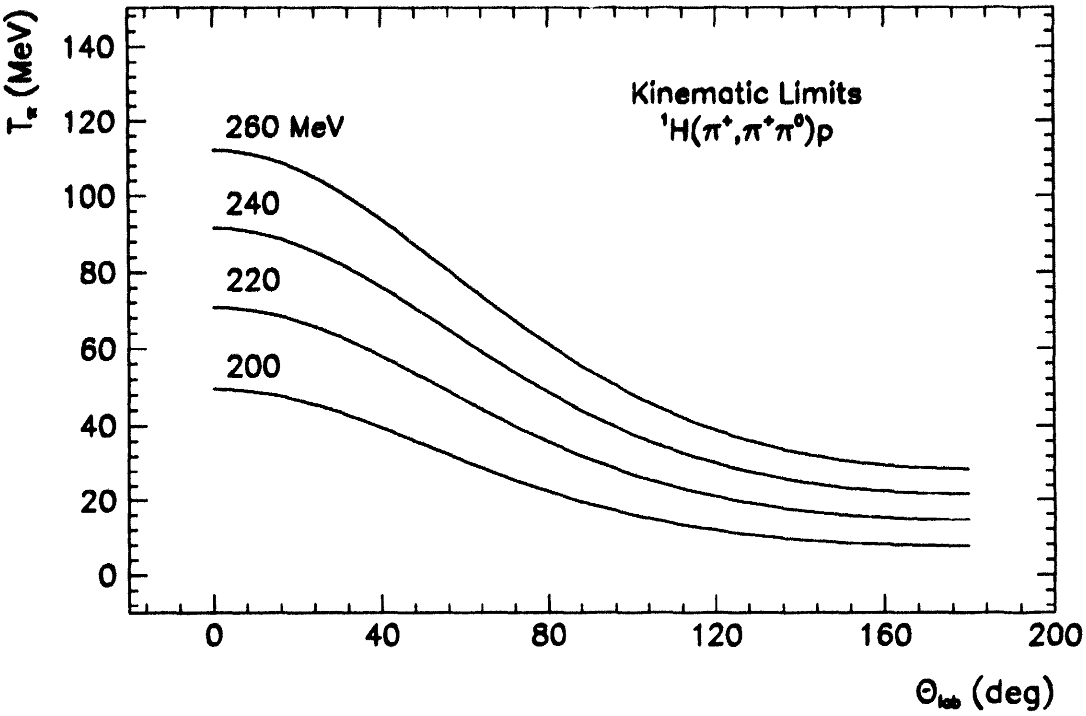

Figure C.2 Maximum laboratory kinetic energy for final state pions in $\pi^+p \rightarrow \pi^+\pi^0p$ shown as a function of the pion laboratory polar angle. The curves correspond to four E1179 incident pion energies.

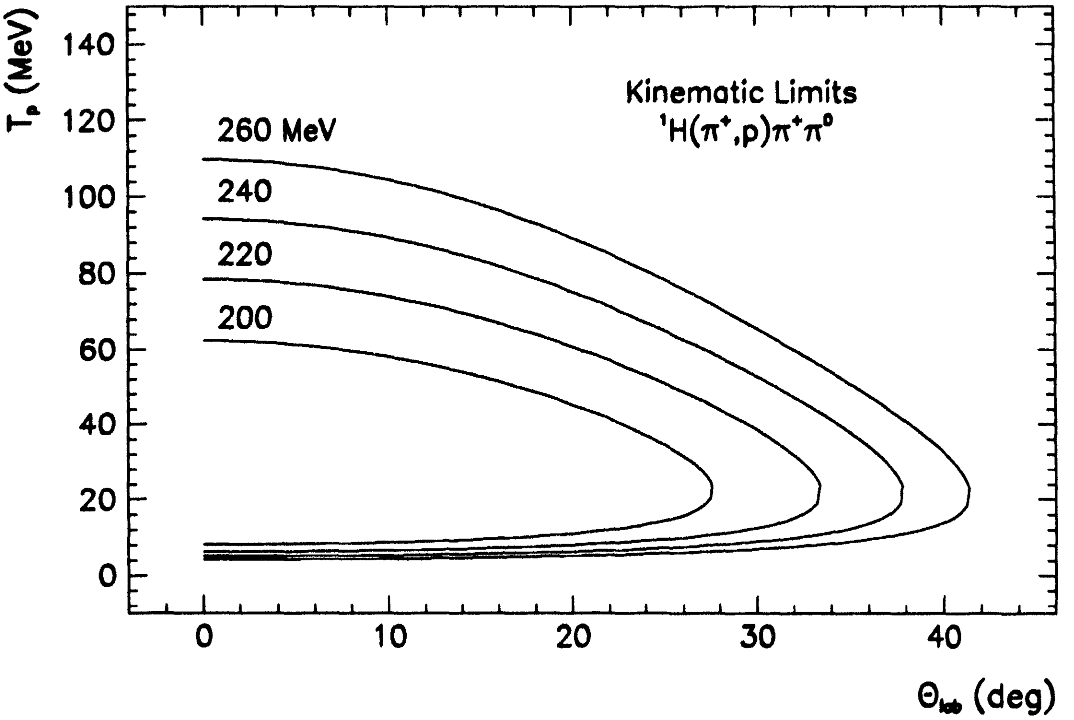

Figure C.3 Kinematical limits in the laboratory polar angle- kinetic energy space for recoil protons in $\pi^+p \rightarrow \pi^+\pi^0p$. Knowledge of the maximum and minimum proton kinetic energies in the reaction $\pi^+p \rightarrow \pi^+\pi^0p$ at given laboratory angle constrains the design of charged particle counters.

The kinematical boundaries of the Chew-Low plot are:

$$t_1^{\pm} = m_a^2 + m_1^2 - \frac{1}{2s}[(s + m_a^2 - m_b^2)(s - s_2 + m_1^2 \pm \lambda^{\frac{1}{2}}(s, m_a^2, m_b^2)\lambda^{\frac{1}{2}}(s, s_2, m_1^2))], \qquad (C.34)$$

$$s_2^{\pm} = s + m_1^2 - \frac{1}{2m_a^2}[(s + m +{}_a^2 - m_b^2)(m_a^2 + m_1^2 - t_1) \pm \lambda^{\frac{1}{2}}(s, m_a^2, m_b^2)\lambda^{\frac{1}{2}}(t_1, m_a^2, m_1^2)], \qquad (C.35)$$

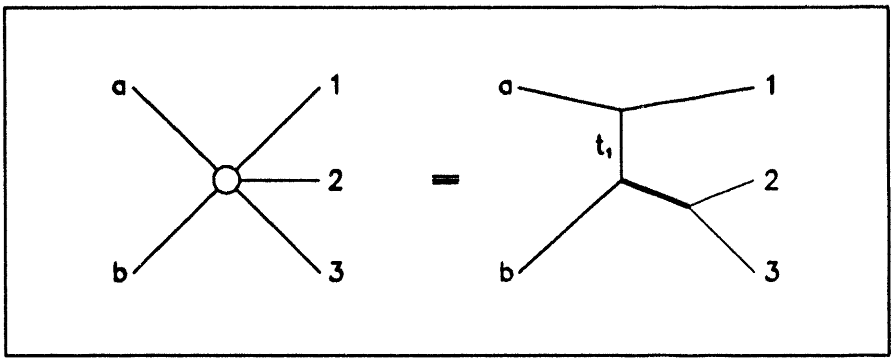

Figure C.4 Factorization of the three-particle final state phase space integral. Kinematics of the 2 → 3 scattering process can be described stepwise as two processes 2 → 2 and 1 → 2.

Introducing the matrix element $\mathcal{M}(s_2, t_1, \Omega)$, the physical angular distributions are proportional to

$$\mathcal{P}(\cos\theta, \phi) \propto \int dt_1 ds_2 \frac{\lambda^{\frac{1}{2}}(s_2, m_2^2, m_3^2)}{8s_2} \mathcal{M}(s_2, t_1, \Omega), \qquad (C.36)$$

where the direction Ω specifies the vector $\mathbf{p}_3$ in the dipion rest frame, $\mathbf{p}_2 + \mathbf{p}_3 = \mathbf{0}$. Specific choice of $\mathbf{p}_b$ as the z axis and of $\mathbf{p}_1\mathbf{p}_b$ plane as the xz plane in Figure C.5 defines the Jackson "frame" for which the polar and azimuthal angle of particle 3 are called the Jackson angle and the Treiman-Yang angle, respectively.

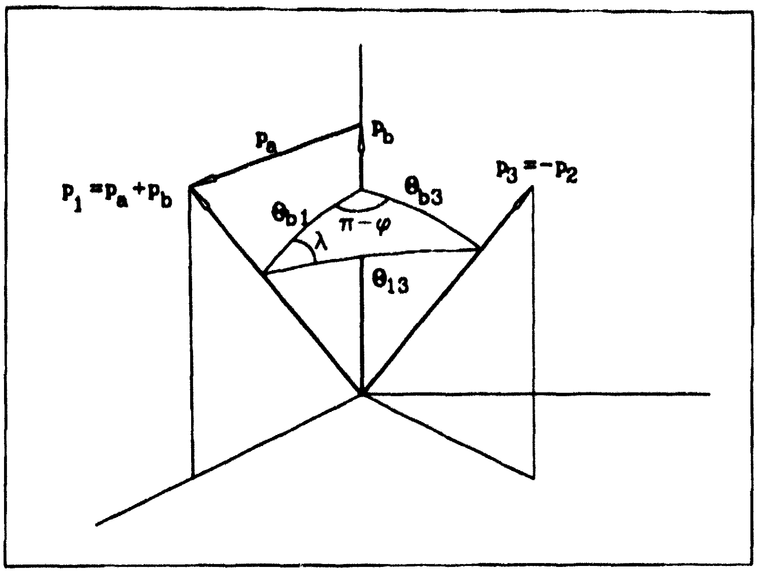

Figure C.5 Definition of the Treiman-Yang angle ϕ_b and the helicity angle λ in the $\pi\pi$ rest frame, $\mathbf{p}_2 + \mathbf{p}_3 = \mathbf{0}$. $\mathbf{p}_a$ and $\mathbf{p}_b$, the momentum vectors of the proton and pion in the pre- interaction state, together with $\mathbf{p}_1$, the final state proton momentum vector, define the production plane. The Jackson angle and the Treiman-Yang angle are the polar and azimuthal angle of the final state pion with respect to the production plane.

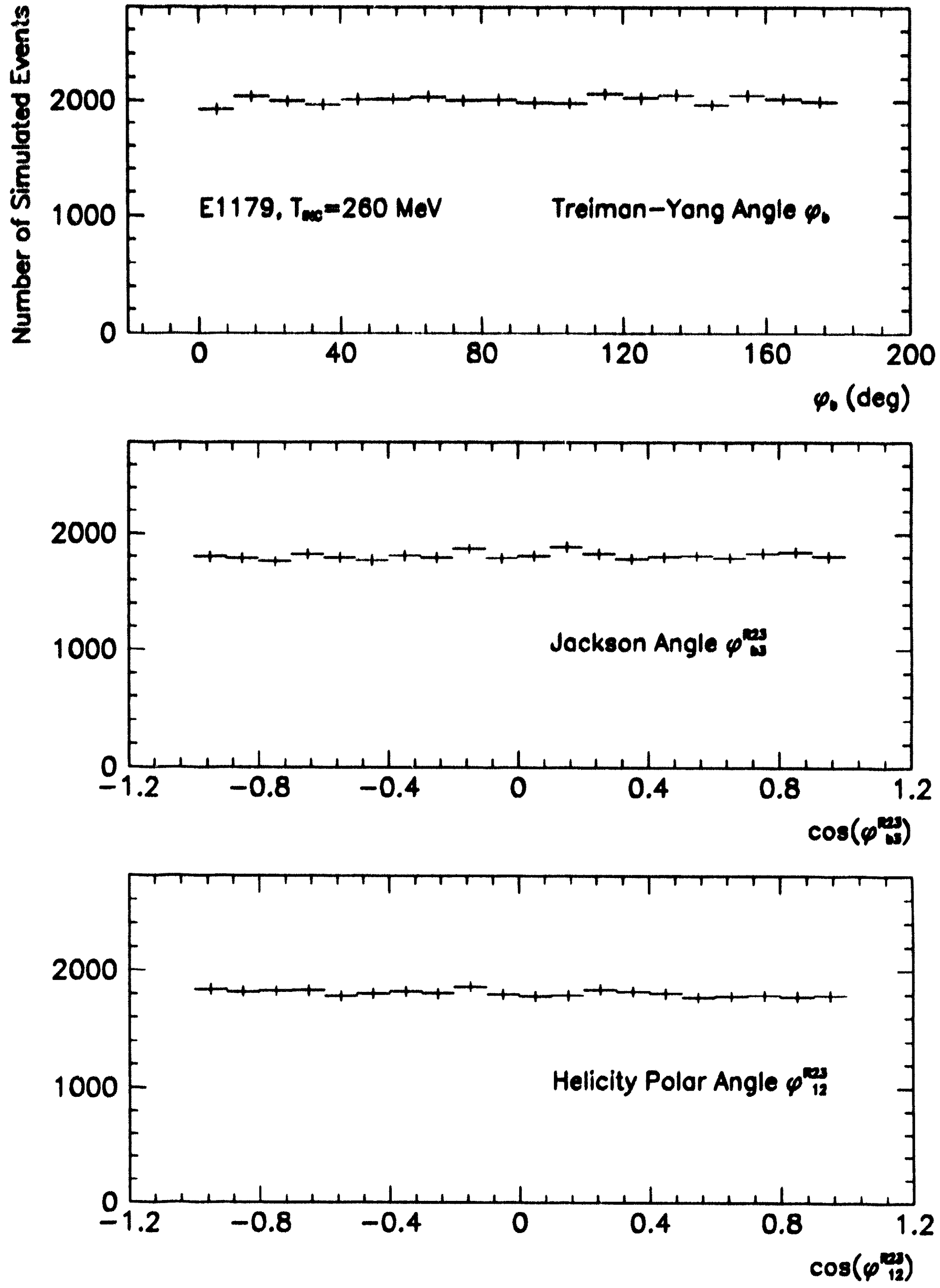

Figure C.6 The $\pi^+p \to \pi^+\pi^0p$ Monte Carlo final state angular distributions at 260 MeV. The s-wave pion-pion interaction and the non-resonant dipion-proton final state lead to flat distributions in polar and azimuthal angles.

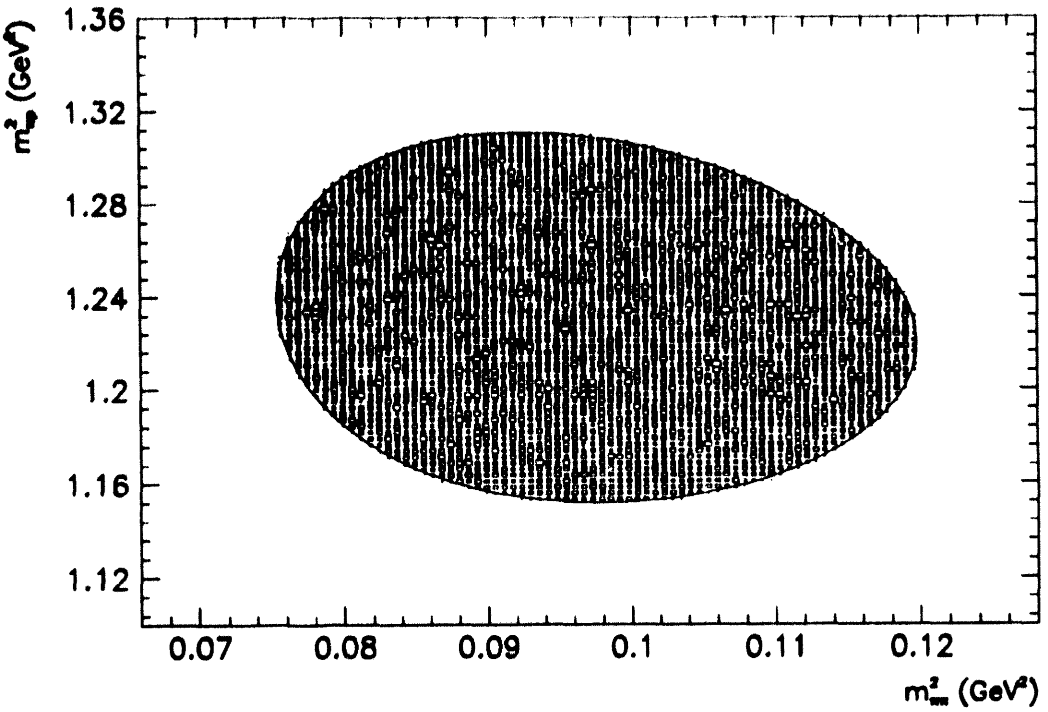

Figure C.7 The $\pi^+p \to \pi^+\pi^0p$ Monte Carlo Dalitz plot at 260 MeV. The density of the points on the Dalitz plot is proportional to the matrix element squared: a constant matrix element in the calculation leads to a uniform population density of events.

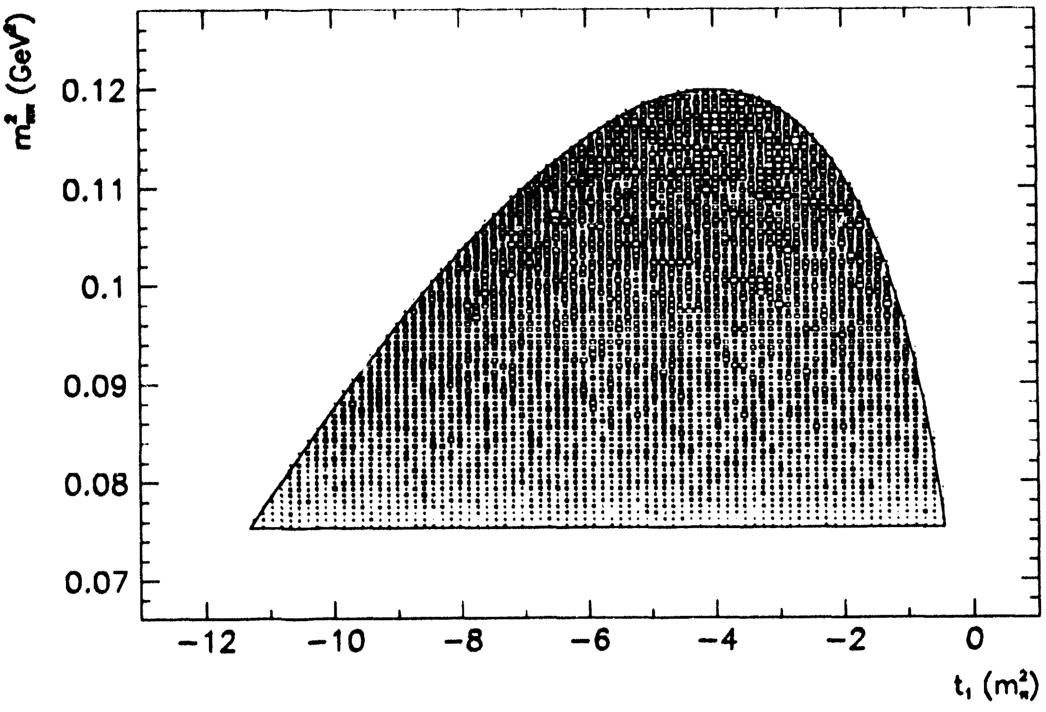

Figure C.8 The $\pi^+p \to \pi^+\pi^0p$ Monte Carlo Chew-Low plot at 260 MeV. A total of 10^5 simulated events are plotted, each weighted according to the phase space factor.

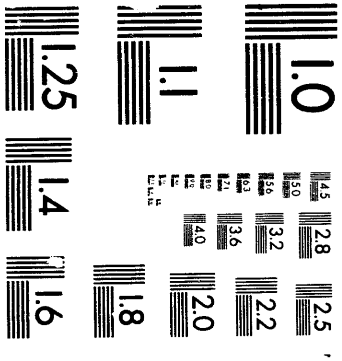
1.0
1.1
1.25
1.4
1.6
1.8
2.0
2.2
2.5
2.8
3.2
3.6
4.0
4.5
5.0
5.6
6.3

3 of 3

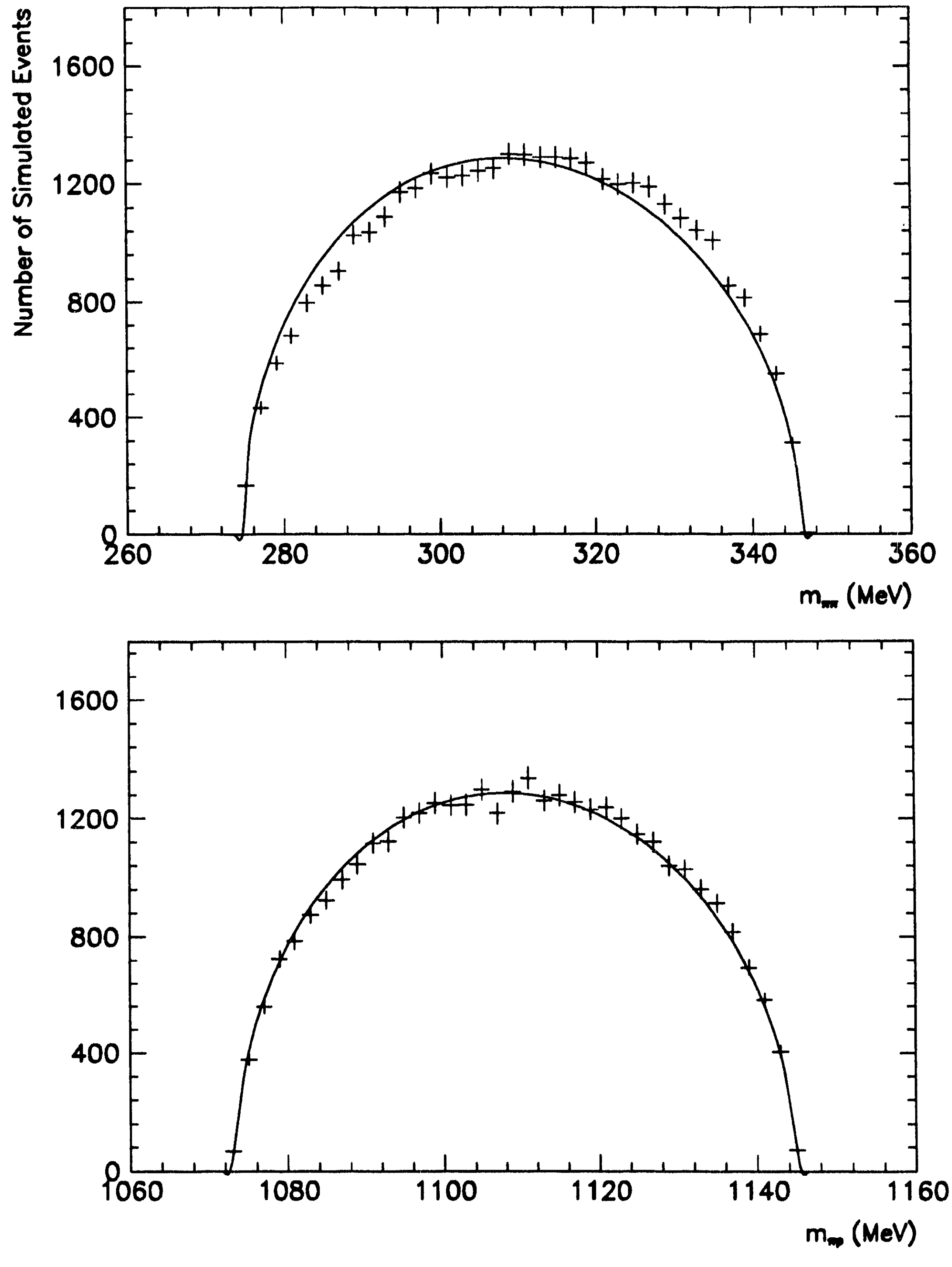

Figure C.9 E1179 Monte Carlo invariant mass spectra at 260 MeV. Agreement between the simulated shape and the curve obtained by numerical integration of the three-body final-state phase space weight confirms the acceptability of the random number generator (Cernlib `RNDM`).

Appendix D

1. Effective Chiral Lagrangians

The historical σ model ([Sch-58], [Pol-58], [Gel-60]) incorporates an isotriplet of pion fields $\boldsymbol{\pi} = (\pi_1, \pi_2, \pi_3)$, an isoscalar σ field and an isodublet of massless nucleon fields $N = (p, n)$, and is derivable from the Lagrangian

$$\mathcal{L} = \frac{1}{2}[(\partial_\mu \sigma)^2 + (\partial_\mu \boldsymbol{\pi})^2] + \overline{N} i \gamma^\mu \partial_\mu N + g\overline{N}(\sigma + i\boldsymbol{\tau}\cdot\boldsymbol{\pi}\gamma_5)N - V(\sigma^2 + \boldsymbol{\pi}^2), \tag{D.1}$$

where $\boldsymbol{\tau}$ are isospin matrices and the potential V can be expanded up to second order into

$$V(\sigma^2 + \boldsymbol{\pi}^2) = \frac{-\mu^2}{2}(\sigma^2 + \boldsymbol{\pi}^2) + \frac{\lambda}{4}(\sigma^2 + \boldsymbol{\pi}^2)^2, \tag{D.2}$$

The σ-model Lagrangian is invariant under transformations of isospin symmetry:

$$\sigma \longrightarrow \sigma' = \sigma \tag{D.3}$$

$$\boldsymbol{\pi} \longrightarrow \boldsymbol{\pi}' = \boldsymbol{\pi} + \boldsymbol{\alpha} \times \boldsymbol{\pi} \tag{D.4}$$

$$N \longrightarrow N' = N + i\boldsymbol{\alpha}\cdot\frac{\boldsymbol{\tau}}{2}N, \tag{D.5}$$

where $\boldsymbol{\alpha}$ is the infinitesimal rotation angle in the isospin space.

The corresponding conserved currents follow from Noether's theorem

$$J^a_\mu = \overline{N}\gamma_\mu\frac{\tau_a}{2}N + \epsilon_{abc}\pi^b\partial_\mu\pi^c, \quad \text{for } a = 1, 2, 3, \tag{D.6}$$

while the charges are defined as space integrals of the timelike current component

$$Q^a = \int J^a_0(x) d^3x. \tag{D.7}$$

Axial SU(2) infinitesimal transformations

$$\sigma \longrightarrow \sigma' = \sigma + \boldsymbol{\beta}\cdot\boldsymbol{\pi} \tag{D.8}$$

$$\boldsymbol{\pi} \longrightarrow \boldsymbol{\pi}' = \boldsymbol{\pi} - \boldsymbol{\beta}\cdot\boldsymbol{\pi} \tag{D.9}$$

$$N \longrightarrow N' = N + i\boldsymbol{\beta}\cdot\frac{\boldsymbol{\tau}}{2}\gamma_5 N, \tag{D.10}$$

also leave the form of the Lagrangian unchanged leading to conserved axial currents

$$A^a_\mu = \overline{N}\gamma_\mu\gamma_5\frac{\tau^a}{2}N + (\partial_\mu\sigma)\pi^a - (\partial_\mu\pi^a)\sigma, \tag{D.11}$$

and charges

$$Q^{5a} = \int A_0^a(x) d^3x. \tag{D.12}$$

In this model, the pion and the σ are massive and stable particles. The charges defined by (D.7) and (D.12) satisfy the following commutation relations:

$$[Q^a, Q^b] = i\epsilon^{abc}Q^c, \tag{D.13}$$

$$[Q^a, Q^{5a}] = i\epsilon^{abc}Q^{5c}, \tag{D.14}$$

$$[Q^{5a}, Q^{5b}] = i\epsilon^{abc}Q^c. \tag{D.15}$$

This algebra can be simplified by defining right-handed and left-handed charges

$$Q_R^a = \frac{1}{2}(Q^a + Q^{5a}), \tag{D.16}$$

$$Q_L^a = \frac{1}{2}(Q^a - Q^{5a}) \tag{D.17}$$

Q_R's and Q_L's generate separate SU(2) charge algebras transforming into each other under the parity transformation:

$$[Q_R^a, Q_R^b] = i\epsilon^{abc}Q_R^c, \tag{D.18}$$

$$[Q_L^a, Q_L^b] = i\epsilon^{abc}Q_L^c, \tag{D.19}$$

$$[Q_R^a, Q_L^b] = 0. \tag{D.20}$$

These commutation relations correspond to the chiral $\mathrm{SU}(2)_L \times \mathrm{SU}(2)_R$ algebra which is isomorphic to the O(4) group. Imagining chiral transformations as "Lorentz boosts" in isospin space, and drawing the parallel between Q^a and the angular momentum operator L^a, as well as between Q^{5a} and the boost operator A^a, the σ field can be identified as the timelike component of the pion field. That explains the absence of the nucleon mass term in the chiral invariant Lagrangian (D.1): $\overline{N}N$ is just the fourth component of a chiral vector and not a chiral scalar. The transformation properties of pion, σ- and nucleon fields can be redefined in the following way

$$\begin{array}{llll}
(\mathrm{D.21}) & [Q^a, \pi^b] = i\epsilon_{abc}\pi^c, & [Q^a, \sigma] = 0, & (\mathrm{D.24}) \\
(\mathrm{D.22}) & [Q^{5a}, \pi^b] = -i\delta_{ab}\sigma, & [Q^{5a}, \sigma] = i\pi^a, & (\mathrm{D.25}) \\
(\mathrm{D.23}) & [Q^a, N] = -\frac{1}{2}\tau^a N, & [Q^{5a}, N] = -\frac{1}{2}\tau^a\gamma_5 N & (\mathrm{D.26})
\end{array}$$

or in terms of left- and right-handed charges

$$\begin{array}{llll}
(\mathrm{D.27}) & [Q_R^a, N_R] = -\frac{1}{2}\tau^a N_R, & [Q_L, N_R] = 0, & (\mathrm{D.29}) \\
(\mathrm{D.28}) & [Q_R, N_L] = 0, & [Q_L^a, N_L] = -\frac{1}{2}\tau^a N_L & (\mathrm{D.30})
\end{array}$$

where $N_{L,R} = \frac{1}{2}(1 \pm \gamma_5)N$, (D.31).

Considering only the mesonic part of the σ model Lagrangian (D.1), the potential energy minimum is obtained brom the condition

$$\left.\begin{array}{ll} \text{(D.32)} & \dfrac{\partial \mathcal{H}}{\partial \sigma} = 0 \\ \text{(D.33)} & \dfrac{\partial \mathcal{H}}{\partial \boldsymbol{\pi}} = 0 \end{array}\right\} \qquad \begin{array}{lr} \sigma[\mu^2 - \lambda(\boldsymbol{\pi}^2 + \sigma^2)] = 0 & \text{(D.34)} \\ \boldsymbol{\pi}^a[\mu^2 - \lambda(\boldsymbol{\pi}^2 + \sigma^2)] = 0. & \text{(D.35)} \end{array}$$

Besides the trivial solutions $\sigma = 0$ and $\boldsymbol{\pi} = 0$, the physically interesting case is the perturbation around the points $\sigma' = \sigma \pm \sqrt{\mu^2/\lambda} = 0$ in $(\boldsymbol{\pi}, \sigma)$ space. Introducing the notation $\sigma = \sigma' + b$ where $\lambda b = \mu^2$, the pion Lagranginan can be rewritten in the form

$$\mathcal{L} = \frac{1}{2}[(\partial_\mu \boldsymbol{\pi})^2 + (\partial_\mu \sigma')^2 - \mu^2(\boldsymbol{\pi}^2 + \sigma'^2)] - \frac{1}{2}\underbrace{(\mu^2 - \lambda b^2)}_{0}\boldsymbol{\pi}^2 - \frac{1}{2}\underbrace{(\mu^2 - 3\lambda b^2)}_{-2\mu^2,}\sigma'^2$$
$$+ \frac{1}{4}(\sigma'^2 + \boldsymbol{\pi}^2) + b\lambda\sigma'(\boldsymbol{\pi}^2 + \sigma'^2). \quad \text{(D.36)}$$

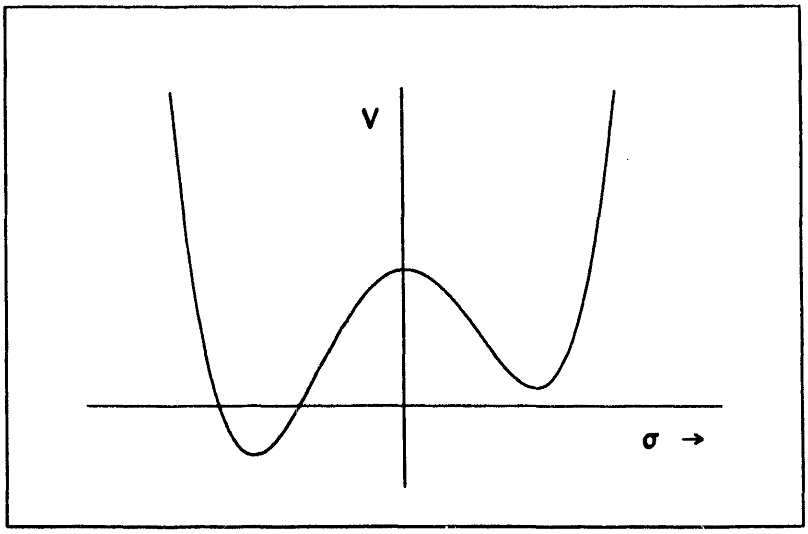

Figure D.1 Potential in the effective Lagrangian with broken chiral symmetry. The addition of isospin scalar term $c\sigma$ to the original manifestly chiral invariant Lagrangian select a unique minimum of the potential, introduces the mass term and changes the current divergence [Alf-73].

Axial vector current A^a_μ now aquires the additional term $b\partial_\mu \pi^a$ and in the full Lagrangian nucleon aquires a mass. The σ model can be used as a starting point for calculation of $\pi\pi$ and πN scattering. Weinberg has devised, however, the chiral Lagrangian that contains only a pion field with derivative interactions. Redefining the physical pion field $\boldsymbol{\pi}$

$$\phi = \frac{2f_\pi}{f_\pi - \sigma}\boldsymbol{\pi}, \qquad \text{(D.37)}$$

and introducing the covariant derivative

$$D_\mu \boldsymbol{\pi} = (f_\pi - \sigma)\partial_\mu \frac{1}{f_\pi - \sigma}\boldsymbol{\pi}, \quad \text{or} \quad D_\mu \boldsymbol{\phi} = \frac{1}{1+\frac{\boldsymbol{\phi}^2}{4f_\pi^2}}\partial_\mu \boldsymbol{\phi}, \tag{D.38}$$

one arrives at nonlinear relization of SU(2)×SU(2) with the field transformation law

$$[Q^{5a}, \phi^b] = if_\pi \left[\delta_{ab}\left(1 - \frac{\boldsymbol{\phi}^2}{4f_\pi^2}\right) + \frac{\phi^a\phi^b}{2f_\pi^2}\right], \tag{D.39}$$

The Weinberg Lagrangian restricted to the pionic degrees of freedom has the form

$$\mathcal{L}_\pi = \frac{1}{2}(D_\mu \boldsymbol{\phi})^2 + \mathcal{L}_N = \frac{1}{2}\frac{1}{1+\frac{\boldsymbol{\phi}^2}{4f_\pi^2}}(\partial_\mu \boldsymbol{\phi})^2 + \mathcal{L}_N \approx \frac{1}{2}(\partial_\mu \boldsymbol{\phi})^2 - \frac{1}{4f_\pi^2}\boldsymbol{\phi}^2(\partial_\mu \boldsymbol{\phi})^2 + \ldots + \mathcal{L}_N, \tag{D.40}$$

where $\mathcal{L}_N$ is chiral-symmetry breaking part to be determined from the experiment. The term $\mathcal{L}_N$ can be naturally classified in terms of its chiral transformation properties. The function $\mathcal{L}_N$ is supposed to transform according to the $(N/2, N/2)$ representation of SU(2)×SU(2). Using the isomorphism of that group with O(4) one can make an assumption that

$$\mathcal{L}_N = t^N_{00\ldots0}, \tag{D.41}$$

where $t^N_{ab\ldots c}$ is a traceless symmetric tensor of rank N. Weinberg [Wei-68] showed that ordinary rules of the tensor algebra and zero trace of t^N lead to the commutation relation

$$\left[Q^{5a}, [Q^{5a}, \mathcal{L}_N]\right] = N(N+2)\mathcal{L}_N. \tag{D.42}$$

A second order differential equation can be written for arbitrary function $\mathcal{L}(\boldsymbol{\phi})$ that satisfies (D.42) and solved in a power series of $\boldsymbol{\phi}$:

$$\mathcal{L}_N(\boldsymbol{\phi}^2) = -\frac{1}{2}m_\pi^2\left[-\frac{3}{2}\frac{4f_\pi^2}{2N(N+2)} + \boldsymbol{\phi}^2 - \frac{1-\frac{\xi}{2}}{4f_\pi^2}(\boldsymbol{\phi}^2)^2 + \ldots\right], \tag{D.43}$$

where the chiral-symmetry-breaking parameter is defined as

$$\xi = \frac{2}{5}[3 - N(N+2)]. \tag{D.44}$$

Taking into account the symmetry-breaking term (D.43) to the pion Lagrangian one obtains

$$\mathcal{L}_{\text{pion}} = \frac{1}{2}[(\partial_\mu \boldsymbol{\phi})^2 - m_\pi^2\boldsymbol{\phi}^2] \underbrace{- \frac{1}{4f_\pi^2}\left[\boldsymbol{\phi}^2(\partial_\mu \boldsymbol{\phi})^2 - \frac{1-\frac{\xi}{2}}{2}m_\pi^2(\boldsymbol{\phi}^2)^2\right]}_{\mathcal{L}_{\pi\pi}}. \tag{D.45}$$

Olsson and Turner [Ols-68] extended Weinberg's covariant-derivative formalism to the full Lagrangian containing pion-nucleon fields relevant to single-pion production and found

$$\mathcal{L}_{\text{int}} = \mathcal{L}_{NN\pi} + \mathcal{L}_{NN\pi\pi\pi} + \mathcal{L}_{NN\pi\pi} + \mathcal{L}_{\pi\pi}, \tag{D.46}$$

where

$$\mathcal{L}_{NN\pi} = \frac{g_{\pi N}}{2m_N}\overline{N}\gamma^\mu\gamma^5\boldsymbol{\tau}N \quad \partial_\mu\boldsymbol{\phi}^2, \tag{D.47}$$

$$\mathcal{L}_{NN\pi\pi\pi} = \frac{g_{\pi N}}{2m_N}\frac{1}{4f_\pi^2}\overline{N}\gamma^\mu\gamma^5\boldsymbol{\tau}N \cdot (\partial_\mu\boldsymbol{\phi})\boldsymbol{\phi}^2, \tag{D.48}$$

$$\mathcal{L}_{NN\pi\pi} = -\frac{1}{4f_\pi^2}\overline{N}\gamma^\mu\gamma^5\boldsymbol{\tau}N \cdot (\boldsymbol{\phi} \times \partial^\mu\boldsymbol{\phi}), \tag{D.49}$$

$$\mathcal{L}_{\pi\pi} = -\frac{1}{4f_\pi^2}\left[\boldsymbol{\phi}^2(\partial^\mu\boldsymbol{\phi})^2 - \frac{1-\frac{\xi}{2}}{2}m_\pi^2(\boldsymbol{\phi}^2)^2\right] \tag{D.50}$$

This Lagrangian provides the basis for calculation of $\pi N \rightarrow \pi\pi N$ production amplitudes near threshold, the equation (4.20). The $\pi N \rightarrow \pi\pi N$ total cross sections and the s-wave $\pi\pi$ scattering lengths are expressed in terms of the single parameter, ξ. The physical meaning of ξ is revealed in σ commutator

$$[Q^{5a}, \partial_\mu A_\mu^b] = if_\pi m_\pi^2\left[\delta^{ab}\left(f_\pi - \frac{\phi^2}{2f_\pi}\right) + \frac{\xi}{4f_\pi}(\delta^{ab}\phi^2 + 2\phi^a\phi^b)\right], \tag{D.51}$$

where it is a measure of $I = 2$ component and expresses a departure from an assumption that σ commutator is proportional to the σ field. In the quark model the commutator (D.51) reduces to a pure isospin scalar $\langle m_q\rangle(\bar{u}u + \bar{d}d)$, favouring value $\xi = 0$.

Appendix E

1. Design of the Charged Particle Detectors

The overall mechanical and optical characteristics of the charged particle detectors used in the experiment are described in the main body of the thesis. This Appendix justifies the particular design decisions.

The design of our charged particle detectors had to accommodate several conflicting requirements. Fast timing response and good light output were factors in deciding to build the counters from plastic material. The Bicron BC408 plastic (equivalent to PILOT F from Nuclear Enterprises) was chosen for the scintillator detector and ultraviolet-transparent (UVT) acrylic plastic for the light guide. BC 408, when cast in 2 × 20 × 200 cm^3 sheet, has a measured risetime of 0.9 ns and a decay time of 2.1 ns, resulting in a 2.5 FWHM ns pulse width. The light output relative to anthracene is 64%, light attenuation length 210 cm, and the wavelength of maximum emission is 425 nm [Bic-89]. The figure-of-merit defined as an integral of relative light output from the scintillator convoluted with the light guide wavelength transparency was 2.08 times better than that of the poorest choice (BC 404 plastic and commercial grade ultraviolet-absorbing guide).

The need for tight packaging of the CP detectors and very limited space available between the π^0 spectrometer detector arms guided the selection of the detector shape in the form of truncated pyramids. The kinetic energies of the ejectiles from $\pi^+ p \rightarrow \pi^+ \pi^0 p$ reaction at the highest incident pion energy of 260 MeV determined the length of the detectors.

The scattering of pions, the target geometry and the beam profile forced the choice of angles of the truncated pyramidal shapes. All these effects were taken into account in a Monte Carlo simulation based on `PSTOP` modular codes [Zio-86]. Figure E.1 shows the most constraining case: the stopping size distribution of 100 MeV pions in detector material relative to the detector surface.

Previous experience with the LEP beam line indicated that the incident pion beam with an intensity of 1-5 × 10^7 π^+ s^{-1} could be focused into a well collimated spot ~1.0 cm FWHM regardless of target. The front face detector dimensions were limited by the expected background flux of scattered pions and by muons coming from in-flight pion decays and desired angular resolution. Signal pile-up were kept below 5%. Bigger "pion" detectors positioned at polar angles $\geq 40°$ used 4×4 cm^2 hodoscope arrays in line with the desired charged particle direction resolution of ~3°.

Treatment of the detector surfaces and light guide design were determined by the stringent requirement on uniformity of the scintillator light collection. The starting point is an

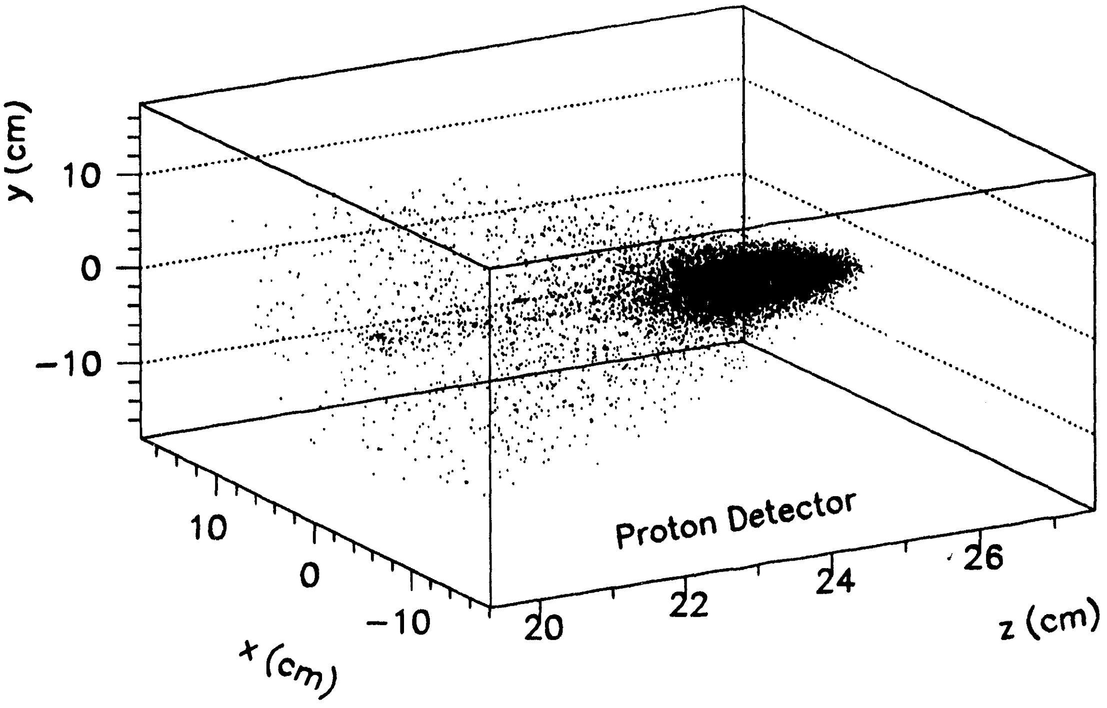

Figure E.1 The three dimensional stopping distribution of 100 MeV π^+'s incident along the z axis of plastic $CH_{1.1}$ detector ($\rho = 1.032$ g/cm^3). The FWHM of the distribution in x and y is 0.9 cm and in z 1.4cm. The FWTM widths are 5.0 cm in x and y and 3.0 cm along the incident axis.

assumption that for every MeV of energy deposited in plastic 100 scintillation photons are generated [Leo-87]. In the Monte Carlo code the detector volume was subdivided into 4128 one cubic centimeter bins and 10^4 photons were generated with an isotropic distribution from the center of every bin and propagated through the geometrical volume of detector. This CPU-intensive calculation was run on a DECstation 5000 computer using a highly optimized program `OPTICS` [Wri-89]. The propagating material was described by a refractive index and attenuation length. Different types of the light reflection were associated with different surface types, and the detection circle was defined at the light guide exit side. The possible processes at interfaces are specular and diffuse reflection with predefined probabilities as well as absorption and refraction. Output of the `OPTICS` photon-propagating code is the number of photons processed, the number of photon lost to attenuation, number of surface absorptions, number of "overbounced" photons (making $\geq$1000 steps inside a detector) and number of detected photons. Quantum efficiency of the PM tube entered as an input constant.

A variety of diverse detectors, with light guide shapes and dimensions consistent with

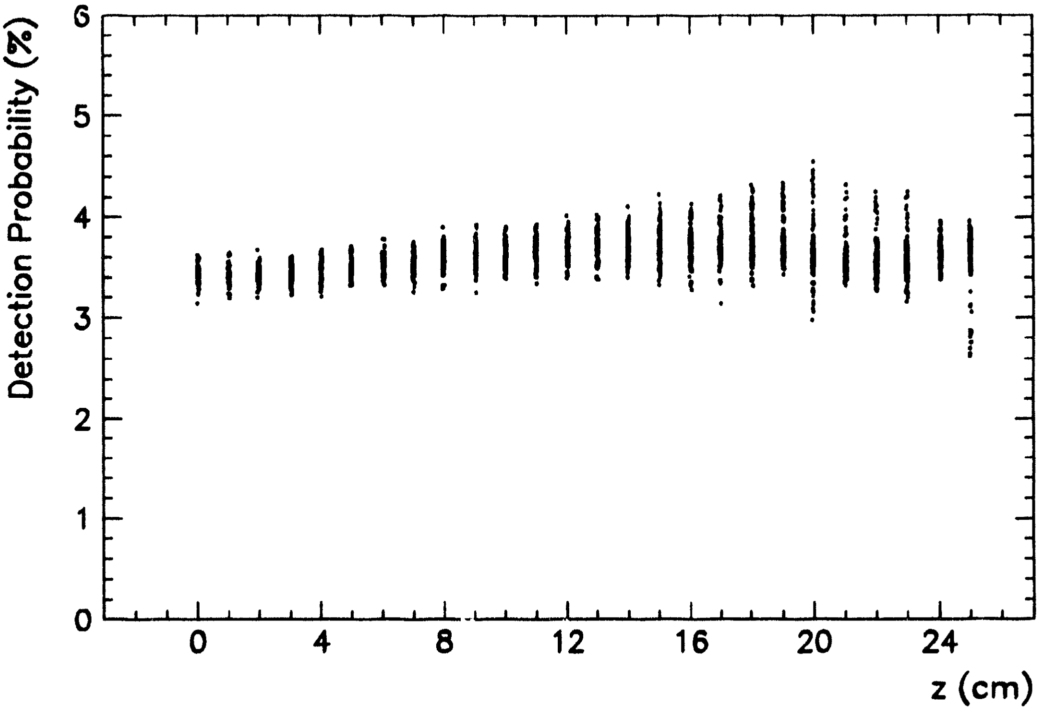

Figure E.2 Monte Carlo simulated light collection throught the volume of an E "pion" counter coupled to 12 cm phototube with quantum efficiency $QE = 0.27$. The detector side surfaces were diffuse reflectors ($dI/d\theta \propto \cos\theta_{\text{out}}$) with reflectivity coefficient 96%, the front face is covered with the imperfect "black" absorber (reflectivity 10%) over the air gap and the end face is polished. The acceptable ($\leq 5\%$) non-uniformity along 25 cm long detector z axis is revealed in this scatter-plot for unrestricted transverse coordinates.

the requirements described in preceding paragraphs, and different surface treatments, PMT's sizes and efficiencies was studied in high-statistics Monte Carlo runs.

The conclusions were: (i) the detector side surfaces had to be covered with high-reflectivity diffuse paint, (ii) the detector entrance face had to be polished and covered with black paper in order to insure linearity between the generated and detected light through the active volume of the detector. The selected dimensions of the counter front and end faces were $10\times18\times25$ cm^3 to $20\times32\times3$ cm^3 for the "pion" detectors and 7×7 to 8×8 cm^2 for the smaller "proton" detectors. The light guides were chosen to be 16 cm long. Bicron BC620 diffuse reflector paint, based on a special grade of titanium oxide in a water soluble binder, was applied directly to the detector side surfaces. It is a highly efficient reflector particularly above 410 nm where its reflectivity coefficient levels off at 96% [Bic-91]. The quality of our design for the main "pion" detectors is illustrated in Figure E.2: the PMT detection probability of scintillation photons is shown as a function of distance along the detector axis. The predicted position-dependent non-uniformity of energy resolution is ~ 5%.

The average collection probability of $(3.63 \pm 0.19)\%$. The resolution measured later with a monoenergetic radioactive ^{90}Sr source indicated ~ 300 photoelectrons per MeV.

To reinforce confidence in these results, a relatively complicated shape was cut from plastic scintillator sheet and incorporated into a cosmic ray coincidence setup (Figure E.3). Light output for cosmic ray triple coincidences was measured at four different points along the axis of the calibration detector. Absolute photon detection probability for the same points are calculated in the Monte Carlo package `OPTICS` described above. Very good agreement was found (Figure E.4), reaffirming the confidence in the design simulation tools. Increase in the photon collection probability for sources originating near front (end) faces is a simple solid-angle effect. For a long rectangular plastic piece with thickness a and the index of refraction n_r a straightforward derivation [Wri-90] indicates that collection probability is proportional to

$$P \sim \sqrt{(1 - \frac{1}{n_r^2})} - \frac{2z}{\sqrt{(4z^2 + a^2)}}, \tag{E.1}$$

where z is the source distance from the perfectly polished (front) face. The behavior for our detectors is modified by light refraction losses on the slanted detector side surfaces.

The absolute probability of scintillator light collection as a function of a position within the counter were passed to the `GEANT3` general purpose detector simulation package [Bru-87]. Monoenergetic positive pions and protons were "thrown" into charged particle fiducial areas from the target space. Energy deposited by the particles in each interaction step in the detector volume was converted into a number of scintillating photons and multiplied with the photon collection probability stored in the look-up table. The resulting simulated detector responses to the positively charged pions is shown in Figure E.6. They have energy resolution $\Delta E/E \sim 5\%$ in the region 10-100 MeV and deliver $\sim$250 photoelectrons/MeV throughout these energies. The simulated photoelectric responses to the stopping protons have equally satisfactory energy resolution.

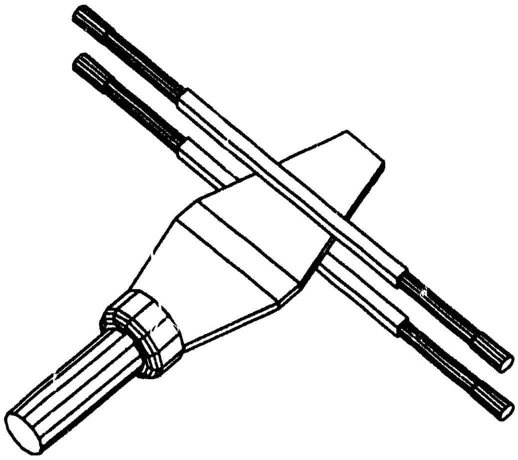

Figure E.3 Shematic drawing of the cosmic ray calibration setup. A 1 cm thick shape was cut from BICRON BC 408 plastic sheet and wrapped with aluminum foil that approximately a 90% specular reflector. A 7.5 cm THOR-EMI 9821QB phototube was grease-coupled to the tapered detector end. Two 30 cm long plastic tags with 1.5 × 1.5 cm^2 cross section viewed from the both ends with 1-1/8 inch HAMAMATSU R1355 phototubes were placed above and below the detector. The data acquisition electronics were triggered by triple coincidences between the tag counters and detector, and all five channels of ADC and TDC data were written to tape. The Landau-shaped spectra were recorded for four different positions of the tag detectors along the detector axis.

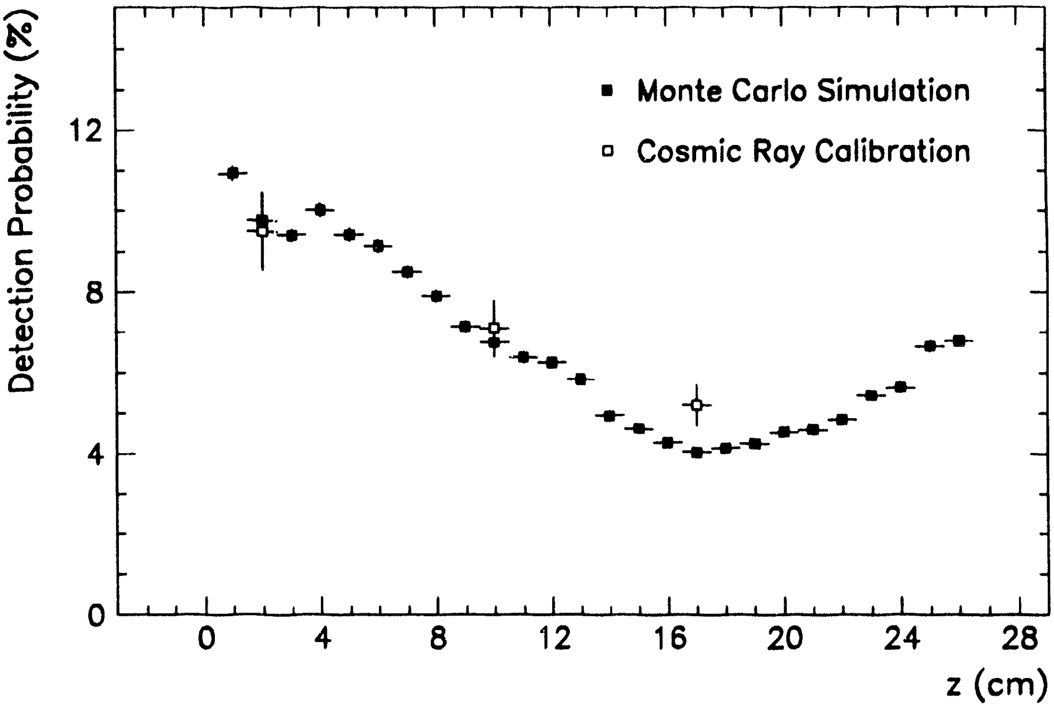

Figure E.4 Agreement between the Monte Carlo simulated light collection probability distribution and laboratory measurements performed with the cosmic ray calibration apparatus in Figure E.3. Dependence of photon detection probability upon the cosmic ray position along the detector axis is shown. Three measurements are expressed relative to the fourth one that was 1 cm away from the PMT face.

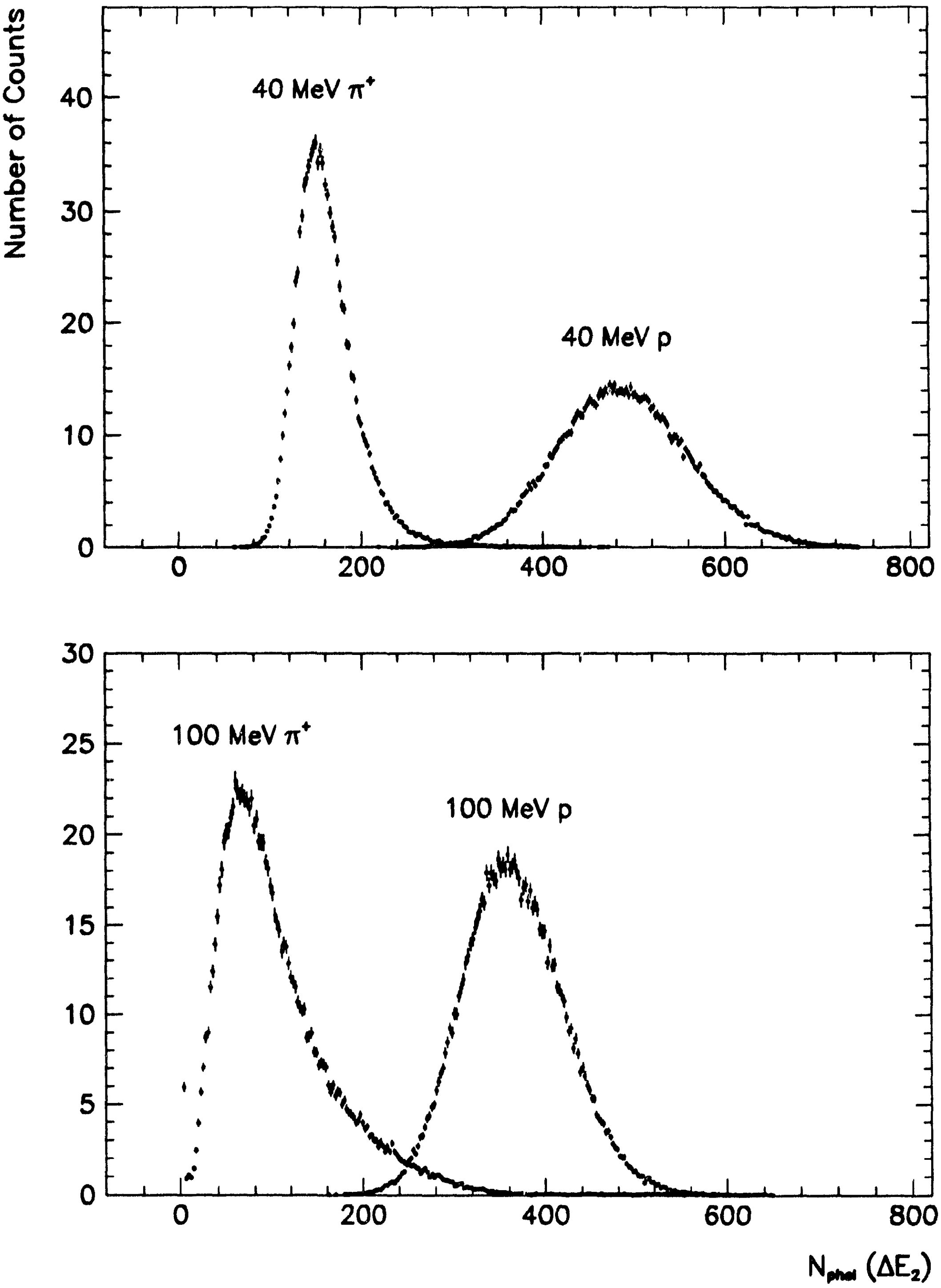

Figure E.5 Monte Carlo energy spectra of monoenergetic pions and protons in 2.5 cm thick ΔE_2 detector. Landau straggling calculated using the PSTOP code [Zio-85] is additionally broadened by photoelectron statistics, and 10% gain drifts. For the highest energy particles of interest (100 MeV), particle identification efficiency is $\geq 97\%$, based on the ΔE_2 counter alone.

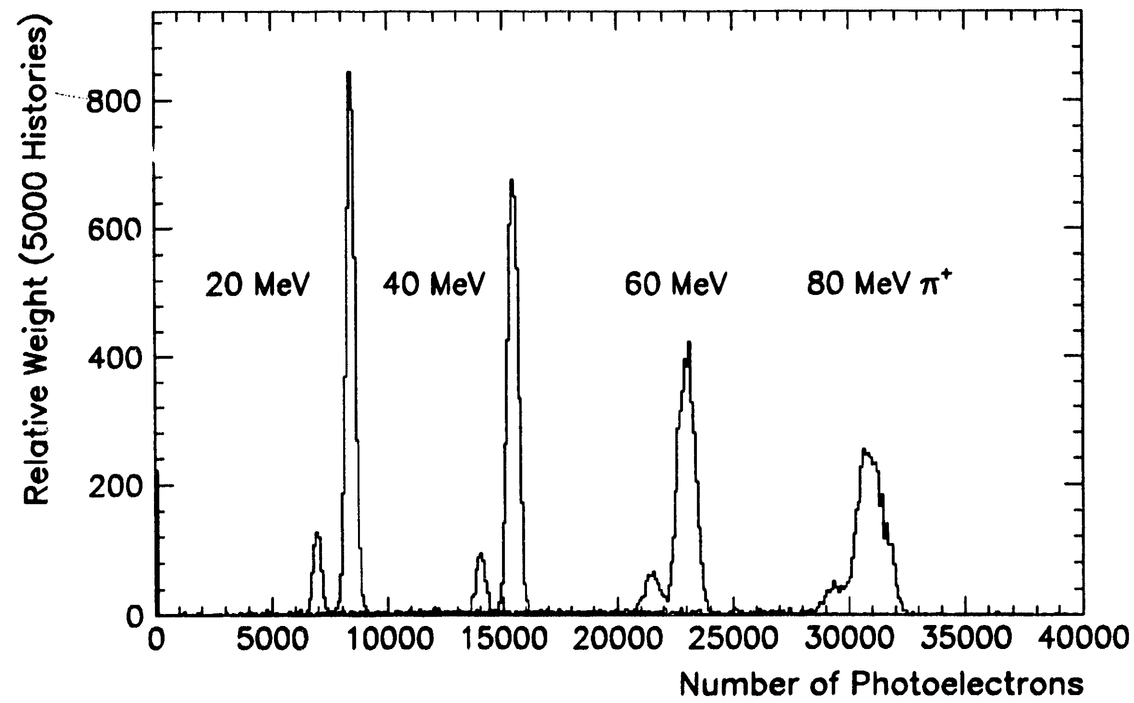

Figure E.6 Monte Carlo simulated responses of a "pion" detector to monoenergetic pion ejectiles from the reaction $\pi^+p \rightarrow \pi^+\pi^0p$. The expected energy resolution $\Delta E/E$ is ~5%. Scintillator light collection probabilities illustrated in Figure E.2 were used as an input to the GEANT3 calculation of pion energy deposition.

Appendex F

List of Symbols

The quantities listed below are defined, explaned or first used on the pages indicated

$\|a(\pi\pi \rightarrow \pi\pi N\|$	dimensionless magnitude of the reduced matrix element	159
$\|a_0(\pi\pi \rightarrow \pi\pi N\|$	dimensionless magnitude of the reduced matrix element at threshold	143
A	atomic weight	78
$\mathcal{A}^D_{ab}$	acceptance for *ab* final state in detector D	121
$\mathcal{A}^{(i)}$	matrix element for Feynman diagram (i)	141
B_i	π^0 spectrometer lead glass total absorption blocks, $i = 1, \ldots, 15$	36
c	speed of light	78
C_i	π^0 spectrometer converter planes, $i = 1, 2, 3$	36
CM	center of momentum frame	119
d_{γ_1}, d_{γ_2}	distances of π^0's gammas from the center of scattering chamber end plates (cm)	26
$\mathrm{d}\Omega$	element of solid angle	57
E_i, E_f	nucleon energies in the initial and final state	140
E_{γ_1}, E_{γ_2}	energies of gamma rays in π^0 decay	31
f_A	weak axial current form factor	2
f_{abs}	loss due to the absorption of π^0 photons preceding conversion	123
f_e	beam electron fraction	86
f_p	beam proton fraction	77
f_V	weak vector current form factor	2
f_π	pion decay constant	2
$G(p_1, \ldots)$	unsymmetric Gram Determinant	176
$g_{\pi N}$	pion-nucleon coupling constant	2
I	particle isospin	140
i_m	beam ion chamber scaler count	78
I_c	beam ion chamber constant	86
I_{ex}	ionization potential (eV)	79
$I_{\pi\pi}$	isospin of $\pi\pi$ system	5
$\mathcal{H}$	Hamiltonian	178
$\mathcal{L}$	Lagrangian	176
$\mathcal{L}_{\mathrm{int}}$	interaction Lagrangian	180
$\mathcal{L}_N$	chiral-symmetry-breaking part of the Lagrangian, tensor of rank N	179
LAB	laboratory reference frame	170
m	nucleon mass	140
m_e	electron mass	78
MIP	minimum ionizing particle	54
m_3	mass of the missing third (undetected) particle	123
m_π	pion mass	31
n	index of refraction	184

$n_{\rm rl}$	π^0 spectrometer fiducial area constraint expressed in terms of RL	89
N	nucleon field	176
N_a	Avogardo's number	78
N_L, N_R	left- and right-handed nucleon fields	177
$N_{\rm phel}$	number of photoelectrons	186
$N_{\pi^\pm}$	incident $\pi^\pm$ intensity (s^{-1})	92
p	four-momentum	140
p_0	$\pi N \to \pi\pi N$ threshold momentum, nominal beam momentum (MeV/c)	78
$\mathbf{p}$	spacelike part of p, $\mathbf{p} = (p^1, p^2, p^3)$	171
$p_{\pi^\pm}$	magnitude of incident $\pi^\pm$ momentum (MeV/c)	17
P	magnitude of $\mathbf{p}$	168
$\mathbf{Q}$	3-momentum vector of incident pion in CM frame	140
$r_k, r^{(i)}, \bar{r}^{(i)}$	random number uniformly distributed within $(0, 1)$	175
R	nominal spectrometer radius, target-to-first-converter distance (cm)	35
$R_{e^\pm}$, R_γ, $R_{e\gamma}$	positron, gamma and coincidence activation rates	165
R_3	three particle final state phase space integral	141
r_e	classical electron radius	78
s	total energy squared in the center-of-momentum system	167
s_i	two-particle invariant mass squared, $s_i = (p_i + p_{i+1})^2$	167
s_{ij}	two-particle invariant mass squared, $s_{ij} = (p_i + p_j)^2$	167
S_i	π^0 spectrometer scintillator, $i = 1, 2, 3$	36
s_{ij}	geometrical solid angle subtended by the scintillator pair ij	48
s_f	prescaled fraction for CP singles events	78
λ_1	helicity angle in the dipion rest frame	171
t, t_i	invariant momentum transfer squared	167
$t^\pm$	values of t in forward and backward directions	171
t_x	target thickness in terms of the number of scattering centers per barn	78
T_0	beam LAB kinetic energy at threshold of $\pi N \to \pi\pi N$	155
T	matrix element squared	140
$t^r_{\pi^0}$	raw π^0 TDC value (ns)	45
$t^c_{\pi^0}$	software-corrected π^0 timing (ns)	45
T_p	proton kinetic energy (MeV)	99
$T_{\pi^\pm}$	incident $\pi^\pm$ kinetic energy (MeV)	17
T_{π^0}	π^0 LAB kinetic energy (MeV)	31
V_i	π^0 spectrometer veto, $i = 1, 2$	36
w_k	weight in Monte Carlo integration	171
$w(x)$	distribution in variable x	171
X	γ-γ energy sharing parameter	31
$x_{\rm J(K)}, y_{\rm J(K)}, z_{\rm J(K)}$	π^0 conversion point coordinates in the J(K) arm	45
$Y_{ab\to 123}$	measured yield for $ab \to 123$ reaction	92
z	charge of the incident particle in units of e	78
Z	atomic number	78

α	infinitesimal rotation angle in isospin space 176
α_l^I	$\pi\pi$ scattering length in the state with isospin I and angular momentum J 143
β	infinitesimal parameter of chiral transformation 176
η	opening angle of the π^0 spectrometer crates 31
η_{cl}	computer live time fraction 71
η_{vp}	J×K π^0 spectrometer veto live time fraction 71
ΔE_1	light-equivalent energy deposited in thin ΔE_1 counter 57
ΔE_2	light-equivalent energy deposited in a thick ΔE_2 counter 57
ΔE	light-equivalent energy deposited in the total absorption CP detector 57
Δp	beam momentum spread (MeV) 7
$\Delta x_b \times \Delta y_b$	horizontal and vertical FWHM beam profiles 17
$\Delta x_m \times \Delta y_m$	x and y MWPC conversion point resolution 89
$\Delta x_2 \times \Delta y_2$	fiducial area cut at the second converter 88
ϵ_b	detection efficiency correction due to electromagnetic shower baksplash 48
ϵ_{ct}	π^0 spectrometer J×K converter "transparency" to charged particles 48
ϵ_c^γ	single-plane γ conversion efficiency 48
$\epsilon_{e^\pm}$, ϵ_γ, $\epsilon_{e\gamma}$	instrumental efficiencies of the activation apparatus 165
ϵ_m	weighted MWPC instrumental efficiency 48
ϵ_s	weighted J×K scintillator efficiency 48
ϵ_t	efficiency of the π^0 tracking algorithm 48
ϵ_{π^0}	overall π^0 detection efficiency 48
$\epsilon_{\pi^0}^{jk}$	π^0 conversion probability in J×K arms 48
ϕ	renormalized pion field 178
$\Gamma_{\pi^0\rightarrow\gamma\gamma}$	branching ratio for the decay $\pi^0 \rightarrow \gamma\gamma$ 92
Γ_J	photon triggerin J arm 37
Γ_K	photon trigger in K arm 37
Γ_9	π^0 trigger—EVENT 9 36
χ_i, χ_f	spinors of the initial and final state nucleon 140
θ	polar angle, polar angle of the π^0 spectrometer crates 31
θ^μ	beam muon cone opening angle 22
θ_{12}	angle between $\mathbf{p}_1$ and $\mathbf{p}_2$ 119
Θ	step function 169
ϕ_b, ϕ_a	Treiman-Yang angle in the rest frame of particles 2 and 3 (1 and 2) 119
λ_1, λ_3	helicity angle in the rest frame of particles 2 and 3 171
$\lambda(x, y, z)$	kinematic function related to Δ_2 169
μ	particle mass 2
π	pion field 176
θ_{γ_1}, θ_{γ_2}	LAB polar angle of gamma rays π^0 decay 31
θ_{π^0}	π^0 LAB polar angle 31
$\theta_{\pi\pi}$	dipion polar angle in the $\pi\pi N$ barycentric frame 123
σ	Pauli spin matrices 142
σ^{scx}	single charge exchange cross section 92

σ_t	angle-intergated cross section	8
$\sigma_{\pi^\pm}$, $\sigma_{e^\pm}$, σ_p	activation cross sections for pions, electrons and protons	79
τ	lifetime	1
$\boldsymbol{\tau}$	Pauli isospin matrices	176
ϕ	azimuthal angle	57
Ω	solid angle	57
ξ	chiral-symmetry-breaking parameter	2
ω_Q, ω_1, ω_2	energies of the incident and outgoing pions	140
$*$	superscript for CMS quantities	143
θ_{b3}^{R23}	Jackson angle in the dipion rest frame	119

Appendix G

List of Physical Constants

Quantity	Symbol, Equation	Value	Reference
speed of light	c	299792458 m s^{-}1	[Her-90]
Planck constant	h	$6.6260755(40) \times 10^{-34}$ J s	[Her-90]
reduced Planck constant	$\hbar \equiv h/2\pi$	$1.05457266(63) \times 10^{-34}$ J s	[Her-90]
conversion constant	$(\hbar c)^2$	$3.8937966(23) \times 10^{8}$ MeV$^{-2}\mu b$	[Her-90]
proton mass	m_p	938.27231 ± 0.00028 MeV	[Her-90]
neutron mass	m_n	939.56563 ± 0.00028 MeV	[Her-90]
nucleon mass	$m_N = \frac{1}{2}(m_p + m_n)$	938.91897 MeV	[Her-90]
charged pion mass	$m_{\pi^\pm}$	139.5675 ± 0.0004 MeV	[Her-90]
neutral pion mass	m_{π^0}	134.9739 ± 0.0006 MeV	[Her-90]
πNN coupling constant	$g_{\pi NN}/4\pi$	13.4 ± 0.1	[Arn-90]
$g_{\pi NN}$ in chiral limit	$g_{\pi NN}^{CL}$	13.0	[Coo-90]
pion decay constant	f_π	92.6 ± 0.2 MeV	[Hol-90]
axial vector form factor	$g_A(q^2 = 0)$	1.261 ± 0.004	[Hol-90]
$g_A(q^2 = 0)$ in chiral limit	$g_A^{CL}(0)$	1.29	[Coo-90]

Appendix H

Program PIANG_PAW.FOR

```
C     PROGRAM PIANG86—PARAM‹OUT‹OUTPUT/OUT‹INPUT/PARAM‹TAPE5/INPUT
C     $‹TAPE1/INPUT‹
C     $TAPE6/OUTPUT—
C
C Sign convention———lab coord system
C       The Z axis is the direction of the initial beam
C       The X axis is up
C       THE Y axis is beam right
C       X—Y—Z form a right—handed coord system▷
C
C
C 1—POST.POST / 1▷0
C        Scattering plane is horizontal
C        Sign convention———detector coords
C                —X—direction is towards larger opening angles
C                —Z is into the detector
C                X—Y—Z form a right—handed coord system▷
C        Sign convention———target coords
C                —THTGT has tgt normal pointing beam left
C                —D0 is downstream displacement from nominal tgt position
C
C 2—POST.POST / 2▷0
C        Scattering plane is vertical
C        Sign convention———detector coords
C                —X—direction is towards larger opening angles
C                —Z is into the detector
C                X—Y—Z form a right—handed coord system▷
C        Sign convention———target coords
C                —THTGT has tgt normal pointing down
C                —D0 is downstream displacement from nominal tgt position
c
C INPUT CARDS
C
C        CARD 1—2 are for detector coords and resolutions▷
C        CARD 3 are for beam properties
C        CARD 4 is for target properties
C        CARD 5 is for general program parameters
C        CARD 6 gives theta bins
C
C         FORMAT—8F10▷0—
C         CARD 1        R1‹X1‹Y1‹R2‹X2‹Y2
C         CARD 2        ETA‹THTA—DETECTOR—‹GAMR‹RMSX‹RMSY
C         CARD 3        TP‹DETP‹XSIZE‹YSIZE‹Q
C         CARD 4        THTGT—TARGET—‹D0‹DEDX‹THCK‹ESTRAG
C         CARD 5        POST‹XCUT‹FMAX‹TIMLMT‹THCUT‹CSTART
C         CARD 6        THETCT—1—‹▷▷▷▷    ‹THETCT—6—
C         CARDS 7 to 17 title cards for plots —may be blank—
C
```

```
C
CARD 1
C R←1←‘R←2← is distaance from target to detectors←CM←
C X←1←‘X←2← is X-WIDTH←MWPC← of detector←CM←,XMAX/X←I←/2
C Y←1←‘Y←2← is Y-WIDTH←MWPC← of detector←CM←,YMAX/Y←I←/2
C
CARD 2
C ETA is the angle between the detector bisectors▷ ←DEG←
C THTA is the nominal setup scattering angle ←DEG←
C GAMR is the energy resolution fwhm in ϱ for gammas at 100 MEV
C RMSX  is full width position resolution ←GAMMA← in X Direction ←CM←
C RMSY is full width position resolution ←GAMMA← in Y direction ←CM←
C
CARD 3
C TP is the kinetic energy of the incident beam▷ ←MEV←
C DETP is the incident beam smearing ←MEV-full width square dist←
C XSIZE is the vertical   rms beam size of a gaussian distribution▷ ←CM←
C YSIZE is the horizontal rms beam size of gaussian distribution▷ ←CM←
C Q is the reaction Q-value
C
CARD 4
C THTGT is the angle between the targetφs normal and the Z axis▷ ←DEG←
C D0 is target displacement ←CM←
C DEDX is the incident beam DE/DX ←MEV/CM← in the target
C THCK is the target thickness ←CM←
C ESTRAG is the straggling parameter SIGMA/SQRT←DEDX→THCK→ESTRAG←
C
CARD 5
C POST / 1▷0 OR 2▷0
C XCUT is the cutoff value in detected X such that ABS←X← is ▷LE▷ XCUT
C FMAX is the number of success through monte carlo loop
C TIMLMT is the time limit imposed for running the code
C THCUT and CSTAR are cuts to limit the range of phase space for pizero▷
C They speed up the program▷
C The pizero direction is thrown uniformly into a cone centered on
C the detector bisector the cone has a half angle of THCUT ←DEGREES←
C CSTAR---cosine of gamma center of mass angle ranges from →CSTAR to
C -CSTAR▷
C Start with CSTAR / XCUT→2→FWHM gamma resolution at WPI0
C Start with THCUT/45▷
C To determine final value look at graph 8 for CSTAR
C Set CSTAR/XCUT→3→SIGMA←8←
C Look at graph 3 for THCUT
C Set THCUT so that the detector acceptance shown in plot 3
C goes to zero at an angle less than THCUT
C
CARD 6
C THTTCT←1←‘←2← are limits of the first angle bin←DEG←
C    φφ    3  4        φφ          second    φφ
C    φφ    5  6                    third   φφ
C    φφ    7  8        φφ           fourth    φφ
C
C         Variables of 2 gammas and 2 arms
```

```
REAL*4 XX(6), TT(10), CC(25)
REAL*4 M3PP, M3PR
COMMON /PAWC/H(1000000)
COMMON/GENIN/NP,ATECM,AMAS(18),KGENEV
COMMON/GENOUT/APCM(5,18),AWT

DIMENSION BIN(4)     !Counts in each angle bin
DIMENSION CE(2)      !Cosine of ETA/2, J/K arm
DIMENSION CF(2)      !Direction cosine of floor angle
DIMENSION CI(2)      !Direction cosine of inclination
DIMENSION COSX(2) !Direction cosine from
DIMENSION COSY(2) !        face of target
DIMENSION COSZ(2) !        center of crate
DIMENSION COSXL(2) !Direction cosine between
DIMENSION COSYL(2) !       lab gamma momentum and
DIMENSION COSZL(2) !       detector position vector
DIMENSION COS0(2)  !Ang. betwn. interaction pt. vector and detector
DIMENSION COSDD(2,2) !Ang. betwn. gamma direction and detector center
DIMENSION CT(2)      !Cosine theta-spectrometer, J/K arm
DIMENSION DDX(2,2) !Smeared conversion pt. in detector
DIMENSION DDY(2,2) !        coordinate system
DIMENSION DSAB(4) !dSAB, also error in monte carlo solid angle
DIMENSION DX(2,2)   !Physical conversion pt. coordinates
DIMENSION DY(2,2)   !        in detector coordinate
DIMENSION DZ(2,2)   !        system
DIMENSION EG(2)      !Smeared lab gamma energies
DIMENSION EPH(2)    !Thrown lab gamma energies
INTEGER*2 ERRORCOUNT !PI0s w/non-physical energies EP
LOGICAL*2 GAMMA_ARM !Function, .T. if gammas hit both arms
DIMENSION IBIN(4)   !Integer counts in angle bins
INTEGER*2 JK         ! =1 J arm, =2 K arm
DIMENSION PGX(2)    !Measured lab gamma vector
DIMENSION PGY(2)    !        momentum
DIMENSION PGZ(2)    !        components
DIMENSION PHG(2)    !Measured lab gamma phi
DIMENSION PX(2)     !Thrown gamma vetor
DIMENSION PY(2)     !        momentum
DIMENSION PZ(2)     !        components
DIMENSION R(2)      !Radius from target to face of detector
DIMENSION RGAM(2,2) !Magnitude of Gamma position vector
DIMENSION SAB(4)    !Solid Angle of bin
DIMENSION SE(2)     !Sine of ETA/2, J/K arm
DIMENSION ST(2)     !Sine of theta-spectrometer, J/K arm
DIMENSION THETCT(8) !Bin theta limits, 4 bins
DIMENSION THG(2)    !Measured lab theta-gamma rel. to beam direction
DIMENSION VX(2)     !Trown lab gamma vector
DIMENSION VY(2)     !        direction cosines
DIMENSION VZ(2)     !        from center of face of target
DIMENSION WW(2)     !Gamma vector momentum magnitude
DIMENSION WWX(2) !Smeared lab gamma vector
DIMENSION WWY(2) !       from interaction pt.
DIMENSION WWZ(2) !       to detector face
```

```
        DIMENSION WX(2,2) !Thrown lab gamma
        DIMENSION WY(2,2) !          from interaction pt.
        DIMENSION WZ(2,2) !          to detector face
        DIMENSION X(2)    !X-MWPC width (CM)
        DIMENSION XMAX(2) !X half width of detector (CM)
        DIMENSION Y(2)    !Y-MWPC width (CM)
        DIMENSION YMAX(2) !Y half width of detector (CM)
        REAL*4   DET_I(14),DET_F(14),DET_DI(14),DL(14),DET_R(14)
        REAL*4     DET_TH(14),DET_PH(14)
        REAL PP_THR(150), PR_THR(150) ! charged particle thresholds

        COMMON/HISTCM/NXT(60),XZERO(60),XWIDTH(60)
      CHARACTER*4 TAGM(6),TAGT(10),TAGC(25)
      REAL*4 MPR,MPP,MP0
c detector inclinations
      DATA DET_I /-53.41,-49.42,-65.00,40.00,60.00,80.00,
     +            -18.00,-22.77,-18.09,-30.00,-35.35,-30.85,-42.00,20.00/
c detectors floor angles
      DATA DET_F /-32.98,28.15,4*0.00,
     +            0.00,-12.90,12.73,0.00,-14.96,15.05,2*0.00/
c detectors delta_inclination
      DATA DET_DI/10.78,10.78,11.89,5.57,6.01,6.01,
     +            8*2.86/
c detectorsφ half-widths
      DATA DL/3*4.,3*8.,8*2.5/
c detector-to-target distance
      DATA DET_R/2*42.,38.,41.,2*38.,8*50./
c detector polar angles
      DATA DET_TH/60.,55.,65.,40.,60.,80.,18.,26.,22.,30.,38.,34.,
     +             42.0,20./
c detector azimuthal angles
      DATA DET_PH/202.,158.,180.,0.,0.,0.,180.,208.,146.,180.,
     +             200.,156.5,180.,0./
c pion threshold
      DATA PP_THR/3*0.,0.037037,0.111111,0.137931,0.241379,0.627907,
     +             0.868421,0.952381,140*1./
c proton threshold
      DATA PR_THR/10*0.,0.013158,0.063830,0.093333,0.180451,0.20000,
     +             0.232432,0.331288,0.367232,0.460674,0.510753,
     +             0.573529,0.697115,0.75,0.815166,0.945545,0.979592,
     +             0.989305,123*1./

      DATA    NXT/60*120/                 !NXT is the number of channels, max 121
      DATA    XZERO/2*-30.,3*.0,3*-1.,0.,-12.,!XZERO is the centre of the first bin
     1        4*-30.,4*0.,4*0.0,2*-60.,36*0./
      DATA    XWIDTH/2*.5,.5,1.0,1.0,3*.02,1.,! XWIDTH is the bin width
     1        .2,4*.5,4*1.0,4*1.0,2*1.0,36*0./

      DATA TAGM,TAGT/'KIM','THM','PHM','PM','XM','WM',
     1              'KIT','THT','PHT','PT','WT','TY','J','A',2*' '/
      DATA TAGC/'PRH','PPH','KIM','THM','PHM','BIS','XM','WM',
     1        'TPR','TPP','MPP','MRP','TM','TY','J','H','A','TMS',
     1        'MPPS','MRPS','TYS','JS','HS','AS',' '/
```

```
      ICOINC=0
      AWTTOT=0.0
      MPR=0.93827231
      MPP=0.13956755
      MP0=0.1349734

      CALL HLIMIT(1000000)
      CALL HROPEN(2,'E1179NTP','E1179NTP.RZ','N',1024,ISTAT)

      CALL HBOOKN(30,'THROWN PIOS',10,'E1179NTP',2000,TAGT)
      CALL HBOOKN(31,'DETECTED PIOS',6,'E1179NTP',2000,TAGM)
      CALL HBOOKN(33,'COINCIDENCES',25,'E1179NTP',2000,TAGC)
      CALL HBOOK1(41,'THROWN WEIGHTS',40,-2.,2.,0.)

      OPEN (UNIT=1, FILE='PIANG_PAW.INP', STATUS='OLD')
      OPEN (UNIT=101, FILE='AWTTOT.OUT', STATUS='NEW')
      OPEN (UNIT=37, FILE='DISK20:[SCRATCH_LONG.EMIL.TRACK_EFF]
     +                  TR_HIT_260PIO.OUT', STATUS='NEW')

  998 READ(1,1,END=999) ((R(I),X(I),Y(I)), I=1,2)
      READ(1,1) ETA, THTA, GAMR, RMSX, RMSY
      READ(1,1) TIN, DETP, XSIZE, YSIZE, HMAX
      READ(1,1) THTGT, D0, DEDX, THCK, ESTRAG
      READ(1,1) POST, XCUT, FMAX, TIMLMT, THCUT, CSTAR
    1 FORMAT (8F10.0)

C
C     Print out data input page
      IPOST = POST
      IF (IPOST.EQ.1) THEN
      WRITE(6,3998)
 3998 FORMAT(1H1,4X,'PIANG1    1-POST    26.MAR.86  H.BAER'/)
      ELSE
      WRITE(6,3999)
 3999 FORMAT(1H1,4X,'PIANG2    2-POST    26.MAR.86  H.BAER'/)
      ENDIF

      WRITE(6,4000)
 4000 FORMAT(10X,'FIRST DETECTOR')
      WRITE(6,4001)R(1),X(1),Y(1)
 4001 FORMAT(5X, 'RADIAL DISTANCE FROM TARGET  ='F10.3' CM'/5X,
     1          'XWIDTH                       ='F10.3' CM'/5X,
     2          'YWIDTH                       ='F10.3' CM')
      WRITE(6,5000)
 5000 FORMAT(10X,'SECOND DETECTOR')
      WRITE(6,4001)R(2),X(2),Y(2)
      WRITE(6,4500)
 4500 FORMAT(10X,'DETECTOR ORIENTATION')
      WRITE(6,4501)ETA,THTA
 4501 FORMAT(5X, 'ARM SEPARATION              ='F10.3' DEGREES'/
     1       5X, 'SCATTERING ANGLE            ='F10.3' DEGREES')
      WRITE(6,6000)
```

```
 6000 FORMAT(10X,'PIZERO')
      WRITE(6,6001)TIN,XCUT,GAMR,RMSX,RMSY,THTGT
 6001 FORMAT(5X, 'BEAM ENERGY                ='F10.3' MEV'/
    1       5X, 'X CUT                      ='F10.3/
    2       5X, 'GAMMA RES                  ='F10.3' % AT 100 MEV'/
    3       5X, 'GAM POS RES(X)             ='F10.3' CM'/
    4       5X, 'GAM POS RES(Y)             ='F10.3' CM'/
    5       5X, 'TARGET ANGLE               ='F10.3' DEGREES')
      WRITE(6,6002)THCK,D0,XSIZE,YSIZE,DEDX,DETP,HMAX
 6002 FORMAT(5X, 'TARGET THICKNESS           ='F10.3' CM'/
    1       5X, 'TARGET OFF SET             ='F10.3' CM'/
    2       5X, 'RMS BEAM SIZE(X)           ='F10.3' CM'/
    3       5X, 'RMS BEAM SIZE(Y)           ='F10.3' CM'/
    4       5X, 'DEDX IN TARGET             ='F10.3' MEV/CM'/
    5       5X, 'BEAM ENERGY VARIATION      ='F10.3' MEV'/
    6       5X, 'MAX NUMBER OF HITS         ='F10.3' MEV')
      WRITE(6,6003)ESTRAG
 6003 FORMAT(5X, 'DE/DX STRAGGLING PARAMETER  ='F10.3' MEV')
C
C       Constants for monte carlo loop

        PI = ACOS(-1.00)       !3.1415...
        RAD = PI/180.0         !Radians per degree
        XM = 134.964           !PI0 rest mass
        XM2 = XM/2
        ETA = ETA*RAD          !Nominal spectrometer opening angle, radians
        ETA2 = ETA/2
        THTA = THTA*RAD        !Nominal spect. angle rel. to beam, radians
        THTGT = THTGT*RAD
        CA = COS(ETA2)
        SA = SIN(ETA2)
        CH = COS(THTA)
        SH = SIN(THTA)

C     Direction cosines for detector postion vectors
C     2-POST.detector-1 is beam-left' detector-2 is right
C     1-POST.dtector-1 is up'detector-2 is down
      IF (IPOST.EQ.1) THEN
        CE(1) = CA
        CE(2) = -CE(1)
        SE(1) = SA
        SE(2) = -SE(1)
        CT(1) = CH
        CT(2) = -CT(1)
        ST(1) = SH
        ST(2) = -ST(1)

        DO 9 JK =1,2
        COSX(JK) = SE(JK)
        COSY(JK) = CE(JK)*ST(JK)
        COSZ(JK) = CE(JK)*CT(JK)
        XMAX(JK) = X(JK)/2
        YMAX(JK) = Y(JK)/2
```

```
    9   CONTINUE
       ELSE
C         Direction cosines of detector position vectors
C         in terms of floor angle←F←‘inclination←I←
C         used for 2–post transfomations‘lab to MWPC
        SI = CA*SH
        CI(1) = SQRT(1.-SI**2)
        CI(2) =-CI(1)
        SF = SA/CI(1)
        CF(1) = SQRT(1.-SF**2)
        CF(2) = -CF(1)
        COSY(1) = -SA
        COSY(2) =  SA

        DO 10 JK = 1,2
        COSX(JK) = CA*SH
        COSZ(JK) = CA*CH
        XMAX(JK) = X(JK)/2
        YMAX(JK) = Y(JK)/2
   10   CONTINUE
       ENDIF
C
C      Begin monte carlo calculation

       ERRORCOUNT = 0 !No. PI0s w/non–physical energy
       LCT = 0          !No. of PI0 decays which fail XCUT
       MCT = 0          !Monte carlo loop count, no. of trials
       FCT = 0          !FCT replaces NCT in previous version
       DFCT = 1         !DFCT is the increment in FCT.  It takes into account
       ND1 = 0          !        the dependence of conversion efficiency on gamma
       ND2 = 0          !        angle with the detector face.
       NOUT = 0         !No. of PI0 decays whose gammas miss either arm
       NCYCLE = 0       !
       MAX = FMAX       !FCT weighted max number of successes

C        CCUT / 1▷0 – COS←THCUT→RAD←
C        XZERO←4← / THTA–30▷
C        IF ←XZERO←4←▷LT▷0▷← XZERO←4← / 0▷0

C       Zero the event tabs and the histograms
C        CALL HISTZZ←1‘60←

C        DO 100 K/1‘4
C100     BIN←K← / 0▷0

200    CONTINUE
C
C      Enter monte carlo loop
777    MCT = MCT + 1                   !Increment no. of trials

C      Calculate target energy loss and beam energy smearing
       Z00    = THCK*RANF(D)/COS(THTGT)
       ELOSS = DEDX*Z00
```

```
      STRAG = SQRT(ESTRAG*ELOSS)
      STRAG = STRAG*GRAUS(D)
      ELOSS = ELOSS + STRAG
      TINN=0.001*TIN                 ! incident energy in GeV
      TINC   = TIN - ELOSS + .5*(1.-2.*RANF(D))*DETP
      TINC   = TINC*0.001
      CALL GEN_EVENT(TINC,
     +                    CXP,CYP,CZP,
     +                    X3,Y3,Z3,
     +                    X1,Y1,Z1,
     +                    TP0,T3,T1)
c     Scattering angle of thrown pizero
      PP0=SQRT(CXP*CXP+CYP*CYP+CZP*CZP)
      X2=CXP
      Y2=CYP
      Z2=CZP
***
      XT1=X1
      YT1=Y1
      ZT1=Z1
      XT2=X2
      YT2=Y2
      ZT2=Z2
      XT3=X3
      YT3=Y3
      ZT3=Z3
      CALL ANGLES(TINN,XT1,YT1,ZT1,XT2,YT2,ZT2,XT3,YT3,ZT3,
     +             TY,R23_B3,R23_12,ATH)
      CXP=CXP/PP0
      CYP=CYP/PP0
      CZP=CZP/PP0
      POLAR = ACOS(CZP)/RAD       !PI0 lab polar angle rel. to beam direction
      AZIMU = ATAN2(CYP,CXP)/RAD        !PI0 lab azimuthal angle
      IF (AZIMU.LT.0) AZIMU = AZIMU + 360.
      CTI=CXP*SH+CZP*CH
      POLT=ACOS(CTI)/RAD
***
      TT(1)=TP0
      TT(2)=POLAR
      TT(3)=AZIMU
      TT(4)=POLT
      TT(5)=AWT
      TT(6)=TY
      TT(7)=R23_B3
      TT(8)=ATH
      TT(9)=0.
      TT(10)=0.
      AWTTOT=AWTTOT+AWT
      IF (MCT.LT.100000) CALL HFN(30,TT)
***
      T2=TP0
      TP0= 1000.*TP0
```

```
      IF (ABS(CTI).GT.1.) GOTO 777
      IF(CTI.LE.0.001) GOTO 777
      STI=SQRT(1.-CTI*CTI)
      IF (ABS(STI).LE.1.E-37) GOTO 777
      CAZ=CYP/STI
      SAZ=(CXP*CH-CZP*SH)/STI

      THETE = ACOS(CTI)/RAD           !PI0 angle rel to spectrometer bisector

      EP    = TP0 + XM
      IF ((EP*EP).LT.(XM*XM)) THEN
        ERRORCOUNT = ERRORCOUNT + 1
        GOTO 4662                     !Exit monte carlo loop
      ENDIF

      P     = SQRT(EP*EP - XM*XM)
      BETA  = P/EP
      GAM   = SQRT(1./(1. - BETA*BETA))
      PXX   = P*CXP
      PYY   = P*CYP
      PZZ   = P*CZP

C     Throw decay direction in pizero rest frame
      COST = (1.-2.*RANF(D)) !COS(theta-gamma) rel. to PI0 direction

C     Check to see if event passes XCUT
C     Lorentz transform gamma energies to coordinate system with
C     Z-axis along pizero direction
      EPH(1) = XM2*GAM*(1.+BETA*COST)
      EPH(2) = XM2*GAM*(1.-BETA*COST)

C     Spread measured energies by their detector resolutions
      ERR = GAMR / 23.5

      DO 20 I=1,2
   20 EG(I) = EPH(I)+ERR* SQRT(EPH(I))*GRAUS(D)

      XMEAS = (EG(1)-EG(2))/(EG(1)+EG(2))

C     Lorentz transform gamma momenta to coordinate system
c     with Z-axis along pizero direction
      SINT  = SQRT(1.-COST*COST)
      PHY   = 2.0*PI*RANF(D)          !Gamma polar angle rel. to PI0 direction
      PZ(1) = XM2*GAM*(BETA+COST)
      PY(1) = XM2*SINT*SIN(PHY)
      PX(1) = XM2*SINT*COS(PHY)
      PZ(2) = XM2*GAM*(BETA-COST)
      PY(2) = -PY(1)
      PX(2) = -PX(1)

C     Momenta and direction cosines for gammas in lab system
      DO 23 I =1,2
        IF (IPOST.EQ.1) THEN
```

```
          VX(I) = PX(I)*CTI*CAZ - PY(I)*SAZ + PZ(I)*STI*CAZ
          VY(I) = PX(I)*(CTI*SAZ*CH-STI*SH) + PY(I)*CAZ*CH +
     1          PZ(I)*(STI*SAZ*CH+CTI*SH)
          VZ(I) = PX(I)*(-CTI*SAZ*SH-STI*CH) - PY(I)*CAZ*SH +
     1          PZ(I)*(-STI*SAZ*SH+CTI*CH)
        ELSE
          VX(I) = PX(I)*CAZ*CH + PY(I)*(CTI*SAZ*CH-STI*SH) +
     1          PZ(I)*(STI*SAZ*CH+CTI*SH)
          VY(I) = PX(I)*(-SAZ) + PY(I)*CTI*CAZ + PZ(I)*STI*CAZ
          VZ(I) = PX(I)*(-CAZ*SH) - PY(I)*(CTI*SAZ*SH+STI*CH) +
     1          PZ(I)*(-STI*SAZ*SH+CTI*CH)
        ENDIF
        COSXL(I) = VX(I)/EPH(I)
        COSYL(I) = VY(I)/EPH(I)
        COSZL(I) = VZ(I)/EPH(I)
   23 CONTINUE

C     Choose interaction point in target
      X0 = XSIZE*GRAUS(D)
      Y0 = YSIZE*GRAUS(D)

      IF (IPOST.EQ.1) THEN
        Z0 = Z00 + Y0*TAN(THTGT) + D0
      ELSE
        Z0 = Z00 + X0*TAN(THTGT) + D0
      ENDIF

      R0 = SQRT(X0*X0 + Y0*Y0 + Z0*Z0)
      IF (R0.LE.0.0) R0 = 1.
      COSX0 = X0/R0
      COSY0 = Y0/R0
      COSZ0 = Z0/R0

      DO 26 I=1,2
   26 COS0(I) = COSX0*COSX(I) + COSY0*COSY(I) + COSZ0*COSZ(I)

C ▷▷▷▷▷▷▷▷▷▷▷▷▷▷▷▷▷▷▷▷▷▷▷▷▷▷▷▷▷▷▷▷▷▷▷
C       Cosines between lab gamma momenta ←first subscript← and
C       detector position vectors ←second subscript←'

      DO 30 I=1,2
      DO 30 JK=1,2
      COSDD(I,JK)=COSXL(I)*COSX(JK)+COSYL(I)*COSY(JK)+COSZL(I)*COSZ(JK)

C      Length of gamma ray position vectors
      IF (COSDD(I,JK).EQ.0.0) COSDD(I,JK)=1.0E-6
      RGAM(I,JK) = (R(JK)-R0*COS0(JK))/COSDD(I,JK)

C      Lab coordinates of the 4 hit points in the 2 detector planes
      WX(I,JK) = X0 + RGAM(I,JK)*COSXL(I)
      WY(I,JK) = Y0 + RGAM(I,JK)*COSYL(I)
      WZ(I,JK) = Z0 + RGAM(I,JK)*COSZL(I)
```

```
C      Detector coordinates for the hit points
       IF (IPOST.EQ.1) THEN
         CALL ROT1(WX(I,JK),WY(I,JK),WZ(I,JK),CE(JK),SE(JK),
      1            CT(JK),ST(JK),DX(I,JK),DY(I,JK),DZ(I,JK))
       ELSE
         CALL ROT2(WX(I,JK),WY(I,JK),WZ(I,JK),CI(JK),SI,
      1            CF(JK),SF,DX(I,JK),DY(I,JK),DZ(I,JK))
       ENDIF
    30 CONTINUE !do I,JK = 1,2

C      The following replaces original code‘ see REVISIONS▹FOR
C      See if gamma 1 in arm 1‘ gamma 2 in arm 2
       IF (GAMMA_ARM(1,2,DX,DY,XMAX,YMAX)) THEN
         ND1 = ND1 + 1
         JK = 1
C      See if gamma 1 in arm 2‘ gamma 2 in arm 1
       ELSE IF (GAMMA_ARM(2,1,DX,DY,XMAX,YMAX)) THEN
         ND2 = ND2 + 1
         JK = 2
       ELSE                          !Gamma(s) missed
         NOUT = NOUT + 1
         GOTO 200
       ENDIF


C      Smear position vectors and find gamma momenta —detector coordinates—
       DFCT = 1.0
       DO 35 I=1,2
         DDX(I,JK) = DX(I,JK) + RMSX*(0.5-RANF(D))
         DDY(I,JK) = DY(I,JK) + RMSY*(0.5-RANF(D))
         IF (IPOST.EQ.1) THEN        !(lab coordinates, WWX,WWY,WWZ)
         CALL ROT1IV(DDX(I,JK),DDY(I,JK),DZ(I,JK),CE(JK),SE(JK),
      1            CT(JK),ST(JK),WWX(JK),WWY(JK),WWZ(JK))
         ELSE
         CALL ROT2IV(DDX(I,JK),DDY(I,JK),DZ(I,JK),CI(JK),SI,
      1            CF(JK),SF,WWX(JK),WWY(JK),WWZ(JK))
         ENDIF
         DFCT = DFCT/COSDD(I,JK)     !Bin weighted
         JK = 3 - JK
    35 CONTINUE
       XX1 = DDX(JK,1)
       YY1 = DDY(JK,1)
       FCT = FCT + DFCT              !Increment total weighted-counts
C End of revisions
C      The next block of code does not effect solid angle computation▹

C      Compute measured lab quantities for histograms
C      Calculate measured lab gamma vector momenta
       DO 461 I=1,2
       WW(I)  = SQRT(WWX(I)**2 + WWY(I)**2 + WWZ(I)**2)
       PHG(I) = ATAN2(WWY(I),WWX(I))
       THG(I) = ACOS(WWZ(I)/WW(I))
       PGZ(I) = EG(I)*COS(THG(I))
```

```
      PGY(I) = EG(I)*SIN(THG(I))*SIN(PHG(I))
      PGX(I) = EG(I)*SIN(THG(I))*COS(PHG(I))
  461 CONTINUE

C     Calculate measured pizero vector momentum ←from EGφs smeared by gamma
C     energy resolution⊳←
      PPIX = PGX(1) + PGX(2)
      PPIY = PGY(1) + PGY(2)
      PPIZ = PGZ(1) + PGZ(2)

C     Calc measured pizero opening angle
      COSETA = (WWX(1)*WWX(2)+WWY(1)*WWY(2)+WWZ(1)*WWZ(2))/(WW(1)*WW(2))
      ETAP = ACOS(COSETA)/RAD        !Measured ETA
      XTHRO = BETA*COST              !Physical X, not measured X
      CET = 1. - 2./((GAM**2)*(1.-XTHRO**2))
      ETHRO = ACOS(CET)/RAD          !Physical ETA
      DIFET = ETHRO - ETAP
      DIFX = XTHRO - XMEAS           !Note: XMEAS is not energy smeared
C                                    ω        as with the real data⊳ 30-JAN-88
C     Calculate measured pizero scattering angle ←2 ways←
CC       DEN / SQRT←EG←1←−→2→EG←2←−→2→2→EG←1←−→EG←2←−→COSETA←
CC       COSTPI / ←PGZ←1←−→PGZ←2←−←/DEN
CC       THT1 / ACOS←COSTPI←/RAD
C     alternately`
      THTPI = ATAN2(SQRT(PPIX**2+PPIY**2),PPIZ)/RAD
      DIFANG = THTPI - POLAR

C     Calc measured pizero kinetic energy
      ESQ = 2.*XM*XM/((1.-COSETA)*(1.-XMEAS*XMEAS))
      IF(ESQ.LE.0.) GOTO 777
      TTPI = SQRT(ESQ) - XM
      DIFTP = TTPI - TP0
C     Calc measured pizero azimuthal angle
      PHPI=ATAN2(PPIY,PPIX)/RAD
      IF (PHPI.LT.0.) PHPI= PHPI+360.

      XX(1)=TTPI
      XX(2)=THTPI
      XX(3)=PHPI
      XX(4)=POLT
      XX(5)=XMEAS
      XX(6)=AWT*ABS(DFCT)
      CALL HFN(31,XX)

 Coincidence

      XINPP=ATAN2D(X3,SQRT(Y3*Y3+Z3*Z3))
      XFLPP=ATAN2D(Y3,Z3)

      XINPR=ATAN2D(X1,SQRT(Y1*Y1+Z1*Z1))
      XFLPR=ATAN2D(Y1,Z1)

      IF(Z3.LE.0..OR.PP_THR(IFIX(1000.*T3)).LT.RANF(D)) GOTO 6662
```

```
      DO 737 IDET=1,14
      CDELIN_PP=COSD(ABS(XINPP-DET_I(IDET)))
      IF (CDELIN_PP.LE.0.1) GOTO 737
      DET_RN=DET_R(IDET)/CDELIN_PP
      DF=ATAN2D(DL(IDET),DET_RN*COSD(XINPP))
      IF(ABS(XINPP-DET_I(IDET)).LT.DET_DI(IDET)) THEN
        IF(ABS(XFLPP-DET_F(IDET)).LT.DF) PPH=IDET
      ENDIF
 737  CONTINUE

6662  IF(Z1.LE.0..OR.PR_THR(IFIX(1000.*T1)).LT.RANF(D)) GOTO 8662
      DO 738 IDET=1,14
      CDELIN_PR=COSD(ABS(XINPR-DET_I(IDET)))
      IF (CDELIN_PR.LE.0.1) GOTO 738
      DET_RN=DET_R(IDET)/CDELIN_PR
      DF=ATAN2D(DL(IDET),DET_RN*COSD(XINPR))
      IF(ABS(XINPR-DET_I(IDET)).LT.DET_DI(IDET)) THEN
        IF(ABS(XFLPR-DET_F(IDET)).LT.DF) PRH=IDET
      ENDIF
 738  CONTINUE

8662  IF((PPH+PRH).EQ.0.) GOTO 4662

C WE HAVE A HIT
      IF(JK.EQ.1) THEN
       WRITE(37,3721) DX(1,1),DY(2,2),EPH(JK),
     +                  DX(2,2),DY(1,1),EPH(KJ),TTPI,THTPI,dwww
      ELSE
       WRITE(37,3721) DX(1,2),DY(2,1),EPH(JK),
     +                  DX(2,1),DY(1,2),EPH(KJ),TTPI,THTPI,dwww
      ENDIF
 3721 FORMAT(9F8.2)

      CC(1)=PRH
      CC(2)=PPH
      CC(3)=TTPI
      CC(4)=THTPI
      CC(5)=PHPI
      CC(6)=POLT
      CC(7)=XMEAS
      CC(8)=AWT*ABS(DFCT)
      CC(9)=T1
      CC(10)=T3
      CC(11)=(T2+T3+MP0+MPP)**2-(X2+X3)**2-(Y2+Y3)**2-(Z2+Z3)**2
      CC(12)=(T1+T3+MPR+MPP)**2-(X1+X3)**2-(Y1+Y3)**2-(Z1+Z3)**2
      CC(13)=-2.*MPR*T1/(0.5*(MPP+MP0))**2
      XX1=X1
      YY1=Y1
      ZZ1=Z1
      XX2=X2
      YY2=Y2
      ZZ2=Z2
```

```
      XX3=X3
      YY3=Y3
      ZZ3=Z3
      CALL ANGLES(TINC,XX1,YY1,ZZ1,XX2,YY2,ZZ2,XX3,YY3,ZZ3,
     +            TY,R23_B3,R23_12,ATH)
C these are sharp values
      CC(14)=TY
      CC(15)=R23_B3
      CC(16)=R23_12
      CC(17)=ATH
C now come the smeared values of mpp‘ mprp‘ tman‘ ty‘ r23_b3
      TTPI=0.001*TTPI
      PPIX=0.001*PPIX
      PPIY=0.001*PPIY
      PPIZ=0.001*PPIZ
      IF(PRH.GT.0.) THEN
        CALL SMEAR(PRH,PPH,
     +            T1,X1,Y1,Z1,DET_TH(IFIX(PRH)),DET_PH(IFIX(PRH)))
        CALL MISS_M(X1,Y1,Z1,PPIX,PPIY,PPIZ,X3,Y3,Z3)
        CC(18)=-2.*MPR*T1/(0.5*(MPP+MP0))**2
      ELSE
        CALL SMEAR(PRH,PPH,
     +            T3,X3,Y3,Z3,DET_TH(IFIX(PPH)),DET_PH(IFIX(PPH)))
        CALL MISS_M(X3,Y3,Z3,PPIX,PPIY,PPIZ,X1,Y1,Z1)
        CC(18)=-2.*MPR*(0.26-0.1349734-T3-TTPI)/(0.5*(MPP+MP0))**2
      ENDIF

      CC(19)=(T2+T3+MP0+MPP)**2-(PPIX+X3)**2-(PPIY+Y3)**2-(PPIZ+Z3)**2
      CC(20)=(T1+T3+MPR+MPP)**2-(X1+X3)**2-(Y1+Y3)**2-(Z1+Z3)**2
      CALL ANGLES(TINN,X1,Y1,Z1,PPIX,PPIY,PPIZ,X3,Y3,Z3,
     +            TY,R23_B3,R23_12,ATH)
      CC(21)=TY
      CC(22)=R23_B3
      CC(23)=R23_12
      CC(24)=ATH
      CALL HFN(33,CC)
      ICOINC=ICOINC+1
      PRH=0.
      PPH=0.

C     End monte carlo loop
C
 4662 CONTINUE
      NCT = FCT
      IF (ICOINC .LT. IFIX(HMAX)) GOTO 200
 4661 MCT = MCT + LCT                !No. trials plus XCUT fails

C     Calculate monte carlo solid angle
      SANG = FLOAT(NCT)/FLOAT(MCT)*(4*PI)*CCUT*(CSTAR/2.0)

C     Calculate solid angle using analytic expression‘ it applies to
C     1-post at all scatt angles and to 2-post at 0 deg
      P1 = SQRT((TP0+XM)**2-XM*XM)
```

```
      BET1 = P1/(TP0+XM)
      RHO = PI*BET1*SIN(ETA)*R(1)**3
      ASA = X(1)*Y(1)**2*XCUT/RHO

C
C     Output results
      WRITE(4,1053)THCUT,CSTAR
1053  FORMAT(5X, 'THCUT          = 'F10.3' DEGREES'/
     1       5X, 'CSTAR          = 'F10.3//)
      WRITE(4,1050)SANG,XCUT
 1050 FORMAT(5X, 'SOLID ANGLE    = '1PE10.3' (SR)   FOR XCUT = '0PF5.3)
      WRITE(4,1051)ASA
 1051 FORMAT(5X, 'ANALYTIC S.A. = '1PE10.3' (SR)'/)
      WRITE(4,1052)ND1,ND2,NCT,MCT
 1052 FORMAT(5X, 'NO. WITH GAM1 IN ARM1 = 'I8/
     1       5X, 'NO. WITH GAM1 IN ARM2 = 'I8/
     2       5X, 'NO. OF SUCCESSES      = 'I8/
     3       5X, 'NO. OF TRIALS         = 'I8)
      WRITE(4,1999)LCT,NOUT,ERRORCOUNT,DELTA
 1999 FORMAT(5X, 'LCT (XCUT fails)      = 'I8/
     1       5X, 'NOUT (gamma misses)   = 'I8/
     2       5X, 'ERRORCOUNT            = 'I8/
     3       5X, 'CPU TIME    ',F10.1,' SECONDS'//)

      CALL HROUT(0,ICYCLE,' ')
      CALL HREND('E1179NTP')
      WRITE(101,9421) AWTTOT
 9421 format(g30.10)

C
      GOTO 998
  999 CONTINUE
      END                            !End of program PIANG86

C
C
      FUNCTION RANF(D)
      DATA I1/323/
      RANF=RAN(I1)
      RETURN
      END
C
      SUBROUTINE ROT1(PX,PY,PZ,CE,SE,CT,ST,VX,VY,VZ)
      VX = PX*CE - PY*SE*ST - PZ*SE*CT
      VY = PY*CT - PZ*ST
      VZ = PX*SE + PY*CE*ST + PZ*CE*CT
      RETURN
      END
C
      SUBROUTINE ROT1IV(PX,PY,PZ,CE,SE,CT,ST,VX,VY,VZ)
      VX = PX*CE + PZ*SE
      VY =-PX*SE*ST + PY*CT + PZ*CE*ST
      VZ =-PX*SE*CT - PY*ST + PZ*CE*CT
```

```
      RETURN
      END
C
      SUBROUTINE ROT2(PX,PY,PZ,CI,SI,CF,SF,VX,VY,VZ)
      VX =-PY*CF - PZ*SF
      VY = PX*CI + PY*SI*SF - PZ*SI*CF
      VZ = PX*SI - PY*CI*SF + PZ*CI*CF
      RETURN
      END
C
      SUBROUTINE ROT2IV(PX,PY,PZ,CI,SI,CF,SF,VX,VY,VZ)
      VX = PY*CI + PZ*SI
      VY =-PX*CF + PY*SI*SF - PZ*CI*SF
      VZ =-PX*SF - PY*SI*CF + PZ*CI*CF
      RETURN
      END

C
      FUNCTION GAMMA_ARM(FIRST,SECOND,DX,DY,XMAX,YMAX)
C        True if gamma corresponding to FIRST hits arm 1 and SECOND hits arm 2▷

      INTEGER*2 FIRST,SECOND
      LOGICAL*2 GAMMA_ARM
      DIMENSION DX(2,2)
      DIMENSION DY(2,2)
      DIMENSION XMAX(2)
      DIMENSION YMAX(2)

      GAMMA_ARM = .FALSE.
      IF (ABS(DX(FIRST,1)).LE.XMAX(1)) THEN
        IF (ABS(DX(SECOND,2)).LE.XMAX(2)) THEN
          IF (ABS(DY(FIRST,1)).LE.YMAX(1)) THEN
            IF (ABS(DY(SECOND,2)).LE.YMAX(2)) GAMMA_ARM = .TRUE.
          ENDIF
        ENDIF
      ENDIF
      RETURN
      END
C
      FUNCTION GRAUS(D)

C     Program to calculate gaussian psuedo random numbers▷
C     Generates distribution with mean zero and sigma one▷
C     Program is set up to run on 66‘
C     to run on 66 substitute EXP for QEXP and ALOG for QLOG▷
C     Subroutine calls RANDOM two times per subroutine call▷

1     P=RANF(D)
      IF (P-.6666666666) 10,10,20
10    GRAUS=P*3-1
      Q=RANF(E)
 1006 FORMAT(1H+,20X,80A1/)
 1007 FORMAT(1H ,A1,5X,'.',122A1)
```

```
 1008 FORMAT(/40X,'MEAN =',G16.6,10X,'STANDARD DEVIATION =',G16.6)

      IF (Q- EXP(-.5*GRAUS*GRAUS)) 11,11,1
20    P=6*P-5
      IF (P) 50,1,60
   50 GRAUS=.5*ALOG(-P)-1
      T=GRAUS+2
      GOTO 70
   60 GRAUS=-.5*ALOG(P)+1
      T=GRAUS-2
70    Q=RANF(F)
      IF (Q- EXP(-.5*T*T)) 11,11,1
11    RETURN
      END

C
      SUBROUTINE HISTMK(X,N)

C     Program to form and plot sixty histograms
C     The control parameters are entered thru COMMON/HISTCM/
C     NXT is the number of bins‘ MAX 121
C     XZERO is the left endpoint of the first bin
C     XWIDTH is the bin width
C     Calling sequence        HISTZZ to initialize the limits
C                             HISTMK to increment one of the histograms
C                             HISTPT to plot one or more histograms
C     NTITLE/0 for no titles‘ 1 for main title only‘ 3 for all titles
C        TH is the main title  max 80 char
C        TX is the abscissa title  max 80 char
C        TY is the ordinate title  max 50 char

      COMMON/HISTCM/NXT(60),XZERO(60),XWIDTH(60)

      DIMENSION TH(80),TX(80),TY(50),IPLT(60),IOVER(60),IUNDER(60),XX(7)
     1,XSUM(60),XDEV(60),IRRAY(121,60)

      REAL A(121,50),CHAR(10),SSCALE(5)

      EQUIVALENCE (YDUM,MX)

      DATA CHAR/1H0,1H1,1H2,1H3,1H4,1H5,1H6,1H7,1H8,1H9/
      DATA BLK/1H /,XCHAR/1HX/,PERIOD/1H./,PLUS/1H+/
      DATA MINHIS/61/,MAXHIS/0/,TY/50*1H /,TH/80*1H /
      DATA SSCALE/2.,3.,5.,7.,10./

C     Change following card to allow 0-3 titles
      DATA NTITLE/1/
 1001 FORMAT(' ERROR IN SETTING UP HISTOGRAMS ',I2,' THRU ',I2)
 1004 FORMAT(' ERROR IN PLOTTING HISTOGRAMS ',I2,' THRU ',I2)
 1005 FORMAT(1H1,I3)
 1006 FORMAT(1H+,20X,80A1/)
 1007 FORMAT(1H ,A1,5X,'.',122A1)
 1008 FORMAT(/40X,'MEAN =',G16.6,10X,'STANDAERD DEVIATION=',G16.6)
```

```
 1009 FORMAT(1H+,I5,'-')
 1010 FORMAT(7X,'.',122A1)
 1011 FORMAT(2X,6(G11.4,9X),G11.4)
 1012 FORMAT(/  I6,' POINTS PLOTTED',I6,' BINS    BIN WIDTH =',G11.4,
     1I6,' OVER RANGE (GE ',G11.4,')',I6,' UNDER RANGE (LT ',G11.4,')')
 1013 FORMAT(/21X,80A1)
 1014 FORMAT('1THERE WERE ',I5,' CALLS TO HISTMK WITH THE SECOND ARGUEME
     1NT OUT OF THE RANGE INITIALIZED')
 1016 FORMAT(////I4,15H  *** EMPTY ***  )
 1018 FORMAT(8X,12(A1,9X),A1)
 2000 FORMAT(80A1)

C     Increment the N th histogram vector with the value X
C     Check N
      IF (N .LE. MAXHIS .AND. N .GE. MINHIS) GOTO 102
      IBAD=IBAD+1
      RETURN
  102 I=(X-XZERO(N))/XWIDTH(N) + 1.0

C     Check for valid channel
      IF (I.GE.1) GOTO 100
      IUNDER(N)=IUNDER(N)+1
      RETURN
  100 IF (I.LE.NXT(N)) GOTO 101
      IOVER(N)=IOVER(N)+1
      RETURN
  101 IRRAY(I,N)=IRRAY(I,N)+1
      IPLT(N)=IPLT(N)+1
      XDEV(N)=XDEV(N)+X**2
      XSUM(N)=XSUM(N)+X
      RETURN

      ENTRY HISTPT

C     Plot histograms M thru MM
      YDUM=X
      M=MX
      MM=N

C     Check the value of M‘MM
      IF (MIN0(M,MM) .LT. MINHIS) GOTO 214
      IF (MAX0(M,MM) .GT. MAXHIS) GOTO 214

C     Read the titles
      DO 200 I=M,MM
      IF (NTITLE .GT. 0) READ(1,2000)TH
      IF (NTITLE .GT. 1) READ(1,2000)TX,TY
      NBINS=NXT(I)
      XMAX=XZERO(I)+XWIDTH(I)*NBINS
      IF (IPLT(I) .LE. 0) GOTO 230

C     Find maximum value in the vector
      MAXX=IRRAY(1,I)
```

```
      DO 212 J=2,NBINS
  212 MAXX=MAX0(MAXX,IRRAY(J,I))
      IF (MAXX.GT.50) GOTO 201
      YDIV=1.
      ISCALE=1
      GOTO 203

C     Calculate the scaling factor
  201 SCALE=0.1
  202 SCALE=SCALE*10.
      IF (MAXX.GE.SCALE*50) GOTO 202

C     Try for tighter scale
      S=SCALE*5.

      DO 211 J=1,5
      IF (MAXX.LE.S*SSCALE(J)) GOTO 205
  211 CONTINUE

      STOP
  205 ISCALE=SCALE*SSCALE(J)/10.   +0.5
      YDIV=1./ISCALE
  203 CONTINUE

C     Now fill the plot buffer
      DO 204 J=1,NBINS

C     Get the number to plot
      IX=IRRAY(J,I)

C     Find out how many units to plot
      NX=IX*YDIV + 0.5
      IF (NX.EQ.0.AND.IX.GT.0) NX=1

C     How many digits do we print - JJ
      JJ=-1
  215 JJ=JJ+1
      IF (IX.GE.10**JJ) GOTO 215
      IF (JJ.GT.NX) JJ = 0

C     Put in the blanks
      NNN=50-NX
      IF (NNN.EQ.0) GOTO 207
      DO 206 K=1,NNN
  206 A(J,K)=BLK

C     Put in the digits
  207 IF (JJ.EQ.0) GOTO 208
      ID=0
      JJJ=JJ-1
      NNF=NNN+1
      NNN=NNN+JJ
```

```
      DO 209 K=NNF,NNN
      IDD=IX/10**JJJ - ID
      ID=(IDD+ID)*10
      JJJ=JJJ-1
  209 A(J,K)=CHAR(IDD+1)

C     Put in the Xφs
  208 IF (NNN.GE.50) GOTO 204
      NNN=NNN+1
      DO 213 K=NNN,50
  213 A(J,K)=XCHAR
  204 CONTINUE

C     Now plot the graph
      WRITE(6,1005)I
      IF (NTITLE .GT. 0) WRITE(6,1006)TH
      WRITE(6,1010)(PERIOD,J=1,NBINS),PERIOD
      II=50

      DO 210 J=1,50
      WRITE(6,1007)TY(J),(A(K,J),K=1,NBINS),PERIOD
      IF (MOD(J,10).NE.1) GOTO 210
      IX=II*ISCALE
      WRITE(6,1009) IX
      II=II-10
  210 CONTINUE

      DO 216 K=1,7
  216 XX(K)=XZERO(I)+(K-1)*20.*XWIDTH(I)

      WRITE(6,1010)(PERIOD,J=1,NBINS),PERIOD
      NXX1=NBINS/10+1
      NXX2=NBINS/20+1
      WRITE(6,1018)(PLUS,J=1,NXX1)
      WRITE(6,1011)(XX(J),J=1,NXX2)
      IF (NTITLE .GT. 1) WRITE(6,1013)TX
      WRITE(6,1012)IPLT(I),NBINS,XWIDTH(I),IOVER(I),XMAX,IUNDER(I),
     1  XZERO(I)
      IF (IPLT(I) .LE. 1) GOTO 200
      Z=IPLT(I)
      XMEAN=XSUM(I)/Z
      XSTDEV=SQRT((XDEV(I)-XSUM(I)**2/Z)/(Z-1.0))
      WRITE(6,1008)XMEAN,XSTDEV
      GOTO 200

C     Empty histogram
  230 WRITE(6,1016)I
      IF (NTITLE .GT. 0) WRITE(6,1006)TH
      WRITE(6,1012)IPLT(I),NBINS,XWIDTH(I),IOVER(I),XMAX,IUNDER(I),
     1  XZERO(I)
  200 CONTINUE

      IF (IBAD.EQ.0) RETURN
```

```
      WRITE(6,1014)IBAD
      IBAD=0
      RETURN

C     Plot error -STOP-
  214 WRITE(6,1004)M,MM
      STOP

      ENTRY HISTZZ

C     Zero histograms M thru MM
      YDUM=X
      MM=N
      M=MX

C     Check values of M‘MM
      IF (MIN0(M,MM).LE.0) GOTO 12
      IF (MAX0(M,MM).GT.60) GOTO 12

C     Zero the vectors M thru MM
      DO 10 I=M,MM
      DO 11 J=1,121
      IRRAY(J,I)=0
   11 CONTINUE

C     Zero the monitors
      IUNDER(I)=0
      IOVER(I)=0
      IPLT(I)=0
      XSUM(I)=0.
      XDEV(I)=0.
      IBAD=0
      IF (M .LT. MINHIS) MINHIS=M
      IF (MM .GT. MAXHIS) MAXHIS=MM

C     Check the vector size
      IF (NXT(I).GT.121) GOTO 12
   10 CONTINUE
      RETURN

C     Error response  -STOP-
   12 WRITE(6,1001)M,MM
      STOP
      END

      SUBROUTINE GEN_EVENT(TINC,
     +                     X1,Y1,Z1,
     +                     X2,Y2,Z2,
     +                     X3,Y3,Z3,
     +                     T1,T2,T3)
      IMPLICIT REAL (M)
      COMMON/GENIN/NP,ATECM,AMAS(18),KGENEV
      COMMON/GENOUT/APCM(5,18),AWT
```

```
save
MPR=0.93827231
MNE=0.93956563
MPP=0.1395675
MP0=0.1349739
NP=3
AMAS(1)=MP0
AMAS(2)=MPP
AMAS(3)=MPR
KGENEV=1
MA=MPP
MB=MPR
P0=SQRT(TINC*TINC+2.*TINC*MA)
ATECM=SQRT(MA*MA+MB*MB+2.*(MA+TINC)*MB)
CALL GENBOD
X1=APCM(1,1)
X2=APCM(1,2)
X3=APCM(1,3)
Y1=APCM(2,1)
Y2=APCM(2,2)
Y3=APCM(2,3)
Z1=APCM(3,1)
Z2=APCM(3,2)
Z3=APCM(3,3)
E1=APCM(4,1)
E2=APCM(4,2)
E3=APCM(4,3)

CALL BOOST(ATECM,0.,0.,P0,E1,X1,Y1,Z1)
CALL BOOST(ATECM,0.,0.,P0,E2,X2,Y2,Z2)
CALL BOOST(ATECM,0.,0.,P0,E3,X3,Y3,Z3)
T1=E1-AMAS(1)
T2=E2-AMAS(2)
T3=E3-AMAS(3)
RETURN
END

SUBROUTINE BOOST(XM0,X0,Y0,Z0,E1,X1,Y1,Z1)
BG1=X0/XM0
G1=SQRT(1+BG1**2)
BG2=Y0/(XM0*G1)
G2=SQRT(1+BG2**2)
BG3=Z0/(XM0*G1*G2)
G3=SQRT(1+BG3**2)

E=G1*G2*G3*E1+BG1*G2*G3*X1+BG2*G3*Y1+BG3*Z1
X=G1*X1+BG1*E1
Y=G2*Y1++BG1*BG2*X1+G1*BG2*E1
Z=G3*Z1+BG2*BG3*Y1+BG1*G2*BG3*X1+BG3*G2*G1*E1

E1=E
X1=X
Y1=Y
```

```
      Z1=Z
      RETURN
      END

      SUBROUTINE MISS (M3,P1,T1,TH1,FI1,P2,T2,TH2,FI2)

      REAL*4 M3

      X3=-P1*COSD(FI1)*SIND(TH1)-P2*COSD(FI2)*SIND(TH2)
      Y3=-P1*SIND(FI1)*SIND(TH1)-P2*SIND(FI2)*SIND(TH2)
      Z3=374.4-P1*COSD(TH1)-P2*COSD(TH2)
      P3SQ=X3*X3+Y3*Y3+Z3*Z3

      T3=260.-134.9734-T1-T2
      M3=0.5*(X3*X3/T3+Y3*Y3/T3+Z3*Z3/T3-T3)

      RETURN
      END


      SUBROUTINE ANGLES  (TINC,X1,Y1,Z1,X2,Y2,Z2,X3,Y3,Z3,
     +                    TY,R23_B3,R23_12,ATH)

      IMPLICIT REAL*4 (M,K)
      DATA M1,M2,M3/0.93827231,0.1349734,0.13956755/
      DATA MA,MB/0.93827231,0.13956755/

      K1=SQRT(X1*X1+Y1*Y1+Z1*Z1+M1*M1)-M1
      K2=SQRT(X2*X2+Y2*Y2+Z2*Z2+M2*M2)-M2
      K3=SQRT(X3*X3+Y3*Y3+Z3*Z3+M3*M3)-M3
      XB=X1+X2+X3
      YB=Y1+Y2+Y3
      ZB=Z1+Z2+Z3

      E1=K1+M1
      E2=K2+M2
      E3=K3+M3
      S=MA*MA+MB*MB+2.*MA*(MB+TINC)
      S1=(E1+E2)**2-(X1+X2)**2-(Y1+Y2)**2-(Z1+Z2)**2
      S2=(E2+E3)**2-(X2+X3)**2-(Y2+Y3)**2-(Z2+Z3)**2
      S3=(E1+E3)**2-(X1+X3)**2-(Y1+Y3)**2-(Z1+Z3)**2
      T1=(K1+M1-MA)**2-X1*X1-Y1*Y1-Z1*Z1
      T2=(TINC+MB-K3-M3)**2-((XB-X3)**2+(YB-Y3)**2+(ZB-Z3)**2)

      ER23=E2+E3
      BB1=(X2+X3)/ER23
      BB2=(Y2+Y3)/ER23
      BB3=(Z2+Z3)/ER23
      GG=1./SQRT(1.-BB1*BB1-BB2*BB2-BB3*BB3)
      EB=TINC+MB

      CALL GBOOST(GG,BB1,BB2,BB3,E2,X2,Y2,Z2)
      CALL GBOOST(GG,BB1,BB2,BB3,E3,X3,Y3,Z3)
```

```
 CALL GBOOST(GG,BB1,BB2,BB3,E1,X1,Y1,Z1)
 CALL GBOOST(GG,BB1,BB2,BB3,EB,XB,YB,ZB)

 CALL VPRODUCT(XB1,YB1,ZB1,
+              XB,YB,ZB,X1,Y1,Z1)
 CALL VPRODUCT(XB3,YB3,ZB3,
+              XB,YB,ZB,X3,Y3,Z3)
 CALL VPRODUCT(X13,Y13,Z13,
+              X1,Y1,Z1,X3,Y3,Z3)
 CALL VPRODUCT(X12,Y12,Z12,
+              X1,Y1,Z1,X2,Y2,Z2)

 A_B3=SQRT(XB3*XB3+YB3*YB3+ZB3*ZB3)
 A_B1=SQRT(XB1*XB1+YB1*YB1+ZB1*ZB1)
 A_B =SQRT(XB*XB+YB*YB+ZB*ZB)
 A_1 =SQRT(X1*X1+Y1*Y1+Z1*Z1)
 A_2 =SQRT(X2*X2+Y2*Y2+Z2*Z2)
 A_3 =SQRT(X3*X3+Y3*Y3+Z3*Z3)
 A_12=SQRT(X12*X12+Y12*Y12+Z12*Z12)

 IF(ABS(A_B*A_3).GE.1.E-35) THEN
  COS_R23_B3=(XB*X3+YB*Y3+ZB*Z3)/(A_B*A_3)
 ELSE
  COS_R23_B3=0.
 ENDIF

 IF(ABS(A_B1*A_B3).GE.1.E-35) THEN
  COS_TY=-(XB1*XB3+YB1*YB3+ZB1*ZB3)/(A_B1*A_B3)
  SIN_TY=-A_B*(XB*X13+YB*Y13+ZB*Z13)/(A_B1*A_B3)
 ELSE
  COS_TY=0.
  SIN_TY=1.
 ENDIF

 A_1212=(A_12/(A_1*A_2))**2
 IF(A_1212.LT.1.) THEN
   COS_R23_12=SQRT(1.-(A_12/(A_1*A_2))**2)
 ELSE
   COS_R23_12=0.
 ENDIF

 IF(ABS(COS_TY).LT.1.) THEN
   TY=ACOSD(COS_TY)
 ELSEIF(COS_TY.GE.1.) THEN
   TY=0.
 ELSE
   TY=180.
 ENDIF

 IF(SIN_TY.LT.0.) TY=360.-TY

 IF(ABS(COS_R23_B3).LT.1.) THEN
   R23_B3=ACOSD(COS_R23_B3)
```

```
      ELSEIF(COS_R23_B3.GE.1.) THEN
        R23_B3=0.
      ELSE
        R23_B3=180.
      ENDIF

      IF(ABS(COS_R23_12).LT.1.) THEN
        R23_12=ACOSD(COS_R23_12)
      ELSEIF(COS_R23_12.GE.1.) THEN
        R23_12=0.
      ELSE
        R23_12=180.
      ENDIF
**
      ER23=E1+E2+E3
      BB1=(X1+X2+X3)/ER23
      BB2=(Y1+Y2+Y3)/ER23
      BB3=(Z1+Z2+Z3)/ER23
      GG=1./SQRT(1.-BB1*BB1-BB2*BB2-BB3*BB3)

      CALL GBOOST(GG,BB1,BB2,BB3,E1,X1,Y1,Z1)
      CALL GBOOST(GG,BB1,BB2,BB3,E2,X2,Y2,Z2)
      CALL GBOOST(GG,BB1,BB2,BB3,E3,X3,Y3,Z3)

      ATH=(Z2+Z3)/SQRT((X2+X3)**2+(Y2+Y3)**2+(Z2+Z3)**2)

      IF(ABS(ATH).LE.1.) THEN
         ATH=ACOSD(ATH)
      ELSEIF(ATH.LE.-1.) THEN
         ATH=180.
      ELSE
         ATH=0.
      ENDIF

      RETURN
      END


      SUBROUTINE GBOOST(G,B1,B2,B3,E1,X1,Y1,Z1)

      B=B1*B1+B2*B2+B3*B3

      A11=G
      A12=-G*B1
      A13=-G*B2
      A14=-G*B3
      A21=-G*B1
      A22=1.+(G-1.)*B1*B1/B
      A23=(G-1.)*B1*B2/B
      A24=(G-1.)*B1*B3/B
      A31=-G*B2
      A32=(G-1.)*B1*B2/B
      A33=1.+(G-1.)*B2*B2/B
```

```
      A34=(G-1.)*B2*B3/B
      A41=-G*B3
      A42=(G-1.)*B1*B3/B
      A43=(G-1.)*B2*B3/B
      A44=1.+(G-1.)*B3*B3/B

      E=A11*E1+A12*X1+A13*Y1+A14*Z1
      X=A21*E1+A22*X1+A23*Y1+A24*Z1
      Y=A31*E1+A32*X1+A33*Y1+A34*Z1
      Z=A41*E1+A42*X1+A43*Y1+A44*Z1

      E1=E
      X1=X
      Y1=Y
      Z1=Z

      RETURN
      END


      SUBROUTINE VPRODUCT(X,Y,Z,X1,Y1,Z1,X2,Y2,Z2)

      X=Y1*Z2-Y2*Z1
      Y=X2*Z1-X1*Z2
      Z=X1*Y2-X2*Y1

      RETURN
      END


      SUBROUTINE MISS_M(X1,Y1,Z1,X2,Y2,Z2,X3,Y3,Z3)

      X3=-X1-X2
      Y3=-Y1-Y2
      Z3=0.3744-Z1-Z2

      RETURN
      END


      SUBROUTINE SMEAR(PRH,PPH,T,X,Y,Z,TH,PH)

      REAL*4 DETTH(80),DETPH(80)
      DATA DETTH/18.,26.,22.,30.,38.,34.,42.,20.,
     +     68.50,67.51,63.23,62.18,57.92,56.81,52.68,51.51,
     +     62.41,63.53,57.10,51.76,58.29,53.03,46.48,47.84,
     +     73.99,73.99,68.04,68.04,62.03,62.03,56.08,56.08,
     +     37.99,43.44,37.30,42.87,37.30,42.87,37.99,43.44,
     +     57.44,63.37,57.04,63.05,57.04,63.05,57.44,63.37,
     +     77.15,83.10,77.01,83.02,77.01,83.02,77.15,83.10,
     +     67.98,62.67,57.33,52.05, 62.94,57.66,52.35,47.10,
     +     73.97,68.01,61.99,56.03, 40.71,40.08,40.08,40.71,
     +     60.40,60.04,60.04,60.40, 80.12,80.01,80.01,80.12/
```

```
      DATA DETPH/180.,208.,146.,180.,200.,156.5,180.,0.,
     + 203.12,197.40,204.39,198.37,205.79,199.45,207.35,200.67,
     + 163.03,157.11,161.89,160.59,155.60,153.91,159.10,151.98,
     + 183.10,176.90,183.24,176.76,183.41,176.59,183.59,176.41,
     + 346.41,347.86,355.39,355.90,  4.61,  4.10, 13.59, 12.14,
     + 349.35,349.97,356.41,356.62,  3.59,  3.38, 10.65, 10.03,
     + 350.81,350.97,356.91,356.97,  3.09,  3.03,  9.19,  9.03,
     + 200.27,201.39,202.64,204.03,160.06,158.73,157.22,155.50,
     + 180.00,180.00,180.00,180.00,347.17,355.66,  4.34, 12.83,
     + 349.67,356.52,  3.48, 10.33,350.89,356.94,  3.06,  9.11/

      DELM=-1.
      XYZ=SQRT(X*X+Y*Y+Z*Z)
      UX=X/XYZ  ! charged particles unit direction vectors
      UY=Y/XYZ
      UZ=Z/XYZ

      IF(PRH.GT.0.) THEN
c average loss inside target --proton--
        DT=0.00643-0.0000493*T
        T=T+DT*(RANF(D)-0.5)
c gain uncertainty
        T=T*(1+0.05*GRAUS(D))
        IDET=IFIX(PRH)
        IF(PRH.LE.6.) THEN     ! pion detector hit
          IF(T.LE.0.018) THEN  ! proton stops in DE1
            DO JJ=1,4
              IND=56+4*(IDET-1)+JJ
              DEL=UX*SIND(DETTH(IND))*COSD(DETPH(IND))+
     +             UY*SIND(DETTH(IND))*SIND(DETPH(IND))+
     +             UZ*COSD(DETTH(IND))
              IF(DEL.GT.DELM) THEN
                 DELM=DEL
                 TH=DETTH(IND)
                 PH=DETPH(IND)
              ENDIF
            ENDDO
          ELSE
            DO JJ=1,8
              IND=8*(IDET-1)+JJ+8
              DEL=UX*SIND(DETTH(IND))*COSD(DETPH(IND))+
     +             UY*SIND(DETTH(IND))*SIND(DETPH(IND))+
     +             UZ*COSD(DETTH(IND))
              IF(DEL.GT.DELM) THEN
                 DELM=DEL
                 TH=DETTH(IND)
                 PH=DETPH(IND)
              ENDIF
            ENDDO
          ENDIF ! T<18 MeV
        ENDIF ! PRH<7

        P=SQRT(T*T+2.*T*0.93827231)
```

```
      X=P*SIND(TH)*COSD(PH)
      Y=P*SIND(TH)*SIND(PH)
      Z=P*COSD(TH)
    ELSE
c average loss inside target --pion--
      DT=0.00179-0.0000129*T
      T=T+DT*(RANF(D)-0.5)
c gain uncertainty
      T=T*(1+0.05*GRAUS(D))
      P=SQRT(T*T+2.*T*0.13956755)

      IDET=IFIX(PPH)
      IF(PPH.LE.6.) THEN       ! pion detector hit
        IF(T.LE.0.008) THEN   ! proton stops in DE1
          DO JJ=1,4
            IND=56+4*(IDET-1)+JJ
            DEL=UX*SIND(DETTH(IND))*COSD(DETPH(IND))+
     +          UY*SIND(DETTH(IND))*SIND(DETPH(IND))+
     +          UZ*COSD(DETTH(IND))
            IF(DEL.GT.DELM) THEN
              DELM=DEL
              TH=DETTH(IND)
              PH=DETPH(IND)
            ENDIF
          ENDDO
        ELSE
          DO JJ=1,8
            IND=8*(IDET-1)+JJ+8
            DEL=UX*SIND(DETTH(IND))*COSD(DETPH(IND))+
     +          UY*SIND(DETTH(IND))*SIND(DETPH(IND))+
     +          UZ*COSD(DETTH(IND))
            IF(DEL.GT.DELM) THEN
              DELM=DEL
              TH=DETTH(IND)
              PH=DETPH(IND)
            ENDIF
          ENDDO
        ENDIF
      ENDIF

      X=P*SIND(TH)*COSD(PH)
      Y=P*SIND(TH)*SIND(PH)
      Z=P*COSD(TH)
    ENDIF

    RETURN
    END
```

Appendix I

Program E1179.FOR

```
*CMZ :
*--
      SUBROUTINE UFILES
*
*           To open FFREAD and HBOOK files
*
      OPEN(UNIT=4,FILE='E1179.INP',STATUS='UNKNOWN')
      END
*CMZ :          13/05/89  19.04.22  by  Rene Brun
*-- Author :
*CMZ :          07/01/90  Emil Frlez
*-- Author :
      SUBROUTINE UGINIT
*
************************************************************************
*                                                                      *
*             To initialise GEANT3 program and read data cards          *
*                                                                      *
************************************************************************
*
      COMMON/GCUNIT/LIN,LOUT,NUNITS,LUNITS(5)
      INTEGER LIN,LOUT,NUNITS,LUNITS
      COMMON/GCMAIL/CHMAIL
      CHARACTER*132 CHMAIL
      CHARACTER*4 TAG(30)
      DATA TAG/30*'A'/
C
      COMMON/GCKINE/IKINE,PKINE(10),ITRA,ISTAK,IVERT,IPART,ITRTYP
     +      ,NAPART(5),AMASS,CHARGE,TLIFE,VERT(3),PVERT(4),IPAOLD
C
      COMMON/GCTMED/NUMED,NATMED(5),ISVOL,IFIELD,FIELDM,TMAXFD,DMAXMS
     +      ,DEEMAX,EPSIL,STMIN,CFIELD,CMULS,IUPD,ISTPAR,NUMOLD
*
      FIELDM=0.0
      IFIELD=0
      TMAXFD=0.0
      DMAXMS=3.0
      DEEMAX=0.010
      EPSIL=0.01
      STMIN=0.1
      CMULS=0.5
*
*     ---------------------------------------------------------------
*
*           Open user files
*
      CALL UFILES
*
```

```
*          Initialize GEANT
*
      CALL GINIT
*
*          Prints version number
*
      WRITE(LOUT,1000)
*
*          Read data cards with FFREAD
*
      CALL GFFGO
*
*          Initialize GEANT/ZEBRA data structures
*
      CALL GZINIT
*
*
*          Initialize graphics package
*
      CALL GDINIT
*
*          Geometry and materials description.
*
      CALL GECDHS
*
*          Particle table definition and energy loss initialization.
*
      CALL GPART
      CALL GPHYSI
*
*          Create a view bank
*
      CALL VIEWYZ(1)
      CALL UINIT
*
 1000 FORMAT(/,' PI_PI VERSION 1.00 : ',/)
      END
*CMZ :          12/06/89  17.04.08  by  Rene Brun
*-- Author :
      SUBROUTINE UINIT
*
************************************************************************
*                                                                      *
*          To book the user s histograms                              *
*                                                                      *
************************************************************************
*
      COMMON/GCKINE/IKINE,PKINE(10),ITRA,ISTAK,IVERT,IPART,ITRTYP
     +        ,NAPART(5),AMASS,CHARGE,TLIFE,VERT(3),PVERT(4),IPAOLD
C
*     ---------------------------------------------------------------------
*
*          Open a HBOOK4 direct access file
```

```
*
      CALL HROPEN(2,'E1179NTP','E1179NTP.RZ','N',1024,ISTAT)
      CALL HBOOKN(51,'PIPIP NTP',30,'E1179NTP',2000,TAG)
*
      END
*CMZ :          02/03/89  08.37.38  by  Rene Brun
*-- Author :
      SUBROUTINE GECDHS
*
************************************************************************
*                                                                      *
*          Routine to define the geometry of the set-up.              *
*                                                                      *
************************************************************************
*
*
      COMMON/GCFLAG/IDEBUG,IDEMIN,IDEMAX,ITEST,IDRUN,IDEVT,IEORUN
     +        ,IEOTRI,IEVENT,ISWIT(10),IFINIT(20),NEVENT,NRNDM(2)
*
      COMMON/GCKINE/IKINE,PKINE(10),ITRA,ISTAK,IVERT,IPART,ITRTYP
     +      ,NAPART(5),AMASS,CHARGE,TLIFE,VERT(3),PVERT(4),IPAOLD
*
      COMMON/GCTMED/NUMED,NATMED(5),ISVOL,IFIELD,FIELDM,TMAXFD,DMAXMS
     +      ,DEEMAX,EPSIL,STMIN,CFIELD,CMULS,IUPD,ISTPAR,NUMOLD
*
      DIMENSION AMYL(3),ZMYL(3),WMYL(3)
      DIMENSION ASCI(2),ZSCI(2),WSCI(2)
      DIMENSION ACH2(2),ZCH2(2),WCH2(2)
      DIMENSION APOL(2),ZPOL(2),WPOL(2)
      DIMENSION ZLG(6),ALG(6),WLG(6)
      DIMENSION ABRASS(2),ZBRASS(2),WBRASS(2)
      DIMENSION PMAM(3),PLEP(3),PTMY(3),PEND(16),
     +          PSCA(3),PG10(3),PHAR(3),PLH2(3),PVET(3),
     +          PBLO(3),PCRA(3),PCON(3),PSCI(3)
      DIMENSION PCH2(3),PALF(10),P12C(3),PRE1(3),PRE2(3),
     +          PREE(37),PPE1(3),PPE2(3),PPEA(5),PPEB(3),
     +          PPRB(3)
C
C          Lead glass mixture parameters
C
      DATA ZLG/  82.00,  19.00,  14.00,  11.00,  8.00,  33.00/
      DATA ALG/ 207.19,  39.102,  28.088,  22.99, 15.999,  74.922/
      DATA WLG/ .65994, .00799, .126676, .0040073,.199281, .00200485/
C
C          Mylar parameters
C
      DATA AMYL,ZMYL,WMYL/12.01,1.01,16.00,6.,1.,8.,5.,4.,2./
C
C          Scintillator parameters
C
      DATA ASCI,ZSCI,WSCI/12.01,1.01,6.,1.,1.,1.1/
C
C          CH2 Target parameters
```

```
C
      DATA ACH2,ZCH2,WCH2/12.01,1.01,6.,1.,1.,2./
C
C                 Polyethylene parameters
C
      DATA APOL,ZPOL,WPOL/12.01,1.01,6.,1.,1.,2./
C
C                 Brass Parameters
C
      DATA ABRASS,ZBRASS,WBRASS/63.54,65.37,29.,30.,0.7,0.3/
C
C     PCH2/CH2 TARGET‘ PHAR/HARDENER‘ PVET/PLASTIC VETO
C
C                 Dimensions of Volumes

      DATA PMAM,PLEP/3*1000.,3*800./
C LH2 Target
      DATA PLH2/0.,1.905,2.54/
      DATA PTMY/1.905,1.9126,2.54/
      DATA PEND/0.,360.,8,4,-1.35,1.745,1.905,1.19,1.745,1.905,
     +           1.19,0.,1.905,1.35,0.,1.905/
C Scattering Chamber
      DATA PSCA/27.178,27.94,24.13/
      DATA PG10/0.,30.48,0.635/
C PIo Spectrometer
      DATA PHAR/20.,32.,0.4047/
      DATA PVET/20.,32.,0.15/
      DATA PBLO/7.5,7.5,30./
      DATA PCRA/22.5,37.5,300./
      DATA PCON/20.,32.,1.2/
      DATA PSCI/20.,32.,0.15/
C CH2 Target and Al Frame
      DATA PCH2/4.,4.,0.3886/
      DATA PALF/0.,360.,4,2,-0.1588,5.,6.2,0.1588,5,6.2/
C 12C Target --C--
      DATA P12C/8.35,5.25,0.2475/
C Proton Detector
      DATA PPRB/7.,7.,100./
      DATA PRE1/2.5,2.5,0.1588/
      DATA PRE2/3.,3.,1.27/
C       DATA PREE/0▹‘360▹‘4‘3‘2▹9‘0▹‘3▹5‘26▹9‘0▹‘7▹‘29▹9‘0▹‘7▹/
      DATA PREE/0.,360.,4,11, 0.,0.,2.5, 0.3175,0.,2.5,
     +           0.3175,0.,0., 0.4175,0.,0.,
     +           0.4175,0.,3.,
     +           2.9575,0.,3., 2.9575,0.,0., 3.0575,0.,0.,
     +           3.0575,0.,3.5, 27.0575,0.,7.,
     +           30.0575,0.,7./
C Pion Detector
      DATA PPE1/4.,8.,0.1588/
      DATA PPE2/4.5,8.5,1.27/
      DATA PPEA/5.,8.6,9.,15.5,10./
      DATA PPEB/8.6,15.5,1.5/
*
```

```
*    -----------------------------------------------------------------
*
*              Defines materials

      CALL GSMATE(1,'LIQUID HYDROGEN$',1.01,1.0,0.071,865.0,790.0,0,0)
      CALL GSMATE(6,'CARBON$', 12.01,6.,2.265 , 18.8,49.9,0,0)
      CALL GSMATE(9,'ALUMINIUM$', 26.98,13.,2.7    , 8.9,37.2,0,0)
      CALL GSMATE(10,'IRON$', 55.85,26.,7.87,1.76,17.1,0,0)
      CALL GSMATE(15,'AIR$',14.61,7.3,0.001205,30423.24,6750.,0,0)
      CALL GSMATE(16,'VACUUM$',1.E-16,1.E-16,1.E-16,1.E+16,1.E+16,0,0)
      CALL GSMIXT(17,'MYLAR$',AMYL,ZMYL,1.39,-3,WMYL)
      CALL GSMIXT(18,'CH2$',ACH2,ZCH2,0.935,-2,WCH2)
      CALL GSMIXT(19,'POLYETHYLENE HARD$',APOL,ZPOL,3.600,-2,WPOL)
      CALL GSMIXT(20,'PLASTIC SCINT$',ASCI,ZSCI,1.032,-2,WSCI)
      CALL GSMIXT(21,'LEAD GLASS$',ALG,ZLG,3.23,6,WLG)
      CALL GSMIXT(22,'BRASS$',ABRASS,ZBRASS,8.560,2,WBRASS)
      CALL GSMATE(23,'G10$',8.67,20.03,1.70,19.4,90.2,0,0)

C
      CALL GSTMED( 1,'VACUUM$'     , 16 , 0 , IFIELD,
     *           FIELDM,TMAXFD,DMAXMS,DEEMAX, EPSIL, STMIN, 0 , 0 )
      CALL GSTMED( 2,'AIR$', 15 , 1 , IFIELD,
     *           FIELDM,TMAXFD,0.,0., EPSIL, STMIN, 0 , 0 )
      CALL GSTMED( 3,'LIQUID HYDROGEN$'    , 1 , 0 , IFIELD,
     *           FIELDM,TMAXFD,DMAXMS,DEEMAX, EPSIL, STMIN, 0 , 0 )
      CALL GSTMED( 4,'MYLAR$'     , 17 , 1 , IFIELD,
     *           FIELDM,TMAXFD,DMAXMS,DEEMAX, EPSIL, STMIN, 0 , 0 )
      CALL GSTMED( 5,'CARBON$'     , 9 , 1 , IFIELD,
     *           FIELDM,TMAXFD,DMAXMS,DEEMAX, EPSIL, STMIN, 0 , 0 )
      CALL GSTMED( 6,'CH2$'     , 18 , 1 , IFIELD,
     *           FIELDM,TMAXFD,DMAXMS,DEEMAX, EPSIL, STMIN, 0 , 0 )
      CALL GSTMED( 7,'POLYETHYLENE HARD$'     , 19 , 1 , IFIELD,
     *           FIELDM,TMAXFD,DMAXMS,DEEMAX, EPSIL, STMIN, 0 , 0 )
      CALL GSTMED( 8,'PLASTIC SCINT$'     , 20 , 1 , IFIELD,
     *           FIELDM,TMAXFD,DMAXMS,DEEMAX, EPSIL, STMIN, 0 , 0 )
      CALL GSTMED( 9,'ALUMINUM$'     , 9 , 1 , IFIELD,
     *           FIELDM,TMAXFD,DMAXMS,DEEMAX, EPSIL, STMIN, 0 , 0 )
      CALL GSTMED(10,'LEAD GLASS$'     , 21 , 1 , IFIELD,
     *           FIELDM,TMAXFD,DMAXMS,DEEMAX, EPSIL, STMIN, 0 , 0 )
      CALL GSTMED(11,'BRASS$'     , 22 , 1 , IFIELD,
     *           FIELDM,TMAXFD,DMAXMS,DEEMAX, EPSIL, STMIN, 0 , 0 )
      CALL GSTMED(12,'IRON$'     , 10 , 1 , IFIELD,
     *           FIELDM,TMAXFD,DMAXMS,DEEMAX, EPSIL, STMIN, 0 , 0 )
      CALL GSTMED(13,'G10$'     , 23 , 1 , IFIELD,
     *           FIELDM,TMAXFD,DMAXMS,DEEMAX, EPSIL, STMIN, 0 , 0 )
*
*              Defines geometry of the set-up
*
      CALL GSVOLU ('MAMA','BOX ', 1,PMAM,3,IMAMA)  ! mama
      CALL GSVOLU ('CLEP','BOX ', 2,PLEP,3,ICLEP)  ! LEP air
*
C     Define Setup
      R0=PKINE(4)
```

```
      CALL GSROTM(1,90.,0.,0.,0.,90.,270.) ! to neg Y
      CALL GSROTM(2,90.,0.,180.,0.,90.,90.) ! to pos Y
      CALL GSROTM(3,90.,315.,90.,45.,0.,0.) ! 45 deg z ROT
      CALL GDOPT('PROJ','PERS')
C Ro/48▷12 cm THETA/20▷0 deg TPIo/22▷28 MeV
      IF (R0.EQ.48.12) THEN
        CALL GSROTM(11,149.124,270.,90.,0.,59.124,270.)
        CALL GSROTM(12,149.124,90.,90.,180.,59.124,90.)
      ENDIF
C Ro/50▷0 CM THETA/20▷0 deg TPIo/25▷0 MeV
C Ro/55▷0 cm THETA/20▷0 deg TPIo/25▷0 MeV
      IF (R0.EQ.50.0.OR.R0.EQ.55.0) THEN
        CALL GSROTM(11,149.127,270.,95.406,9.107,59.707,282.276)
        CALL GSROTM(12,149.127,90.,84.594,170.893,59.707,77.724)
      ENDIF
C Ro/73▷0 cm THETA/50▷0 deg TPIo/33▷0 MeV
      IF (R0.EQ.73.0) THEN
        CALL GSROTM(11,154.537,270.,101.306,24.825,67.503,299.574)
        CALL GSROTM(12,154.537,90.,78.694,155.175,67.503,60.426)
      ENDIF
*
      CALL GSPOS ('CLEP',1,'MAMA',0.,0.,0.,0,'ONLY')
      CALL GSATT ('CLEP','SEEN',0)
*
C     1991 Liquid Hydrogen Target
      IF (ISWIT(1).EQ.1) THEN
        CALL GSVOLU ('LH2T','TUBE', 3,PLH2,3,ILH2T)  ! LH2
        CALL GSVOLU ('TMYL','TUBE', 4,PTMY,3,ITMYL)  ! targ mylar
        CALL GSVOLU ('SEND','PGON',12,PEND,16,ISEND) ! steel endcap
        CALL GSVOLU ('SCAC','TUBE', 9,PSCA,3,ISCAC)  ! Al chamber
        CALL GSVOLU ('G10P','TUBE',13,PG10,3,IG10P)  ! G10 plate
        CALL GSPOS ('TMYL',1,'CLEP',0.,0.,0.,1,'ONLY')
        CALL GSPOS ('SEND',1,'CLEP',0.,3.89,0.,2,'ONLY')
        CALL GSPOS ('SEND',2,'CLEP',0.,-3.89,0.,1,'ONLY')
        CALL GSPOS ('SCAC',1,'CLEP',0.,0.,16.51,1,'ONLY')
        CALL GSPOS ('G10P',1,'CLEP',0.,24.765,16.51,1,'ONLY')
        CALL GSPOS ('G10P',2,'CLEP',0.,-24.765,16.51,1,'ONLY')

C     1990 Liquid Hydrogen Target
      ELSEIF (ISWIT(1).EQ.2) THEN
        CONTINUE
C     CH_2 Target
      ELSEIF (ISWIT(1).EQ.3) THEN
        CALL GSVOLU ('ALFR','PGON', 9,PALF,13,IALFR)  ! Al Frame
        CALL GSVOLU ('CH2T','BOX ', 6,PCH2,3,ICH2T)   ! CH2 Target
        CALL GSPOS  ('ALFR',1,'CLEP',0.,0.,PALF(3),0,'ONLY')
        CALL GSPOS  ('CH2T',1,'CLEP',0.,0.,-PCH2(3),3,'ONLY')
C     12C Target
      ELSEIF (ISWIT(1).EQ.4) THEN
        CALL GSVOLU ('12CT','BOX ', 5,P12C,3,I12CT)
        CALL GSPOS  ('12CT',1,'CLEP',0.,0.,0.,0,'ONLY')
      ENDIF
```

```
      IF (ISWIT(2).EQ.1.OR.ISWIT(3).EQ.2) THEN
        ZH=-6.+R0
        ZV=-3.+R0
        ZC1J=1.2+R0
        ZC2J=ZC1J+10.93
        ZC3J=ZC2J+10.74
        ZS1J=ZC1J+2.35
        ZS2J=ZS1J+10.93
        ZS3J=ZS2J+10.74
        ZBJ=ZC3J+11.83-1.2+PBLO(3)
*
        ZC1K=1.2+R0
        ZC2K=ZC1K+11.19
        ZC3K=ZC2K+10.66
        ZS1K=ZC1K+2.35
        ZS2K=ZS1K+11.19
        ZS3K=ZS2K+10.66
        ZBK=ZC3J+11.83-1.2+PBLO(3)
        CALL GSVOLU ('HARD','BOX ', 7,PHAR,3,IHARD)  ! PVT hardener
        CALL GSVOLU ('VETO','BOX ', 8,PVET,3,IVETO)  ! PI0 veto
        CALL GSVOLU ('SCIN','BOX ', 8,PSCI,3,ISCIN)  ! scintillator
        CALL GSVOLU ('CONV','BOX ',10,PCON,3,ICONV)  ! convertor
        CALL GSVOLU ('BLOC','BOX ',10,PBLO,3,IBLOC)  ! blocks
        CALL GSVOLU ('JCRA','BOX ', 2,PCRA,3,IJCRA)  ! J crate
        CALL GSVOLU ('KCRA','BOX ', 2,PCRA,3,IKCRA)  ! K crate
      ENDIF
*
C Turn on J Crate
      IF (ISWIT(2).EQ.1) THEN
      CALL GSPOS ('JCRA',1,'CLEP',0.,0.,0.,11,'ONLY')
      CALL GSATT ('JCRA','SEEN',0)
      CALL GSPOS ('HARD',1,'JCRA',0.,0.,ZH,0,'ONLY')
      CALL GSPOS ('VETO',1,'JCRA',0.,0.,ZV,0,'ONLY')
      CALL GSPOS ('CONV',1,'JCRA',0.,0.,ZC1J,0,'ONLY')
      CALL GSPOS ('CONV',2,'JCRA',0.,0.,ZC2J,0,'ONLY')
      CALL GSPOS ('CONV',3,'JCRA',0.,0.,ZC3J,0,'ONLY')
      CALL GSPOS ('SCIN',1,'JCRA',0.,0.,ZS1J,0,'ONLY')
      CALL GSPOS ('SCIN',2,'JCRA',0.,0.,ZS2J,0,'ONLY')
      CALL GSPOS ('SCIN',3,'JCRA',0.,0.,ZS3J,0,'ONLY')
      ENDIF
C Turn on K Crate
      IF (ISWIT(3).EQ.2) THEN
      ZKC=R0+PCRA(3)
      CALL GSPOS ('KCRA',1,'CLEP',0.,0.,0.,12,'ONLY')
      CALL GSATT ('KCRA','SEEN',0)
      CALL GSPOS ('HARD',2,'KCRA',0.,0.,ZH,0,'ONLY')
      CALL GSPOS ('VETO',2,'KCRA',0.,0.,ZV,0,'ONLY')
      CALL GSPOS ('CONV',4,'KCRA',0.,0.,ZC1K,0,'ONLY')
      CALL GSPOS ('CONV',5,'KCRA',0.,0.,ZC2K,0,'ONLY')
      CALL GSPOS ('CONV',6,'KCRA',0.,0.,ZC3K,0,'ONLY')
      CALL GSPOS ('SCIN',4,'KCRA',0.,0.,ZS1K,0,'ONLY')
      CALL GSPOS ('SCIN',5,'KCRA',0.,0.,ZS2K,0,'ONLY')
      CALL GSPOS ('SCIN',6,'KCRA',0.,0.,ZS3K,0,'ONLY')
```

```
      ENDIF
*
C Position Blocks Inside the Crates
*
      NJ=0
      DO 87 IB=2,-2,-1
       DO 87 JB=1,-1,-1
        NJ=NJ+1
        NK=NJ+15
        YB=15.*IB
        XB=15.*JB
        CALL GSPOS('BLOC',NJ,'JCRA',XB,YB,ZBJ,0,'ONLY')
        CALL GSPOS('BLOC',NK,'KCRA',XB,YB,ZBK,0,'ONLY')
 87   CONTINUE

      IF (ISWIT(4).EQ.1) THEN
        CALL GSROTM(21,110.,0.,90.,90.,20.,0.)
        CALL GSVOLU ('PRBX','BOX ', 2,PPRB,3,IPRBX)  ! PR Box
        CALL GSATT  ('PRBX','SEEN',0)
        CALL GSVOLU ('PRO1','PGON', 8,PREE,37,IPRO1)
        CALL GSPOS  ('PRBX', 1,'CLEP',0.,0.,0.,21,'ONLY')
        CALL GSPOS  ('PRO1', 1,'PRBX',0.,0.,50.,0,'ONLY')
      ENDIF

      CALL GGCLOS
*
      END
*CMZ :          30/05/89  09.13.13  by  Rene Brun
*-- Author :
      SUBROUTINE GUKINE
*
************************************************************************
*                                                                      *
*             Read or Generates Kinematics for primary tracks          *
*                                                                      *
************************************************************************
*
      COMMON/GCFLAG/IDEBUG,IDEMIN,IDEMAX,ITEST,IDRUN,IDEVT,IEORUN
     +        ,IEOTRI,IEVENT,ISWIT(10),IFINIT(20),NEVENT,NRNDM(2)
C
      COMMON/GCKINE/IKINE,PKINE(10),ITRA,ISTAK,IVERT,IPART,ITRTYP
     +      ,NAPART(5),AMASS,CHARGE,TLIFE,VERT(3),PVERT(4),IPAOLD
C
      COMMON/GPFLAG/IFLAG,ISELECT,X1,Y1,Z1,E1,X2,Y2,Z2,E2,X3,Y3,Z3,E3
*
      DATA RT,IFLAG/1.905,0/
*
      REAL VERTEX(3),PLAB(3),RRR,XXX,YYY,ZZZ
*
*     -----------------------------------------------------------------
*
      IFLAG=IFLAG+IKINE
      ISELECT=MOD(IFLAG,3)
```

```
C     IPARTICLE/4→ISELECT→ISELECT→11→ISELECT→14
      IPARTICLE=7
      IF(IPARTICLE.EQ.7) THEN
         CALL GEN_EVENT(PKINE(3),X1,Y1,Z1,X2,Y2,Z2,X3,Y3,Z3,T1,T2,T3)
         PLAB(1)=X1
         PLAB(2)=Y1
         PLAB(3)=Z1
 634     CALL GRANOR(RANX,RANY)
         VERTEX(1) = RANX*PKINE(1)
         IF (ABS(VERTEX(1)).GE.RT) GOTO 634
         VERTEX(2) = RANY*PKINE(2)
         IF (ABS(VERTEX(2)).GE.5.08) GOTO 634
         VERTEX(3) = SQRT(RT*RT-VERTEX(1)**2)*(1.-2.*RNDM(X))
      ELSEIF(IPARTICLE.EQ.8) THEN
         PLAB(1)=X2
         PLAB(2)=Y2
         PLAB(3)=Z2
      ELSE
         PLAB(1)=X3
         PLAB(2)=Y3
         PLAB(3)=Z3
      ENDIF

      CALL GSVERT(VERTEX,0,0,0,0,NVERT)
      CALL GSKINE(PLAB,IPARTICLE,NVERT,0,0,NT)
*
      END
*CMZ :          13/05/89  19.04.22  by  Rene Brun
*-- Author :
      SUBROUTINE GUTREV
*
************************************************************************
*                                                                      *
*             User routine to control tracking of one event           *
*                                                                      *
*             Called by GRUN                                           *
*                                                                      *
************************************************************************
*
      COMMON/GCFLAG/IDEBUG,IDEMIN,IDEMAX,ITEST,IDRUN,IDEVT,IEORUN
     +        ,IEOTRI,IEVENT,ISWIT(10),IFINIT(20),NEVENT,NRNDM(2)
C
*
*     ---------------------------------------------------------------------
*
      CALL GTREVE
*
      END
*CMZ :          13/05/89  19.04.22  by  Rene Brun
*-- Author :
      SUBROUTINE GUSTEP
*
************************************************************************
```

```
*                                                                    *
*           User routine called at the end of each tracking step     *
*           MEC    is the mechanism origin of the step               *
*           INWVOL is different from 0 when the track has reached    *
*                  a volume boundary                                 *
*           ISTOP is different from 0 if the track has stopped       *
*                                                                    *
**********************************************************************
*
      COMMON/GCTMED/NUMED,NATMED(5),ISVOL,IFIELD,FIELDM,TMAXFD,DMAXMS
     +      ,DEEMAX,EPSIL,STMIN,CFIELD,CMULS,IUPD,ISTPAR,NUMOLD
C
      COMMON/GCKINE/IKINE,PKINE(10),ITRA,ISTAK,IVERT,IPART,ITRTYP
     +      ,NAPART(5),AMASS,CHARGE,TLIFE,VERT(3),PVERT(4),IPAOLD
C
      COMMON/GCKING/KCASE,NGKINE,GKIN(5,100),TOFD(100),IFLGK(100)
      INTEGER       KCASE,NGKINE ,IFLGK
      REAL          GKIN,TOFD
C
      COMMON/GCFLAG/IDEBUG,IDEMIN,IDEMAX,ITEST,IDRUN,IDEVT,IEORUN
     +        ,IEOTRI,IEVENT,ISWIT(10),IFINIT(20),NEVENT,NRNDM(2)
C
      COMMON/GCTRAK/VECT(7),GETOT,GEKIN,VOUT(7),NMEC,LMEC(30),NAMEC(30)
     + ,NSTEP ,MAXNST,DESTEP,DESTEL,SAFETY,SLENG ,STEP  ,SNEXT ,SFIELD
     + ,TOFG  ,GEKRAT,UPWGHT,IGNEXT,INWVOL,ISTOP ,IDECAD,IEKBIN
     + , ILOSL, IMULL,INGOTO,NLDOWN,NLEVIN,NLVSAV,ISTORY
C
      COMMON/GCVOLU/NLEVEL,NAMES(15),NUMBER(15),
     +LVOLUM(15),LINDEX(15),INFROM,NLEVMX,NLDEV(15),LINMX(15),
     +GTRAN(3,15),GRMAT(10,15),GONLY(15),GLX(3)
C
      COMMON/GCCUTS/CUTGAM,CUTELE,CUTNUE,CUTHAD,CUTMUO,BCUTE,BCUTM,
     +DCUTE,DCUTM,PPCUTM,TOFMAX,GCUTS(5)
C
      COMMON /CONVERSION/LCONV,EDEPTOT
      DATA LCONV/0/
      DATA EDEPTOT/0./
      DATA  ISEED/71539/
*
*     -----------------------------------------------------------------
*
*           Accumulate energy deposited in scintillator
*
*           Something generated ?
*

      IF (NMED.EQ.10) THEN
        NMED=10
        ZZZ=ZZZ*2
      ELSE
        CONTINUE
      ENDIF
```

```
      IF(NGKINE.GT.0) THEN
        DO 5 I=1,NGKINE
          ITYPA  = GKIN(5,I)
          IF(ITYPA.NE.4) CALL GSKING(I)
   5    CONTINUE
      ENDIF
*

*             Debug/plot event
*
      CALL GPJXYZ(0)
      CALL GDCXYZ(0)
      CALL GDPART(0,11,PKINE(5))

      END
*CMZ :          02/03/89  08.37.38  by  Rene Brun
*-- Author :
      SUBROUTINE GUOUT
*
C▷    -----------------------------------------------------------------
C▷    -                                                  -
C▷    -          User routine called at the end of each event▷    -
C▷    -                                                  -
C▷    -----------------------------------------------------------------
C▷
C▷
      COMMON/GCUNIT/LIN,LOUT,NUNITS,LUNITS(5)
      INTEGER LIN,LOUT,NUNITS,LUNITS
      COMMON/GCMAIL/CHMAIL
      CHARACTER*132 CHMAIL
C
      COMMON/GCFLAG/IDEBUG,IDEMIN,IDEMAX,ITEST,IDRUN,IDEVT,IEORUN
     +        ,IEOTRI,IEVENT,ISWIT(10),IFINIT(20),NEVENT,NRNDM(2)
C
      COMMON/GPFLAG/IFLAG,ISELECT,X1,Y1,Z1,T1,X2,Y2,Z2,T2,X3,Y3,Z3,T3
      COMMON/GNTP/XNTP(30)
      COMMON /CONVERSION/LCONV,EDEPTOT

      IF(ISELECT.EQ.1) THEN
        XNTP(1)=1.
        XNTP(2)=2.
      ELSEIF(ISELECT.EQ.2) THEN
        XNTP(11)=3.
        XNTP(12)=4.
      ELSEIF(ISELECT.EQ.0) THEN
        XNTP(21)=5.
        XNTP(22)=6.
        CALL HFN(51,XNTP)
        CALL VZERO(XNTP,30)
      ENDIF
*
      END
*CMZ :          26/05/89  08.50.35  by  Rene Brun
```

```
*-- Author :
      SUBROUTINE GUPHAD
C▷
C▷    ⇀⇀⇀⇀⇀⇀⇀⇀⇀⇀⇀⇀⇀⇀⇀⇀⇀⇀⇀⇀⇀⇀⇀⇀⇀⇀⇀⇀⇀⇀⇀⇀⇀⇀⇀⇀⇀⇀⇀⇀⇀⇀⇀⇀⇀
C▷    ⇀                                                  ⇀
C▷    ⇀                                                  ⇀
C▷    ⇀      GEANT3 user routine called at each step     ⇀
C▷    ⇀      to evaluate the next hadronic interaction point  ⇀
C▷    ⇀                                                  ⇀
C▷    ⇀           ↼TATINA↼ uses R▷Barlow cross-sections tables  ⇀
C▷    ⇀           ↼GHEISHA↼uses the GHEISHA cross-sections    ⇀
C▷    ⇀                                                  ⇀
C▷    ⇀⇀⇀⇀⇀⇀⇀⇀⇀⇀⇀⇀⇀⇀⇀⇀⇀⇀⇀⇀⇀⇀⇀⇀⇀⇀⇀⇀⇀⇀⇀⇀⇀⇀⇀⇀⇀⇀⇀⇀⇀⇀⇀⇀⇀
C▷
C▷
C▷    ------------------------------------------------------------
C▷
      CALL GPGHEI
C
      END
*CMZ :          26/05/89  08.50.35  by  Rene Brun
*-- Author :
      SUBROUTINE GUHADR
C▷
C▷    ⇀⇀⇀⇀⇀⇀⇀⇀⇀⇀⇀⇀⇀⇀⇀⇀⇀⇀⇀⇀⇀⇀⇀⇀⇀⇀⇀⇀⇀⇀⇀⇀⇀⇀⇀⇀⇀⇀⇀⇀⇀⇀⇀⇀⇀
C▷    ⇀                                                  ⇀
C▷    ⇀                                                  ⇀
C▷    ⇀      GEANT3 user routine called when a hadronic process  ⇀
C▷    ⇀      has been selected in the current step▷     ⇀
C▷    ⇀⇀⇀⇀⇀⇀⇀⇀⇀⇀⇀⇀⇀⇀⇀⇀⇀⇀⇀⇀⇀⇀⇀⇀⇀⇀⇀⇀⇀⇀⇀⇀⇀⇀⇀⇀⇀⇀⇀⇀⇀⇀⇀⇀⇀
C▷
C▷
C▷    ------------------------------------------------------------
C▷
      CALL GHEISH
C
      END
*CMZ :          13/05/89  19.04.22  by  Rene Brun
*-- Author :
      SUBROUTINE UGLAST
*
************************************************************************
*                                                                      *
*           Termination routine to print histograms and statistics    *
*                                                                      *
************************************************************************
*
      COMMON/GCFLAG/IDEBUG,IDEMIN,IDEMAX,ITEST,IDRUN,IDEVT,IEORUN
     +        ,IEOTRI,IEVENT,ISWIT(10),IFINIT(20),NEVENT,NRNDM(2)
C
*
*     ------------------------------------------------------------
*
```

```
      CALL GLAST
*
      CALL HROUT(0,ICYCLE,' ')
      CALL HREND('E1179NTP')
      CALL IGEND
*
      END
*CMZ :          13/05/89  19.04.22  by  Rene Brun
*-- Author :

      SUBROUTINE VIEWYZ(IVIEW)
      CALL GSATT('MAMA','SEEN',0)
      END

      SUBROUTINE QNEXT

      END

      SUBROUTINE GEN_EVENT(TINC,
     +                     X1,Y1,Z1,
     +                     X2,Y2,Z2,
     +                     X3,Y3,Z3,
     +                     T1,T2,T3)
      IMPLICIT REAL (M)
      COMMON/GENIN/NP,ATECM,AMAS(18),KGENEV
      COMMON/GENOUT/APCM(5,18),AWT
      COMMON/GNTP/XNTP(30)
      DATA MPR,MNE,MPP,MP0/0.93827231,0.93956563,
     +                     0.1395675,0.1349739/
      DATA NP/3/
      AMAS(1)=MP0
      AMAS(2)=MPP
      AMAS(3)=MPR
      KGENEV=1
      MA=MPP
      MB=MPR
      P0=SQRT(TINC*TINC+2.*TINC*MA)
      ATECM=SQRT(MA*MA+MB*MB+2.*(MA+TINC)*MB)
      CALL GENBOD
      X1=APCM(1,1)
      X2=APCM(1,2)
      X3=APCM(1,3)
      Y1=APCM(2,1)
      Y2=APCM(2,2)
      Y3=APCM(2,3)
      Z1=APCM(3,1)
      Z2=APCM(3,2)
      Z3=APCM(3,3)
      E1=APCM(4,1)
      E2=APCM(4,2)
      E3=APCM(4,3)

      CALL BOOST(ATECM,0,0,P0,E1,X1,Y1,Z1)
```

```
CALL BOOST(ATECM,0,0,P0,E2,X2,Y2,Z2)
CALL BOOST(ATECM,0,0,P0,E3,X3,Y3,Z3)
T1=E1-AMAS(1)
T2=E2-AMAS(2)
T3=E3-AMAS(3)
RETURN
END

SUBROUTINE BOOST(XM0,X0,Y0,Z0,E1,X1,Y1,Z1)
BG1=X0/XM0
G1=SQRT(1+BG1**2)
BG2=Y0/(XM0*G1)
G2=SQRT(1+BG2**2)
BG3=Z0/(XM0*G1*G2)
G3=SQRT(1+BG3**2)

E=G1*G2*G3*E1+BG1*G2*G3*X1+BG2*G3*Y1+BG3*Z1
X=G1*X1+BG1*E1
Y=G2*Y1++BG1*BG2*X1+G1*BG2*E1
Z=G3*Z1+BG2*BG3*Y1+BG1*G2*BG3*X1+BG3*G2*G1*E1

E1=E
X1=X
Y1=Y
Z1=Z
RETURN
END
```

Appendix J

Program REDUCED_AMPLITUDES.FOR

```
      PROGRAM REDUCED_AMPLITUDES
C     CALCULATES REDUCED AMPLITUDES FOR PIN->PIPIN
      IMPLICIT REAL*8 (A-H,M,O-Z)
      EXTERNAL DR3
      PARAMETER (PI=3.141592654)
      COMMON/KIN3/MA,MB,MC,ECM2
      DATA MPP,MP0,MN,MP,MNUC/139.5675,134.9739,
     +                   939.56563,938.27231,938.91897/
C
C SET THE FINAL STATE MASSES APPROPRIATE FOR PARTICULAR REACTIONω
C BE SURE TO SET SPIN FACTOR S TOOωωω

      MA=MN
      MB=MPP
      MC=MPP

      WRITE(6,*)('ENTER T_INC,DT_INC (MEV),S,DS_STAT,DS_SYS (uB): ')
      ACCEPT *, TINC, DTINC, S, DSSTAT,DSSYS

      ECM2=MPP*MPP+MP*MP+2.*(TINC+MPP)*MP
      ECM=SQRT(ECM2)
Cω
      TCM=SQRT(ECM2)-MPP-MPP-MN

      M1=MPP
      M2=MP

      DS=SQRT(DSSTAT**2+DSSYS**2)
      PLAB=SQRT(TINC*TINC+2.*MPP*TINC)
      E=TINC+MPP
      DP=E*DTINC/PLAB
      ECM=SQRT(M1*M1+M2*M2+2.*(TINC+MPP)*M2)
      DECM=M2*DTINC/ECM
      PCM=M2*PLAB/ECM
      DPCM=M2*SQRT((DP/ECM)**2+((PLAB*DECM)/(ECM*ECM))**2)
Cω      EDIT THIS LINE FOR THE PARTICULAR REACTIONωω

      TCM=ECM-MPP-MPP-MN
      DTCM=DECM
*
      B=(SQRT(ECM2)-MA)**2
      A=(MB+MC)**2
      CALL QGAUS(DR3,A,B,R)

      CF=3.8937966E8       ! MeV**-2->uB
C     CONSTANTS FROM COON AND SCADRON ♭1990♮ AT CHIRAL LIMIT
      Q2_PS=CF*13.0**3*(1./1.29)**4*(1./(8*PI*MNUC**5))*PCM*PCM*R/PLAB
```

```
      WRITE(6,9)
 9    FORMAT(//)
      WRITE(6,*) ('  PCM      DPCM    ECM       DECM    TCM       DTCM')
      WRITE(6,7) PCM,DPCM,ECM,DECM,TCM,DTCM
 7    FORMAT(6F8.1,//)

C     IF IDENTICAL PARTICLES IN FINAL STATE‘ S/o▷5
c      SP/o▷5
C     ELSE SP/1
      SP=1.
C     WHAT IS THE RIGHT FACTOR*
C
      A2=S/(SP*Q2_PS)
      A=SQRT(A2)
      DA2=(1./(24.994*SP))*SQRT(((ECM**2*DS)/(PCM*TCM**2))**2+
     +     ((2.*ECM*S*DECM)/(PCM*TCM**2))**2+
     +     ((S*ECM**2*DPCM)/(PCM**2*TCM**2))**2+
     +     ((2.*S*ECM**2*DTCM)/(PCM*TCM**3))**2)
      DA=DA2/(2.*A)
      WRITE(6,*) ('  A          DA  ')
      WRITE(6,8) A,DA
 8    FORMAT(2F8.2//)


**
      XXX=S/(24.994*PCM*TCM*TCM*SP/(ECM*ECM))
      XXX=SQRT(XXX)
      WRITE (6,*) XXX

      STOP
      END

      REAL*8 FUNCTION DR3(X)
      implicit REAL*8 (a-h,m,o-z)
      COMMON/KIN3/MA,MB,MC,ECM2
      DR3=R2(ECM2,MA*MA,X)*R2(X,MB*MB,MC*MC)
      RETURN
      END

      REAL*8 FUNCTION R2(S,T,U)
      implicit REAL*8 (a-h,m,o-z)
      REAL*8 LAMBDA
      LAMBDA(X,Y,Z)=(X-Y-Z)**2-4.*Y*Z
      R2=DMAX1(0.D0,LAMBDA(S,T,U))
      R2=0.5*3.141592654*SQRT(R2)/S
      RETURN
      END

      SUBROUTINE QSIMP(FUNC,A,B,S)
      PARAMETER (EPS=1.E-4, JMAX=20)
      IMPLICIT real*8 (A-H,M,O-W)
      OST=-1.E30
      OS= -1.E30
```

```
      DO 11 J=1,JMAX
        CALL TRAPZD(FUNC,A,B,ST,J)
        S=(4.*ST-OST)/3.
        IF (ABS(S-OS).LT.EPS*ABS(OS)) RETURN
        OS=S
        OST=ST
11    CONTINUE
      PAUSE 'Too many steps.'
      END

      SUBROUTINE QGAUS(FUNC,A,B,SS)
      IMPLICIT real*8 (A-H,M,O-W)
      DIMENSION X(5),W(5)
      DATA X/.1488743389,.4333953941,.6794095682,.8650633666,.9739065285
     */
      DATA W/.2955242247,.2692667193,.2190863625,.1494513491,.0666713443
     */
      XM=0.5*(B+A)
      XR=0.5*(B-A)
      SS=0
      DO 11 J=1,5
        DX=XR*X(J)
        SS=SS+W(J)*(FUNC(XM+DX)+FUNC(XM-DX))
11    CONTINUE
      SS=XR*SS
      RETURN
      END
```

VII. References

[Aar-79] R. Aaron, R. A. Arndt, J. B. Cammarata, D. A. Dicus, and V. L. Treplitz, Phys. Rev. Lett. **44**, 66 (1979).

[Abe-73] E. Abers and B. W. Lee, Phys. Rep. **9C**, 1 (1973).

[Adl-68] S. L. Adler and R. F. Dashen, *Current Algebras and Applications to Particle Physics*, W. A. Benjamin, New York, 1968.

[Aja-87] Z. Ajaltouni, A. Falvard, J. Jousset, B. Michel, J. C. Montret, Ph. Mutter, D. Pallin, A. Courau, J. E. Augustin, A. Cordier, G. Cosme, F. Couchot, B. Delcourt, B. Dudelzak, F. Fulda, B. Grelaud, G. Grosdidier, J. Haissinski, B. Jean-Marie, S. Jullian, D. Lalanne, V. Lepeltier, F. Mane, C. Paulot, R. Riskalla, Ph. Roy, F. Rumpf, G. Szklarz, R. Baldini, S. Calcaterra, G. Capon, D. Bisello, G. Busetto, L. Pescara, P. Sartori, and L. Stanco, Phys. Lett. **B194**, 573 (1987).

[Alf-73] V. de Alfaro, S. Fubini, G. Furlan, and C. Rosseti, *Currents in Hadron Physics*, North-Holland, Amsterdam, 1973.

[All-89] R. C. Allen, H. H. Chen, M. E. Potter, R. R. Burman, J. B. Donahue, D. A. Krakauer, R. L. Talaga, E. S. Smith, and A. C. Dodd, Nucl. Instr. and Meth. **A282**, 347 (1989).

[Alm-67] B. Almgren, Arkiv för Fysik, **38**, 161 (1967).

[Als-71] M. Alston-Garnjost, A. Barbaro-Galtieri, S. M. Flatté, J. H. Friedmann, G. R. Lynch, S. D. Protopopescu, M. S. Rabin, and F. T. Solmitz, Phys. Lett. **36B**, 152 (1971).

[Als-74] J. Alster, J. D. Bowman, M. A. Moinester, R. Heffner, M. Johnson, C. Hoffman, M. Cooper, J. Potter, *Angular Distribution Measurements for Pion-Nucleus Single Charge Exchange Reactions*, LAMPF Proposal E181, unpublished, LAMPF, Los Alamos, 1974.

[Amm-88] J. F. Amman and M. A. Oothourt, *A Data Testing Package under VMS*, MP-1-3412-3, LAMPF, Los Alamos, 1988.

[And-61a] J. A. Anderson, V. X. Bang, P. G. Bruke, D. D. Carmony, and N. Schmitz, Rev. Mod. Phys. **33**, 431 (1961).

[And-61b] J. A. Anderson, V. X. Bang, P. G. Bruke, D. D. Carmony, and N. Schmitz, Phys. Rev. Lett. **6**, 365 (1961).

[And-85] G. T. Anderson, *Dynamical Parameter Array Sub-system*, MP-1-3404-4, LAMPF, Los Alamos, 1985.

[And-89] G. T. Anderson and M. A. Oothourt, *General Purpose Memory Management Region*, MP-1-3409-1, LAMPF, Los Alamos, 1989.

[Ani-62] V. V. Anisovich, A. A. Ansel'm and V. N. Gribov, JETP **15**, 159 (1962).

[Ani-66] V. V. Anisovich and A. A. Ansel'm, Sov. Phys. Usp. **9**, 117 (1966).

[Ans-59] A. A. Ansel'm and V. N. Gribov, JETP **10**, 354 (1959).

[Ape-82] W. D. Apel, K. H. Augenstein, E. Bertolluci, S. V. Donskov, A. V. Inyakin, V. A. Kachanov, R. N. Krasnokutsky, M. Kruğer, G. Leder, A. A. Ledner, I. Mannelli, Yu. V. Mikhailov, H. Müller, G. M. Pierazzini, Yu. D. Prokoshkin, M. Quaglia, H. Schneider, A. Scribano, F. Sergiampietri, R. S. Shuvalov, G. Sigurdsson, and M. L. Vincelli, Nucl. Phys. **B201**, 197 (1982).

[Apo-89] V. D. Apokin, Yu. I Arestov, N. I. Belikov, N. S. Borisov, A. N. Vasil'ev, O. A. Grachev, A. A. Derevshchikov, Yu. M. Kazarinov, M. Yu. Liburg, V. N. Matafonov, Yu. A. Matulenko, A. P. Meshchanin, A. I. Mysnik, A. B. Neganov, S. B. Nurushev, A. F. Prudkoglyad, V. L. Rykov, L. F. Solov'ev, V. L. Solov'yanov, Yu. A. Usov, B. A. Khachaturov, and B. Yu. Khodyrev, Sov. J. Nucl. Phys. **42**, 278 (1989).

[Are-67] A. V. Aref'ev, Yu. D. Bayukov, Yu. M. Zaïtsev, M. S. Kozodaev, G. A. Leskin, V. T. Osipenkov, D. A. Suchkov, V. V. Telenkov, and V. B. Fedorov, Sov. J. Nucl. Phys. **5**, 757 (1967).

[Arm-72] M. Arman, D. J. Blasberg, R. P. Haddock, K. C. Leung, B. M. K. Nefkens, B. L. Schrock, D. I. Sober, and J. M. Sperinde, Phys. Rev. Lett. **29**, 962 (1972).

[Arn-79] R. A. Arndt, J. B. Cammarata, Y. N. Goradia, R. H. Hackman, V. L. Treplitz, D. A. Dicus, R. Aaron, and R. S. Longacre, Phys. Rev. D **20**, 651 (1979).

[Arn-85] R. A. Arndt, J. M. Ford, and L. D. Roper, Phys. Rev. D **32**, 1085 (1985).

[Arn-87] R. A. Arndt, *Phase Shift Analysis for* πN *Scattering*, Computer Program SAID, unpublished (1987).

[Ash-81] D. Ashery, I. Navon and G. Azuelos, Phys. Rev. C **23**, 2173 (1981).

[Ash-84a] D. Ashery, D. F. Geesaman, R. J. Holt, H. E. Jackson, J. R. Specht, K. E. Stephenson, R. E. Segel, P. Zupranski, H. W. Baer, J. D. Bowman, M. D. Cooper, M. Leitch, A. Erel, J. Comuzzi, R. P. Redwine, and D. R. Tieger, Phys. Rev. C **30**, 946 (1984).

[Ash-84b] D. Ashery, D. F. Geesaman, R. J. Holt, H. E. Jackson, J. R. Specht, K. E. Stephenson, R. E. Segel, P. Zupranski, H. W. Baer, J. D. Bowman, M. D. Cooper, M. Leitch, A. Erel, R. Chefetz, J. Comuzzi, R. P. Redwine, and D. R. Tieger, Phys. Rev. Lett. **50**, 482 (1984).

[Au-87] K. L. Au, D. Morgan, and M. R. Pennington, Phys. Rev. D **35**, 1633 (1987).

[Aue-62] L. B. Auerbach, T. Elioff, W. B. Johnson, J. Lach, C. E. Wiegand, and T. Ypsilantis, Phys. Rev. Lett. **9**, 173 (1962).

[Bae-80a] H. W. Baer, π^0 *Spectrometer Alignment Constants*, unpublished, LAMPF, Los Alamos, 1980.

[Bae-80b] H. W. Baer, π^0 *Spectrometer MWPCs and Trigger Logic*, unpublished, LAMPF, Los Alamos, 1980.

[Bae-81] H. W. Baer, R. D. Bolton, J. D. Bowman, M. D. Cooper, F. H. Cverna,R. H. Heffner, C. M. Hoffman, N. S. P. King, J. Piffaretti, J. Alster, A. Doron, S. Gilad, M. A. Moinester, P. R. Bevington, and E. Winkelmann, Nucl. Instr. and Meth. **180**, 445 (1981).

[Bae-84] H. W. Baer, G. O. Bolme, J. D. Bowman, A. A. Browman, M. D. Cooper, D. H. Fitzgerald, P. Heusi, F. Irom, D. M. Lee, R. J. Macek, D. E. Nagle, E. Piasetzky, and U. Sennhauser, *Measurement of the Differential Cross Section for* $\pi^- p \rightarrow \pi^0 n$ *at 10, 20 and 40 MeV*, LAMPF Proposal E882, unpublished, LAMPF, Los Alamos, 1984.

[Bag-88] A. Bagheri, K. A. Aniol, F. Entezami, M. D. Hasinoff, D. F. Measday, J-M. Poutissou, M. Salomon, and B. C. Robertson, Phys. Rev. C **38**, 885 (1988).

[Bai-71] P. Baillon, F. Bulos, R. K. Carnegie, G. E. Fischer, E. E. Kluge, D. W. G. S. Leith, H. L. Lynch, B. Ratcliff, B. Richter, H. H. Williams, and S. H. Williams, Phys. Lett. **35B**, 453 (1971).

[Bal-67] N. F. Bali, G. F. Chew, A. Pignotti, Phys. Rev. **163**, 1572 (1967).

[Bar-88] R. Baran, U. Bohnert, M. Dillig, G. Herrmann, P. Helbig, A. Hofmann, O. Jäkel, W. Kluge, H. Krüger, D. Malz, H. Matthäy, R. Müller, W. Menzel, H.-W. Ortnar, L. Schweinzer, and S. Wirth, PSI Annual Report Annex I, 29 (1988).

[Bar-89] R. Baran, U. Bohnert, M. Dillig, W. Eyrich, G. Herrmann, A. Hofmann, P. Helbig, O. Jäkel, W. Kluge, R. Kraft, H. Krüger, D. Malz, H. Matthäy, W. Menzel, R. Müller, H.-W. Ortnar, L. Schweinzer, and S. Wirth, PSI Annual Report Annex I, 39 (1989).

[Bar-61] B. C. Barish, R. J. Kurz, P. G. McManigal,V. Perez-Mendez, and J. Solomon, Phys. Rev. Lett. **6**, 297, (1961).

[Bar-64] B. C. Barish, R. J. Kurz, V. Perez-Mendez, and J. Solomon, Phys. Rev. **135B**, 416, (1964).

[Bar-63] V. E. Barnes, D. V. Bugg, I. Derado, A. Minguzzi, L. Montanet, R. T. van de Walle, R. Carrara, M. Cresti, A. Grigoletto, A. Loria, L. Peruzzo, and R. Santangelo, CERN 63-27, Geneva, 1963.

[Bar-87] T. Barnes, K. Dooley, and N. Isgur, Phys. Lett. **B183**, 210 (1987).

[Bar-80] K. W. Barnham, S. L. Glickman, W. A. C. Mier-Jedrzejowicz, S. J. Orebi Gann, R. A. Stevens, and A. P. White, Nucl. Phys. **B168**, 243 (1980).

[Bas-70] J. L. Basdevant and B. W. Lee, Phys. Rev. D **2**, 1680 (1970).

[Bas-72a] J. L. Basdevant, Springer Tracts in Modern Physics **61**, 1 (1972).

[Bas-72b] J. L. Basdevant, J. C. Le Guillou, and H. Navelet, Nuovo Cimento **7A**, 363 (1972).

[Bat-67] J. P. Baton, G. Laurens, and J. Reignier, Phys. Lett. **25B**, 419 (1967).

[Bat-70a] J. P. Baton, G. Laurens, and J. Reignier, Phys. Lett. **33B**, 525 (1970).

[Bat-70b] J. P. Baton, G. Laurens, and J. Reignier, Phys. Lett. **33B**, 528 (1970).

[Bat-61] Yu. A. Batusov. S. A. Bunyatov, V. M. Sidorov, and V. A. Yarba, JETP **12**, 1290 (1961).

[Bat-63] Yu. A. Batusov, S. A. Bunyatov, V. M. Sidorov, and V. A. Yarba, JETP **16**, 1422 (1963).

[Bat-64] Yu. A. Batusov, S. A. Bunyatov, V. M. Sidorov, and V. A. Yarba, unpublished, JINR P-1823, Dubna, 1964.

[Bat-65] Yu. A. Batusov, S. A. Bunyatov, V. M. Sidorov, and V. A. Yarba, Sov. J. Nucl. Phys. **1**, 492 (1965).

[Bat-75] Yu. A. Batusov, S. A. Bunyatov, G. R. Gulkanyan, V. M. Sidorov, M. Musakhanov, G. Ionice, E. Losnianu, V. Mihul, and D. Tuvdendorzh, Sov. J. Nucl. Phys. **21**, 162 (1975).

[Bee-69a] M. De Beer, B. Deler, J. Dolbeau, M. Neveu, N. T. Diem, G. Smadja, and G. Valladas, Nucl. Phys. **B12**, 599 (1969).

[Bee-69b] M. De Beer, B. Deler, J. Dolbeau, M. Neveu, N. T. Diem, G. Smadja, and G. Valladas, Nucl. Phys. **B12**, 617 (1969).

[Bel-78] A. A. Bel'kov, S. A. Bunyatov, B. Zh. Zalikhanov, V. S. Kurbatov, and A. Khalbaev, Sov. J. Nucl. Phys. **28**, 657 (1978).

[Bel-79] A. A. Bel'kov, S. A. Bunyatov, K. N. Mukhin, O. O. Patarakun, V. M. Sidorov, M. M. Sulkovskaya, A. F. Sustavov, and V. A. Yarba, JETP Lett. **29**, 597 (1979).

[Bel-80] A. A. Bel'kov, S. A. Bunyatov, B. Zh. Zalikhanov, V. S. Kurbatov, A. Khalbaev, and V. A. Yarba, Sov. J. Nucl. Phys. **31**, 96 (1980).

[Bel-82] A. A. Bel'kov and S. A. Bunyatov, Sov. J. Part. Nucl. **13**, 1 (1982).

[Bel-82] A. A. Bel'kov and A. V. Lanev, Sov. J. Nucl. Phys. **45**, 312 (1987).

[Ben-68] J. Benecke and H. P. Durr, Nuovo Cimento **56A**, 269 (1968).

[Bha-84] R. S. Bhalerao and L. C. Liu, Phys. Rev. C **30**, 224 (1984).

[Bic-89] *BICRON Catalog*, Bicron Corporation, Newbury, 1989.

[Bir-51] J. B. Birks, Proc. Phys. Soc. **A64**, 874 (1951).

[Bjo-65] J. D. Bjorken and S. D. Drell, *Relativistic Quantum Mechanics*, McGraw-Hill, New York, 1965.

[Bjo-80] C. W. Bjork, S. E. Jones, T. R. King, D. M. Manley, A. T. Oyer, G. A. Rebka, J. B. Walter, R. Carawon, P. A. M. Gram, F. T. Shively, C. A. Bordner, and E. L. Lomon, Phys. Rev. Lett. **44**, 62 (1980).

[Bla-70] I. M. Blair, H. Müller, G. Torelli, and E. Zavattini, Phys. Lett. B **32**, 528 (1970).

[Blo-63] T. D. Blokhintseva, V. G. Grebinnik, V. A. Zhukov, G. Libman, L. L. Nemenov, G. I. Selivanov, and Yüan Jung-Fang, JETP **17**, 80 (1963).

[Blo-65] T. D. Blokhintseva, V. G. Grebinnik, V. A. Zhukov, V. A. Kravtsov, G. Libman, L. L. Nemenov, G. I. Selivanov, and Yüan Jung-Fang, Sov. J. Nucl. Phys. **1**, 71 (1965).

[Boc-90] R. K. Bock, H. Grote, D. Notz, and M. Regler, *Data Analysis Techniques for High-Energy Physics Experiments*, Cambridge University Press, New York, 1990.

[Bol-88a] A. A. Bolokhov, V. V. Vereshchagin, and S. G. Sherman, Sov. J. Nucl. Phys., **45**, 319 (1987).

[Bol-88b] A. A. Bolokhov, V. V. Vereshchagin, and S. G. Sherman, Sov. J. Nucl. Phys., **46**, 322 (1988).

[Bol-88c] A. A. Bolokhov, V. V. Vereshchagin, and S. G. Sherman, Sov. J. Nucl. Phys., **47**, 311 (1988).

[Bol-88d] A. A. Bolokhov, V. V. Vereshchagin, and S. G. Sherman, Sov. J. Nucl. Phys., **48**, 517 (1988).

[Bol-89] A. A. Bolokhov, V. V. Vereshchagin, and S. G. Sherman, LNPI Preprint No. 1542, Leningrad, 1989.

[Bol-91] A. A. Bolokhov, V. V. Vereshchagin, and S. G. Sherman, Nucl. Phys. **A530**, 660 (1991).

[Bol-80] R. D. Bolton, H. W. Baer, J. D. Bowman and L. Gordon, Nucl. Instr. Meth. **174**, 411 (1980).

[Bou-89] R. L. Boudrie, C. L. Morris, and and J. L. Matthews, *Proposal for a High Resolution Spectrometer for Neutral Mesons*, LAMPF, Los Alamos (1989).

[Bow-70] M. G. Bowler and R. J. Cashmore, Nucl. Phys. **B17**, 331 (1970).

[Bow-81] T. J. Bowles, D. F. Geesaman, R. J. Holt, H. E. Jackson, J. Julien, R. M. Laszewski, J. R. Specht and E. J. Stephenson, Phys. Rev. C **23**, 439 (1981).

[Boy-84] K. G. Boyer, W. J. Braithwaite, W. B. Cottingame, S. J. Greene, L. E. Smith, C. F. Moore, C. L. Morris, H. A. Thiessen, G. S. Blanpied, G. R. Burleson, J. F. Davis, J. S. McCarthy, R. C. Minehart and C. A. Goulding, Phys. Rev. C **29**, 182 (1984).

[Bra-86] J. T. Brack, J. J. Kraushaar, J. H. Mitchell, R. J. Peterson, R. A. Ristinen, J. L. Ullmann, D. R. Gill, R. R. Johnson, D. Ottewell, F. M. Rozon, M. E. Sevior, G. R. Smith, F. Tervisidis, R. P. Trelle, and E. L. Mathie, Phys. Rev. C **34**, 1771 (1986).

[Bro-74] K. L. Brown and Ch. Iselin, *Decay Turtle*, CERN 74-2, Geneva, 1974.

[Bro-80] K. L. Brown, D. C. Carey, Ch. Iselin, and F. Rothacker, *Transport*, CERN 80-04, Geneva, 1980.

[Bro-86] G. E. Brown and M. Rho, Comments Nucl. Part. Phys. **15**, 245 (1986).

[Bru-87] R. Brun, F. Bruyant, M. Maire, A. C. McPherson, and P. Zanarini, *GEANT 3*, DD/EE/84-1, Cern, Geneva, 1987.

[Bru-89] R. Brun, O. Couet, C. Vandoni, and P. Zanarini, *PAW—Physics Analysis Workstation*, CN/Q121, Cern, Geneva, 1989.

[Bry-80] R. K. Bryan, Ph. D. Thesis, unpublished, University of Cambridge, Cambridge, (1980).

[Bul-69] F. Bulos, R. E. Lanou, A. E. Pifer, MA. M. Shapiro, C. A. Bordner, A. E. Brenner, M. E. Law, E. E. Ronat, F. D. Rudnick, K. Strauch, J. J. Szymanski, P. Bastien, B. B. Brabson, Y. Eisenberg, B. T. Feld, V. K. Kistiakowsky, I. A. Pless, L. Rosenson, R. K. Yamamoto, G. Calvelli, F. Gasparini, L. Guerriero, G. A. Salandin, A. Tomasin, L. Ventura, C. Voci, and F. Waldner, Phys. Rev. **187**, 1827 (1969).

[Bun-77] S. A. Bunyatov, G. V. Zholobov, B. Zh. Zalikhanov, V. S. Kurbatov, M. M. Musakhanov, A. Khalbaev, and V. A. Yarba, Sov. J. Nucl. Phys. **25**, 177 (1977).

[Bur-83] S. F. Burch, S. F. Gull, and J. Skilling, Comp. Vis. Graph. Im. Proc., **23**, 113, (1983).

[Bur-86] W. J. Burger, E. Beise, S. Gilad, R. P. Redwine, P. G. Roos, N. S. Chant, H. Breuer, G. Ciangaru, J. D. Silk, G. S. Blanpied, B. M. Preedom, B. G. Ritchie, M. Blecher, K. Gotow, D. M. Lee and H. Ziock, Phys. Rev. Lett. **57**, 58 (1986).

[Bur-91] H. Burkhardt and J. Lowe, Phys. Rev. Lett. **67** 2622, (1991).

[Bur-75a] R. L. Burman, R. L. Fulton, and M. Jakobson, Nucl. Instr. and Meth. **131**, 29 (1975).

[Bur-75b] R. L. Burman and P. F. Chavez, *TRACE: A Beam Design Program for LEP*, unpublished, LAMPF, Los Alamos, 1975.

[But-82] G.W. Butler, B.J. Dropesky, C.J. Orth, R.E. Green, R.G. Korteling, and G.K.Y. Lam, Phys. Rev. C **26**, 1737 (1982).

[Byc-69] E. Byckling and K. Kajantie, Phys. Rev. **187**, 2008 (1969).

[Byc-73] E. Byckling and K. Kajantie, *Particle Kinematics*, John Wiley & Sons, New York, 1973.

[Cam-93] P. Camerini, N. Grion, and R. Rui, Nucl. Phys. **A552**, 451 (1993).

[Car-62a] D. D. Carmony and R. T. Van de Walle, Phys. Rev. **127**, 959 (1962).

[Car-62b] D. D. Carmony and R. T. Van de Welle, Phys. Rev. Lett. **8**, 73 (1962).

[Cas-83] N. M. Cason, P. E. Cannata, A. E. Baumbaugh, J. M. Bishop, N. N. Biswas, T. J. Dauwe, V. P. Kenney, R. C. Ruchti, and W. D. Shephard, Phys. Rev. D **28**, 1586 (1983).

[Cec-79] R. A. Cecil, B. D. Anderson, and R. Madey, Nucl. Instr. and Meth. **161**, 439 (1979).

[Cha-67a] L. N. Chang, Phys. Rev. **162**, 1497 (1967).

[Cha-67b] P. Chang and F. Gürsey, Phys. Rev. **164**, 1752 (1967).

[Cha-67c] Chang Hong-Mo, K. Kaajantie, and G. Ranft, Nuovo Cimento, **49A**, 157 (1967).

[Cha-67c] Chang Hong-Mo, K. Kaajantie, G. Ranft, W. Beusch, and E. Flaminio, Nuovo Cimento, **49A**, 696 (1967).

[Che-84] T. P. Cheng and L. F. Li, *Gauge Theory of Elementary Particle Physics*, Oxford University Press, New York, 1984.

[Che-59] G. F. Chew and F. E. Low, Phys. Rev. **113**, 1640 (1959).

[Che-60a] G. F. Chew and S. Mandelstam, Phys. Rev. **119**, 467 (1960).

[Che-60b] G. F. Chew, S. Mandelstam, and H. P. Noyes, Phys. Rev. **119**, 478 (1960).

[Chi-67] C. B. Chiu, R. D. Eandi, A. C. Helmholz, R. W. Kenney, B. J. Moyer, J. A. Poirier, W. B. Richards, R. J. Cence, V. Z. Peterson, N. K. Sehgal, and V. J. Stenger, Phys. Rev. **156**, 1415 (1967).

[Cho-75] A. Chodos and C. B. Thorn, Phys. Rev. D **12**, 2733 (1975).

[Chu-77] K. H. Chung and R. S. Willey, Phys. Rev. D **16**, 1339 (1977).

[Ciu-69] S. Ciulli, Nuovo Cimento **61**, 787 (1969).

[Cla-85] R. K. Clark, P. M. Barlow, R. N. Diamond, V. Hagopian, J. E. Lannutti, M. Spencer, M. Ferguson, T. Glanzman, A. T. Goshaw, P. Lucas, N. Morgan, W. Robertson, W. D. Walker, W. Bugg, G. Condo, T. Handler, E. Hart, A. Rogers, H. O. Cohn, I. J. Kim, R. C. Sun, and R. Gearhart, Phys. Rev. D **32**, 1061 (1985).

[Col-74] J. S. Colonias, *Particle Accelerator Design: Computer Programs*, Academic Press, New York, 1974.

[Com-75] J. Comiso, T. Meyer, F. Schlepuetz, and K. O. H. Ziock, Phys. Rev. Lett. **35**, 13 (1975).

[Com-76] J. C. Comiso, F. Schlepuetz, and K. O. H. Ziock, Nucl. Inst. and Meth. **133**, 121 (1976).

[Coo-90] S. A. Coon and M. D. Scadron, Phys. Rev. D **42**, 2256 (1990).

[Coo-74] M. D. Cooper, *Time-of-Flight Measurements at the LAMPF Low-Energy Pion Channel*, LA-5529-MS, Informal Report UC-28, LAMPF, Los Alamos, 1974.

[Coo-82] M. D. Cooper, H. W. Baer, J. D. Bowman, F. H. Cverna, R. H. Heffner, C. M. Hoffman, N. S. P. King, J. Piffaretti, J. Alster, A. Doron, S. Gilad, M. A. Moinester, P. R. Bevington and E. Winklemann, Phys. Rev. C **25**, 438 (1982).

[Cum-63] J. B. Cumming, Ann. Rev. Nucl. Sci. **13**, 261 (1963).

[Cut-68] R. E. Cutkosky and B. B. Deo, Phys. Rev. **174**, 1859 (1968).

[Cra-70] R. L. Craun and D. L. Smith, Nucl. Inst. and Meth. **80**, 239 (1970).

[Czy-68] O. Czyževsky, in *Kinematics and Multiparticle Systems*, Herceg-Novi, Yugoslavia, 1965, edited by M. Nikolić (Gordon and Breach, New York, 1968).

[Dav-77] M. David, G. Villet, R. Ayed, P. Bateyre, P. Borgeaud, J. Ernwein, J. Feltesse, Y. Lemoigne, and A. V. Stirling, Phys. Rev. D **16**, 2027 (1977).

[Dea-75] L. Deahl, M. Derrick, J. Fetkovich, T. Fields, and G. B. Yodh, Phys. Rev. **124**, 1987 (1961).

[Deb-65] J. Debaisieux, F. Grard, J. Heughebaert, R. Servranckx, and R. T. van de Walle, Nucl. Phys. **63**, 273 (1965).

[Dil-72] J. P. Dilley and R. Teshima, Nucl. Phys. **B46**, 275 (1972).

[Dor-81] A. Doron, Ph. D. Thesis, unpublished, Tel-Aviv University, Tel-Aviv, 1981.

[Dor-82] A. Doron, J. Alster, A. Erell, M. A. Moinester, R. A. Anderson, H. W. Baer, J. D. Bowman, M. D. Cooper, F. H. Cverna, C. M. Hoffman, N. S. P. King, M. J. Leitch, J. P. Piffaretti and C. D. Goodman, Phys. Rev. C **26**, 189 (1982).

[Dre-61] S. D. Drell, Rev. Mod. Phys. **33**, 458 (1961).

[Dro-75] B. J. Dropesky, G. W. Butler, C. J. Orth, R. A. Williams, G. Friedlander, M. A. Yates and S. B. Kaufman, Phys. Rev. Lett. **34**, 821 (1975).

[Dro-79] B. J. Dropesky, G. W. Butler, C. J. Orth, R. A. Williams, M. A. Yates-Williams, G. Friedlander, and S. B. Kaufman, Phys. Rev. C **20**, 1844 (1979).

[Dum-83] O. Dumbrajs, R. Koch, H. Pilkuhn, G. C. Oades, H. Behrens, J. J. de Swart, and P. Kroll, Nucl. Phys. **B216**, 277, (1983).

[Dür-65] H. P. Dur̈r and H. Pilkuhn, Nuovo Cimento **40A**, 899 (1965).

[Dyc-79] O. B. van Dyck, E. W. Hoffman, R. J. Macek, G. Sanders, R. D. Werbeck, and J. K. Black, IEEE Trans. Nucl. Sci. **NS-26**, 3197 (1979).

[Ead-71] W. T. Eadie, D. Drijard, F. E. James, M. Roos, and B. Sadoulet, *Statistical Methods in Experimental Physics*, North-Holland, Amsterdam, 1971.

[Efi-89] G. V. Efimov and M. A. Ivanov, Sov. J. Part. Nucl. **20**, 479 (1989).

[EGG-89] *EG&G ORTEC Nuclear Instruments Catalog*, EG&G ORTEC Corporation, Oak Ridge, 1989.

[Ere-84] A. Erell, Ph. D. Thesis, unpublished, Tel-Aviv University, Tel-Aviv, 1984.

Eri-91] T. E. O. Ericson, V. W. Hughes, and D. E. Nagle, *The Meson Factories*, University of California Press, Berkeley, 1991.

[Erw-61] A. R. Erwin, R. March, W. D. Walker, and E. West, Phys. Rev. Lett. **6**, 628 (1961).

[Est-75] P. Estabrooks and A. D. Martin, Nucl. Phys. **B95**, 322 (1975).

[Fau-84] J. A. Faucett, B. E. Wood, D. K. McDaniels, P. A. M. Gram, M. E. Hamm, M. A. Oothoudt, C. A. Goulding, L. W. Swenson, K. S. Krane, A. W. Stetz, H. S. Plendl, J. Norton, H. Funsten and D. Joyce, Phys. Rev. C **30**, 1622 (1984).

[Fer-62] E. Ferrari and F. Selleri, Suppl. Nuovo Cimento **24**, 453 (1962).

[Fes-85] H. Fesefeldt, *The Simulation of Hadronic Showers*, PITHA 85/02, Physikalisches Institut, Aachen, 1985.

[Fit-86] D. H. Fitzgerald, H. W. Baer, J. D. Bowman, M. D. Cooper, F. Irom, N. S. P. King, M. J. Leitch, E. Piasetsky, W. J. Briscoe, M. E. Sadler, K. J. Smith, and J. N. Knudson, Phys. Rev. C **34**, 619 (1986).

[Fro-69] C. D. Froggatt and D. Morgan, Phys. Rev. **187**, 2044 (1969).

[Fro-77] C. D. Froggatt and J. L. Peterson, Nucl. Phys. **B129**, 89, (1977).

[Fra-83] J. S. Frank, A. A. Browman, P. A. M. Gram, R. H. Heffner, K. A. Klare, R. E. Mischke, D. C. Moir, D. E. Nagle, J. M. Potter, R. P. Redwine, and M. A. Yates, Phys. Rev. D **28**, 1569 (1983).

[Fra-75] J. Franklin, Phys. Rev. D **11**, 513 (1975).

[Fri-64] G. Friendlander, J. W. Kennedy and J. M. Miller, *Nuclear and Radiochemistry*, 2nd Edition, John Wiley & Sons, New York, 1964.

[Frl-92a] E. Frlež, *PIANG_3B Computer Code and Notes*, unpublished, University of Virginia, Charlottesville, 1992.

[Frl-92b] E. Frlež, *PIANG_PAW Computer Code and Notes*, unpublished, University of Virginia, Charlottesville, 1992.

[Ful-73] R. L. Fulton, *Mechanical Design of the LAMPF Low-Energy Pion Channel*, LA-5222-MS, Informal Report UC 34 & 38, LAMPF, Los Alamos, 1973.

[Gai-84] F. C. Gaille, V. L. Highland, L. B. Auerbach, W. K. McFarlane, G. E. Hogan, C. M. Hoffman, R. J. Macek, R. E. Morgado, J. C. Pratt, and R. D. Werbeck, Phys Rev. D **30**, 2408 (1984).

[Gal-92] H. Galić, C. G. Wohl, B. Armstrong, D. C. Dodder, V. I. Klyukhin, Yu. G. Ryabov, N. S. Illarionova, F. Lehar, Y. Oyanagi, A. Olin, R. Frosch, *Current Experiments in Elementary Particle Physics*, LBL-91 revised, UC-414, (1992).

[Gas-83] J. Gasser and H. Leutwyler, Phys. Lett. **125B**, 321, 325, (1983).

[Gas-84] J. Gasser and H. Leutwyler, Ann. Phys. **158**, 142 (1984).

[Gas-85] J. Gasser and H. Leutwyler, Nucl. Phys. **B250**, 465, 517, 539 (1985).

[Gas-88] J. Gasser, M. E. Sainio, and A. Švarc, Nucl. Phys. **B307**, 779 (1988).

[Geo-84] H. Georgi, *Weak Interactions and Modern Particle Physics*, Benjamin/Cummings, Melno Park, 1984.

[Gil-77] S. Gilad, J. D. Bowman, M. D. Cooper, R. H. Heffner, C. M. Hoffman, M. A. Moinester, J. M. Potter, F. H. Cverna, H. W. Baer, P. R. Bevington, and M. W. McNaughton, Nucl. Inst. Meth. **144**, 103 (1977).

[Gil-79] S. Gilad, Ph. D. Thesis, unpublished, Tel-Aviv University, Tel-Aviv, 1979.

[Gil-84] S. Gilad, E. Piasetsky, W. J. Burger, G. W. Dodson, S. Høibråten, R. P. Redwine, H. W. Baer, J. D. Bowman, F. H. Cverna, M. J. Leitch, J. Alster, D. Ashery, J. Lichtenstadt, M. A. Moinester, S. A. Wood, Z. Fraenkel, R. Minehart, C. Smith, R. Whitney and G. S. Kyle, *Study of the* $^3He,^3H(\pi^+,\pi^0p)$ *Reactions by Detecting Neutral Pions and Protons in Coincidence*, LAMPF Proposal E921, unpublished, LAMPF, Los Alamos, 1984.

[Gil-86] S. Gilad, S. Høibråten, W. J. Burger, G. W. Dodson, L. D. Pham, R. P. Redwine, E. Piasetzky, H. W. Baer, J. D. Bowman, F. H. Cverna, M. J. Leitch, U. Sennhauser, Th. S. Bauer, C. H. Q. Ingram, G. S. Kyle, D. Ashery, S. A. Wood, and Z. Fraenkel, Phys. Rev. Lett. **57**, 2637 (1986).

[Ged-75] H. B. Geddes and R. H. Graham, Phys. Rev. D **12**, 855, (1975).

[Ged-76] H. B. Geddes and R. H. Graham, Phys. Rev. D **13**, 56, (1976).

[Gel-60] M. Gell-Mann and M. Lévy, Nuovo Cimento **16**, 53 (1960).

[Gel-62] M. Gell-Mann, Phys. Rev. **125**, 1067 (1962).

[Gel-64] M. Gell-Mann, Physics **1**, 63 (1964).

[Gel-68] M. Gell-Mann, R. J. Oakes, and B. Renner, Phys. Rev. **175**, 175 (1968).

[Goe-58] C. Goebel, Phys. Rev. Lett. **1**, 337 (1958).

[Gol-58] M. L. Goldberger and S. M. Treiman, Phys. Rev. **111**, 354 (1958).

[Gor-81] V. A. Gordeev, V. P. Koptev, S. P. Kruglov, L. A. Kuz'min, A. A. Kulbardis, Yu. A. Malev, S. M. Mikirtich'yants, I. I. Strakovsky, and G. V. Scherbakov, Nucl. Phys. **A364**, 408 (1981).

[Gor-70] M. Gormley, E. Hayman, W. Lee, T. Nash, J. Peoples, C. Schultz, and S. Stein, Phys. Rev. D **2**, 501 (1970).

[Gre-87] L. G. Greeniaus, *TRIUMF Kinematics Handbook*, 2nd Edition, TRIUMF, Vancouver, 1987.

[Gun-77] J. F. Gunion, P. C. McNamee, and M. D. Scadron, Nucl. Phys. **B123**, 445 (1977).

[Gri-89] N. Grion, R. Rui, F. M. Rozon, M. Hanna, R. R. Johnson, J. McAlister, R. Olszewski, C. Ponting, M. E. Sevior, V. Sossi, D. R. Gill, G. Sheffer, M. J. Vicente-Vacas, and E. Oset, Nucl. Phys. **A492**, 509 (1989).

[Gut-69a] L. J. Gutay, F. T. Meiere, D. D. Carmony, F. J. Loeffler, and P. L. Csonka, Nucl. Phys. **B12**, 31 (1969).

[Gut-69b] L. J. Gutay, F. T. Meiere, and J. H. Scharenguivel, Phys. Rev. Lett. **23**, 431 (1969).

[Hag-66] V. Hagopian, W. Selove, J. Alitti, J. P. Baton, and M. Neveu-René, Phys. Rev. **154**, 1128 (1966).

[Hag-73] S. Hagopian, V. Hagopian, J. D. Kimel, and N. D. Pewitt, Phys. Rev. D **7**, 1271 (1973).

[Hel-87] L. Heller, S. Kumano, J. C. Martinez, and E. J. Moniz, Phys. Rev. C **35**, 718, (1987).

[Her-75a] D. J. Herndon and P. Söding, Phys. Rev. D **11**, 3165 (1975).

[Her-75b] D. J. Herndon, R. Longacre, L. R. Miller, A. H. Rosenfeld, G. Smadja, P. Söding, R. J. Cashmore, and D. W. G. S. Leith, Phys. Rev. D **11**, 3183 (1975).

[Her-90] J. J. Hernández, J. Stone, F. C. Porter, R. J. Morrison, L. Montanet, K. Gieselmann, M. Aguilar-Benitez, G. Comforto, C. Caso, M. Roos, N. A. Törnqvist, K. G. Hayes, K. R. Schubert, G. Höhler, K. Hagiwara, K. Hikasa, S. Kawabata, R. M. Barnett, J. J. Eastman, D. E. Groom, G. R. Lynch, A. Rittenberg, M. Suzuki, T. G. Trippe, C. G. Wohl, G. P. Yost, B. Armstrong, G. S. Wagman, K. A. Olive, R. E. Shrock, R. H. Schindler, and R. A. Eichler, *Review of Particle Properties*, Phys. Lett. **239B** (1990).

[Heu-74] C. A. Heusch, R. V. Kline, and S. J. Yellin, Nucl. Inst. and Meth. **120**, 237 (1974).

[Hil-70] H. Hilsher, W.-D. Krebs, G. Sepp and V. Soergel, Nucl. Phys. **A158**, 602 (1970).

[Hoe-82] M. V. Hoehn and D. H. Fitzgerald, LAMPF Report No. A82-01, LAMPF, Los Alamos, 1982.

[Høib-85] S. Høibråten, Ph. D. Thesis, unpublished, Los Alamos, 1985.

[Hoo-77] W. Hoogland, S. Peters, G. Grayer, B. Hyams, P. Weilhammer, W. Blum, H. Dietl, G. Hentschel, W. Koch, E. Lorenz, G. Lïjens, G. Lutz, W. Männer, B. Richter, and U. Stierlin, Nucl. Phys. **B126**, 109 (1977).

[How-87] H. Howard, *LAMPF User's Handbook*, MP-DO-1-UHB, 3rd revision, LAMPF, Los Alamos, 1987.

[Hub-69] J. H. Hubbell, *Photon Cross Sections, Attenuation Coefficients, and Energy Absorption Coefficients from 10 keV to 100 GeV*, NSRDS-NBS **29** (969).

[Hum-86] S. Humphries, *Principles of Charged Particle Acceleration*, John Wiley & Sons, New York, 1986.

[Hum-90] S. Humphries, *Charged Particle Beams*, John Wiley & Sons, New York, 1990.

[Ing-83] C. H. Q. Ingram, P. A. M. Gram, J. Jansen, R. E. Mischke, J. Zichy, J. Bolger, E. T. Boschitz, G. Pröbstle and J. Arvieux, Phys. Rev. C **27**, 1578 (1983).

[Iro-83] F. Irom, J. R. Comfort, R. Jeppesen, J. J. Kraushaar, R. A. Ristinen, W. Tew, J. L. Ullmann, H. W. Baer, J. D. Bowman, M. D. Cooper, E. Piasetsky, U. Sennhauser, A. Erell, M. A. Moinester and E. R. Siciliano, Phys. Rev. C **28**, 2565 (1983).

[Iro-85] F. Irom, J. D. Bowman, H. W. Baer, E. Piasetzky, and J. Alster, unpublished, LAMPF, Los Alamos, 1985.

[Iva-86] A. N. Ivanov and N. I. Troitskaya, Sov. J. Nucl. Phys. **43**, 260 (1986).

[Jac-64] J. D. Jackson, Nuovo Cimento **34**, 1644 (1964).

[Jac-82] R. J. Jacob and M. D. Scadron, Phys. Rev. D **25**, 3073 (1982).

[Jäk-90] O. Jäkel, H.-W. Ortner, M. Dillig, and C. A. Z. Vasconcellos, Nucl. Phys. **A511**, 733 (1990).

[Jam-89a] F. James and M. Roos, *MINUIT—Function Minimization and Error Analysis*, CERN D506, Geneva, 1989.

[Jam-89b] F. James, in *CERN Computer Center Program Library W515*, edited by G. Benassi (CERN, Geneva, 1989).

[Jam-89c] F. James, in *CERN Computer Center Program Library V150*, edited by G. Benassi (CERN, Geneva, 1989).

[Jan-82] J. F. Janni, *Atomic Data and Nuclear Data Tables* **27**, 150 (1982).

[Joh-80] M. K. Johnson, Phys. Rev. C **22**, 192 (1980).

[Jon-74] J. A. Jones, W. W. A. Allison, and D. H. Saxon, Nucl. Phys. **B83**, 93 (1974).

[Käl-83] G. Kälbermann and J. M. Eisenberg, Phys. Rev. D **28**, 66 (1983).

[Käl-64] G. Källén, *Elementary Particle Physics*, Addison-Wesley, Reading, 1964.

[Kan-67] G. L. Kane, Phys. Rev. **163**, 163 (1967).

[Kan-69] G. L. Kane and M. Ross, Phys. Rev. **177**, 2353 (1969).

[Kar-77] A. A. Kartamyshev, V. K. Makar'in, K. N. Mukhin, O. O. Patarakin, M. M. Sulkovskaya, and A. F. Sustavov, JETP Lett. **26**, 296 (1977).

[Ker-83] G. Kernel, P. Križan, M. Mikuž, A. Stanovnik, D. Zavrtnik, C. Engster, E. G. Michaelis, A. G. Zaphat, J. Harvey, and K. O. H. Ziock, Nucl. Instr. and Meth. **214**, 273 (1983).

[Ker-86a] G. Kernel, in *Proceedings of the Fifth Course of the International School of Intermediary Energy Nuclear Physics*, Verona, 1986, edited by R. Bergere, S. Costa and C. Schaerf (World Scientific, Singapore, 1986).

[Ker-86b] G. Kernel, D. Korbar, P. Križan, M. Mikuž, F. Sever, A. Stanovnik, M. Starič, D. Zavrtanik, C. W. E. van Eijk, R. W. Hollander, W. Lourens, S. A. Clark, J. D.

Davies, N. W. Tanner, E. G. Michaelis, S. M. Playfer, J. Lowe, and J. V. Jovanovich, Nucl. Instr. and Meth. **A244**, 367 (1986).

[Ker-89a] G. Kernel, D. Korbar, P. Križan, M. Mikuž, U. Seljak, F. Sever, A. Stanovnik, M. Starić, D. Zavrtanik, C. W. E. van Eijk, R. W. Hollander, W. Lourens, E. G. Michaelis, N. W. Tanner, S. A. Clark, J. V. Jovanovich, J. D. Davies, J. Lowe, and S. M. Playfer, Phys. Lett. **216B**, 244 (1989).

[Ker-89b] G. Kernel, D. Korbar, P. Križan, M. Mikuž, U. Seljak, F. Sever, A. Stanovnik, M. Starić, D. Zavrtanik, C. W. E. van Eijk, R. W. Hollander, W. Lourens, E. G. Michaelis, N. W. Tanner, S. A. Clark, J. V. Jovanovich, J. D. Davies, J. Lowe, and S. M. Playfer, Phys. Lett. **225B**, 198 (1989).

[Ker-90] G. Kernel, D. Korbar, P. Križan, M. Mikuž, U. Seljak, F. Sever, A. Stanovnik, M. Starić, D. Zavrtanik, C. W. E. van Eijk, R. W. Hollander, W. Lourens, E. G. Michaelis, N. W. Tanner, S. A. Clark, J. V. Jovanovich, J. D. Davis, J. Lowe, and S. M. Playfer, Z. Phys. C **48**, 201 (1990).

[Ker-91a] G. Kernel, D. Korbar, P. Križan, M. Mikuž, U. Seljak, F. Sever, A. Stanovnik, M. Starić, D. Zavrtanik, E. G. Michaelis, N. W. Tanner, C. W. E. van Eijk, R. W. Hollander, W. Lourens, S. A. Clark, J. D. Davis, J. Lowe, S. M. Playfer, and J. V. Jovanovich, Z. Phys. C **51**, 377 (1991).

[Ker-91b] G. Kernel, D. Korbar, P. Križan, M. Mikuž, U. Seljak, F. Sever, A. Stanovnik, M. Starić, D. Zavrtanik, E. G. Michaelis, N. W. Tanner, C. W. E. van Eijk, R. W. Hollander, W. Lourens, S. A. Clark, J. D. Davis, J. Lowe, S. M. Playfer, and J. V. Jovanovich, in *Particle Production Near Threshold*, Nashville, 1990, edited by H. Nann and E. J. Stephenson (American Institute of Physics, New York,1991).

[Kin-90] B. H. King, W. J. Cummings, G. E. Dodge, S. S. Hanna, S. Kuhn, K. Assamagan, E. Frlež, K. Keeter, D. Počanić, LAMPF Experiment E1181 Logbook, unpublished, LAMPF, Los Alamos, 1990.

[Kir-62] J. Kirz, J. Schwartz, and R. D. Tripp, Phys. Rev. **126**, 763 (1962).

[Kir-63] J. Kirz, J. Schwartz, and R. D. Tripp, Phys. Rev. **130**, 2481, (1963).

[Kle-92] S. P. Klevansky, Rev. Mod. Phys. **64**, 649 (1992).

[Kli-78] F. J. Kline and E. Hayward, Phys. Rev. **17**, 1531 (1978).

[Kno-89] G. F. Knoll, *Radiation Detection and Measurement*, 2nd Edition, John Wiley & Sons, New York, 1989.

[Knu-86] J. N. Knudson, *The PI0 Spectrometer Data Acquisition System*, MP-1-3408-2, LAMPF, Los Alamos, 1986.

[Knu-89] J. N. Knudson, *The PI0 Spectrometer Electronics Diagrams*, unpublished, LAMPF, Los Alamos, 1989.

[Koz-89] T. Kozlowski and M. A. Oothourt, *Q—Programmer's Information Manual*, MP-1-3401-5, LAMPF, Los Alamos, 1989.

[Kra-74] A. V. Kravtsov, A. V. Kuptsov, L. L. Nemenov, E. A. Starchenko, and D. M. Khazins, Sov. J. Nucl. Phys. **20**, 500 (1974).

[Kra-78] A. V. Kravtsov, E. A. Lobachev, M. M. Makarov, V. I. Medvedov, V. V. Nelyubin, G. Z. Obrant, V. I. Pomorov, V. V. Sarantsev, S. G. Sherman, V. M. Sirin, G. L. Sokolov, and L. N. Tkack, Nucl. Phys. **B134**, 413 (1978).

[Kri-71] S. Krinsky, Phys. Rev. D **4**, 1046 (1971).

[Kri-86] P. Križan, G. Kernel, and F. Sever, Nucl. Instr. and Meth. **A248**, 451 (1986).

[Kri-87] P. Križan, Ph. D. Thesis, unpublished, University of Ljubljana, Ljubljana, 1987.

[Koc-80] R. Koch and E. Pietarinen, Nucl. Phys. **A336**, 331 (1980).

[Kuh-72] G. Kuhl and U. Kneissl, Nucl. Phys. **A195**, 559 (1972).

[Küh-71] H. Kühnelt, Z. Phys. **246**, 447 (1971).

[Kyl-84] G. S. Kyle, P.-A. Amaudruz, Th. S. Bauer, J. J. Domingo, C. H. Q. Ingram, J. Jansen, D. Renkar, J. Zichy, R. Stamminger, and F. Volger, Phys. Rev. Lett. **52**, 974 (1984).

[LeC-91] *LeCroy 1992 Research Instrumentation Catalog*, LeCroy Corporation, Chestnut Ridge, 1991.

[Lee-72] B. W. Lee, *Chiral Dynamics*, Gordon and Breach, New York, 1972.

[Lei-86] M. J. Leitch, H. W. Baer, J. D. Bowman, M. D. Cooper, E. Piasetsky, U. Sennhauser, H. J. Ziock, F. Irom, P. B. Siegel and M. A. Moinester, Phys. Rev. C **33**, 278 (1986).

[Lei-84] M. J. Leitch, B. J. Dropesky, A. Cui, D. Fitzgerald, G. C. Giesler, J. A. McGill, C. J. Orth, and L. E. Ussery, *Measurement of Low Energy Cross Sections for the* $^{12}C(\pi^{\pm},\pi N)^{11}C$ *Reactions*, LAMPF Proposal E942, unpublished, LAMPF, Los Alamos, 1984.

[Lei-90] M.J. Leitch, private communication, 1990.

[Les-71] G. A. Leskin, Sov. Phys. Usp. **13**, 704 (1971).

[Lio-77] M. K. Liou and W. T. Nutt, Phys. Rev. D **16**, 2176, (1977).

[Lon-70] W. F. Long and J. S. Kovacs, Phys. Rev. D **1**, 1333 (1970).

[Low-91a] J. Lowe, N. W. Tanner, J. P. Miller, B. L. Roberts, M. D. Hasinoff, A. J. Noble, M. Sevior, C. E. Waltham, M. Sakitt, W. J. Fickinger, D. K. Robinson, D. Horvath, B. Bassalleck, J. R. Hall, K. D. Larson, and D. M. Wolfe, BNL 34518, Brookhaven, 1989.

[Low-91b] J. Lowe, B. Bassalleck, H. Burkhardt, W. J. Fickinger, J. R. Hall, M. D. Hasinoff, D. Horvath, G. Koch, K. D. Larson, J. P. Miller, A. J. Noble, B. L. Roberts, D. K. Robinson, M. Sakitt, M. E. Sevior, N. W. Tanner, C. E. Walthman, T. M. Warner, and D. M. Wolfe, Phys. Rev. C **44**, 956 (1991).

[Lyb-84] M. Lybanon, Am. J. Phys. **52**, 276 (1984).

[Mad-78] R. Madey, F. M. Waterman, A. R. Baldwin, J. N. Knudson, J. D. Carlson, and J. Rapaport, Nucl. Instr. and Meth. **151**, 445 (1978).

[Man-81] D. M. Manley, Ph. D. Thesis, unpublished, VPI and State University, Blacksburg, 1981.

[Man-84] D. M. Manley, Phys. Rev. D **30**, 536 (1984).

[Mar-85] R. M. Marshall and K. O. H. Ziock, *RANGER Computer Code*, unpublished, University of Virginia, Charlottesville, 1985.

[Mar-73] B. R. Martin, D. Morgan, and G. Shaw, *Pion-Pion Interaction in Particle Physics*, Academic Press, New York, 1976.

[Mar-78] A. D. Martin and M. R. Pennington, Ann. Phys. **114**, 1 (1978).

[McF-85] W. K. McFarlane, L. B. Auerbach, F. C. Gaille, V. L. Highland, E. Jastrzembski, R. J. Macek, F. H. Cverna, C. M. Hoffman, G. E. Hogan, R. E. Morgado, J. C. Pratt, and R. D. Werbeck, Phys. Rev. D **32**, 547 (1985).

[Mea-69a] D. F. Measday and C. Richard-Serre, Nucl. Instr. and Meth. **76**, 45 (1969).

[Mea-69b] D. F. Measday and C. Richard-Serre, *Loss of Protons by Nuclear Interactions in Various Materials*, CERN 69-17, Geneva, (1969).

[Mey-88] C. A. Meyer, C. Amsler, A. Bosshard, K. M. Crowe, M. Döbeli, M. Doser, L. van Elmbt, R. P. Haddock, Q. Ingram, S. Ljungfelt, J. F. Loude, J. P. Perroud, J. Riedlberger, D. Renker, M. Schaad, D. I. Sober, and P. Truöl, Phys. Rev. D **38**, 754, (1988).

[Mei-91] U.-G. Meissner, Comments Nucl. Part. Phys. **20**, 119 (1991).

[Mid-73] A. B. Midgal, Nucl. Phys. **A210**, 421 (1973).

[Miy-62] K. Miyake, K. F. Kinsey, and D. E. Knapp, Phys. Rev. **126**, 2188 (1962).

[Mon-82] E. J. Moniz, Nucl. Phys. **a374**, 557c, (1982).

[Mor-70] D. Morgan, Phys. Rev. D **2**, 520 (1970).

[Mor-73] D. Morgan and J. Pišút, Springer Tracts in Modern Physics **55**, 1 (1973).

[Muh-81] K. N. Mukhin and O. O. Patarakin, Sov. Phys. Usp. **24**, 161 (1981).

[Nag-67] D. E. Nagle, E. A. Knapp, and B. C. Knapp, Rev. Sci. Instrum. **38**, 1583 (1967).

[Nam-60] Y. Nambu, Phys. Rev. **4**, 380 (1960).

[Nam-62] Y. Nambu and Lurié, Phys. Rev. **125**, 1429 (1962).

[Neg-81] J. W. Negele and K. Yazaki, Phys. Rev. Lett. **47**, 71 (1981).

[Nov-88] J. Novak, *Cryogenic Targets Coooled by a 10 Watt Closed-Cycle Refrigerator*, unpublished, LAMPF, Los Alamos, 1988.

[Nov-91] J. Novak and N. C. Hoffman, Experiment 1179 Refrigerated Liquid Hydrogen Target, SOP 153, unpublished, Los Alamos, 1991.

[New-63] P. C. A. Newcomb, Phys. Rev. **132**, 1283 (1963).

[Nyb-66] P. Nyborg, Am. J. Phys. **34** 932 (1966).

[Nyb-70] P. Nyborg, Nuovo Cimento, **65A**, 544 (1970).

[Ols-66a] M. G. Olsson and G. B. Yodh, Phys. Rev. **145**, 1309 (1966).

[Ols-66b] M. G. Olsson and G. B. Yodh, Phys. Rev. **145**, 1327 (1966).

[Ols-68] M. G. Olsson and L. Turner, Phys. Rev. Lett. **20**, 1127 (1968).

[Ols-69] M. G. Olsson and L. Turner, Phys. Rev. **181**, 2141 (1969).

[Ols-72] M. G. Olsson and L. Turner, Phys. Rev. D **6**, 3522 (1972).

[Ols-77a] M. G. Olsson, E. T. Osypowski, and L. Turner, Phys. Rev. Lett. **38**, 296 (1977).

[Ols-77b] M. G. Olsson, E. T. Osypowski, and L. Turner, Phys. Rev. Lett. **39**, 52 (1977).

[Oot-85] M. A. Oothourt, *A Guide to Writing an RSX-11M or VMS Q Analyzer*, MP-1-3417-1, LAMPF, Los Alamos, 1985.

[Oot-89] M. A. Oothourt, *Histogram Support System for VMS*, MP-1-3403-4, LAMPF, Los Alamos, 1989.

[Ore-82] J. Orear, Am. J. Phys. **50**, 912 (1982).

[Ore-84] J. Orear, Am. J. Phys. **52**, 278 (1984).

[Ort-78] C. J. Orth, M. W. Johnson, J. D. Knight, and K. Wolfsberg, *Fast Muon Reactions with* ^{12}C, ^{48}Ti *and* ^{58}Ni, LAMPF Proposal E331, unpublished, LAMPF, Los Alamos, 1978.

[Ort-90] H.-W. Ortner, R. Baran, U. Bohnert, M. Dillig, G. Herrmann, A. Hofmann, P. Helbig, O. Jäkel, W. Kluge, H. Krüger, D. Malz, H. Matthäy, R. Müller, W. Menzel, L. Schweinzer, and S. Wirth, Phys. Rev. Lett. **64**, 2759 (1990).

[Ort-93] H.-W. Ortner, U. Bohnert, M. Dillig, D. Malz, and R. Müller, Phys. Rev. C **47**, 447 (1993).

[Ose-86] E. Oset and M. J. Vincente-Vacas, Nucl. Phys. **A454**, 637 (1986).

[Pag-75] H. Pagels, Phys. Rep. **16**, 219 (1975).

[Pas-78] P. Pascual and R. Tarrach, Nucl. Phys. **B134**, 133, (1978).

[Per-60] W. A. Perkins III, J. C. Caris, R. W. Kenney, and V. Perez-Mendez, Phys. Rev. **118**, 1364 (1960).

[Pen-71] M. R. Pennington and P. Pond, Nuovo Cimento **3A**, 548 (1971).

[Pen-72] M. R. Pennington and S. D. Protopopescu, Phys. Lett. **40B**, 105 (1972).

[Pen-73] M. R. Pennington and S. D. Protopopescu, Phys. Rev. D **7**, 1429 (1973).

[Pet-71] J. L. Peterson, Phys. Rep. **C2**, 155 (1971).

[Pet-77] J. L. Peterson, *The $\pi\pi$ Interaction*, CERN 77-04, Geneva, 1977.

[Pia-82a] E. Piasetsky, A. Altman, J. Lichtenstadt, A. I. Yavin, D. Ashery, W. Bertl, L. Felawka, H. K. Walter, F. W. Schlepütz, R. J. Powers, R. G. Winter and J. v. d. Pluym, Phys. Rev. C **26**, 2702 (1982).

[Pia-82b] E. Piasetsky, R. L. Burman, N. J. DiGiacomo, R. M. DeVries, W. E. Sondheim, J. W. Sunier, J. Lichtenstadt, J. Alster, D. Ashery and Z. Fraenkel, *Pion Production in Pion-Nucleus Collisions*, LAMPF proposal E784, unpublished, LAMPF, Los Alamos, 1982.

[Pia-84] E. Piasetzky, P. A. M. Gram, D. W. MacArthur, G. A. Rebka, C. A. Bordner, S. Høibråten, E. R. Kinney, J. L. Matthews, S. A. Wood, D. Ashery, and J. Lichtenstadt, Phys. Rev. Lett. **53**, 540 (1984).

[Pic-61] E. Pickup, D. K. Robinson, and E. O. Salant, Phys. Rev. Lett. **7**, 192 (1961).

[Pic-62] E. Pickup, D. K. Robinson, and E. O. Salant, Phys. Rev. Lett. **9**, 170 (1962).

[Pil-79] H. M. Pilkuhn, *Relativistic Particle Physics*, Springer-Verlag, New York, 1979.

[Piš-73] J. Pišút, Springer Tracts in Modern Physics **55**, 43 (1973).

[Poč-89] D. Počanić, D. Day, E. Frlež, R. M. Marshall, J. S. McCarthy, R. C. Minehart, L. C. Smith, K. O. H. Ziock, W. J. Cummings, G. E. Dodge, S. S. Hanna, B. H. King, S. E. Kuhn, J. D. Bowman, and J. N. Knudson, *Reaction $\pi^+p \to \pi^+\pi^0p$ Near Threshold*, LAMPF Proposal E1179, unpublished, LAMPF, Los Alamos, 1989.

[Poč-91] D. Počanić, K. A. Assamagan, D. Day, E. Frlež, K. J. Keeter, R. M. Marshall, J. S. McCarthy, R. C. Minehart, L. C. Smith, B. K. Wright, K. O. H. Ziock, W. J. Cummings, G. E. Dodge, S. S. Hanna, B. H. King, S. E. Kuhn, J. D. Bowman, J, N. Knudson, M. Furić, T. Petković, and N. Šimičević, *Reaction $\pi^+p \to \pi^+\pi^0p$ Near Threshold*, LAMPF E1179 Progress Report, unpublished, LAMPF, Los Alamos, 1991.

[Poi-66] C. P. Poirier, C. A. Tilger, E. D. Alyea, Jr., H. J. Martin, Jr., and J. H. Scandrett, Phys. Rev. **143**, 1092 (1966).

[Pra-90a] M. Praszałowicz, Ph. D. Thesis, unpublished, Jagellonian University, Kraków, 1991.

[Pra-90b] M. Praszałowicz and G. Valencia, Nucl. Phys. **B341**, 27 (1990).

[Pre-81] B. M. Preedom, S. H. Dam, C. W. Darden III, R. D. Edge, D. J. Malbrough, T. Marks, R. L. Burman, M. Hamm, M. A. Moinester, R. P. Redwine, M. A. Yates, F.

E. Bertrand, T. P. Cleary, E. E. Gross, N. W. Hill, C. A. Ludemann, M. Blecher, K. Gotow, D. Jenkins, and F. Milder, Phys. Rev. C **23**, 1134 (1981).

[Pre-86] W. H. Press, B. P. Flannery, S. A. Teukolsky, and W. T. Vetterling, *Numerical Recipes—The Art of Scientific Computing*, Cambridge University Press, Cambridge, 1986.

[Pre-92] W. H. Press and S. A. Teuklosky, Comp. in Physics, **6**, 82 (1992).

[Pre-71] P. Prešnajder and J. Pišut, Nuovo Cimento **3A**, 603 (1971).

[Pro-73] S. D. Protopopescu, M. Alston-Garnjost, A. Barbaro-Galtieri, S. M. Flatté, J. H. Friedman, T. A. Lasinski, G. G. Lynch, M. S. Rabin, and F. T. Solmitz, Phys. Rev. D **7**, 1279 (1973).

[Pru-74] J. P. Prukop, O. R. Sander, J. A. Poirier, C. A. Rey, A. J. Lennox, B. C. J. Chen, N. N. Biswas, N. M. Carson, V. P. Kenney, and W. D. Shephard, Phys. Rev. D **10**, 2055, (1974).

[Pup-63] G. Puppi, Ann. Rev. Nucl. Sci. **13**, 287 (1963).

[Ray-87] G. Rayna, *REDUCE—Software for Algebraic Computation*, Springer-Verlag, New York, 1987.

[Rey-74] E. Reya, Rev. Mod. Phys. **46**, 545 (1974).

[Rho-81] M. Rho and G. E. Brown, Comments Nucl. Part. Phys. **10**, 201 (1981).

[Roc-75] R. M. Rockmore, Phys. Rev. C **11**, 1953 (1975).

[Roc-83] R. M. Rockmore, Phys. Rev. C **27**, 2150 (1983).

[Roc-84] R. M. Rockmore, Phys. Rev. C **29**, 1534 (1984).

[Rok-87] S. H. Rokni, Ph. D. Thesis, unpublished, Los Alamos, 1987.

[Ros-69] L. Rosen, Science Journal **5A**, 2 (1969).

[Ros-77] L. Rosselet, P. Extermann, J. Fischer, O. Guisan, R. Mermod, R. Sachot, A. M. Diamant-Berger, P. Bloch, G. Bunce, B. Devaux, N. Do-Duc, G. Marel, and R. Turlay, Phys. Rev. D **3**, 574, (1977).

[Roy-71] S. M. Roy, Phys. Lett. **36B**, 353 (1971).

[Sad-87] M. E. Sadler, W. J. Briscoe, D. H. Fitzgerald, B. M. K. Nefkens, and C. J. Seftor, Phys. Rev. D **35**, 2718 (1987).

[Sad-90] M. E. Sadler, LAMPF Experiment 882, private communication, 1990.

[Sag-81] B. Saghai, B. M. Preedom, B. J. Dropesky, B. Sachai, G. Fournier, P. Vernin, C. Samour, P. Bertin, R. P. Redwine and G. C. Giesler, *Pion Production in Pion-Nucleon and Pion-Nucleus*, LAMPF Proposal E730, unpublished, LAMPF, Los Alamos, 1981.

[Sal-84] M. Salamon, D. F. Measday, and J-M. Poutissou, Nucl. Phys. **A414**, 493 (1984).

[Sax-70] D. H. Saxon, J. H. Mulvey, and W. Chinowsky, Phys. Rev. **D2**, 1790 (1970).

[Sca-81] M. D. Scadron, Rep. Prog. Phys. **44**, 213 (1981).

[Sch-69] J. H. Scharenguivel, L. J. Gutay, D. H. Miller, L. D. Jacobs, R. Keyser, D. Huwe, E. Marquit, F. Oppenheimer, W. Schultz, S. Marateck, J. D. Prentice, and E. West, Phys. Rev. **186**, 1387 (1969).

[Sch-70] J. H. Scharenguivel, L. J. Gutay, D. H. Miller, R. L. McIlwain, F. T. Meiere, D. Morgan, L. D. Jacobs, S. Marateck, C. D. Froggatt, D. Huwe, and E. Marquit, Phys. Rev. Lett. **24**, 332 (1970).

[Sch-75] *SCHOTT Optical Glass Catalog*, Mainz, Germany (1975).

[Sch-67] J. Schwinger, Phys. Lett. **24B**, 473 (1967).

[Sch-77] J. Schwinger, in *Proceedings of the 7th Hawaii Topical Conference on Particle Physics*, Honolulu, Hawaii, 1977, edited by R. J. Cence, P. N. Dobson, Jr., S. Pakvasa, S. F. Tuan (The University Press of Hawaii, Manoa/Honolulu, 1977).

[Sen-83] U. Sennhauser, E. Piasetsky, H. W. Baer, J. D. Bowman, M. D. Cooper, H. S. Matis, H. J. Ziock, J. Alster, A. Erell, M. A. Mionester and F. Irom, Phys. Rev. Lett. **51**, 1324 (1983).

[Sev-91a] M. E. Sevior, A. Ambadar, J. T. Brack, P. Camerini, F. Duncan, J. Ernst, A. Feltham, N. Grion, R. R. Johnson, G. Koch, O. Meirav, D. F. Ottewell, R. Rui, G. R. Smith, V. Sossi, D. Theis, and D. Vetterli, Phys. Rev. Lett. **66**, 2569 (1991).

[Sev-91b] M. E. Sevior, Nucl. Phys. **A527**, 425c (1991).

[Shi-70] E. I. Shibata, D. H. Frisch, and M. A. Wahlig, Phys. Rev. Lett. **25**, 1227 (1970).

[Siv-90] D. S. Sivia, Los Alamos Science, Summer 1990, 180, (1990).

[Ski-84] J. Skilling and R. K. Bryan, Mon. Not. R. Astr. Soc. **211**, 111, (1984).

[Sob-75] D. I. Sober, M. Arman, D. J. Blasberg, R. P. Haddock, K. C. Leung, B. M. K. Nefkens, B. L. Schrock, and J. M. Sperinde, Phys. Rev. D **11**, 1017 (1975).

[Sob-79] D. I. Sober, Nucl. Instr. and Meth. **166**, 555 (1979).

[Sou-77] A. M. Sourkes, M. S. de Jong, C. A. Goulding, W. T. H. van Oers, E. A. Ginkel, R. F. Carlson, A. J. Cox, and D. J. Margaziotis, Nucl. Instr. Meth. **143**, 589 (1977).

[Thé-80] S. Théberge, A. W. Thomas, and G. A. Miller, Phys. Rev. D **22**, 2838 (1980).

[Tre-62] S. B. Treiman and C. N. Yang, Phys. Rev. Lett. **8**, 140 (1962).

[Tur-69] L. Turner, Ph. D. Thesis, unpublished, University of Wisconsin, Madison, 1969.

[Ull-86] J. L. Ullmann, P. W. F. Alons, J. J. Kraushaar, J. H. Mitchell, R. J. Peterson, R. A. Ristinen, J. N. Knudson, J. R. Comfort, H. W. Baer, J. D. Bowman, D. M. Cooper,

D. H. Fitzgerald, F. Irom, M. J. Leitch, and E. Piasetzky, Phys. Rev. C **33**, 2092 (1986).

[Vie-87] D. J. Viera, *Operating Instructions for Counter 49*, unpublished, LAMPF, Los Alamos, 1987.

[Wan-71] G. Wanders, Springer Tracts in Modern Physics **57**, 22 (1971).

[Wei-66a] S. Weinberg, Phys. Rev. Lett. **16**, 879 (1966).

[Wei-66b] S. Weinberg, Phys. Rev. Lett. **17**, 616 (1966).

[Wei-67] S. Weinberg, Phys. Rev. Lett. **18**, 188 (1967).

[Wei-68] S. Weinberg, Phys. Rev. **166**, 1568 (1968).

[Wei-70] S. Weinberg, in *Lectures on Elementary Particles and Quantum Field Theory*, 1970 Brandeis University Summer Institute in Theoretical Physics, Volume I, 1970, edited by S. Deser, M. Grisaru, and H. Pendleton (The M.I.T. Press, Cambridge/Massachusetts 1970).

[Wei-79] S. Weinberg, Physica **96A**, 327 (1979).

[Wei-91] S. Weinberg, Nucl. Phys. **B363**, 3 (1991).

[Wil-70] P. K. Williams, Phys. Rev. D **1**, 1312 (1970).

[Wil-59] W. J. Willis, Phys. Rev. **113**, 753 (1959).

[Wan-66] G. Wanders, Helv. Phys. Acta **39**, 228 (1966).

[Wil-59] W. J. Willis, Phys. Rev. **116**, 753 (1959).

[Wil-88] S. L. Wilson, R. Hofstadter, E. B. Hughes, Y. C. Lin, R. Parks, M. W. Ritter, J. Rolfe, R. D. Bolton, J. D. Bowman, M. D. Cooper, J. S. Frank, A. L. Hallin, P. Heusi, C. M. Hoffman, G. E. Hogan, F. G. Mariam, H. S. Matis, R. E. Mischke, D. E. Nagle, L. E. Piilonen, V. D. Sandberg, G. H. Sanders, U. Sennhauser, R. Werbeck, R. A. Williams, D. P. Grosnick, S. C. Wright, and J. McDonough, Nucl. Instr. and Meth. **A264**, 263 (1988).

[Win-87] J. R. Winkelman, M. S. Thesis, unpublished, University of Virginia, Charlottesville, 1987.

[Wri-89] B. Wright, *OPTICS Programs*, unpublished, University of Virginia, Charlottesville, 1989.

[You-60] D. E. Young and L. H. Johnston, Phys. Rev. **119**, 313 (1960).

[Zav-84] G. Zavrtanik, F. Sever, M. Pleško, M. Mušič, G. Kernel, N. W. Tanner, E. G. Michaelis, and A. Stanovnik, Nucl. Instr. and Meth. **227**, 237 (1984).

[Zio-85] K. O. H. Ziock and R. M. Marshall *PSTOP Computer Code*, unpublished, University of Virginia, Charlottesville, 1985.

*U.S. GOVERNMENT PRINTING OFFICE 1993-0-573-024/87051

DATE
FILMED

2/3/94

END